PROCEEDINGS BOOK OF THE 2ND INTERCONTINENTAL GEOINFORMATION DAYS

05 - 06 MAY 2021
MERSİN, TURKEY

MERSIN UNIVERSITY - ENGINEERING FACULTY
DEPARTMENT OF GEOMATICS ENGINEERING

IGD
Intercontinental Geoinformation Days

ISBN: 978-625-44303-2-9 | http://igd.mersin.edu.tr/2020/

The proceedings of the

2nd Intercontinental Geoinformation Days

Editor-in-Chief

Prof. Dr. Murat YAKAR

Editors

Prof. Dr. İsmail ŞANLIOĞLU

Assoc. Prof. Dr. Erdinç AVAROĞLU

Asst. Prof. Dr. Muzaffer Can İBAN

Asst. Prof. Dr. Ali ULVİ

Asst. Prof. Dr. Osman ORHAN

Asst. Prof. Dr. Lütfiye KUŞAK

Asst. Prof. Dr. Fatma BÜNYAN ÜNEL

Res. Asst. Aydın ALPTEKİN

Res. Asst. Abdurahman Yasin YİĞİT

Res. Asst. Mehmet Özgür ÇELİK

Eng. Engin KANUN

ISBN: 978-625-44303-2-9

Mersin, 2021

HONOR BOARD

Ali İhsan SU - Governor of Mersin Province
Prof. Dr. Ahmet ÇAMSARI - Rector of Mersin University
Prof. Dr. Orhan AYDIN - Rector of Tarsus University
Mehmet Zeki ADLI – Director of Turkish Land Registry and Cadastre
Prof. Dr. Rudolf STAIGER - FIG President
Prof. Dr. Christian HEIPKE - ISPRS President
Prof. Dr. Chryssy POTSIOU - FIG President (2015-2018)
Prof. Dr. Haluk ÖZENER – Boğaziçi University Director of Kandilli Observatory
Dr. Orhan ERCAN - FIG Vice President

EXECUTIVE COMMITTEE

Prof. Dr. Abdurrahman EYMEN – Erciyes University, TURKEY
Prof. Dr. Alexander SAGAYDAK – State University of Land Use Planning, RUSSIA
Prof. Dr. Alias Abdul RAHMAN – Universiti Teknologi Malaysia (UTM), MALAYSIA
Prof. Dr. Andreas GEORGOPOULOS – National Technical University of Athens, GREECE
Prof. Dr. Ariel BLANCO – University of Philippines at Daliman, PHILIPPINES
Prof. em. Dr.-Ing. Dr.h.c. Armin GRÜN – ETH Zürich, SWITZERLAND
Prof. Dr. Ashutosh MOHANTY – Shoolini University, INDIA
Prof. Dr. Aydın ÜSTÜN – Kocaeli University, TURKEY
Prof. Dr. Bashkim IDRIZI – University of Prishtina, KOSOVO
Prof. Dr. Bülent BAYRAM – Yıldız Technical University, TURKEY
Prof. Dr. Charles TOTH – Ohio State University, USA
Prof. Dr. Chryssy POTSIOU – National Technical University of Athens, GREECE
Prof. Dr. Çetin CÖMERT – Karadeniz Technical University, TURKEY
Prof. Dr. Dursun Zafer ŞEKER – Istanbul Technical University, TURKEY
Prof. Dr. Erkan BEŞDOK – Erciyes University, TURKEY
Prof. Dr. Ferruh YILDIZ – Konya Technical University, TURKEY
Prof. Dr. Fevzi KARSLI – Karadeniz Technical University, TURKEY
Prof. Dr. Füsun BALIK ŞANLI – Yıldız Technical University, TURKEY
Prof. Dr. Hacı Murat YILMAZ – Aksaray University, TURKEY
Prof. Dr. Hediye ERDOĞAN – Aksaray University, TURKEY
Prof. Dr. Haluk ÖZENER – Boğaziçi University, TURKEY
Prof. Dr. Hande DEMİREL – Istanbul Technical University, TURKEY
Prof. Dr. Jiyoon KIM – University of Seoul, REPUBLIC OF KOREA
Prof. Dr. Maria Antonia BROVELLI – Politecnico di Milano, ITALY
Prof. Dr. Mevlüt YETKİN – İzmir Katip Çelebi University, TURKEY
Prof. Dr. Muhammad Bilal – Nanjing University of Information Science and Technology, CHINA
Prof. Dr. Mustafa YANALAK – Istanbul Technical University, TURKEY
Prof. Dr. Naser EL-SHEIMY – University of Calgary, CANADA
Prof. Dr. Nebiye MUSAOĞLU – Istanbul Technical University, TURKEY
Prof. Dr. Nilanchal PATEL – Birla Institute of Technology Mesra, INDIA
Prof. Dr. Niyazi ARSLAN – Çukurova University, TURKEY
Prof. Dr. Pal NIKOLLI – University of Tirana, ALBANIA
Prof. Dr. Reha Metin ALKAN – Istanbul Technical University, TURKEY
Prof. Dr. Sebahattin BEKTAŞ – Ondokuz Mayıs University, TURKEY
Prof. Dr. Sujit MANDAL – Diamond Harbour Womens' University, INDIA
Prof. Dr. Tahsin YOMRALIOĞLU – Beykent University, TURKEY
Prof. Dr. Tayfun ÇAY – Konya Technical University, TURKEY
Prof. Dr. Tamer BAYBURA – Afyon Kocatepe University, TURKEY
Prof. Dr. Tarık TÜRK – Cumhuriyet University, TURKEY
Prof. Dr. Taşkın KAVZOĞLU – Gebze Technical University, TURKEY
Prof. Dr. Uğur DOĞAN – Yıldız Technical University, TURKEY
Prof. Dr. Yasemin ŞİŞMAN – Ondokuz Mayıs University, TURKEY
Prof. Dr. Youkyung HAN – Kyungpook National University, REPUBLIC OF KOREA
Assoc. Prof. Dr. Anargha DHORDE – Nowrosjee Wadia College, INDIA
Assoc. Prof. Dr. Aziz ŞİŞMAN – Ondokuz Mayıs University, TURKEY
Assoc. Prof. Dr. Bihter EROL – Istanbul Technical University, TURKEY
Assoc. Prof. Dr. Cevdet Coşkun AYDIN – Hacettepe University, TURKEY
Assoc. Prof. Dr. Erol YAVUZ – Uşak University, TURKEY
Assoc. Prof. Dr. Fatih DÖNER – Gümüşhane University, TURKEY
Assoc. Prof. Dr. Fatih POYRAZ – Cumhuriyet University, TURKEY
Assoc. Prof. Dr. Halil AKINCI – Artvin Çoruh University, TURKEY
Assoc. Prof. Dr. Khalil Valizadeh KAMRAN – University of Tabriz, IRAN
Assoc. Prof. Dr. Lyubka PASHOVA – Bulgarian Academy of Sciences, BULGARIA
Assoc. Prof. Dr. Murat UYSAL – Afyon Kocatepe University, TURKEY
Assoc. Prof. Dr. Özgün AKÇAY – Çanakkale Onsekiz Mart University, TURKEY
Assoc. Prof. Dr. Serdar EROL – Istanbul Technical University, TURKEY
Assoc. Prof. Dr. Şükran YALPIR – Konya Technical University, TURKEY

Assoc. Prof. Dr. Uğur AVDAN – Eskişehir Technical University, TURKEY
Assoc. Prof. Dr. Zaide DURAN – Istanbul Technical University, TURKEY
Asst. Prof. Dr. Berk ANBAROĞLU – Hacettepe University, TURKEY
Asst. Prof. Dr. Esra TEKDAL YILMAZ – Nicholls State University, USA
Asst. Prof. Dr. Jorge ROCHA – University of Lisbon, TURKEY
Asst. Prof. Dr. Kemal ÇELİK – Gümüşhane University, TURKEY
Asst. Prof. Dr. Khalid MAHMOOD – University of Punjab, PAKISTAN
Asst. Prof. Dr. Mahmut Oğuz SELBESOĞLU – Istanbul Technical University, TURKEY
Asst. Prof. Dr. Mustafa Utkan DURDAĞ – Artvin Çoruh University, TURKEY
Asst. Prof. Dr. Mustafa ÜSTÜNER – Artvin Çoruh University, TURKEY
Asst. Prof. Dr. Nizar POLAT – Harran University, TURKEY
Asst. Prof. Dr. Osman Sami KIRTILOĞLU – İzmir Katip Çelebi University, TURKEY
Asst. Prof. Dr. Sadra KARIMZADEH – University of Tabriz, IRAN
Asst. Prof. Dr. Serdar BİLGİ – Istanbul Technical University, TURKEY
Asst. Prof. Dr. Subija IZEIROSKI – Geo-SEE Institute, NORTH MACEDONIA
Asst. Prof. Dr. Surendra Pal SINGH – Wollega University, ETHIOPIA
Asst. Prof. Dr. Süleyman Sefa BİLGİLİOĞLU – Aksaray University, TURKEY
Asst. Prof. Dr. Serdar BİLGİ – Istanbul Technical University, TURKEY
Asst. Prof. Dr. Tae-Suk BAE– Sejong University, REPUBLIC OF KOREA
Asst. Prof. Dr. Tirthankar BANERJEE – Banaras Hindu University, INDIA
Asst. Prof. Dr. Volkan YILMAZ – Artvin Çoruh University, TURKEY
Dr. Abdel Aziz ELFADALY – Nat. Auth. for Remote Sensing and Space Science, EGYPT
Dr. Abdul-Lateef BALOGUN – Universiti Teknologi PETRONAS (UTP), MALAYSIA
Dr. Artur GIL – University of the Azores, PORTUGAL
Dr. Ajoy DAS – Gujarat University, INDIA
Dr. Bayartungalag BATSAIKHAN – Chairwoman of Mongolian Geo-spatial Association, MONGOLIA
Dr. Cesar CAPINHA – University of Lisbon, PORTUGAL
Dr. Erman ŞENTÜRK – Kocaeli University, TURKEY
Dr. Gábor Remetey-FÜLÖPP – GIS Association Hungary, HUNGARY
Dr. Gojko NIKOLIC – University of Montenegro, MONTENEGRO
Dr. Ismail KABASHI – Angst, AUSTRIA
Dr. Krishna Prasad BHANDARI– Tribhuvan University, NEPAL
Dr. Olalekan Adekunle ISIOYE – Ahmadu Bello University, NIGERIA
Dr. MD Firoz KHAN – University of Malaya, MALAYSIA
Dr. Muhammad IMZAN BIN HASSAN – Universiti Teknologi Malaysia, MALAYSIA
Dr. Eng. Colonel Altan YILMAZ – Turkish Gen. Directorate of Mapping, TURKEY
M.Sc. R.S. AJIN – Dpt. Of Disaster Management, Govt. Of Kerala, INDIA
M.Sc. Ochirkhuyag LKHAMJAV – Mongolian Geo-spatial Association, MONGOLIA
Dereje SUFA – Wollega University, ETHIOPIA
Byeong-Hyeok YU – Korean Soc. of Environment & Ecology, REPUBLIC OF KOREA

International Association of Turkish Literature Culture Education (TEKE Derneği)
Prof. Dr. Cengiz ALYILMAZ –Bursa Uludağ University
Assoc. Prof. Dr. Onur ER – Düzce University
Assoc. Prof. Dr. Faruk POLATCAN – Sinop University
Assoc. Prof. Dr. Beyhan KOCADAĞİSTAN – Atatürk University
Dr. İsmail ÇOBAN – Artvin Çoruh University

ORGANIZING COMMITTEE

Mersin University - Faculty of Engineering - Department of Geomatics Engineering

Prof. Dr. Murat YAKAR – Conference Chairman – Head of Department
Asst. Prof. Dr. Muzaffer Can İBAN – Conference Secretary
Prof. Dr. İsmail ŞANLIOĞLU
Assoc. Prof. Dr. Erdinç AVAROĞLU
Asst. Prof. Dr. Ali ULVİ
Asst. Prof. Dr. Fatma BÜNYAN ÜNEL
Asst. Prof. Dr. Lütfiye KUŞAK
Asst. Prof. Dr. Osman ORHAN
Dr. Hakan DOĞAN – Turkish State Meteorological Service
Lect. Atilla KARABACAK
Lect. Şafak FİDAN
Res. Asst. Abdurahman Yasin YİĞİT
Res. Asst. Aydın ALPTEKİN
Res. Asst. Mehmet Özgür ÇELİK
Res. Asst. Semih KAHVECİ
Eng. Abdulkadir KAYA
Eng. Binnaz SARI
Eng. Emircan BUĞA
Eng. Engin KANUN
Eng. Ganime Melike OĞUZ
Eng. İldeniz Leyla ÖZTÜRK
Eng. Seda Nur Gamze HAMAL
Eng. Şafak BOZDUMAN
Eng. Veli YILDIZ
Eng. Mücahit Emre ORUÇ
Urb. Plan. Bilal ÖZAY
Urb. Plan. Ezgi ŞAHİN

5 May 2021 - Wednesday	
08:30-09:00	Opening
09:00-10:15	Photogrammetry and Remote Sensing - 1 (Chair: Prof. Dr. Dursun Zafer ŞEKER - Rapporteur: Asst. Prof. Dr. Osman ORHAN) **Forest health assessment using hyper spectral image and multi-criteria analysis: A case study: Ramsar Forest, North of Iran** Khalil Valizadeh Kamran*, Behnam Khaorrami **Geological mapping and mineral exploration based on the application of remote sensing in North Waziristan, Pakistan** Muhammad Yaseen*, Jawerai Mehboob, Adil Nawaz **Mapping evapotranspiration with vegetation index - temperature difference method using the products for the moderate resolution imaging spectroradiometer** Ali Levent Yağcı **A medium-sized rainfall-induced landslide detection using L- and C-band SAR images: A comparative study in agricultural lands** Ayub Mohammadi*, Khalil Valizadeh Kamran, Sadra Karimzadeh, Masashi Matsuoka **Effect of first wave COVID-19 outbreak lockdown measures on satellite-based tropospheric NO_2 over Mersin Province, Turkey** Fatemeh Ghasempour*, Aliihsan Şekertekin, Hakan Kutoğlu **The estimation of the Sky glow by using the nighttime light satellite imagery in Northern Thailand** Anurak Chakpor*, Xi Li, Vanisa Surapipit, Phattraporn Soithong
10:15-10:30	Break
10:30-12:00	Surveying and Geodesy - 1 (Chair: Asst. Prof. Dr. Mahmut Oğuz SELBESOĞLU - Rapporteur: Prof. Dr. İsmail ŞANLIOĞLU)
	The efficiency of high-rate RTK for structural health monitoring Güldane Oku Topal*, Burak Akpınar, Vahap Engin Gülal **The analysis process of robotic total station data to determine structural deformations** Hüseyin Pehlivan **Recent advances and perspectives for accurate positioning with low-cost smart devices** Reha Metin Alkan*, Can Delice **Accuracy of GPS single point positioning solution using IGS precise products** Sinan Birinci*, M. Halis Saka **Improvement of SPP NMEA output using correction projection method** Furkan Soğukkuyu*, M. Halis Saka **The impact of variable neighbor numbers on Wi-Fi fingerprint-based indoor positioning using the KNN and WKNN algorithms** Behlül Numan Özdemir*, Ayhan Ceylan **Brief history of early marine navigation** Hatice Şeyma Selbesoğlu*, Burak Barutçu, Aytekin Çökelez
12:00-12:45	Lunch Break
12:45-14:15	Geographic Information Systems and Cartography - 1 (Chair: Asst. Prof. Dr. Muzaffer Can İBAN - Rapporteur: Asst. Prof. Dr. Lütfiye KUŞAK)
	A quantitative approach for geographical vulnerability assessment of Bhasan Char, Bangladesh, using remote sensing and GIS Md. Tariqul Islam*, Mohammad Tarikul Islam, Atta Rabbi* **Accuracy of digital elevation models: under canopy vs. open field** Halit Altun, Arif Oğuz Altunel* **Geostatistical mapping of reference crop evapotranspiration (ETo)** Fatma Bünyan Ünel*, Lütfiye Kuşak, Murat Yakar, Abdullah Şahin, Hakan Doğan, Fikret Demir **Mapping of local soil conditions in GIS environment: A case study in Çukurkeşlik village** Aydın Alptekin*, Murat Yakar **Using an integrated approach for mapping soil salinity risk in Tadla plain, Morocco** Abdelwahed Chaaou*, Mohamed Chikhaoui, Mustapha Naimi, Aissa Kerkour El Miad **GIS-Based landslide susceptibility mapping using weight of evidence (WoE) and random forest (RF)** Aslan Cihat Basara*, Yasemin Şişman **The status of wheelchair-tagged OpenStreetMap point data in European capital cities** Müslüm Hacar*, Özge Öztürk Hacar **Digital terrain and detail mapping of part of ABU Phase 2, Kaduna state Nigeria** Kaka Atta, Abdulmajid Bukhari, Lukman Giwa
14:15-14:30	Break
14:30-16:00	Land Administration, Cadastre and Land Use (Chair: Asst. Prof. Dr. Muzaffer Can İBAN - Rapporteur: Asst. Prof. Dr. Fatma Bünyan ÜNEL)
	Legal aspect of space activities in international context Mehmet İşiler*, Mahmut Oğuz Selbesoğlu, Mustafa Yanalak **Content analysis of real estate valuation courses taught in geomatics engineering departments in Turkey** Nuri Erdem **Using artificial neural networks in land use/change** Esat Fikri Kılıç*, Eray Köksal **Generating temporal cadastral parcels with artificial intelligence algorithms within the scope of cadastre 2034** Fatma Betül Yıldız*, İsmail Ercüment Ayazlı, Hidayet Takcı **Easement right valuation for electric power tranmission lines** Mustafa Yılmaz*, Reha Metin Alkan **The urban agriculture approach to evaluating urban-rural interfaces** İrem Yurday*, Ceren Yağcı, Fatih İşcan **Anthropogenic intrusions leading to variability in vegetated vs non-vegetated land dynamics over the past two decades in India** Rahul Kashyap*, A.C. Pandey **Usability of wearable mobile laser systems in cadastral studies** Seda Nur Gamze Hamal*, Binnaz Sarı, Ali Ulvi, Murat Yakar
16:00-16:15	Break
16:15-17:30	Photogrammetry and Remote Sensing - 2 (Chair: Dr. Muzaffer Can İBAN - Rapporteur: Res. Asst. Abdurahman Yasin YİĞİT)
	Checking Landsat 8 OLI's predictive power in the retrieval of chlorophyll-a and phycocyanin concentrations of a reservoir with high frequency field data Güray Hatipoğlu **Investigation and modeling of physical growth of urban areas using night-time light data** Samaneh Bagheri*, Sadra Karimzadeh, Bakhtiar Feizizadeh **Rapid flood mapping with Sentinel-1 SAR images: A case study of Maritsa River** Ahmet Batuhan Polat*, Özgün Akçay **Assessment of spatiotemporal distribution of anchovy catches based on Vessel Monitoring System (VMS) and MODIS satellite data in the Gulf of Thailand** Nittaya Katekaew, Jianzhong Lu, Anukul Buranapratheprat, Dudsadee Leenawarat **Use of photogrammetric techniques for virtual modeling of historical heritage. Application: Santa Bárbara Bridge (Almería, Spain)** Ahlem Nezreg, Patricio Martínez-Carricondo, Fernando Carvajal-Ramírez, Francisco Agüera-Vega **Investigation of the effects of vegetation indices derived from UAV-based RGB imagery on land cover classification accuracy** Muhammed Yusuf Öztürk, İsmail Çölkesen

6 May 2021 - Wednesday	
09:00-10:15	Photogrammetry and Remote Sensing - 3 (Chair: Prof. Dr. Taşkın KAVZOĞLU - Rapporteur: Prof. Dr. Murat YAKAR)
	Prediction chlorophyll content of Zizania Latifolia using hyperspectral data and machine learning Adenan Yandra Nofrizal*, Rei Sonob, Hiroto Yamashita, Akio Morita, Takashi Ikka **The effect of auxiliary data (slope, aspect and elevation) on classification accuracy of Sentinel – 2A image using random forest classifier** Furkan Bilücan*, Taşkın Kavzoğlu **Mangrove forests changes and responses to sea level rise based on remote sensing and GIS in PKWS, Cambodia** Nayelin Phorn, Jianzhong Lu, Pakorn Petchprayoon **Effect of elevation on land surface temperature (LST) variation in Jos and Environs, Nigeria** Bello Abubakar Abubakar*, Sani Abubakar Abubakar **Application of UAV-Based multispectral images for accessing oil palm trees health using online AI platform** Hong Lay, Zhenfeng Shao, Sanara Hor **Sentinel-1 and -2 time-series data-fusion for olive tree identification in heterogeneous land surfaces using Google Earth Engine** Haydar Akçay*, Şinasi Kaya, Elif Sertel, Uğur Algancı, Samet Aksoy
10:15-10:30	Break
10:30-12:00	Geographic Information Systems and Cartography - 2 (Chair: Prof. Dr. Hande DEMİREL - Rapporteur: Asst. Prof. Dr. Lütfiye KUŞAK)
	Temporal analysis and future prediction of CO_2 emissions of solid, liquid and gas fuels in python with FBProphet model Metin Kaynaklı, Mehmet Emin Tabar* **Using analytical hierarchy process (AHP) for flood susceptibility mapping of Mersin, Turkey** Bilal Özay*, Osman Orhan **Analysing influence of abandoned mining sites on land use land cover and terrain in Jos, Nigeria** Adamu Bala*, Samuel Sule Garba, Taiye Oluwafemi Adewuyi, AbdulAzeez Aliyu Onotu **2D flood modeling with the help of GIS: Mersin / Lamas River** Vahdettin Demir*, Aydın Alptekin, Mehmet Özgür Çelik, Murat Yakar **Using modern methods to determine the suitable area for rain harvesting** İldeniz Öztürk*, Lütfiye Kuşak **Analysis of carbon absorption amount of urban forests by spatial interpolation methods** Elif Akyel*, Fatih Kenar
12:00-12:45	Lunch Break
12:45-14:15	Geographic Information Systems and Cartography - 3 (Chair: Assoc. Prof. Dr. Khalil Valizadeh KAMRAN - Rapporteur: Asst. Prof. Dr. MuzafferCan İBAN)
	Analysis urban green space classification using landscape pattern analysis based on GIS and remote sensing in Pattaya, Thailand Sopaphan Chinnabut*, Nengcheng Chen, Haoran Zhang **Trend analysis of temperature and precipitation data of 9 stations located in Mediterranean region** Cavit Berkay Yılmaz, Vahdettin Demir*, Mehmet Faik Sevimli, Fikret Demir, Murat Yakar **Creating and evaluating pollution distribution map in Aegean Region by using geographical information system (GIS) and air quality data** Ömer Bilginer*, Elif Akyel, Güzide Miray Perihanoğlu, Sena Tekavcu **Determination of effective predisposing factors using random forest-based Gini index in landslide susceptibility mapping** Alihan Teke*, Taşkın Kavzoğlu **Trend analysis of precipitation data using Mann Kendall and Sen's slope tests** Osman Enes Güneş*, Aslan Cihat Basara, Yasemin Şişman **Investigation of the shadow effect of urbanization on green areas with shadow impact analysis** Halil İbrahim Şenol **Spatial flood analysis to determine possible economic damage: Case study of the European side of Istanbul** Buğrahan Özcihan, Enes Doğukan Özgener, İlker Karakap, Levent Doğukan Özlü, Yusuf Göktuğ Bağcı, Ömer Akın, Hande Demirel
14:15-14:30	Break
14:30-15:45	Photogrammetry and Remote Sensing - 4 (Chair: Asst. Prof. Dr. Youkyung HAN - Rapporteur: Asst. Prof. Dr. Ali ULVİ)
	Analysis and investigation on spatio-temporal dynamic pattern of drought in Thailand Arpakorn Wongsit*, Nengcheng Chen, Tanita Suepa **Using terrestrial lidar data in 3D CAD modeling applications** Lütfiye Karasaka, Neslişah Ulutaş* **Road extraction through satellite imagery processing and visual interpretation** Aikaterini Karagianni **Construction of 3D modeling based on vertical and oblique unmanned aerial vehicle imagery for efficient national park management** Changhui Lee, Taeheon Kim, Jueon Park, Youkyung Han* **Photogrammetric analysis of multispectral and thermal close-range images** Özgün Akçay **Tree detection from high-resolution unmanned aerial vehicle (UAV) images** Halil İbrahim Şenol, Abdurahman Yasin Yiğit, Yunus Kaya
15:45-16:00	Break
16:00-17:15	Photogrammetry and Remote Sensing - 4 (Chair: Asst. Prof. Dr. Süleyman Sefa BİLGİLİOĞLU - Rapporteur: Res. Asst. Mehmet Özgür ÇELİK)
	Supervised machine learning classification in Google Earth Engine: Time series analysis in Akkuyu, Turkey Muzaffer Can İban*, Şafak Bozduman, Ezgi Şahin **Analysis of the effect of training sample size on the performance of 2D CNN models** Elif Özlem Yılmaz*, Taşkın Kavzoğlu **Documentation of cultural heritage with Backpack lidar usage on photogrammetric purpose** Kasım Erdal, Hasan Bilgehan Makineci* **Extraction of high-precision built-up areas from SENTINEL-2B imagery via multi-index approach and Fuzzy C-Means algorithm** Imane Bachri*, Ruth Virginia Zonkouan Badjo, Abdelmajid Benbouziane, Mohammed Raji, Mustapha Hakdaoui, Diomande Beh Ibrahim **The availability of local laser technique in forest management planning** Mücahit Emre Oruç, İldeniz Leyla Öztürk*, Ali Ulvi **Monitoring the stability of highway cut slopes utilizing drone photogrammetry** Ufuk Kader, Arif Oğuz Altunel* **Using drone mapping to analyze risky areas and predict LULC at Sichang Island, Chonburi province, Thailand** Suwatcharapong Surasanpreedee*, Kitsanai Charoenjit, Zhenfeng Shao

CONTENTS **Page**

Intercontinental Geoinformation Days

igd.mersin.edu.tr

Forest health assessment using hyper spectral image and multi-criteria analysis: A case study: Ramsar Forest, North of Iran

Khalil Valizadeh Kamran*[1], Behnam Khorrami [2]

[1]*University of Tabriz, Faculty of Planning and Environmental Sciences, Department of Remote Sensing and GIS, Tabriz, Iran.*
[2]*Dokuz Eylul University, Graduate School of Natural and Applied Sciences, Department of GIS, Izmir, Turkey.*

Keywords
Hyperspectral
Fuzzy set
Forest health
Vegetation indices

ABSTRACT

The hyperspectral images have so far been widely used to monitor and detect environmental changes in vast areas. The analysis of hyperspectral images provides the spatial distribution (maps) of terrain physical and ecological characteristics. In this study, fuzzy set theory integrated with a decision-making algorithm in a Geographic Information Systems (GIS) was used to map Ramsar forest health. In the fuzzy set theory, all classes must have a certain boundary or grouping. (i.e., fuzzy) and consist of a rule base, membership functions, and an inference procedure. For forest health assessment, NDWI, CRI1, PSRI, PRI, and NDVI indices were used to infer the causative factors of forest health. Spectral indices can provide different methods for identifying vegetation coverings. The results of this study are quite useful in identifying potential forest health, where forest health protection measures can be taken in advance. The results also suggest that the southern and the western aspects of the study area are of "very low to low" forest health. Furthermore, the results introduce the potentiality of multi-criteria analysis integrated with GIS as an effective tool in assessing the fire-prone areas of forests.

1. INTRODUCTION

The majority of the current assessments of forest conditions are limited to ground-based visual evaluation. Although these conventional field assessments are valuable, they do not reveal physiological changes that characterize early stress responses (Sampson et al., 2000). Assessing physiological conditions can indicate productivity and adaptability to environmental stress (Chapin, 1991; Colombo and ParAcker,1999) and may provide an early indication of the decline in stand vigor and productive capacity (Zarco et al, 2002). The applications of hyperspectral imaging to natural resources, vegetation, and surface water, have been widely tested (Mouroni et al, 2013). The spectral signature of vegetation is influenced by the presence of pigments (mainly chlorophyll-a, chlorophyll-b, xanthophylls, and carotenoids), canopy water component, whose content varies depending on the chemical and biological activity and the physical structure of plants as well (Blachborn, 1998; Baret, 1998; Sims and Gamon, 2002). The reflectance spectrum of plants provides information on the degree of senescence, the deterioration of leaf structure, or any diseases and abnormalities that plants may be affected from. [Baret, 1998, Blachborn, 1998, Carter and Miller, 1994). Gamon and Surfus (1999) reported quantitative estimates of chemical content in leaves and canopies using indices derived from spectral reflectance at specific wavelengths. Several important eco-physiological properties can be inferred from these reflectance indices based on the links which exist between chemical content, leaf structure, and function. Thenkabail et al (2002) determined the optimal hyperspectral narrow wavebands, in the visible and near-infrared portion of the spectrum, that best characterize agricultural crop characteristics. Vegetation indices derived from narrow and broad wavebands were used to establish relationships with crop biophysical variables and yield.

Moreover, integration of multi-criteria decision-making (MCDM) methods in a spatial domain provides a novel framework for addressing several environmental problems, such as quantifying "fire risk", "forest health" etc. MCDM methods have been developed to solve conflicting preferences among criteria (Keeney and Raiffa 1976). Rational decision-making requires combining both objective and subjective criteria (Pomerol and Barba-Romero2000), most notably in a

* **Corresponding Author**

*(valizadeh@tabrizu.ac.ir) ORCID ID 0000-0003-4648-842X
(behnam.khorrami@ogr.deu.edu.tr) ORCID ID 0000-0003-3265-372X

Cite this study

Kamran K V, Khorrami B (2021). Forest health assessment using hyper spectral image and multi-criteria analysis: A case study: Ramsar Forest, North of Iran. Intercontinental Geoinformation Days (IGD), 1-4, Mersin, Turkey

collaborative participatory framework for which MCDM methods can provide a useful framework (Saaty 1994; Malczewski 2002; Sadiq and Husain 2005). MCDM is believed to be a powerful technique for analysis and prediction. It also provides a rich collection of technique for structuring decision problem and designing, evaluating, and prioritizing alternative decisions (Feizizadeh et al, 2012 and Feizizadeh and Blaschke, 2012a)

Forest health mapping is useful for detecting pest and blight conditions in a forest and is useful for assessing areas of timber harvest. Within the gamut of the current study, a forest health map was generated for the study area by using five different spectral indices in conjunction with a Fuzzy set.

2. METHODOLOGY

2.1. Study Area

Ramsar is the capital city of Ramsar County, Mazandaran Province, Iran. Green coverage of forests contributes to the majority of the city area and is one of the main vegetation hotspots in Iran regarding the volume of the produced trees. These forests are graded from 1 to 3 with an area of 42,894 ha, 32,758 ha, and 52,972 ha respectively. The commercial utilization is 21,202 m^3 (6,505,000 cu ft) and the non-commercial utilization is 32,173 m^3 (4,455,800 cu ft). The Total Annual Precipitation (TAP) of Ramsar is about 1200 mm. The study area is located between the following geo-coordinate: 50° 22' 06"- 50° 59' 31"N 36° 11' 08"- 36° 45' 06" E.

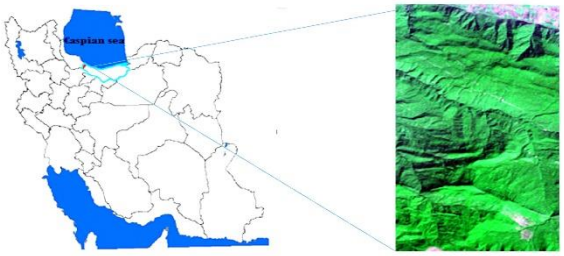

Figure 1. The geographic location of Ramsar Forest in North of Iran

The methodology of the current study consists of three different components: (1), A Fuzzy Inference System for forest health (2), Fuzzy Degree Membership Functions, (3) Performing Scenarios.

2.2. Fuzzy Inference System for Forest Health

Fuzzy logic is a human Knowledge embodying tool through operational algorithms. Several intelligent Systems have been developed globally for forest health assessment on an annual basis (Yan and Yang, 2001) and also for the estimation of risk due to natural hazards (Iliadis et al., 2005). According to fuzzy Algebra, every element of the universe may belong to any fuzzy set (FS) with a degree of membership that varies from 0 to 1 (Ilidias et al, 2009). We used NDWI, CRI1, PSRI, PRI, and NDVI indices for evaluating forest health in the study area.

2.2.1. Canopy Water Content

Water content is an important quantity of vegetation because higher water content indicates healthier vegetation that is likely to grow faster and be more fire-resistant (Penules et al, 1992). Plants of different species inherently contain different amounts of water based on their leaf geometry, canopy architecture, and water requirements. Among plants of one species, there is still significant variation, depending upon leaf thickness, water availability, and plant health. Water features center around the 970 nm and 1190 nm of the microwave spectrum and can be readily measured from hyperspectral sensors. However, they cannot be sampled by multispectral sensors.

2.2.2. NDWI (Normalized Difference Water Index)

NDWI is sensitive to variations in vegetation canopy water content because reflectance at 857 nm and 1241 nm has similar but slightly different liquid water absorption properties. The scattering of light by vegetation canopies enhances the weak liquid water absorption at 1241 nm. Applications of NDWI include forest canopy stress analysis, leaf area index studies in densely foliated vegetation, plant productivity modeling, and fire susceptibility studies (Gao, 1995). NDWI is defined by the following equation:

$$NDWI = \frac{857 - 1241}{857 + 1241} \qquad \text{Equation1}$$

2.2.3. Leaf Pigments

There are three main categories of leaf pigments in plants: chlorophyll, carotenoids, and anthocyanin. These pigments are critical to the function and health of vegetation. Vegetation with a high concentration of chlorophyll is generally very healthy. Conversely, carotenoids and anthocyanin often appear in higher concentrations in less healthy vegetation (Gitelson et al, 2002). The main pigments involved in photosynthesis are chlorophylls and carotenoids. One of the structural characteristics of carotenoids is their ability to absorb visible light: p delocalized electrons suffer a photo-induced transformation through which a single state (s2) is produced, then energy is efficiently transferred to chlorophyll (CHL) to form singlet CHL with slightly higher energy (Delgado et al, 2000). In this study, NDVI and CRI1 were used to evaluate chlorophylls and carotenoids.

The Carotenoid Reflectance Index 1 (CRI1) and NDVI are defined as follow:

$$CRI1 = \frac{1}{510} - \frac{1}{550} \qquad \text{Equation 2}$$

$$NDVI = \frac{800-670}{800+670} \qquad \text{Equation 3}$$

2.2.4. Dry or Senescent Carbon

Senescence marks the final phase of a leaf's development thereby launching degradation processes integral to the recycling and redistribution of the leaf's nutrients. Plant growth regulators, reproduction, cellular differentiation, and hormone levels are internal factors that influence senescence (Thomas and Stoddart 1980; Smart 1994) In this study, the Plant Senescence Reflectance Index (PSRI) was utilized to assess the Dry or Senescent Carbon status.

PSRI is designed to maximize the sensitivity of the index to the ratio of bulk carotenoids (for example, alpha-carotene and beta-carotene) to chlorophyll. An increase in PSRI indicates increased canopy stress (carotenoid pigment), the onset of canopy senescence, and plant fruit ripening. PSRI is defined by the following equation:

$$PSRI = \frac{680-500}{750} \qquad \text{Equation 4}$$

2.2.5. Light Use Efficiency

Light use efficiency is highly related to carbon uptake efficiency and vegetative growth rates and is somewhat related to fractional absorption of photosynthetically active radiation (FAPAR). Light use Vegetation Indices (VI's) use reflectance measurements in the visible spectrum to take advantage of relationships between different pigment types to assess the overall light use efficiency of the vegetation (Gamon et al, 1997). In this study for Light use efficiency assessment, The Photochemical Reflectance Index (PRI) index was used.

PRI is a reflectance measurement that is sensitive to changes in carotenoid pigments in live foliage (Penuelas et al, 1992). Carotenoid pigments are indicative of photosynthetic light use efficiency, or the rate of carbon dioxide uptake by foliage per unit energy absorbed. PRI is defined by the following equation:

$$PRI = \frac{531-570}{531+570} \qquad \text{Equation 5}$$

2.3. Fuzzy Degree Membership Functions

There is no optimal method for choosing the most appropriated Fuzzy Membership Functions (FMFs) and their respective parameters; these are generally selected according to the preference of the decision-makers (Feizizadeh et al, 2013). In this respect, the sigmoidal membership function was used (Fig.3). The Fuzzy Membership tool reclassifies or transforms the input data to a 0 to 1 scale based on the possibility of being a member of a specified set. 0 is assigned to those locations that are not a member of the specified set, 1 is assigned to those values that are a member of the specified set, and the entire range of possibilities between 0 and 1 are assigned to some level of possible membership (the larger the number, the greater the possibility) (Zadeh, 1968).

2.4. Sigmoidal Membership Function

The Sigmoidal ("s-shaped") Membership function is perhaps the most commonly used function in Fuzzy Set theory. It is produced using a cosine function. In use, FUZZY requires the positions (along the X-axis) of 4 points governing the shape of the curve (Zadeh, 1968).

2.5. Performing Scenarios

By linking environmental factors and efficient forestry, GIS can perform as a tool for operational and practical monitoring of forest health assessment and management. As a planning tool, it may also play an important role in forest and land-use studies in a broader sense (Jaiswal et al. 2001).

2.6. Defining membership function

In this study, the Sigmoidal function was used as a membership function and layer overlay was done in the GIS environment. On account of the optimal wizard availability issue for defining the Sigmoidal membership function in GIS, the authors utilized coding. (Fig.4)

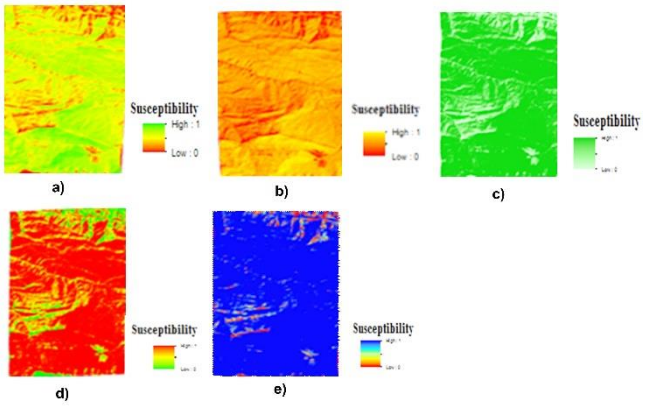

Figure 2. Parameters Susceptibility Maps: *WBI (a), CRI1 (b), NDVI (c), PSRI (d), and PRI (e).*

3. Results and discussion

The locations with at least a 0.5 or greater suitability for all the criteria were satisfied for this study thus the Fuzzy AND function was used. The forest health map (Fig 5) suggests that the southern and western aspects in the study area are of "very low to low" forest health while the other aspects belong to "medium to very high" health zones. Determination of the fuzzy membership boundaries was implemented according to the opinions of four experts.

The results underline a highly dynamic and spatial nature of forest health in the study area. Results also indicate that it is essential to improve our understanding of the causative factors of forest health to manage forest health as well as to prioritize the related measures.

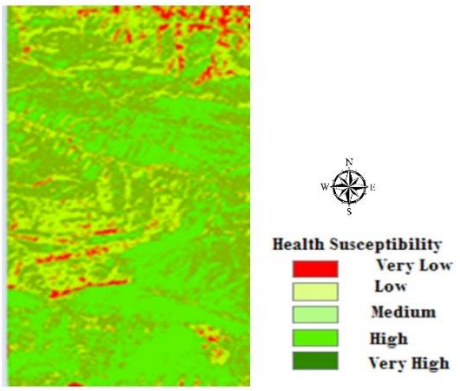

Figure 3. Forest Health Susceptibility Map

4. CONCLUSION

In this study, Ramsar forest health was quantified in terms of canopy water component, carotenoid and chlorophyll pigments in plant foliage, plant senescence, and photochemical reflectance. To address the "fuzziness" in the spatial dataset and also to include the subjective judgments in the modeling process, a fuzzy analytical hierarchy approach in GIS was utilized to assess the fire risk in the study area. Results are quite useful in delineating potential "forest health" zones at a district level. The findings of the current study can be used as a strategic planning tool. They may also be applied to assess the health susceptibility of any vegetation coverage.

Overall, the findings of this study demonstrate the potential of GIS technology, Multi-criteria Decision Making (MCDM), and its viability for the assessment of forest health by integrating objective as well as subjective data in a Fuzzy Logic.

Acknowledgment

We would like to express our warmest gratitude to the geology organization of the USA for providing this study with the EO-1 images.

Reference

Canadian Forest Service, 1999.Forest health in Canada: An overview. Vogelmann, J.E., B.N. Rock, and D.M. Moss, 1993. Red edge spectralNat. Resour. Canada, Ottawa, ON

Chapin, F.S, 199. Integrated responses of plants to stress.BioScience41:29–36.

Colombo, S.J., and W.C. Parker, 1999. Does Canadian forestry need .physiology researchFor. Chronicle 75:667–673.

Feizizadeh, B, Blaschke, T and Roodposhti, M, S, 2013. Integrating GIS based fuzzy set theory in Multi Criteria evaluation methods for Landslide susceptibility mapping. International Tournal of Geoinformatic, Vol 9 No.3 Sep 2013

Feizizadeh, B, Blaschke, T and Zamani, H, 2012.GIS based ordered weigthed averaging and Dempstershafermwthodfor landslide susceptibility map in Uromia lake basin, Iran. International journal of digital earth . DOI: 10:1080. 17538,2012.

Feizizadeh, B, Blaschke, T , 2012a.Comparing GIS Multi criteria decision analysis for land slide susceptibility mapping for the Uromia lake basin Iran, (IGARSS)2012 IEEE International 10.1109, IGARSS 2012.

Gamon JA, Surfus JS, 1994. Assessing leaf pigment content and activity with a reflectometer.New Phytol1999;143:105-117.

Gamon, J.A.,J. Penuelas, and C.B. Field, 1992. A Narrow-Waveband Spectral Index That Tracks Diurnal Changes in Photosynthetic Efficiency. Remote Sensing of Environment 41:35-44.

Gitelson, A.A., Y. Zur, O.B. Chivkunova, and M.N. Gao, B.C., 1995. Normalized Difference Water Index for Remote Sensing of Vegetation Liquid Water from Space. Proceedings of SPIE 2480: 225-236.

Iliadis L., 2007, Intelligent Information Systems and Applications in Risk Estimation (in Greek) Stamoulis Publishing Thessaloniki, Greece

Jaiswal RK, Mukherjee S, Raju DK, 2001. Forest fire risk zone mapping from satellite imagery and GIS. International Journal of Applied Earth Observation and Geo information 4 :1-10.

Malczewski, J, 2002. Fuzzy screening for land suitability analysis. Geographical and Environmental Modelling 6, 27–39. doi: 10.1080/13615930220127279

Pomerol, J. C., &Barba-Romero, S, 2000. Multi criterion decision in management: Principles and management .Boston: Kluwer Academic

P. J. Zarco-Tejada, J. R. Miller, G. H. Mohammed, T. L. Noland, and P. H. Sampson, 2002, Vegetation Stress Detection through Chlorophyll a + b Estimation and Fluorescence Effects on Hyperspectral Imagery, Journal of.Environ. Qual. 31:1433–1441

Saaty. 1968, Fuzzy sets. Information and Content,8, 338–356. doi: 10.1016/S0019-9958(65)90241-X.

Sadiq, R. &Husain, T. (2005).A fuzzy-based methodology for aggregative environmental risk assessment: A case study of drilling waste. Environmental Modelling&Software, 20, 33–46. doi:10.1016/j.envsoft.2003.12.007.

Sampson, P.H., G.H. Mohammed, P.J. Zarco-Tejada, J.R.Miller, T.L, Noland, D. Irving, P.M. Treitz, S.J. Colombo, and J. Freementle, 2000. The bioindicators of forest condition project:Aphysiological, remote sensing approach. For. Chronicle 76(6):941–952.

Sims AD, Gamon JA, 2002. Relationships between leaf pigment content and spectral reflectance across a wide range of species, leaf structures and developmental stages. Remote Sensing of Environment 2002;81:337- 354. (a)

Thenkabail PS, Smith RB, De Pauw E, 2002, Evaluation of Narrowband and Broadband Vegetation Indices for Determining Optimal Hyperspectral Wavebands for Agricultural Crop Characterization. Photogrammetric Engineering and Remote Sensing 2002;68(6):607-621.

Zadeh, L. A, (1968 and 1972). Fuzzy sets. Information and Content, 8, 338–356. doi: 10.1016/S0019-9958(65)90241-X.

Intercontinental Geoinformation Days

igd.mersin.edu.tr

Geological mapping and mineral exploration based on the application of remote sensing (RS) in North Waziristan Pakistan

Muhammad Yaseen[*1], **Jaweria Mehboob**[2], **Adil Nawaz** [3]

[1] *Abdul Wali Khan University, Mardan, Pakistan*
[2] *Postgrduate College of Science, Dir Lower, Pakistan*
[3] *Faculty of Geology Geophysics and Environmental Protection, AGH University of Science and Technology, Krakow 30-59, Poland*

Keywords
Remote sensing
Alteration zone
Color composites
Geological mapping
North Waziristan

ABSTRACT

In mineral exploration, remote sensing tools are important and cost effective. Minerals occur in a variety of genetic associations, commercial deposits of minerals are limited in genetic types and modes of occurrences. This forms the basis of modern concept based prospecting and is also responsible for the significant role of remote sensing in exploration. Remote sensing data can help to differentiate metalogenic provinces/belts/sides and mineral guides in a larger terrain. Keeping In view the importance of RS Tools, digitally enhanced OLI Landsat 8 images are applied to find alteration zones and for geological mapping of North Waziristan Pakistan. The territory is rough with sparse vegetation; the exposure of the Waziristan ophiolite, related sedimentary-igneous lithologies and inaccessibility to the area made the utilization of Landsat information helpful in this investigation. Spectral signatures recorded by Landsat 8 data were used to differentiate different rock units and alteration zones. RS tool i.e. band ratios, band combinations, principal component analysis and image classification are helpful in this regard. Final detection of the lithology and alteration zones is based on correlation between classes generated in the thematic map and the referenced geological map. On the basis of the image classification techniques; unsupervised classification, band ratios, five principles lithological units and alteration zones with highest percentage of clay and iron ratio, results are satisfactory with overall accuracy 63.07 % in comparison with referenced geological map using confusion matrix analysis. The results are subject to discussion and need to examine about the utility and confinements of remote sensing strategy on the investigation zone.

1. INTRODUCTION

The aim of the project is to use remote sensing tools in identifying alterations zones for mineral perspective and to create a map of lithology of rocks, sediments and their residuals exposed on the land surface. The new map which would depends on unsupervised classification, colour composites band ratios and principal component analysis expand limited mapping of the ophiolite, approves and enhances past general conclusions and reveals new prospects in the territory. The application of multispectral imaging to the Northwest of Pakistan makes the construction of definite geologic maps economical and efficient. Applying appropriate band rationing and Principal Component analysis (PCA) is part of the analysis which entitles additional lithologic information from the ground. Modified map is verified with referenced geological map published by Geological Survey of Pakistan (GSP), high resolution airborne ortho photomap and different field reports. For the research purpose, Landsat 8 images are freely downloaded from USGS online repository. Satellite images are processed and analysed using software i.e. Ermapper, QGIS, ArcGIS and Global Mapper. The result of study are satisfactory enough to apply remote sensing as a tool to differentiate lithological units in the study area. Visual evaluation of multispectral images using RS tools i.e. band ratios, PCA and unsupervised classification, we can differentiate between different rock units as usually geological materials are not homogeneous even within specific rock units.

2. METHOD

The study goes in five stages.

1. Creating an updated lithological map with the use of image processing and analysis
2. Highlighting alteration zones.

* **Corresponding Author**

*(yaseengeo@awkum.edu.pk) ORCID ID 0000-0002-0740-0635
(sjiya6548@gmail.com) ORCID ID 0000-0002-2228-1857
(adil_pu@hotmail.com) ORCID ID xxxx – xxxx – xxxx – xxxx

Cite this study

Yaseen M, Jaweria M & Adil N (2021). Geological mapping and mineral exploration based on the application of remote sensing (RS) in North Waziristan Pakistan. 2nd Intercontinental Geoinformation Days (IGD), 5-8, Mersin, Turkey

3. Rectification of the map obtained by comparison and statistical validation with referenced data.
4. Modification of processing parameters.
5. Final rectification of the map.

The ophiolite belt of Waziristan is having potential for certain type of ore deposits, consisting VMS type of copper deposits, podiform chromite & banded manganese(Jan 1985). The occurrences of these deposits in the ophiolite belt of Waziristan was first reported by Asrarullah of Geological survey of Pakistan, Taher Kheli, Aftab Ahmed (1959), Afzal (1970). A number of principal geological criteria for mineral prospecting, which are helpful in this study, have been setup by Mckinstry in 1948 includes: 1-statigraphical–lithological, 2 Geomorphology, 3-Structural, 4-Rock alterations, and 5-Geobotnical, 6-Geochemical and geophysical anomalies (Gupta 1991).

Seven clear, cloud free Landsat-8 images were downloaded from online repository of the United States Geological Survey (USGS) in tiff format, specifications of the images are shown in Table 1. The study area (Path/row-152/37) is captured by Landsat 8 scenes acquired on 15 May, 2016. Fig. 1 shows the Landsat image of the study area. Following techniques are applied on the satellite imagery. While displaying a color composite, three primary colours i.e. red, green and blue (RGB) for three bands of multispectral images are selected. Fig. 2-3 shows the Colour composites. When combining three colours in different proportions, they create different colours in the visible spectrum. Involving every spectral band (not necessarily a visible band) to an isolated primary colour, resultant will give us a colour composite. Details of band number and their usage is explained in Table 2. Colour visualization will always make it easier to interpret the multispectral images and capture differences between single bands. In LANDSAT 8 OLI scanner; by combining band 4 (red), band 3 (green) and band 2 (blue), resultant color composite image shows closely what would be seen by the human eye. In natural colour composite (Fig. 1) bands are in the visible range and features on the ground appears in their natural colour. Fig. 1 shows iron oxide coloration in the soil, Rocks rich in iron oxide can be seen in dark reddish colour. Recent superior sediments and alluvial fan deposits are in light brown colour. This band combination used for urban studies as well as it provides the most water penetration and bathymetric information. Vegetation types are not easily distinguishable in natural colour composites as we do in false colour combinations. Similarly, natural composite 321 is not good to distinguish shallow water from soil as it in 753 combination. The false colour display assignment can be done in an absolutely random way for any band of a multispectral image so that the colour of a target in the displayed image does not show any resemblance to its actual colour. The resultant image is known as a false colour composite. However, some methods can be more appropriate for the detection of certain features in the image. False colour composite schemes for exhibiting a Landsat 8 OLI multispectral image used in this research are RGB 653 and RGB 543. Fig. 2-3 shows false colour composites. In lithological mapping, RGB color combinations that use bands with low correlation coefficients are giving us better results due to the spectral diversity in the bands. Lithology interpretation is based on the following remote sensing tools:

I. Colour composites
II. Band ratios- Clay, iron-oxide, NDVI and its derivatives.
III. Unsupervised classification (ISO CLASS)

Geological colour Composite in fig. 2 shows RGB 653 which creates an enhanced image with strongly green vegetation, bluish water and light to dark brown rock or soil. Limestone and shale are most probably pinkish or light in colours. RGB 753 and 652 are alternatives of this combination. Quaternary fan deposits are visible in light brownish-greyish colour, dark brown colour could be dunite and wherlite.

Fig. 3 shows RGB 543 In a tropical setting, it replicate a conventional Infrared aerial image with red vegetation and grayish to bluish rock or soil. It focuses on the boundaries between barren and vegetated land. Equivalent in L5/7 to this band is RGB 432. Chlorophyll content in leaves is different in different types of vegetation which results different shades of red in every plant. That's why 543 composite images are very convenient in determining the extent of vegetation cover and in the classification of vegetation in remote sensing. Band rationing is very simple and powerful technique in the remote sensing; Fig. 4, 6 & 7 shows band rationing images. Different band ratios like NDVI used by (Bannari 1995), iron oxide, clays ratio and principle component (PCS) (Mudrov 2010) could give us better understanding of the geology. Basic idea of this technique is to emphasize or exaggerate the anomaly of the target object as used by (Abrams 1983). In Fig. 4 band ratio is created with b7/b6 in red, b6/b5 in green and b2/b3 in blue. It is clear from the image that geology is giving map like appearance with small relief in topography. Rocks composed of clay mineral are in blue shades, light reddish colour could be of chert and light yellow colour could be of Limestone. Clay ratio in Fig. 6 is produced through the combination of band b6/b7. Clays, carbonates and micas can produce the light grey to white zones in greyscale images. In pseudo color, clay with red colour is showing maximum value which is 1.65. It can be due to the reason that hydrous minerals as said by (Knepper 1975) or alteration zone have high absorption as compare to band 7. Fig. 7, Iron oxide ratio is created through band b4/b3 combination. Iron oxide ratio increases the existence of iron bearing minerals which can be the reason of strong absorption in b4 and alteration in iron oxide, also it causes strong absorption in band 3 and higher reflectance in band 4. Oxides of iron seems to be reddish with higher values i.e. 1.357.

Unsupervised classification (ISO CLASS) is created (Fig. 5) with 70 number of classes using different classification parameters; results are verified visually and statistically with reference data, colour composites and band ratios. Unsupervised classification is executed using Iterative Self Organizing Data Analysis Algorithm Technique (ISODATA) as used by (Tou & Gonzalez 1974). In this classifier we don't use training samples data as a base for classification. Instead, these classifiers involve algorithms. Undefined pixels are analyzed by these

algorithms in the image and collect them into number of classes established on the natural clusters or grouping present in the image values. Geological referenced map is reclassified in ER mapper using algorithms written under Table 4 and shown in Fig. 8. Five major lithlogic units are marked on the referenced geological map, which are discussed under section 4 stratigraphy and Table 3. Thematic map with unsupervised classification is shown in Fig. 9. This map is showing 5 lithologies which are giving quite satisfactory results when we compared with referenced geological map. Fig. 10 shows referenced geological map prepared by Geological Survey of Pakistan.

Error (Confusion) Matrix (Awad, N.M.A., 2011) allows for quantitative estimation of the overall accuracy of classification. The correct classifications results are presented diagonally from upper left to lower right corner. Table 4 and 5 shows confusion matric analysis. The values (Tables 3) which are not found in the diagonals are considered as errors said by (Congalton 1991; Congalton 1999). The ISO classified image with 70 clusters or classes shown in Fig. 5, each represented by a different color. Each class was labeled and identified as geology or non-geology with the help of high resolution ortho photomap and geological referenced map using ARCGIS and QGIS online imagery. The confusion matrix was generated through ER mapper. Confusion matrix between referenced geological map and the classified multispectral image with 70 classes was created to check the accuracy of the classification as shown in Table 4 and 5.

There was confusion between classes and just 5 classes were showing satisfactory results out of 16 which are shown in Table 3. As far other lithologies are concerned, there was confusions in following set of lithologies; JZEF, TKF, JVV, JWV, QRS, KML, JZF and QTG (See Stratigraphy). After calculation of confusion matrix, highlighted maximum numbers in rows and columns (Table 4, 5). In this way we reduced the classes and just 5 classes were retained. For the second time, image was reclassified using algorithm shown in Table 5 with just 5 classes which are giving satisfactory results. Geological referenced map is also reclassified using 5 corresponding lithologies. After reclassification of both images, confusion matrix analysis giving us 63.071 % overall accuracy with kappa statistics 0.521 as used by (Jensen 2005).

3. RESULTS AND DISCUSSION

The purpose of the study is to generate a revised map of the rocks revealed on the surface in geologically complex area and to identify VMS type deposits using RS tools. Geological referenced map was having 20 major lithologies; JUM, QFD, JPS, JUM, JWV ,QFD, QTG, JSD, DOLORITE DYKE, KML, JVV, JG, QRS, JPG, ZEF, TKF, JAF, JZF, TRF and QAL (See Stratigraphy). Study shows that on a broad scale, the use of 70 classes in unsupervised classification produced more precise distribution of lithology. The result of study are satisfactory enough to apply remote sensing as a tool to differentiate lithological units in the study area. Visual evaluation of multispectral images using RS tools i.e. band ratios, PCA and unsupervised classification, we can differentiate between different rock units as usually geological materials are not homogeneous even within specific rock units. Within the ophiolite complex different igneous rock types like gabbroic rocks, ultramafic rocks, and the sheeted dike complex can be differentiated on the basis of spectral ratio, false color composites and PCs.

The reference data used in this study was the geological map of North Waziristan on the scale 1:50,000. For further studies and to minimize uncertainties caused by vegetation, complex geologic history and local landscape evolution events, it would be valuable to use other data (field data, geophysical data) for reference purposes. Different systems like Landsat allows efficient, consistent data collection for geological studies. Combination of more information and with the help of higher resolution data, like high resolution spectral data, spatial and morphometric datasets, we can get better geological view of the area. Keeping in view the complex geological history of the area, I suggest that a combination of remote sensing with sampling on ground and geophysical data; magnetics and gravity could produce more accurate results. Information could be changed due to geomorphic processes and different factors; erosion and deposition, so evaluating the accuracy of unsupervised classification, results of Landsat 8 OLI data through error matrix and kappa hat shows that remote sensing using digital image processing techniques can generate moderate to high level results in lithological mapping especially in arid regions.

ACKNOWLEDGEMENT

We are grateful to all faculty Professors for providing assistance during the research. We are Professor Dr. Janusz Magiera for his understanding, endless support and encouragement.

REFERENCES

Abrams MJ, Brown D, Lepley L, Sadowski R (1983). Remote sensing for porphyry copper deposits in southern Arizona. Economic Geology 78: 591- 604.

Anwar M, Fatmi AN, Hyderi IH (1993) Stratigraphic analysis of the Permo Triassic and Lower Middle Jurassic Rocks from the "Axial Belt" Region of the Northern Baluchistan, Pakistan. The Geological Bulletin of the Punjab University 28: 1–20.

Awad NMA (2011) Evaluating the effectiveness of multi-spectral remote sensing data for lithological mapping in arid regions : A quantitative approach with examples from the Makkah Neoproterozoic region, Saudi Arabia. Dissertation, Missouri University of Science and Technology.

Bannari A, Morin D, Bonn F, Huete AR (1995) A review of vegetation indices. Remote Sensing Reviews 13: 95–120.

Beck RA (1995) Late Cretaceous ophiolite obduction and Paleocene India-Eurasia collision in the westernmost Himalaya. Dissertation, University of Southern California.

Congalton RG (1991) A review of assessing the accuracy of classification of remotely sensed data. Remote Sensing of Environment 37: 35–46.

Congalton RG, Green K (1999) Assessing the accuracy of remotely sensed data: principles and applications. Lewis Publishers, Boca Raton, Fla.

Fatmi A N (1974) Lithostratigraphic units of the Kohat-Potwar range, Indus basin, Pakistan. Memoirs of the Geological Survey of Pakistan 10: 1–80

Federal Administrated Tribal Areas. Geography. http://fata.gov.pk/facility- home.php?fid=%2036 Accessed 26 June 2018.

Jan MQ, Windley BF, Khan A (1985). The Waziristan ophiolite, Pakistan; general geology and chemistry of chromite and associated phases. Economic Geology 80: 294-306.

Jensen JR (2005) Introductory digital image processing (3rd edition). International journal of remote sensing: Prentice hall. http://web.pdx.edu/~nauna/week3a-changedetection.pdf

Johnson BD, Powell CMA, Weavers JJ (1976) Spreading history of the Eastern Indian Ocean and greater India's northward flight from Antarctica and Australia. GSA Bull, Vol. 87: 1560–1566.

Khan SR (1999) Stratigraphy of the passive margin of the Indian plate, Waziristan, NW Pakistan, Geologica Vol.4: 47–68.

Khan SR (2000) Petrology and Geochemistry of a part of the Waziristan ophiolite complex NW Pakistan. Dissertation, Peshawar University: 253.

Knepper DH, Simpson SL (1975) Remote sensing in Geology and mineral resources of the Altiplano and Cordillera Occidental, Bolivia. USGS Bulletin: 47–55.

Mckinstry HE (1948) Mining geology. Englewood cliffs, New Jersey, Prentice Hall Inc: 407-428

Mudrova M (2010) Principal component analysis in image processing. Department of Computing & Control Engineering. https://pdfs.semanticscholar.org/76a7/fc9d87736c8383576865cf50403e53e74848.pdf

Sohail MT, Huang D, Bailey E et al (2013) Regulatory framework of mineral resources sector in Pakistan and investment proposal to Chinese companies in Pakistan. American Journal of Industrial and Business Management 3: 514.

Tou JT, Gonzalez RC (1974) Pattern recognition principles. New York, Addison-Wesley, Reading, MA: 377.

Intercontinental Geoinformation Days

igd.mersin.edu.tr

Mapping evapotranspiration with vegetation index-temperature difference method using the products of the moderate resolution imaging spectroradiometer

Ali Levent YAGCI *1

[1]*Gebze Technical University, Faculty, Department of Geomatics Engineering, Kocaeli, Turkey*

Keywords
Remote sensing
Evaporative Fraction
Evapotranspiration
NDVI
Land Surface Temperature
MODIS

ABSTRACT

Evapotranspiration (ET) is a crucial variable to monitor agricultural water consumption, map irrigated agriculture and identify agricultural droughts. ET maps can be used to analyze agricultural water use practices of farmers, identify irrigated farms and drought-stricken regions. In this study, a simple model capable of producing evaporative fraction (EF) and then ET from minimal remotely sensed and meteorological inputs in a trapezoidal framework is presented. So far, the model has successfully validated against ground data collected at three different eddy-covariance (ECOR) flux towers in the US. Overall, this methodology shows promise to estimate ET from field to regional scales in regions with limited data like Turkey.

1. INTRODUCTION

Evapotranspiration (ET) is the second largest component in water balance after precipitation and an indispensable surface variable to monitor agricultural water use and droughts (Anderson et al. 2013; Mueller et al. 2011). Therefore, monitoring ET is an immediate concern especially for a country like Turkey which agriculture heavily relies on water supply through irrigation to grow agricultural crops during dry summers.

ET is a combination of evaporation from soils and transpiration from plants. While surface soil moisture, surface available energy and atmospheric resistance to water vapor transport drive evaporation rate from soil, transpiration is controlled by a combination of factors including moisture availability in the plant's root zone, available energy, and atmospheric and canopy resistances to water vapor transport (Monteith 1965).

In recent years, remote sensing products and methods have become a promising tool to map spatially continuous ET information across the Earth's surface (Aksu and Arikan 2017) thanks to a key remotely sensed surface variable, Land Surface Temperature (T_s). T_s is a good indicator of plant stress caused by moisture deficiencies in the plant root-zone (Anderson and Kustas 2008). When soil moisture is not adequate to meet plant demands, stomata in the plant leaves is closed. Afterwards, photosynthesis and transpiration are slowed, thereby causing canopy temperature to rise. Elevated plant canopy temperatures, considered as a sign of non-transpiring vegetation, can be detected from space. Therefore, the ET models based on remotely sensed thermal data capitalize on these features of T_s to develop ET estimates from space.

2. MATERIALS and METHOD

2.1. Material

The 16-day NDVI composites obtained by the Moderate Resolution Imaging Spectroradiometer (MODIS) instrument onboard the Terra satellite as well as daily T_s products acquired by the MODIS instrument mounted on both the Terra and Aqua satellites were retrieved from the Land Processes Distributed Active Archive Center (LPDAAC; https://lpdaac.usgs.gov/). The vegetation products acquired by the MODIS instrument are in 1-km spatial resolution and found to be very consistent to represent vegetation information (Huete et al. 2002). In the same way, the errors of T_s products were generally within ±1 K according to validation with in situ T_s observations of various land-cover types such as bare soil, grassland, open water and rice fields around the world (Wan et al. 2002; Wang, Liang, and Meyers 2008).

* **Corresponding Author**

*(alyagci@gtu.edu.tr) ORCID ID 000 – 0003 – 1094 – 9204

Cite this study

Yagcı A L (2021). Mapping evapotranspiration with vegetation index-temperature difference method using the products of the moderate resolution imaging spectroradiometer. 2nd Intercontinental Geoinformation Days (IGD), 9-12, Mersin, Turkey

Daily minimum (T_{min}) and maximum (T_{max}) air temperatures were obtained from the Daily Surface Weather and Climatological Summaries (Daymet, Version 2) dataset (Thornton et al. 2014). Later, daily average air temperature (T_a) datasets were produced from daily T_{min} and T_{max} datasets by calculating the arithmetic mean of T_{min} and T_{max} .These products are in 1-km spatial resolution, as well.

2.2. Method

Moran et al. showed (1994) that the measurements of fractional vegetation cover (fr) and surface minus air temperature ($T_s - T_a$) would theoretically compose a trapezoidal shape (Fig. 1) and named the concept, vegetation index-temperature trapezoid (VITT). Going left to right within this shape, soil moisture conditions change from wet to dry. The edges of this shape represent hydrological extremes (wet and dry conditions). A computer program in Python programming language were written to locate the critical points, P1, P2, P3 and P4 as shown in Fig. 1. All the computation in the model were fully automated and it doesn't require human intervention. Detailed information about the model can be found in these works (Yagci et al. 2017; Yagci and Santanello 2018).

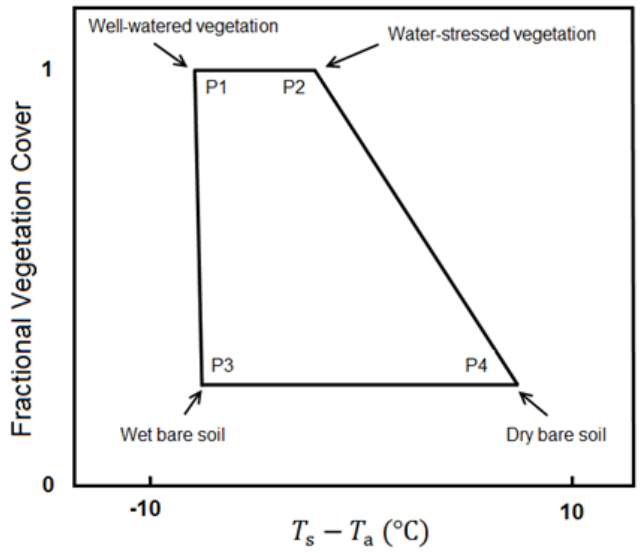

Figure 1. A theoretical trapezoidal space that would from the relationship between surface minus air temperature ($T_s - T_a$) and Fractional Vegetation Cover (fr)

2.3. Study Area

All three validation sites are in the US. The first site, US-Skr: Shark River Slough (Tower SRS-6) Everglades, is registered in AmeriFlux dataset. The flux tower is situated in the protected wilderness area by the Shark River in the Everglades National Park, Florida, U.S.A. The site is characterized by mangrove forests whose heights range from 15 to 20 m. The climate is humid subtropical and characterized by a mild, dry season (October–May) and warm, very wet season (June–September).

The other two validation sites, EF-14 and EF-21, in the US Southern Great Plains (SGP) were selected to validate model estimates. These sites were established by the Department of Energy's under the Atmospheric Radiation Measurement (ARM) program. The crop type at EF-14 site is winter wheat, while forest (e.g., mixed deciduous forest) dominates the EF-21 site. According to Köppen–Geiger classification, both validation sites are characterized by temperate humid climate with hot summers (Cfa).

3. RESULTS

The scatterplots that show validation done at flux towers, US-Skr, EF-14 and EF-21, are given in Fig. 2, Fig. 3 and Fig. 4, respectively. The observation count (N) and errors measures, such as Bias and Root Mean Square Error (RMSE) are shown in Table 1 and Table 2 for T_s products of MODIS-Terra and MODIS-Aqua, respectively. EF is a unitless measure, while ET has a unit of Watts per meter square (Wm^{-2}).

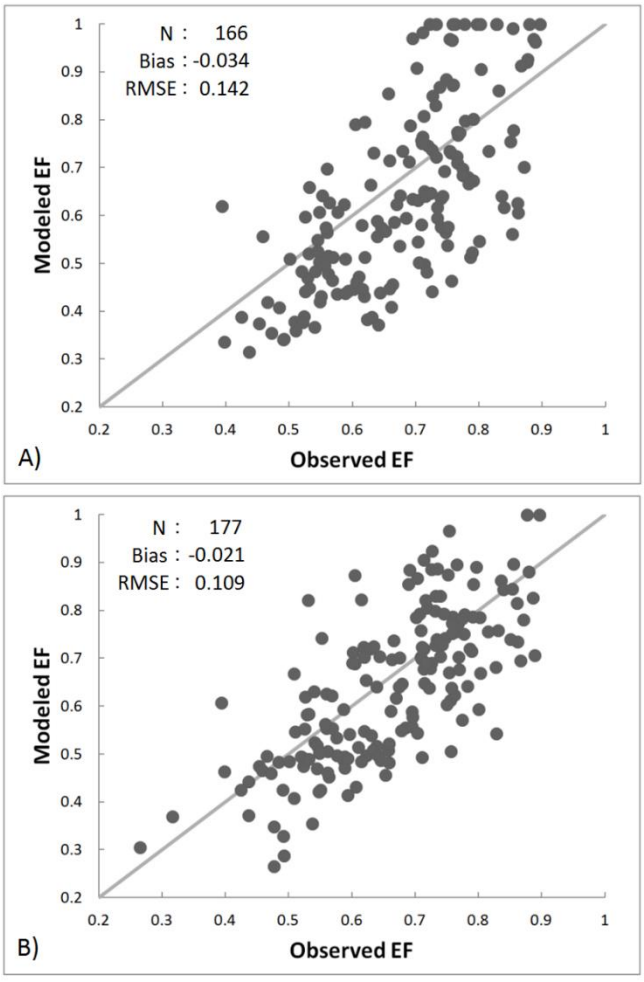

Figure 2. The validation of the Terra-based (A) and Aqua-based (B) evaporative fraction (EF) against eddy covariance tower-based EF at US-Skr in 2009.

The results indicates that the model was able to reproduce EF and ET variability at US-Skr station in 2009 (Fig. 2) as well as EF-14 and EF-21flux stations in 2011 (Fig. 3 and Fig. 4). Both EF and ET results when the model is run with the T_s products from MODIS-Aqua satellite, were more accurate in comparison to the model results of the T_s products from MODIS-Terra satellite. The MODIS instrument mounted on the Terra satellite collects morning surface temperature, while afternoon

surface temperature is acquired by the MODIS instrument onboard the Aqua satellite.

Table 1. Validation of EF (unitless) and ET (Wm^{-2}) using T_S products acquired by the MODIS-instrument on board the Terra satellite. EF validation was done at US-Skr site, while ET validation was carried out at EF-14 and EF-21 sites. N is the number of observations, while RMSE is root mean square error.

Site	N	Bias	RMSE
US-Skr	166	-0.034	0.142
EF-14	132	-4.648	0.532
EF-21	244	50.674	49.886

Table 2. Validation of EF (unitless) and ET (Wm^{-2}) using T_S products acquired by the MODIS-instrument on board the Aqua satellite. EF validation was done at US-Skr site, while ET validation was carried out at EF-14 and EF-21 sites. N is the number of observations, while RMSE is root mean square error.

Site	N	Bias	RMSE
US-Skr	177	-0.021	0.109
EF-14	135	2.237	-2.174
EF-21	249	39.304	34.902

4. DISCUSSION

Estimation ET is a crucial task to budget water in agriculture and monitor water consumption by farmers to irrigate their crops especially in countries which possess semi-arid climates like Turkey. It is not feasible and economical to keep account of agricultural water use using point-based tower observations. Satellite observations of vegetation condition and skin temperature of the Earth's surface are required to overcome this daunting task.

5. CONCLUSION

According to the validation carried out at the eddy covariance (ECOR) flux towers in two study areas with different climates characteristics across the US, the model was able to generate spatially continuous daily EF and ET from minimal remotely-sensed and meteorological inputs in a trapezoidal framework both cloud-free and partial-cloudy conditions.

The model outputs can be used to monitor agricultural water consumption, calibrate, and validate of hydrological, climate, and land surface models and track agricultural drought.

Given the models' success in the study areas across the US, the author was awarded a Career Development Program (CAREER) grant from the Scientific and Technological Research Council of Turkey (TÜBİTAK) to further test the model and produce ET maps in the study areas of Turkey.

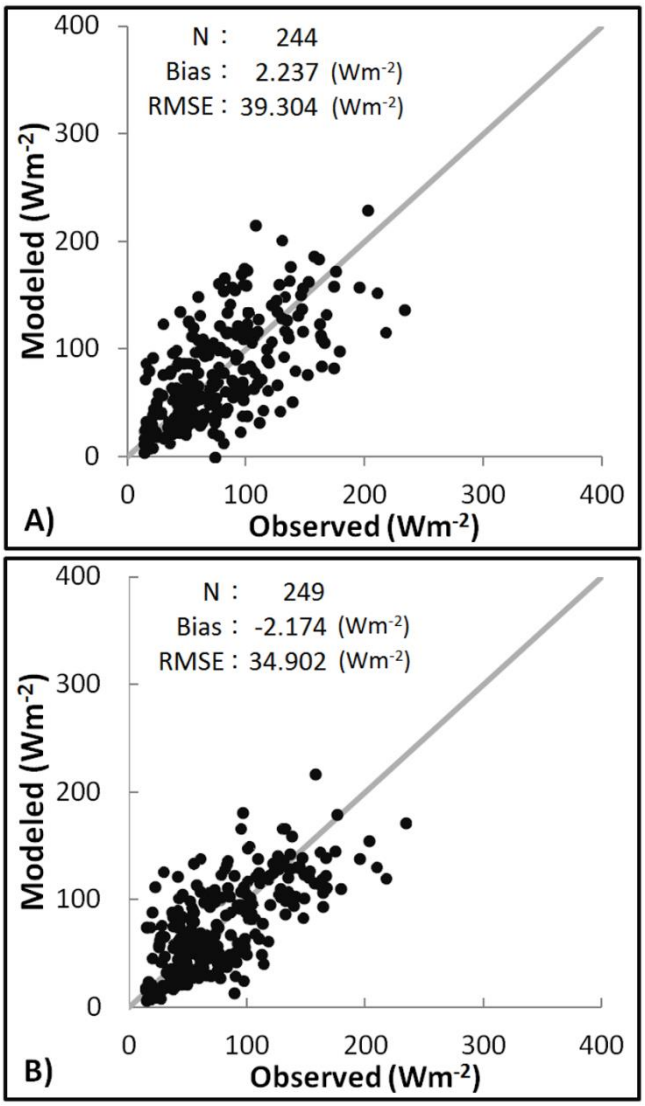

Figure 3. The validation of the Terra-based (A) and Aqua-based (B) evapotranspiration in Wm^{-2} units (ET) against eddy covariance tower-based ET at EF-14 in 2011.

ACKNOWLEDGEMENT

This research was supported by an appointment to the NASA Postdoctoral Program at the Goddard Space Flight Center (GSFC), administered by Universities Space Research Association under a contract, NNH15C048B. Additionally, funding support was provided by the U.S. Geological Survey (USGS) Land Remote Sensing and Land Change Science Programs.

Author would like to thank John W. Jones of USGS Eastern Geographic Science Center and Joseph A. Santanello of NASA-GSFC for their invaluable contributions to the development of this model and their guidance to make this research possible

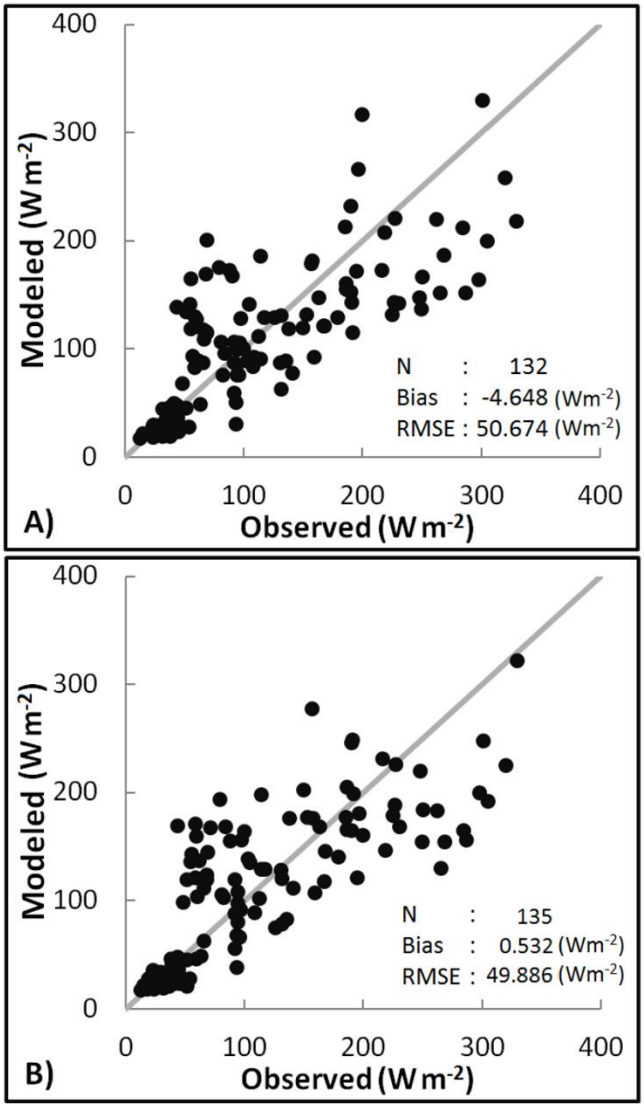

Figure 4. The validation of the Terra-based (A) and Aqua-based (B) evapotranspiration in Wm^{-2} units (ET) against eddy covariance tower-based LE at EF-21 in 2011.

REFERENCES

Aksu, Hakan, and Alparslan Arikan. 2017. "Satellite-Based Estimation of Actual Evapotranspiration in the Buyuk Menderes Basin, Turkey." *Hydrology Research* 48(2):559–70. doi: 10.2166/nh.2016.226.

Anderson, Martha C., Christopher Hain, Jason Otkin, Xiwu Zhan, Kingtse Mo, Mark Svoboda, Brian Wardlow, and Agustin Pimstein. 2013. "An Intercomparison of Drought Indicators Based on Thermal Remote Sensing and NLDAS-2 Simulations with U.S. Drought Monitor Classifications." *Journal of Hydrometeorology* 14(4):1035–56. doi: 10.1175/JHM-D-12-0140.1.

Anderson, Martha C., and William Kustas. 2008. "Thermal Remote Sensing of Drought and Evapotranspiration." *Eos, Transactions American Geophysical Union* 89(26):233–34. doi: 10.1029/2008EO260001.

Huete, A. R., K. Didan, T. Miura, E. P. Rodriguez, X. Gao, and L. G. Ferreira. 2002. "Overview of the Radiometric and Biophysical Performance of the MODIS Vegetation Indices." *Remote Sensing of Environment* 83(1–2):195–213. doi: 10.1016/S0034-4257(02)00096-2.

Monteith, J. L. 1965. "Evaporation and Environment." Pp. 205–34 in *Symposia of the Society for Experimental Biology*. Vol. 19.

Moran, M. S., T. R. Clarke, Y. Inoue, and A. Vidal. 1994. "Estimating Crop Water Deficit Using the Relation between Surface-Air Temperature and Spectral Vegetation Index." *Remote Sensing of Environment* 49(3):246–63. doi: 10.1016/0034-4257(94)90020-5.

Mueller, B., S. I. Seneviratne, C. Jimenez, T. Corti, M. Hirschi, G. Balsamo, P. Ciais, P. Dirmeyer, J. B. Fisher, Z. Guo, M. Jung, F. Maignan, M. F. McCabe, R. Reichle, M. Reichstein, M. Rodell, J. Sheffield, A. J. Teuling, K. Wang, E. F. Wood, and Y. Zhang. 2011. "Evaluation of Global Observations-Based Evapotranspiration Datasets and IPCC AR4 Simulations." *Geophysical Research Letters* 38(6):L06402. doi: 10.1029/2010GL046230.

Thornton, P. E., M. M. Thornton, B. W. Mayer, N. Wilhelmi, Y. Wei, R. Devarakonda, and R. B. Cook. 2014. "Daymet: Daily Surface Weather Data on a 1-Km Grid for North America, Version 2." *Oak Ridge National Laboratory Distributed Active Archive Center, Oak Ridge, Tennessee, USA*. doi: 10.3334/ORNLDAAC/1219.

Wan, Z., Yulin Zhang, Zhao-liang Li, Ruibo Wang, Vincent V. Salomonson, Arnaud Yves, Roland Bosseno, and Jean Francois Hanocq. 2002. "Preliminary Estimate of Calibration of the Moderate Resolution Imaging Spectroradiometer Thermal Infrared Data Using Lake Titicaca." *Remote Sensing of Environment* 80(3):497–515. doi: 10.1016/S0034-4257(01)00327-3.

Wang, Wenhui, Shunlin Liang, and Tilden Meyers. 2008. "Validating MODIS Land Surface Temperature Products Using Long-Term Nighttime Ground Measurements." *Remote Sensing of Environment* 112(3):623–35. doi: 10.1016/j.rse.2007.05.024.

Yagci, Ali Levent, and Joseph A. Santanello. 2018. "Estimating Evapotranspiration From Satellite Using Easily Obtainable Variables: A Case Study Over the Southern Great Plains, USA." *IEEE Journal of Selected Topics in Applied Earth Observations and Remote Sensing* 11(1):12–23. doi: 10.1109/JSTARS.2017.2753723.

Yagci, Ali Levent, Joseph A. Santanello, John W. Jones, and Jordan Barr. 2017. "Estimating Evaporative Fraction from Readily Obtainable Variables in Mangrove Forests of the Everglades, U.S.A." *International Journal of Remote Sensing* 38(14):3981–4007. doi: 10.1080/01431161.2017.1312033.

Intercontinental Geoinformation Days

igd.mersin.edu.tr

A medium-sized rainfall-induced landslide detection using L- and C-band SAR images: A comparative study in agricultural lands

Ayub Mohammadi [*1], **Khalil Valizadeh Kamran** [1], **Sadra Karimzadeh** [1,2,3], **Masashi Matsuoka** [3]

[1]*University of Tabriz, Department of Remote Sensing and GIS, Tabriz, Iran*
[2]*University of Tabriz, Institute of Environment, Tabriz, Iran*
[3]*Tokyo Institute of Technology, Department of Architecture and Building Engineering, Yokohama, Japan*

Keywords
Remote sensing
SAR data
Landslide
Gilan province
Iran

ABSTRACT

Because of landslides, rapid volume of materials fall or move along the steep slopes. This research consists of a comparative study for creating landslide inventory maps (LIM) in agricultural lands of Gilan province, Iran using the ALOS-2 PALSAR-2 and Sentinel-1 (both ascending and descending directions). A pixel-based RGB band combination model and interferometric synthetic aperture radar (InSAR) technique were used to detect the occurred landslides. The landslide was detected using ALOS-2 PALSAR-2, while, it was not detected using Sentinel-1. The google earth and GPS were employed to validate the study. The results showed the potential of L-band ALOS-2 PALSAR-2 compared to C-band Sentinel-1.

1. INTRODUCTION

Landslide is one of the geo-hazards in terms of damage (Schlögel et al., 2015). Landslides are almost happen everywhere on the Earth (Adriano et al., 2020; Bui et al., 2016). In Gilan province, landslide cause many damages to the agricultural lands (Moroor, 2020). Remote sensing technologies present the best methods for detecting post-disaster damage, including landslides (Adriano et al., 2020). SAR data have widely been used for landslide monitoring (Catani et al., 2005; García-Davalillo et al., 2014; Jebur et al., 2015; Strozzi et al., 2018). InSAR is a valuable technique for landslide inventory (Calabro et al., 2010; Zhao et al., 2012). The accurate identifying of landslides is vital for disaster response management (Adriano et al., 2020). Pixel-based RGB band combination method detects Landslides directly from the satellite data. The current study can be significant, because it compares either ascending or descending directions of Sentinel-1 (C-band) with ALOS-2 PALSAR-2 (L-band) for detecting an occurred landslide. Many researches have conducted landslide through different models and techniques such as convolutional network, hot-spot analysis, differential interferometric synthetic aperture radar (DInSAR), NDVI, random forest, InSAR (Chen et al., 2014; Furuta and Tomiyama, 2008; García-Davalillo et al., 2014; Jebur et al., 2015; Lv et al., 2020; Schlögel et al., 2015). The main objective of this study was to compare the suitability of Sentinel-1 and ALOS-2 PALSAR-2 on landslide detection in the agricultural lands of a part of Gilan Province, Iran (Figure 1).

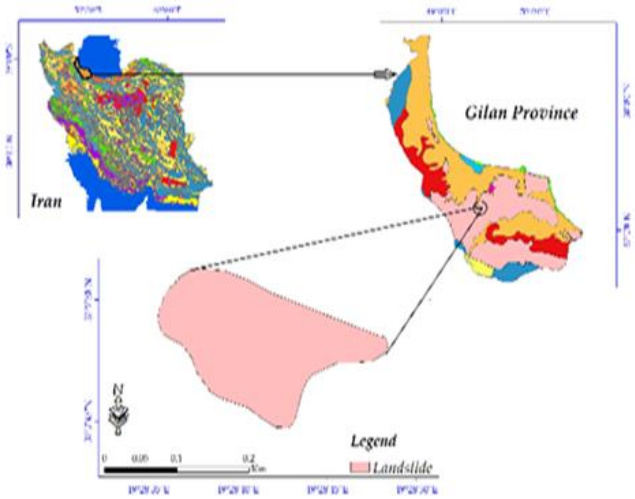

Figure 1. Geographical extent of the study

2. METHOD

2.1. Data Acquisition and Methodology

A pair image of ALOS-2 PALSAR-2 and Sentinel-1 (pre- and post-event) were acquired (date of the event 10 / 4 / 2020). Table 1 shows the attributes of the data used.

* **Corresponding Author**

*(mohammadi.ayub@tabrizu.ac.ir) ORCID ID 0000-0001-8848-8917
(valizadeh@tabrizu.ac.ir) ORCID ID 0000-0003-4648-842X
(sa.karimzadeh@tabrizu.ac.ir) ORCID ID 0000-0002-5645-0188
(matsuoka.m.ab@m.titech.ac.jp) ORCID ID 0000-0003-3061-5754

Cite this study

Mohammadi A, Kamran K V, Karimzadeh S, Matsuoka M (2021). A medium-sized rainfall-induced landslide detection using L- and C-band SAR images: A comparative study in agricultural lands. 2nd Intercontinental Geoinformation Days (IGD), 13-15, Mersin, Turkey

Table 1. Technical characteristics of the data used

Imagery	Orbit Type	Date acquired	Product
Sentinel-1	Ascending	01-04-2020 13-04-2020	SLC
	Descending	27-03-2020 20-04-2020	
ALOS-2 PALSAR-2	Ascending	29-01-2020 22-05-2020	SLC

The RGB methodology used in this study represents a series of pixels to detect the landslides. The processing steps is summarized in Figure 2. This flowchart is managed into three main sections of data used, preprocessing and output. In the pre-processing task, two operators of TOPS split and TOPS deburst (shown in orange color) belong only to Sentinel-1 data, while the other operators are common tasks for both ALOS-2 PALSAR-2 and Sentinel-1. For landslide detection using RGB band combination, intensity band of pre-event image was used for R window and intensity band of post-event for G window. Finally, GPS and the Google Earth images were applied for validation processes.

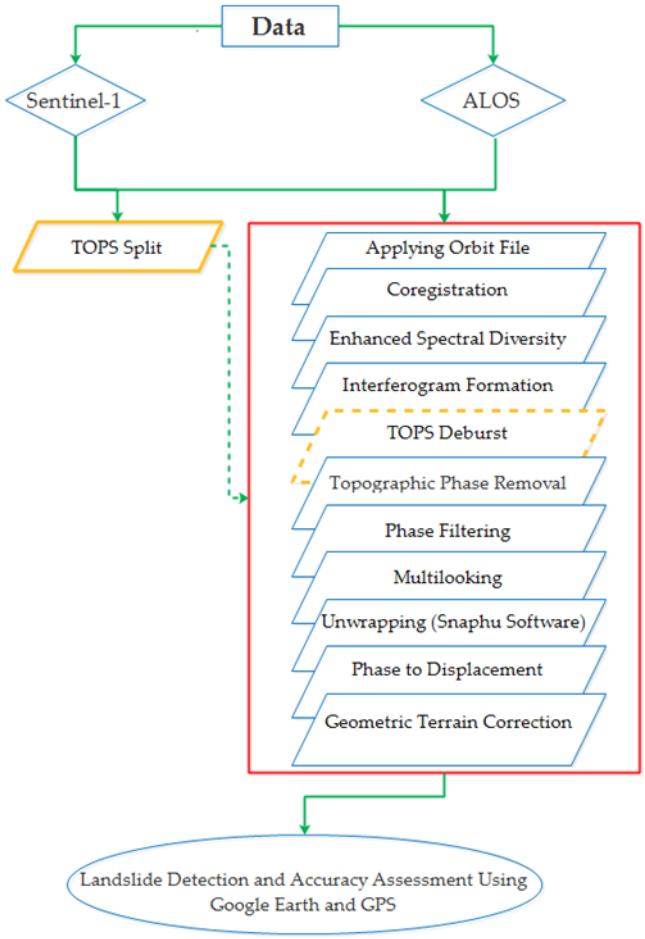

Figure 2. Methodology

3. RESULTS

3.1. Landslide Detection

Figure 3 shows the proposed RGB band combination of ALOS-2 PALSAR-2 data. The green color represents areas where the landslide occurred. It is worth mentioning that the yellow colors show the correctly co-registered pixels in both slave and master data.

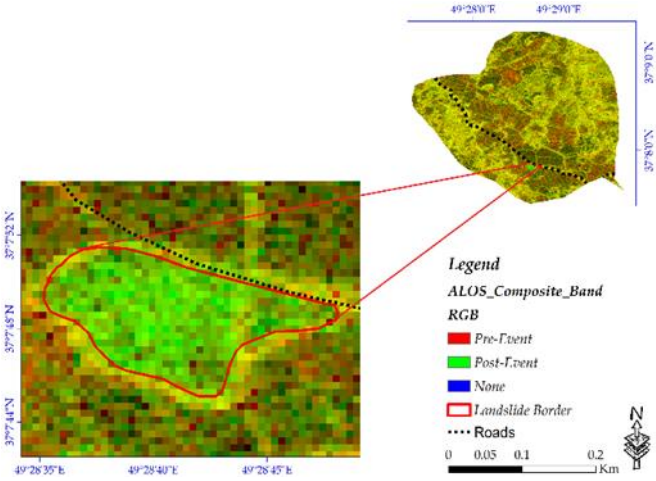

Figure 3. Landslide detection using ALOS-2 PALSAR-2

Figure 4 represents results for ascending and descending directions of Sentinel-1. Firstly, we performed the analysis for ascending direction, but no good finding was obtained. We thought that maybe it is because of the view angle; therefore, the operations were done on the descending direction as well. Unfortunately, it was not also capable of detecting the occurred landslide.

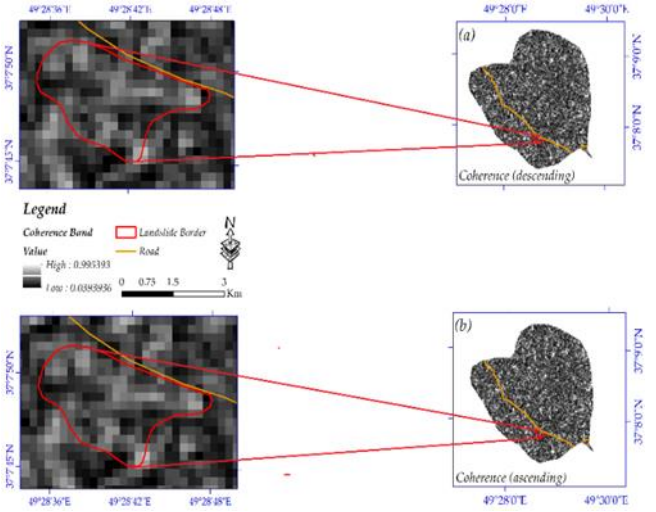

Figure 4. Landslide inventory using Sentinel-1 data; (a) descending and (b) ascending

3.2. Validation

Because, this study was focused only on one rainfall-induced landslide and it was occurred near to the main road; therefore, it was validated by GPS and the Google Earth as well (Figure 5).

4. DISCUSSION

We employed SAR satellite data of L- and C-bands of ALOS-2 PALSAR (wavelength 24 cm) and Sentinel-1 (wavelength 5.7 cm) images, respectively (Hein, 2003; Strozzi et al., 2018). Because of the physical situation of Gilan province, C- band cannot detect the occurred landslide, while L-band was able to detect it. Because of

smaller wavelength and penetration power into vegetation coverages, results from Sentinel-1 showed a lower quality than ALOS-2 PALSAR-2. The findings indicate that the technique is suitable for rapid response planning to such disasters using ALOS-2 PALSAR-2. On the other hand, applying C-band satellite data including Sentinel-1 for vegetated areas is a time-consuming effort.

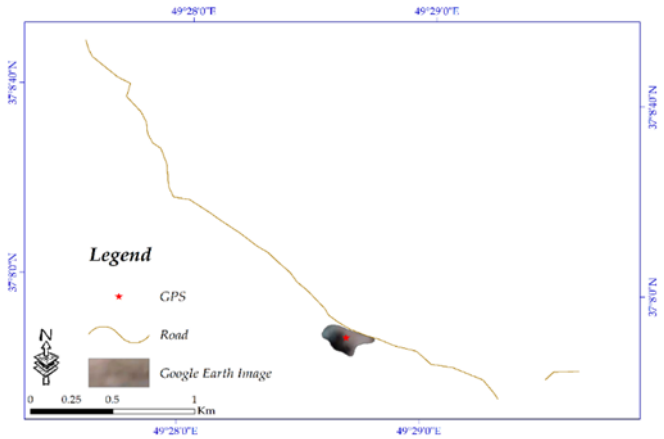

Figure 5. Validation using GPS and the Google Earth

5. CONCLUSION

InSAR and a pixel-based RGB band combination method were applied for detecting a rainfall-induced landslide in vegetated area of Gilan Province, Iran. ALOS-2 PALSAR-2 (L-band) and Sentinel-1 (C-band) were acquired and used to detect an occurred landslide in the study area. From ALOS-2 PALSAR-2 the landslide was identified, while C-band Sentinel-1 was not able to detect it. GPS and the Google Earth were applied to validate the results.

ACKNOWLEDGEMENT

Many thanks are given to the National Elites Foundation of Iran and the University of Tabriz for funding this research. Grant number: (No. 102/1670).

REFERENCES

Adriano, B., Yokoya, N., Miura, H., Matsuoka, M., Koshimura, S., (2020). A semiautomatic pixel-object method for detecting landslides using multitemporal ALOS-2 intensity images. Remote Sensing, 12(3), 561.

Bui, D.T., Tuan, T.A., Klempe, H., Pradhan, B., Revhaug, I., (2016). Spatial prediction models for shallow landslide hazards: a comparative assessment of the efficacy of support vector machines, artificial neural networks, kernel logistic regression, and logistic model tree. Landslides, 13(2), 361-378.

Calabro, M., Schmidt, D., Roering, J., (2010). An examination of seasonal deformation at the Portuguese Bend landslide, southern California, using radar interferometry. Journal of Geophysical Research: Earth Surface, 115(F2).

Catani, F., Farina, P., Moretti, S., Nico, G., Strozzi, T., (2005). On the application of SAR interferometry to geomorphological studies: estimation of landform attributes and mass movements. Geomorphology, 66(1-4), 119-131.

Chen, W., Li, X., Wang, Y., Chen, G., Liu, S., (2014). Forested landslide detection using LiDAR data and the random forest algorithm: A case study of the Three Gorges, China. Remote sensing of environment, 152, 291-301.

Furuta, R., Tomiyama, N., (2008). A Study of Detection of Landslide Disasters due to the Pakistan Earthquake using ALOS data. PRISM, 2008(11/07).

García-Davalillo, J.C., Herrera, G., Notti, D., Strozzi, T., Álvarez-Fernández, I., (2014). DInSAR analysis of ALOS PALSAR images for the assessment of very slow landslides: the Tena Valley case study. Landslides, 11(2), 225-246.

Hein, A. Processing of SAR data: Springer, (2003).

Jebur, M.N., Pradhan, B., Tehrany, M.S., (2015). Using ALOS PALSAR derived high-resolution DInSAR to detect slow-moving landslides in tropical forest: Cameron Highlands, Malaysia. Geomatics, Natural Hazards and Risk, 6(8), 741-759.

Lv, Z., Liu, T., Kong, X., Shi, C., Benediktsson, J.A., (2020). Landslide Inventory Mapping with Bitemporal Aerial Remote Sensing Images Based on the Dual-path Full Convolutional Network. IEEE Journal of Selected Topics in Applied Earth Observations and Remote Sensing.

Moroor, (2020). Human factors, the cause of landslides in Gilan. https://moroor.org/

Schlögel, R., Doubre, C., Malet, J.-P., Masson, F., (2015). Landslide deformation monitoring with ALOS/PALSAR imagery: A D-InSAR geomorphological interpretation method. Geomorphology, 231, 314-330.

Strozzi, T., Klimeš, J., Frey, H., Caduff, R., Huggel, C., Wegmüller, U., Rapre, A.C., (2018). Satellite SAR interferometry for the improved assessment of the state of activity of landslides: A case study from the Cordilleras of Peru. Remote sensing of environment, 217, 111-125.

Zhao, C., Lu, Z., Zhang, Q., de La Fuente, J., (2012). Large-area landslide detection and monitoring with ALOS/PALSAR imagery data over Northern California and Southern Oregon, USA. Remote Sensing of Environment, 124, 348-359.

Intercontinental Geoinformation Days

igd.mersin.edu.tr

Effect of first wave COVID-19 outbreak lockdown measures on satellite-based tropospheric NO_2 over Mersin Province, Turkey

Fatemeh Ghasempour [1], Aliihsan Sekertekin [*2], Hakan Kutoglu [1]

[1]*Bulent Ecevit University, Department of Geomatics Engineering, Zonguldak, Turkey*
[2]*Cukurova University, Department of Geomatics Engineering, Adana, Turkey*

Keywords
Remote sensing
COVID-19
GEE
Sentinel 5P
NO_2

ABSTRACT

In recent years, greenhouse-trace gases pollution is one of challenging problems all over the world. Due to the coronavirus (COVID-19) epidemic in the world, almost all countries implemented some restrictions that reduced human activities in cities and industries. As a result of these restrictions, an opportunity occurred to monitor the changes in anthropogenic (human-made) air quality. Among the other air pollutants, NO_2 is one of the important trace gases on the atmosphere which can arise with anthropogenic and natural sources. This study investigated NO_2 pollution derived from Sentinel-5P satellite associated with the first wave lockdown of COVID-19 pandemic over Mersin city, located at the Mediterranean coast of Southern Turkey. The tropospheric NO_2 vertical column density (VCD) data were derived from TROPOMI instrument onboard the Sentinel 5P satellite, and Google Erath Engine (GEE) platform was used for the analyses. The results showed that the substantial 35 % reduction in NO_2 concentration was observed over Mersin when comparing the lockdown time in 2020 and the corresponding days in 2019.

1. INTRODUCTION

Nitrogen dioxide (NO_2), as one of six common air pollutants listed by World Health Organization (WHO) (Bert and Stephen 1999; Oo et al. 2021), is a short life pollutant in the atmosphere (Dutta et al. 2021). Moreover, its concentration rises due to the increase in the anthropogenic and natural sources of emission comprising industrial activities, the fossil fuel combustion in land-water-space transports and thermal power plants (Center 1999; Hilboll et al. 2017), lightning and forest fires (Smith 2020; Solomon 2007), and open biomass burning (Biswal et al. 2021; Castellanos et al. 2014).

The COVID-19 outbreak emerged in Wuhan, China, in late 2019 and it was extremely spread around the world. The first case of COVID-19 in Turkey reported on March 11 2020 (Sahin et al. 2021; Sarialioglu Gungor et al. 2021). Then, the information about the COVID-19 was always announced and up-to-dated by the Ministry of Health-Turkey. However, the partial restrictions formally started on April 2020.

Since COVID-19 restrictions made it possible to monitor the anthropogenic variations in air quality, many researchers investigated the spatiotemporal changes in NO_2 concentration over different areas of the world during the nationwide lockdown of COVID-19 outbreak with remote sensing techniques (Biswal et al. 2021; Dutta et al. 2021; Ghahremanloo et al. 2021; Naqvi et al. 2021; Nichol et al. 2020; Oo et al. 2021; Roşu et al. 2021; Smith 2020).

The aim of this study is to examine the changes in satellite-based tropospheric NO_2 vertical column density (VCD) during the first wave of the lockdown over Mersin Province, Turkey. The tropospheric NO_2 data were derived from The TROPOspheric Monitoring Instrument (TROPOMI) onboard the Sentinel 5P satellite, and we used Google Erath Engine (GEE) platform with Java script API capability for the analyses. Since Turkish Government did not apply full lockdown, we considered only lockdown days of 2020 (weekends combined with official and religious holidays presented in Figure 1) in the analysis rather than presenting average monthly images. Then, the lockdown days of 2020 were compared with the corresponding days (considering the same weekend periods) in 2019.

* **Corresponding Author**

*(f.ghasempour2019@gmail.com) ORCID ID 0000-0002-7078-431X
(asekertekin@cu.edu.tr) ORCID ID 0000-0002-4715-5160
(kutogluh@hotmail.com) ORCID ID 0000-0001-6587-3417

Cite this study

Ghasempour F, Sekertekin A & Kutoglu H (2021). Effect of first wave COVID-19 outbreak lockdown measures on satellite-based tropospheric NO_2 over Mersin Province, Turkey. 2nd Intercontinental Geoinformation Days (IGD), 16-19, Mersin, Turkey

2. STUDY AREA

Mersin, formerly known as İçel province with having 13 district and 1,868,757 populations (https://www.nufusu.com/), is eleventh most populous cities located on the Mediterranean coast of Southern Turkey (Figure 1: in red boundary). Therefore, it includes the Mediterranean climate and the subtropical climate. On the other hand, there is Turkey's largest seaport in this city.

3. DATA USED AND METHOD

The TROPOspheric Monitoring Instrument (TROPOMI) onboard Sentinel-5P, the first Copernicus mission, was launched on 13 October 2017 (Butz et al. 2012). The TROPOMI as a passive remote sensing instrument is an advanced multispectral imaging spectrometer with nadir-viewing and wavelengths of Ultraviolet-Visible, Near Infrared and Shortwave Infrared. Besides, it is monitoring several atmospheric gases density in different parts of the electromagnetic spectrum. It works in a cross direction, with ~ 2600 km swath width over the ground surface. The nadir view for NO_2 product is 7x3.5 km^2 (Veefkind et al. 2012). Many researchers have studied monitoring and retrieval of NO_2 pollutants using Sentinel-5P TROPOMI data (Wang et al. 2021; Zheng et al. 2019).

Fig. 1 illustrates the methodology used in this study in Google Earth Engine (GEE). GEE Java script API was utilized for downloading TROPOMI-based tropospheric NO_2 raster data (COPERNICUS/S5P/OFFL/L3_NO2), preprocessing, visualization, analyzing the NO_2 level changes, and exporting for the first wave periods.

Firstly, we considered the first wave lockdown period around Mersin on specific days in April and May 2020 and also the nearest equivalent days in 2019. The days in 2019 and 2020 do not match since we considered related weekend periods. For example, 13-14 April 2019 is the second weekend in 2019, while 11-12 April 2020 is the corresponding second weekend in 2020.

Here the preprocessing step was the most substantial stage including satellite local pass time(s) filtering and cloudy pixel masking (Fioletov et al. 2020; Ialongo et al. 2020), moreover, to produce one mosaicked image for each day. Eventually, after calculating mean daily images, to create NO_2 maps of the first wave, we generated two mean images for 2019 and 2020.

4. RESULTS

Fig. 2 shows the spatial distribution of mean tropospheric NO_2 vertical column density (VCD) on Mersin at first wave duration for 2020 and corresponding days in 2019. With comparing two maps in 2019 and 2020, we observed a significant reduction, especially in the southeastern part of the interested region, which is the city center of Mersin Province. We also extracted statistical results from mean images during the first wave lockdown in Table 1. As seen in the Table 1, the variation in column density ranged between $-0.351*10^{15}$ molec/cm^2 to $5.238*10^{15}$ molec/cm^2 with a mean of $1.298*10^{15}$ molec/cm^2 and between $-0.557*10^{15}$ molec/cm^2 to $3.936*10^{15}$ molec/cm^2 with a mean of $0.847*10^{15}$ molec/cm^2 in 2019 and 2020, respectively. The minimum and maximum values were decreased from $-0.351*10^{15}$ molec/cm^2 to $-0.557*10^{15}$ molec/cm^2 and $5.238*10^{15}$ molec/cm^2 to $3.936*10^{15}$ molec/cm^2 respectively. In addition, we indicated the change rate (CR) by -0.35 value compared to the according days in 2019. The whisker box plot is displayed using the extracted statistical description of NO_2 VCD for 2019 and 2020 in Fig. 3. As seen in Fig. 3, median, quartile 25% and 75% values are closer to minimum value that these demonstrated a higher value of NO_2 concentration in some of geographical areas. Figure 3 also proves that the height of the boxes indicates the reduction of NO_2 VDC in 2020 lockdown days compared to the same period in the previous year 2019.

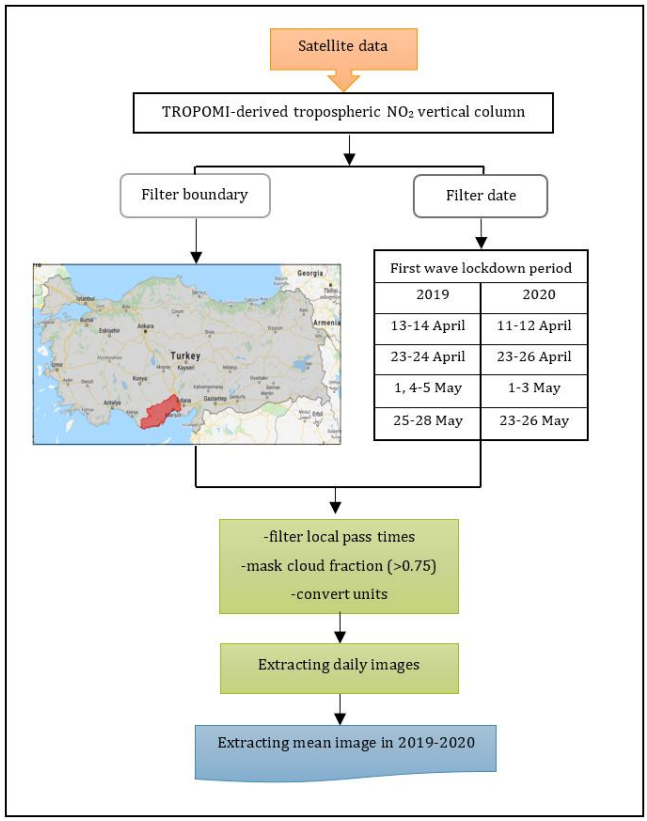

Figure 1. The workflow of the used methodology

Table 1. Descriptive statistics of NO2 concentration by year. The values should be multiplied by 10^{15} except for change rate (CR)

Year	2019	2020
Min	-0.351	-0.557
Q25	0.828	0.578
Median	1.140	0.766
Mean	1.298	0.847
Q75	1.484	1.015
Max	5.238	3.936
STD	0.775	0.486
CR	-0.35	

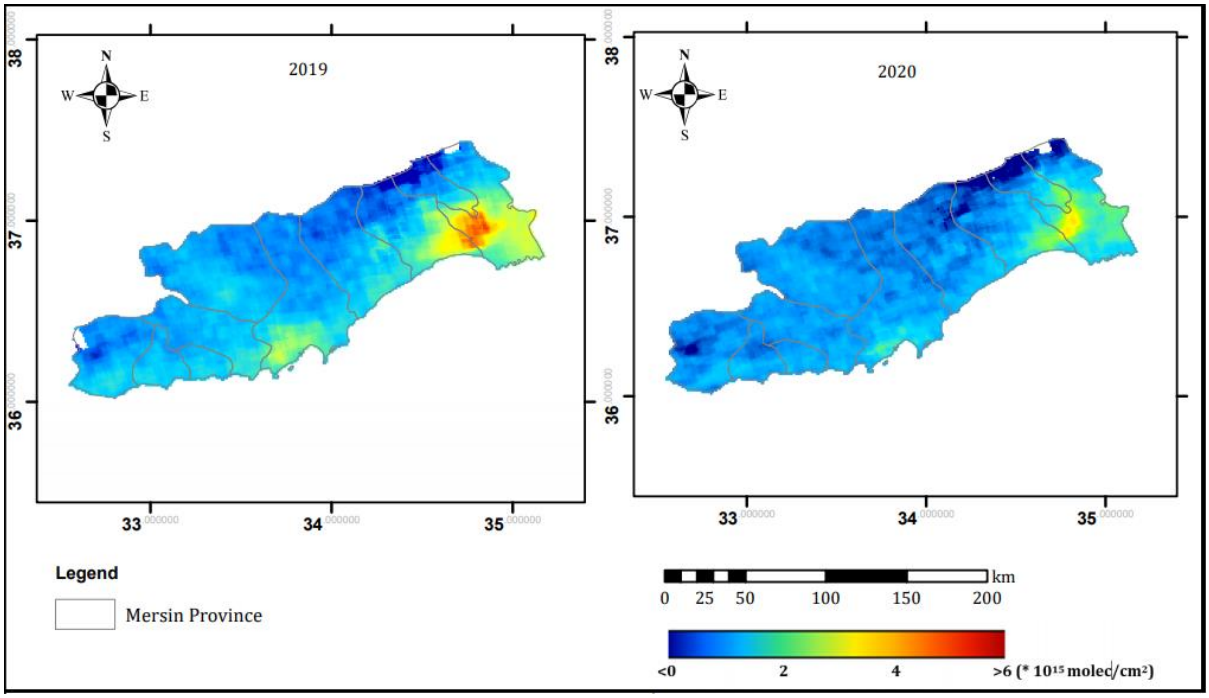

Figure 2. Comparison the average NO_2 VCD in the troposphere first wave lockdown period in 2019 and 2020

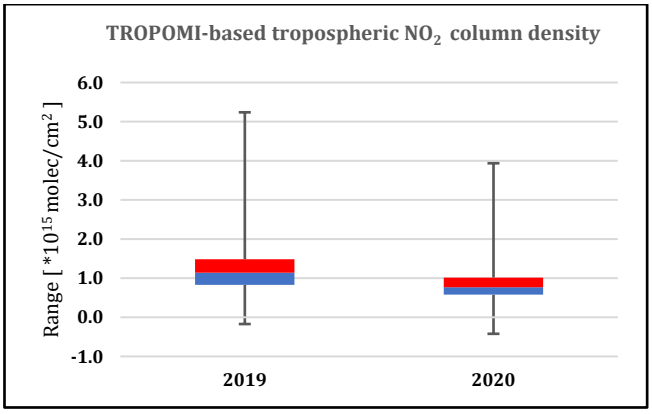

Figure 3. Whisker box plot for mean images derived from the first wave lockdown period in 2020 and previous year 2019

5. DISCUSSION

The derived results represented an important reduction over Mersin with comparing the first wave lockdown on special days of April-May in 2019-2020. However, the possible effect of the meteorological conditions on the air pollutants was ignored in this preliminary study. Besides, due to the fact that having no air quality monitoring station observation in 2019-2020 in the study area, we could not compare TROPOMI-derived NO_2 VCD and NO_2 ground station concentration.

6. CONCLUSION

In this study, we investigated the change of NO_2 VCD concentration as an air pollutant in the first wave lockdown duration over Mersin city in Turkey. We used the NO_2 product derived from TROPOMI instrument onboard Sentinel 5P. Moreover, all operations such as importing the raster data, preprocessing, visualizing, calculating and exporting were conducted using GEE Java script API. Results represented a significant decrease about 35% over the study area in first wave lockdown period times in 2020 comparing with the according days in 2019. These changes were observed mostly in southeast areas, around the city center, and a part of south of Mersin, close to Silifke district. As a future work, we are going to investigate the relationship between the NO_2 derived from Sentinel 5P images and the meteorological parameters.

ACKNOWLEDGEMENT

The authors wish to thank Google Earth Engine (https://earthengine.google.com/), for providing the needed data for this study.

REFERENCES

Bert B & Stephen H. (1999). Air pollution and health, Air Pollut. Heal, 360, 115-148.

Biswal A, Singh V, Singh S, Kesarkar A P, Ravindra K, Sokhi R S, Chipperfield M P, Dhomse S S, Pope R J & Singh T. (2021). COVID-19 lockdown-induced changes in NO 2 levels across India observed by multi-satellite and surface observations. Atmospheric Chemistry and Physics, 21(6), 5235-5251.

Butz A, Galli A, Hasekamp O, Landgraf J, Tol P & Aben I. (2012). TROPOMI aboard Sentinel-5 Precursor: Prospective performance of CH4 retrievals for aerosol and cirrus loaded atmospheres. Remote Sensing of Environment, 120, 267-276.

Castellanos P, Boersma K & Van Der Werf G. (2014). Satellite observations indicate substantial spatiotemporal variability in biomass burning NOx emission factors for South America. Atmospheric Chemistry and Physics, 14(8), 3929-3943.

Center C A T (1999). Nitrogen Oxides (NOx): Why and How they are controlled: Research Triangle Park ^ eNorth Carolina North Carolina.

Dutta V, Kumar S & Dubey D. (2021). Recent advances in satellite mapping of global air quality: evidences

during COVID-19 pandemic. Environmental Sustainability, 1-19.

Fioletov V, McLinden C A, Griffin D, Theys N, Loyola D G, Hedelt P, Krotkov N A & Li C. (2020). Anthropogenic and volcanic point source SO 2 emissions derived from TROPOMI on board Sentinel-5 Precursor: first results. Atmospheric Chemistry and Physics, 20(9), 5591-5607.

Ghahremanloo M, Lops Y, Choi Y & Mousavinezhad S. (2021). Impact of the COVID-19 outbreak on air pollution levels in East Asia. Science of The Total Environment, 754, 142226.

Hilboll A, Richter A & Burrows J P. (2017). NO2 pollution over India observed from space–the impact of rapid economic growth, and a recent decline. Atmospheric Chemistry and Physics Discussions, 1-18.

Ialongo I, Virta H, Eskes H, Hovila J & Douros J. (2020). Comparison of TROPOMI/Sentinel-5 Precursor NO 2 observations with ground-based measurements in Helsinki. Atmospheric Measurement Techniques, 13(1), 205-218.

Naqvi H R, Mutreja G, Shakeel A & Siddiqui M A. (2021). Spatio-temporal analysis of air quality and its relationship with major COVID-19 hotspot places in India. Remote Sensing Applications: Society and Environment, 22, 100473.

Nichol J E, Bilal M, Ali M & Qiu Z. (2020). Air pollution scenario over China during COVID-19. Remote Sensing, 12(13), 2100.

Oo T K, Arunrat N, Kongsurakan P, Sereenonchai S & Wang C. (2021). Nitrogen Dioxide (NO2) level changes during the control of COVID-19 pandemic in Thailand. Aerosol and Air Quality Research, 21, 1-0.

Roşu A, Constantin D-E, Voiculescu M, Arseni M, Roşu B, Merlaud A, Van Roozendael M & Georgescu P L. (2021). Assessment of NO2 Pollution Level during the COVID-19 Lockdown in a Romanian City. International Journal of Environmental Research and Public Health, 18(2), 544.

Sahin S K, Arslan E, Atalay Ü M, Demir B, Elboga G & Altındağ A. (2021). Psychological impact of COVID-19 outbreak on health workers in a university hospital in Turkey. Psychology, Health & Medicine, 1-10.

Sarialioglu Gungor A, Donmez N & Uslu Y S. (2021). Knowledge, stress levels, and clinical practice modifications of Turkish dentists due to COVID-19: a survey study. Brazilian Oral Research, 35.

Smith J (2020). Coronavirus Lockdowns and the Impact on Global Nitrogen Dioxide.

Solomon S. (2007). IPCC (2007): Climate change the physical science basis. Paper presented at the Agu fall meeting abstracts.

Veefkind J, Aben I, McMullan K, Förster H, De Vries J, Otter G, Claas J, Eskes H, De Haan J & Kleipool Q. (2012). TROPOMI on the ESA Sentinel-5 Precursor: A GMES mission for global observations of the atmospheric composition for climate, air quality and ozone layer applications. Remote sensing of environment, 120, 70-83.

Wang Z, Uno I, Yumimoto K, Itahashi S, Chen X, Yang W & Wang Z. (2021). Impacts of COVID-19 lockdown, Spring Festival and meteorology on the NO2 variations in early 2020 over China based on in-situ observations, satellite retrievals and model simulations. Atmospheric Environment, 244, 117972.

Zheng Z, Yang Z, Wu Z & Marinello F. (2019). Spatial variation of NO2 and its impact factors in China: An application of sentinel-5P products. Remote Sensing, 11(16), 1939.

Intercontinental Geoinformation Days

igd.mersin.edu.tr

The estimation of the Skyglow by using the nighttime light satellite imagery in Northern Thailand

Anurak Chakpor*[1,2,4] Xi Li*[2] Vanisa Surapipith*[3] Phattraporn Soythong*[1] Tanita Suepa*[4]

[1]*Burapha University, Geoinformatics, Chonburi, Thailand*
[2]*Wuhan University, State Key Laboratory of Information Engineering in Surveying, Mapping and Remote Sensing, Wuhan, China*
[3]*National Astronomical Research Institute of Thailand (Public Organization), Chiang Mai, Thailand*
[4]*Geo-Informatics and Space Technology Development Agency, SCGI: Sirindhorn Center for Geo-Informatics, Chonburi, Thailand*

Keywords
Skyglow
Nighttime Light
Light Pollution
Spatial Distribution
Bortle's scale

ABSTRACT

The skyglow is scattering from natural light sources and non-natural light, which maximizes night sky brightness, resulting in visual impairment and star visualization loss. This phenomenon leads to an impoverished environment and surroundings. SNPP - VIIRS Day/Night Band (DNB) is a source for monitoring skyglow phenomena and Nighttime Light (NTL) spatial expansion trend in northern Thailand. A scatter plot model was applied to the data. The sky brightness and radiance from SNPP-VIIRS exhibited R2 values of 0.9488. And the correlation of sky brightness in summer and winter had a value of 0.888. During summer, the Aerosol Optical Depth (AOD) value increased by 2.3-times and the natural sky rose to 1 times magnitude brighter than winter. In contrast, the amount of brightness in the city area decreased, resulting from the NTL released skyward by luminaires with aerosol particles, generating a luminous background. This research estimates and illustrating the skyglow map for a more straightforward astronomical interpretation. Consequently, Bortle's map and the skyglow profile are crucial research tools for monitoring light pollution and understanding the skyglow characteristics of skyglow which varies upon the specific AOD value, a substantial amount of aerosol and intensity of light directed upward.

1. INTRODUCTION

Interestingly, less than 10 decades ago, the human could see a spectacular starry night sky with the naked eye. Nowadays, people around the world have never seen the Milky Way from their residences, especially in the big city. The massive amount of artificial light leads to visual impairment of seeing the starry night. Furthermore, there are substantial impacts on the environment.

Light pollution was a significant factor for astronomical observation in the second half of the 20 century when finding new locations for the astronomical observatories. The astronomers have addressed and concerned about the skyglow because it can limit human visual acuity to see the celestial objects. Also, the skyglow can brighten up the dark sky areas, which decreases the contrast of stars or other celestial objects against the dark sky background.

This concept demonstration study uses the Visible/Infrared Imager/Radiometer Suite (VIIRS) Day/Night Band (DNB) observations on the Suomi National Polar-orbiting Partnership (SNPP) satellite data. The method is applied for retrieving Aerosol Optical Depth (AOD)(τ) (Johnson, Zhang et al. 2013), utilizing the contrast among designated areas and artificial surface light data of the NTL satellite over the north of Thailand. Due to the summer situation, open biomass burning, including forest, bush and field fires, caused air pollution in northern Thailand. Most Northern Thailand was severely affected by smoke-haze pollution episodes caused by the emissions of forest and crop fires (Supasri, Itsubo et al. 2020)

Therefore, this research emphasizes estimating and illustrating the skyglow map from NTL satellite imagery and determining the correlation between the radiance values of the VIIRS DNB image and sky brightness in the magnitude unit. This study expresses the differences in the sky brightness in summer and winter by means of the Bortle's scale and skyglow profile.

2. METHOD

2.1 Study Area

In northern Thailand, the growth of urban areas of Chiang Mai, Chiang Rai, Lampang, etc. were selected to

* **Corresponding Author**

*(anurak@narit.or.th) ORCID ID 0000-0002-0876-1889
(lixi@whu.edu.cn) ORCID ID 0000-0003-0788-5692
(vanisa@narit.or.th) ORCID ID 0000-0002-4647-4493
(phattraporn@go.buu.ac.th) ORCID ID 0000-0002-6617-2257
(tanita@gistda.or.th) ORCID ID 0000-0002-5560-0965

Cite this study

Chakpor A, Li X, Surapipith V, Soythong P & Suepa T (2021). The estimation of the Skyglow by using the nighttime light satellite imagery in Northern Thailand. 2nd Intercontinental Geoinformation Days (IGD), 20-23, Mersin, Turkey

be the study area. Satellite imagery products from 2014 to 2019 were analyzed. By focusing on Chiang Mai, were recognized as a capital city of Northern Thailand

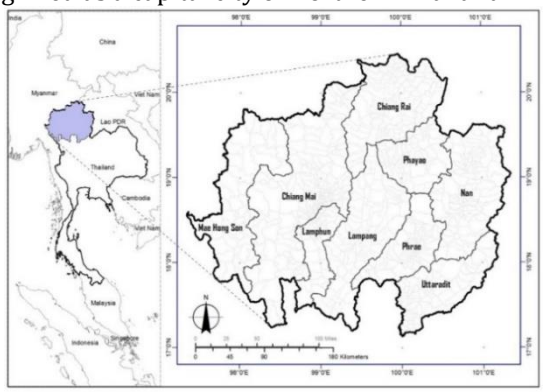

Figure 1. Map of studying area in Northern Thailand

2.2 Data collection step

Data collecting and data preprocessing are study methods for diagnosing information and supporting this research. The correction data were obtained from the NOAA and NASA Comprehensive Large Array-Data Google Earth Engine (GEE) site. The datasets were used to study the skyglow and dark sky. The SNPP/ VIIRS datasets were also downloaded and preprocessed in GEE by means of filling gap correction, mosaic image, re-projection, resampling, and co-registration to parallels with The NTL from VIIRS DNB and MODIS AOD product. Data from 2014 to 2019 were downloaded to analyze the relationship between the NTL radiance and AOD at 500 m resolution(Wang, Mu et al. 2020).

Table 1. Satellite imagery information

Imagery	Platform	Instrument	Image Resolution	Sensor Resolution
DNB	SNPP	VIIRS	500 m	750 m
AOD (550nm)	SNPP	VIIRS	500 m	750 m

2.3 Converting The VIIRS-DNB Image Data to Estimated Astronomical Units

The correspondence between VIIRS-DNB and SQM (de Miguel, Kyba et al. 2020) is quite essential to estimate the sky brightness. Typically, nW / cm^2 * sr is a SI radiometry unit for radiance. Radiance is radiant flux emitted, reflected, transmitted and received by a surface per unit solid, angle per unit projected area for satellite imagery data. Radiance can compare the raster of data from the sky's brightness measurement using the Sky Quality Meter (SQM) device to calculate it in units of mag/$arcsec^2$. The SQM is a device to measure the light of the incident sky on the CCD sensor and measure the number of photons against the standard value. Collecting the brightness quality data of the observed celestial area is helpful in studying the changes in the brightness of the sky. That makes the instrumentation accurate in international system units of astronomy.

The VIIRS DNB image's radiance values are relationships to brightness values using the following Alejandro Sanchez de Miguel's equation.

$$S = 20.0 - (1.9 * Log (VIIRS\ DNB)) \quad (1)$$

S is sky brightness in the magnitude unit. To convert the pixel value of VIIRS-DNB image data to mag/$arcsec^2$ in the astronomical unit for the analysis of the data in NTL satellite imagery.

2.4 Spatial Distribution

The spatial structure and variability of NTL were analyzed using geostatistical methods. Geostatistics analysis uses the 6-year mean values of the sky brightness were computed across the study area to analyze the spatial patterns (Suepa, Qi et al. 2016) of the spatio-temporal trends of NTL. In this research, NTL data were analyzed the brightness mean deviation by raster calculation of NTL monthly data using QGIS software to reduce the data between 2014 and 2019.

2.5 Bortle's scale

The Bortle's Scale, a nine-class numerical scale, is acknowledged as a technique used to estimate the surface sky brightness from the observation ground point during the night. Astronomically, it measures the observational capabilities of celestial objects and the intervention that occurred by light pollution. John E. Bortle (Bortle 2001) built the scale and published it in 2001. The scale clearly classifies from level 1, as the darkest sky in the world, up to level 9, the brightest sky in the city center. In the current study, the Bortle's Scale was criticized for the reliable results and the usefulness for classifying a separate map of the sky's brightness levels. The chart below shows Bortle's descriptive explanation of each level. Every single level differs from the one beside it, such as in Figure 2.

Figure 2. The Bortle's show the night sky's brightness by compared with the observational area of the constellations

2.6 Scatter Plots with Regression Model

The scatter plot model was used to evaluate the brightness's correlation in modelling the skyglow between the winter sky brightness data and the summer sky brightness data. This model also performed a regression analysis for quantifying the relationship between the two-period data (Li, Xu et al. 2013).

3. RESULTS

3.1 Skyglow Map

This experiment's results revealed the converting of the radiance from the VIIRS DNB satellite imagery to the universal astronomical sky brightness (mag/ $arcsec^2$) show in Figure 3.

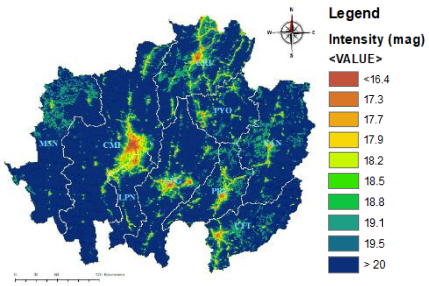

Figure 3. Optimized the nighttime light map for estimating the skyglow over northern Thailand. on December 11, 2019

The map shows the brightness (mag/arcsec ^{2}) of the night sky in northern Thailand. The sky in urban areas of Northern Thailand, specifically Chiang Mai, Chiang Rai, Lampang, Phrae, Uttaradit Phayao etc., was most brilliantly lit, approximately 16 mag/arcsec^2. In contrast, the night sky brightness in rural and forest areas was about 18 mag/arcsec^2 and more than 20 mag/arcsec^2, respectively.

3.2 Trend Analysis of NTL

The diagram in Figure 4 showed the Spatial Distribution NTL lighting. It presented the trends between 2014 and 2019, with bright tones representing the NTL change in more brilliant. In contrast, Dark tones show a dimmed light area. By the trend of changes since 2014, the spatial area has changed a lot. The urban area is much brighter than other areas. Chiang Mai Province tends to have the most changes in the northern provinces of Thailand.

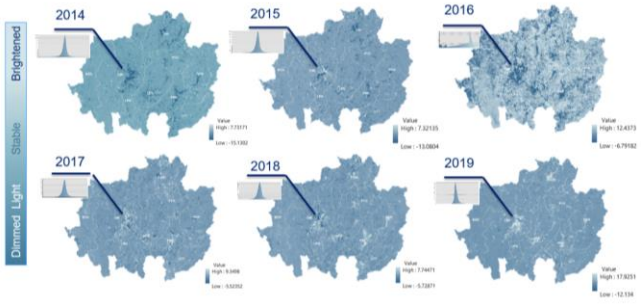

Figure 4. Nighttime light spatial distribution of brightness mean deviation from 2014 to 2019

3.3 Bortle's scale Map

The Bortle's Scale map presented a nine-scale numerical scale used to measure the night sky brightness and classify the light pollution levels, with each colour shade clearly identifying the different level of the sky brightness.

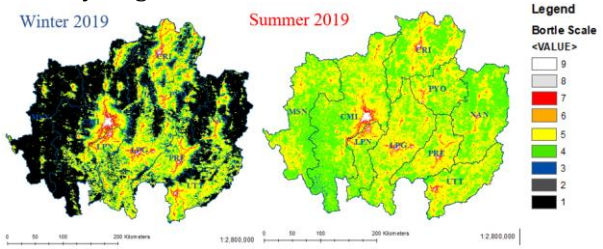

Figure 5. Skyglow map in 2019 to show light pollution in northern Thailand classified by using Bortle's scale model of light pollution between winter and summer.

Level 1(Black), considered the darkest is the light pollution-free zones, including the province's border. level 9(White) in the city of Chiang Mai regarded as the brightest, is the highest light pollution zone; meanwhile, level 7 (red) covered the other city center of each province. Maps in figure 5 revealed that light pollution in summer is distinctively more than in winter. The level 1 areas in winter became to level 4 in summer.

3.4 The Scatter Diagram of the Correlation

The graph (Figure 6 A.) shows empirical data and plots the correlation between the radiance (nW /cm^2 * sr) and brightness (mag/ arcsec^2) that occurred significantly as a nonlinear correlation. This can be explained by the nonlinear regression coefficient of determination known as R^2 value of 0.9488, which was considered as a higher correlation.

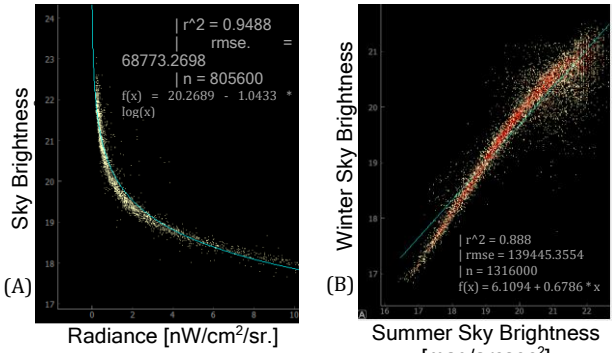

Figure 6. (A) A scatter plot of the relationship between radiance and sky brightness. **(B)** Correlation between the sky brightness model during winter and summer in Chiang Mai

Figure 6 (B) shows that R2 of the sky brightness between winter and summer in Chiang Mai is 0.888, which is perfectly correlated in 17 – 19.5 mag/arcsec^2 (Brighten) and dispersed about 19.5 – 22 mag/arcsec^2 .

3.5 The Skyglow Profile

In comparison, the AOD value of sky brightness in winter was 0.2725, but the summer value was relatively high 0.6254. The skyglow profile (Figure 7 A) showed the spotlight areas in winter had a high brightness value, whereas the dark areas had a low brightness value. In contrast, in summer, the brightness value was inversely proportional to winter. The brightness value of the Spotlight areas decreased. Particularly, the dark areas in summer, the background brightness had higher than in winter.

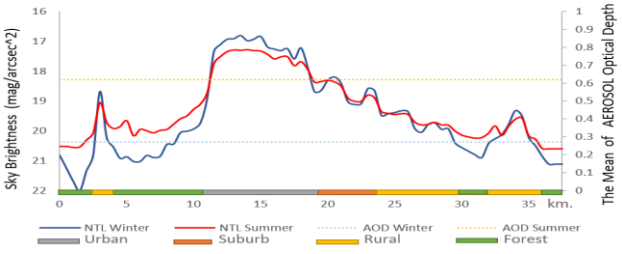

(A)

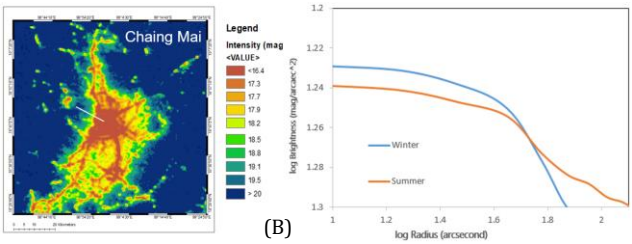

(B)

Figure 7. (A) The skyglow profile graph compares Chiang Mai's brightness during winter and summer and **(B)** Sérsic Skyglow Profile Model

4. DISCUSSION

In physics, the equation converter radiance (nW / cm^2 * sr) to brightness (mag / $arcsec^2$) was not found. This research reviewed and examined the conversion from correlation, based on the research of Alejandro Sanchez de Miguel and his team, in a study of the nature of the diffuse light near cities and the correlation between the sky brightness at the zenith (The UCM sky brightness survey) and VIIRS imagery which were found to strongly correlated from the observational data(de Miguel, Kyba et al. 2020). Therefore, it is possible to convert the value by using the above equation.

The scatters plot model performed as a regression analysis to describe the relationship for quantifying the relationship between the two-period data (Li, Xu et al. 2013) as well as other NTL regression model. The scatters plot model could build the simple fit graph linear and nonlinear regression.

The Bortle's Scale map can be applied to identify and specify the degree of sky brightness and the area affecting light pollution by the colour differentiation. In observing the areas affected by light pollution, figures 5, 6 and 7 present interactions with forest fire dust expressed through AOD. The impact of the skyglow was severe. Remarkably, not only the amount of brightness in rural and national park areas increased but also the amount of brightness in the city area decreased. Significantly. This led to very little chance of seeing starlight with the naked eye in the affected area. Outstandingly, the dark sky during the winter season and the light pollution with the highest skyglow effect rate in the summer season were associated with changes in radiances over artificial light sources between aerosol-free and high aerosol loading (and cloud-free) nights(Zhang, Jaker et al. 2019).

5. CONCLUSION

This research exhibited the correspondence between radiance VIIRS-DNB imagery convert to sky brightness unit and then analyzed the Nighttime light spatial distribution of brightness mean deviation from 2014 to 2019. The trend of changing, mainly Chiang Mai city center, has the most change to brighten and the city center of each province also brighten too.

The Bortle's scale map to compare light pollution severity was accounted for the heart of estimating the attribute of skyglow in night time from satellite imagery. The Bortle's scale colour shades were efficiently implemented to compare the brightness maps and describe the sky brightness differences in winter and summer. The imagery was also interpreted more clearly.

Furthermore, the skyglow cross-section profile provided a noticeable ratio of the brightness range of the sky. A typical urban night sky usually is 5 times magnitude brighter at the zenith than the natural sky. In summer, the zenith of the natural sky rose up to 1 times brighter than winter. While the AOD value increased by 2.3-times in the summer, the effect of the sky brightness in the city center and the typical natural sky were inversely proportional to winter.

In addition, Sérsic Skyglow Profile Model was described when the nighttime light has been affected by aerosols in summer, then the intensity of the skyglow will be decreased but the radius of the skyglow will be expanded.

Eventually, this research was carried out towards achieving all of the objectives.

ACKNOWLEDGEMENT

I fully appreciate Wuhan University, Burapha University and GISTDA for supporting this work. Last but not least, this research could not be completely done without the comments and contributions from the anonymous reviewers and supporting valuable data from NARIT team members.

REFERENCES

Bortle J E (2001). Introducing the Bortle dark-sky scale. S&T 101(2): 126.

de Miguel, A. S., et al. (2020). "The nature of the diffuse light near cities detected in nighttime satellite imagery." Scientific reports 10(1): 1-16.

Johnson, R. S., et al. (2013). "Preliminary investigations toward nighttime aerosol optical depth retrievals from the VIIRS Day/Night Band." Atmospheric Measurement Techniques 6(5): 1245.

Li, X., et al. (2013). "Potential of NPP-VIIRS nighttime light imagery for modeling the regional economy of China." Remote Sensing 5(6): 3057-3081.

Suepa, T., et al. (2016). "Understanding spatio-temporal variation of vegetation phenology and rainfall seasonality in the monsoon Southeast Asia." Environmental research 147: 621-629.

Supasri, T., et al. (2020). "Life cycle assessment of maize cultivation and biomass utilization in northern Thailand." Scientific reports 10(1): 1-13.

Wang, X., et al. (2020). "Quantitative Analysis of Aerosol Influence on Suomi-NPP VIIRS Nighttime Light in China." IEEE Journal of Selected Topics in Applied Earth Observations and Remote Sensing 13: 3557-3568.

Zhang, J., et al. (2019). "Characterization and application of artificial light sources for nighttime aerosol optical depth retrievals using the Visible Infrared Imager Radiometer Suite Day/Night Band." Atmospheric Measurement Techniques 12(6): 3209-3222.

Intercontinental Geoinformation Days

igd.mersin.edu.tr

The efficiency of high-rate RTK for structural health monitoring

Güldane OKU TOPAL*[1], Burak AKPINAR [1], Vahap Engin GÜLAL[2]

[1] *Yildiz Technical University, Department of Geomatics Engineering, Istanbul, Turkey*
[2] *Atlas University, Rectorate, Turkey*

Keywords
Structural Health Monitoring
High-Rate RTK
Shake Table
Time Series

ABSTRACT

The purpose of Structural Health Monitoring (SHM) is to monitor the conditions of important structures, to determine natural behaviors, and to take necessary precautions in advance by determining the possible accidents. In recent years, Global Navigation Satellite Systems (GNSS) are widely used because of their high accuracy and ease of use in SHM applications. The purpose of this study is to show that high-rate RTK GNSS measurement methods can detect the behavior of engineering structures with high accuracy and to investigate that they can be used effectively in SHM. Experiments were carried out with a single-axis shake table to determine the performance of the RTK GNSS method in SHM studies. The shake table was moved harmonically to simulate possible structural movements and it is aimed to determine these movements with the 20 Hz multi-GNSS equipment. The obtained data were analyzed by time series analysis and fast Fourier transform techniques, and the frequency and amplitude values of the movements were calculated. The accuracy of the results was determined by comparing GNSS displacements with the results obtained by LVDT (Linear Variable Differential Transformer) which is the position sensor of the shake table. As a result of experiments, it was determined that the high-rate RTK GNSS method can be used in observing the behavior and natural frequencies of engineering structures with a precision of a few mm.

1. INTRODUCTION

Improving technology, increasing population due to increased construction and these areas' largest economy has increased the importance of structural observation. These observations have great importance in terms of structural health monitoring (SHM) and disaster management.

There are many different methods and equipments used in SHM applications. However, today High Rate Global Navigation Satellite Systems (GNSS) method has been widely used to detect dynamic deformations and determine structural vibrations for long bridges, towers and tall buildings (Wells et al. 1987).

GNSS is a three-dimensional positioning system with the help of radio signals broadcast from GNSS satellites, in all weather conditions, day and night, quickly, accurately and economically, without the need for sight between points. The system, designed for the navigation need, offers a very sensitive time and speed determination as well as positioning (Wells et al. 1987). With the help of the developing GNSS Method, SHM studies have also gained a new dimension and have become able to present instant results with the help of data obtained simultaneously. So last years, Real-time GNSS positioning methods have been used to detect dynamic displacement of tall slender structures and long or short span bridges frequently (Çelebi and Şanlı 2002; Li et al. 2006; Meng and Roberts 2007; Park et al. 2008; Moschas and Stiros 2011; Xu et al. 2017; Górski 2017). Besides, various shake table tests have been carried out to simulate the natural frequencies of engineering structures, create high oscillations and determine these displacements with GNSS equipment. (Wang et al. 2012 ; Önen et al. 2014; Nie et al. 2016; Akpınar et al. 2017; Dindar et al. 2018)

There are 3 main techniques used in broadcasting corrections and point coordinates in RTK positioning which can be used effectively and practically in SHM. These are Virtual Reference Station Method (VRS), Field Correction Parameters Method (FKP), Main-Auxiliary Reference Station Method (MAC) techniques. In this study, the results of the high-rate RTK GNSS measurements performed with the single-axes shake

* **Corresponding Author**

*(guloku@yildiz.edu.tr) ORCID ID 0000-0001-7548-2276
(bakpinar@yildiz.edu.tr) ORCID ID 0000-0002-3076-1578
(engingülal@gmail.com) ORCID ID 0000-0002-5397-3303

Cite this study

Oku Topal G, Akpınar B & Gülal V E (2021). The efficiency of high-rate RTK for structural health monitoring. 2nd Intercontinental Geoinformation Days (IGD), 24-27, Mersin, Turkey

table will be analyzed using Time Series and Fast Fourier Transform Analysis. The results of these three Network RTK (NRTK) GNSS methods have been analyzed and the advantages and disadvantages of the methods compared to each other have been determined.

2. METHOD

Spectra Precision SP80 GNSS Receiver was mounted on the shake table and experiments were carried out in the field of Yıldız Technical University Davutpaşa Campus Faculty of Civil Engineering to determine whether structural vibrations can be determined by NRTK GNSS methods. Data on the movements of selected amplitudes and frequencies were collected from the GNSS receiver mounted on the shake table while the shake table was stationary and in motion. The measurement results obtained from GNSS were compared with the position sensor (LVDT) data of the shake table and the results were examined. For each of the VRS, FKP and MAC methods, GNSS data was collected with a sampling rate of 20 Hz for a total of ten minutes, with the first and last 4 minutes being still and 2 minutes moving ''Table 1''.

Table 1. All events same frequencies and equal observation times on the shake table

Shake Table				
GNSS	Stationary	Motion	Stationary	Duration
VRS	4 min	2 min(5 Hz)	4 min	11.00-11.10
FKP	4 min	2 min(5 Hz)	4 min	11.10-11.20
MAC	4 min	2 min(5 Hz)	4 min	11.20-11.30

2.1. The Network-RTK

In the Network-RTK measurement technique, corrections are not from a single reference station, but a system consisting of multiple reference stations. The biggest advantage of the method is that the 15 km working area limit required to obtain cm accuracy is pulled to a 100 km base distance. In Turkey national CORS-TR system (TUSAGA-AKTİF) is operating according to the Network-RTK measurement principle. The CORS-TR system has a total of 146 stations spread across the country (Yıldırım et al. 2011). Some other networks work in the Network-RTK technique, not nationally, but regionally. For example, the ISKI-UKBS network, which has 8 fixed stations covering the whole of Istanbul, is one of these local networks. In our study ISKI-UKBS network has been used to compare VRS, FKP, and MAC methods.

2.1.1. VRS, FKP and MAC methods

The VRS (Virtual Reference Station) method is based on the determination of the position of mobile receivers with respect to a virtual reference station created using data of reference stations covering the working area. In the VRS method, it is assumed that there is a virtual station without equipment installed on it only a few meters away from the roaming receiver. With this method, even if there is a malfunction in the operation of any reference station in the network, the necessary GNSS corrections can be calculated using other station data (Arslan et al 2002).

FKP (Field Correction Parameters Method) is the same as the basic principle VRS method. In FKP method, which is the German translation FKP (Flächen Korrektur Parameter), surfaces are used as a reference in the calculation of correction parameters. The transfer of data at the reference stations to the browsing receiver requires that the approximate location of the browsing receiver be known (Eren et al. 2009).

The basic principle of the MAC Method is based on determining the location of the mobile receiver within the network, which consists of one master station and several auxiliary stations. The critical point of this method is that most of the calculations are made in the mobile receiver (Kahveci and Yıldız 2001)

2.2. Shake Table

A shake table is called a platform that realizing harmonic motion at defined frequencies and imitates earthquake movements by artificially generating vibration movements. The QUANSER Shake Table II (SHII) used in the experiments is an earthquake simulator with a single-axis 9.5 cm displacement capability. The range of motion of the table is determined with the help of LVDT sensors that provide precise position feedback integrated into the hardware ''Fig. 1''. The LVDT measures the position of the table at 0.0006 mm accuracy with 50 samplings per second (50 Hz). The movements created by the shaking table can be determined as harmonic and random values. Harmonic motions are the function of a sinusoidal wave defined by amplitude, frequency, and number of cycles (Yiğit et al. 2018). In this study, results regarding a harmonic motion was observed.

Figure 1. Shake Table

2.3. Time Series and Fast Fourier Analysis

In the time series analysis, it is ensured that the time-dependent graph of the series is generated, filtering operations to eliminate blunders, then the trend, periodic and stochastic components in the series are analyzed and removed from the series. A detected trend component in the series represents the long time changes in the series and is defined as a polynomial function which is given below:

$$Y(ti)\text{Trend} = \sum_{k=1}^{m} Ckti^{k-1} \quad (1)$$

Where Ck, (k=1,2,...,m) are the parameters that depend on the degree of function(Erdoğan and Gülal 2013). By separating these calculated trends from the series, de-trended series and graphs are created. Then, the spectral analysis should be done to determine the frequency and amplitude of the series.

The transformation of series from the time domain to frequency domain is done by Fast Fourier Transform (Erdoğan 2006). The basis of the Fourier Technique is based on the separation of the signals that make up the time series. In the FFT, as in other time series, the series should be de-trended. In FFT a function with period T can be approached as the sum of sine and cosine functions.

$$f(x) = a_0 + \sum_{n=1}^{\infty} \left(a_n \cos\frac{n\pi x}{L} + b_n \sin\frac{n\pi x}{L} \right) \quad (2)$$

After the Fast Fourier Transform is applied to the time series, the frequency and amplitude values of the motion will be given in the results section.

3. RESULTS

The 5 Hz harmonic oscillation data of all 3 network RTK methods were analyzed by time series and fast Fourier analysis. The amplitude and frequency values are expressed in "Table 2".

Table 2. Peak frequency and amplitude difference from LVDT value for all methods

Methods	GPS		LVDT		Difference	
	Amp. (mm)	Freq. (Hz)	Amp. (mm)	Freq. (Hz)	Amp. (mm)	Freq. (Hz)
VRS	14.6	5.00	16.1	5.00	1.5	0.0
FKP	15.0	5.00	17.0	5.00	2.0	0.0
MAC	15.0	5.00	16.4	5.00	1.4	0.0

When the differences are examined, it is seen that the best result from the NRTK GNSS methods is obtained with the VRS and MAC method. Lower accuracy was obtained from the FKP method with the highest difference value compared to the other two methods.

During the RTK measurements, data were collected in stationary time with GNSS for four minutes after the oscillations started and the oscillations ended. The data regarding this period when the shake table is at rest were determined by time series analysis and the amplitude and frequency values were calculated. The expected frequency and amplitude of the motion for the stationary time is zero. Results belonging to stationary time were used as RMSE (root-mean-square-error) in our measurements. When ''Table 3'' is examined, it is seen that the lowest RMSE belongs to the VRS method and the highest RMSE belongs to the FKP method. The RMSE results are consistent with the accuracy of the LVDT differences for harmonic motion.

Table 3. Peak frequency and amplitude of stationary time

STATIONARY	VRS	FKP	MAC
Amplitude(mm)	1.5	2.2	1.6
Frequency(Hz)	0.01	0.04	0.01

Figure 2 shows the LVDT and GNSS detrended time series and the Fast Fourier Transform (FFT) spectra of a representative event selected for comparing the methods. It can be seen in ''Fig. 2'' all three methods of displacement show good agreement with the LVDT displacements.

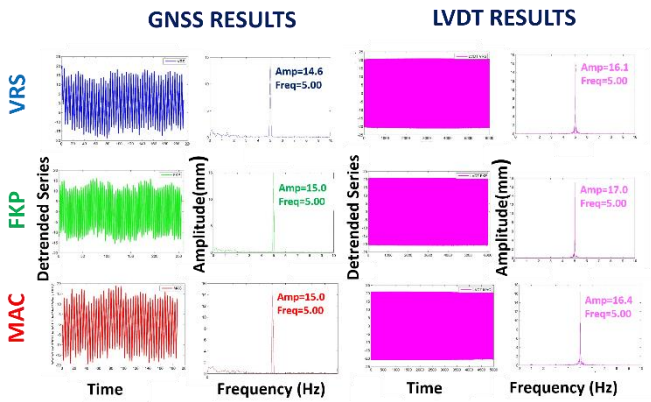

Figure 2. Ground motion test: free vibration responses of GNSS (VRS, FKP, MAC) derived time series and FFT spectrum.

4. DISCUSSION & CONCLUSION

Exactly the same analysis procedures were applied to RTK GNSS and LVDT measurement data and the differences between the determined frequency and amplitude values were calculated. The same frequency values were obtained for all methods with LVDT and GNSS methods. The differences between the amplitude values were determined as 1.5 mm for VRS, 2 mm for FKP, and 1.4 mm for MAC. Although frequency values can be determined with high accuracy in all measurement methods, differences were detected in the amplitudes compared to LVDT measurements, but these differences are exceptionally low. In this study, the relative accuracy of the methods were determined as below cm. Also, the data when the shake table was stationary was analyzed by time series analysis, and the amplitude and frequency values were calculated. Since the differences between these values and the amplitude and frequency values calculated during motion are very close to each other, these differences are found to be meaningless.

The natural frequencies of large engineering structures are in the range of 0.5 - 1 Hz. The determination of oscillations at a frequency of 5 Hz with high accuracy with high rate RTK measurement methods has shown that the RTK-GNSS method can be used effectively in monitoring the structural behaviors.

In conclusion, Network-RTK GNSS methods are potentially good methods for determining the natural frequencies of engineering structures. All test results

revealed that all three Network RTK GNSS methods are efficient in SHM studies.

ACKNOWLEDGEMENT

We would like to thank Ahmet Anıl Dindar, and Fahri Karabulut for their support for this work.

REFERENCES

Akpınar B, Aykut N O, Dindar A A, Gürkan K & Gülal V E (2017). Ağ RTK GNSS Yönteminin Yapı Sağlığı İzleme Çalışmalarında Kullanımı, Afyon Kocatepe University Journal of Science and Engineering 2017. 035504. (1030-1040).

Arslan N, Aydın C, Üstün A & Demirel H (2002). Sanal Referans İstasyonu Sistemi (VRS), 30th Anniversary Symposium in Geodesy and Photogrammetry Education 16-18 October 2002, Selçuk University, Konya

Celebi M & Sanli A (2002). GPS in Pioneering Dynamic Monitoring of Long-Period Structures. Earthquake Spectra, 18(1), 47-61. https://doi.org/10.1193/1.1461375

Dindar A A, Akpınar B, Gurkan K, Aykut N O & Gulal E (2018). Development of LowCost Hybrid Measurement System 16. Europen Confrence on Earthquake Engineering 2018, Thessolaniki.

Erdoğan H (2006). Mühendislik Yapılarındaki Dinamik Davranışların Jeodezik Ölçmelerle Belirlenmesi, PhD Thesis, Yıldız Technical University, Institute of Science and Engineering, İstanbul(in Turkish).

Erdoğan H & Gülal E (2013). Ambient Vibration Measurements of the Bosphorus Suspension Bridge by Total Station and GPS. Experimental Techniques. 37. https://doi.org/10.1111/j.1747-1567.2011.00723.x.

Eren K, Uzel T, Gülal E, Yıldırım O & Cingöz A (2009). Results from a Comprehensive GNSS Test in the CORS-TR Network: Case Study. Journal of Surveying Engineering, 135(1): 10-18.

Górski P (2017). Dynamic characteristic of tall industrial chimney estimated from GPS measurement and frequency domain decomposition. Eng. Struct. 148.

Kahveci M & Yıldız F (2001).Global Konum Belirleme Sistemi Teori-Uygulama. Nobel Yayın Dağıtım, Ankara.

Li X, Linlin G, Ambikairajah E, Rizos C, Tamura Y & Yoshida A (2006). Full-scale structural monitoring using an integrated GPS and accelerometer system. GPS Solutions, 10(4), 233-247

Meng X, Dodson A H & Roberts G W (2007). Detecting bridge dynamics with GPS and triaxial accelerometers. Eng. Struct. 29 (11):3178–3184. https://doi.org/10.1016/j.engstruct.2007.03.012.

Moschas F & Stiros S (2011). Measurement of the dynamic displacements and of the modal frequencies of a short-span pedestrian bridge using GPS and an accelerometer. Engineering Structures, 33(1), 10-17.celerometers, Engineering Structures, 29, 3178-3184, doi: 10.1016/j.enstruct.2007.03.2012.

Nie Z, Zhang R, Liu G, Jia Z, Wang D, Zhou Y & Lin M (2016). GNSS seismometer: Seismic phase recognition of real-time high-rate GNSS deformation waves. Journal of Applied Geophysics, 135, 328-337. https://doi.org/10.1016/j.jappgeo.2016.10.026.

Önen Y H, Dindar A A, Gülal E, Gürkan G, Gürkan K & Akpınar B (2014). Use of High-Frrequency GNSS Sebsors in Dynamıc Motions. Second European Conference on Eartquake Engineering and Seismology, 25-29 August, İstanbul.

Park H S, Sohn H G, Kim I S, & Park J H. (2008). Application of GPS to monitoring of wind-induced responses of high-rise buildings. Struct. Des. Tall Spec. Build. 17 (1): 117–132. https://doi.org/10.1002 /tal.335.

Wang G, Blume F, Meertens C, Ibanez P & Schulze M (2012). Performance of High-rate Kinematic GPS during Strong Shaking: Observations from Shake Table Tests and the 2010 Chile Earthquake. Journal of Geodetic Science, 2(1): 15-30.

Wells D E, Beck N, Delikaraoğlu D, Kleusberg A, Krakiwsky E E, Lachapelle G, Langey R B, Nakiboğlu M, Schwarz K P, Tranquilla J M, Vanicek P (1987). Guide To GPS Positioning, Second Edition, Canadian GPS Associates, New Brunswick, Canada.

Xu Y, Brownjohn J M W, Hester D & Koo K Y (2017). Long-span bridges: Enhanced data fusion of GPS displacement and deck accelerations. Eng. Struct. 147 (Sep): 639– 651. https://doi.org/10.1016/j.engstruct.2017.06.018.

Yıldırım Ö, Bakıcı S & Mekik Ç (2011). TUSAGAAKTİF (CORSTR) Sisteminin Tapu ve Kadastro Genel Müdürlüğüne Katkıları. Journal of HKM Jeodezi, Jeoinformasyon ve Arazi Yönetimi, 11(2), 134-139.

Yigit C O, Dindar A, Bezcioglu M & El-Mowafy A (2018). Evaluation of HighRate GNSS-PPP for Monitoring Structural Health and Seismogeodesy Applications. In XXVI FIG Congress 2018: Proceedings (pp. 1-18).

Intercontinental Geoinformation Days

igd.mersin.edu.tr

The analysis process of robotic total station data to determine structural deformations

Hüseyin Pehlivan[1]

[1]*Gebze Technical University, Faculty of Engineering, Department of Geomatics Engineering, Kocaeli, Turkey*

Keywords
Total station
SHM
RTS
Deformation
Least Squares Method

ABSTRACT

Monitoring structural deformations and taking measures for building safety are considered almost synonymous with important concepts such as human health, public safety and prevention of economic losses. For this reason, new structural monitoring application techniques are being developed in parallel with the developments in building construction technologies and architecture. In particular, GNSS satellite-based measurement systems have found wide application areas for determining structural oscillations and deformations. In addition, the direction of the studies in this field has focused on lower cost and more practical measurement systems. One of the alternative measurement devices used for this purpose is angle and distance measurements with the classical total station. Total stations, which have been automated and gained robotic features in recent years, are easily used in the determination of the most critical structural monitoring and deformations with their programmable structure. In this study, angle-distance measurements performed with a robotic total station at a simultaneous and constant sampling interval for 6 hours were processed and analyzed. Coordinate values and position errors were calculated by balancing according to the least-squares method for each measuring range. Structural displacement values were determined from the coordinate values calculated as a function of time.

1. INTRODUCTION

In structural monitoring, electronic theodolites (ET) or total stations (TS) are commonly used to calculate the time-dependent changes of Cartesian coordinates of observation points. These instruments are the most basic geodetic measuring instruments used in engineering measurements and scientific studies. Firstly, with the development of electronic theodolites, TSs emerged and later with automatized Robotic total stations (RTS), which allow new generation robotic measurements, have found a wide area of use (Schofield and Breach 2007).

RTS or Robotic theodolites are a modern version of TS. In sampling intervals determined according to the features of the program used, RTS can direct itself to the target point, make measurements and record. Nowadays, by programming RTSs, it has been reached the level of observing with a sampling interval of 5-10 Hz and monitoring moving reflectors. Because of these advantages, it is widely used in many surveying and other engineering projects (Psimoulis and Stiros 2008; Psimoulis and Stiros 2011; Moschas et al. 2012; Lienarth et al. 2016). In addition to general engineering research, it can also be used in more scientific experiments to record oscillations with a high frequency greater than 1 Hz and small amplitude (a few mm). With this capacity, RTS can also be used for monitoring large engineering structures under the influence of wind or traffic load (Pehlivan 2009).

In this study; horizontal angle, vertical angle and oblique distance measurements were carried out in order to model the building movements by using a robotic featured total station from the control points located at long distances. Post-process and instant data were analyzed in order to determine the changes (structural deformations) in the positions of the monitoring points, and the details in the data analysis were examined.

* **Corresponding Author**

*(hpehlivan@gtu.edu.tr) ORCID ID 0000 – 0002 – 0018 - 6912

Cite this study

Pehlivan H (2021). The analysis process of robotic total station data to determine structural deformations. 2nd Intercontinental Geoinformation Days (IGD), 28-31, Mersin, Turkey

2. MEASUREMENTS WITH TOTAL STATION

The RTS sends laser light to the prism mounted on the observed structure and can record the horizontal distance and the horizontal and zenith angles values using the round trip time of the returning light. Each observation record can be converted into coordinate values and its change over time helps us calculate the direction and trace of motion. Under normal atmospheric conditions, be making angle measurements with 0.5' and distance measurements with 1mm + 1ppm accuracy allows us to determine the position with 1mm accuracy. Repeated measurements at regular intervals defined by a total station with automatic target recognition (ATR) system; It automatically performs the process of guiding to the target point, measuring and recording, as programmed. The speed of this automated measurement and recording process is directly proportional to the sampling rate of the measurement process (Psimoulis and Stiros 2011; Moschas et al. 2012; Pehlivan et al. 2013)

Distance and angle values from the observation point to the points to be measured can be measured automatically at certain intervals with RTS. Modern RTSs can measure the angle value with 0.5cc. While angle measurements in the range of 5-10cc can be performed with normal total stations, precise distance measurements can be performed with an accuracy of 0.1 mm and normal distance measurements with an accuracy of 1 mm. With this sampling range and measurement accuracy, RTS will continue to maintain its place as an indispensable measuring instrument in many engineering works as well as in many SHM (Structural Health Monitoring) works (Pehlivan 2019).

3. DATA PROCESSING STRATEGY IN DETERMINE STRUCTURAL DEFORMATIONS

Different data processing strategies can be used depending on the expected type of movement in structural motion tracking studies. If slow deformation is expected at a constant rate, the data can be processed in static sessions from a few hours to several days, generally assuming no movement during the session. If the building movement or deformation in question does not pose an imminent threat to the structure or its surroundings or people living in the area, this is usually done after the procedure (Pehlivan 2009).

However, if the movement expected from the structure is expected to be "sudden deformation" for a short period of time and/or "continuous deformation" changes over time, the sampling interval should be increased accordingly. If the deformation could cause the deformed body to fail, a real-time solution is desired to detect the deformation as soon as it occurs and initiate the warning and evacuation processes. In the test study of this work, structural deformations are expected to have a slow character. In normal weather conditions, while the movement is slow, increasing impact loads such as temperature, wind, etc. will cause an increasing effect on the building movements. For these reasons, it is thought that in monitoring the constant and regular motion expected in normal atmospheric conditions, performing our observations with a few minutes sampling interval of RTS measurements will give us the opportunity to capture the expected movements. However, over a relatively short period of time, it can be preferred as a solution in real-time monitoring to detect movements of the structure.

3.1. Determining the Coordinates of the Monitored Point with the Least Squares Method

The linear-angular intersection method has been used in order to determine the accuracy of the coordinates to be determined by the angle-distance measurements performed with the total station to the Observation Point (Prism P) and to benefit from the advantages of the least-squares method (Ehigiator et al. 2010; Okwuashi et al. 2014). In the test measurements, four observations so two distances and two angular directions were carried out with the automated total station instrument from two fixed station points. With an angular-linear intersection, the number of observations is greater than the unknown, so the least-squares method can be used to determine the coordinates of the 3rd point (Figure 1.).

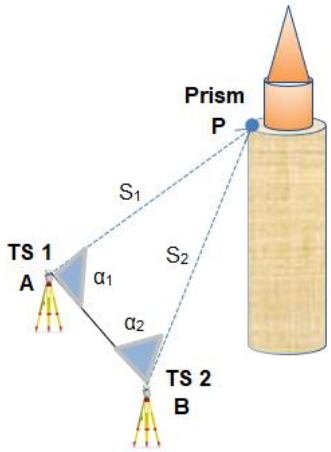

Figure 1. Test measurements and the geometry of angular-linear intersection.

The weight of all measurements performed was assumed to be equal (W = I). Observations were made to Prism point with two total stations installed and levelled at TS1 and TS2 points. Horizontal and vertical angle values and oblique length values were recorded in equal time intervals for six hours. Vertical angles and oblique length measurements and horizontal distances S_1 and S_2 were calculated. Horizontal angles α_1 and α_2 and horizontal distances S_1 and S_2 measurements were obtained as time series for each measurement interval. Using these data, the coordinates of the Prism point were be determined by observations made from TS1 and TS2. Balancing of the calculated coordinates will be done using the observation equation method. The coordinates of the observed Prism point are (Xp, Yp), the coordinates of the fixed station points TS1 and TS2 are (X_A, Y_A) and (X_B, Y_B), respectively.

The adjustment will be carried out in this case by using the observation equation method. In this adjustment model (observational least square), the number of equations is equal to the number of observations (n=4), each equation contains one observation and one or more unknowns. In this case, observations are (S_1, S_2, α_1, α_2) and unknowns (Xp, Yp). The two lengths (S_1, S_2) of the lines in the horizontal projection can be written in a coordinate form as follows:

$$S_1 = \sqrt{(X_P - X_A)^2 + (Y_P - Y_A)^2}$$
$$S_2 = \sqrt{(X_P - X_B)^2 + (Y_P - Y_B)^2} \quad (1)$$

The horizontal angles (α_1 and α_2) from figure 1 can be calculated as follows:

$$\alpha_1 = cos^{-1}\left(\frac{\overline{AP}^2 + \overline{AB}^2 - \overline{PB}^2}{2\,\overline{AP}\,\overline{AB}}\right)$$
$$\alpha_2 = cos^{-1}\left(\frac{\overline{BA}^2 + \overline{BP}^2 - \overline{AP}^2}{2\,\overline{BA}\,\overline{BP}}\right) \quad (2)$$

Using the coordinates of the points, we can write equations 2 as follows:

$$\alpha_1 = cos^{-1}\left[\frac{(X_P - X_A)^2 + (Y_P - Y_A)^2 + AB^2 - (X_P - X_B)^2 + (Y_P - Y_B)^2}{2\,AB\,\sqrt{(X_P - X_A)^2 + (Y_P - Y_A)^2}}\right]$$
$$\alpha_2 = cos^{-1}\left[\frac{(X_P - X_B)^2 + (Y_P - Y_B)^2 + \overline{AB}^2 - (X_P - X_A)^2 + (Y_P - Y_A)^2}{2\,\overline{AB}\,\sqrt{(X_P - X_B)^2 + (Y_P - Y_B)^2}}\right] \quad (3)$$

The four observational equations given in equations 1 and 3 are nonlinear functions of both parameters and observations; they can be processed by the least-squares adjustment technique. Before starting the solution, approximate values of unknown parameters are calculated. Approximate values of the coordinates of the P point are calculated using the angular intersection according to the following formulas (Ehigiator et al., 2010):

$$X_P^0 = \frac{X_A\,cot\,\alpha_2 + X_B\,cot\,\alpha_1 - Y_A + Y_B}{cot\,\alpha_1 + cot\,\alpha_2}$$
$$Y_P^0 = \frac{Y_A\,cot\,\alpha_2 + Y_B\,cot\,\alpha_1 - X_A + X_B}{cot\,\alpha_1 + cot\,\alpha_2} \quad (4)$$

Using these X_P and Y_P values, the approximate values of the observation equations (Lo) are calculated. Then the misclosure vector (L) is calculated as:

$$L = L^0 - L_{abs} \quad (5)$$

We can express the linearized model in matrix form as follows:

$$V_{4\times1} = A_{4\times2} \cdot X_{2\times1} + L_{4\times1} \quad (6)$$

Where, A: The coefficients matrix of parameters, L: The misclosure vector, V: The residuals vector. Matrix A may be computed by differentiation of the four equations with respect to the two unknowns and can be written in the form:

$$A_{(4\times2)} = \begin{bmatrix} \frac{\partial S_1}{\partial X_P} & \frac{\partial S_1}{\partial Y_P} \\ \frac{\partial S_2}{\partial X_P} & \frac{\partial S_2}{\partial Y_P} \\ \frac{\partial \alpha_1}{\partial X_P} & \frac{\partial \alpha_1}{\partial Y_P} \\ \frac{\partial \alpha_2}{\partial X_P} & \frac{\partial \alpha_2}{\partial Y_P} \end{bmatrix} \quad (7)$$

With the Matlab program, the elements of the matrix A (a_{ij}) can be found by differentiating the four observation equations. Then the normal equation system using the Matlab program can be solved.

The positional error at point P can be computed using the following equation (Allan 1988):

$$M_P = \frac{b\,m_\alpha''}{\rho''\,\sin\gamma}\sqrt{sin^2\alpha_1 + sin^2\alpha_2} \quad (8)$$

Where; b: Base line (the distance between total stations) (b=AB in fig. 1); $m_\alpha{}^{cc}$: Mean square error of measuring horizontal angles (taken from specifications of the using total stations); ρ^{cc}=206265, γ: The horizontal angle at point P.

In order to accept the observations of the point P from the triangle ABP and its adjusted coordinates to be sufficiently accurate, the coordinates must satisfy the following condition (Ashraf 2010).

$$r_P = \sqrt{\Delta_X + \Delta_Y} \leq 3\,M_t \quad (9)$$

Where;

$\Delta_X = X_i^P - X_k^P$, $\Delta_Y = Y_i^P - Y_k^P$ ve $M = \sqrt{M_i^2 - M_k^2}$,

X_i^P , Y_k^P: The adjusted coordinates of the point P at the time i of measurement; X_j^P, Y_k^P: The adjusted coordinates of the point P at the time k of the measurement; M_i, M_k : The position errors of the point P at time i and k (Ashraf 2010).

4. EVALUATION OF EXPERIMENTAL TESTS RESULTS

As seen in Figure 1; From the fixed station points (TS1 and TS2), observations were made to the P observation point every 2 minutes and the data sets (2 edges and 2 angle values) were recorded as a function of time. Each observation data set was analyzed within itself and it was aimed to determine the change of total displacement with respect to time by creating 30-minute observation sets. For this purpose, the balanced coordinate values and position errors of the P observation point for each half-hour time between 11:00 and 17:00 were calculated using the MATLAB program. And also, the positional errors (M_p) at point P was calculated by equation (8) for each adjusting time. The position errors for each epoch are approximately equal to each other, as they depend on approximately the same parameters. The results are presented in Table 1 below.

Table 1. The adjusted coordinates and position errors of the observed point

Time	x	y	M_p
11:00	914.90597	449.46749	2.4791642
11:30	914.90584	449.46670	2.4791642
12:00	914.90571	449.46591	2.4791642
12:30	914.90545	449.46434	2.4791642
13:00	914.90532	449.46355	2.4791642
13:30	914.90507	449.46197	2.4791642
14.00	914.90480	449.46122	2.4791642
14:30	914.90467	449.46045	2.4791641
15:00	914.90391	449.45903	2.4791638
15:30	914.90433	449.45824	2.4791642
16:00	914.90421	449.45745	2.4791642
16:30	914.90395	449.45587	2.4791642
17:00	914.90382	449.45508	2.4791642

Table 2. The displacement changes of the observed point

Time	Δx (mm)	Δy (mm)	dn (mm)	pn (mm)
11:30	-0.12938	-0.78940	0.80	3.51
12:00	-0.12938	-0.78940	0.80	3.51
12:30	-0.25877	-1.57881	1.60	3.51
13:00	-0.12938	-0.78940	0.80	3.51
13:30	-0.25876	-1.57881	1.60	3.51
14.00	-0.26506	-0.74507	0.80	3.51
14:30	-0.12735	-0.77701	0.79	3.51
15:00	-0.76594	-1.41306	1.61	3.51
15:30	0.42666	-0.79438	0.90	3.51
16:00	-0.12938	-0.78940	0.80	3.51
16:30	-0.25876	-1.57881	1.60	3.51
17:00	-0.12938	-0.78940	0.80	3.51

The adjusted coordinates obtained during the observation period are presented in Table 1. Measurements, which started at 11 o'clock, were completed at 17:00, and coordinate values were calculated for each 30 minutes. Coordinate differences are calculated for each measurement moment in Table 2. Since the adjusted coordinates of the P point provide equation (9), it is accepted as correct. Accordingly, from the adjusted coordinate differences, the total displacement during the observation period was calculated as 1.29 cm in the X-direction.

5. CONCLUSION

Monitoring structures and determining their deformation characteristics will provide an important prediction for preventing catastrophic events. In addition, taking into account the structural features, the monitoring period and the most appropriate measurement system should be selected and evaluated with the most appropriate analysis methods. Because it is a known fact that incorrect analysis of measurement data prevents some deformations from being noticed. The analysis process of the data recorded with RTS also requires an accurate deformation analysis.

For this purposes; Within the scope of this study, structural monitoring data was recorded with RTS under normal meteorological conditions for 6 hours. The coordinate values balanced by the least-squares method and their mean errors were calculated and the displacement vectors for each measurement instant were calculated. As a result of analysis and evaluation; It was concluded that the movement of the structure was within known and predicted limits and the measurements were made with sufficient accuracy.

REFERENCES

Allan A L (1988). The Principles of Theodolite Intersection Systems A. L. Allan Survey Rev. 226-234.

Ashraf A B (2010). Development and Innovation of Technologies for Deformation Monitoring of Engineering Structures Using Highly Accurate Modern Surveying Techniques and Instruments, Ph.D. thesis, Siberian State Academy of geodesy SSGA, Novosibirsk, Russia, 205 p. [Russian language].

Ehigiator-Irughe R, Ehiorobo J O & Ehigiator M O 2010. Distortion of oil and Gas infrastructure from Geomatics support view, Journal of Emerging Trends in Engineering and Applied Sciences (JETEAS) Vol 1 (2010) 14-23 Toronto, Canada.

Lienhart W, Ehrhart M & Grick M (2016). High frequent total station measurements for the monitoring of bridge vibrations, J. Appl. Geodesy 2017; 11(1): 1–8, DOI 10.1515.

Moschas F, Psimoulis P & Stiros S (2012). GPS-RTS data fusion to overcome signal deficiencies in certain bridge dynamic monitoring projects, Smart Structures and Systems, Vol. 12, No. 3-4 (2013) 251-269.

Pehlivan H, Aydin Ö, Gülal E & Bilgili E (2013). Determining the behaviour of high-rise structures with geodetic hybrid sensors. Geomatics Nat Hazard Risk. doi:10.1080/19475705.2013.854280

Pehlivan H (2009). The Investigation of Dynamic Behaviors in Structures With Real-Time Kinematic GPS, PhD Thesis, Yildiz Technical University, Istanbul, (in Turkish).

Pehlivan H (2019). Robotik Total Station ve GNSS Ölçümlerinin Analizi. Erzincan University Journal of Science and Technology 2019, 12(2), 1018-1027.

Psimoulis P & Stiros S (2008). Experimental assessment of the accuracy of GPS and RTS for the determination of the parameters of oscillation of major structures. Computer-Aided Civil and Infrastructure Engineering, 23, 389-403.

Psimoulis P & Stiros S (2011). Robotic Theodolites (RTS) Measuring Structure Excitation. GIM International, 25(4), 29-33.

Schofield W and Breach M (2007). Engineering Surveying. UK. Elsevier Ltd., 2007. 622 pp. ISBN 978-0-7506-6948-8.

Okwuashi O and Asuquo I (2014). Basics of Least Squares Adjustment Computation in Surveying. International Journal of Science and Research (IJSR). Volume 3 Issue 8, ISSN (Online): 2319-7064.

Intercontinental Geoinformation Days

igd.mersin.edu.tr

Recent advances and perspectives for accurate positioning with low-cost smart devices

Reha Metin ALKAN *[1], **Can DELİCE** [1]

[1] *Istanbul Technical University, Civil Engineering Faculty, Geomatics Engineering Department, Istanbul, Turkey*

Keywords
GNSS
Low-cost GNSS Positioning
Static Survey
Kinematic Survey
PPP

ABSTRACT

Nowadays, satellite-based positioning systems have become the most widely used method for fast, reliable and accurate positioning in many different areas. With this method, 3D position of fixed or moving objects can be determined in the range of meters to cm level depending on the method used and the experimental setups. Among them, when it is possible to determine the position in meters with code measurements using a single GNSS receiver, this accuracy can reach cm (even mm) levels in case the carrier phase measurements are used. With the conventional GNSS positioning approach, it is sufficient to use receivers of a few hundred USD for the first method, however, the second group that requires high accuracy should use geodetic-grade receivers with prices about 10,000 USD or more. Recently, several low-cost systems have been used as an alternative to highly expensive geodetic GNSS receivers for precise positioning. The most prominent of these are hand-held GNSS receiver, smart-phones / tablets, and OEM-type GNSS receivers, and these devices are widely used in many fields, including geodetic applications. In this study, the usability of these different mobile devices in geodetic measurements was reviewed and shared in the light of the literature.

1. INTRODUCTION

Today, satellite-based positioning techniques have become widely used tools for positioning and timing in many different areas. At the beginning, there was only NAVigation Satellite Timing And Ranging-Global Positioning System (NAVSTAR-GPS) developed by the United States Department of Defense, later operated by Russia, GLObal'na NAvigatsionnaya Sputnikovaya Sistema (GLONASS), Galileo operated by the European Union and BeiDou Navigation Satellite System (BDS) operated by the People's Republic of China, an integrated global positioning system called the Global Navigation Satellite System (GNSS) has emerged. With GNSS, depending on the method applied and the equipment used, 3D position of static or moving objects can be determined within the accuracy level of meters to cm. Some of the main features of these systems are given in Table 1.

It is routinely possible to determine the 3D position with meter-level accuracy by using the code measurements collected with a single GNSS receiver. Unfortunately, this accuracy cannot meet the requirements for many surveying applications that require high-accuracy. In this case, the carrier phase observations should also be used. While the hand-held GNSS receivers of a few hundred USD may be sufficient for the first one, the second one requires multi-frequency geodetic-grade GNSS receivers (and antennas) whose prices can reach up to USD 10,000 or even more.

Table 1. The main features of Global Positioning Systems

Parameter	GPS	GLONASS	Galileo	BDS
First Launch Date, FOC	22-Feb-78 17-Jul-95	12-Oct-82 95	21-Oct-11 -	31-Oct-00 -
Total Sat. in Constellation	32	27	30	49
Orbital Planes	6	3	3	3
Inclination with Equator	55°	64.8°	56°	55°
Coordinate Frame	WGS-84	PZ-90	GTRF	CGCS2000
Time System	GPST	UTC (SU)	GST	BDT
Signal / Frequencies (MHz)	L1(C/A): 1575.42 L1(C): 1575.42 L2(C): 1227.60 L2(P): 1227.60 L5: 1176.45	L1(C/A): 1598.0625-1609.3125 L2(C): 1242.9375-1251.6875 L2(P): 1242.9375-1251.6875 L3(OC): 1202.025	E1: 1575.42 E5a: 1176.45 E5b: 1207.14 E5 AltBOC: 1191.795 E6: 1278.75	B1I: 1561.098 B2I: 1207.14 B3I:1268.52 B1C:1575.42 B2a: 1176.45 B2b: 1207.14

* **Corresponding Author**

*(alkanr@itu.edu.tr) ORCID ID 0000-0002-1981-9783
(delice@itu.edu.tr) ORCID ID 0000-0002-2864-0494

Cite this study

Alkan RM & Delice C (2021). Recent advances and perspectives for accurate positioning with low-cost smart devices. 2nd Intercontinental Geoinformation Days (IGD), 32-35, Mersin, Turkey

Recently, as an alternative to high-cost geodetic type GNSS receivers, hand-held GNSS receiver, Android mobile devices (i.e. smart-phones, tablets etc.), and OEM-type GNSS receiver, which allow to collect and process the raw data, have been widely used in many areas. These types of devices can perform single or multi-frequency pseudorange and carrier phase measurements and provide a significant alternative to geodetic GNSS receivers in many applications by providing positioning at different levels as post-mission and/or RTK modes.

In this study, the geodetic surveying performances of different kinds of devices that can be used as an alternative to the widely used geodetic type GNSS receivers will be reviewed.

2. BRIEF REVIEW of GNSS POSITIONING TECHNIQUE

In general, GNSS positioning is carried out in two main ways: Absolute Positioning and Relative Positioning Methods. For Absolute Positioning, it is possible to determine the position within an accuracy of a few meters, depending on the environment in which it is used, also the number and geometry of the satellites. However, the attainable accuracy of this method is not sufficient for many surveying applications.

Recent advances in satellite geodesy, data analysis and processing techniques have led to the emergence of many algorithms and approaches that make it possible to determine the position with high accuracy (cm-dm) using GNSS data collected with only a single receiver. One of these is the technique called Precise Point Positioning (PPP), which is widely used all over the world in several different applications. By using code and carrier phase observations obtained by a single GNSS receiver, PPP method performs 3D point positioning either in real-time and/or in post-mission, combines with precise orbit and clock corrections produced by mainly International GNSS Service (IGS) and others to obtain centimeter-level positioning accuracy. However, using a single GNSS receiver with PPP technique also has a disadvantage such as necessity of the long occupation time for convergence (of the order of 20 minutes or more). It is important for the ambiguity float solution to converge in order to obtain centimeter-level positioning accuracy (Rizos et al. 2021).

In the Relative Positioning Method, the coordinates of the point(s) can be determined with very high accuracy according to a reference station having known coordinates. In this method, in order to make high accurate positioning, the data collected in the field should be processed in the office with a proper GNSS data processing software. This is a major drawback of the method. It also limits the use of it in real-time applications. For such applications, a method called Real-Time Kinematics (RTK) is used. However, the prominent difficulties of the method are that there is a distance limitation between the rover receiver and its reference, it requires additional equipment for data communication and may not be used due to possible problems in data communication. Instead, with another method called Network-RTK (such as CORS-TR in Turkey), it is possible to determine coordinates of a point in real time with high accuracy in a very efficient, easy and economical way. Network-RTK method requires GSM connection and therefore the field survey is limited with the coverage area of the service provider. Some of the prominent disadvantages of this method are that the GNSS receivers to be used are relatively more expensive, the installation and operation difficulties and costs of such a system.

The methods mentioned above are compared with each other in terms of their prominent features in Figure 1.

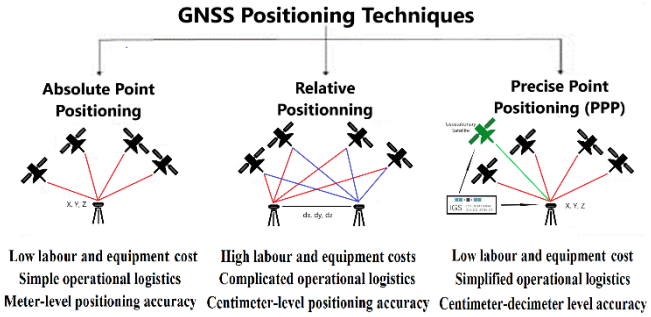

Figure 1. Comparison of GNSS positioning techniques

It should be emphasized that, in order to make high accurate positioning (i.e., within accuracy level of the cm to dm) with PPP or Relative Positioning Method, carrier phase measurements should be made together with the pseudorange measurements. However, in this case, it is required to use geodetic grade GNSS receivers (at least one for PPP and at least two for the relative method) with a unit price of USD 10,000 or more.

As an alternative to highly costly geodetic grade GNSS receivers, hand-held GNSS receivers, smart-phones/tablets and OEM-type receivers have been used in geodetic surveys as a result of developments in technology and communication. Generally, these types of systems are used today and their general performances are given below.

2.1. Positioning with hand-held GNSS receivers

Hand-held GNSS receivers have a large market for navigation, may be purchased by 100-500 USD depending on their features. At the origin, hand-held GNSS receivers perform continuously 3D positions in real-time by using only GPS satellites. Nowadays, multi-constellation hand-held receivers are available on the market.

The Department of Defense has released the latest "Global Positioning System Standard Positioning Service (SPS) Performance Standard" in April, 2020 (note that, this document can be accessed via U.S. Coast Guard Navigation Center web site, https://www.navcen.uscg.gov). The latest performance standard, for GPS SPS PVT (Position, Velocity and Time) accuracy standards are given in Table 2. As can be seen from Table 2, GPS provides global average position accuracy of 8 m (95%) for horizontal component and 13 m (95%) for vertical component; however, site environment conditions can cause severe effect on accuracy. The reason behind the limited accuracy is high level of noise that is caused by integrated low-cost GNSS antenna, in addition to satellite orbit and clock errors, ionospheric and tropospheric delays as well as multipath effects. The typical low-cost hand-held GNSS receivers

can fulfill the needs of navigation users; however, geodetic positioning requires higher accuracies with geodetic type receivers.

Table 2. GPS SPS Position, Velocity and Time Transfer Accuracy Standards (as of April 2020)

Position/Time Accuracy Standard	Conditions and Constraints
Global Average Position Accuracy • ≤ 8 m 95% Horizontal Error • ≤ 13 m 95% Vertical Error	• Defined for a position/time solution meeting the representative user conditions • Position/time solution is available
Worst Site Position Accuracy • ≤ 15 m 95% Horizontal Error • ≤ 33 m 95% Vertical Error	• Defined for a position/time solution meeting the representative user conditions • Position/time solution is available
Global Average Velocity Accuracy • ≤ 0.2 m/sec 95% velocity error, any axis	• Defined for a position/velocity/time solution meeting the representative user conditions • Position/velocity/time solution is available
Time Transfer Accuracy • ≤ 30 ns Time Transfer error 95% of time (SIS only)	• Defined for a time transfer solution meeting the representative user conditions • Time transfer solution is available

Today, some hand-held GNSS receivers can start to log raw data (pseudorange and carrier phase measurement) in RINEX format. In this case, the user can make positioning with cm-dm level of accuracy by processing the collected data. Lachapelle et al. (2018.a) investigated the GPS and GLONASS raw measurements with single frequency GNSS receiver, Garmin Rino 750 hand-held receiver. They obtained dm or better level of positioning accuracy with relative static method. PPP results produced positioning accuracies between 0.5 and 2 meters as a function of the occupation time. According to the kinematic application with the same receiver, it was possible to reach an accuracy of 2 meters (RMS) in position and 2 times lower than in height. In another research of Lachapelle et al. (2018.b), decimeter-level accuracy was obtained by processing code and carrier-phase data collected with single-frequency Garmin GPS Map66 hand-held GNSS receiver and external geodetic antenna in static and kinematic modes.

2.2. Positioning with Android Mobil Devices

In May 2016, Google introduced APIs giving access to GNSS raw measurements from Android Nougat operating system (version 7.x or 8.x). After this improvement, users will be able to log GNSS raw data. This opens the possibility to reach low-cost positioning devices for Android mobile devices including smartphones and tablets. Nowadays, almost all android devices have an integrated GNSS receiver/chip; however, the accuracy of measurements made with this type of device is much lower than it is received with geodetic receivers, and even hand-held GNSS receivers. One of the reasons for this is that the carrier-to-noise density ratios (C/N0) of smart devices are about 10 dB lower than those of geodetic receivers. Another reason is that the pseudo range measurements made in smart devices cause high levels of noise and gross errors along with the multipath caused by the internal antenna (Wang et al. 2021).

Several studies have been conducted on this topic, and very promising results have been obtained. These studies have shown that the positioning accuracy was affected from the length of the session, receiver characteristics (i.e. single or multi-frequency, multi constellation) and used antenna type. This type of devices typically provides level of a few meters accuracy and even more, depending on experimental setups and environmental conditions for navigational purposes. However, more accurate results can be obtained when carrier phase measurements are used along with the pseudo ranges. One of the important issues affecting the result here is the type of antenna used. In general, it has been seen that by processing the carrier phase data collected using device's own internal antennas, the positioning can be made with an accuracy of meters or better. It should be noted that, the GNSS measurement with smartphones/tablets etc. is closely affected by the high noise and multipath. Thus, if the code measurements are used, it is seen that the position can be determined at the order of meters. In the case of using a geodetic grade antenna, it is possible to obtain accuracies at the order of cm-dm as a result of the processing of the code and phase measurements in static mode. For kinematic positioning approach, lower accuracies are obtained (Humphreys et al. 2016; Dabove et al. 2019; Geng and Li 2019; Håkansson 2019; Lachapelle and Gratton 2019; Robustelli et al. 2019; Uradziński and Bakuła 2020; Wen et al. 2020).

In general, it can be concluded that, use of android smart devices having multi-frequency and multi-constellation GNSS receiver with an external geodetic antenna shows promising results to use them as an alternative to geodetic receivers.

2.3. Positioning with OEM-Type GNSS receivers

The use of low-cost systems, commonly referred to as Original Equipment Manufacturers (OEM) type GNSS receivers, began in the late 1990s. OEM receivers, with their accuracy, have been an important alternative to highly expensive geodetic grade GNSS receivers and have been used successfully in several surveying projects (Figure 2).

Figure 2. OEM-type GNSS receiver boards

It is possible to measure and record multi-frequency, multi-constellation pseudorange and carrier phase data with these types of receivers. However, in such systems, connections between components (e.g., board, antenna, power supply, data collection unit, etc.) have to be assembled by user. Besides, lack of easy user interfaces and the need for users to develop many stages by themselves cause such systems to be used only in certain areas. In general, OEM-type GNSS receivers with geodetic antennas can provide cm-dm level accuracy in static and kinematic modes by fixing the carrier phase ambiguities (Lu et al. 2019; Dabove et al. 2020).

3. CONCLUSION

Position data will continue to be more important in many areas and applications on future as it is today. This means that the need for accurate and fast positioning will

continue to increase day by day. Therefore, the production of position data at different accuracy levels will always maintain its importance.

Today, geomatics engineers and many technicians around the world are using satellite-based positioning techniques for accurate, fast and cost-effective positioning. Traditionally high-cost geodetic receivers were required for this purpose, however, in the current situation, new type of low-cost mobile platforms like hand-held receivers, smart devices, OEM-type GNSS receivers, have been started to be used as economical alternatives. Indeed, it is possible to determine the position with dm or better level of accuracy with these type of low-cost devices (<500-1,000 USD). The use of these devices will be a serious alternative to geodetic type receivers and will decrease the necessity of geodetic receivers.

REFERENCES

Dabove P, Di Pietra V, Hatem S & Piras M (2019). GNSS Positioning using Android Smartphone. In Proc. of the 5th International Conference on Geographical Information Systems Theory, Applications and Management-Volume 1: GISTAM, pp.135-142, May 3-5, Heraklion, Crete, Greece. https://doi.org/10.5220/0007764801350142

Dabove P, Di Pietra V & Piras M (2020). GNSS Positioning Using Mobile Devices with the Android Operating System. ISPRS International Journal of Geo-Information, 9(4):220. https://doi.org/10.3390/ijgi9040220

Geng J & Li G (2019). On the Feasibility of Resolving Android GNSS Carrier-phase Ambiguities. Journal of Geodesy, 93, pp.2621-2635. https://doi.org/10.1007/s00190-019-01323-0

Håkansson M (2019). Characterization of GNSS Observations from a Nexus 9 Android Tablet. GPS Solutions, 23, Article number: 21. https://doi.org/10.1007/s10291-018-0818-7

Humphreys T E, Murrian M, van Diggelen F, Podshivalov S & Pesyna K M (2016). On the Feasibility of Cm-Accurate Positioning via a Smartphone's Antenna and GNSS Chip. In Proc. of the 2016 IEEE/ION Position, Location and Navigation Symposium (PLANS 2016), pp.232-242, April 11–14, Savannah, USA.

Lachapelle G, Gratton P, Horrelt J & Lemieux E (2018.a). Performance Assessment of Low-Cost Hand Held GNSS Receiver's Raw Code and Carrier Phase Data. In Proceedings of the 16th World Congress of the International Association of Institutes of Navigation, 28 November-1 December 2018, Tokyo, Japan.

Lachapelle G, Gratton P, Horrelt J, Lemieux E & Broumandan, A (2018.b). Evaluation of a Low Cost Hand Held Unit with GNSS Raw Data Capability and Comparison with an Android Smartphone. Sensors, 18(12): 4185. https://doi.org/10.3390/s18124185

Lachapelle G & Gratton P (2019). GNSS Precise Point Positioning with Android Smartphones and Comparison with High Performance Receivers. In Proc. of the 2019 IEEE International Conference on Signal, Information and Data Processing (ICSIDP), December 11-13, Chongqing, China. https://doi.org/10.1109/ICSIDP47821.2019.9173062

Lu L, Ma L, Wu T & Chen X (2019). Performance Analysis of Positioning Solution Using Low-Cost Single-Frequency U-Blox Receiver Based on Baseline Length Constraint. Sensors, 19(19):4352. https://doi.org/10.3390/s19194352

Rizos C, Janssen V, Roberts C & Grinter T (2012). Precise Point Positioning: Is the Era of Differential GNSS Positioning Drawing to an End?, In Proc. of the FIG Working Week 2012, May 6-10, Roma, Italy.

Robustelli U, Baiocchi V & Pugliano G (2019). Assessment of Dual Frequency GNSS Observations from a Xiaomi Mi 8 Android Smartphone and Positioning Performance Analysis. Electronics, 8(1):91. https://doi.org/10.3390/electronics8010091

Uradziński M & Bakuła M (2020). Assessment of Static Positioning Accuracy Using Low-Cost Smartphone GPS Devices for Geodetic Survey Points' Determination and Monitoring. Applied Sciences, 10(15):5308. https://doi.org/10.3390/app10155308

Wang L, Li Z, Wang N & Wang Z (2021). Real-time GNSS Precise Point Positioning for Low-cost Smart Devices. GPS Solutions, 25(69). https://doi.org/10.1007/s10291-021-01106-1

Wen Q, Geng J, Li G & Guo, J (2020). Precise Point Positioning with Ambiguity Resolution Using an External Survey-Grade Antenna Enhanced Dual-Frequency Android GNSS Data. Measurement, 157:107634. https://doi.org/10.1016/j.measurement.2020.107634

Intercontinental Geoinformation Days

igd.mersin.edu.tr

Accuracy of GPS single point positioning solution using IGS precise products

Sinan BİRİNCİ*[1], M. Halis SAKA [1]

[1]*Gebze Technical University, Department of Geomatics Engineering, Gebze-Kocaeli, Turkey*

Keywords
Single Point Positioning (SPP)
Accuracy
IGS Precise Products
Weighted Least Square

ABSTRACT

GPS Single Point Positioning (SPP) is the common usage of navigation and meets the meter-level positioning requirements. The error sources including orbital error and satellite clock offset significantly affect the accuracy of the SPP solution. International GNSS Service (IGS) focuses on improvements of orbital and clock products since 1994. In this study, the SPP solution was performed with IGS final precise products using an in-house Matlab program. The ten-days dataset was evaluated with the program. Systematic errors decreasing the accuracy of the SPP solutions were modeled and then removed. Estimating GPS SPP solution was performed by the weighted least squares method for each epoch. It was observed that the accuracy of the solutions was associated with the number of satellites and GDOP values. The results revealed that the positioning accuracy was achieved at a maximum 21 centimeter level for the daily average, and RMSE values of all components were less than 1 meter. It was also clearly seen that the IGS precise products contributed to the accuracy of the GPS-SPP solution.

1. INTRODUCTION

Single point positioning (SPP) is a method that estimates receiver coordinates and clock offset by using the pseudorange measurements. The technique solves the user position at a single epoch with the meter-level positioning accuracy. The accuracy of the results is dependent on many factors, such as satellite clock offset, receiver clock offset, satellite orbital error, ionosphere delay, tropospheric delay, satellite and receiver antenna offsets, multipath, and noise. In addition, the number of visible satellites and satellite geometry plays an important role for positional accuracy (Cai and Gao 2009; Satirapod et al. 2001).

The atmospheric effects resulting from the ionosphere and troposphere are the main sources of error for SPP, and it should be suitably corrected, mitigated, or eliminated. The Saastamoinen tropospheric model is widely used for hydrostatic and wet delays from the zenith directional effect of the troposphere (Saastamoinen 1972). For the slant tropospheric corrections, several types of mapping functions are used. In this study, the tropospheric effect was removed from the data using the UNB3m hybrid model (Leandro et al. 2006). The Ionospheric delay is frequency-dependent; therefore, the effect of the ionosphere is eliminated by ionosphere-free combination in the dual-frequency receivers.

By using dual-frequency receivers and International GNSS Service (IGS) precise products, the daily mean of the positional difference between the SPP solution and the true position was reported to be at 1 meter level for the north, east, and up components (Satirapod et al. 2001). On the other hand, using the single frequency receiver with broadcast ephemeris and ionospheric model, the average error was obtained as about 1m and 2m level for horizontal and vertical components, respectively (Angrisano et al. 2013). In a study conducted by Cai et al. (2014), the accuracy of the vertical component was increased by 10% by the use of GPS and Galileo data together. Also, the triple-constellation combination and quad-constellation use of GLONASS, Galileo, and BeiDou satellite systems together with GPS significantly increased the SPP accuracy (Pan at al. 2017; Kwasniak 2018).

The aim of this study is to investigate the maximum accuracy that can be obtained from GPS SPP solution with IGS precise products using 10-day GPS data collected for ANKR.

* **Corresponding Author**

*(s.birinci@gtu.edu.tr) ORCID ID 0000-0001-6668-9160
(saka@gtu.edu.tr) ORCID ID 0000-0002-5283-9065

Cite this study

Birinci S & Saka M. H (2021). Accuracy of GPS single point positioning solution using IGS precise products. 2nd Intercontinental Geoinformation Days (IGD), 36-39, Mersin, Turkey

2. METHOD

2.1. Functional and Stochastic Model

In the SPP method, the functional model of the code observation for dual-frequency receivers can be expressed as follows;

$$P_{IF} = \rho + cdt_R - cdT + d_{trop} + \varepsilon_p \quad (1)$$

where, P_{IF} is the ionosphere-free combination of measured pseudorange in meters, dt_R is the receiver clock offset in second, dT is the satellite clock offset from in second, d_{trop} is the tropospheric delay in meters, c is the speed of light in meters per second, ρ is the geometric range between the satellite and the receiver in meters, ε_p is the unmodelled errors such as multipath error, orbital error, and measurement noise in meters. Tropospheric delay (d_{trop}) was corrected using the UNB3m tropospheric model as suggested by Leandro et al. (2006). This model calculates the tropospheric delay using the station's latitude, ellipsoidal height and time (day of year), and the satellite elevation angles.

The adjustment model of the Eq. (1) can be written as follows (Kouba and Héroux 2001);

$$A\delta + l - v = 0 \quad (2)$$

where, A is the design coefficient matrix, δ is the correction vector for unknown parameters, l is the misclosure vector, v is the residual vector of measurements in Eq. (2). Matrix A can be written as follows;

$$\begin{bmatrix} -\frac{X^{S(1)}-X_{0,R}}{\rho_{0,R}^{S(1)}} & -\frac{Y^{S(1)}-Y_{0,R}}{\rho_{0,R}^{S(1)}} & -\frac{Z^{S(1)}-Z_{0,R}}{\rho_{0,R}^{S(1)}} & 1 \\ -\frac{X^{S(2)}-X_{0,R}}{\rho_{0,R}^{S(2)}} & -\frac{Y^{S(2)}-Y_{0,R}}{\rho_{0,R}^{S(2)}} & -\frac{Z^{S(2)}-Z_{0,R}}{\rho_{0,R}^{S(2)}} & 1 \\ \cdots & \cdots & \cdots & \cdots \\ -\frac{X^{S(n)}-X_{0,R}}{\rho_{0,R}^{S(n)}} & -\frac{Y^{S(n)}-Y_{0,R}}{\rho_{0,R}^{S(n)}} & -\frac{Z^{S(n)}-Z_{0,R}}{\rho_{0,R}^{S(n)}} & 1 \end{bmatrix} \quad (3)$$

$$\rho_{0,R}^{S} = \sqrt{(X^S - X_{0,R})^2 + (Y^S - Y_{0,R})^2 + (Z^S - Z_{0,R})^2} \quad (4)$$

where X^S, Y^S, Z^S are the coordinates of satellites, $X_{0,R}, Y_{0,R}, Z_{0,R}$ are the approximate coordinates of the receiver, n shows the number of satellites and $\rho_{0,R}^{S}$ is the geometric range. The weighted least squares method has been applied to solve the adjustment model given in Eq. (2).

$$\delta = (A^T PA)^{-1}(A^T Pl) \quad (5)$$

$$\delta = \begin{bmatrix} \Delta X & \Delta Y & \Delta Z & cdt_R \end{bmatrix}^T \quad (6)$$

where P is the weight matrix of which the diagonal elements are obtained from the elevation angle of the satellites and it can be shown as follows;

$$P_i = (\sin(e_i))^2 / \sigma_0^2 \quad (7)$$

where, e is the satellites elevation angle, σ_0^2 is the *a priori* variance of the ionosphere-free code measurement and the subscript i identifies the satellite number.

2.2. Data and Processing Strategy

For the implementation of the SPP solution, ten-day data of the ANKR station in Ankara in Turkey, one of the IGS stations, was used. The selected data ranged from 12 to 21 July 2020, provided by IGS (available at: https://cddis.nasa.gov/archive/gnss/data/daily/). Precise orbits and clock products are released by IGS. The products of *.eph files, and *.clk files, provided by Center for Orbit Determination in Europe (CODE), were used in the processing stage for daily solutions (available at: https://cddis.nasa.gov/archive/gnss/products). The RINEX data was collected by LEICA GR30 receiver with observation types: C1, P2. Consequently, the Differential Code Bias (DCB) file provided by CODE was used to upscale the C code to the P code in Eq. (8) (Schaer 2012).

$$P1 = C1 + DCB_{P1-C1} \quad (8)$$

where DCB_{P1-C1} is the DCB between C1 and P1 code.

Table1. Processing Strategy of SPP

Parameters	Used in the Study
Processing Mode	Epoch-by-Epoch
Adjustment Model	Weighted Least Square
Satellite Orbit/Clock	Final CODE products
Antenna Phase Center	igs14.atx
Ionosphere	Ionosphere-Free
Troposphere	UNB3m Model
Relativistic Effect	Corrected (Ashby 2003)
Elevation Mask	10°
Sampling Interval	30s
Standard deviation of code measurements	±0.30 m

It should be pointed that all processing stages were carried out by using an in-house software developed on Matlab by the authors. The input files, as outlined in Table 1, are the RINEX observation, satellite orbit and clock, antenna offset, and DCB files. The elevation mask was set to 10°. An epoch-by-epoch solution was performed using the ordinary weighted least squares method. At the processing stage, if there is no data or the Geometric Dilution of Precision (GDOP) value greater than 30, the epoch is skipped, and moved to the next epoch. GDOP is a crucial factor for SPP solution which reflects the numerical condition of matrix A. The accuracy of the SPP result depends primarily on the value of GDOP that is computed from Eq. (9).

$$GDOP = \sqrt{trace((A^T A)^{-1})} \quad (9)$$

Besides, the outlier data were discarded according to the residual of the measurements. Finally, an accuracy comparison was conducted on the SPP results and the true coordinates of the station. The true coordinates of the station were taken from International Earth Rotation and Reference System Service (IERS).

3. RESULT

The purpose of this paper is to improve the SPP positioning performance using the IGS precise products together with modeling of the common systematic error sources. The data were processed epoch-by-epoch and the errors of the north, east, up components, the number of satellites in each epoch, and the GDOP values were estimated (Figure 1). The error of the up component is larger than the other components. It should be outlined that the results were strongly related to the GDOP value and number of visible satellites. The processing results of about 25 epochs were not shown in the Figure1 when the cases of the number of observed satellites less than 5 or GDOP greater than 30.

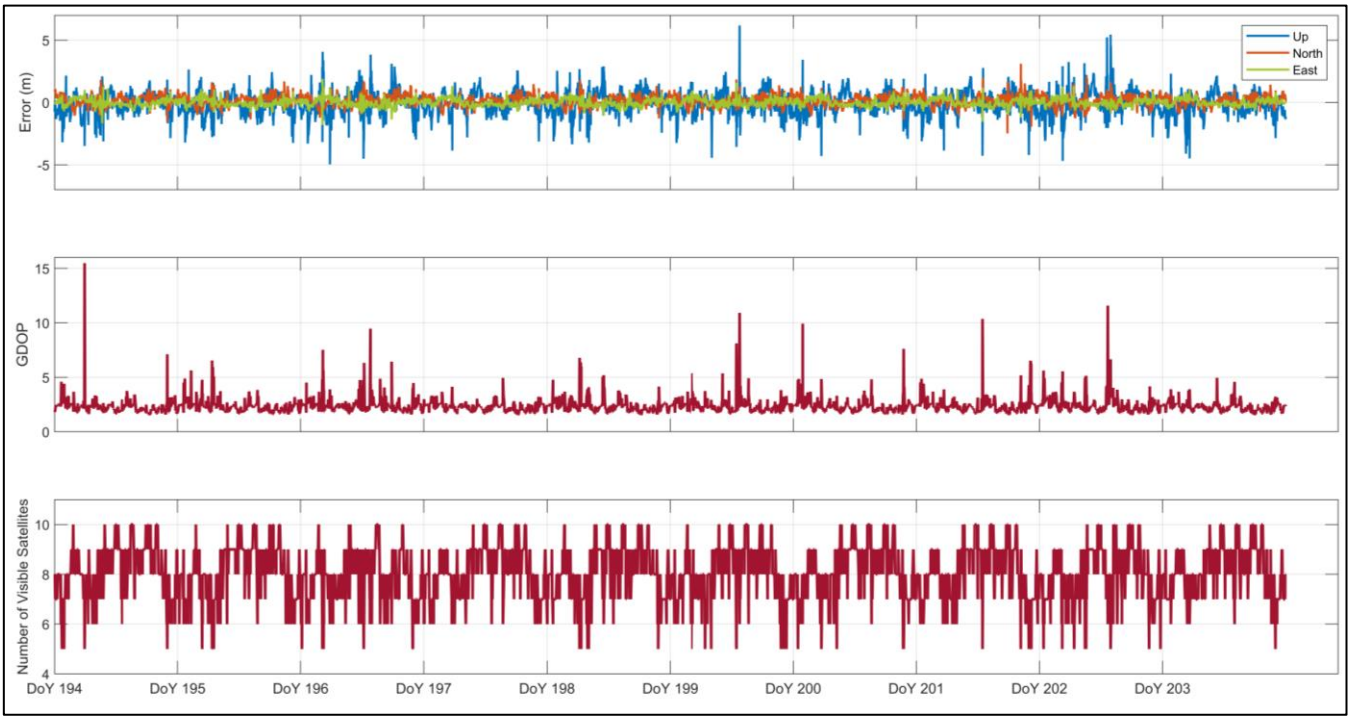

Figure 1. Epoch-by-Epoch Positioning Error, GDOP and Number of Visible Satellites from 13 to 21 July 2020

Table 2 summarizes the daily average error, root mean square error (RMSE), and maximum absolute error for the north, east, and up components that are obtained from the results of the epoch-by-epoch solution for the ANKR station. It was observed that the daily averaged absolute values for all three components were calculated less than 21 cm as shown in Table 2. In particular, the average values of the east component were at the centimeter level.

In addition, more accurate results were calculated for the east component compared to others. The calculated RMSE values were almost at the decimeter level for all three components. Analysis of the result for the error ranges showed that the maximum absolute error of the vertical component was greater than the horizontal components.

Table 2. Statistical Summary of the Processing Results

DoY	Mean (m)			RMSE (m)			Absolute Max. Error (m)		
	N	E	U	N	E	U	N	E	U
194	0.17	-0.02	-0.12	0.43	0.28	0.75	1.82	1.69	3.49
195	0.20	-0.01	-0.18	0.43	0.27	0.80	1.69	1.08	3.24
196	0.21	-0.02	-0.06	0.45	0.30	0.92	1.71	1.91	4.96
197	0.18	-0.01	-0.05	0.40	0.27	0.73	1.48	1.33	3.85
198	0.17	-0.01	0.02	0.42	0.29	0.83	1.80	1.05	3.36
199	0.15	0.02	-0.08	0.42	0.28	0.83	1.85	1.57	6.19
200	0.17	0.01	-0.10	0.41	0.28	0.82	1.39	0.94	4.31
201	0.18	0.01	-0.09	0.44	0.28	0.82	3.12	1.54	4.28
202	0.15	0.02	0.00	0.43	0.28	0.96	2.10	1.30	5.45
203	0.15	0.02	-0.21	0.40	0.27	0.88	1.43	1.06	4.49

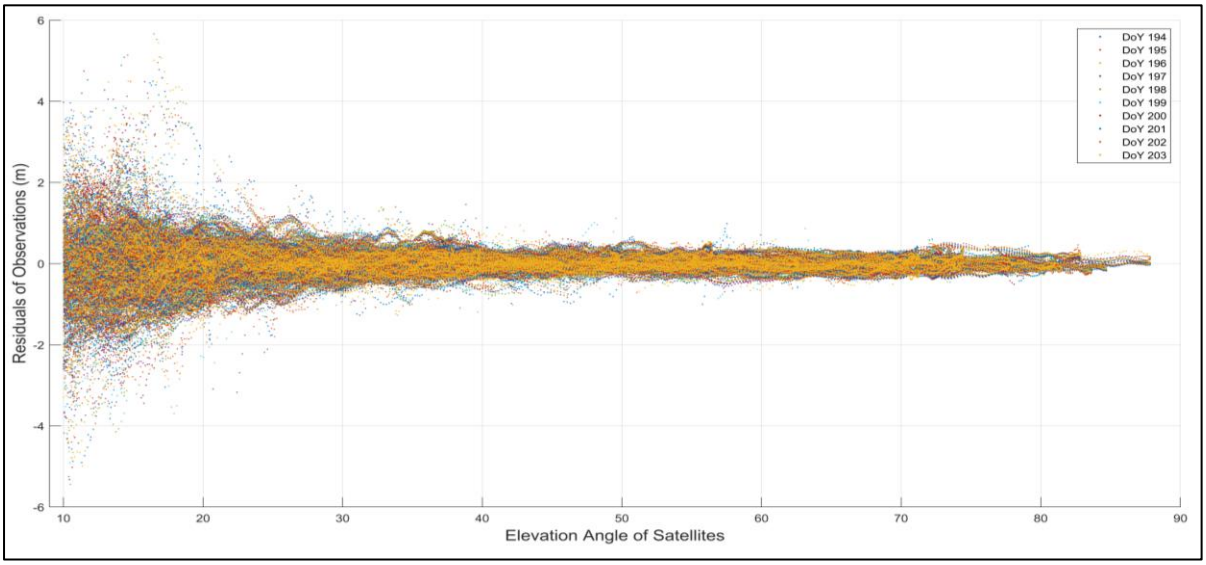

Figure 2. Ionosphere-Free Code Measurement Residual from 13 to 21 July 2020

Figure 2 shows ten-day residuals of the SPP solution with respect to the satellite elevation angle. It can be shown that when the satellite is at low elevation, its residuals get higher. The reason can be explained as the satellites near the user horizon were considerably affected by the multipath and the tropospheric effects.

CONCLUSION

In this study, the performance of GPS SPP was analyzed focusing on the elimination of systematic errors. The test was performed using ten days of observation data of the IGS permanent station called as ANKR. In the processing stage, IGS precise orbit and clock products were utilized. Results produced in this study confirm the effectiveness of the applied strategy, thus improved and comparable results were obtained with the current literature. Daily average coordinate solution was identical to the true positions with a maximum 21 cm error. The RMSE values of all components were at the decimeter level. Furthermore, the up error component was higher than the other two components, as given in Table 2. The results are needed to be clarified using different experiments on different datasets. Improvements of the software will be our priority in future studies to enhance the positional accuracy estimated using the SPP method with other GNSS systems.

REFERENCE

Angrisano A, Gaglione S, Gioia C, Massaro M & Troisi S (2013). Benefit of the NeQuick Galileo Version in GNSS Single-Point Positioning. *International Journal of Navigation and Observation*, *2013*, 1–11. https://doi.org/10.1155/2013/302947

Ashby N (2003). Relativity in the Global Positioning System Imprint / Terms of Use. *Living Reviews in Relativity*, *6*(1), 1–42.

Cai C & Gao Y (2009). A Combined GPS/GLONASS Navigation Algorithm for use with Limited Satellite Visibility. *Journal of Navigation*, *62*(4), 671–685. https://doi.org/10.1017/S0373463309990154

Cai C, Luo X, Liu Z & Xiao Q (2014). Galileo Signal and Positioning Performance Analysis Based on Four IOV Satellites. *Journal of Navigation*, *67*(5), 810–824. https://doi.org/10.1017/S037346331400023X

Kouba J & Héroux P (2001). Precise Point Positioning Using IGS Orbit and Clock Products. *GPS Solutions*, *5*(2), 12–28. https://doi.org/10.1007/PL00012883

Kwasniak D L (2018). Single Point Positioning Using GPS, Galileo and BeiDou System. *2018 Baltic Geodetic Congress (BGC Geomatics)*, 310–315. IEEE. https://doi.org/10.1109/BGC-Geomatics.2018.00065

Leandro R, Santos M & Langley R B (2006). UNB neutral atmosphere models: Development and performance. *Proceedings of the Institute of Navigation, National Technical Meeting*, *2*(September), 564–573. https://doi.org/242114590

Pan L, Cai C, Santerre R & Zhang X (2017). Performance evaluation of single-frequency point positioning with GPS, GLONASS, BeiDou and Galileo. *Survey Review*, *49*(354), 197–205. https://doi.org/10.1080/00396265.2016.1151628

Saastamoinen J (1972). *Atmospheric Correction for the Troposphere and Stratosphere in Radio Ranging Satellites*. https://doi.org/10.1029/GM015p0247

Satirapod C, Rizos C & Wang J (2001). GPS SINGLE POINT POSITIONING WITH SA OFF: HOW ACCURATE CAN WE GET? *Survey Review*, *36*(282), 255–262. https://doi.org/10.1179/sre.2001.36.282.255

Schaer S (2012). Overview of GNSS biases. *IGS Workshop on GNSS Biases*. Retrieved from http://www.biasws2012.unibe.ch/pdf/bws12_1.3.1.pdf

Intercontinental Geoinformation Days

igd.mersin.edu.tr

Improvement of SPP NMEA output using correction projection method

Furkan Soğukkuyu[*1], **M. Halis Saka** [1]

[1]*Gebze Technical University, Faculty of Engineering, Dept. of Geomatics Engineering, Kocaeli, Turkey*

Keywords
DGNNS
Accuracy
NMEA
Low-cost GNSS receiver

ABSTRACT

Differential Global Navigation Satellite Systems (DGNSS) positioning is a relative technique used for meter level accuracy requirements that needs an extra communication link between the base and the rover in real-time. For the offline user, the technique can be also used by considering the raw data for both receivers. In the last decade, smartphones with GNSS hardware enormously boomed. In this study, the DGNSS method for low-cost receivers, DGNSS Correction Projection (DGNSS-CP) algorithm was developed and applied for the low-cost, u-blox M8P single-frequency GNSS receiver. The results were analyzed with in-house software developed in MATLAB environment. Detailed analysis of the results outlined that the DGNSS-CP algorithm produced identical results with the position correction in short distance uses. The differential correction in coordinate space (DGNSS-CP) can be applied successfully to all smartphone users.

1. INTRODUCTION

Global Navigation Satellite Systems (GNSS), the satellite-based positioning systems, provide positioning requirements of the worldwide users in different accuracy levels. Single Point Positioning (SPP), usually called a navigation solution in real-time positioning, is an essential processing method of GNSS using pseudorange data of the receiver. This method can be also used in the meter-level accuracy requirements of users in the field of geodesy and GIS.

Improvement of the results with the other augmentation systems such as DGNSS, Local Area Differential GNSS (LADGNSS), Wide Area Differential GNSS (WADGNSS), Satellite Based Augmentation Systems (SBAS), European Geostationary Overlay Service (EGNOS) has been widely used in the literature (Ashkenazi et al. 1998; Enge et al. 1996; Krasuski et al. 2020; Specht et al. 2019; Tabti et al. 2020). Some of these systems require extra communication methods and hardware. These systems also need transferring a common data format (e.g. Radio Technical Commission for Maritime Service (RTCM)) and the computation is performed with corrected observation. In some applications, SPP solutions at National Marine Electronics Association (NMEA) data format are corrected via the Correction Projection Method (Park et al. 2013; Weng et al. 2020; Yoon et al. 2016). The method is widely used compared to the others, as it can be used without GNSS raw data.

The aim of this study was to improve the SPP performance by using the DGNSS Correction Projection method with the implementation of design matrices.

2. METHOD

2.1. NMEA 0183 Protocol

Most low-cost GNSS receivers transmit basic location information and satellite information to the users in the NMEA 0183 protocol, although they do not record GNSS raw data (pseudoranges). Examples of GGA, GSA, and GSV data types are given in Table 1.

Table 1. NMEA 0183 Messages

Data Type	Message
GGA	$GPGGA,113330.00,4048.57208,N,02921.67575,E,1,07,1.37,17.7,M,37.8,M,,*6E
GSA	$GPGSA,A,3,06,32,02,12,19,24,25,,,,,,2.60,1.37,2.22*0E
GSV	$GPGSV,3,1,09,02,41,128,46,06,36,079,45,12,66,325,48,15,07,198,32*79

Position information in a SPP solution is provided via GGA message. The satellite ID and Dilution of Precision (DOP) existing in this solution are included in the GSA

* **Corresponding Author**

*(fsogukkuyu@gtu.edu.tr) ORCID ID 0000-0003-2904-8713
(saka@gtu.edu.tr) ORCID ID 0000-0002-5283-9065

Cite this study

Sogukkuyu F, Saka M.H (2021). Improvement of SPP NMEA output using correction projection method. 2nd Intercontinental Geoinformation Days (IGD), 40-43, Mersin, Turkey

message. Besides, the elevation and azimuth angles between the satellites and the GNSS receiver are transmitted through the GSV message.

2.2. DGNSS Correction Projection Algorithm

DGNSS, a relative positioning technique, contains two GNSS receivers, one of which is established at the known point. The distance ($\hat{d}^i_{RS}$) between the known point (x_{RS}, y_{RS}, z_{RS}) and satellite i (x^i, y^i, z^i) is estimated by the following equation,

$$\hat{d}^i_{RS} = \sqrt{(x_{RS} - x^i)^2 + \left(y_{RS} - y^i\right)^2 + (z_{RS} - z^i)^2} \quad (1)$$

Pseudorange correction (PRC^i) is generated at the known point and then sent to the user receiver, as follows;

$$PRC^i = \hat{d}^i_{RS} - \rho^i_{RS} \quad (2)$$

where ρ^i_{RS} is the measured pseudorange for each satellite.

To calculate the design matrix *H,* the position information of the satellites and GNSS receiver is required. There are two methods for calculating the positions of the satellites. In the first method, satellite position information (x^i, y^i, z^i) is computed using the algorithm for ephemeris determination in IS-GPS-200 using the broadcast navigation message collected by the GNSS receiver at the reference station. Then, *H* design matrix defines as,

$$H = \begin{bmatrix} \frac{x_R - x^1}{\rho^1_0} & \frac{y_R - y^1}{\rho^1_0} & \frac{z_R - z^1}{\rho^1_0} & 1 \\ \frac{x_R - x^2}{\rho^2_0} & \frac{y_R - y^2}{\rho^2_0} & \frac{z_R - z^2}{\rho^2_0} & 1 \\ \vdots & \vdots & \vdots & \vdots \\ \frac{x_R - x^n}{\rho^n_0} & \frac{y_R - y^n}{\rho^n_0} & \frac{z_R - z^n}{\rho^n_0} & 1 \end{bmatrix} \quad (3)$$

where x_R, y_R, and z_R denote approximate coordinates of the receiver in the Earth-centered Earth-Fixed (ECEF) system, ρ^i_0 is the geometric range between satellite *i* and receiver, and *n* is the number of satellites.

In the second method, the design matrix *H* is established from the parameters of the local topocentric system. The vector line-of-sight (LOS) is achieved by the azimuth (*Az)* and elevation (*El)* angles obtained via the GSV sentence, which can be expressed by the following equation;

$$LOS^i_{local} = \begin{bmatrix} \cos(El^i)\sin(Az^i) \\ \cos(El^i)\cos(Az^i) \\ \sin(El^i) \end{bmatrix} \quad (4)$$

LOS^i_{local} is converted to LOS^i_{ecef} by the rotation matrix (R) that is formed by the receiver's latitude and longitude as shown in Equation 5.

$$LOS^i_{ecef} = R(\varphi, \lambda).LOS^i_{local} \quad (5)$$

The design matrix of *H* is obtained for *n* number of satellites as;

$$H = \begin{bmatrix} LOS^1_{ecef} & 1 \\ LOS^2_{ecef} & 1 \\ \vdots & \vdots \\ LOS^n_{ecef} & 1 \end{bmatrix} \quad (6)$$

The position correction (Δx) can be computed from;

$$\Delta x = (H^T H)^{-1} H^T \left(\hat{I} + \hat{T} - \hat{B} + PRC\right) \quad (7)$$

where $\hat{I}$ is an ionospheric delay, $\hat{T}$ is a tropospheric delay, and $\hat{B}$ is the satellite clock offset (Weng et al., 2020).

SPP accuracy can be improved by applying position correction to the stand-alone position (x_0) obtained from the GGA sentence. Then, the DGNSS position is calculated by the following equation;

$$x_{DGNSS} = x_0 + \Delta x \quad (8)$$

2.3. Study Area and Experimental Setup

The study area is Çayırova Campus of Gebze Technical University (Fig. 1). To assess the performance of DGNSS Correction Projection method, the CHC i80 GNSS receiver was established at the reference station and u-blox C94-M8P (Fig. 2) at the rover station. Then, the low-cost u-blox C94-M8P receiver was connected to NovAtel Flexpack 4 antenna. Data collection started at 11:33 UTC on 19 March 2021 and lasted about 75 min with an interval of 1 Hz. The reference and rover receivers collected data at Receiver Independent Exchange (RINEX) and NMEA formats, respectively.

Figure 1. Study Area

Figure 2. u-blox C94-M8P Evaluation Kit

Position correction was applied by performing SPP solution at reference station with satellites used by rover station in SPP solution. In this solution, satellite clock error, ionosphere delay correction and troposphere delay correction were calculated using broadcasting satellite clock error parameters, the Klobuchar model, and the Saastamoinen model (Klobuchar 1987; Saastamoinen 1972).

3. RESULTS

For the processing of the collected data, an in-house MATLAB program was developed. The program performs the common SPP solution for L1 frequency data using broadcast messages with standard atmospheric models. Besides, the data from the rover receiver at NMEA 0183 format is handled by a sub-program.

The processing results are shown in Table 2 and Fig. 3 where the mean error, standard deviation (STD) and root mean square error (RMSE) for the north, east, and up components was estimated from the solution of the rover station.

Table 2. Summary of Statistical Results

		Mean (m)	STD (m)	RMSE (m)
Stand-Alone	E	0.69	0.60	0.91
	N	1.61	0.70	1.75
	U	-3.03	2.47	3.91
DGNNS-CP with NMEA	E	0.19	0.65	0.68
	N	0.12	0.75	0.76
	U	1.40	2.26	2.66
DGNNS-CP with Eph	E	0.19	0.65	0.68
	N	0.12	0.75	0.75
	U	1.40	2.26	2.66

It was observed that RMSE values obtained from DGNSS-CP solutions were smaller than those of the stand-alone solution for all three components. However, no significant differences were found between the DGNSS-CP solutions and the stand-alone solution in terms of the standard deviation values. As it can be seen from Fig. 3 and Table 2 that the DGNNS and DGNSS-CP methods give similar results for short distances, as it is the case in this study (~200 m). Results revealed that that the construction of the design matrix *H* with ECEF coordinates instead of local coordinates did not contribute to solution.

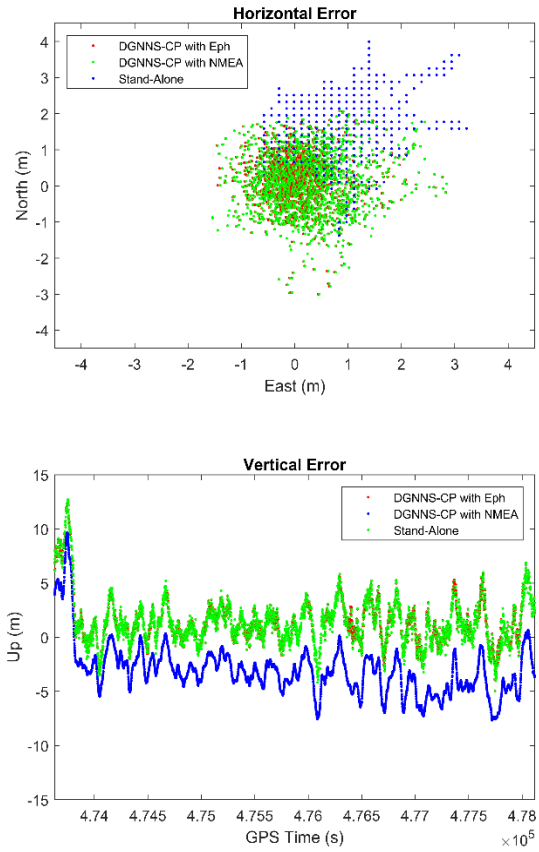

Figure 3. Positioning errors estimated for DGNNS-CP and SPP methods

4. CONCLUSION

The results obtained from the DGNSS-CP were compared with the SPP solution of a low-cost GNSS receiver. The test demonstrated that DGNSS-CP methods provided positioning within meter-level accuracy for horizontal components. In the analysis of North, East, and Up components, it was seen that the performances of the correction methods were identical. Since the navigation message did not contribute to the solution of DGNSS-CP method, the use of DGNSS-CP method with NMEA is found sufficient for the estimation of the positions with low-cost GNSS receivers. In future studies, the performance of DGNSS-CP method will be investigated for longer distances and data from the International GNSS Service (IGS) precise products.

REFERENCES

Ashkenazi V, Chen W, Hill C J & Moore T (1998). Wide area and local area augmentations: design tools and error modelling.Journal of Navigation,51(1),58–66. https://doi.org/10.1017/S0373463397007522

Enge P, Walter T, Pullen S, Kee C, Chao Y & Tsai Y (1996). Wide area augmentation of the Global Positioning System. Proceedings of the IEEE, 84(8), 1063–1088. https://doi.org/10.1109/5.533954

Klobuchar J (1987). Ionospheric Time-Delay Algorithm for Single-Frequency GPS Users. IEEE Transactions on Aerospace and Electronic Systems, *AES-23*(3), 325–331. https://doi.org/10.1109/TAES.1987.310829

Krasuski K, Ciećko A, Bakuła M & Wierzbicki D (2020). New strategy for improving the accuracy of aircraft

positioning based on GPS SPP solution. Sensors, *20*(17),4921. https://doi.org/10.3390/s20174921

Park B, Lee J, Kim Y, Yun H & Kee C (2013). DGPS enhancement to GPS NMEA output data: DGPS by Correction Projection to Position-Domain. Journal of Navigation, 66(2), 249–264. https://doi.org/10.1017/S0373463312000471

Saastamoinen J (1972). Atmospheric Correction for the Troposphere and Stratosphere in Radio Ranging Satellites. Environment Science, 15(4), 247–251. https://doi.org/10.1029/GM015p0247

Specht C, Pawelski J, Smolarek L, Specht M & Dabrowski P (2019). Assessment of the Positioning Accuracy of DGPS and EGNOS Systems in the Bay of Gdansk using Maritime Dynamic Measurements. Journal of Navigation, 72(3), 575–587. https://doi.org/10.1017/S0373463318000838

Tabti L, Kahlouche S, Benadda B & Beldjilali B (2020). Improvement of Single-Frequency GPS Positioning Performance Based on EGNOS Corrections in Algeria. Journal of Navigation, *73*(4), 846–860. https://doi.org/10.1017/S037346331900095X

Weng D, Gan X, Chen W, Ji S & Lu Y (2020). A New DGNSS Positioning Infrastructure for Android Smartphones. Sensors, *20*(2), 487. https://doi.org/10.3390/s20020487

Yoon D, Kee C, Seo J & Park B (2016). Position Accuracy Improvement by Implementing the DGNSS-CP Algorithm in Smartphones. Sensors, 1*6*(6), 910. https://doi.org/10.3390/s16060910

Intercontinental Geoinformation Days

igd.mersin.edu.tr

The impact of variable neighbor numbers on Wi-Fi fingerprint-based indoor positioning using the KNN and WKNN algorithms

Behlül Numan Özdemir*[1], Ayhan Ceylan [1]

[1]*Konya Technical University, Faculty of Engineering and Natural Sciences, Geomatics Engineering Department, Konya, Turkey*

Keywords
IPS
Wi-Fi
Fingerprinting
WKNN

ABSTRACT

Indoor positioning is an area where GNSS signals are either not available or very weak to provide sufficient positioning accuracy. We use smart mobile devices, which are technologically advanced today, as a solution to this issue. Despite the fact that they contain GNSS receivers and some also have dual-band chips, they currently do not have solutions for indoor spaces. As a result, we use Wi-Fi infrastructure, which is as widely used as GNSS. Although the purpose of its emergence is wireless communication, it is now one of the most popular indoor positioning applications. This study used the fingerprint approach, which is among the most successful methods of indoor positioning using this technology. We looked at two parameters related to both the positioning and calibration stages. The 2-meter point interval had the lowest mean errors when these parameters, which are the number of neighbors in KNN and WKNN algorithms and the point frequency in the calibration process, were examined. Furthermore, it has been observed that the KNN algorithm produces significant errors as the number of closest neighbors selected increases. Given the method's simplicity, we may conclude that the NN algorithm's results are quite respectable.

1. INTRODUCTION

There has been a rapid increase in indoor positioning applications due to the widespread use of smart phones and their technical advancements (Wi-Fi 6, Dual-Band GPS, inertial sensors etc.). The Wi-Fi fingerprinting method is one of the most well-known of these applications. Consisting of two phases, Offline (Calibration) and Online (Positioning) Phase, fingerprinting method has its strengths and weaknesses. The main drawback of this approach is the Calibration Phase, which takes a long time and necessitates a lot of human effort. Although some studies concentrate on decreasing the necessary manpower (Wu et al., 2015; Yang et al., 2013) or looking for solutions with autonomous robots (Bakri et al., 2020), others propose a variety of time-saving approaches (Bi et al., 2019). To provide an example of how Wi-Fi Fingerprinting differs from other approaches, it makes use of existing WLAN infrastructure, obviating the need for additional hardware. Since almost all smartphones and majority of smart mobile devices have Wi-Fi hardware readily available, this method is highly applicable to anywhere needed.

In the aforementioned calibration phase a point grid is generated homogeneously in indoor space. These are referred to as calibration points, and the signal fingerprint is the vector formed by the measurements made on them. A typical fingerprint consists of 2D point coordinates, received signal strength (RSS) information from nearby WAPs (Wireless Access Point) and floor information. Data from inertial sensors such as magnetic field sensors and accelerometers is also included in the fingerprint in more sophisticated systems. RSS measurements are performed multiple times at each calibration point due to signal fluctuations. The RSS values obtained from an unknown point are compared to the RSS values obtained from all calibration points during the Positioning Phase. While Euclidean signal distance is the most commonly used distance/similarity measure in this comparison, several other distance/similarity measures are also used (Cha, 2007; Torres-Sospedra et al., 2015). Finally, the location of the unknown point is estimated from the point (s) with the smallest signal distance. If a single calibration point is used to determine this smallest signal distance, the nearest neighbor algorithm (NN), and if more than one calibration point is used, K-Nearest Neighbor (KNN) algorithms are used. In this study, for the KNN algorithm

* **Corresponding Author**

*(bnozdemir@ktun.edu.tr) ORCID ID 0000-0001-7351-1870
(aceylan@ktun.edu.tr) ORCID ID 0000-0003-4408-4245

Cite this study

Özdemir B.N. & Ceylan A (2021). The impact of variable neighbor numbers on Wi-Fi fingerprint-based indoor positioning using the KNN and WKNN algorithms. 2nd Intercontinental Geoinformation Days (IGD), 44-47, Mersin, Turkey

and Weighted-KNN algorithm, different K values were tested and the changes in position accuracy were examined. The primary goal of this research is to determine the K number in an indoor space under real-world conditions and to compare the results obtained with weighted measurements.

2. METHOD

This study was carried out in the Faculty of Engineering and Natural Sciences building of Konya Technical University (Fig. 1). The wireless network infrastructure of the building consists of approximately 80 wireless access points broadcasting 2.4GHz and 5GHz signals.

Figure 1. Aerial view of the building where the measurements were taken

The methodology of the study was carried out in the following order.

I. Obtaining and coordinating the CAD plan of the building
II. Establishment of calibration points as routes along corridors at desired intervals
III. Conducting coordinated signal strength measurements at each calibration point on the routes prepared with the measurement setup and software (Fig. 2).
IV. Conducting coordinated signal strength measurements at random points to test positioning accuracy
V. Analyzing the collected data with the prepared software

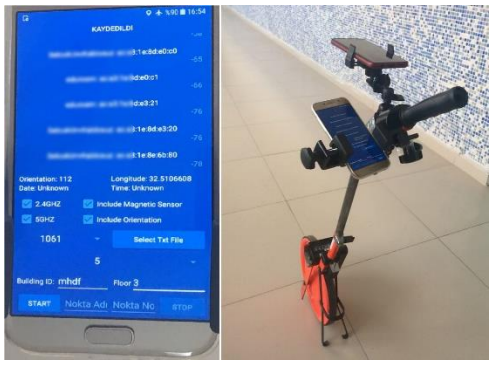

Figure 2. Signal acquisition software(left), measurement setup(right)

Using measurements taken with a total station at the corner points, the CAD plan of the building was adjusted to the correct scale and position. NetCAD 8 software was used to create measurement routes and mark calibration points on the plan. The signal strength measurements were completed with the measurement setup by importing the coordinate list of these marked points into the mobile data collection software. To determine the point positioning accuracy, measurements were taken at 237 test points and 1771 calibration points. In addition, the table below shows the number of calibration points for data arranged between 1 to 5 meters to investigate the effect of various neighbor numbers. (Table 1).

Table 1. Total calibration points for each scenario

Gap between two calibration points	Total Calibration Points
1 m	1771
2 m	907
3 m	606
4 m	471
5 m	366

2.1. Position Estimation

The Euclidean distance used to determine similarity is calculated as (1), where P and Q are two signal vectors and j is the vector length.

$$d_{euclidean}(P,Q) = \sqrt{\sum_{i=1}^{j} |P_i - Q_i|^2} \quad (1)$$

When using the nearest neighbor algorithm to determine location, the calibration point with the shortest Euclidean distance is used, and the KNN algorithm selects the closest K number of calibration points, then estimates the point position as the average of the Y and X coordinates of the K number of closest neighbors found (2).

$$P(X,Y) = \frac{1}{K}\sum_{i=1}^{K}(x_i, y_i) \quad (2)$$

In this process, a certain amount of error is made (Δs) since the influence of each neighbor on the point is evaluated equally in this method (Fig. 3).

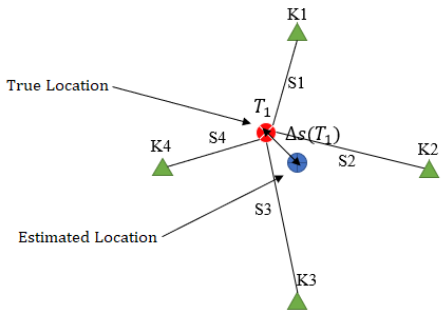

Figure 3. Position estimation with KNN algorithm

The WKNN algorithm, on the other hand, alleviates the problem's impact by weighting neighboring points in proportion to their Euclidean distances (3).

$$w_i = \frac{1/D_i}{\sum_{j=1}^{k} 1/D_j} \quad i = 1,2,\dots,k \qquad (3)$$

2.2. Analysis Software

The results of the measurements were analyzed using the software we developed for Wi-Fi fingerprint positioning (Fig. 4). Main features of the program are;

- Thresholding to remove WAPs under certain signal strength
- Plotting signal strength changes over time
- Viewing calibration points on the map
- Interpolation module
- Position estimation with weighted measurements
- Analyzing with Euclidean, Manhattan, Minkowski L3-5 and Sørensen distances
- Different data representation schemes (dBm, Exponential Function and Powed (Torres-Sospedra et al., 2015), Positive, Normalized and Experimental Functions)

Figure 4. Analysis software, plotting screen(top), main screen (bottom)

3. RESULTS AND DISCUSSIONS

To begin with, as the number of neighbors chosen in the KNN algorithm exceeded 2, the average errors increased by up to 6 meters. More importantly, it is seen that the relationship between different neighbor numbers and the accuracies obtained as a result of the change in the calibration point frequency does not change (Fig. 5). This is due to the fact that as the search for the nearest neighbor progresses, less and less relevant points are chosen. This is particularly true in corridor-style indoor spaces. However, this scenario can produce different results in hall-type indoor spaces where the number of relevant neighboring calibration point count is much higher (Shin et al., 2012)

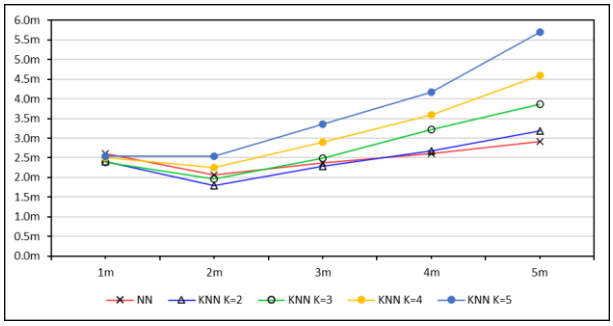

Figure 5. Mean errors of KNN with different neighbor numbers and calibration point gaps

The WKNN algorithm, which has lower average errors, produces similar effects (Fig. 6). WKNN is rather more effective in this situation because it decreases the effect of less important points on position estimation.

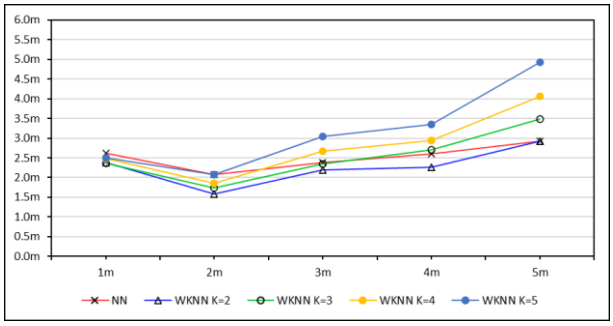

Figure 6. Mean errors of WKNN with different neighbor numbers and calibration point gaps

When each case is looked at individually to decide the best point spacing, it is clear that the 2-meter distribution has the lowest mean errors. In second place, distributions of 1- and 3-meter intervals generated the best results (Fig. 7-8-9-10). It is also clear that the NN algorithm produces respectable result in all ranges, especially above 3 meters.

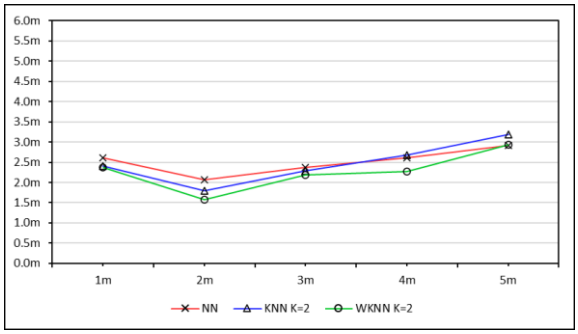

Figure 7. Mean errors of different neighbor numbers for each algorithm, K=2

Total test point count and their locations are clearly linked to the NN algorithms success, which generates comparable average errors at intervals greater than 3 meters. The reason for this is that although the distance between successive calibration points is large in a corridor type closed area, we can say that the closest calibration point to a point in that corridor will be equal or closer to the selected interval.

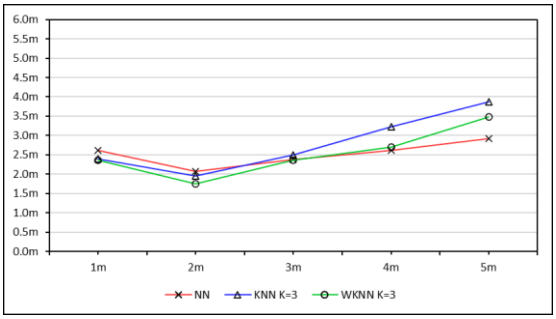

Figure 8. Mean errors of different neighbor numbers for each algorithm, K=3

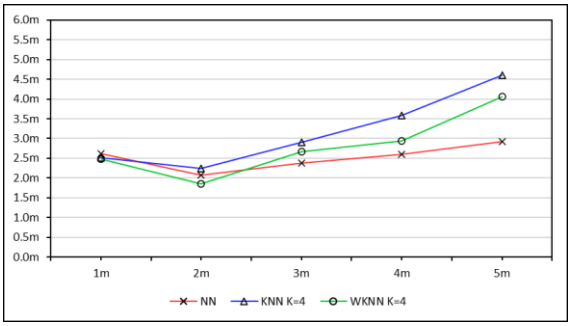

Figure 9. Mean errors of different neighbor numbers for each algorithm, K=4

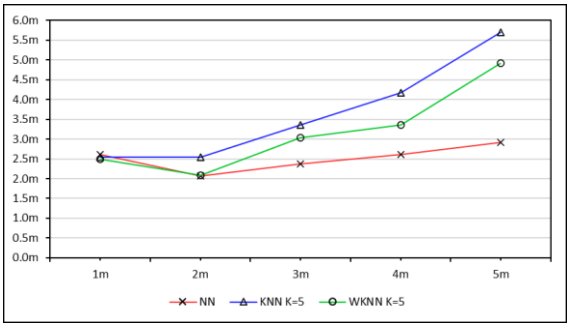

Figure 10. Mean errors of different neighbor numbers for each algorithm, K=5

In addition, the standard deviations obtained from each scenario are shown in Table 1 and Table 2.

Table 1. Standard deviations of NN and KNN algorithms

Gap between two calibration point	NN	KNN K=2	KNN K=3	KNN K=4	KNN K=5
1 m	2.45	2.33	2.22	2.34	2.29
2 m	2.38	1.79	1.70	1.80	1.87
3 m	2.16	2.05	1.70	2.17	2.27
4 m	2.71	2.20	2.40	2.61	2.85
5 m	2.42	2.76	2.65	3.11	3.52

Table 2. Standard deviations of NN and WKNN algorithms

Gap between two calibration point	NN	WKNN K=2	WKNN K=3	WKNN K=4	WKNN K=5
1 m	2.45	2.32	2.21	2.31	2.25
2 m	2.38	1.81	1.65	1.81	1.79
3 m	2.16	2.01	1.64	1.99	2.09
4 m	2.71	2.19	2.23	2.40	2.53
5 m	2.42	2.62	2.39	2.75	3.18

4. CONCLUSION

The application of Wi-Fi fingerprint indoor position determination was investigated in this study. Since the calibration phase is a time-consuming and labor-intensive process, it has been determined that selecting the best point range to determine the number of calibration points is critical. According to this research, the most appropriate calibration point density for the application area is around 2 meters.

It has been observed that as the number of closest neighbors increases, the point positioning accuracy declines. Although this is related to the geometry of the indoor space (Corridor-Type) and fixed K-value, algorithms based on dynamic K-value can provide better results in various scenarios.

We can conclude that the NN algorithm achieves results that are almost as good as KNN and WKNN but it produces higher standard deviation.

REFERENCES

Bakri M Q, Ismail A H, Hashim M S M, Muhamad Azmi M S, Safar M J A & Marhaban M H (2020). Design and Development of a Service Robot for Wi-Fi RSSI Fingerprint Data Collection. *IOP Conference Series: Materials Science and Engineering*, *920*, 012003. https://doi.org/10.1088/1757-899X/920/1/012003

Bi J, Wang Y, Li Z, Xu S, Zhou J, Sun M & Si M (2019). Fast Radio Map Construction by using Adaptive Path Loss Model Interpolation in Large-Scale Building. *Sensors*, *19*(3), 712. https://doi.org/10.3390/s19030712

Cha S H (2007). *Comprehensive Survey on Distance/Similarity Measures between Probability Density Functions*. *1*(4), 8.

Shin B, Lee J H, Lee T & Kim H S (2012). Enhanced Weighted K-Nearest Neighbor Algorithm for Indoor Wi-Fi Positioning Systems. *International Journal of Networked Computing and Advanced Information Management*, *2*(2), 15–21. https://doi.org/10.4156/ijncm.vol2.issue2.2

Torres-Sospedra J, Montoliu R, Trilles S, Belmonte Ó & Huerta J (2015). Comprehensive analysis of distance and similarity measures for Wi-Fi fingerprinting indoor positioning systems. *Expert Systems with Applications*, *42*(23), 9263–9278. https://doi.org/10.1016/j.eswa.2015.08.013

Wu C, Yang Z, Xiao C, Yang C, Liu Y & Liu M (2015). Static power of mobile devices: Self-updating radio maps for wireless indoor localization. *2015 IEEE Conference on Computer Communications (INFOCOM)*, 2497–2505. https://doi.org/10.1109/INFOCOM.2015.7218639

Yang S, Dessai P, Verma M & Gerla M (2013). FreeLoc: Calibration-free crowdsourced indoor localization. *2013 Proceedings IEEE INFOCOM*, 2481–2489. https://doi.org/10.1109/INFCOM.2013.6567054

Intercontinental Geoinformation Days

igd.mersin.edu.tr

The brief history of early marine-navigation

Hatice Şeyma SELBESOĞLU [1], Burak BARUTÇU [2], Aytekin ÇÖKELEZ [1]

[1]*Istanbul Technical University, Faculty of Science and Letters, Department of Humanities and Social Sciences, Istanbul, Turkey*
[2]*Istanbul Technical University, Energy Institute, Renewable Energy Department, Istanbul, Turkey*

Keywords
Early Navigation
Transportation
Navigational Instrument
Compass
Armillary Sphere
Dead-Reckoning
Nautical Almanac
Ancient Greek
Classics
De Magnete
Eratosthenes

ABSTRACT

The aim of this study is to examine in the beginnings and development of early navigation systems and to reveal their relationship with disciplines such as astronomy, cartography, horology and map-making. Since prehistoric times, people have been travelling using waterways and highways. Before the transporting by air, oceans was the only way for early intercontinental transportation. Thus, people learned building simple boats to cross seas. As progressing of marine-navigation technologies, the importance of calculating route made it necessary to measure time and distance. Early navigators sailed by observing the celestial bodies such as the sun, moon and stars through the astronomical information. Especially the transition from the earth-centered universe model to heliocentric (Copernican) has astronomically affected the entire early navigation period. Moreover, navigators used early navigation tools such as dead reckoning and cross-staff. And also, they made nautical almanac called ''parapegmata'' in Greek and used primitively designed compasses. Despite all these developments sailors mostly have lost their route due to misinterpreted rotations. Also it has not been easy to make accurate measurements on ships until the eighteenth-nineteenth centuries.

1. HISTORY OF NAVIGATION

Transportation has been necessary since the beginning of human history. Human populations who initially settled near rivers, needed to travel more as their population grows and new settlements are needed. Travelling by road was possible up to limited distance because there were not sufficient highways. In addition, oceans was the only way of the intercontinental travel. Thus, travelling on water could be improved faster. The only thing that matters in the first place was to stay on the water and dry. Human firstly learned how to make raft to cross rivers. But as time passed, people learned to build larger boats and galleys, and it became extremely important to take these vehicles from one point to another. So, the history of navigation has begun. Navigation term etymologically derived from the verb Navigare[1], which means traveling in Latin, especially traveling in the sea. Today, navigation word is used in both sea and land. One of the most important tools of navigating on the sea are maps in addition to navigational instruments throughout the history. People were able to divide the land they lived on into meaningful pieces thanks to the maps. Major terms such as ''map'', ''charta'' or ''karte'' and ''mappa mundi'' stand out in the history of cartography. It is important to separate these terms from each other for reading history. While the map represents maps made in a more general sense, charts in most sources represent nautical charts. It comes from the word - χάρτης (kartes) which means paper in Greek. The term '' karte'' was first used in the history of cartography by the German cartographer Laurent Fries. And the map term come from the word ''mappa'' in Latin, meaning a napkin, table-napkin or cloth. The term of '' mappa mundi''[2] in Late Latin, it may represent the boundaries of the known world of that time, and this mappa could

[1] Navig/o, are, avi, atum. (Lat.)

[2] Mundus word could be used to mean the world in Vulgar Latin but that is the meaning of "order" in Latin.

* **Corresponding Author**

*(seyma.selbesoglu@itu.edu.tr) ORCID ID 0000-0002-8636-6593
(barutcub @itu.edu.tr) ORCID ID 0000-0002-8834-2317
(cokelez@itu.edu.tr) ORCID ID 0000-0002-8742-3246

Cite this study

Selbesoğlu H Ş, Barutçu B & Çökelez A (2021). The brief history of early marine-navigation. 2nd Intercontinental Geoinformation Days (IGD), 48-51, Mersin, Turkey

contain texts, surveying notes and pictures. The term ''mappa'' was used because of them who called Gromatici in Latin, recorded drawings and notes of their surveying on cloth, parchment or pieces of vellum[3].

2. DEVELOPMENT OF NAVIGATION INSTRUMENTS

The development of technology over time, the distance traveled on the sea has begun to be measured. Primitive measurements on the sea are based on determining time intervals starting from a certain point. Lack of instruments measuring time as we know it today required calculations over time intervals. Instruments such as the hourglass and sundial play an important role in ancient navigation as primitive timers for measuring time over elapsed time. One of the most primitive scientific instruments for measuring time are water clocks called Clepsydra (κλεψύδρα)[4] in Greek. The most primitive form of water clock is a bowl-shaped outflow form date back to Egypt. One of the most advanced examples of water clocks in ancient times belongs to the famous mechanist and inventor of principles of pneumatic science Ctesibius. The instrument developed by Ctesibius also works over time intervals and an alarm system. Measuring certain time periods is not enough for journey on the sea. In order to achieve a useful result, the starting point must be positioned. This is exactly the point that expresses the inseparable part of the history of cartography and navigation. We cannot create a route on the sea without knowing where we are right now. And confirming this thesis, we can witness that mapmaking and navigation technologies are growing simultaneously on the stage of history. It can be said as follows to be more precise: Mapmaking made the development of navigation possible. Besides the science of cartography, astronomy and horology have been the main supporters of navigation science.

The oldest known maps are attributed to the Middle East. Greek geographer Eratosthenes, made one of the earliest scientific world maps. He is also the inventor of the geographic coordinate system (GCS). Eratosthenes has determined latitude using stallers and longitude with the lunar eclipse method. GCS is vital in development of sea navigation. Although the science of astronomy emerged and developed in civilizations such as Egypt, Mesopotamia and China, Ancient Greek offers a wider field to research in terms of the abundance of written sources that have survived to the present day. Greek philosophers/scientists[5] travelling to Egypt and China, they learned the science of astronomy and mathematics belonging to that geography and carried it to their hometown. The final step is the transfer of all this knowledge to the west by the Romans and so the historical background of the scientific revolution is almost formed.

The beginning of Ancient Greek Astronomy dates to the Ionian Age. Mesopotamia is rarely mentioned in the Ancient Greek writing sources, but astronomy studies in the Mesopotamian Seleucids era and Ionian age were on the same period. (Unat, 2013). The Greeks who first explained planetary motions with geometric-kinematic systems, were able to describe planetary systems at a level that could explain astronomical phenomena (Unat, 2013). Thus, it did not take long for the μῦθος (myths) and λόγος (logos) to separate in Ancient Greek. People used myths and epics for knowledge (getting information, and oral tradition. Information from mythological narratives remained valid even after the emergence of sciences. The term '' logos '' (reason) represents scientific thinking. Logos word was used in various meanings.[6] It was used especially by the Sophists and Greek philosopher Heraclitus in the sense of the first power, the first principle in the universe. It was the force that brought order to the primordial chaos. This corresponds to the first people thinking over the epic tradition. In this sense, it represents the cosmic flux in the meaning of a transition from chaos to order corresponds to the human thought which evolving from mythos to the logos phase[7]. Scientific thought and rational knowledge fully formed in Greek created a background that Western science. Greek curiosity (periergia)[8] creates the roots of the tree of science. Theories about the cosmology of philosophers can be accepted as the beginning of astronomy in Greek. It has an important role to play in history of astronomy. The image of perfection reached the peak in Ancient Greek and it was accepted and carried to later times, especially through Aristotle's universe and Platonic ideas. The main reason why geocentric universe model cannot be rejected is expulsion of human from center of the universe. This means acceptance of heliocentric universe model (Copernican).

Tens of thousands of years ago, peoples sailed across open oceans. More recently, within the past four thousand years, Egyptians and other peoples in the Mediterranean Sea, Persian Gulf, and Indian Ocean dared longer-distance sea travel. Early mariners navigated from island to island by observing the sun and stars, the wind and waves. They noted some objects such as large rocks as guiding points. They observed the behavior of fish and birds. They sailed into the winds, making use of

[3] Vellum, i (Lat) : a cloth or calf.

[4] Clepsydra : Water Thief; water-clock, a water-butt with a narrow orifice underneath, through which the water trickled slowly, for measuring periods of time, used to time speeches in the law-courts. (Liddell & Scott, 2009), [κλέπτω (kléptō, "steal") + ὕδωρ (húdōr, "water"].

[5] φῑ́λο- (philo-, "beloved, loving") + σοφός (sophós, "wise") – the term of φῑλόσοφος in Ancient Greek includes the title of scientist in today's sense

[6] reason, word,expression

[7] For more reading : Kahn, C. H., Heraclitus, ., & Kahn, C. H. (2004). The art and thought of Heraclitus: An edition of the fragments with translation and commentary. Cambridge [England: Cambridge University Press]., Dürüşken, C., & Bayrak, M. F. (2014). Antikçağ felsefesi: Homeros'tan Augustinus'a bir düşünce serüveni.,
Gregory, A. (2013). Ancient Greek cosmogony.,
Laks, A., Most, G. W., Journée, G., Iribarren, L., & Lévystone, D. (2016). *Early Greek philosophy*.,
In Laks, A., In Most, G. W., In Journée, G., In Lévystone, D., Protagoras, ., Protagoras, ., Gorgias, ., ... Harvard University. (2016). *Early Greek philosophy: Volume VIII, Part 1*.

[8] For more reading: Assmann, J. (2017). Periergia: Egyptian reactions to Greek Curiosity.

winds that blow east to west just north and south of the equator.

The navigation benefitted from the position of the sun with the knowledge of astronomy. Early navigators prepared handbooks of recorded ocean routes and nautical almanacs. Almanac, known as parapegmata in Greek, had been composed for centuries. Parapegmata or nautical almanacs are the publication describing the cyclical phenomena such as stellar phases, weather, lunar cycles, and more. The Almanacs or parapegmata as astronomical diaries, were not enough alone to travel by sea. Therefore, various technological instruments and navigational systems were additionally used.

Dead reckoning is one of the primary and oldest method of marine navigation. It was first developed by Mediterranean navigators. The oldest dead reckoning chart is Carta Pisana dating back to thirteenth century. The oldest surviving nautical chart called Carta Pisana, because it was acquired by the Bibliothèque Nationale from a family old-established in Pisa. Dead reckoning that preferred method when celestial observation is unavailable, is a method of navigation relying on estimating one's current position using a previously obtained position. In earlier versions of reckoning, during the cruise, a floating object was thrown into the sea from the fore and the time of this object until it reached the stern of the ship was determined. Then, with the proportionality method, the distance the ship traveled in an hour, in other words its speed was calculated. In later times, different instruments using properties such as hydrodynamics and electromagnetic, have been made to determine the speed of the ship.

Development of navigation instruments continued throughout the history of ancient maritime. The backstaff is one of them that was used to measure the altitude of a celestial body. Scientific navigational instrument that especially used to measure the altitude of the moon and sun, was invented by English navigator John Davis (Seaman's Secrets in 1594). Therefore backstaff was called Davis quadrant which is the most dominant tool in the history of navigation instruments evolved from the Cross-staff. And Cross-staff also called Jacob's Staff or '' baculum'' (bone) or '' radius'' (staff) in Latin words (Rossi & Russo, 2009).

Compass also was one of the major instrument for marine navigation. Term of ''compass'' etymology derives Latin verb ''compassare'' (in italian and also may be in Vulgar Latin) combines with ''com'' (with) and the ''passus'' (step). In addition to meaning such as measuring with steps, it can be thought to be etymologically related to circular motion because of the name similarity with the drafting compass. The compass as an instrument of navigation and measuring based on stones with magnetic properties. Loadstones which referred to as ''magnetum'' in Late Latin writings, made the development of the compass with magnetized needle possible. Loadstones and their properties were known in Greek. The first known compass is dated to China, during the Han Dynasty (between 2nd c.BC - 2nd c.AD). Chinese realized that the lodestone always points in the same direction when floated in water but it isn't unclear whether the Chinese understood that this direction was north, as little was known about global direction finding at that time. Also, it is not certain that the earliest knowledge about lodestones is dated to China. Fundamental property of the lodestone of attracting iron was certainly known before. The close of the seventh century B.C, loadstones and their magnetic properties were known by the Ancient Greek. Even a legend attributed to the Ida Mountain confirms the existence of information about magnets (the legend of magnes the shepherd). 9In the texts of many ancient authors such as Thales (640-546 B.C.) and Pliny (23-79 A.D.), the mentions of ''loadstones'' were frequently cited. But the first reference to the use of the compass for navigational purposes is found in a Chinese encyclopedia in probably during the Han or Tsin Dynasty. But there was no definite mention of the use of the compass until ''De Utensilibus'' written by an English monk, Alexander Neckam. This work occurs in middle ages around the twelfth century (Author, 1919). It became difficult to find the first inventors for advanced compasses (as mariner's compass or advanced magnetic compasses), which spread over many geographies and was developed by different people after the middle Ages and the period of discoveries. Peregrinus is the first that describes the compass with pivoted needle. The first writer to attribute a special knowledge of the compass to the Amalfians was Flavio Biondo, was later cited in other works as the inventor of the mariner compass (Nelson, 1962). The four chief improvements applied to Peregrinus compass in late times: the cap-and-pivot support, the movable fly, the divided needle, and the gimbal suspension (Nelson, 1962). Next developments of compass extend to modern period and technologies developing in time of war.

3. RESULT

In this study, main issues were how navigation in the sea emerges and develops. Related astronomical concepts, traditions of thought and primitive navigation instruments such as compass, cross-staff and system of dead-reckoning were especially examined. Research on instruments only in technical terms does not bring historical integrity. Furthermore, it is not possible to investigate to the history of navigation without examining their relations between other disciplines such as astronomy, cartography, horology and map-making. Philology and History sciences help to see all these in a meaningful framework. In addition to the given instruments, there were early instruments that we cannot include in a brief study, used in marine-navigation such as the mariner's quadrant, armillary sphere and astrolabe. These historical navigation instruments will be examined in future studies.

REFERENCES

Author U, (1919). Principal Facts of The Earth's Magnetism and Methods of Determining the True Meridian and The Magnetic Declination. (E. JONES,

[9] It is a legend that describes the discovery of the magnetic property of Mount Ida. (*For more reading: Mourino, M. R. (1991). From Thales to Lauterbur, or from the lodestone to MR imaging: Magnetism and medicine.*)

Dü.) Department of Commerce U.S.Coast and Geodetic Survey, Washington.

Bagrow L. (1966). History of Cartography. (R. Skelton, Dü.) C.A.Watts & Co, London.

Johnston A, Connor R, Stephens C & Ceruzzi P (2015). Time and Navigation The Untold Story of Getting from Here to There. (G. McNamee, Dü.) Smithsonian Books, Washington.

Liddell H & Scott R (2009). Greek-English Lexicon. Salt Digitized by the Genealogical Society of Utah, Lake City, Utah.

McLeod A (2016). Astronomy in the Ancient World Early and Modern Views on Celestial Events. Springer International Publishing AG.

Nelson J H (1962). Magnetism of the Earth. U.S. Govt.Print.Off. Washington.

Rossi C & Russo F (2009). Ancient Engineers' Inventions Precursors of the Present. Springer, Milano.

Unat P (2013). İlkçağlardan Günümüze Astronomi Tarihi. Nobel Akademik Yayıncılık, Ankara (in Turkish).

Intercontinental Geoinformation Days

igd.mersin.edu.tr

A quantitative approach for geographical vulnerability assessment of Bhasan *Char*, Bangladesh, using Remote sensing and GIS

Md. Tariqul Islam*[1], Mohammad Tarikul Islam [2], Atta Rabbi [3]

[1]*University of Nottingham, Faculty of Engineering, Nottingham, United Kingdom*
[2]*Swedish Maritime Administration, Source Data Division, Norrkoping, Sweden*
[3]*Huddinge Municipality, Environment and Building Permit Administration, Geo-data Unit, Huddinge, Sweden*

Keywords
Bhasan *Char,* Bangladesh
Rohingya refugee
Vulnerability assessment
Remote sensing
GIS

ABSTRACT

The relocation of 100 thousand Rohingya refugees is expected from camps in Cox's Bazar to Bhasan *Char* (BC) (island), Bangladesh. The BC is located at the mouth of the Ganga-Brahmaputra-Meghna river system in the Bay of Bengal, ~30-40 km from the nearest water port of the mainland. This study aims to assess geographical vulnerability based on frequent erosion and deposition of the island. Therefore, Landsat satellite images during 1975-2020 are used to detect the areal changes using Geographic Information System (GIS). Since the BC didn't appear 20 years back, nearby islands are studied as similar geographical characteristics. A normalized difference water index is applied to identify the land area. Further, the erosion-deposition and migration of shorelines are identified and quantified. The islands are expanded since 1975. Most erosion occurs along the direction of the main flow of upstream water and the islands' southern face, including BC. Temporarily, a settlement at BC may be no harm by maintaining engineering works of infrastructure, e.g., cyclone against standing buildings, tidal wave, and surge-protected infrastructures. However, the most important, sustainable components, e.g., economic stability and social interaction among the refugees in BC and camps in Cox's Bazar, need to be implemented.

1. INTRODUCTION

Rohingya is a minor Muslim ethnic group in Rakhine State, Myanmar, facing force migration to mainly Bangladesh and other countries in the world since the 1970s as ethnic cleansing (Grundy-Warr and Wong 1997). In the most recent massive migration of ~742,00 Rohingya people crossed the border to Bangladesh during September–November 2017 (OCHA 2020). Now, more than one million refugees live in Cox's Bazar District, Bangladesh, due to the proximity of Myanmar (Fig. 1). They are currently residing overcrowdedly in unhumanitarian conditions with predominantly support from foreign aid. Their housing comprises a room of ~16-22 m^2, including a kitchen and bathing (for women) place. It is bamboo based which is covered by polythene sheets for fence and roofing. Men and children use a communal bathing place, and all refugees use a communal toilet. To improve this situation, Bangladesh Government (BG) constructed a Bangladeshi Taka (Tk) of 2,312-crore (US$274.011 million) housing project at Bhasan *Char* (BC) (Island) (Fig. 1) under Ashrayan-3 policy (Palma and Jinnat 2020). The island is ~40 km^2 and consists of 120 cyclone shelters (CSs) cum schools, medical and community centers, two helipads, and housing blocks built above a four-foot concrete structure from the ground, and protected by a 3-m height 13-km long flood protected embankment. BG aims to relocate 100 thousand refugees to this area, expecting little gardening and cultivation opportunities (Palma and Jinnat 2020).

BG started to shift 1,642 refugees on 4th December 2020 with the help of the Bangladesh Navy Ship and so far (by 3 March 2021), 12,276 refugees are shifted (Prothom Alo 2021). BC is located at the mouth of the Ganga-Brahmaputra-Meghna river system in the Bay of Bengal (Fig. 1). It is a sandy island with an average altitude of 2.86 m from the sea level, which did not exist 20 years ago (Banerjee 2020; DW News 2020). BG stated that the refugees are relocated by their own choice, so-called "Willingly"; however, the mainstream media reported that the refugees' relocation is forcefully by pressuring (DW News 2020). Whether the relocation is willingly or forcefully is out of the scope of this study. This study aims to assess BC's geographical vulnerability by comparing neighboring islands using Landsat remote sensing image and geographic information system (GIS).

* **Corresponding Author**

*(md.islam5@nottingham.ac.uk) ORCID ID 0000 – 0003 – 2831 – 2252
(tarikul020819@gmail.com) ORCID ID 0000 – 0001 – 7969 – 9544
(atta.rabbi@huddinge.se) ORCID ID 0000 – 0002 – 8239 – 3746

Cite this study

Islam M T, Islam M T & Rabbi A (2021). A quantitative approach for geographical vulnerability assessment of Bhasan *Char*, Bangladesh, using Remote sensing and GIS. 2nd Intercontinental Geoinformation Days (IGD), 52-55, Mersin, Turkey

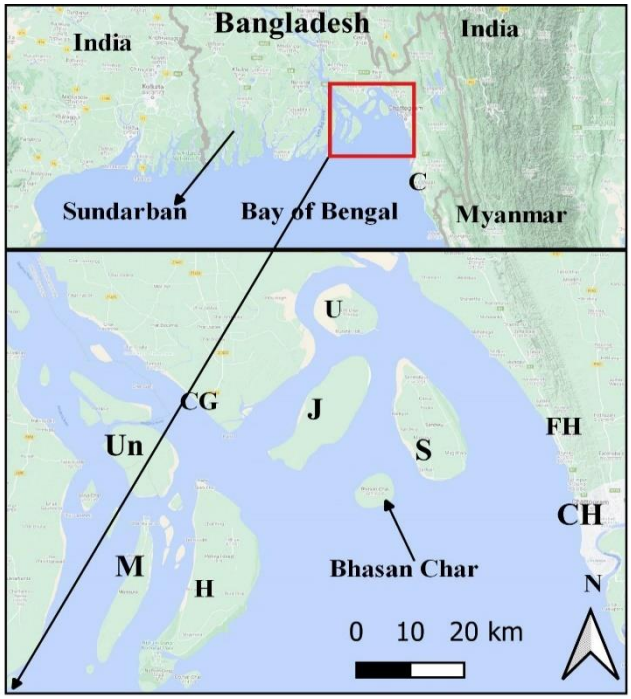

Figure 1. Location of the study area. Location of Chairman Ghat (CG), Cox's Bazar (C), Chittagong seaport (CH), Faujdarhat (FH), Hatiya *Char* (H), Jahangir *Char* (J), Manpura (M), Sandwip (S), Urirchar (U) and an un-named *char* (Un) is also illustrated.

2. METHOD

The geographical vulnerability is assessed by quantifying how often the nearby Islands, e.g., Hatiya *Char*, Sandwip is eroded and deposited since the BC was not existed 20 years back, despite the natural calamities e.g., severe tropical cyclones (TCs), similar to Islam (2013, 2010). First, the data set for BC is obtained from OpenStreetMap Foundation (2018), giving the most updated features' location, e.g., built-up area, housing, road network, flood protection embankment, tidal wave protection infrastructure. The area of polygon features and length of line features are calculated applying ArcGIS pro 2.4.3 using reference system UTM Zone 46N (Fig. 2a). Second, the Landsat satellite images are used, processed, and quantified to estimate the islands' physical sustainability, what is commonly used for such studies (e.g., Islam 2009, 2009a, 2010a). The images are accessed from EarthExplorer, science for a changing world archive of USGS (United States Geological Survey-USGS n.d.). All these data sets are cloud-free and sensed during the dry seasons (November–February), except an MSS data set on 15 April 1978 due to considering better data quality (Tab. 1). The data sets during 1972-1978 (MSS) and 1999-2001 (ETM+) are expected to present the landcover in 1975 and 2000, respectively. This approach was followed to maintain data quality, similar to Islam (2014) (Tab. 1). The Used data sets are georeferenced by the European Petroleum Survey Group (EPSG) with Projection Coordinate System: WGS (World Geodetic System) 1984 UTM (Universal Transverse Mercator) Zone 46N, Linear Unit: Meters.

The images are processed by applying the Normalized Difference Water Index (NDWI) following the equation as Li et al. (2013):

Table 1. Properties of Landsat remote sensing data.

Sensor	Path	Row	Acq. date	Representing yr.
OLI/TRIS	136	45	04 Feb 2020	2020
OLI/TRIS	136	44	04 Feb 2020	
OLI/TRIS	137	44	11 Feb 2020	
OLI/TRIS	137	45	11 Feb 2020	
ETM+	136	44	07 Feb 2001	2000
ETM+	136	45	19 Dec 1999	
ETM+	137	44	24 Nov 1999	
ETM+	137	45	26 Nov 2000	
MSS	146	44	15 Apr 1978	1975
MSS	146	45	03 Nov 1972	
MSS	147	44	08 Feb1977	
MSS	147	45	03 Jan 1977	

$$NDWI = (R_{GREEN}-R_{NIR})/(R_{GREEN}+R_{NIR})$$

where R_{GREEN} is reflected/radiated digital numbers (DNs) value of green band, R_{NIR} is DNs value of near-infrared band. The spectral range of green band is 0.53-0.59 µm for OLI/TRIS, 0.52-0.60 µm for ETM+, 0.50-0.60 µm for MSS, and the near-infrared band is 0.85-0.88 µm for OLI/TRIS, 0.77-0.90 µm for ETM+ and 0.70-0.80µm for MSS. The spatial resolution of the visible bands blue, green, red, and near-infrared for MSS is 60 m and for ETM+ and OLI/TRIS is 30 m. Usually, the NDWI value is obtained from -1 to +1. Ideally, -1 to 0 and 0 to 1 NDWI values represent non-water and waterbody land cover.

However, this classification scheme was slightly modified and judge by comparing it with a visual interpretation of False Color Composited images (e.g., Manugula and Bommakanti 2017) where near-infrared, red, and green bands were set to the red, green and blue channel, respectively, applying the ArcGIS Pro tools: Imagery Composite Bands. The classified NDWI layers of different years were converted to a polygon with two majors land covers: waterbody and non-water. The polygons were converted to polyline, generalized and modified as the shoreline of different years, and visually compared the most eroded and deposited location. A cross-section was made at each nearby island of BC and quantified the erosion and deposition of shorelines/boundaries of islands (Fig. 2b).

3. RESULTS

The Bhasan *Char* is located in the Bay of Bengal, ~35-40 km from the nearest water ports of Faujdarhat and Chairman *Ghat* (Fig. 1). It is an isolated island between the Hatiya *Char* and Sandwip (Fig. 1). The primary transportation system between the BC and the mainland of Bangladesh is the waterway, and a Navy ship takes ~3 hours from the Chittagong seaport. Two helipads can be used emergency basis. The BC consists of two blocks of islands with ~35 km^2, where the bigger block is ~32 km^2. The habitable area is ~6.95 km^2 (the project area), protected by a tidal protection embankment (Fig. 2a).

The built-up area is ~144 hectares with mainly housing and road network within the island (Figs. 2a, 3a). A pond of ~3.9 hectare (38854 m^2) exits here for a fresh water source and some fisheries opportunity. Some part of this area is tried to protect by sandbags (Fig. 3b).

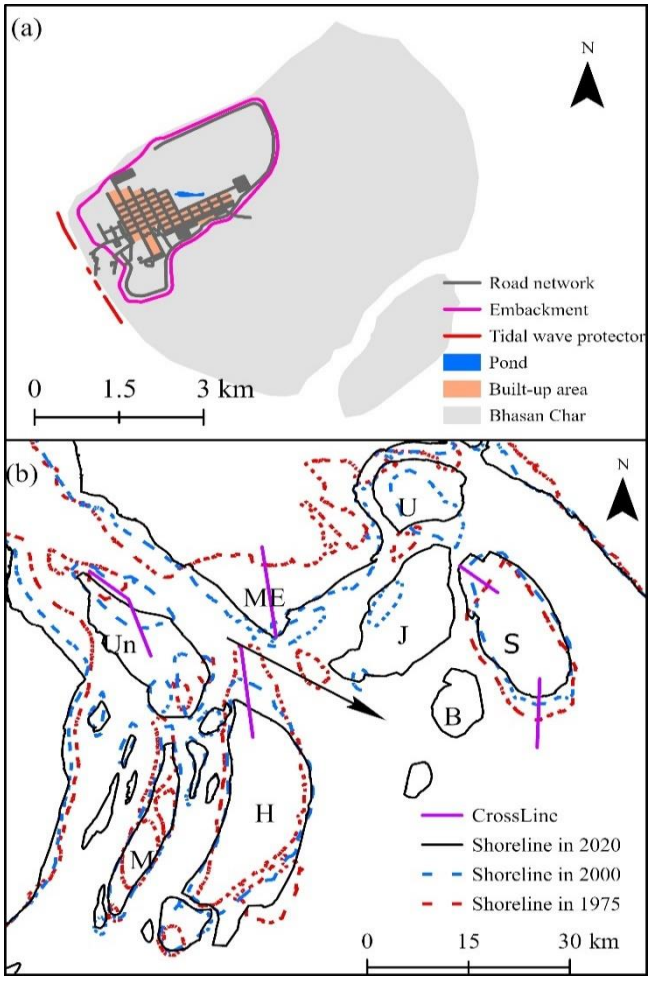

Figure 2. Features in Bhasan char (a). Different year shorelines at the mouth of Ganga-Brahmaputra-Meghna river system at Bay of Bengal (b). Location of Bhasan *Char* (B), Hatiya *Char* (H), Jahangir *Char* (J), Manpura (M), Sandwip (S), Urirchar (U), an un-named *char* (Un) and easter part of the mouth (ME) is also illustrated. Arrow indicates general flow direction.

A tidal wave-protected metallic infrastructure of ~2.3 km locates at the island's southwest face (Figs. 2a, 3c). There are 120 CSs in BC for 100 thousand persons that mean 833 people per CS can be accommodated during the cyclonic events.

The erosion and deposition of the islands at the mouth of the Ganga-Brahmaputra-Meghna river system are very regular (Fig. 2b). In 1975, the Hatiya *Char* and Sandwip were visible, including some tiny pieces of Manpura islands those become united to ~97 km^2 and visible in 2020 (Fig. 2b). About 31.7 km^2 of a piece of an island (un-named in Fig. 2b) appeared at the rivers systems mouth in 1975, which was getting larger to ~73 km^2 during 1975-2000 and shifted ~7.3 km towards southeast. Further, it's shape becomes ~192 km^2 in 2020 and moves 9.6 km in the same direction. The northern shoreline of Hatya *Char* shifted ~5.6 km and ~4.5 km during 1975-2000 and 2000-2020, respectively, towards the south. The northern and southern shorelines of Sandwip migrated ~5.2 km and ~3.5 km toward the northwest and northeast, respectively, during 1975-2020 (Fig. 2b). The area of Urirchar in 1975 was ~11 km^2 that is expanded to ~73.5 km^2 during 1975-2000 and become ~117 km^2 in 2020.

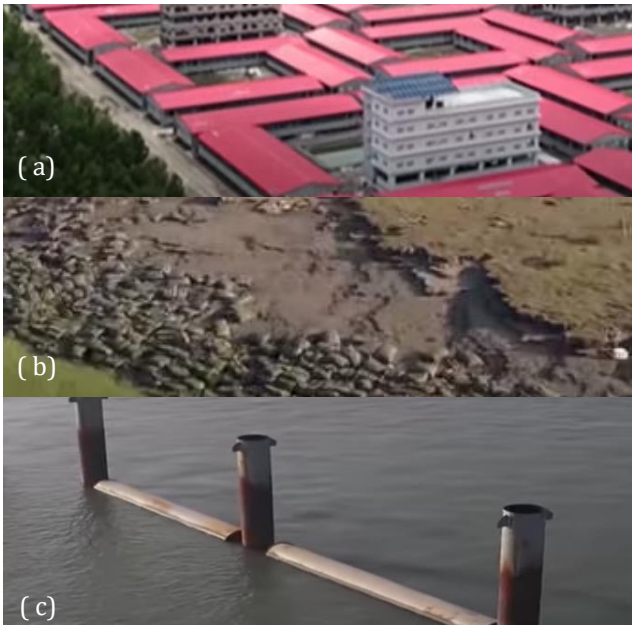

Figure 3. Bhasan char; Housing infrastructure (a), sandbag to protect the coastal erosion (b) and metallic infrastructure to protect from tidal wave (c).

The Jahangir *Char* did not appear in 1975 but became visible ~17 km^2 in 2000; however, in 2020, it becomes ~216 km^2 (Fig. 2b). Erosion at the northern shoreline at the Hatya is clearly influenced by the upstream water flow force (Fig. 2b). A massive deposition happens during 1975-2020 at the southeast mouth (ME in Fig. 2b), and the shoreline moves ~11.5 km toward the south.

4. DISCUSSION

The Bhasan Char is a sandy, newly formed island (2005-2006) with an altitude of 2.5 m that makes the island very susceptible, and many claims that it may be eroded and/or washed away by a strong flood and cyclone (Banerjee 2020; Castell 2021). This assumption becomes valid for the other surrounding islands that have eroded and migrated frequently (Fig. 2b) (Ciavola et al. 2015). During the monsoon, the rivers' flow increases, and it overflows the *Chars*, damage the infrastructure, including CSs, flood-protected embankments, crops, and livestock (Banerjee 2020; Castell 2021). A remote sensing study during 2015-2017 also suggests that BC experiences erosion at the south face and migration towards the north (Banerjee 2020).

However, some living condition in BC is far better than camps in Cox's Bazar, e.g., security and safety, housing situation and in context of landslide hazard. Some physical infrastructure in BC, e.g., CSs, embankment, wave protector is better than the nearby islands, Sandwip (450,000 population in 2016) and Hatiya *Char* (452,463 population in 2011) where the host community lives. For example, a CS for 1000 person available in Sandwip, whereas in BC, a CS is for 833 people (Castell 2021; WION 2020). But economic and social concerns may be an issue regarding a sustainable settlement.

Global warming causes an average temperature increasing of 0.019 °C/yr on the Bay of Bangle (Islam 2014; Islam et al. 2021). It increases the frequency and more intense TCs, and the Northern Indian basin shares

4%-10% TCs globally (Islam et al. 2021). Bangladesh shares 1% TCs and 53% of deaths globally (Islam et al. 2021). Before the 1990s, one severe TC occurred; however, now, 2-3 severe TCs per decade are experienced by the coastal communities in Bangladesh (Islam et al. 2021). The refugees' relocation's complete phase increases 100,000 more people in the vulnerable group in coastal Bangladesh. To protect these coastal communities from the tidal surge of a severe TC, an embankment of an average height of the tidal surge of TCs (six meters), plus one meter for expected sea-level rises by 2050, is necessary (Islam et al. 2021).

BC is a Ashrayan-3 (temporary solution for homeless) policy, not a permanent solution for the refugees. However, geopolitical behavior between Bangladesh and Myanmar suggests that the Rohingya refugee reparation is a long-term conflict since 1970s. Bangladesh enjoys very little success on this issue. An international effort, including the foreign policy of Bangladesh, could not resolve this issue, and therefore many Rohingya refugees have been living in Bangladesh since 1970s (Banerjee 2020; Grundy-Warr and Wong 1997).

5. CONCLUSION

Indeed, the Bhasan *Char* is a vulnerable place to live in terms of sustainable concept. However, this is not a place for the refugees to live permanently. Infrastructure in BC is better than that in the camps in Cox's Bazar and even in the nearby island where host communities live. If the present-day infrastructure in BC can withstand a severe TC and devastating flood, on the temporary, it may be a better place than the existing camps in Cox's Bazar.

However, many claims that BC would be like an open jail for the refugees (Castell 2021) and, therefore, sustainable parameters, e.g., economic activities, particularly income generation and social activities and network among the refugees within the Bhasan *Char* and the camps area in Cox's Bazar need to be researched.

REFERENCES

Banerjee S (2020). From Cox ' s Bazar to Bhasan Char : An Assessment of Bangladesh ' s Relocation Plan for Displaced Rohingyas. Observer Research Foundation Brief, 1–16.

Castell J (2021). Rohingya Relocation: A ground report from Bangladesh. WION Wideangle. https://www.youtube.com/watch?v=CMdHPzVUYWg (acc. 2.28.21).

Ciavola P, Uddin M M, Duo E, Fakhruddin S H M (2015). Vulnerability of the Bangladesh coastline to inundation under cyclone activity: Past records and DRR Strategies at Sandwip Island. 36th IAHR World Congress, 1–6, The Hague.

DW News (2020). Bangladesh begins relocating Rohingya refugees to remote island Bhasan Char. https://www.youtube.com/watch?v=VxLM2bYXt6g&t=1s (acc. 2.28.21).

Grundy-Warr C & Wong E (1997). Sanctuary Under a Plastic Sheet – The Unresolved Problem of Rohingya Refugees. IBRU Boundary and Security Bulletin Autumn, 79–91.

Islam M T (2014). Vegetation changes of Sundarbans based on Landsat imagery analysis between 1975 and 2006. Landscape & Environment 8, 1–9.

Islam M T (2013). Time Series Landsat Remote Sensing Images and Geographical Information System to Environmental Evaluation of Sites for the Padma River Bridge. Int. J. Remote Sensing & GIS 2, 114–121.

Islam M T (2010). Evaluation of Sites For A River Bridge: A GIS And Remote Sensing. Master Thesis, Royal Institute of Technolongy, Stockholm.

Islam M T (2010a). River channel migration: A remote sensing and GIS analysis. ESA Living Planet Symposium, 1-6, Bergen.

Islam M T (2009). Quantification of eroded and deposited riverbanks and monitoring river's channel using RS and GIS. 17th Int. Con. Geoinformatics, 12-14, Fairfax, VA. https://doi.org/10.1109/GEOINFORMATICS.2009.5293151

Islam M T (2009a). Bank erosion and movement of river channel: A study of Padma and Jamuna Rivers in Bangladesh using Remote sensing and GIS. Master Thesis, Royal Institute of Technolongy, Stockholm.

Islam M T, Charlesworth M, Aurangojeb M, Hemstock S, Sikder S K, Hassan M S, Dev P K & Hossain M Z (2021). Revisiting disaster preparedness in coastal communities since 1970s in Bangladesh with an emphasis on the case of tropical cyclone Amphan in May 2020. Int. J. Disaster Risk Reduction, 58, 1–15. https://doi.org/10.1016/j.ijdrr.2021.102175

Li W, Du Z, Ling F, Zhou D, Wang H, Gui Y, Sun B & Zhang X (2013). A comparison of land surface water mapping using the normalized difference water index from TM, ETM+ and ALI. Remote Sensing 5, 5530–5549. https://doi.org/10.3390/rs5115530

Manugula S S & Bommakanti V (2017). Photogrammetry, GIS & Remote Sensing. Edu. Pub., Chhattisgarh.

OCHA (2020). Rohingya Refugee Crisis. https://www.unocha.org/rohingya-refugee-crisis (acc. 4.5.20).

OpenStreetMap Foundation (2018). Terms of Use. Open Street Map. https://wiki.osmfoundation.org/w/index.php?title=Terms_of_Use&oldid=5789 (acc. 2.21.21).

Palma P & Jinnat M A (2020). Facilities in Bhashan Char: Rohingya leaders satisfied after trip. The Daily Star.

Prothom Alo (2021). Fifth phase, 2280 Rohingya going to Bhasanchar (পঞ্চম দফায় আরও ২২৬০ রোহিঙ্গা ভাসানচরেযাচ্ছেন). https://www.prothomalo.com/bangladesh/পঞ্চম-দফায়-আরও-২২৬০-রোহিঙ্গা-ভাসানচরে-যাচ্ছেন (acc. 3.26.21).

United States Geological Survey (n.d.). United State Department of the Interior, Washington D.C. https://earthexplorer.usgs.gov/ (acc. 8.19.19).

WION, 2020. Gravitas: Bangladesh is re-locating 1,00,000 Rohingya Refugees. https://www.youtube.com/watch?v=X-SbvpxwL00 (acc. 3.26.21).

Intercontinental Geoinformation Days

igd.mersin.edu.tr

Accuracy of digital elevation models; under canopy vs. open field

Halit ALTUN[1], **Arif Oguz ALTUNEL**[*1]

[1]Kastamonu University, Department of Forestry Engineering, Kastamonu, Turkey

Keywords
Remote sensing
Digital Elevation Models
Accuracy Assessment
RMSE

ABSTRACT

Digital Elevation Models have been known as the representations of terrain elevation data captured, processed and released by remote sensing capabilities. They could either be called Digital Surface Models, which include elevation data of the Earth along with the objects later placed by the humans, or Digital Terrain Models, which only reflect the real z values of the bare ground. This is a conundrum for the latter definition since a considerable amount of earth surface is covered with natural and artificial objects, forests being the most noteworthy. Furthermore, the usage of them on areas covered by forests is a popular phenomenon deserving an in depth questioning. For this reason, the measurement of how accurate they are, is necessary on terrains covered by forests vs. on terrains which barely involves vegetation or no vegetation at all. In this study, the elevation data of Shuttle Radar Topography Mission C-band SAR 30 m Global DEM, Shuttle Radar Topography Mission X- band SAR 25 m partial Global DEM, ALOS Phased Array type L-band SAR 12.5 m Global DEM, ALOS World 3D Precise 30 m Global Digital maps and Advanced Spaceborne Thermal Emission and Reflection Radiometer (ASTER v3) 30 m Global DEM were compared to a high density sample of z values generated by Real Time Kinetic Global Positioning System. Results showed that under the forest canopy, the margin of error increased across the elevation data.

1. INTRODUCTION

Digital Elevation Models (DEMs) are 3 dimensional images which are composed of grids that have elevation values in. They are important datasets used in many fields (Aronoff, 2005) such as management perspectives in natural resources, engineering and infrastructure, disaster and risk analysis, archaeology, security, aviation, forestry, energy, topographic mapping, landslide and flood analysis (Makineci & Karabörk 2016), with ease. They can be manipulated and various new geographical information like elevation, gradient, aspect, topographical roughness, etc. (Ravibabu & Jain, 2008) can be derived from them through Remote Sensing (RS) and Geographical Information System (GIS) capabilities. The first ever Global DEMs were produced by NASA and European Space Agency (ESA) after an 11-day shuttle program equipped with C-band and X-band Synthetic Aperture Radar (SAR) sensors in 2000. However, for remote sensing capabilities, acquiring the elevation information of the ground is difficult to achieve when the ground is covered by natural and artificial objects. Forest vegetation is one of the most encountered obstacle in the way among them. Accuracy in spatial information is a must for forestry, natural resource management, landscape planning, decision making and many other areas, (Murphy et al. 2008). For this purpose, investigating how much accuracy DEMs have under the forest canopy compared to those from the open fields is necessary. In this paper, the acknowledged open source DEMs which are Shuttle Radar Topography Mission C-band SAR 30 m Global DEM (SRTM C-band), Shuttle Radar Topography Mission X- band SAR 25 m partial Global DEM (SRTM X-band), ALOS Phased Array type L-band SAR 12.5 m Global DEM (ALOS PALSAR), ALOS World 3D Precise 30 m Global Digital maps (AW3D30) and Advanced Spaceborne Thermal Emission and Reflection Radiometer (ASTER v3) 30 m Global DEM are compared to Real Time Kinetic Global Positioning System (RTK-GPS) elevation values taken in the province of Kastamonu, Turkey. The result values of Root Mean Square Error (RMSE), which were

* **Corresponding Author**

(haltun@ogr.kastamonu.edu.tr) ORCID ID 0000-0002-1027-7666
*(aoaltunel@kastamonu.edu.tr) ORCID ID 0000-0003-2597-5587

Cite this study

Altun, H & Altunel, A. O. (2021). Accuracy of digital elevation models; under canopy vs. open field. 2nd Intercontinental Geoinformation Days (IGD), 56-59, Mersin, Turkey

indication of the value of difference between the model and an observed value, showed that the absolute error of elevation values extracted from DEMs under forest canopy were greater than the ones on the open lands.

2. METARIAL AND METHODOLOGY

Turkey has been undertaken watershed rehabilitation projects to fight the effects of global warming. Water deposition projects were devised throughout the country. The study area which had previously been surveyed using high precision RTK-GPS in order to get a better view of the topography in this context, was chosen because it also expanded over forest canopy. The location of the study area was situated between 41°12'49'' - 41°14'20'' Northern Latitudes and 33°22'12'' - 33°28'11'' Eastern Longitudes in Kastamonu, Turkey (Figure 1).

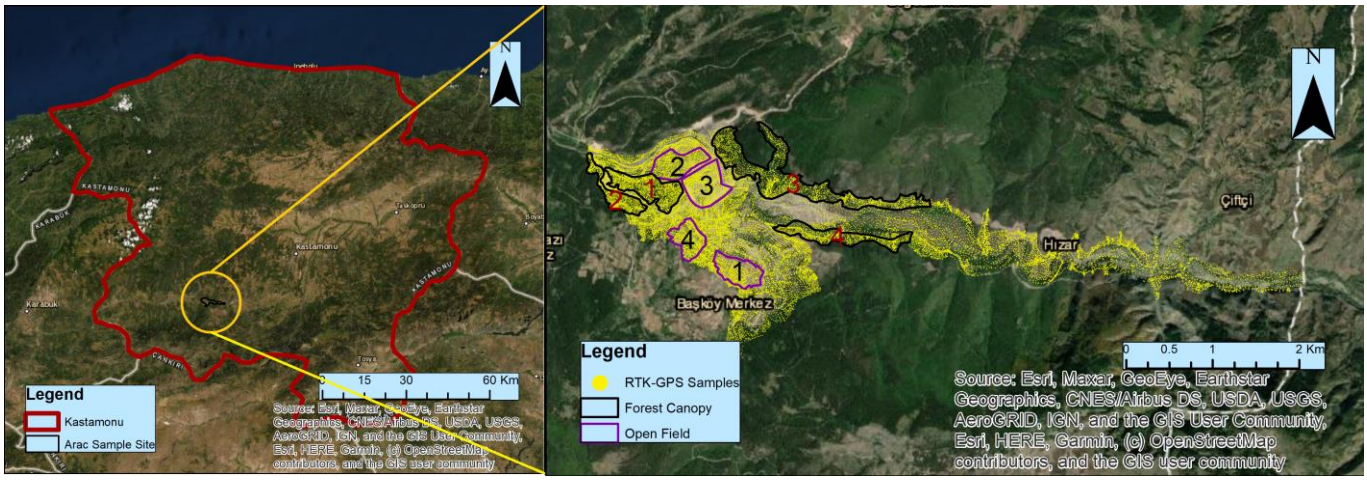

Figure 1. Study Area

Table 1. Land cover type information

Forest Canopy	Area(ha)	Number Of RTK-GPS Points	RTK-GPS Points/Hectare
1	20.57	2714	131.95
2	11.95	1596	133.52
3	57.86	3430	59.28
4	19.19	2343	122.12
Open Field			
1	14.34	2378	165.81
2	15.17	2421	159.61
3	18.21	2794	153.44
4	12.10	2380	196.73

Land cover types for the study were classified as forest canopy and open field. Four locations with enough location readings were selected for each class. Sample sites of forest canopy 1, 2, 3 and 4 had the areas of 20.57, 11.95, 57.86 and 19.19 hectares, respectively. The areas of open field 1, 2, 3 and 4 were 14.34, 15.17, 18.21 and 12.1 hectares, respectively. Google Earth Pro was used for the selection process. The fields of forest canopy were picked from highly dense forest vegetation. Although site number 3 was not as much dense as the others, it still had significant amount of canopy in it. The land use in three of the open fields was agriculture. Site number 3 of open field was a construction site which was predominantly bare ground. GPS point density was ranging from 59,28/ha to 196,73/ha for sampling sites (Table 1).

Data from the mentioned open source DEMs and GPS survey points were processed using ArcMap 10.5. GPS point location z values within the specified class sites were compared to those of the open source DEM extracted z values and root mean square errors (RMSE) were calculated for each class site.

In ArcMap, first, a raster DEM model was generated, using the random GPS points. The procedure allowed us to produce a spatial resolution of 22.7 meter through points to raster conversion (Figure 2). Second, utilizing this newly generated DEM, four sets of systematic points were produced for each land cover type by assigning a point to the center of each raster cell in the model (Figure 3). Third, new systematic points were placed on each open source DEM, and new elevations were extracted for each point from the them (Altunel 2020). Finally, RMSEs were calculated for each land cover class from each DEM.

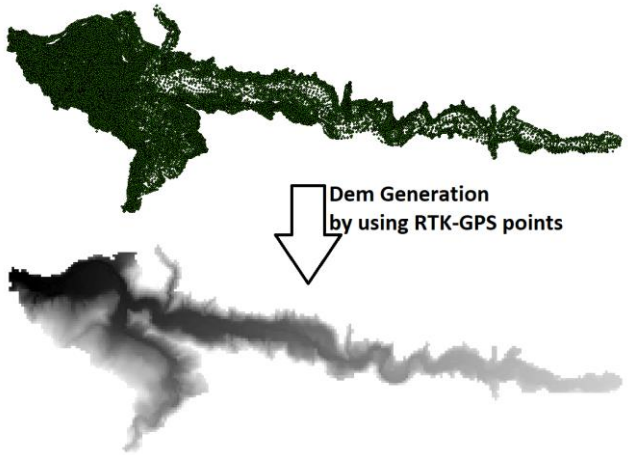

Figure 2. High resolution DEM generated from random GPS points

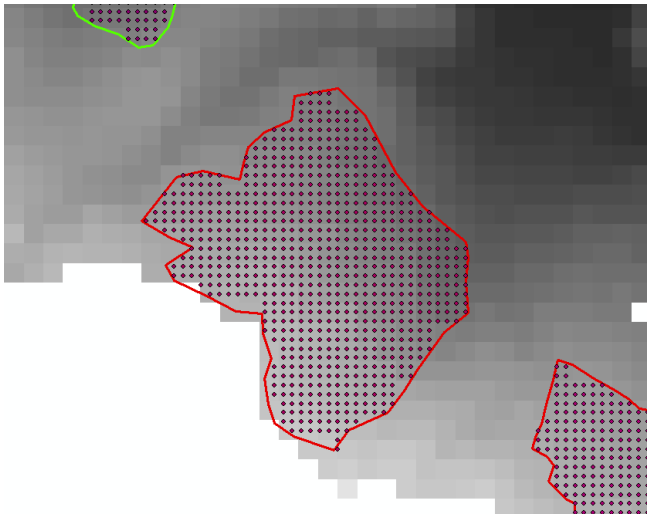

Figure 3. Systematical points, produced from high resolution DEM

RMSE, which has been a frequently used formula for measuring the difference between the measured and model elaborated values, was utilized to evaluate the difference between the GPS measured and open source DEM extracted values.

3. RESULTS

RMSEs between the elevations of GPS, as field measured values, and the elevations of SRTM, SRTM X-band, ALOS PALSAR, AW3D30 and ASTER, as model extracted values, were calculated (Table 2).

It was expected that RMSE values in forest canopy sites would be greater than RMSE values in open field sites for each test of DEMs, individually. The results of all sites in SRTM, SRTM X-band and AW3D30 indicated that this was the case because the difference in RMSE value between forest canopy and open field were considerable. However, site 4 in open field in ASTER had a RMSE value of 12.78 which exceeded the RMSE value of site 2, 3 and 4 in forest canopy. Moreover, site 3 in forest canopy in ALOS PALSAR had a RMSE value of 37.68 which was less than site 3 and 4 in open field.

Regardless of these two sites in ASTER and ALOS PALSAR, as shown in Table 2, RMSE values of all forest canopy sites were greater than RMSE values of all open field sites.

Table 2. RMSE values distributed with respect to open field and forest canopy sites

Sample Sites	RMSE Values of The DEMs (m)				
Forest Canopy	SRTM C-band	SRTM X-band	ASTER v3	ALOS PALSAR	AW3D30
1	10.05	41.64	12.85	45.69	9.45
2	10.66	42.02	10.51	45.66	8.09
3	8.53	38.27	12.51	37.68	9.22
4	10.33	38.77	12.14	48.02	7.92
Open Field					
1	2.69	34.08	9.27	36.42	3.12
2	2.66	33.72	7.58	36.63	3.3
3	6.13	36.68	7.69	39.4	5.21
4	4.76	34.88	12.78	38.51	3.39

4. DISCUSSION and CONCLUSION

This paper set out to evaluate the accuracy of the most acknowledged open source DEMs under forest canopy against open field. It was expected to find out that under canopy accuracy level would decrease. When the DEMs were compared to the GPS sample points, the results of RMSE values indicated that this was indeed the case with the exception of two sites.

SRTM C-band, SRTM X-band and ALOS PALSAR were the synthetic aperture radar (SAR) signal based DEMs which used the microwaves of the electromagnetic spectrum to predict the elevation of target areas. It was shown that longer wavelengths of microwaves penetrate vegetation to a far greater extent (Churchill et al. 1985). While C-band wavelengths were ranging from 3.75cm to 7.5cm, in the case of X-band on the other hand, they were ranging from 2.5cm to 3.75cm. So this can explain why SRTM C-band was better than SRTM X-band under canopy, although in open field, accuracy difference was approximately the same between them.

ALOS PALSAR used L-band whose wavelengths are ranging from 15cm to 30cm and longer than SRTM C-band and SRTM X-band. However, the results of RMSE values from it were counterintuitive to the fact that longer wavelengths of microwaves penetrated the canopy more. Alaska Satellite Facility which is the open source data provider for ALOS PALSAR used in this paper made the project of Radiometric Terrain Correction (RTC) so that the SAR data and the derivatives produced from them were more reliable to a broader community of users. In the validation trials, SRTM and National Elevation Datasets (NED) were used as comparison source data. However, the vast range topographical differences all across the world were probably much more than what it could efficiently represent. In this particular study, the results indicated that it failed to deliver more desirable

outcome than one of the other comparison data, SRTM C-band, used in this paper.

ASTER v3 and AW3D30 utilized stereo correlation to produce DEM by using the stereo pairs. Their results of RMSE values in line with the argument that accuracy level of DEMs would decrease under forest canopy except the result of ASTER v3 for site 4 in open field. Both give better results than SRTM X-band and ALOS PALSAR. However, AW3D30 performed better than ASTER v3 and its results were very similar to the SRTM C-band as the recent study suggests (González-Moradas & Viveen 2020).

Overall, all of the DEMs put to the test in this study performed better in open field sites than forest canopy sites which is in the line with the expectancy of this research. In future, this kind of study should be done bigger areas and more remote sample sites to each other should be selected than the sample sites in this paper.

REFERENCES

Altunel, A. O. (2020). Questioning the effects of raster-resampling and slope on the precision of TanDEM-X 90 m digital elevation model. *Geocarto International*. https://doi.org/10.1080/10106049.2020.1840636.

Aronoff, S. (2005). *Remote sensing for Gis managers* ESRI Press. 1st ed., p.487.

Churchill, P. N., Horne, A. I., & Kessler, R. (1985). A Review of Radar Analyses of Woodland. In *Microwave remote sensing applied to vegetation: proceedings of an EARSeL Workshop*, pp. 25–34. essay, European Space Agency.

González-Moradas, M. del R., & Viveen, W. (2020). Evaluation of ASTER GDEM2, SRTMv3.0, ALOS AW3D30 and TanDEM-X DEMs for the Peruvian Andes against highly accurate GNSS ground control points and geomorphological-hydrological metrics. *Remote Sensing of Environment*, *237*.

Makineci, H. B., & Karabörk, H. (2016). Evaluation Digital Elavation Model Generated by Synthetic Aperture Radar Data. *Remote Sensing and Spatial Information Sciences*, *XLI-B1*, 57–62.

Murphy, P. N. C., Ogilvie, J., Meng, F.-R., & Arp, P. (2008). Stream network modelling using lidar and photogrammetric digital elevation models: a comparison and field verification. *Hydrological Processes*, *22*, 1747–1754.

Ravibabu, M. V., & Jain, K. (2008). Digital Elevation Models Accuracy Aspects. *Journal Of Applied Sciences*, *8*, 134–139.

Intercontinental Geoinformation Days

igd.mersin.edu.tr

Geostatistical mapping of reference crop evapotranspiration (ETo)

Fatma BUNYAN UNEL*[1], Lutfiye KUSAK[1], Murat YAKAR[1], Abdullah SAHIN[2], Hakan DOGAN[3], Fikret DEMIR[4]

[1]*Mersin University, Engineering Faculty, Department of Geomatics Engineering, Mersin, Turkey*
[2]T.C. Governorship of *Sinop, Sinop, Turkey*
[3]*Turkish State Meteorological Service, Ankara, Turkey*
[4]*Mersin Provincial Directorate of Meteorological Department, Mersin, Turkey*

Keywords
Meteorological Data
Reference Crop Evapotranspiration
Penman Monteith Method
Geostatistical Mapping

ABSTRACT

Usable natural water resources on the earth's surface are decreasing. The water mostly used in agriculture should be consumed as much as the plant needs and irrigation plans should be prepared for this. Reference Crop Evapotranspiration (ETo) can be estimated according to climatic conditions. The aim of this study is to estimate the Reference Crop Evapotranspiration of Mersin province using Penman Monteith method and produce its geostatistical map. For this, temperature, humidity, sunshine duration, wind speed and meteorological data of the month of May 2017-2020 of 28 meteorological stations provided from Mersin Provincial Directorate of Meteorology were used. The equation used in Penman Monteith method was written with buttons in MatLAB guide programming language and ETo values were calculated and estimated. Mersin province's reference crop evapotranspiration map was created as geostatistical by correlating the Eto values for the years 1 May 2017-2020 with each station and it was observed that the highest water requirement was found on May 1, 2018.

1. INTRODUCTION

Although 70% of the earth's surface is covered with water, the amount of natural spring water available is approximately 2.5%. 69.5% of this water is in glacial or frozen soil layer at the poles, approximately 30.1% is in groundwater, and the remaining 0.4% is in atmospheric and surface waters. The demand for water in the world is increasing day by day due to the increase in population, global warming, natural disasters and environmental pollution. 70% of the natural spring water is used in agriculture (Development Planı, 2014; Smedley, 2017). It is necessary to protect, manage and recycle freshwater to support human health and sustainable development (United Nations, 2017; 2018).

The reference crop evapotranspiration is the water consumption resulting from the evaporation of natural objects on the land surface and the sweating of plants (TAGEM, 2017). Reference Evapotranspiration (ETo), taken as a reference to the water consumption of grass, can be calculated with the water consumption of other plant species (Allen et al., 1998; TAGEM, 2017).

In national studies on reference crop evapotranspiration; water consumption for the selected plant (Biber & Kara, 2006; Emekli & Baştuğ, 2007; Uçar et al., 2017), forecast models (Taş & Kırnak, 2011; Şarlak & Bağçacı, 2020), seasonal impact on climate change (Bayramoğlu, 2013), geographical issues such as the use of information systems (Güler, 2014), reference crop evapotranspiration values and irrigation programs (Gürgülü & Ul, 2017), spatial and temporal distribution (Karaca et al., 2017), use of AGROS software in irrigation water management (Köksal, 2018). has been taken. In international studies; Water consumption for the selected plant (Fenech et al., 2019), crop evapotranspiration database (Tomas-Burguera et al., 2019), Bangladeş historical background of reference crop evapotranspiration due to climate (Mousumi et al., 2019) were examined. In Bosnia and Herzegovina, with the Penman-Monteith method, the annual ETo was found to be 716 mm, and it was stated that approximately 78%

* **Corresponding Author**

*(fatmabunel@mersin.edu.tr) ORCID ID 0000-0002-9949-640X
(lutfiyekusak@mersin.edu.tr) ORCID ID 0000-0002-7265-245X
(myakar@mersin.edu.tr) ORCID ID 0000-0002-2664-6251
(absahin@hotmail.com) ORCID ID 0000-0002-2405-5837
(hadogan@mgm.gov.tr) ORCID ID 0000-0003-3505-5864
(fidemir@mgm.gov.tr) ORCID ID 0000-0001-7675-9492

Cite this study

Unel, F.B., Kusak, L., Yakar, M., Sahin, A., Dogan, H. & Demir, F. (2021). Geostatistical mapping of reference crop evapotranspiration (ETo). 2nd Intercontinental Geoinformation Days (IGD), 60-63, Mersin, Turkey.

of this occurred in the vegetation period (April-September) (Čadro et al., 2019). In addition, the reference crop evapotranspiration estimates were made from satellite images (Granger, 2000).

The aim of this study is to calculate the Reference Crop Evapotranspiration (ETo) using the Penman Monteith method in the province of Mersin in MatLAB guide programming language and show the results with a geostatistical map. Equation (1) in Penman-Monteith method is coded in MatLAB guide programming language. Meteorological data of 28 Automatic Meteorological Observation Stations (OMGI) obtained from the General Directorate of Meteorology and Mersin Provincial Directorate of Meteorology were used. ETo values were calculated with 31-day meteorological data in May of 2017, 2018, 2019 and 2020. These values were matched with the station points in ArcGIS software and their map was produced with IDW (Inverse distance weighted), one of the geostatistical analysis methods.

2. METHOD

Study area is located in Mersin Province, which is in the Mediterranean region, Turkey, is between 36 ° 01' - 37° 25' north latitude 32° 47' - 35 ° 23' east longitude (Figure 2). The study area is characterized by Mediterranean climate, which is hot and dry in summers, and warm and rainy in winters (MGM, 2020). It has fertile agricultural lands and there are four savanna within the borders of Mersin province (BKK, 2017). Especially in the dry summer months, plants need maximum water.

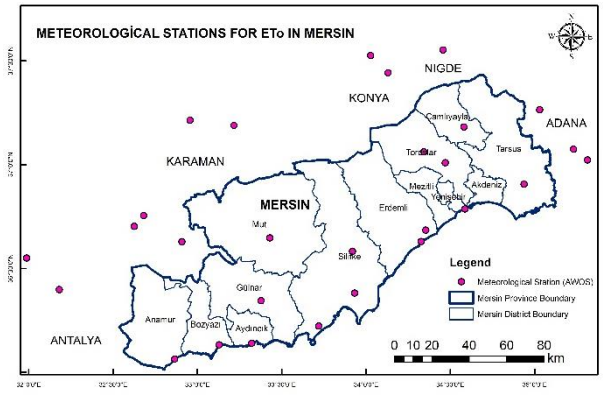

Figure 1. Meteorological stations

Automated Weather Observing System (AWOS) is a system that is sensitive to changes in meteorological parameters and consists of sensors that measure the amount of these changes and transmit data automatically (MGM, 2020). This system constitutes the whole of the meteorological stations in the field. 28 Meteorological station information and their data were obtained from Meteorology Mersin Provincial Directorate. The meteorological data, which are maximum-minimum temperature and relative humidity, wind speed and sunbathing time, belonging to a total of 28 stations, 15 in Mersin and 13 in neighboring provinces, were arranged. In addition, the height of the station and the height at which the wind was measured, the maximum possible sunshine duration and radiation reaching the outer surface of the atmosphere were collected. The raw data set of May for each station between 2017-2020 was made ready to be used in the Penman-Monteith method.

Penman-Monteith is a method adopted by the United Nations-UN, Food and Agriculture Organization-FAO in 1998. The guidelines are presented for computing crop water requirements in FAO Irrigation and Drainage Paper No. 56 (Allen et al., 1998). Since it is the closest method to real measurements made with Lysimeter, it is also accepted in the literature and is taken as a reference in model estimates (Saggi & Jain, 2019; Sanikhani et al., 2019). In addition, when calculating the evapotranspiration of a specific plant, the value found from the Penman-Monteith method is taken into account as ETo (Bruin & Trigo, 2019; Fenech et al., 2019).

$$ET_o = \frac{0{,}408\Delta(R_n - G) + \gamma \frac{900}{T+273} u_2 (e_s - e_a)}{\Delta + \gamma(1 + 0{,}34u_2)} \quad (1)$$

In Penman-Monteith Method, Equation (1) is mean following (Allen et al., 1998).
ET_o, Reference Crop Evapotranspiration (mm/gün)
Δ, slope of saturation vapour pressure curve [kPa °C-1],
R_n, net radiation [MJ m-2 day-1]
G, soil heat flux [MJ m-2 day-1],
γ, psychrometric constant [kPa °C-1],
T, average air temperature [°C]
u_2, wind speed at 2 m above ground surface [m s-1],
$(e_s - e_a)$, saturation vapour pressure deficites.

Value estimates can be found by downloading the "ETo calculator" published by FAO. The symbols seen in Penman-Monteith Equation (1) have expansions. Sub-variables of these symbols that depend on each other and the station latitude are calculated. But for this study, ETo values were estimated by using original programming.

3. RESULTS AND DISCUSSION

Reference Crop Evapotranspiration was calculated using the program written by the authors using the Penman-Monteith method. For each of the 28 meteorological stations, the days of May 1-31 were found between 2017-2020.

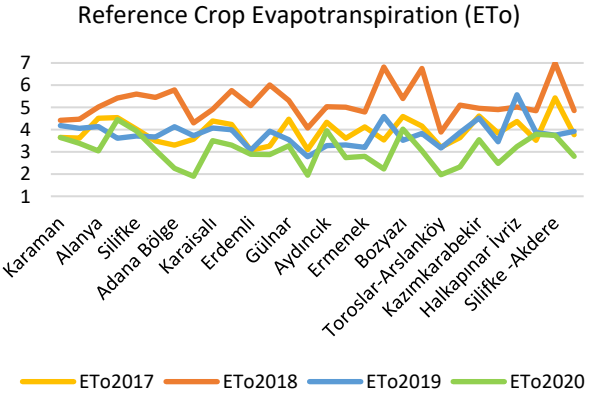

Figure 3. ETo in 2017-2020

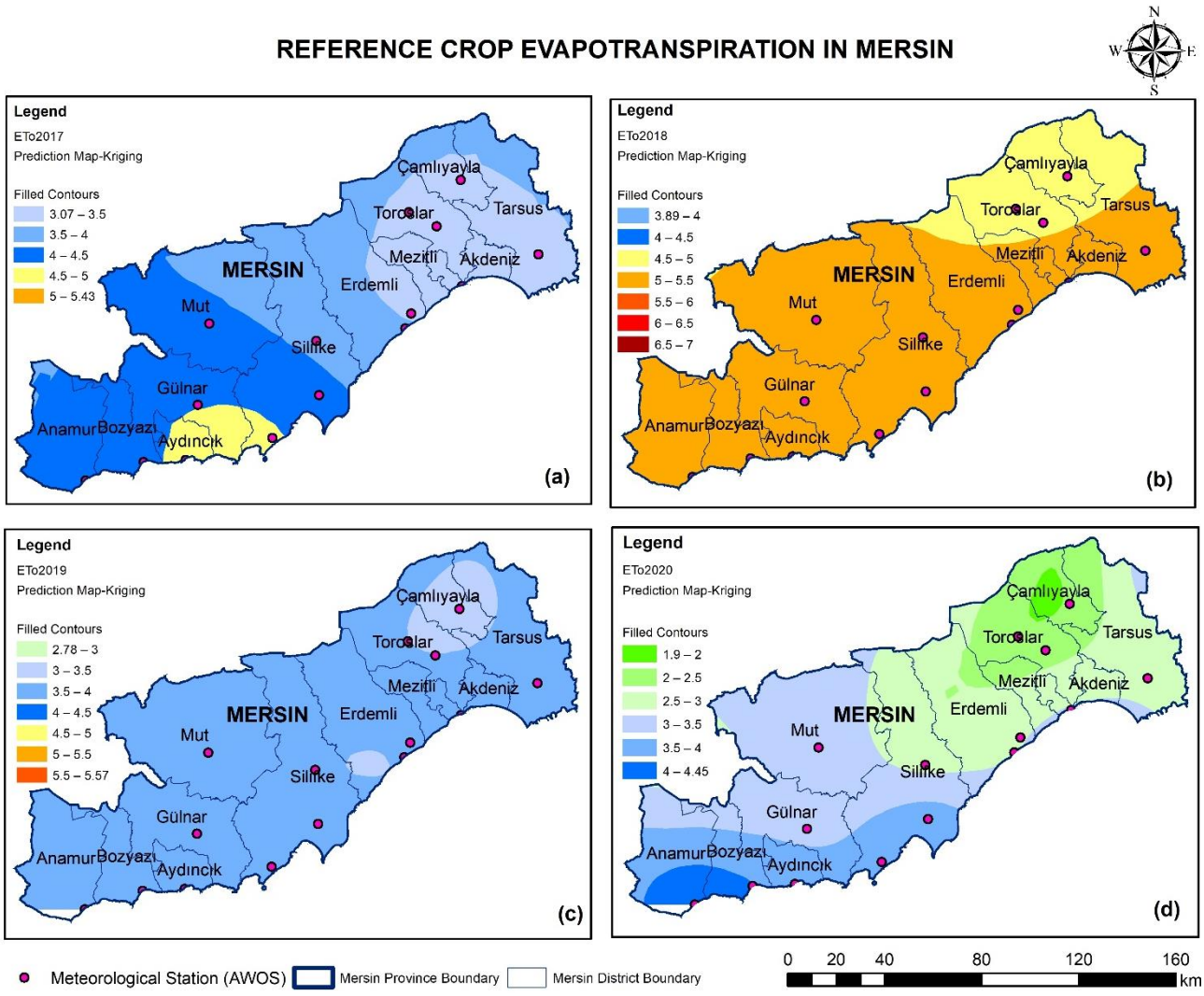

Figure 4. Maps of reference crop evapotranspiration (mm/gün)

The amount of water consumed by each plant is different, and ETo is required to find this amount. ETo shows the amount of water consumed by the grass plant, taken as a reference. Figure 3 shows that in 2018, there was a greater need for water than others. For Çamlıyayla, Toroslar and Ulukışla districts, there is a consistently low water need every year (Figure 3).

Mersin province and district borders and 28 meteorological stations were transferred to ArcGIS 10.5 geographic information system software in order to produce the statistical map of Eto. Separate map of each day of May can be created. However, in this study, maps of reference crop evapotranspiration were prepared for the years 2017-2020, taking into account only May 1. It was used kriging which is one of method of Geostatistical analyst. Not all colors in Legends appear on the maps. Because the geostatistical map is arranged according to Mersin provincial border (Figure 4).

When the maps were examined, it was observed that there was a high water requirement in Mersin on May 1, 2018. On May 1, 2017 and 2019, ETo remained especially in the range of 3-4.5 mm / day. On May 1, 2020, it was determined that the minimum water requirement was found in Çamlıyayla and its surroundings from the ETo value.

4. CONCLUSION

The basic requirements of the world's population are water and food. Agricultural areas need to be cultivated / planted for food production. It is known that most of the water consumption is used for agricultural purposes. For this reason, planning of crop evapotranspiration is of great importance. When the dam, artificial lake, pond is established, the dimensions of the irrigation canals can be determined according to the water needs of the surrounding agricultural areas. In agricultural areas, water need can be determined according to the cultivated plant type and irrigation can be done accordingly. In this case, both soil, water resources and plant will be protected.

In future studies, the ETo value estimated using the Penman-Monteith method can actually be compared with the ETo value obtained from the measurement result using the lysimeter. ETo can be predicted using modern methods.

ACKNOWLEDGEMENT

This study is one of products of research project between Governorship of Mersin, Turkish State Meteorological Service, Mersin Provincial Directorate of

Meteorological Department and Mersin University, Department of Geomatics Engineering on 04/02/2019-29/12/2020.

REFERENCES

Allen, R.G., Pereira, L.S., Raes, D. & Smith, M. (1998). Crop evapotranspiration - Guidelines for computing crop water requirements - FAO Irrigation and drainage paper 56, FAO - Food and Agriculture Organization of the United Nations, Rome.

Bayramoğlu, E. (2013). Trabzon İlinde İklim Değişikliğinin Mevsimsel Bitki Su Tüketimine Etkisi: Penman-Monteith Yöntemi. Kastamonu Üni., Orman Fakültesi Dergisi, 13(2), 300-306.

Biber, Ç, & Kara, T. (2006). Mısır Bitkisinin Bitki Su Tüketimi ve Kısıtlı Sulama Uygulamaları, OMÜ Zir. Fak. Dergisi, 21(1), 140-146.

BKK, (2017). Büyük Ova Koruma Alanı, 2016/9620 sayılı Bakanlar Kurulu Kararı, Resmi Gazete Tarihi: 21 Ocak 2017, Sayısı: 29955.

Bruin, H. A. R. D. & Trigo, I. F. (2019). A New Method to Estimate Reference Crop Evapotranspiration from Geostationary Satellite Imagery: Practical Considerations, Water, 11(382), doi:10.3390/w11020382

Čadro, S., Cherni-Čadro, S., Marković, M. & Žurovec, J. (2019). A reference evapotranspiration map for Bosnia and Herzegovina, International Soil and Water Conservation Research, 7(1), 89-101.

Development Planı, (2014). 10. Development Plan (T.C. Onuncu Kalkınma Planı), Su Kaynakları Yönetimi ve Güvenliği. Özel İhtisas Komisyonu Raporu, Ankara.

Emekli, Y. & Baştuğ, R. (2007). Antalya'da Tarla Koşullarında Bermuda Çiminin Su Tüketimi ve Bazı Kıyas Bitki Su Tüketimi Eşitliklerinin Geçerliliğinin Belirlenmesi, Akdeniz Üniversitesi Ziraat Fakültesi Dergisi, 20(1), 45-57.

Fenech, S., Knox, J., Borg, M., Camilleri, C. & Rizzo, A. (2019). Estimating Impacts of Land Use Change on Evapotranspiration for Three Agricultural Crops in Malta—A Preliminary Assessment, Journal of Agricultural Science, 11(3).

Granger, R.J. (2000). Satellite-derived estimates of evapotranspiration in the Gediz basin. Journal of Hydrology, 229(1–2), 70-76. https://doi.org/10.1016/S0022-1694(99)00200-0

Güler, M. A. (2014). Comparison of Different Interpolation Methods Using the Geographical Information System for the Production of Reference Evapotranspiration Maps in Turkey, Journal of the Meteorological Society of Japan, 92(3), 227–240.

Gürgülü, H. & Ul, M. A. (2017). İzmir'de Yetiştirilen Bazı Bitkiler İçin Bitki Su Tüketimi Değerleri ve Sulama Programları. Ege Üniv. Ziraat Fak. Derg., 54 (3), 311-317.

Karaca, C. Büyüktaş, D., Baştuğ, R. Aydinşakir, K. & Tekelioğlu, B. (2017). Antalya koşullarında kıyas bitki su tüketiminin alansal ve zamansal dağılımının belirlenmesi, Derim, 34(2), 158-171.

Köksal, E. S. (2018). Sulama Suyu Yönetiminde Yeni Geliştirilen AGROS Bilgisayar Yazılımının Kullanılma Olanakları, Süleyman Demirel Üniversitesi Ziraat Fakültesi Dergisi, 1. Uluslararası Tarımsal Yapılar ve Sulama Kongresi Özel Sayısı, 457-467.

MGM, (2020). https://www.mgm.gov.tr 15.11.2020

Mousumi, K.A., Mojid, A., Ahmad, T., Uddin, Z. & Parvez, F. (2019). Climate-induced historical drift of reference evapotranspiration in Mymensingh region of Bangladesh, J Bangladesh Agril Univ, 17(2), 258–264.

Saggi, M. K. & Jain, S. (2019). Reference evapotranspiration estimation and modeling of the Punjab Northern India using deep learning, Computers and Electronics in Agriculture, 156, 387–398.

Sanikhani, H., Kisi, O., Maroufpoor, E. & Yaseen, Z. M. (2019). Temperature-based modeling of reference evapotranspiration using several artificial intelligence models: application of different modeling scenarios. Theoretical and Applied Climatology, 135, 449–462. https://doi.org/10.1007/s00704-018-2390-z

Smedley, T. (2017). Is the world running out of fresh water? BBC Future, Erişim Tarihi: 20.03.2021 http://www.bbc.com/future/story/20170412-is-the-world-running-out-of-fresh-water

Şarlak, N. & Bağçacı, S. Ç. (2020). Ampirik Potansiyel Evapotranspirasyon Tahmin Yöntemlerinin Değerlendirilmesi: Uygulama Konya Kapalı Havzası, Teknik Dergi, 9755-9772, Yazı 565.

TAGEM, (2017). Türkiye'de Sulanan Bitkilerin Bitki Su Tüketimleri. Ar-Ge & İnovasyon, TAGEM ve DSİ, Ankara.

Taş, İ., & Kırnak, H. (2011). Yarı Kurak İklim Bölgelerinde Bitki Su Tüketiminin Tahmininde Kullanılabilecek Ampirik Modeller, ADÜ Ziraat Fakültesi Dergisi, 8(1), 57 – 66.

Tomas-Burguera, M., M. Vicente-Serrano, S. Beguería, S., Reig, F. & Latorre, B. (2019). Reference crop evapotranspiration database in Spain (1961–2014), Earth Syst. Sci. Data, 11, 1917–1930, 2019 https://doi.org/10.5194/essd-11-1917-2019

Uçar, Y., Kazaz, S. İnal, F. E. & Baydar, H. (2017). Empirical Models Likely to Be Used to Estimate the Evapotranspiration of Oil Rose (Rosa damascena Mill.), Süleyman Demirel Üniversitesi Ziraat Fakültesi Dergisi, 12 (1), 1-10.

United Nations, (2017). Freshwater Strategy 2017-2021. United Nations Environment Programme, UN Environment's Inter-Divisional Water Group.

United Nations, (2018). Nature-Based Solutions for Water. The United Nations World Water Development Report 2018, UNESCO, Paris, France.

Intercontinental Geoinformation Days

igd.mersin.edu.tr

Mapping of local soil conditions in GIS environment: A case study in Çukurkeşlik village

Aydın Alptekin*[1], Murat Yakar[2]

[1]Mersin University, Engineering Faculty, Geological Engineering Department, Mersin, Turkey
[2]Mersin University, Engineering Faculty, Geomatics Engineering Department, Mersin, Turkey

Keywords
GIS
MASW
Borehole
Microzonation

ABSTRACT

Turkey has frequently exposed to natural disasters due to its geomorphological structure. Urbanization should be well planned in order to survive disasters with the least damage. Local ground conditions need to be determined in order to create healthy cities. Soil parameters need to be mapped in order to design the earthquake-resistant building and predict the liquefaction potential of the land. In this study, it is aimed to map soil geo-engineering parameters for Mersin Province Çukurkeşlik District. Engineering geological maps were created from the data obtained from drilling and seismic studies in the region using Geographic Information System (GIS). Ground dominant vibration period, the average shear wave velocity of the top 30 m of the soil, soil amplification and Atterberg Limits were modeled in GIS. In this study, the landslide area was mapped with a small data set and a base was created for future microzonation studies.

1. INTRODUCTION

New settlement areas are needed parallel to the population growth. It is essential for the city planners to know the local soil conditions of the area before starting construction works in a region. Planning of settlement areas is useful in determining possible problems that may be encountered later.

Turkey, located on active fault zones and is exposed to frequent natural disasters. Earthquake is one of the leading disasters that result in death. Seismic microzonation studies should be carried out in the Geographical Information System (GIS) environment using geological, geophysical and geotechnical studies in order to minimize the loss of life and property in earthquakes (Sarı and Turk, 2020). The importance of microzonation studies comes to the fore in Turkey where it is located in the active earthquake zone. The map obtained as a result of the microzonation study will reduce the damages that may be caused by the earthquake and provide correct land use.

Microzonation studies are of great importance for modern urbanization. GIS is of great importance in urban planning. Microzonation can be done by different disciplines working together. Creating microzonation maps depends on the detailed study of the region's geology and the comprehensive geotechnical ground survey and seismic studies. The soil class can be determined after these studies are performed. In addition, these maps are guides in the master development plan.

Mapping of local soil properties is very important in selecting new settlements and planning existing settlements. Generally, attention is not paid to the engineering properties of soils in underdeveloped countries. This situation causes natural disasters to result in loss of life and property.

GIS is frequently used in the mapping of soil parameters. GIS provides the analysis and visualization of the information about the earth surface in computer environment. GIS offers great advantages in terms of cost, time and ease of operation. A database was created from the results of field and laboratory tests.

Compression and swelling index mapping study obtained from the consolidation test for the vicinity of Mersin Port was conducted by (Alptekin and Taga 2017).

* **Corresponding Author**

*(aydinalptekin@mersin.edu.tr) ORCID ID 0000 – 0002 – 5605 – 0758
(myakar@mersin.edu.tr) ORCID ID 0000 – 0002 – 2664 – 6251

Cite this study

Alptekin A & Yakar M (2021). Mapping of local soil conditions in GIS environment: A case study in Çukurkeşlik village. 2nd Intercontinental Geoinformation Days (IGD), 64-67, Mersin, Turkey

Özyazıcıoğlu et al. 2019, produced a microzonation map by evaluating the ground amplification effects.

2. STUDY AREA

Çukurkeşlik village, is located in Mersin city, is characterized by typical Mediterrenean climate. In parallel with the rapid increase in the population of the city, uncontrolled construction occurs in the city. The region is located in left-lateral Ecemiş Fault Zone. A landslide event has been observed in the study area (Alptekin and Yakar 2020).

3. METHOD

The physical properties of the environment where earthquake waves spread affect the degree of damage in buildings (Uyanık 2015). Therefore, it is vital to know the engineering properties of soils.

In the study area, the Geological-Geotechnical Survey Report was prepared by Yenişehir Municipality in 2017 as a basis for the development plan. We used the engineering properties of soils obtained from drilling and seismic investigation results. A data set containing geotechnical and geophysical properties has been created.

3.1. Borehole

The purpose of drilling is to monitor the change of geological units with depth, to define the engineering properties of rocks and soils, and to obtain data with groundwater.

In Çukurkeşlik district, six boreholes, each 10 m deep, were drilled. Groundwater was not found in these drillings. Disturbed and undisturbed samples were taken from the boreholes. Atterberg Limits Tests were performed on the disturbed samples.

The soil may appear in four states such as solid, semi-solid, plastic and liquid. The water content at which soil changes from one state to other is known as Atterberg limits. Atterberg limits, which are Liquid limit (LL) and Plastic limit (PL) outlined in ASTM D4318.

LL is the water content that soil changes from the liquid state to plastic state. PL is the water content that soil changes from plastic to semi-solid state. Plasticity index (PI) is the difference of LL and PL (Eq.1).

$$PI = LL - PL \quad (1)$$

In this study, we mapped the Atterberg limits, which were taken 1.5m depth. The results are shown in Table 1. It was determined that the soil samples are in the clay with intermediate plasticity (CI) group in the Unified Soil Classification System (USCS) soil classification.

Table 1. Atterberg limit tests results

Borehole	Depth (m)	LL (%)	PL (%)	PI (%)
1	1.5-3	41.2	23.58	17.62
2	2.0-3.5	41.3	22.96	18.34
3	1.5-2.5	44.8	25.20	19.60
4	1.5-3	42.0	23.15	18.85
5	2.0-3.0	43.2	23.00	20.20
6	1.5-3.0	43.8	22.79	21.01

3.2. Multichannel Analysis of Surface Waves (MASW)

MASW data was obtained by 4.5 Hz geophone and 12-channel seismogram, which can obtain V_P and V_S accurately. A sledgehammer was used to obtain data. Ground dominant vibration period (T_0), soil amplification. The results are shown in Table 2.

Soil was classified according to Desing of Structures for Earthquake Resistance (Eurocode 8), National Earthquake Hazards Reduction Program (NEHRP) and average shear wave velocity in the upper 30 metres (Vs30). The results are shown in Table 3.

Table 2. MASW results

Seismic	T_0 (sn)	V_s30 (m/s)	Soil amplification
1	0.35	543	1.55
2	0.30	645	1.40
3	0.39	501	1.63
4	0.56	343	2.04
5	0.44	437	1.77

Table 3. Soil classes

Seismic	EUROCODE	NEHRP	Vs30
1	B	C	C
2	B	C	C
3	B	C	C
4	C	D	C
5	B	C	C

4. RESULTS

GIS is a platform that performs the storage, processing, management and querying of data. It has been frequently used in engineering projects since 1990s. It is not possible to obtain data from every point in the study area. Interpolation allows us to predict missing points.

The obtained engineering properties were mapped in ArcGIS software by using spatial analysis module. Inverse Distance weighted (IDW) interpolation method was used. Atterberg limits distribution maps, LL (Figure 1) and PL (Figure 2) were prepared. Vs30, T0 and soil amplification values were determined with MASW analyses. The distribution maps (Figure 3-5) were prepared.

The Vs30 values of the near surface soils varies from 343 m/s to 645 m/s. T_o values vary between 0.30 s and 0.56 s. Soil amplification varies between 1.40 and 2.07.

Many researchers (Maheswari et al. 2010; Rahman et al. 2016; Bajaj and Anbazhagan 2019) prepared Vs30 distribution map.

Atterberg Limits Test results show that all of the samples are in CI group. While B and C classes are seen in the study area according to the EUROCODE classification, C and D classes are seen according to the NEHRP classification (Table 3).

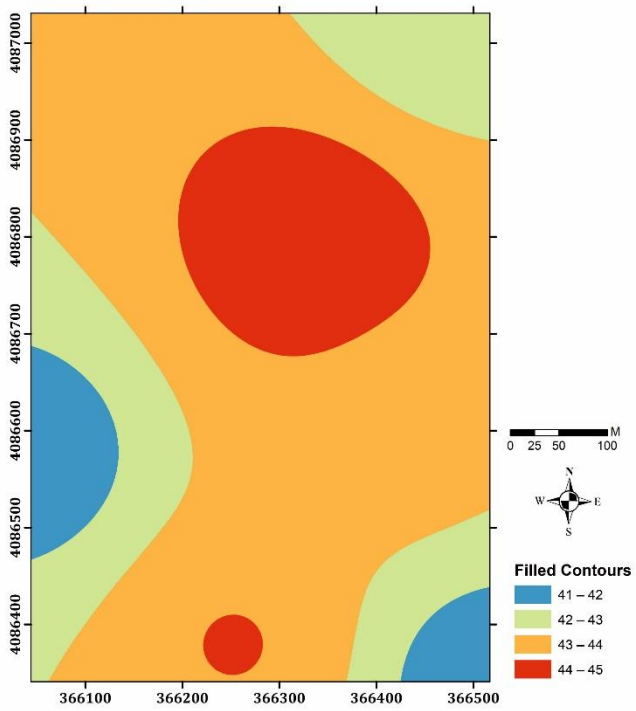

Figure 1. LL distribution

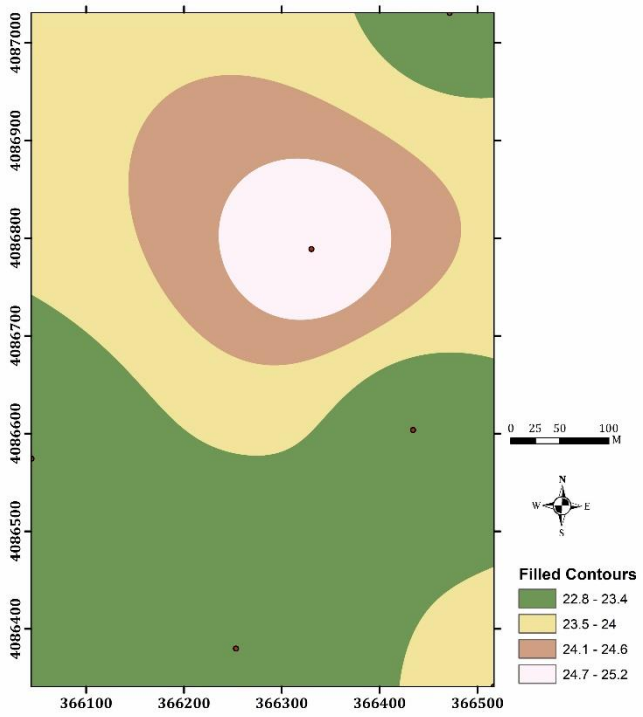

Figure 2. PL distribution

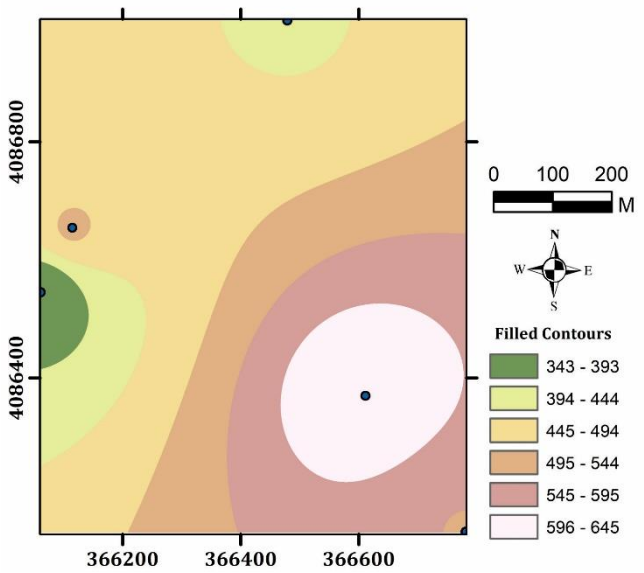

Figure 3. Vs30 distribution

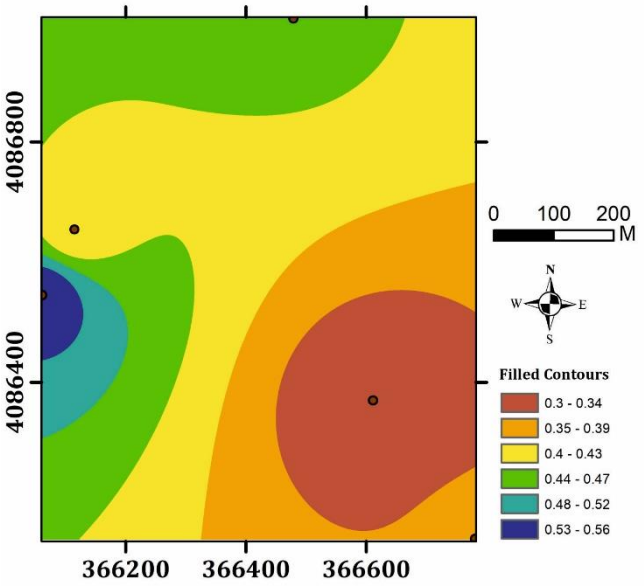

Figure 4. T_0 distribution

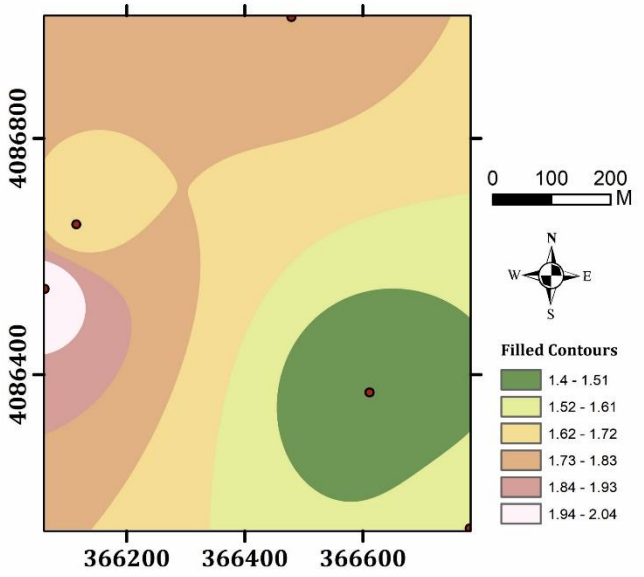

Figure 5. Soil amplification distribution

5. DISCUSSION

Microzonation determines all disaster risks in a region on maps. Microzonation studies should be carried out to determine the suitability of a region for settlement, urban planning, and zoning and land use planning. Urban planning without sufficient research on the geological environment and soil conditions causes natural disasters to come out with more damage. In this study, we prepared a preliminary study for microzonation.

6. CONCLUSION

Engineering properties of soils effects the damage caused by natural disasters. In this study, we mapped the engineering properties of a landslide area. We prepared the basic maps in ArcGIS for microzonation study.

ACKNOWLEDGEMENT

We would like to thank Mersin Yenişehir Municipality for contributing to our data acquisition.

REFERENCES

Alptekin A & Taga H (2017). Mersin Limanı'ndaki zeminlerin indeks ve konsolidasyon özelliklerinin değerlendirilmesi. Ulusal Mühendislik Jeolojisi ve Jeoteknik Sempozyumu, Adana, 200-207.

Alptekin A & Yakar M (2020). Heyelan Bölgesinin İHA Kullanarak Modellenmesi. Türkiye İnsansız Hava Araçları Dergisi, 2(1), 17-21.

ASTM 4318, (2014). Standard Test Methods for Liquid Limit, Plastic Limit, and Plasticity Index of Soils (p. 16). ASTM, West Conshohocken United States

Bajaj K & Anbazhagan P (2019) Seismic site classification and correlation between VS and SPT-N for deep soil sites in Indo-Gangetic Basin. Journal of Applied Geophysics, 163, 55–72

Maheswari R U, Boominathan A & Dodagoudar G R (2010). Seismic site classification and site period mapping of Chennai City using geophysical and geotechnical data. Journal of Applied Geophysics, 72, 152–168.

Özyazıcıoğlu M, Dönmezçelik K, Orhan S N & Özkan M Y (2019). Erzincan İli Zemin Büyütme Etkilerine Dayalı Mikrobölgeleme Çalışması. Doğal Afetler ve Çevre Dergisi, 5(2), 247-256.

Rahman M Z, SiddiquaS & Kamal A S M M (2016) Shear wave velocity estimation of the near-surface materials of Chittagong City, Bangladesh for seismic site characterization. Journal of Applied Geophysics, 134, 210–225

Sarı s & Turk t (2020). Depremde Meydana Gelebilecek Bina Hasarlarının Coğrafi Bilgi Sistemleri ile İncelenmesi. Türkiye Coğrafi Bilgi Sistemleri Dergisi, 2(1), 17-25.

Uyanık O (2015). Deprem Ağır Hasar Alanlarının Önceden Belirlenmesi ve Şehir Planlaması için Makro ve Mikro Bölgelendirmelerin Önemi. Süleyman Demirel Üniversitesi Fen Bilimleri Enstitüsü Dergisi, 19(2), 24-38.

Intercontinental Geoinformation Days

igd.mersin.edu.tr

Using an integrated approach for mapping soil salinity risk in Tadla Plain, Morocco

Abdelwahed Chaaou*[1], Mohamed Chikhaoui [2], Mustapha Naimi [3], Aissa Kerkour El Miad[4]

[1 2 3] *Institut Agronomique et Vétérinaire Hassan II, Département des Ressources Naturelles et Environnement Rabat, Maroc*

[4] *Université Mohamed Premier, Département des Sciences Mathématiques et Informatiques, Oujda, Maroc*

Keywords
Salinization
Soil Salinity
Risk Index
Tadla Plain
Morocco

ABSTRACT

Salinization is form of soil degradation that is expanding dramatically and reveal increasingly worrying aspects. It contributes to the decline of agricultural production in most of the world's irrigated areas, especially those arid or semi-arid climate. This phenomenon results from the synergy effects of climate, bedrock, the aggressiveness of natural conditions and the anthropogenic activities. With this in mind, the present study focuses on the mapping of soil salinity risk in Tadla Plain. To achieve this objective, the approach of Soil Salinity Risk Index (SSRI) was adopted. The necessary variables to calculate SSRI were weighted and overlaid using GIS. This operation allowed to develop a soil salinity risk map of the study area. The use of SSRI-based approach reveals the occurrence of three risk classes: low, moderate and severe. The moderate risk class dominates with a coverage representing 76% of the total area. The results achieved showed the prospect of this approach to delineate areas of soils prone to salinization risk, so as to manage soil salinization and reduce its effects on agricultural production.

1. INTRODUCTION

Salinization is a serious challenge for the development of modern agriculture and the preservation of environment. The global extent of soils affected by primary salinization is about 955 million hectares, while secondary salinization affects nearly 77 million hectares, of which 58% occurs in irrigated areas (Bakacsi et al., 2019; Metternicht and Zinck, 2003). About 20% of irrigated lands are affected by salt, and this proportion tends to increase despite considerable efforts devoted to land reclamation (Metternicht and Zinck, 2003). Human induced or secondary salinization, such as the use of high salt content water, super-irrigation and/or lack of drainage systems, in addition to excess fertilizer (Asfaw et al., 2016; El Gallal et al., 2016; Florinsky et al., 2009; Badraoui, 2006), instigates soluble salts accumulation.

In Morocco, the area of agricultural lands affected by salinity has been increased (Chaaou et al., 2020; Sadiqui et al., 2016) since the launch of irrigation. According to Badraoui (2003), about 16% of irrigated lands were affected by secondary salinization. Given the spread of this problem, Morocco must increase its efforts to evaluate the consequences of soil salinization, but also to develop appropriate conservation programs. In this regard, several studies have been carried out to develop a global strategy for the sustainable development of irrigated areas. In order to analyze the state of soil degradation by salinity and evaluate the risks of its extension and aggravation, several spatio-temporal monitoring approaches have been developed and applied worldwide. The use of models allows the control of salinity by knowing its spatial distribution and its evolution over time (Bouaziz et al., 2018; Lahlou, 2002). However, monitoring the process and mapping of soil salinity are not carried out with sufficient reliability without the integration of several factors (Aswaf et al., 2016; Nosetto et al., 2013). Given the complexity of the processes controlling soil salinity, the use of a multi-criteria approach makes it possible to identify areas at high risk of salinity and ensure spatiotemporal monitoring of chemical soil degradation (Triki et al.,

* **Corresponding Author**

*(abdelwahedchaaou@gmail.com) 0000-0001-8803-873X
(mchikhaoui@gmail.com) 0000-0002-5623-7432
(mnaimi2005@gmail.com) 0000-0001-8395-1431
(mid.kerkour@gmail.com) 0000-0002-0795-4072

Cite this study

Chaaou A, Chikhaoui M, Naimi M & Kerkour El Miad A (2021). Mapping the risk of soil salinity: case of the Tadla Plain, Morocco. 2nd Intercontinental Geoinformation Days (IGD), 68-71, Mersin, Turkey

2017; Bolinder et al., 2000). It is therefore necessary to develop an approach that allows the mapping on the basis of several factors of this (Castro et al., 2019). In this context, Chaaou et al. (2020) have developed a tool in the form of an index that uses several factors (soil types and bedrocks, climate and water table level) for mapping soil salinity risks. This approach allows the development of a soil salinity risk map that can be used as a decision-making tool to manage soil quality. In spite of its extensive use worldwide, this approach has never been implemented in the Mediterranean region, and particularly in Morocco.

2. MATERIAL AND METHODS

2.1. Study area

This study was carried out in the irrigated perimeter of Tadla in central Morocco "Fig .1".

Geologically, the Tadla perimeter is characterized by a vast synclinal depression filled with Neogene (Miocene and Pliocene) and Quaternary deposits (Etienne et al.,1975). Soils studies carried out in the study site show the predominance of chromic Kastanozems soils (WRB,2016).

The climate is arid to semi-arid with average annual temperature of about 17 °C. Mean annual rainfall varies from 200 to 600 mm during 2001-2014 (Chaaou et al.,2020).

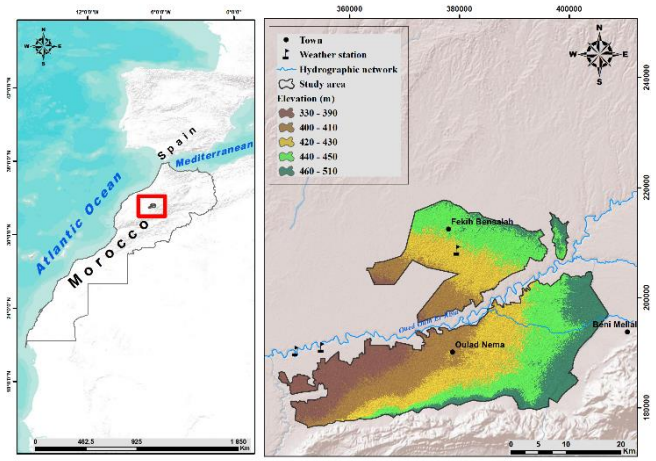

Figure 1. Location of the study area

2.2. Soil Salinization Risk Index (SSRI)

The soil salinization risk index (SSRI) is an additive method (Chaaou et al.,2020), which includes ten factors "Table 1". The SSRI calculation is based on a 5 X 9 matrix with two levels weighting (1 or 2).

To calculate SSRI, the risk class index for each factor is multiplied by its respective weight. The weighted values for each factor are added together to estimate SSRI, which ranges from 10 "very low" to 50 "very high" depending on the risk class "Table 2".

Table 1. Factors used to calculate SSRI

Indicators	Class limits and their rating score				
	None (1)	Slight (2)	Moderate (3)	Severe (4)	Very severe (5)
Depth of water table (m)	>5	3-5	1-3	0.5-1	<0.5
Soil texture	Coarse soils	Coarse to medium and medium	Moderately fine	Fine	Very fine
Slope (%)	>30	15-29	5-14	1-4	<1
Quality of irrigation water EC (ds/cm)	<0,25	0,25-0,75	0,75-2,25	2,25-5	>5
Quality of groundwater EC (ds/cm)	<0,25	0,25-0,75	0,75-2,25	2,25-5	>5
Efficacy of surface geology	<0.1	0.1-0.39	0.39-0.65	0.65-1	>1
Climate	Sub-humid and humid	Slightly semi-arid	Semi-arid	Arid	Very arid
Dry index (P/ETP)	>0.60	0.40-0.59	0.20-0.39	0.05-0.19	<0.05
Status of soil salinity EC (ds/cm)	<4	4-8	8-16	16-32	>32

SSRI original = (Status of soil salinity X 2) + 1 X (Quality of irrigation water + Depth of water table + Ground water quality + Soil texture + Climate + Dry index + Slope + Efficacy of surface geology)

Table 2. Salinity Risk Severity Classes

Class	None	Slight	Moderate	Severe	Very severe
Risk score	10-15	16-25	26-35	36-45	46-50

2.3. Data processing

The data used in this study comes from soil and water quality monitoring networks, established by the Tadla Agricultural Development Office. "Fig. 2" shows the data and the processing performed to calculate SSRI.

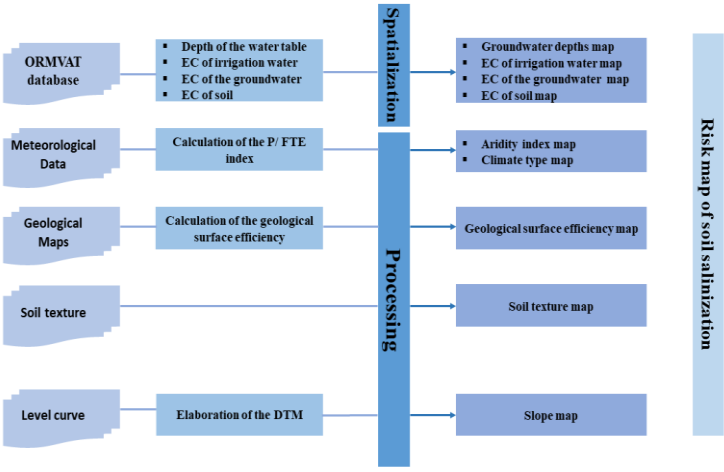

Figure 2. Data used and processing to develop the risk index for salinity.

3. RESULTS

The soil salinization risk map in "Fig.3" illustrates the spatial distribution of salinity risk in the Tadla plain using the SSRI approach. This map includes 4 classes, namely: moderate potential risk, low potential risk, moderate current risk and severe current risk.

The analysis of the spatial distribution of soil salinity risk classes led to conclude that SSRI is relevant for determining the soil salinization risk classes (current and potential) with the predominance of moderate potential risk class (76% of total area) "Fig.4". It can also be noted that the areas of potential salinity risk correspond to the highly sensitive soils. It seems that soils with severe risk class are located in areas with high groundwater and soil salinity. Current severe risk class represents only 0.1% of the total area of the Tadla irrigated perimeter "Fig.4".

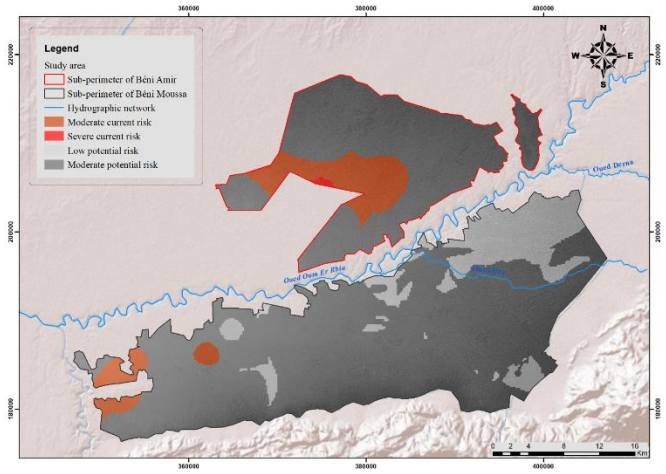

Figure 3. Soil salinization risk map

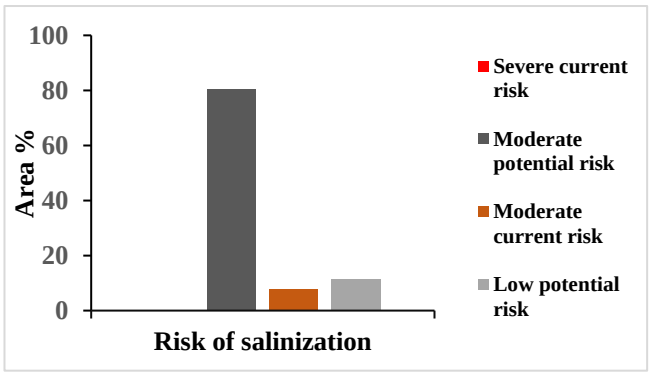

Figure 4. Areas of risk classes using SSRI

4. DISCUSSION

The combination of elements of the biophysical system such as relief, rainfall and lithological structure contributes to the mapping of soil salinity risk, taking into account soil characteristics (Castro et al., 2019).

The index approach allowed us to identify different levels of salinity risk in the irrigated perimeter of Tadla (current and potential). The results show the predominance of moderate potential risk with an extent of 76%. The area with potential risk includes soils that are very sensitive to salinity. On the other hand, area with severe risk class represents only 0.1% of the total surface of the irrigated perimeter of Tadla. In addition, severe risk class is located in area where salinity is high for groundwater and soils. This risk is higher during the dry season when rainfall is low.

Results show the interest of using this approach and the contribution of multi-source data in the study of soil degradation salinity. Moreover, it is noteworthy to mention the strong correlation between groundwater electrical conductivity and soil electrical conductivity. The same observation was also revealed by a study carried out by Badraoui (2003).

In fact, the electrical conductivity of groundwater explains 40% of the variability in the electrical conductivity of soils. Similarly, the depth of water table explains 28% of the variability in soil salinity in Tadla perimeter.

In our case study, the analysis of the results showed that the low spatial variability of the slope was not sufficient to explain the spatial dynamics of soil salinity in this perimeter. However, it should be noted that the current land use and cultivation practices seemed to control soil salinization. Similarly, the irrigation system and its efficiency could probably influence the salinization process.

5. CONCLUSION

In view of these results, we have demonstrated the interest of using the SSRI approach and the integration of multi-source data for the characterization of soil degradation risk by salinity in the irrigated perimeter of Tadla.

The use of this approach is also justified by its simplicity and ease of implementation in a GIS environment. The SSRI identified three classes of risk: low, moderate and severe. The low-risk class, largely represented in the Béni Moussa sub-perimeter, is explained by the low concentration of salts in irrigation water. Whereas the vast majority of the Béni Amir sub-perimeter is subject to a moderate risk of salinization. The severe salinization class is mainly observed in the downstream of the perimeter.

Monitoring the spatio-temporal dynamics of soil salinity is the key to understand the impact of rainfall, irrigation and agricultural practices on the evolution of soil salinity. Consequently, agricultural land users and managers using the SSRI can benefit from key intervention tools to mitigate the effects of soil salinization on agricultural production.

In light of these results, we suggest to improv this study by combining the SSRI with other variables, such as land use and irrigation system.

ACKNOWLEDGEMENT

The authors would like to acknowledge the National Centre for Scientific and Technical Research, the Hassan II Institute of Agronomy and Veterinary Medicine and the Hassan II Academy of Science and Technology (GISEC Project) for their multifaceted support. We also would like to extend our thanks to the Tadla Regional Office for Agricultural Development for their collaboration.

REFERENCES

Asfaw S, Di Battista F & Lipper L (2016). Agricultural technology adoption under climate change in the Sahel: Micro-evidence from Niger. Journal of African Economies, 25(5), 637-669.

Badraoui M (2006). Connaissance et utilisation des ressources en sol au Maroc. Rapport général 50 ans de développement humain et perspectives, 2025, 91-117.

Badraoui M (2003). Etat actuel de la salinité des eaux et des sols dans le Tadla. www.fsagx.ac.be/mf/Agriecoconseil/EFCA/badraoui.pdf.

Bakacsi Z , Tóth T, Makó, A, Barna G, Laborczi A, Szabó J, Szatmári G & Pásztor L (2019). National level assessment of soil salinization and structural degradation risks under irrigation. Hungarian Geographical Bulletin, 68(2), 141-156.

Bolinder MA, Simard RR , Beauchemin S & MacDonald, K.B (2000). Indicator of risk of water contamination by P for soil landscape of Canada polygons. Canadian Journal of Soil Science, 80(1), 153-163.

Bouaziz M, Chtourou MY, Triki I, Mezner S & Bouaziz S (2018). Prediction of Soil Salinity Using Multivariate Statistical Techniques and Remote Sensing Tools.Advances in Remote Sensing, Vol. 7, 313-326.

Castro FC, Araújo JF & dos Santos A M (2019). Susceptibility to soil salinization in the quilombola community of Cupira - Santa Maria da Boa Vista - Pernambuco – Brazil. CATENA 179, 175–183. https://doi.org/10.1016/j.catena.2019.04.005

Chaaou A,Chikhaoui M , Naimi M, El Miad A & Achemrk A (2020). Cartographie Du Risque De Salinité Des Sols À L'aide De L'approche Des Indices Et Des Données Multi-Sources : Cas De La Plaine De Tadla Au Maroc European Scientific Journal, ESJ, 16 (33), 206. https://doi.org/10.19044/esj.2020.v16n33p206

El Gallal M, Fletcher L & Evans B (2016). Assessment of potential risks associated with chemicals in wastewater used for irrigation in arid and semiarid zones: A review. Agricultural Water Management 177. 419–431.

Florinsky IV, Eilers RG, Wiebe BH & Fitzgerald MM (2009). Dynamics of soil salinity in the Canadian Prairies: Application of singular spectrum analysis, Environmental Modelling and Software, vol. 24, p. 1182-1195.

Lahlou M, Badraoui M, Soudi B, Goumari A & Tessier D (2002). Modélisation de l'impact de l'irrigation sur le devenir salin et sodique des sols. In Atelier du PCSI (Programme Commun Systèmes Irrigués) sur une Maîtrise des Impacts Environnementaux de l'Irrigation (pp. 19-p). Cirad-IRD-Cemagref.

Metternicht GI & Zinck JA (2003). Remote sensing of soil salinity: potentials and constraints. Remote Sensing of Environment, 85(1), 1-20.

Nosetto MD, Acosta AM, Jayawickreme DH, Ballesteros S I, Jackson RB & Jobbágy EG. (2013). Land-use and topography shape soil and groundwater salinity in central Argentina. Agricultural Water Management, 129, 120-129.

Sadiki M, Markhi A, Elbelrhiti H, Mrabet H (2016). Cartographie de la Salinité à la surface du sol dans une zone du Prérif : Cas de la région de l'Ouergha, European Scientific Journal. Vol.12, 1857 – 7881.

Triki FH, Bouaziz M, Benzina M & Bouaziz S (2017). Modeling of Soil Salinity within a Semi-Arid Region Using Spectral Analysis. Arabian Journal of Geosciences, 12, 11175-11182.

Intercontinental Geoinformation Days

igd.mersin.edu.tr

GIS-Based landslide susceptibility mapping using weight of evidence (WoE) and random forest (RF)

Aslan Cihat Basara *[1], **Yasemin Sisman** [2]

[1]Ondokuz Mayis University, Institute of Graduate Studies, Department of Geomatics Engineering, Samsun, Turkey
[2]Ondokuz Mayis University, Faculty of Engineering, Department of Geomatics Engineering, Samsun, Turkey

Keywords
Landslide
Susceptibility Map
Weight of Evidence
Random Forest
Machine Learning
GIS

ABSTRACT

In this study, the Landslide Susceptibility Map of Tokat province was produced. Slope classes, elevation classes, land use classes, geology classes, aspect classes and proximity to fault lines classes were used during the study. The Weight of Evidence method was applied to determine the relationship between the classes of the parameters and the landslide events. Random Forest method was used to determine the weights between parameters. Weighted Overlay operation was applied to the classified and weighted map data using ArcGIS program. As a result of the process, the data were divided into 5 classes and the Landslide Susceptibility Map was produced. When susceptibility classes are examined, it was seen that 92,42% of the old landslide events occurred in high and very high classes.

1. INTRODUCTION

Disasters are events that cause material and moral damages in the society they affect and cause great problems in terms of the consequences they cause in the flow of daily life. The landslides can be defined as the downward movement or sliding of parts such as soil and rocks, under the influence of gravity or external factors such as earthquakes and continuous rains (AFAD 2014).

When the negative effects caused by landslides are carefully examined, it is necessary to first reveal the spatial distribution of existing mass movements and inventory information. Using the available inventory data, landslide susceptibility analysis, risk and hazard values can be determined (Van Westen et al. 2008). Landslide susceptibility analysis, which reveals areas susceptible to possible future landslides, reveals the desire for any landslide to ocur (Guzzetti et al. 2006). Landslide susceptibility maps are of great importance in predicting future landslides and providing land use planning (Basara et al. 2020)

In this study, the Landslide Susceptibility Map of Tokat Province was produced. Location Map given in Figure 1.

Figure 1. Location Map

2. MATERIAL AND METHOD

2.1. Material

There is no standard for the parameters to be used in landslide susceptibility analysis studies. Therefore, the parameters may differ depending on the area to be studied. When the parameters used in the landslide susceptibility analysis were analyzed statistically, the rates in Table 1 were obtained (Tetik Biçer 2017).

* **Corresponding Author**

* (aslancihatbasara@gmail.com) ORCID ID 0000 – 0001 – 6644 – 6097
(ysisman@omu.edu.tr) ORCID ID 0000 – 0002 – 6600 – 0623

Cite this study

Basara A.C & Sisman Y (2021). GIS-Based landslide susceptibility mapping using weight of evidence (WoE) and random forest (RF). 2nd Intercontinental Geoinformation Days (IGD), 72-75, Mersin, Turkey

Table 1. Usage Rates of Parameters

Parameters	Rate (%)	Parameters	Rate (%)
Slope	86,47	Land Use	46,62
Lithology	67,29	Curvature	40,60
Aspect	59,77	Fault Lines	28,57
Elevation	55,64	NDVI	24,06
Drainage Density	50,75	Soil	23,68

In this study, Slope, Aspect, Elevation, Geology, Land Use, Proximity to Fault Lines and Landslide Inventory Map were used. Maps of the material are given in Figure 2-8.

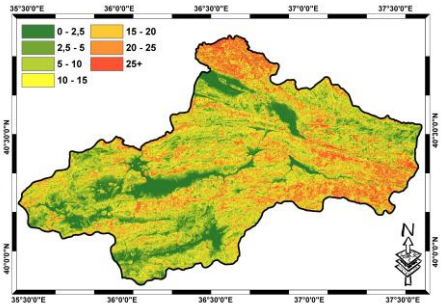

Figure 2. Slope Map

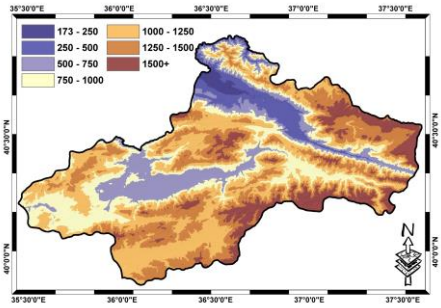

Figure 4. Elevation Map

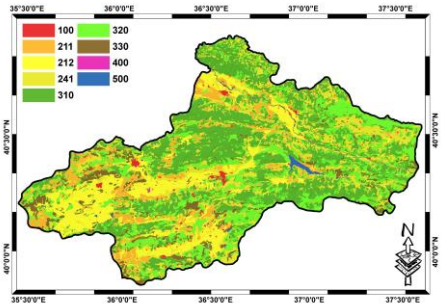

Figure 6. Landuse Map

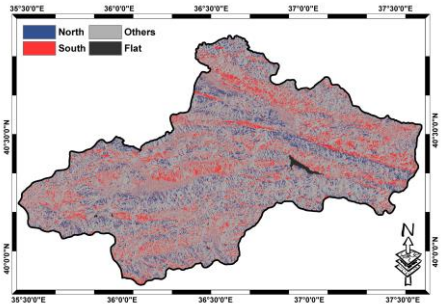

Figure 3. Aspect Map

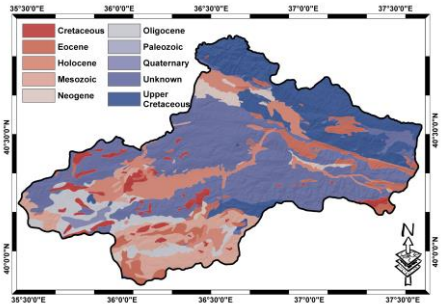

Figure 5. Geology Map

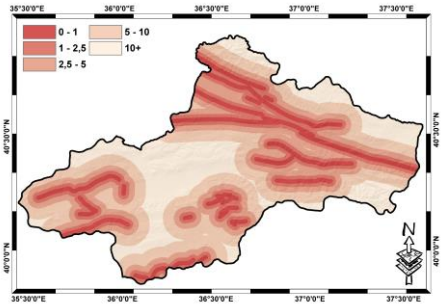

Figure 7. Proximity to Fault Lines Map

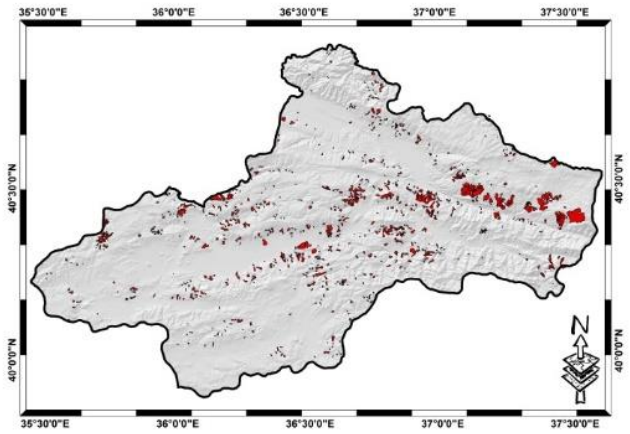

Figure 8. Landslide Inventory Map

2.2. Method

In this study, obtaining the landslide susceptibility map was applied in two stages. In the first part, the Weight of Evidence (WoE) method was applied. In the second part, the weights of the parameters are determined by the Random Forest (RF) algorithm.

2.2.1. Weight of Evidence (WoE)

The Weight of Evidence method has been mathematically expressed by Van Westen et al. (2003) and Regmi et al. (2010). In this study, the weights of the subcategories of the factors affecting the landslide were determined using the equation 1-3 (Regmi et al. 2010; Ozdemir and Altural 2013).

$$W+ = \ln[\,(A1/(A1+A2))\,/\,(A3/(A3+A4))\,] \quad \textbf{(1)}$$

$$W- = \ln[\,(A2/(A1+A2))\,/\,(A4/(A3+A4))\,] \quad \textbf{(2)}$$

$$C = (W+) - (W-) \quad \textbf{(3)}$$

In the equation, A1 refers to the landslide areas in a selected subcategory, A2 refers to the total landslide areas outside the selected category, A3 refers to the areas with no landslides in the selected category, and A4 refers to the total landslide-free areas other than the selected category. While A1 + A2 refers to the total landslide areas, A3 + A4 refers to the total landslide-free areas in the study area. (Regmi et al. 2010).

The difference between the W + and W- weights is called the contrast of the weights (C). The C value shows the final positional relationship between the landslide event and the forecast variable. A value equal to zero indicates that the subcategory of the factor causing the landslide is not important for the analysis. Positive contrast indicates a positive positional relationship, negative contrast indicates the opposite (Ozdemir and Altural, 2013).

Table 2. Aspect Classes

Attribute	Landslide area	Total area	WoE
North	46,76 km^2	1317,89 km^2	0,0945
South	48,81 km^2	1306,85 km^2	0,1566
Others	232,66 km^2	7349,36 km^2	-0,1310
Flat	0,28 km^2	43,39 km^2	-1,6471

Table 3. Geology Classes

Attribute	Landslide area	Total area	WoE
Cretaceous	6,07 km²	407,14 km²	-0,8300
Eocene	38,78 km²	783,26 km²	0,4744
Holocene	8,54 km²	1043,15 km²	-1,5004
Mesozoic	10,74 km²	971,05 km²	-1,1804
Neogene	3,36 km²	250,12 km²	-0,9289
Oligocene	3,52 km²	649,02 km²	-1,8865
Paleozoic	0,26 km²	3,43 km²	0,8992
Quaternary	0,06 km²	72,22 km²	-3,7744
Unknown	155,76 km²	3944,05 km²	0,3386
Upper Cretaceous	101,68 km²	1897,02 km²	0,6777

Table 4. Slope Classes

Attribute	Landslide area	Total area	WoE
0 – 2,5 degree	4,31 km²	1220,36 km²	-2,3784
2,5 – 5 degree	17,53 km²	1169,98 km²	-0,8736
5 – 10 degree	94,69 km²	2432,80 km²	0,2415
10 – 15 degree	104,96 km²	2119,40 km²	0,5816
15 – 20 degree	66,70 km²	1510,13 km²	0,3752
20 – 25 degree	26,93 km²	880,08 km²	-0,0781
25 degree+	13,39 km²	684,72 km²	-0,5610

Table 5. Elevation Classes

Attribute	Landslide area	Total area	WoE
173 – 250 m	0,14 km²	131,32 km²	-3,5079
250 – 500 m	5,52 km²	528,47 km²	-1,2061
500 – 750 m	38,39 km²	1240,21 km²	-0,0677
750 – 1000 m	103,66 km²	1811,46 km²	0,7679
1000 – 1250 m	116,33 km²	2936,22 km²	0,2896
1250 – 1500 m	46,35 km²	2324,58 km²	-0,6265
1500 m+	18,16 km²	1048,20 km²	-0,7091

Table 6. Land Use Classes

Attribute	Landslide area	Total area	WoE
CORINE.100	4,14 km²	135,52 km²	-0,0759
CORINE.211	39,25 km²	808,52 km²	0,4526
CORINE.212	12,31 km²	1337,34 km²	-1,4041
CORINE.241	134,27 km²	1919,02 km²	1,1182
CORINE.310	77,45 km²	3105,39 km²	-0,3883
CORINE.320	49,65 km²	1966,29 km²	-0,3261
CORINE.330	11,25 km²	669,71 km²	-0,7213
CORINE.400	0,00 km²	2,38 km²	-11,2991
CORINE.500	0,31 km²	72,31 km²	-2,0788

Table 7. Proximity to Fault Lines Classes

Attribute	Landslide area	Total area	WoE
0 - 1 km	29,84 km²	1094,26 km²	-0,2117
1 - 2,5 km	52,81 km²	1563,53 km²	0,0358
2,5 - 5 km	91,08 km²	2112,37 km²	0,3746
5 - 10 km	84,38 km²	2829,21 km²	-0,1346
10 km+	70,61 km²	2421,09 km²	-0,1573

2.2.2. Random Forest (RF)

Random Forest Method is one of the collective learning algorithms based on using many decision tree models together to solve a specific classification and regression problem (Breiman 2001). The algorithm is based on the principle of combining the estimates made by each of the decision trees that make up the forest and making the final decision for the relevant sample in the process of estimating a sample with an unknown class label (Kuncheva and Whitaker 2003).

The general formula of the Random Forest algorithm is defined as in Equation 4. Since the algorithm produces K number of decision trees, the predicted value (P) is given by the average of the predicted values (T) in all trees (Costa et al. 2020). Generalization error in Random Forest algorithm is defined as in Equation 6. The "x and y" values here are the landslide conditioning factors showing the x-y space and the probability above mg and are defined as in Equation 5-6. The "I" values here measure the extent to which the average number of votes in random vectors exceeds the average vote for any other output for correct output (Masetic et al. 2016).

$$P = \frac{1}{K}\sum_{k=1}^{K} T \quad \textbf{(4)}$$

$$\mathrm{GE} = P_{x,y}\,(\,\mathrm{mg}\,(\mathrm{x},\mathrm{y}) < 0\,) \quad \textbf{(5)}$$

$$\mathrm{mg}(\mathrm{x},\mathrm{y}) = \mathrm{av_k I}(\mathrm{h_k}(\mathrm{x}) = \mathrm{y}) - \mathrm{max_{j\neq y} av_k I}(\mathrm{h_k}(\mathrm{x}) = \mathrm{j}) \quad \textbf{(6)}$$

Table 8. Random Forest Data

Parameters	Variable İmportance	Standard Deviation	Weight
Land Use	66,909	0,261	27 %
Aspect	10,073	0,036	4 %
Slope	40,407	0,172	16 %
Proximity to Faults	35,912	0,243	14 %
Geology	42,681	0,392	17 %
Elevation	52,508	0,215	21 %

3. RESULTS

The parameters to be used in the study were mapped with the help of ARCGIS. The relationship of the maps with the landslide inventory map was determined using the Weight of Evidence (WoE) Method. Maps were reclassified according to the analysis result. The Random Forest (RF) Algorithm was used to determine the importance of the parameters relative to each other. Finally, the Landslide Susceptibility Map was produced by processing the data with Weighted Overlay analysis. The map produced was reclassified 5 as very low, low, medium, high and very high. Landslide susceptibility map is given in Figure 9.

4. DISCUSSION AND CONCLUSION

The areas and rates of the landslide susceptibility classes are given in Table 9.

Table 9. Landslide Susceptibility Classes

	Landslide area (km²)	Total area (km²)	Landslide incident (%)	Total area (%)
Very Low	0,00	187,79	0,00%	1,88%
Low	0,82	878,77	0,25%	8,78%
Medium	24,13	2160,46	7,33%	21,58%
High	125,91	4905,13	38,25%	48,99%
Very High	178,35	1880,26	54,18%	18,78%

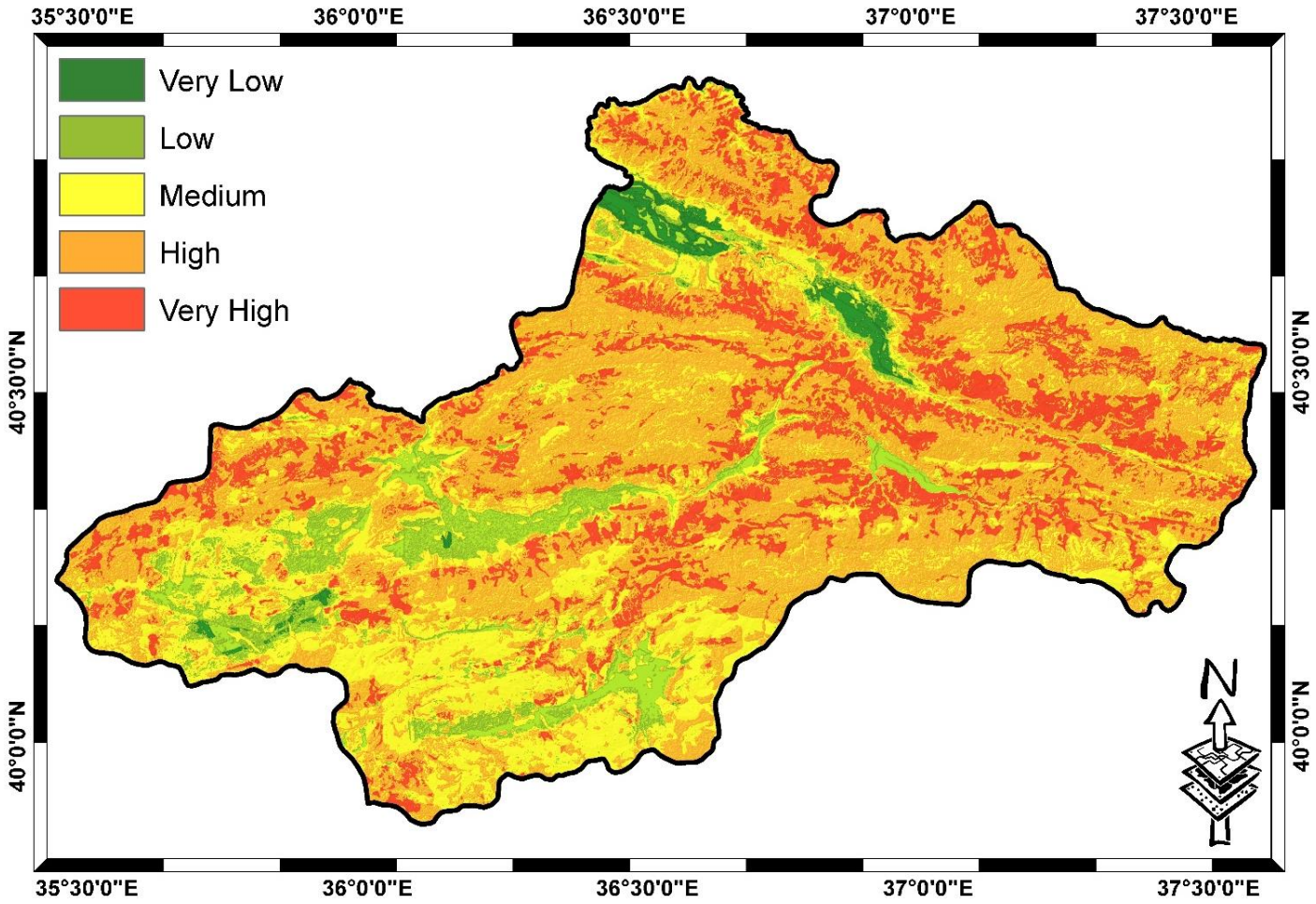

Figure 9. Landslide Susceptibility Map

When susceptibility classes are examined it was seen that 92,42% of the old landslide events occurred in high and very high class, 7,33% occurred in middle class and 0,25% occurred in low and very low class.

In the spatially analysis of landslide events, it was seen that the sensitivity classes are examined spatially, high-risk areas constitute 67,77% of all areas, medium-risk areas constitute 21,58% of all areas and low-risk areas constitute 10,65% of all areas.

As a result, it is possible to say the following. Susceptibility mapping is very important to prevent material and moral losses that may occur due to disasters.

REFERENCES

AFAD 2014. Açıklamalı Afet Yönetimi Terimleri Sözlüğü. TC Başbakanlık Afet ve Acil Durum Yönetimi Başkanlığı Deprem Dairesi Başkanlığı, Ankara.

Basara A C, Tabar M E & Sisman Y (2020). GIS-Based Landslide Susceptibility Mapping Using Frequency Ratio and AHP Methods in Samsun Province. Intercontinental Geoinformation Days (IGD), 223-226, Mersin, Turkey.

Breiman L (2001). Random forests. Machine learning, 45(1), 5-32.

Costa I S L, Serafim I C C D O, Tavares F M & Polo H J D O (2020). Uranium anomalies detection through Random Forest regression. Exploration Geophysics, 51(5), 555-569.

Guzzetti F, Reichenbach P, Ardizzone F, Cardinali M & Galli M (2006). Estimating the quality of landslide susceptibility models. Geomorphology, 81:1-2, 166-184.

Kuncheva L I & Whitaker C J (2003). Measures of diversity in classifier ensembles and their relationship with the ensemble accuracy. Machine learning, 51(2), 181-207.

Masetic Z & Subasi A (2016). Congestive heart failure detection using random forest classifier. Comput. Methods Programs Biomed. 2016, 130, 54–64.

Ozdemir A & Altural T (2013). A comparative study of frequency ratio, weights of evidence and logistic regression methods for landslide susceptibility mapping: Sultan Mountains, SW Turkey. Journal of Asian Earth Sciences, 64, 180-197.

Regmi N R, Giardino J R & Vitek J D (2010). Modeling susceptibility to landslides using the weight of evidence approach: Western Colorado, USA. Geomorphology, 115(1-2), 172-187.

Van Westen C, Rengers N & Soeters R (2003). Use of geomorphological information in indirect landslide susceptibility assessment. Natural Hazards, 30:3, 399-419.

Van Westen C J, Castellanos E & Kuriakose S L (2008). Spatial data for landslide susceptibility, hazard, and vulnerability assessment: an overview. Engineering Geology, 102:3-4, 112-131.

Tetik Biçer Ç (2017). Heyelan Risk Haritalaması Üzerine Yarı Sayısal Bir Değerlendirme.

Intercontinental Geoinformation Days

igd.mersin.edu.tr

The status of *wheelchair*-tagged OpenStreetMap point data in European capital cities

Müslüm Hacar [*1], **Özge Öztürk Hacar** [1]

[1]*Yildiz Technical University, Faculty of Civil Engineering, Department of Geomatic Engineering, Istanbul, Turkey*

Keywords
VGI
Crowdsourcing
OpenStreetMap
Accessibility
POI

ABSTRACT

For a person with walking disability, one of the important information is whether a street has a wheelchair-friendly infrastructure or not. Accessing this information quickly and accurately is crucial. Believing that it will be very convenient to get this information from a single platform, some volunteers enrich OpenStreetMap (OSM) data with a *wheelchair*=* tag that provides information whether a street, building, or any feature in OSM is suitable (or not) for wheelchair use. However, since the tagged data is insufficient in many urban areas, OSM data still requires contributions. This study examines points of interest in Ankara comparing with five capital cities of Europe in terms of the statistics of the *wheelchair* tag contributions. The result shows that Ankara has fewer POIs compared to other cities and volunteers should be attracted to increase the number of *wheelchair* tagged POIs.

1. INTRODUCTION

Learning which places are suitable for wheelchair use and which are not, requires challenging experiences. Volunteered geographic information (VGI) helps us to easily present this information from a single window. In short, a VGI is a platform that is fed by the geometric and semantic contributions of volunteers and presents them openly and freely (Goodchild 2007). OpenStreetMap (OSM) is one of the popular VGI projects. In OSM, while geographical features are contributed with several geometric elements (i.e. node, way and relation), semantic information is contributed as tags (*key = value*) (OSM 2021). It is possible for contributors to add a semantic tag freely on any subject to a geographic location (OSM Wiki: Map Features 2021). Specifically, there are also various tags for wheelchairs, but the most preferred one is *wheelchair = ** (Taginfo 2021). This tag presents whether a feature is wheelchair-friendly or not.

Mobesheri et al. (2017) explained the technical details and framework of the Wheelmap project where OSM infrastructure was used. The application shares with users whether or not geographical contents are accessible for wheelchairs. In addition, the study introduced how contributors can add the compatibility information of wheelchair to the features. Basiri (2017) proposed an approach that identifies wheelchair barriers with visibility graph analysis and calculates routes based on factors that are important for wheelchairs. The suggested routes offered a higher level of user satisfaction than Google Maps suggests. Kocaman and Özdemir (2020) proposed a conceptual (law and geography) and methodological (identifying the barriers) framework by using GIS in order to reduce the social inequality faced by people with physical disabilities. Moutinho et al. (2020) carried out NOVA-MAS project using the sensors and traffic lights as the sources. It enables that wheelchair users can get accessibility information from the urban environment and infrastructures. Götzelmann and Kreimeier (2020) presented a simulator in which virtual reality is integrated with urban plans. According to the approach, wheelchair users are able to interpret 3D city plans and learn about the accessibility. In addition, some other projects for wheelchair users and individuals with reduced mobility are carried out within the scope of cartography (Hoy and Rogala 2018; Tannert et al. 2019; Biagi et al. 2020; Zastudi et al. 2020).

In this study, since OSM is an important source for the previous projects, the *wheelchair = ** tag contributions in OSM were examined. Other tags contributed most to the *wheelchair* tagged points have also been evaluated to understand the contribution trends. The paper continues with the following section describing the study area and the evaluation schema. Then, the results are evaluated over the statistics of the analysed data for six cities. The study ends with some discussions and further studies.

* **Corresponding Author**

*(mhacar@yildiz.edu.tr) ORCID ID 0000-0002-8737-8262
(ozgeo@yildiz.edu.tr) ORCID ID 0000-0002-9017-9651

Cite this study

Hacar M & Öztürk Hacar Ö (2021). The status of wheelchair-tagged OpenStreetMap point data in European capital cities. 2nd Intercontinental Geoinformation Days (IGD), 76-79, Mersin, Turkey

2. MATERIAL & METHOD

2.1. The study areas and data

In this study, we examined six capital cities in Europe (Figure 1). While Ankara, Sofia, and Warsaw represent the urban settlements from the developing countries, Berlin, London, and Paris are the developed countries.

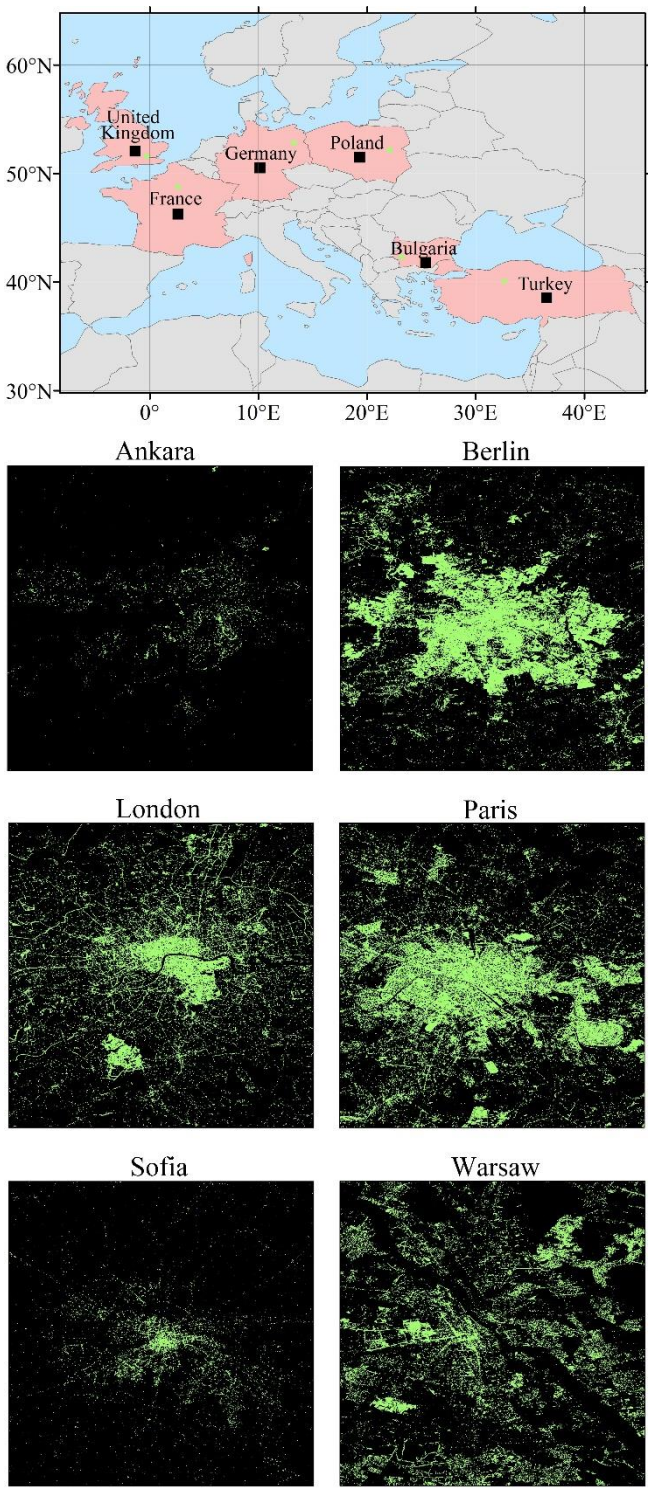

Figure 1. The density representations of POIs (Country boundaries are taken from [2])

[2]https://ec.europa.eu/eurostat/web/gisco/geodata/reference-data/administrative-units-statistical-units/countries

OSM point data in the cities was used for the evaluation. The data consists of non-linear and non-polygonal objects. This means that the points constituting lines (node) and polygons (vertices) are excluded from the dataset. The rest of the point data represents the points of interest (POIs) used in the study. The statistics of data given in Table 1 shows that there is no correlation between the urban characteristics (i.e. population, and total area of buildings) and the number of POIs.

Table 1. Urban and POI statistics of the study areas.

City	Population [1]	Total area of buildings in OSM (km²)	Number of POIs
Ankara	4,725,000	43.1	11,594
Berlin	3,972,000	104.7	614,903
London	10,979,000	79.1	252,495
Paris	11,020,000	225.9	623,244
Sofia	934,000	20.1	20,345
Warsaw	1,935,000	65.2	244,015

[1] http://www.demographia.com

2.2. The evaluation approach

According to the original approach in Hacar (2020), the semantic information in OSM data is analysed in a direction from the most general framework to the target tag value. The most used keys in the OSM planet dataset and the most used tag values together with these keys are determined and preliminary information about the weights of the semantic data is obtained. Our proposed approach was adopted from the approach in Hacar (2020). The evaluation of the *wheelchair* tag contributions relies on the depicted schema below in Figure 2. The tag contributions are assessed from popular tags used in *wheelchair* tagged POIs to the *wheelchair* tag values. Hereafter, the tags contributed most to the *wheelchair* tagged points are called popular tags. While the schema enables the evaluation of *wheelchair* tagged points with and without popular tags, it also examines used *wheelchair* values such as *yes*, *no*, and *limited*.

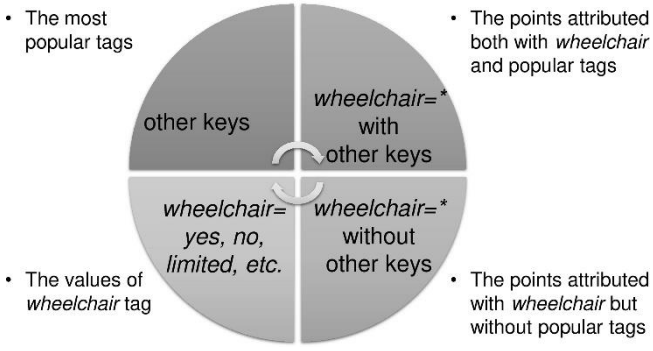

Figure 2. The schema of the evaluation.

3. RESULTS

Four popular tags in POIs contributed with *wheelchair* tag are *name*, *amenity*, *shop*, and *building*

(Taginfo 2021). The stacked bar (green+red) in Figure 3 represents the sum of *wheelchair* tags used with the POIs in the regarding city. While green color shows the number of used respective popular tag with *wheelchair* tag, red color is for the number of unused popular tags. For instance, while the number of *name* tags contributed to the *wheelchair* tagged POIs in Ankara is 65, the number of empty tags for *name* key is 2. This means that 67 points in Ankara have the *wheelchair* attribute. While 65 of them also have the name information, rests have no name.

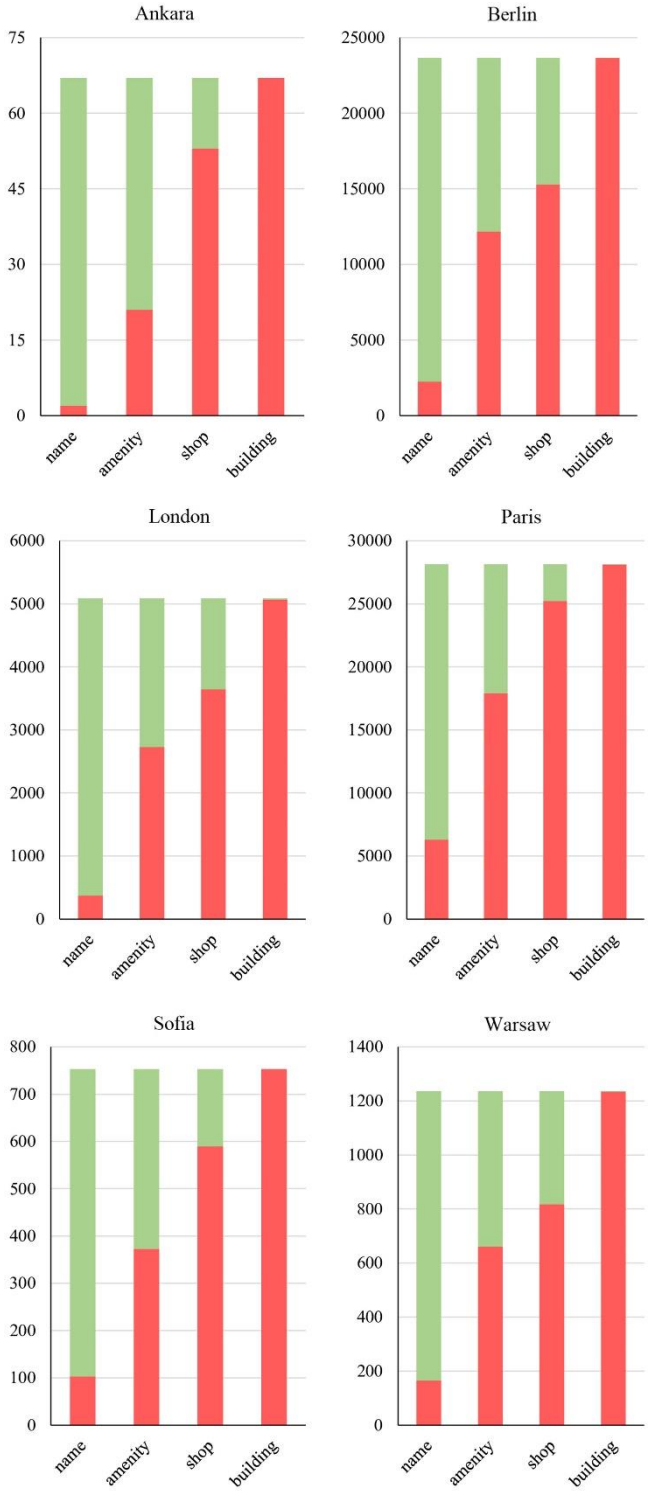

Figure 3. The distribution of popular tags in the *wheelchair* tagged POIs: existent (green) and non-existent (red).

Briefly, the *name* tag exists in 97%, 91%, 93%, 78%, 86%, and 87% of *wheelchair* tagged POIs of Ankara, Berlin, London, Paris, Sofia, and Warsaw, respectively. At least 36% of the wheelchair tagged POIs have the *amenity* tag. Also, while over 10% of the wheelchair tagged POIs have *shop* tag, less than 0.5% of them have the *building* tag. The distribution trends of popular keys in wheelchair tagged POIs of the cities are similar. However, as seen in Figure 3, there are dramatic differences in the numbers of used tags among the cities. While the capitals in developed countries have the maximum numbers, the others have the less numbers. Figure 3 also shows that all of the cities have the same contribution trend of popular tags. The trend from the most used tags to the least is occurred as the *name*, *amenity*, *shop*, and *building* tags, respectively.

Wheelchair tag was used on a small number of POIs in each city (Figure 4). Paris and Berlin, which has the largest numbers of POIs, are also the cities where the *wheelchair* tag is used the most (4.5% and 3.8%, respectively). Surprisingly, although Sofia has about 12 times less POIs than London, it is more complete (3.7%) than London (2.0%) in terms of the *wheelchair* tag rate in POIs. The capital cities where the tag is used the least are Ankara (0.6%) and Warsaw (0.5%), respectively. It can be said that the volunteers' interest in contributing information about wheelchair suitability were the less in Ankara and Warsaw.

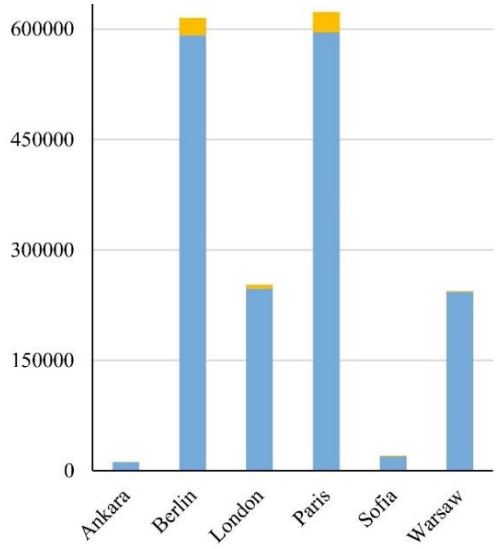

Figure 4. The distribution of the *wheelchair* tagged POIs in all POIs: existent (yellow) and non-existent (blue).

The suitability information of *wheelchair* tag is represented by several tag values such as *yes*, *no*, *limited*, and so on. Figure 5 shows the percentage of the used values in each city. Warsaw (69%) and London (64%) are the cities that *yes* value is used the most for the *wheelchair* tag. In Berlin and Paris, *yes* value is approximately half of the *wheelchair* values. Moreover, while Paris, Sofia, Ankara, and Berlin have *no* tag value more than 30% of *wheelchair* tags, London (21%) and Warsaw (17%) has the less. Thus, it can be interpreted that the volunteers contributed in Warsaw and London preferred focusing the wheelchair-friendly entities the most. However, in Ankara, Berlin, Paris, and Sofia, they

contributed the values homogeneously. In other words, the contributors focused not only the wheelchair-friendly entities, but also unsuitable or restrictedly available entities.

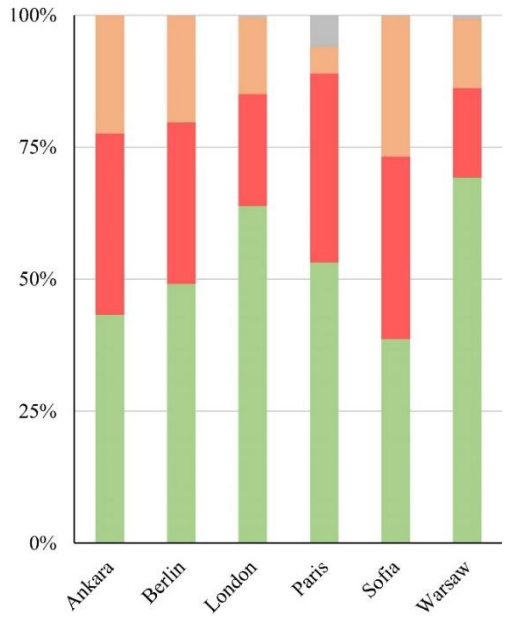

Figure 5. The distribution of the wheelchair tag values: *yes* (green), *no* (red), *limited* (orange), and the others (grey).

4. CONCLUSION

The contributors focused on not only the wheelchair-friendly entities, but also unsuitable or restrictedly available entities in Ankara, Berlin, Paris, and Sofia. However, it seems that the interest of volunteers is mostly in wheelchair-friendly entities in Warsaw and London.

Volunteers contributed the popular tags with the same trend in all cities. The trend from the most used tags to the least is occurred as the *name*, *amenity*, *shop*, and *building* tags, respectively.

Ankara has the least number of POIs comparing with other capitals. Also, the city ranks second from the last after Warsaw in terms of the number of *wheelchair* tagged POIs. Paris and Berlin, which has the largest numbers of POIs, are also the cities where the wheelchair tag is used the most. Considering the population and urbanization of the case cities, it is expected that Ankara would have much more POIs and also *wheelchair* tagged POIs than it has. It can be said that the volunteers' interest in contributing information about wheelchair suitability were the less in Ankara and Warsaw.

Future works about this topic will be focusing on a framework increasing the amount of *wheelchair* tagged POIs in OSM.

REFERENCES

Basiri A (2020). Open area path finding to improve wheelchair navigation. arXiv preprint arXiv:2011.03850 and arXiv:2011.03850v1.

Biagi L, Brovelli M A & Stucchi L (2020). Mapping the accessibility in openstreetmap: A comparison of different techniques. International Archives of the Photogrammetry, Remote Sensing and Spatial Information Sciences-ISPRS Archives, XLIII-B4-2020, 229-236. https://doi.org/10.5194/isprs-archives-XLIII-B4-2020- 229-2020

Goodchild, M F (2007). Citizens as sensors: the world of volunteered geography. GeoJournal, 69 (4), 211-221. https://doi.org/10.1007/s10708-007-9111-y

Götzelmann T & Kreimeier J (2020). Towards the inclusion of wheelchair users in smart city planning through virtual reality simulation. 13th ACM International Conference on Pervasive Technologies Related to Assistive Environments, 1-7, New York, USA.

Hacar M (2020). Analyzing the Contribution Trends of Volunteers by Comparing Tag Metadata of OpenStreetMap Residential Roads [In Turkish: OpenStreetMap Yerleşim-içi Yollarına Ait Etiket Bilgilerinin Karşılaştırılmasıyla Gönüllülerin Katkı Sağlama Eğilimlerinin İncelenmesi]. Harita Dergisi, 164, 77-87.

Hoy K N & Rogala S. (2018). Using a crowdsourcing tool to collect data on the travel behaviour and needs of individuals with reduced mobility. In Scientific and Technical Conference Transport Systems Theory and Practice, 844, 75-84. https://doi.org/10.1007/978-3-319-99477-2_7

Kocaman S & Ozdemir N (2020). Improvement of Disability Rights via Geographic Information Science. Sustainability, 12(14), 5807. https://doi.org/10.3390/su12145807

Moutinho F, Campos-Rebelo R, Lagartinho-Oliveira C, Moreira E, Almeida B & Gomes L (2020). NOVA Mobility Assistive System: Developed and Remotely Controlled with IOPT-Tools. Electronics, 9(8), 1328. https://doi.org/10.3390/electronics9081328

OpenStreetMap Wiki. (2021). Welcome to OpenStreetMap. https://wiki.openstreetmap.org/wiki/Main_Page, accessed 30.03.2021.

OpenStreetMap Wiki. (2021). Map Features. https://wiki.openstreetmap.org/wiki/Map_Features, accessed 30.03.2021.

TagInfo. (2020). OpenStreetMap Taginfo. Erişim Adresi: https://taginfo.openstreetmap.org/ accessed 30.03.2021.

Tannert B, Kirkham R & Schöning J (2019). Analyzing accessibility barriers using cost-benefit analysis to design reliable navigation services for wheelchair users. INTERACT, 11746, 202-223. https://doi.org/10.1007/978-3-030-29381-9_13

Zastudil C, Stewart M, Sprague N & Brady E (2020). Campuspartner: an assistive technology for mobility impaired pedestrians. Companion of the 2020 ACM International Conference on Supporting Group Work, 139-142, Sanibel Island, FL, USA.

Intercontinental Geoinformation Days

igd.mersin.edu.tr

Digital terrain and detail mapping of part of ABU Phase 2, Kaduna state Nigeria

Atta Kaka Zenabu*[1], Abdulmajid Bukhari [1], Giwa Olawunmi Lukman [1]

[1]*Ahmadu Bello University, Faculty of Environmental Design, Department of Geomatics, Kaduna State,Nigeria*

Keywords
Digital Mapping
Perimeter Survey
GIS
Detail Mapping

ABSTRACT

The study is focused on the production of a detailed survey map of part of Ahmadu Bello University Zaria Phase II. The coordinate of each detail both natural and artificial features were obtained by total station and then plotted using ArcGIS software. The Perimeter of the study area was first measured and the total area of the study area was measured to be 1.0168ha which was measured from the temporary control points extended from ABU Barda 2553 and ABU Barda 2554. A total of three departments, a lecture hall, manhole, tress, high tension, electric pole and street light etc. were measured. And then finally the detail survey plan was produced for proper documentation and record keeping.

1. INTRODUCTION

A detail surveying is used to determine and locate the feature and improvement on a parcel of land. The word 'feature' here means both natural and man-made structures on a piece of land such as vegetation, types of soil, buildings, land utilities, fences and boundaries, roads, land marks and so on (Chandra, 2008). A detail survey is completed for design and assessment purposes and it's typically required for a council development application although it has many more uses (Fort, 1993).

They are generally carried out using survey equipment such as total stations and theodolites. The data is then carried to the office for analysis and preparation of detail maps known as Digital terrain models, which provide the details that have been collected in the form of a map. These maps are useful for engineers and architects who use them in their designs and plans. The survey should be carried out by a qualified land surveyor who may be assisted by a chainman (Wolf and Ghilani, 2012).

This project entails in providing detailed geospatial data and producing a detailed survey plan of the existing structures and other relating information about the land mass of the study area for proper documentation and further constructions in the study area.

2. METHOD

The flow chart of the procedures and steps taken to achieve the aim and objectives of this project is shown in figure 1.0 below.

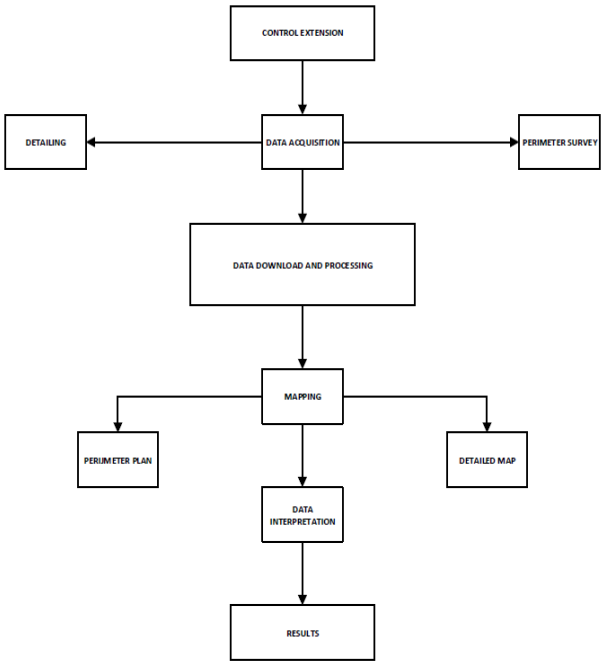

Figure 1. Flow chart diagram of the steps

* **Corresponding Author**

*(kakaattaz@gmail.com) ORCID ID 0000 – 0003 – 0672 – 4862
(e-mail) ORCID ID
(lukmanogiwa@gmail.com) ORCID ID 0000 - 0002 - 5716 - 8985

Cite this study

Zenabu A K, Bukhari A & Lukman G O (2021). Digital terrain and detail mapping of part of ABU Phase 2, Kaduna state Nigeria. 2nd Intercontinental Geoinformation Days (IGD), 80-83, Mersin, Turkey

2.1. Reconnaissance

It is required for the commencement of any survey work to check the possible alternate route to follow while conducting a survey work. Two control points were found to be inter-visible, and then 5 five control points were extended to the project site. The values of the extended controls are tabulated in table 2.1 below. With a recce diagram of the study as seen in figure 2.1 below.

Table 2.1: Showing values of the extended control point.

S/N	Control point	Easting	Northing
1	ABU Barda 2553	351919.8630	1232564.3370
2	ABU Barda 2554	351792.8190	1232468.1010
3	CP1	351775.7975	1232420.6850
4	CP2	351700.3722	1232230.8660
5	CP3	351625.5602	1231975.2330
6	CP4	351656.2913	1231908.4740
7	CP5	351677.5439	1231555.7010

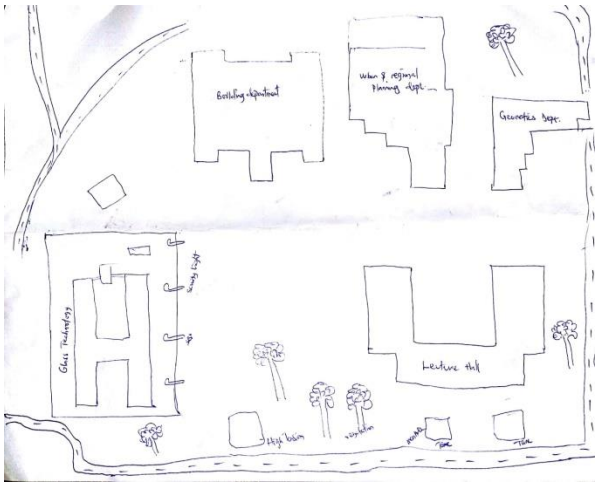

Figure 2.1: Recce diagram of the study area

2.2. Data acquisition

A perimeter survey of part of ABU Phase II was carried out using total station. The closing error is computed from the coordinates of the starting point and that of the last point.

The position of a point on the ground may be established if it's bearing and distance from another known point is measured. This process may be extended to successive points and the resulting series of connecting lines of which their bearing and distance are known is called traverse. Hence a traverse is a means of providing horizontal control in which rectangular coordinates are determined form a combination of angle and distance measurements along lines joining adjacent stations. These are seen in table 2.2 and 2.3 respectively.

Table 2.2: Showing the coordinates of the perimeter survey

S/N	EASTING	NORTHING	POINT ID
	351919.8630	1232564.3370	Barda 2553
2	351792.8190	1232468.101	Barda 2554
4	351570.467	1231668.678	TP1
5	351655.534	1231654.453	TP2
6	351742.176	1231612.465	TP3
7	351835.824	1231606.95	TP4
8	351895.545	1231560.213	TP5
9	351889.49	1231473.456	TP6
10	351882.678	1231380.932	TP7
11	351836.378	1231352.111	TP8
12	351662.785	1231368.291	TP9
13	351472.891	1231393.991	TP10
14	351485.091	1231487.139	TP11
15	351515.902	1231594.092	TP12

Table 2.3: Traverse Computation

Stn From	Bearing	Distance	DN	DE	NORTHINGS	EASTINGS	Stn To
					1232564.337	351919.863	P1
P1	232 51 21	159.379	-96.236	-127.044	1232468.101	351792.819	P2
P2	195 32 36	829.77	-799.423	222.352	1231668.678	351570.467	P3
P3	099 29 35	86.248	-14.225	85.067	1231654.453	351655.534	P4
P4	115 51 19	96.28	-41.988	86.642	1231612.465	351742.176	P5
P5	093 22 13	93.81	-5.515	93.648	1231606.95	351835.824	P6
P6	128 02 46	75.835	-46.737	59.721	1231560.213	351895.545	P7
P7	183 59 32	86.968	-86.757	-6.055	1231473.456	351889.49	P8
P8	184 12 38	92.774	-92.524	-6.812	1231380.932	351882.678	P9
P9	238 05 54	54.538	-28.821	-46.3	1231352.111	351836.378	P10
P10	275 19 29	174.345	16.18	-173.593	1231368.291	351662.785	P11
P11	277 42 27	191.625	25.7	-189.894	1231393.991	351472.891	P12
P12	007 27 42	93.944	93.148	12.2	1231487.139	351485.091	P13
P13	016 04 14	111.303	106.953	30.811	1231594.092	351515.902	P14
P14	022 36 15	1050.98	970.245	403.961	1231564.337	351919.863	P1
Total Distance		3197.799					

Total Area= 10168m^2 or 1.0168ha

3. RESULTS

The plan of the perimeter survey which is surveyed and found the total area of the study area to be approximately 1.0168ha as seen in Figure 3.1 below.

The coordinates of each features within the study area were measured and the features includes both natural and artificial features such as buildings, trees, manhole, road, footpath, manhole, high tension, electric pole etc.

The coordinates of each feature were then exported to ArcGIS and shape file of feature is created in ArcCataloq for plotting and then the features were then digitize to give a 2D shape.

The figure 3.2 below shows the detailing of features within the study area where all the features are shown including both natural and manmade features.

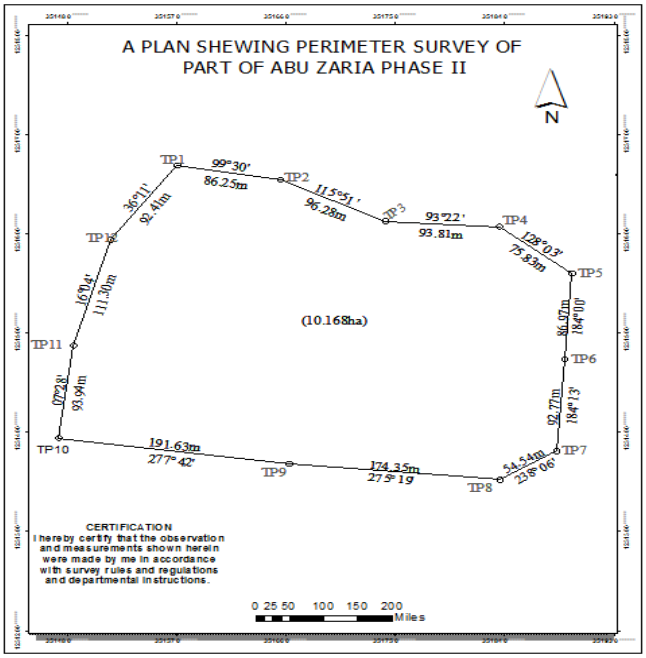

Figure 3.1: Plan shewing perimeter survey of part of ABU phase II

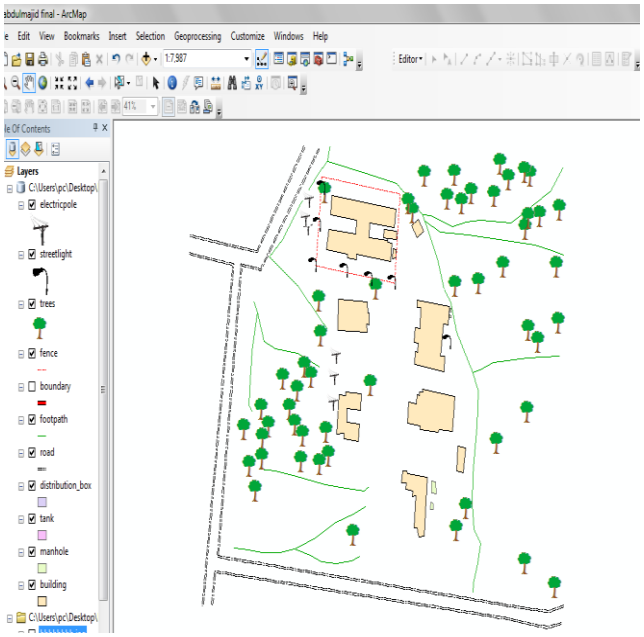

Figure 3.2: Showing detailing of the Study Area.

Below shows the final survey plan of the study area which shows the detailing of each feature which includes the road, trees, boundary (perimeter of the study area), water tank, street light, distribution box, electric pole, manhole and buildings.

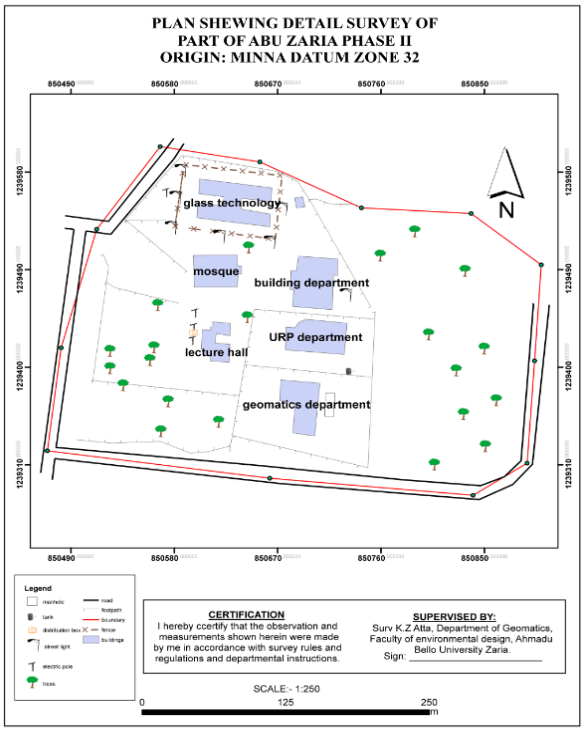

Figure 3.3: shows the final detail plan of part of ABU Phase II

4. DISCUSSION

A total of 1.0168ha was measured from the perimeter survey as the total area of the study area (ABU phase II) and also all the detail both natural and artificial features within study area were identified which includes a total of 4 departments which are; department of glass and silicate technology, department of Geomatics, department of urban and regional planning and Building department and also one lecture hall, a building close to glass technology, manhole, vegetation, road, security light and high tension were both identified and the coordinate of were measured as seen in figure 3.2. The final detail map of the study area was produced in accordance with survey rules and regulations as shown is figure 3.3

5. CONCLUSION

This project work which is sited at Ahmadu Bello University Zaria Phase II covers the perimeter survey total of area of 1.0168ha was measured and also the coordinate of all the details both natural and artificial features within study area were identified and measured where the details includes a total of four (4) departments i.e. department of glass and silicate technology, department of Geomatics, department of urban and regional planning and Building department and also one lecture hall, a building close to glass

technology, manhole, vegetation, road, security light and high tension were both identified and measured.

ACKNOWLEDGEMENT

The authors would like to acknowledge ABU Geomatics Department Zaria for the controls.

REFERENCES

Chandra, A. (2008). Higher Surveying, Revised Second Edition, new Age Internatioal Limited, Publisher. new Delhi, www.newagepublisher.com.

M.J. Fort, (April,1993) 'Software for Surveyors' in civil engineering Surveyor, Vol.18, No.3, Electronic Surveying Supplement, Google Scholar.

M.J. Fort, (Jan, 1993) ' Surveying by computer', in Engineering Surveying Showcase '93, pp. 24,27-31 (PV Publications, 101 Bancroft, itchin, Hertford-shire).

Wolf, P. R., & Ghilani, C. D. (2012). Elementry surveying An introduction to Geomatics. (13 ed.). Upper Saddle River, NJ: Prentice Hall

Intercontinental Geoinformation Days

igd.mersin.edu.tr

Legal aspect of space activities in international context

Mehmet İşiler*[1], M. Oğuz Selbesoğlu [1], Mustafa Yanalak [1]

[1]*Istanbul Technical University, Civil Engineering Faculty, Geomatics Engineering Department, Istanbul, Turkey*

Keywords
Space Law
National Space Program
Geomatics Engineering

ABSTRACT

Land is considered as limited and consumable asset which should be managed with the sustainable development approach. Today, economic, social and cultural activities of humans on the land have obviously increased due to advances in technologies and globalization trends. These rapid developments have caused environmental, housing, food and energy resources management problems. The main requirement for efficient and effective land management is qualified, reliable, correct and up-to-date land information. Especially, space technologies that enable to obtain land related data have provided many opportunities to manage land resources and human activities in local, regional and global context. Communication, earth observation, navigation and meteorology services are among the main usage areas of space technologies for land management purposes. With the rapid advances in science and technology, space has begun to be seen as a new resources area. Space tourism and space mining are emerging as the new topics. All these developments have been transforming space into a commercial and industrial target as well. With the national space program in Turkey, our country has started new studies to develop space abilities. As known geomatics engineering has play key role in organizations that perform many different services by using the space technology products. In this context, local and global initiatives have an effect on our profession. Therefore, it is important to understand current legal regime in this area. In this study, main international agreements concerning space activities under the United Nations are summarized and the role of the International Telecommunication Union on allocation of satellite orbit is mentioned.

1. INTRODUCTION

Space law, which is considered as a sub-branch of international law, is the field of law that regulates studies and activities in outer space. Space law mainly consists of international agreements approved among states under the United Nations General Assembly (UNGA) and national laws.

Space law has emerged as a result of human efforts to launch artificial satellites into earth orbits. It can be stated that the launch of World's first artificial satellite Sputnik-1 into earth orbit in 1957 by Soviet Union is the starting point of legal studies aimed at regulating activities in outer space in the international context. In the following years, several international agreements concerning outer space activities were adopted by the UNGA (Can 2017). The Outer Space Treaty of 1967 which was signed under The UNGA can be stated as the

On the other hand, outer space has begun to seen as an alternative place for extracting mine and producing energy. Some countries have started to make own legal basis legal document which conducts activities of outer space (Can 2017).

In the early years, the scope of space law was formed as a result of the space activities carried out by the USA and the USSR. Depending on the advances in science and technology, the abilities for space activities have increased and new issues that should be regulated by the space law have been emerged.

Today, GNSS data has taken important role in our daily life via mobile phones and navigation devices etc. Many location-based applications receive the necessary data from GNSS satellites. In addition, environmental management, mapping, urban-rural planning, mining and other related activities have become increasingly dependent on data derived from space technology such as earth observation, communication, meteorological and navigation satellites.

On the other hand, outer space has begun to seen as an alternative place for extracting mine and producing energy. Some countries have started to make own legal

* **Corresponding Author**

*(isiler@itu.edu.tr) ORCID ID 0000-0003-0543-0029
(selbesoğlu@itu.edu.tr) ORCID ID 0000-0002-1132-3978
(yanalak@itu.edu.tr) ORCID ID 0000-0001-6805-8768

Cite this study

İşiler M, Selbesoğlu O & Yanalak M (2021). Legal aspect of space activities in international context 2nd Intercontinental Geoinformation Days (IGD), 84-87, Mersin, Turkey

regulations concerning the space mining. For instance; On 25 November 2015, U.S Government signed into law the U.S. Commercial Space Launch Competitiveness Act that has a title named as ""Space Resource Exploration and Utilization" which is about space mining (Can 2017). Considering current trends, it can be easily seen that space has an economic potential on space mining and production in space. All these developments have been transforming space into a commercial and industrial area that should be interested.

Today, countries have realized the economic and civil benefits of space and several countries are making great effort to increase their abilities for space activities. Our country has been working for a long time to take its place in space. The first step of space activities for Turkey was launching of communication satellites. Then, space developments of Turkey have continued with earth monitoring and remote sensing satellites. Our first reconnaissance satellite Göktürk 2 was launched in 2012. Also, several cubic satellite projects have been completed. With the achievement of these steps, Turkish Space Agency was established as an affiliated part of the Ministry of Industry and Technology by Presidential Decree No.23 dated 13.12.2018 (The National Space Program Document).

Recently National Space Program has been announced. Our country has started new studies in many areas including regional satellite navigation and remote sensing systems. Main objectives of National Space Program can be summarized as developing space technologies in Turkey, reducing dependency on foreign resources related to space technologies and increasing the awareness of public on space. By the help of missions that declared in National Space Program, economic and technological capacity can be increased extremely. Furthermore, outcomes of declared programs will contribute to public services and enhance the collaboration with other countries in scientific and commercial area.

Geomatics Engineering has play key role in organizations that perform many different services by using the space technology products such as earth observation and navigation satellites. Local and global developments on space activities have several effects on our profession continuously. Technical, legal and administrative developments will affect our professional directly. Therefore, in addition to technical details, it is also important to understand the legal status of relevant studies.

In this study, sources of international law concerning space activities are summarized in the context of only five main agreements adopted by the UNGA. And also, in order to highlight the status of geostationary orbit satellites, role of the International Telecommunication Union on space activities are mentioned.

2. MAIN SOURCES OF INTERNATIONAL LAW CONCERNING SPACE ACTIVITIES

Committee on the Peaceful Uses of Outer Space (COPUOS), which is considered the most important intergovernmental organization in the space field, became a permanent committee in accordance with the decision of the United Nations General Assembly in 1959 (Soysal et al.2018). Main contributions of the Committee are the creation of five international agreements concerning space activities and many decisions supporting the agreements as well as the creation of legally non-binding international documents (Soysal et al.2018).

Five international agreements were adopted by The UNGA between 1967 and 1979. These international agreements that aim to define general and objective rules in space law are still in force (Danışman 2019). These agreements can be listed as below;

- Treaty on Principles Governing the Activities of States in the Exploration and Use of Outer Space, Including the Moon and Other Celestial Bodies, 27 January 1967, (Outer Space Treaty)
- Agreement on the Rescue of Astronauts, the Return of Astronauts and the Return of Objects Launched into Outer Space, 22 April 1968, (Rescue Agreement)
- Convention on International Liability for Damage Caused by Space Objects, 29 March 1972, (Liability Convention)
- Convention on Registration of Object Launched into Outer Space, 14 January 1975, (Registration Convention)
- Agreement on Governing the Activities of States on the Moon and Other Celestial Bodies, 18 December 1979, (Moon Agreement)

Four Agreements that are expressed in the list with their short titles as Rescue Agreement, Liability Convention, Registration Convention and Moon Agreement elaborate and reaffirm the provisions of the Outer Space Treaty (Soysal et al.2018).

In addition to five agreements mentioned, the main international documents containing the principles on the subject of space by the United Nations General Assembly can be summarized as below (Danışman 2019);

- The Declaration of Legal Principles Governing the Activities of States in the Exploration and Uses of Outer Space, UNGA Res. 1962 (XVIII), (13.12.1963)
- Principles Governing the Use by States of Artificial Earth Satellites for International Direct Television Broadcasting, UNGA Res. 37/92, (10.12.1982).
- The Principles Relating to Remote Sensing of the Earth from Outer Space UNGA Res. 41/65, (03.12.1986).
- The Principles Relevant to the Use of Nuclear Power Sources in Outer Space, UNGA Res. 47/68, (14.12.1992).
- The Declaration on International Cooperation in the Exploration and Use of Outer Space for the Benefit and in the Interest of All States, Taking into Particular Account the Needs of Developing Countries, UNGA Res. 51/122, (13.12.1996).

3. LEGAL STATUS OF SPACE IN ACCORDANCE WITH THE FIVE INTERNATIONAL AGREEMENTS UNDER THE UNGA

First of all, it should be said that boundary of space is not described in international law. Whereas, many countries define the Karman Line which is 100 km above the sea level as the boundaries of outer space, NASA defines the space limit to be about 80,5 km above the sea level (Sarıkaya 2020). Our country states that definition and delimitation of space should be defined by joint work with International Civil Aviation Organization (ICAO).

Outer Space Treaty includes basic principles on international space law. The main purpose of the Treaty is to ensure the exploration and use of space for peaceful purposes (Soysal et al.2018). The most basic principles that stated in Outer Space treaty can be summarized as follows:

- *As stated in Article 1, "the exploration and use of outer space, including the Moon and other celestial bodies, shall be carried out for the benefit and in the interests of all countries, irrespective of their degree of economic or scientific development, and shall be province of all mankind."*
- *As stated in Article 2, "outer space, including Moon and other celestial bodies, is not subject to national appropriation by claim of sovereignty, by means of use or occupation, or by any others means."*
- *As stated in Article 4, "The Moon and other celestial bodies shall be used by all States Parties to Treaty exclusively for peaceful purposes. "*
- Statement in Article 6 can be summarized as states are internationally liable for damage caused by their space activities.

Rescue Agreement elaborates the Article 5 and 8 of Outer Space Treaty. This law consists of 10 articles. The main purpose of this agreement is to guarantee all possible steps must be taken by the all parties to rescue and assist astronauts in cases of accidents, emergencies and compulsory landing that may occur during space mission.

Liability Convention which consist of 28 articles elaborates article 7 of Outer Space Treaty. According to Article 2 in Liability Convention, "*a launching State shall be absolutely liable to pay compensation for damaged caused by its space objects on the surface of the Earth or air craft in the flight*. "The term of "damage", "launching State" and "space objects" are expressed in the Article 1 of this convention. Article 3 and 4 express the types of liability for damages occurred. Also, the procedures for claim to compensation are stated in this convention.

Registration Convention was adopted as a result of Rescue Convention and Liability Convention. This convention also elaborates article 8 of Outer Space Treaty. In accordance with Article 4 of Registration Convention; "*the name of launching State or States, an appropriate designator of the space object or its registration number, date and territory or location of the launch, basic orbital parameters including nodal period, inclination, apogee and perigee, and the general function of launching object*" should be registered in the secretary-General of The United Nations as soon as practicable.

Moon Agreement reaffirms and elaborates many regulations of the Outer Space Treaty. As stated in Article 1.1, "*the provisions of this Agreement relating to the moon shall also apply to other celestial bodies within the solar system other than the earth…*" Moon Agreement uses the expression of *"the common heritage of mankind*" for the Moon and its natural sources and reaffirms that the moon is not subject to national appropriation. Also, Article 11.5 of The Moon Agreement provides to establish an international regime which governs the exploitation of natural resources of the moon when exploitation activities are nearly become feasible. The main purposes of this international regime are listed in article 11.7 as well. Moon Agreement states that an equitable share by all States Parties should be made in benefits from space resources. Ince (2020) claims that several space-capable countries are not a party of this agreement because of article 11.

Status of International Agreements relating to activities in outer space as at 1 January 2020 which was shared by Office for Outer Space Affairs United Nations are on Table 1. In Table 1, TotalR refers to number of ratifications, acceptances, approval accessions or successions, TotalS refers to number of signatures only, TotalD refers to number of declarations of acceptance of rights and obligations.

Table 1. Status of international agreements relating to activities in outer space as at 1 January 2020

Items	1967 OST	1968 ARRA	1972 LIAB	1975 REG	1979 MOON
TotalR	110	98	98	69	18
TotalS	23	23	19	3	4
TotalD	0	3	4	4	0

Turkey ratified five basic international agreements regarding space activities which are mentioned in this paper.

4. THE ROLE OF THE INTERNATIONAL TELECOMMUNICATION UNION

At last, the role of the International Telecommunication Union (ITU) on coordination of the geostationary satellite orbit should be mentioned in briefly.

As stated by ITU webpage, ITU was established in 1865 in order to ensure coordination of international connectivity in communication networks. ITU takes a role on allocation frequencies and satellites orbits. In accordance with the International Telecommunication Convention 1973 and its additional protocols, ITU carries out satellite orbit and frequency allocation (Erdem 2012).

Geostationary orbit is about 36000 km from the Earth equator. Satellites in geostationary orbits travel around the world at about 24 hours. Therefore, satellites in geostationary orbit remain the same location relative to Earth surface. Especially, geostationary orbit is used by telecommunication satellites. Geostationary orbit provides a globally

coverage with minimum satellites. For the reason of physical environment restrictions, satellites that can be used in this orbit is limited. Also, satellites located close to each other may also interfere with each other (İnce, 2020). Therefore, coordination of the satellites to be located in this orbit is inevitable.

A state planning to launch satellite in this orbit should apply to the International Communication Union (ITU). The country should launch its satellite according to the location given by ITU (İnce, 2020).

5. CONCLUSION

Within the scope of this study, it is obviously seen that international law concerning space activities is formed as a result of the developments of space studies. Year by year, space studies have become a significant global topic for all mankind. Today, many researchers have an opinion that some issues in international law concerning space activities should be discussed because capabilities of space works have increased. For example, recently space tourism and space mining have emerged as a new issue that should be regulated in the international context. A few countries such as the U.S Government and Luxembourg made some legal regulations on space mining activities as well.

Turkey is part of five main international agreements that are mentioned in this study. Besides the technical efforts, national laws regarding these activities should be prepared as soon as possible.

Recently, our National Space Program has been declared. Our country aims to start new studies in order to develop our space abilities. As known, space activities are related to several disciplines. Coordination of relevant sub-branches of space activities is important to achieve successful results. With the technical issues, in order to contribute the development of space industry, one of the main requirements is national laws that regulates the priority issues related to space technologies.

Outcomes of space activities support public services and scientific collaboration with other countries as well. These technical and legal improvements will support many public and private sector such as the GIS (geographical information system) and remote sensing industry that are directly related to Geomatics Engineering discipline in Turkey.

REFERENCES

Can N (2017). Space mining, 8th International Conference on Recent Advances in Space Technologies (RAST), 19-22 June 2017,Istanbul

Danışman Z S (2019). Uzayda ve uzaydaki gök cisimleri üzerinde devlet egemenliği ve mülkiyet. MS Thesis, Gazi University, Ankara (in Turkish).

Erdem M (2012) Uzay teknolojisinde meydana gelen gelişmelerin uzay hukukuna etkisi, IV. Ulusal Havacılık ve Uzay Konferansı, 2-14 Eylül 2012, Hava Harp Okulu, İstanbul

Ince F (2020). Uzay bir insanlık serüveni – bilimleri, teknolojisi, hukuku, politikaları. Nobel Yayın Grubu, 2. Basım, ISBN: 978-605-320-179-3

Sarıkaya S (2020). Uzay hukuku ve Türkiye. Nobel Bilimsel Eserler, 1. Basım, ISBN: 978-625-7258-91-3

Soysal M, Doğan G & Kuzu L (2018). Uzay Faaliyetlerine İlişkin Uluslararası Hukukun Kaynakları ve Birleşmiş Milletlerin Rolü, Çankaya Üniversitesi Hukuk Fakültesi Dergisi, Cilt 3 Sayı 2 s.101-133

Intercontinental Geoinformation Days

igd.mersin.edu.tr

Content analysis of real estate valuation courses taught in geomatics engineering departments in Turkey

Nuri Erdem*

Osmaniye Korkut Ata University, Engineering Faculty, Department of Geomatics, Faculty of Engineering, Osmaniye, Turkey

Keywords
Geomatics Engineering
Real Estate Valuation Course
Course Content Analysis

ABSTRACT

In many applications in economic life, the values of immovable property are needed. Experts must also determine the value of these applications. Experts should also be selected from among people who are trained in the field of Geomatics Engineering, Civil Engineering, City/Regional Planning, Architecture related to the world of real estate. In this study, a detailed study was carried out about the real estate valuation courses taught in the Geomatics Engineering Departments of our universities. The features of these courses, such as Hours, content, mandatory or optional, were examined and content analyses were made. In this context, the importance of determining the content of the course in parallel with current developments in this field and its contribution to the training of appraisers was revealed. In particular, the importance of Geomatics Engineering education in the field of real estate valuation was emphasized.

1. INTRODUCTION

The value of real estate is needed in many applications related to the world of real estate. For example, taxation, nationalization, privatization, easements, property, banking, lending, insurance, such as private and public sector applications with the sale, donation, exchange, mortgage, contract to look to death, such as transfer, construction servitude, floor ownership, detached and permanent easement, usufruct right, right of fidelity, right of construction, it must be measured on the basis of such registration transactions immovable in the upper right. Experts must determine the value of these applications. Experts should also be selected from among people who are trained in the field of Geomatics Engineering, Civil Engineering, City/Regional Planning, Architecture related to the world of real estate. In this context, the real estate valuation course taught in the Departments of Geomatics Engineering is of great importance in addressing this need and educating new Real Estate Appraisers.

In general, real estate valuation can be defined as "estimation of the possible value of a real estate, real estate project or rights and benefits related to the real estate on the valuation day based on independent, impartial and objective criteria" (SPK, 2001; Açlar & Çağdaş 2008; AI, 2013). An assessment of real estate can be defined as the expression of a real estate partially or completely in terms of quality and quantity (Yalpır, 2007). Hire an expert valuation of immovable property; they are people employed full-time by real estate valuation companies who will assess a real estate, real estate project or rights and benefits associated with a real estate.

The functioning of the real estate valuation system in our country is at a low level compared to other countries developed in this area. In most European countries, street-based value maps have been created and value data for all real estate has been transferred to an information system. In our country, similar positional studies can only be carried out by Geomatics Engineers who have received adequate training in this field. For this reason, the importance of the trainings given in the Departments of Geomatics Engineering is increasing.

Basic concepts of valuation, legislation, analysis of data and methods of valuation with theoretical and practical applications constitute the basis of the education of undergraduate students in the field of real estate valuation (Erdem, 2016). The development of the country's economies is only increasing with the participation of real estate in the use of finance as liquidity, and therefore the need for Real Estate Appraisers is also increasing.

* **Corresponding Author**

*(*nurierdem@osmaniye.edu.try*) ORCID ID 0000-0002-1850-4616

Cite this study

Erdem N (2021). Content analysis of real estate valuation courses taught in geomatics engineering departments in Turkey. 2nd Intercontinental Geoinformation Days (IGD), 88-91, Mersin, Turkey

2. METHOD

One of the most important elements necessary to create a sustainable real estate valuation system is real estate appraisers. In the training of a real estate appraiser; current, knowing the needs of the sector, prepared in accordance with international development and standards, the contribution of real estate valuation training is great (McParland et al., 2002; Polat and Alkan, 2021). Today, the education needed in this field is mostly met by the real estate valuation course given in the Departments of Geomatics Engineering (Polat and Alkan, 2021).

For the first time in Turkey, academic training in the field of valuation was started in 1978 at Yıldız Technical University under the name "Land Valuation". In 1988, the name of the course was changed to "Real Estate Valuation" (Ertaş, 2019). Looking at the present day, it is seen that the real estate valuation course is given elective or compulsory in almost all cartographic engineering departments. Theoretical education comes to the fore. In addition, there are differences in the name, content, course time, mandatory or optional courses and semesters in which they are taught (Table 1 and Table 2).

Table 1 is examined; real estate valuation course is given under different names such as real estate valuation, real estate valuation, real estate valuation, GIS and real estate valuation. Although the course name is different, it is 80% similar in terms of content. As a resource, they often use similar resources.

Credits, ECTS, compulsory/elective (C/E), theoretical, practical and in which semester they are taught are given in Table 2. Accordingly, it was observed that courses were generally 2 and 3 credits, mostly given theoretically, and that 3 or 4 ECTS were suitable for real estate valuation courses in most universities. On the other hand, given the fact that the course is compulsory/elective, it was determined that half of the universities usually gives this course as an elective course. Examining the semester column in the table, it is seen that the related course is generally taught in 6. or 7. semesters.

The percentage values of the grades based on the homework, midterm exam and final exams of the exams conducted in the real estate valuation course are given in Table 3. Accordingly, visa and final exams are held throughout the universities, and the effect of these exams on the success rate is 40% of the visa, 60% of the final. In addition, it is seen that some universities practice in the form of a short exam (homework), except for the midterm exam. The effect of these assignments varies according to the examination regulations of universities.

Information about the content of The Real Estate Valuation course at some universities is summarized in Table 4.

83% similarity was found when examining the content of the course (Fig. 1). It can be said that this is due to the fact that the courses are given mainly in theory or practice, and in some departments there are applications for the content of the SPL valuation expertise exam.

Table 1. Universities where real estate valuation courses are given at undergraduate level

University Name	Course Name*	Course Time*
AKÜ	Application Of Real Estate Valuation	3
Aksaray	Real Estate Valuation with GIS	3
Artvin	Non-Carry Valuation	2
Avrasya	Real Estate Valuation	3
Bülent Ecevit	Real Estate Valuation	3
Cumhuriyet	Real Estate Valuation	3
Erciyes	Real Estate Valuation	2
Gaziosmanpaşa	Real Estate Valuation Applications	3
Gümüşhane	SPL real estate valuation principles	3
Hacettepe	SPL narrow scope Capital Market legislation	3
Harran	Non-Carrying Valuation	3
İTÜ	Real Estate Valuation	3
KTÜ	Real Estate Valuation	2
Kâtip Çelebi	Real Estate Valuation	2
Kocaeli	Application Of Real Estate Valuation	3
Konya Teknik	Real Estate Valuation	3
Korkut Ata	Real Estate Valuation	2
NEÜ	Real Estate Valuation	3
Okan	Real Estate Valuation	3
Ondokuz Mayıs	Real Estate Valuation	3
Onsekiz Mart	Real Estate Valuation	2
Ömer Halisdemir	Real Estate Valuation	2
Mersin	Real estate development and valuation	-
YTÜ	Real Estate Valuation	2
Uşak	Real Estate Valuation	2

* References: Universities' own websites

Table 2. Course Information

University*	C	T	A	E	C/E	S
Afyon Kocatepe	2	2	1	3	E	6
Aksaray	3	3	0	4	E	8
Artvin Çoruh	3	3	0	4	C	6
Çanakkale 18 Mart	2	2	0	4	C	7
Kayseri Erciyes	3	3	0	3	C	5
Gümüşhane	2	2	0	2	C	7
Şanlıurfa Harran	3	3	0	3	C	5
İzmir Kâtip Çelebi	6	3	0	6	E	6
Karadeniz Teknik	2	2	0	3	C	8
Konya Teknik	2	2	0	3	E	7
Necmettin Erbakan	2	2	0	5	E	5
Niğde Ömer Halisdemir	2	2	0	5	E	8
Samsun Ondokuz Mayıs	3	3	0	4	C	7
Osmaniye Korkut Ata	3	2	0	4	E	6
Sivas Cumhuriyet	2	2	0	5	E	7
Tokat Gaziosmanpaşa	3	3	0	4	E	4
Uşak	2	2	0	4	C	5
Yıldız Teknik	2	2	0	2	C	7
Avrasya	2	2	0	4	E	8
İstanbul Okan	3	3	0	5	C	4
Hacettepe	3	3	0	5	E	6
Zonguldak Bülent Ecevit	3	3	0	4	E	7
İstanbul Teknik	1.	1	1	2	C	6
Mersin	-	-	-	-	-	-

* References: Universities' own websites
C:Credit, T:Theory, A:Application, E:ECTS, S:Semester

Table 3. Effect of universities on homework, midterm exam, final grade percentile

University*	HW	ME	F
Afyon	%0	%40	%60
Aksaray	%20	%30	%50
Artvin	%20	%30	%50
Çanakkale	%0	%40	%60
Kayseri	%0	%40	%60
Gümüşhane	%0	%40	%60
Şanlıurfa	%10	%40	%50
İzmir Katip	%0	%40	%60
Karadeniz	%0	%40	%60
Konya	%20	%40	%40
Necmettin	%0	%40	%60
Niğde Ömer	%20	%30	%50
Samsun 19	%0	%40	%60
Osmaniye	%0	%40	%60
Sivas	%0	%40	%60
Tokat	%0	%40	%60
Uşak	%0	%40	%60
Yıldız	%30	%30	%40
Avrasya	%20	%20	%60
İstanbul	%0	%40	%60
Hacettepe	%20	%30	%50
İstanbul	%0	%40	%60
Zonguldak	%0	%40	%60
Mersin	-	-	-

* References: Universities' own websites
HW: Homework, ME: Midterm exam, F:Final

Table 4. General characteristics of Real Estate Valuation courses given in some universities*

Univ.	Course Content
YTÜ	Taxation, capital market, land regulations and real estate valuation applications for expropriation; valuation data; valuation methods; reporting techniques.
BEÜ	Concepts of value and immovable value. Assessment of urban and rural real estate. Parameters affecting evaluation and their relationships. Real estate legislation and assessment of real estate in terms of expropriation. Methods of evaluating real estate. Statistical analysis on a survey basis for the assessment of real estate. Generating valuation maps
KTÜ	It will be able to learn the concepts of Real Estate, Property and value, understand the importance of real estate valuation in Land Management.

* References: Universities' own websites

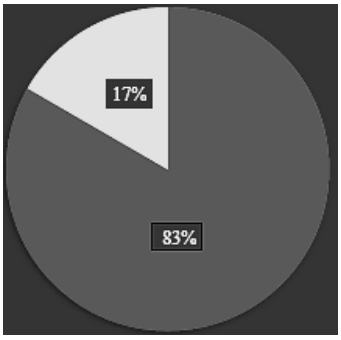

Figure 1. Similarity rate of course content

The results of the analysis of real estate valuation courses for the course hours as credit, ECTS, theory and practice according to the sections are given in Chart 2. Accordingly, 12 universities give 2 credits, 9 universities give 3 credits, and 2 universities give with different credits. When we look at ECTS, 2 universities 2 ECTS, 6 universities 3, 9 universities 4 and 5 universities offer courses with different ECTS. When we look at the theoretical course time, 12 universities 2 Course hours, 10 universities 3 Course hours were sufficient, while 1 university considered a different course time appropriate. It has been explained earlier that the number of universities providing practical education is small. Only 2 universities offer practical training (Fig. 2).

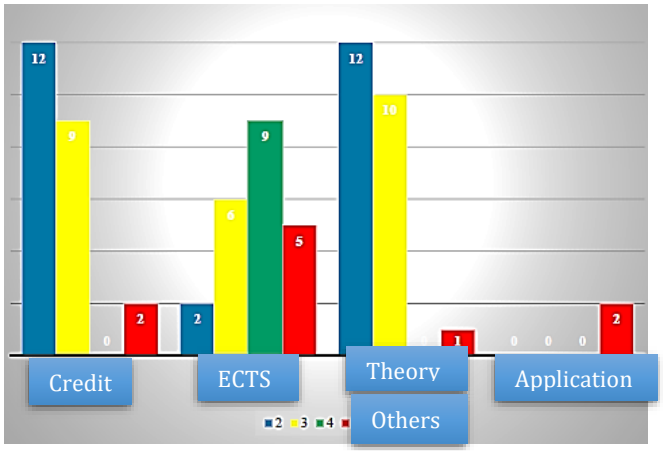

Figure 2. Course hours as credits, ECTS, theory and practice

In the percentage in which semester this course was given, it is compared in Fig. 3. 29% of universities give this course in 7 semesters, 24% in 6 semesters, 19% in 4 and 8 semesters, while 9% give this course in 4 semesters.

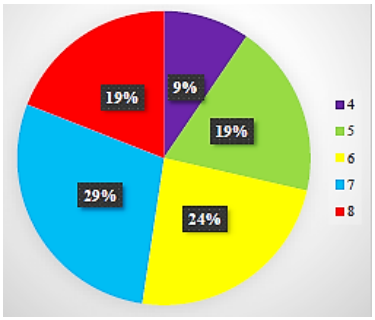

Figure 3. Information about the semester in which the courses are taught

Courses on real estate valuation are elective in 52% of the Geomatics Engineering departments and compulsory in 48% (Fig. 4).

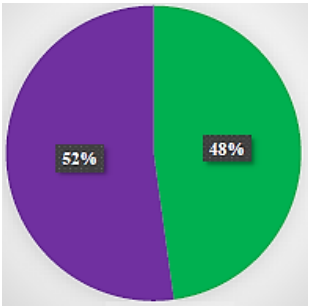

Figure 4. Compulsory or elective courses

3. CONCLUSIONS and RECOMMENDATIONS

- In this study, the course content of real estate valuation course in geomatics engineering departments was examined in ECTS, credit, semester, theoretical, practical, compulsory and elective aspects. The study found that the course content of universities was close to each other. It is seen that the real estate valuation course is given in general in the geomatics engineering departments.
- Many elements of this profession, which require professional experience and expertise, try to eliminate their shortcomings through trial and error, which damages the reputation of the profession. For this reason, education needs to be institutionalized. It is not enough for some of our universities to include undergraduate and graduate level valuations.
- Considering the importance of the valuation profession on behalf of our country in social and economic terms, CMB, BRSA, TDUB and other related institutions and organizations should conduct studies to open this department at universities or to provide courses on valuation in departments related to Real Estate.
- The research showed that universities mostly teach real estate valuation courses in 6 and 7 semesters. This indicates that universities believe that it would be more useful for undergraduate students to have basic professional literature in this field in advance before giving this course.
- Important in the profession is the work done in the field. A person can succeed in the exams by working on modules in the CMB licensing exams, even if they have not received training in valuation expertise. This should not mean that the person has the ability to become an appraiser. SEC licensing exams should be questions about the problems that people experience in the field. In addition, an examination system should be introduced in which the experience periods of appraisers can be measured.
- SPK, real estate (real estate) not related to the world (nursing, Public Administration, international relations... etc.) 4-year university graduates should not open the doors of this profession, should prevent them from applying for exams.
- Today, the issue of real estate valuation has become even more important with the developing country's economy. Universities should take this into account in the education they will give at the undergraduate level.
- Given the lack of experts in the field of real estate valuation, it can be said that universities should update their course content and put practical education at the forefront, as well as the theoretical part. Because only theoretical courses are offered in all but 2 universities.
- In order to conduct practical training, existing lesson hours should be increased, real-life sample applications should be made, and current resources in this field should be included.1".

REFERENCES

Açlar A & Çağdaş V (2008). Real estate valuation, Ankara: Union of Chambers of Turkish Engineers and Architects, Chamber of Surveyors and Cadastre Engineers Publication, ISBN: 975-395-551-0, 500 pages.

AI Appraisal Institute (2013). The appraisal of real estate. 14th ed. Chicago. ISBN: 978-1-935328-38-4.

SPK (2001). Declaration on rules about companies to deliver real estate appraisal service in compliance with capital market legislation; and addition of those companies to the list by the board. Volume: VIII, No: 35, Turkish Official Gazette: August, No. 24491.

Yalpır Ş (2007). Developing, and implementing real estate appraisal model through fuzzy logic modelling: case of Konya. Thesis (PhD). Selçuk University, Institute of Sciences, Konya, 248 pages.

Erdem N (2016). Türkiye de Taşınmaz Değerleme Uzmanlığı ve Haritacılık Eğitimi. International Symposium on Post-Secondary Vocational Education and Training. http://cdn.hitit.edu.tr/hitit/files/18790_161221092331.pdf, sayfa: 64-73.

McParland C, Adair A & McGreal S (2002). Valuation standards: A comparison of four European countries, Journal of Property Investment & Finance, Vol. 20 Issue: 2, pp.127-141, https://doi.org/10.1108/14635780210420025

Polat Z A & Alkan M (2021). Lisans ve lisansüstü düzeyinde verilen taşınmaz değerleme eğitiminin değerleme lisansı sınavı kapsamında değerlendirilmesi. Geomatik, 6(1), 15-30, DOI: 10.29128/geomatik.650766

Ertaş M (2019). Education For Real Estate Valuation in Turkey, International Journal of Engineering and Geosciences (IJEG), Vol; 4, Issue; 1, pp. 008-015, February, ISSN 2548-0960, DOI: 10.26833/ijeg.416336. https://doi.org/10.1007/s13369-013-0853-1

Intercontinental Geoinformation Days

igd.mersin.edu.tr

Using artificial neural networks in land use/change

Esat Fikri Kılıç*[1], Eray Köksal [2]

[1]*Zonguldak Bülent Ecevit University, Institute of Science, Geomatics Engineering, Zonguldak, Turkey*
[2]*Zonguldak Bülent Ecevit University, Engineering Faculty, Geomatics Engineering, Zonguldak, Turkey*

Keywords
Artificial Neural Networks
Maximum Likelihood
Temporal Change
Landsat 8 OLI
QGIS

ABSTRACT

The aim of this study is to detect and control the land cover distribution / change with stylistic shaping based on the satellite images of different times by using remote sensing techniques. These images are used to obtain earth information from satellite images obtained in raw form. The most common method for converting data into information is the classification of satellite images. Different kinds of statistical analysis and interpretation techniques are used to get information regarding the Earth from the images in the raw form. In this study, it is aimed to determine land usage change in order to better understand the land structure by using Landsat 8 OLI satellite images in Çaycuma district of Zonguldak province including the time between 2015 and 2020. The QGIS program was used to determine the change of land usage. In the study, artificial neural networks were used on determining the change of land usage. The values obtained by this method are compared with the maximum likelihood of values and the speed and accuracy of artificial intelligence methods in creating the change of land usage are examined.

1. INTRODUCTION

With remote sensing techniques, it provides important opportunities to determine the changes in different scales and to be able to make comparative analysis through satellite images of different times in order to detect and control the change of land usage.

Land use studies are necessary not only for agriculturally dominant, overpopulated developing regions, but also for all over the world due to their relationship with different human phenomena. The terms land use and land cover change (LU / LC) describe any human activities that occur on the Earth's surface. Land cover refers to the physical and biological cover of the land, including water, vegetation, bare soil and / or artificial structures (Ellis and Pontius, 2006).

Remote sensing is the science of obtaining information about objects without physical contact, recognizing them, distinguishing them from their surroundings and turning this information into the form of images.

With remote sensing technology, the visual and statistical detection of land use and change depending on time and location is an important gain in terms of speed and economy. Thanks to its ability to produce a high rate of data, it can significantly increase the possibilities for analytical evaluation processes about the region and provide users with the opportunity to produce methods and models suitable for its purpose in the planning process (Hellawell, 1991; Banister et al, 1997).

The changes in land cover and land use increase the impact of environmental changes that lead to the change and transformation of the earth. These changes and transformations depend on time. The reason for the change is the decisions taken by local and regional governments in parallel with the economic, cultural, social and ecological processes (Aspinall,2006).

The various statistical analyses and interpretation techniques are used to obtain earth information from satellite images obtained in raw form. The most common method for converting data into information is the classification of satellite images.

Classification is the categorizaton of all pixels in one image nto different classes or themes. It is the creation of homogeneous classes of similar objects in the data, or the creation of previously defined classes using the property of the given object, obtained by mathematical and statistical methods. The purpose of the image

* **Corresponding Author**

*(esatfk@gmail.com) ORCID ID 0000 – 0002 – 5711 – 1663
(eraykoksal@beun.edu.tr) ORCID ID 0000 – 0003– 0329– 8191

Cite this study

Kılıç E.F & Koksal E. (2021). Using artificial neural networks in land use/change. 2nd Intercontinental Geoinformation Days (IGD), 92-95, Mersin, Turkey

classification process is to obtain the thematic map by assigning each pixel to one of the classes that makes up the terrain cover according to a specific rule based on the brightness values of the pixels that make up the image. In this study, it is aimed to determine land usage change in order to better understand the land structure by using Landsat 8 OLI satellite images in Çaycuma district of Zonguldak province including the time between 2015 and 2020.

2. METHOD

In this study, Landsat 8 OLI images from 2015 and 2020 were used in Çaycuma district of Zonguldak province. The following ways are briefly followed in the pre-processing of these images and obtaining a land use map: First, image preprocessing (geometric and atmospheric correction) was performed. The land classes to be used are designed. These classes are the forest area, water surface, structure, agriculture, bare land. Then, test sites that could reveal the earth characteristics in the image were determined and classified with appropriate algorithms. The controlled *classification* method was used in our study. Sample pixels were collected for each terrain class through the image before the classification was initiated. By analyzing the pixel values, the statistical characteristics of the classes were determined and the images were classified using the *Maximum Likelihood* method. In order to get used, artificial neural networks were used on land use change. The values obtained by this method were compared with the *maximum likelihoood* values and the speed and accuracy of the methods of creating classifications were examined. An artificial neural network model was created using Matlab. The results compared with the values obtained with the *maximum likelihood* method and the usability of the methods in the field of land use change are shown.

There are several methods and techniques for satellite image classification. Figure 1 shows the hierarchy of satellite image classification methods. Satellite image classification methods can be broadly classified into three categories: Automated, Manual, Hybrid (Abburu, 2015).

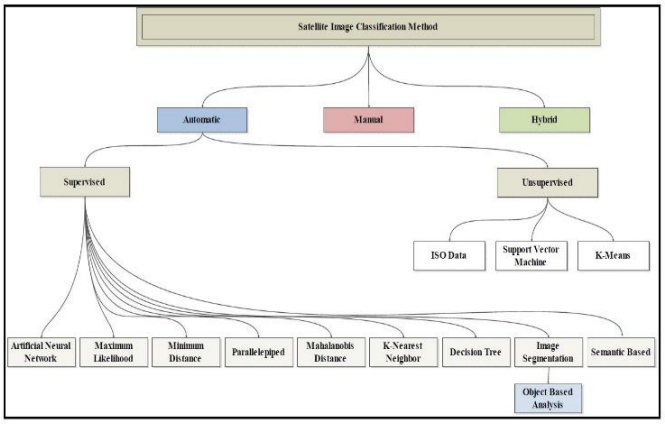

Figure 1. The hierarchy of Satellite image classifications methods (Abburu, 2015)

The controlled classification map for 2015 created with the QGIS program is given in Figure 2.

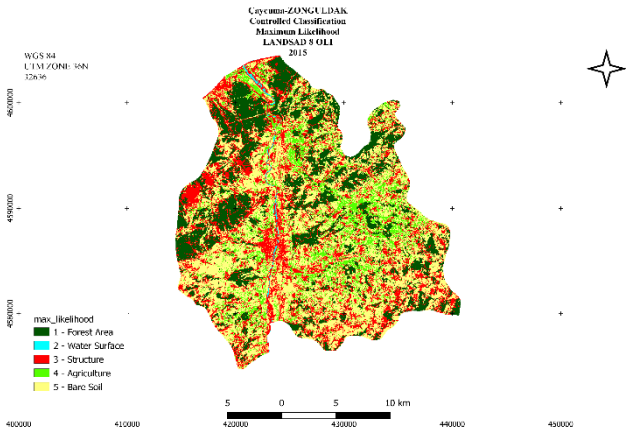

Figure 2. Çaycuma district controlled classification in 2015

The controlled classification map for 2020 created with the QGIS program is given in Figure 3.

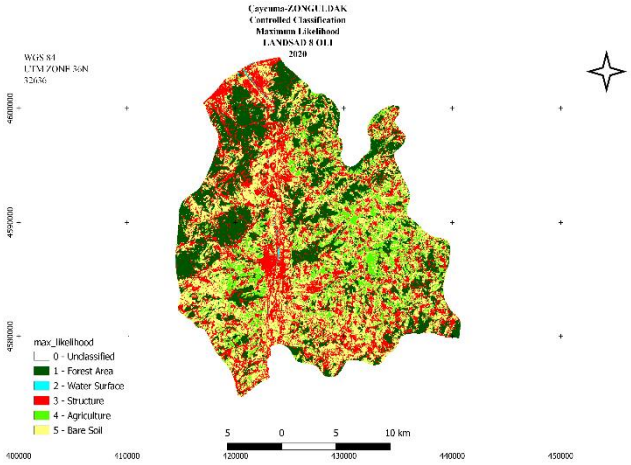

Figure 3. Çaycuma district controlled classification in 2020

The data were obtained as a result of the controlled classification with *maximum likelihood* technique. Classification results for 2015 and 2020 are given in Table 1 and Table 2.

Table 1. Classification results for 2015

Class	PixelSum	Percentage (%)	Area [m^2]
1	130305	23.82676431	117274500
2	2373	0.433912066	2135700
3	130639	23.88783748	117575100
4	63952	11.69386617	57556800
5	219616	40.15761997	197654400

Table 2. Classification results for 2020

Class	PixelSum	Percentage (%)	Area [m^2]
1	144960	26.5063898	130464000
2	1269	0.372040623	1892100
3	146468	26.78213232	131821200
4	65197	11.92147555	58677300
5	188993	34.5579617	170093700

Artificial Neural Networks is an often preferred method because it is successful in learning nonlinear relationships by generalizing with samples. It is a method created based on strong and complex nerves in the human brain (Tabar,2020). It is used to classify complex relationships and nonlinear states. The data is divided into units. Each unit consists of inputs and outputs generating a function that determines the relationship between them. To start the application, the data must first be recognized and the network must be created. After the input and output values are determined, the training phase of the network should be started. The model of artificial neural networks obtained by input and output values is given in Figure 4.

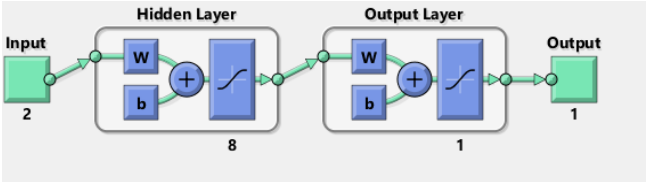

Figüre 4. Artificial Neural Networks Model

Learning-status and test graphs are given in Figure 5.

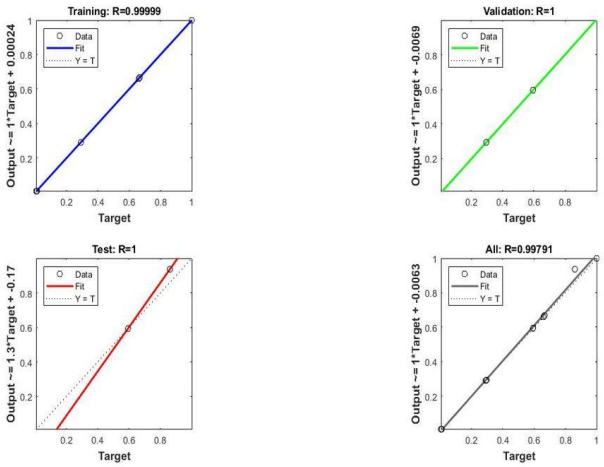

Figure 5. Learning-status and test graphs

Field data and artificial neural networks model were created and then the values of the test result data were compared (Figure 6).

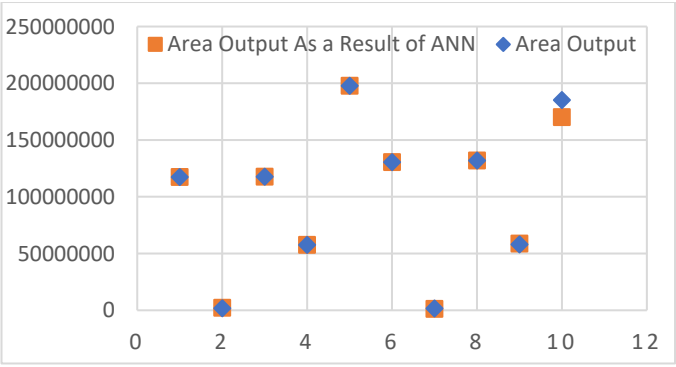

Figure 6. Creating a model of artificial neural networks with field data and then comparing the values of the test result data

Table 3. Artificial neural networks test output for 2015

Class	2015 Area (m^2)	ANN Output
1	117274500	117289335
2	2135700	1779324.79
3	117575100	117589375
4	57556800	57556920.5
5	197654400	197651065

Table 4. Artificial neural networks test output for 2020

Class	2020 Area (m^2)	ANN Output
1	130464000	130463798
2	1892100	1712896.95
3	131821200	131821412
4	58677300	57996906.5
5	170093700	185149415

3. RESULTS

The visual and statistical detection of land usage and change depending on time and location with remote sensing technology provide the possibility of high speed, economy and producing data of higher accuracy. It also contributes to the analytical review processes about the region. This technology is one of the most suitable choices to conduct them. In this study, Çaycuma district of Zonguldak province was examined with satellite images. For this purpose, Landsat 8 OLI satellite images were used. In the working area, there are classes of forest areas, water surface, structure, agricultural land, bare lands. In order to distinguish these classes, controlled classification techniques were applied using satellite imagery. At the same time, it has been investigated whether there will be similar results with artificial neural networks. When the results were examined, it was seen that the data obtained by the maximum likelihood method and the data obtained by artificial neural networks are compatible.

4. DISCUSSION

In the study, the use of artificial intelligence methods in land usage was investigated. Artificial neural networks toolbox was used in Matlab program for application. According to the application results, it was seen that the value obtained from the model established with artificial neural networks was very close to the actual report values. Most methods that use artificial intelligence, such as artificial neural networks, can be used in the change of land usage as it can be used in any field.

5. CONCLUSION

The study based on the change of land usage using Remote Sensing technology is important for numerical analysis with the plans. In addition, the effective analysis of land features involved in planning and the ability to do it quickly and at low costs increase its availability. In this respect, it has been used more frequently in recent years. Artificial neural networks, which are now used in every application, have been shown to give accurate results in

the studies. It should be noted that the number of data should be increased in order for artificial neural networks to give better results.

REFERENCES

Abburu S (2015). Satellite Image Classification Methods and Techniques: A Review. International Journal of Computer Applications (0975 – 8887), Volume 119 – No.8, June 2015.

Aspinall (2006). Mapping Prairie Pothole Communities with Multitemporal Ikonos Satellite Imagery.

Banister D, Watson S & Wood C (1997). Sustainable cities: Transport, energy, and urban form. Environ. Planning. chapter 24, (pp. 125–143).

Ellis E & Pontius R G (2006). Land-use and land-cover change, Encyclopedia of Earth, Environ. Protect, 2, 142-153.

Hellawell J M (1991). Development of a rationale for monitoring.In: Goldsmith, F.B. (Ed.), Monitoring for Conservation and Ecology. London, (pp. 1–14).

Tabar M E (2020). Yapay Sinir Ağları ve Bulanık Mantıkla Gayrimenkul Değerleme Modelinin Oluşturulması: Samsun Örneği. MS Thesis. Samsun Ondokuz Mayis University, Institute of Graduate Studies.

Intercontinental Geoinformation Days

igd.mersin.edu.tr

Generating temporal cadastral parcels with artificial intelligence algorithms within the scope of cadastre 2034

Fatma Betül YIDIZ*[1], İsmail Ercüment AYAZLI [2], Hidayet TAKCI [3]

[1]*Sivas Cumhuriyet University, Engineering Faculty, Department of Geomatics Engineering, Sivas, Turkey*
[2]*Sivas Cumhuriyet University, Engineering Faculty, Survey Engineering Department, Sivas, Turkey*
[3]*Sivas Cumhuriyet University, Engineering Faculty, Computer Engineering Department, Sivas, Turkey*

Keywords
Cadastre 2034
Land Management
Digital Image Processing
Artificial Intelligence
Deep Learning

ABSTRACT

Since real estates are a reliable investment tool, many changes occur in ownership and parcel geometry. Therefore, temporal cadastral data have a great importance in terms of sustainable development policies because cadastre can provide the main data of smart cities. The Cadastre 2034 Vision started by the International Federation of Surveyors (FIG) proposes to record the temporal dimension of the cadastral data. The temporal dimension of cadastral parcels are stored in the documents named as "fenni evraklar" (technical papers) in Turkey. The study aims to develop a new model in which the temporal dimension of cadastral parcels will be automatically digitized in accordance with the four-dimensional cadastral approach targeted in the Vision of Cadastre 2034. Therefore, an interface using artificial intelligence algorithms was created in the Python programming language and changes in cadastral parcels can be monitored at the beginning from the first facility cadastre on any cadastral parcel.

1. INTRODUCTION

Since the second half of the 20th century, due to the rapid increase in the world population, "new policy for sustainable development (land management) about the use and protection of land, and it is a tool for the implementation of these policies, and determining, registering and recording information about the ownership, value and use of real estate and publishing process" (Cagdas & Gur, 2003) has spawned the concepts of land administration. Since the early 2000s, cadastre has been defined as a spatial information system modeling human-land relation (Demir, 2001; Ayazlı, 2006) and evolved into land administration, which is the implementation tool of sustainable development policies (Grant & Williamson, 1999; Enemark, 2001; Cagdas ve Gur, 2003; Enemark, 2009). As it can be perceived from the definition, the cadastre is one of the most important tools necessary for the efficient use of natural and environmental resources, and it is a geospatial information system in which register the real estate properties guaranteed by the constitution. Ownership of the real estates in Turkey starts with the registration date and it may change or end in time by buying and selling and/or land regulations. Therefore, cadastre is a living entity, hence it has a temporal dimension. In this context, cadastre is defined as a four-dimensional (4D) that is a space-time dependent entity. (Stoter, 2004; Ayazli vd., 2011). To design the future of the cadastre after 2014, a paper was published in 2010, the Cadastral Future: Setting Up a New Vision for Nature and the Role of Cadastre (Bennett et al., 2010). In the paper, they discussed the factors affecting the developments in the cadastral field as globalization, urbanized population, good governance, climate change, environmental management, three-dimensional visualization/analysis technologies, wireless networks, standardization and interoperability (Bennett et al.,2010). Under the influence of the factors, the objectives of Cadastre 2034 carried out by FIG are specified as accurate, object-oriented, four dimensional, real-time and global cadastre. (Steudler, 2014; Bennett et al., 2010; LINZ, 2014; Polat and Alkan, 2015; ICSM, 2015). In this context, the cadastre maintains the responsibility to reconstruct the infrastructure that will form the basic data for smart cities and geographical information systems (GIS) by a contemporary perspective (Kaufmann and Steudler 2002; Bennett vd, 2010; (Anzlic Committee on Surveying & Mapping, 2015).

In Turkey, cadastral studies are carried out in accordance with the provisions of the "Cadastral Law" numbered 3402 and 5304. Temporal data in the cadastral system are kept in called technical documents, technical folders, change folders and application folders, and the land registers and the condominium rights. These sources contain over a hundred attribute in total

* **Corresponding Author**

*(20199249005@cumhuriyet.edu.tr) ORCID ID 0000-0002-2152-5661
(eayazli@cumhuriyet.edu.tr) ORCID ID 0000-0003-0782-5366
(htakci@cumhuriyet.edu.tr) ORCID ID 0000-0001-6995-5073

Cite this study

Yıldız F.B, Ayazlı İ.E & Takcı H. (2021). Generating temporal cadastral parcels with artificial intelligence algorithms within the Ssope of cadastre 2034. 2nd Intercontinental Geoinformation Days (IGD), 96-99, Mersin, Turkey

and considering them recorded in whole country, it is obvious that the data density is very high.

In Turkey, cadastral technical documents were scanned within the scope of the "Cadastral Data Consolidation" (CDC) project and converted into "Portable Document Format" (pdf). The aim of this study is to extract temporal data of cadastral parcels from technical documents as fully automatically using artificial intelligence algorithms. In this context, technical documents created within the scope of the CDS project are automatically processed with a prepared software and temporal cadastral parcel data are generated according to the detected coordinate data.

2. METHOD

Within the scope of this study, technical folders with .pdf extension produced in the scope of CDS project in Sancaktepe district of Istanbul were used. At the beginning of the study, the .pdf data were converted into an image format using the Python programming language, then textual expressions and numerical data on the image were separated and saved in a separate file. The data were filtered using digital image processing methods as they contain noises. They were filtered using noise pixel cleaning and "Threshold Gaussian (ATG)" methods.

A graphical user interface (GUI) has been designed. Simultaneous processing has been done in the software with automatic detection.

The process steps followed in the study are as follows:

- GUI design in Python and QT Designer environment.
- Import of libraries to be used (Opencv, PyQt5, Tesseract, NumPy, Matplot, Openpyxl) in Python environment.
- Determination of .exe file locations of the environment where the original textual expressions will be extracted.
- Adjusting the folders to add images in the GUI environment and determining the sizes of the folders.
- Performing image processing steps. These image processing methods are: OpenCv file operations, the control of pixel values in terms of color channels, grayscale image acquisition and thresholding filters.
- Configuration settings for extracting textual and numerical data
- Extracting and printing textual and numerical expressions.
- Performing file processing steps in Python. It covers cases such as opening and closing files in Excel and text document formats, processing values into files and placing them in a meaningful way.
- Final checks in GUI design.

2.1. GUI Design

GUI design was carried out on Python Qt Designer. Functions were created on the design by importing it in Python with PYQT5.

The image adding section, the reading area and the fields showing the separation of the characters are added to the design. The image was read with the "read" button and separation operations can be done. All functions were performed by connected to the button. The scope of functions constitutes image processing and textual expressions in the image. The GUI design is shown in Figure 1.

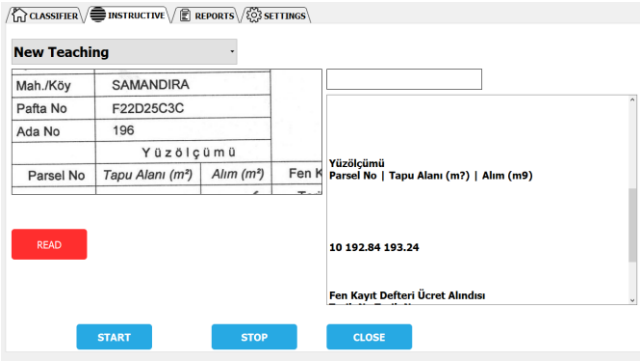

Figure 1. GUI design structure

2.2. Image processing

Image processing techniques have been used as the extraction of text on the image does not give an entirely acceptable result when raw images are used directly. Some image processing steps applied to the image can be listed as follows:

Removing the remaining areas outside the text, finding and sharpening text by converting it to an 8-bit image, resizing the image, clearing unnecessary and non-textual expressions on the text with adaptive thresholding method as images are obtained in different areas and under different lighting conditions and Gaussian Filter, one of the image filters that can make the text more readable, has been applied to soften the image. As a result, the results in Figure 2 were obtained.

Texts may not appear directly in .pdf format as a straight page. In this case, the images must be rotated. For this reason, these images were detected first and this problem was resolved.

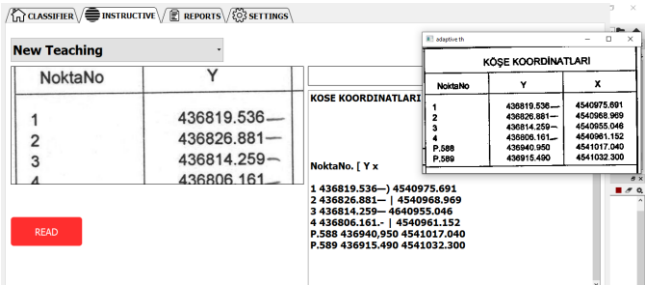

Figure 2. Results from image processing

As represented in the Figure 3, the image was first cleaned, then each character was perceived separately and character segmentation was made as in the Figure 4.

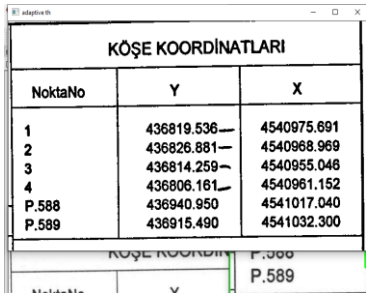

Figure 3. Pre-processed image

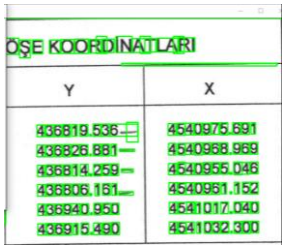

Figure 4. Separating characters from the image

2.2.1. Data processing and extraction

Python-tesseract and EAST deep learning text sensor, Ocular, OCRopus, SwiftOCR (deep learning), LSTM techniques used in text processing were tested in Python language. The best method has been determined.

The texts of the technical folder data with .pdf extension seen in the Figure 5 have been accessed. In the first stage, text files were created for the text extracted with letters, numbers and different signs. Since these need to be cleared, some adjustments have been made on the model to create meaningful text. As settings, fine-tuning has been made, such as language setting, numerical and textual expression detection, navigation setting, and page segmentation mode. Language setting is a setting used to detect different languages and parameter values are given accordingly. Page segmentation mode setting takes and accepts parameters by making a selection according to the numbered list. Thanks to these settings, more meaningful expressions were created in the text and printing operations were realized.

Python-tesseract used in the work is an optical character recognition (OCR) tool for Python. It is an auxiliary tool used to find embedded text on images. Another tool used is the EAST deep learning text detector tool. These two tools offer the best techniques and settings for text recognition. At the same time, these tools can work in real time and perform text finding processes simultaneously.

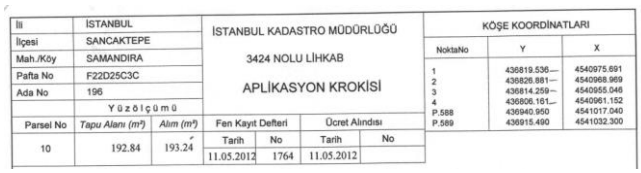

Figure 5. Attributes in technical folder

3. RESULTS

There are a number of problems such as ambiguous texts, light reflections, blurry images in the .pdf extension data created within the scope of the CDS project. To overcome these problems, Python-tesseract and EAST deep learning text detectors are used.

Noises on data used as input images were cleared by passing through filters such as Gaussian, grayscale and thresholding. The cleaned image was processed with the help of the text detector function algorithm. As the result data, the texts were extracted from the image simultaneously.

The Figure 6 shows the process step in which the results obtained as a result of the software are written on the file simultaneously and the accuracy checks are carried out.

The main parts of the software are schematized in the Figure 7.

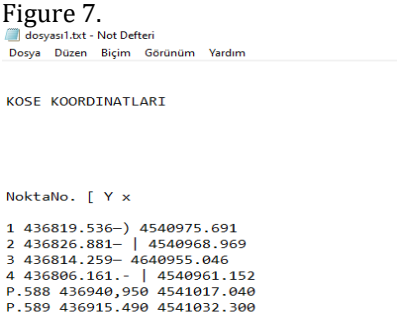

Figure 6. Outputs

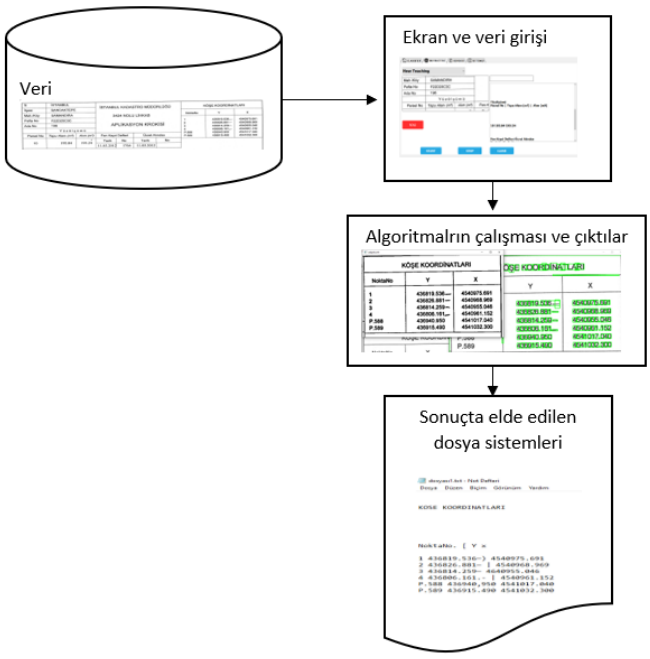

Figure 7. Overwriting files and checking accuracy

4. CONCLUSION

Since real estates are a reliable investment tool, the number of transactions carried out in the land registry and cadastre offices are increasing day by day. In this study, it was aimed to provide a more dynamic tracking system of cadastral records and a solution was presented.

According to the results, it has been possible to digitize the data kept in different file formats automatically, regardless of the format, thanks to the developments in computer technologies.

The proposed solution was encoded in Python programming language, and the texts were extracted and stored with artificial intelligence algorithms on the desktop application. In this way, the changes occurring from starting the first facility cadastre in a cadastral parcel can be monitored graphically.

REFERENCES

Adrian at PyImageSearch (2020). Start Here with Computer Vision, Deep Learning, and OpenCV. Mart 15, 2021- https://www.pyimagesearch.com /start-here/

Anzlic Committee on Surveying & Mapping. (2015). *Cadastre 2034: Powering Land & Real Property*. https://www.icsm.gov.au/sites/default/files/Cadastre2034_0.pdf

Ayazli, I. E., Helvaci, C., Batuk, F., & Stoter, J. (2011). Designing three dimensional property right database. African Journal of Business Management, 5(22), 9440-9447.

By Mathias Lemmens, Delft University of Technology, The Netherlands, Towards Cadastre 2034, September 7,2010,https://www.gim-international.com/content/article/towards-cadastre-2034

Bennett, R., Kalantari, M., & Rajabifard, A. (2010, 06 28). Beyond Cadastre 2014. 12 30, 2017 GIMInternational:https://www.gim-international .com/content/article/beyond-cadastre-2014

Cagdas, V., & Gur, M. (2003). Sustainable Development and Evoulation of the Cadastre. HKM Jeodezi, Jeoinformasyon ve Arazi Yönetimi Dergisi(89), 42-48. http://www.hkmo.org.tr/resimler/ekler/M6K2_f877f38657_ek.pdf

Demir, H. (2001). Kadastro Bilgisi Ders Notları. İstanbul

Enemark, S. (2001). Land Administration Syestems -a major challenge for the surveying profession. A Spatial Odyssey : Proceedings of the XVIII American Surveying Teachers Conference. Penn State University, Wilkes Barre, USA.

Grant, D., & Williamson, I. (1999). The Bathurst Declaration on Land Administration for Sustainable Development. FIG. Retrieved from http://www.fig.net/resources/publications/figpub/pub21/figpub21.asp

Firhan Maulana Rusli, Kevin Akbar Adhiguna, Hendy Irawan (2020). Indonesian ID Card Extractor Using Optical Character Recognition and Natural Language Post-Processing. arXiv:2101.05214v1 [cs.CV] 15 Dec 2020. https://arxiv.org/pdf/2101.05214.pdf

Gorsa Lakshmi Niharika; Shahana Bano; Pavuluri Shyam Kumar; Tinnavalli Deepika; Hampi Thumati (2020). Character Recognition using Tesseract enabling Multilingualism. ISBN:978-1-7281-6388-8 DOI: 10.1109/ICECA49313.2020.9297609

ICSM. (2015). Cadastre 2034: Powering Land and Real Property. 12 30, 2017-The Intergovernmental Committee on Surveying and Mapping Web Page: http://www.icsm.gov.au/cadastral/Cadastre2034.pdf

Kaufmann, J., & Steudler, D. (1998). Cadastre 2014; A VIision for a Future Cadastral System. FIG. Retrieved from http://www.eurocadastre.org/pdf/cadastre_2014 .pdf

LINZ. (2014). Cadastre 2034, A 10–20 Year Strategy for developing the cadastral system: Knowing the 'where' of land-related rights. Land Information New Zealand.

Matthias A Lee (2020). Python Tesseract . Mart 15, 2021 https://github.com/madmaze/ pytesseract

Mehmet Alkan, Hicret Gursoy Surmeneli, Zeynel Abidin Polat, fig congress 2018 - Design and determine cadastral and land management performance of Turkey with Cadastre 2034 Vision, FIG Congress 2018: Embracing our smart world where the continents connect - Enhancing geospatial maturity of societies

Neha Joshi (2019). Text Image Extraction and Summarization. ISSN NO: 2350-1146 I.F-5.11

Polat, Z. A., & Alkan, M. (2015). Türkiye'nin Kadastro 2014 Performansı ve Kadastro 2034'ten Beklentiler. The World Cadastre Summit 2015. Istanbul.

Sahil Thakare; Ajay Kamble; Vishal Thengne; U.R. Kamble (2018). Document Segmentation and Language Translation Using Tesseract-OCR. ISSN: 2164-7011 https://ieeexplore.ieee.org/document/8721372-DOI: 10.1109/ICIINFS.2018.8721372

Sergio Canu (2020). Text recognition (OCR) with Tesseract and Opencv. Mart 15, 2021 https://pysource.com/2020/04/23/text-recognition-ocr-with-tesseract-and-opencv/

Steudler, D. (2014). Cadastre 2014 and Beyond. Copenhagen: FIG.

Stoter, J. E. (2004). 3D Cadastre. Delft: Publication on Geodesy

Sonia Bhaskar, Nicholas Lavassar, Scott Green (2020). Implementing Optical Character Recognition on the Android Operating System for Business Cards. EE 368 Digital Image Processing.

The Tesseract open source OCR engine, http://code.google.com/p/tesseract-ocr.

Open Source Computer Vision (2021). OpenCV Mart 15, 2021- https://docs.opencv.org/master/d6/d00/tutorial_py_root.html

Zeynel Abidin POLAT, Mustafa USTUNER and Mehmet ALKAN, On the Way to Vision of Cadastre 2034: Cadastre 2014 Performance of Turkey, FIG Working Week 2015 From the Wisdom of the Ages to the Challenges of the Modern World Sofia, Bulgaria, 17-21 May 2015

Intercontinental Geoinformation Days

http://igd.mersin.edu.tr/2020/

Easement right valuation for electric power tranmission lines

Mustafa Yılmaz*[1], Reha Metin Alkan[1]

[1]*İstanbul Technical University , Civil Engineering Faculty, Geomatics Engineering Department, İstanbul, Turkey*

Keywords
Expropriation
Easement right
Nominal valuation
Electric power transmission lines

ABSTRACT

Expropriation costs in power transmission line projects reach quite high amounts. Expropriation on these lines is done in two ways as property expropriation and easement right expropriation. Property expropriation is carried out for pylon places and transformer stations. Easement rights are established in cases where an energy transmission line passes over the parcel. In this case, there is no loss from ownership but there is a restriction on usage. For this reason, the decrease value is determined for easement rights and this decrease is paid to the owner. In this contribution, the studies have been carried out on which factors affect the amount of decrease and how the decrease should be determined. For this purpose, factors affecting decrease rate were determined together with their weights, and scoring principles were developed for each factor. Later, a sample application was made to explain the issue and the determined price was compared with the court fee and market value.

1. INTRODUCTION

Generating and transmitting electrical energy both in Turkey and in the world has become a very important goal. The transmission of the generated electricity to users is provided by establishment of substations that enable high voltage electricity to be made suitable for use and by establishment of energy transmission lines that enable transmission of the generated electricity to these substations. When these facilities are established, very high construction costs arise. In addition to all these costs, expropriation costs also constitute an important item. If there is a pylon place or transformer stations in the parcel, these areas are divided from the parcel and expropriated completely; but under transmission line wires easement right is established.

The price to be paid for the right of easement is the decrease caused by this right in value of parcel (Kamulaştırma Kanunu 1983). In Turkey, there is no law or regulation regarding which variables will be taken into account for value decrease of parcel because of the easement right. Both the electricity company valuation commission and the court experts take the Supreme Court decisions into consideration for calculation of the decrease. According to the decisions of the Supreme Court, easement right affects value of the parcel at most 50% in zoned parcels. In agricultural lands, this value is taken as maximum 35% (Yıldırım 2018). In this case, the expropriation value of parcel because of easement right (i.e. easement price), is calculated by using the formula;

$$EP = EA.PV.DC \quad (1)$$

where, EA is easement area, PV is parcel value per unit m^2 and DC is decrease coefficient. As stated above, DC (Decrease Coefficient) must be at most 0.50 for zoning parcels and 0.35 for agricultural parcels. However, the most important thing to remember is that these values are generally accepted maximum values. In other words, the rate of decrease that will occur in parcel due to the establishment of easement should be determined by taking into account the type, nature, use of the parcel, nature of right of easement (pipeline, electric power transmission line etc.), the area and location covered by the easement in the property and direction of easement (Köktürk and Köktürk 2016). However, this coefficient is taken as 0.50 without taking into account the factors affecting decrease rate in the valuation reports prepared by court experts. Even in agricultural lands, maximum 0.35 rule is not followed. Even worse, in some of the expert reports, the decrease coefficient is taken as 0.50 without taking the easement area into account. When the valuation reports are prepared as stated above, the cost to be paid for easement right is determined to be quite high, which causes a serious waste of public resources, a considerable increase in

* **Corresponding Author**

*(yilmazmust18@itu.edu.tr) ORCID ID 0000-0001-8962-4730
(alkanr@itu.edu.tr) ORCID ID 0000-0002-1981-9783

Cite this study

Yılmaz M & Alkan R M (2021). Easement rigt valuation for power lines. 2nd Intercontinental Geoinformation Days (IGD), 100-103, Mersin, Turkey.

costs of energy investments and unjustified enrichment in terms of real estate owners.

In this study, it is aimed to determine the maximum value that this variable should take according to the factors affecting decrease rate. While determining decrease rate, each factor affecting the decrease is evaluated in order to obtain the decrease coefficient.

2. METHOD

In this study, first of all, factors affecting the impairment of easement right were determined by technical personnel who work for Turkish Electricity Transmission Company (TEİAŞ) as Geomatics Engineer, Agricultural Engineer and City Planner and are expert in field of valuation. Then, for each of the factors affecting the decrease, weights were determined. Then scoring were made for each factor. This approach is called nominal valuation method(Yomralıoğlu 1993). Finally, using the nominal valuation method with the help of these factor weights, decrease coefficient (DC) can be calculated with the following formula:

$$DC = (\sum_{i=1}^{n} W_i P_i)0.50 \quad (2)$$

$$P_i = \frac{p_i}{10} \quad (3)$$

where, W_i is weight of each factor, P_i is value of points and p_i is points awarded for each factor. Note that, since scoring made over 10 points, when calculating P_i value, p_i is divided by 10. (0.50) is maximum decrease rate used in Supreme Court decisions for zoning parcels. The easement value is determined by using formula (1).

Factors affecting decrease rate and their weights are explained below:

i-) Building Area Affected by Energy Transmission Line

The weight of this factor is determined as 15%. Buildings built on the parcel are often not affected by the passage of the energy transmission line. Even wires of the line do not pass through the building in any way. The passage of line over the parcel can only be understood from the right of easement registered in the land registry.

The ratio of the building area affected by easement right to total building area is determined as a percentage. One point is allocated for every 10% unit affected. That is, for 0%-9% 1 point, for 10%-19% 2 points, 20%-29% 3 point and so on. For example, since 20% of building on the parcel is affected in Figure 1 (a), the score to be given for this factor is determined as 3. In Figure 1 (b), since almost all of the building is affected, 10 points have been allocated.

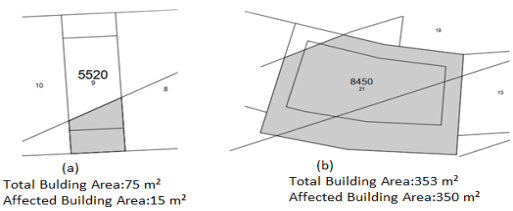

Figure 1. Example of affected building area

ii-) Possible Building Area

The most important factor that determines the decrease of easement right is determination of the building area that can be made before the electric power line crossing on the parcel and the building area to be made after power line crossing. In other words, the amount of lost from the area of the building to be built in normal conditions determines the depreciation. The weight for this factor is set as 35%.

In order to score the effect of this factor, the ratio of the building area to be built in normal conditions and the area lost when the easement right will be registered is calculated as a percentage. Pointing system is determinded as follows:

0%<ratio of lost<10% 2 points; 11%<ratio of lost<25% 4 points; 25%<ratio of lost<50% 6 points; 50% <ratio of lost<60% 8 points and ratio of lost>60% 10 points are allocated. If lost is more than 80%, the option of expropriating entire parcel should be considered.

The most important factor that can affect building area loss is the height of electric power transmission lines passing over the parcel. There are two different types of electric power transmission lines constructed by TEİAŞ, 154 kV and 380 kV. The building to be built under the 154 kV line can approach to wires maximum 5 m vertically. In 380 kV lines, this distance has been determined as 8.70 m. While issuing a building permit, municipalities have to get opinion from TEİAŞ. When asked for opinion, TEİAŞ Mapping Unit sends maximum possible building height to the municipality with an official letter. For TEİAŞ opinion, measurements required in the field should be completed when necessary. The building license is prepared by municipalities according to the information sent by TEİAŞ. When a valuation report is made either by valuation commission or by court experts, the building area that can be built and lost should be determined in consultation with the municipalities.

iii-) Size of the Parcel

The larger the parcel, the less the line crossing will affect the parcel. The weight for this factor was determined as 10%. By calculating affected area of the parcel as a percentage, starting from 1 point in the range of 0-9%, 1 point increase has been made in every 10% segment. In Figure 2, assume that, the area of parcel *A* is 3500 m^2 and the area of parcel *B* is 276 m^2**.** Easement right of 150 m^2 is registered on both parcels. Parcel *A* is affected about 4%, while parcel *B* is affected about 54%. This means that the decreaase rate for two parcels cannot be the same. The point to be given for easement right in *A* parcel is 1 point, since the rate of affection for this parcel is between 0% and 9%. However, the ratio affection for *B* parcel is 54%, that is, the ratio is between 50% and 59%, so for this factor it is allocated 6 points.

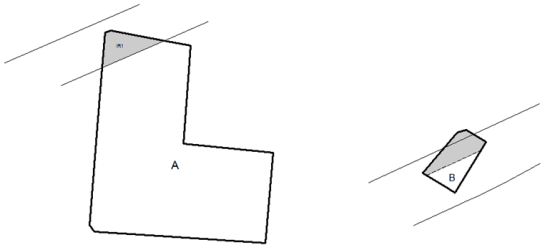

Figure 2. Example of property size

iv-) Easement Shape

The weight of this factor is determined to be 25%. If power line passes through the edge of the parcel, building on property will not be affected much. However, when the line crosses the middle of the parcel, building on it will be affected more. The passage of the line is important in terms of affecting the shape of the new parcel. Scoring should be made after these situations are taken into account.

In Figure 3, easement right passing over parcel *A* does not have any effect on the building to be built on the parcel, but the easement separates the parcel in two pieces and allows the formation of a properly shaped building in the remaining parcel.

Since the parcel the parcel has a smooth geometric feature, 1 point can be allocated for the *A* parcel. When parcel *B* is examined in Figure 3, it is seen that if the easement area is removed, one of the remaining parts will not be suitable for construction because it is triangular and small, and the other part is divided into a trapezoid shape. For this reason the score can be allocated is determined as 8 points.

When the easement area is removed in parcel *C* in Figure 3, it has been determined that although a trapezoid shaped parcel remains, it does not affect the shape of the building to be built. So, 2 points can be allocated for this factor.

When parcel *D* is examined in Figure 3, it is seen that the shape remaining after the easement is trapezoidal, for this reason 5 points can be allocated.

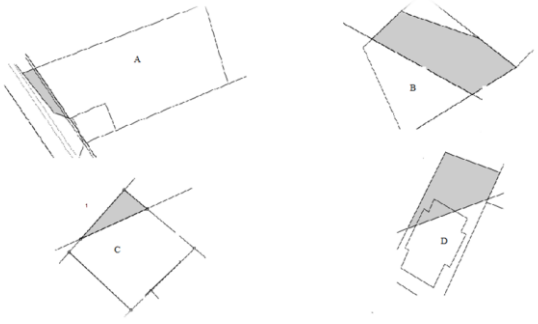

Figure 3. Example of easement shape

If there is a pylon inside the parcel, the parcel shape will often have a broken structure after being divided. In such a case, the shape factor of the line should be scored by considering both the line crossing and pylon location. If the parcel is large, the pylon location may not affect the building that can be built on the parcel. But if the parcel is small and it is not possible to use remaining parcel, paying depreciation may not save the situation. In this case, in accordance with Article 12 of the Turkish Expropriation Law, the entire parcel can be expropriated (Kamulaştırma Kanunu 1983). When making a valuation for the parcel with a pylon in it, the passage of the pylon location through the parcel as a percentage and the way the line passes will be considered together. It can be evaluated in terms of shape, depending on whether there can be made any building or not.

In Figure 4, the pylon passed over a very large parcel, and turned the parcel into a very fractured structure**.** However, it is observed that this situation does not affect the buildings to be built on the parcel in any way. Since the remaining part of the parcel will have a broken structure, 5 points have been allocated and 1 point has been added for the transition of easement. A total of 6 points have been allocated for the power transmission line crossing in this parcel.

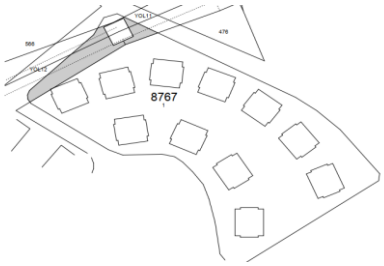

Figure 4. Example of easement shape with pylon

v-) Psychological Factors and Health Effects

The weight of these factors was determined to be 15%. First of all, the fact that the right of easement is registered in the title deed of the parcel will cause reluctance to purchase this parcel in markets where there is a balance of supply and demand, or where demand is less than supply. If the demand is higher and supply is lower, fewer points can be allocated for decrease. When the owner want to withdraw a loan by showing a mortgage on the parcel where the easement right is held, banks generally either do not give any credit or demand for opinion of TEİAŞ. This may cause both time and money loss. If there is an expropriation annotation in the title deed, the owner cannot sell his or her parcel before expropriation process is totally completed. Considering all these situations, it is assumed appropriate to allocate a minimum of 5 points for each parcel to be expropriated. The remaining five points can be allocated over the percentage of the area covered by the easement right on the land. In other words, if the percentage of easement is between 0% and 10%, 1 point; if it is between 11% and 25%, 2 points; if it is between 26% and 50%, 3 points; if between 51% and 60%, 4 points, and 5 points for more than 60% can be allocated.

3. SAMPLE CALCULATION

Our scoring system described above has been implemented on a sample parcel. For this, the expropriation of easement rights on a parcel located within the borders of Pendik district of Istanbul province is taken as an example (Figure 5).

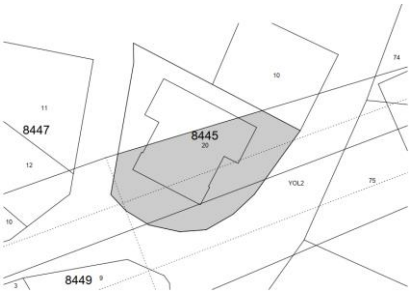

Figure 5. Parcel to be applied

The area of the parcel in the Figure 5 is 645.89 m^2, and 421.63 m^2 of easement is passed over it. A 250 m^2 building can be built on the parcel. 162 m^2 of this building is affected by the easement. In the valuation made by the court, the decrease rate is accepted as 50%. The price per m^2 for the parcel has been determined as 3400 ₺/m^2. From here, the price per m^2 of the easement right has been determined as 1700 ₺/m^2. The expropriation value of easement right is calculated as 1700 ₺/m^2 *x* 421.63 m^2 = 716,771.00 ₺.

The following results are obtained by calculating according to the factors specified in the study.

1. Affected building area: 162m^2/250m^2*x*100=64.8 %. So, 7 points is allocated.

2. Building area that can be built: The building is not affected vertically in this area at all, so 2 points have been allocated.

3. Parcel size: Approximately 65% of the property is affected by the energy transmission line. So, 7 points have been allocated.

4. The way the easement passes through the parcel: Approximately 65% of the property is affected by the energy transmission line. A properly structured parcel is not formed in the part remaining from the energy transmission line. In addition, an independent building cannot be built on the remaining parcel. So, 10 full points have been allocated for this factor.

5. Psychological factors and health effects: for more than %65 of the property is affected by the easement right 10 points have been allocated for this factor.

By using formula (2) and (3):

DC=(0.7*x*0.15 + 0.2*x*0.35 + 0.7*x*0.10 + 1.0*x*0.25 + 1.0*x*0.15)*x*0.50 = 0.645 *x*0.50 = 0.3225

The expropriation value of easement right can be calculated with Eq.(1) as:

EP = 421.63 m^2*x*3400 ₺/m^2 *x* 0.3225 = 462,317.29 ₺

In the study conducted in the real estate market where the parcel is located, the decrease rate was determined to be between 0.30-0.35%. By taking the arithmetic mean of these two values, the rate of impairment will be 0.3250. The obtained value of the handled parcel with different approaches is given Table 1.

Table 1. Data for comparaison

Calculation Type	Decrease Rate	Value (₺)
Court	0.5000	716,771.00
Real Estate Market	0.3250	465,901.15
Nominal Method	0.3225	462,317.29

When the values in Table 1 were compared, it is seen that the market value and nominal value are very close to each other. However, there is a huge difference between these two values and the court value. This causes financial loss of public resources. Furthermore, the owner of the parcel will also receive more than should be received.

4. CONCLUSION

For electric power transmission lines, expropriation expenses are extremely high. This is especially because of the easement rights prices. In this study, factors affecting easement right price are examined and a valuation model is proposed. This model is applied on an example parcel and compared with court and market prices. It is hoped that this study could provide a guide in determination of easement prices and in studies of making law and regulations.

ACKNOWLEDGEMENT

This study is prepared from the master's thesis study prepared by Mustafa YILMAZ under the supervision of Prof.Dr.Reha Metin ALKAN in ITU Graduate School.

REFERENCES

Köktürki E & Köktürk E (2016). Taşınmaz Değerlemesi (Taşınmaz Hukuku–İmar Hukuku–Değerleme Yöntemleri). Seçkin Yayınevi, Ankara, 1376 sayfa.

T.C. Resmi Gazete. 2942 sayılı Kamulaştırma Kanunu(18215), 08.11.1983.

Yıldırım B (2018). Açıklamalı–İçtihatlı Kamulaştırma, Kamulaştırmasız El Atma ve İmar Mevzuatından Doğan Bedel Davaları. Yetkin Yayınları, Ankara.

Yomralioglu T (1993). A nominal asset value-based approach for land readjustment and its implementation using geographical information systems. PhD Thesis, University of Newcastle upon Tyne, UK.

Intercontinental Geoinformation Days

igd.mersin.edu.tr

The urban agriculture approach to evaluating urban-rural interfaces

Irem Yurday [*1], **Ceren Yagci** [2], **Fatih Iscan** [3]

[1]*Konya Technical University, Institute of Graduate Studies, Konya, Turkey*
[2]*Osmaniye Korkut Ata University, Faculty of Engineering, Department of Geomatics Engineering, Osmaniye, Turkey*
[3]*Konya Technical University, Faculty of Engineering and Natural Sciences, Department of Geomatics Engineering, Konya, Turkey*

Keywords
Urban Agriculture
Peri-Urban Agriculture
Land Use Policy
Sustainability

ABSTRACT

Population growth in the world has increased the pressure of urbanization and led to the growth and expansion of urban areas. In addition, this situation has caused some problems in the production of food in cities. These problems can be solved by applying urban agriculture, which is an alternative land use model where interfaces in the urban-rural context can be best evaluated. Urban agriculture contributes to economic, social and environmental branches under the roof of sustainability. In terms of land use, resource management, agriculture, and food security, urban agriculture has emerged as a critical concept. In this study, the concept of urban agriculture, its contribution to sustainability and its benefits are explained. A critical viewpoint on the process of transforming villages in large cities into communities was provided in the light of Law No. 6360. It is aimed to turn the Law No. 6360 into an opportunity and to make suggestions for decision-makers by making the peri-urban agriculture a profitable way out in terms of production. It would be useful to provide a scientific perspective on the development of urban agriculture practices in Turkey.

1. INTRODUCTION

More than half of the world's population lives in cities. As the urbanization rate increases, food production facilities should be located close to the main consumption centers (Orsini et al., 2013). As two-thirds of the world's population is estimated to be concentrated in urban areas within 4 years, a durable food system will become more important for city dwellers . One of the suggested solutions to make cities more sustainable is to implement local urban farming systems (FAO, 2012). In this way, urban agriculture will become increasingly important (Orsini et al., 2013).

Urban agriculture (UA); defined as any agricultural activity located in or within the boundaries of a town, city or metropolis that grows, operates and distributes food and non-food products (Lovell, 2010; Mougeot, 2006).

In another study, urban agriculture was described as an essential component of the growth of cities and their adjacent rural areas, with the potential to dramatically shorten food and ecosystem service supply chains in the face of rising urbanization (René Van Veenhuizen & Danso, 2007). Urban agriculture provides food sources in cities through new technologies, increases the resilience of food systems and ensures food security in urban areas (Grewal & Grewal, 2012; Haberman et al., 2014).

Sustainable urban food production has recently become a topic of interest in professional and academic fields (Bell et al., 2016; Caplow, 2009).

The benefits of urban agriculture are numerous and encompass the economic, social and environmental dimensions (Mougeot, 2006; Peters et al., 2009; Smit et al., 1996). Economic growth, enhanced environmental quality, and meeting food demand are only a few of the many possible benefits of urban agriculture (Saha & Eckelman, 2017). Furthermore, urban and environmental agriculture addresses the issues of urban poverty and food insecurity, providing strategies to reduce them and contribute to approximately 15-20% of the worldwide food demand (Abdulkadir et al., 2012; Armar-Klemesu, 2000).

Urban agriculture is ignored in urban and regional planning, considering its tremendous advantages and positive aspects for individuals and communities (Lovell,

* Corresponding Author

*(yurdayirem@gmail.com) ORCID ID 0000 – 0003 – 2960 – 0926
(cerenyagci@osmaniye.edu.tr) ORCID ID 0000 – 0002 – 4429 – 7809
(fiscan@ktun.edu.tr) ORCID ID 0000 – 0002 – 0669 – 5830

Cite this study

Yurday I, Yagci C & Iscan F (2021). The urban agriculture approach to evaluating urban-rural interfaces. 2nd Intercontinental Geoinformation Days (IGD), 104-107, Mersin, Turkey

2010). As a practice, urban agriculture is very important in both developed and developing countries. Because this practice contributes by addressing three dimensions of sustainability (Ackerman et al., 2014). The definition of urban agriculture and its advantages are discussed in this study, as well as examples of urban agriculture plans and policies implemented by countries.

2. DIMENSIONS OF URBAN AGRICULTURE

Urban agriculture is given below from 3 different aspects.

2.1. Environmental

Urban Agriculture leads to the greening of cities, the reduction of air pollution, the rise of humidity, and the cooling of temperatures (Mougeot, 2006; Smit et al., 1996).

UA expands aesthetic and recreational areas associated with green spaces in cities (Saldivar-Tanaka & Krasny, 2004).

Urban agriculture aims to reduce food insecurity in cities while also helping to solve a number of other environmental concerns such as rising recreational space and biodiversity (Parece & Campbell, 2017).

In addition, urban agriculture has the potential to aid in the productive recovery of contaminated lands, especially in terms of environmental management. While contributing to the utilization of rainwater currents and the reduction of air pollution with the increased vegetation cover thanks to urban agriculture, it increases urban biodiversity and helps to protect species (Kaufman & Bailkey, 2000; Rene Van Veenhuizen, 2006).

2.2. Social

Another reason people participate in urban agriculture is for social reasons. For city dwellers, a garden or rooftop farm is a place where they can come together for mutual benefit and also establish and connect a shared social and cultural identity (Ackerman et al., 2014).

Moreover, the practice of growing food and horticulture rebuilds people's bond with the land and nature, reduces stress in people, and contributes to a healthier diet for some groups (Douglas, 2012; Kortright & Wakefield, 2011).

Although the socio-cultural services and benefits of urban agriculture are difficult to quantify, the majority of them are focused on improving the quality of urban life. Community-based (HOPE Collaborative etc.) UA formats enhance social interactions and mutual communication between citizens of different ages, cultures and social backgrounds (Galluzzi et al., 2010).

By improving ties between different ethnic origins and age groups, community involvement, and social interaction with community gardens, urban agriculture can have a positive impact on health and environmental issues (Hodgson et al., 2011).

Besides that, urban agricultural activities are fertile green spaces that allow people to come together and grow crops at the level of individual parcels. Collectively, these areas form a network of multifunctional, productive features that provide citizens with many benefits beyond just producing food (Balmer et al., 2005).

2.3. Economical

Agriculture will provide various economic benefits in urban areas. It is effective in reducing the maintenance costs of public spaces, increasing local employment and income-generating opportunities for the low-income group levels of the city, processing unused resources (e.g. roofs, roadsides, public services and vacant lands), and increasing property values (Kaufman & Bailkey, 2000; Rene Van Veenhuizen, 2006).

Urban agriculture can also reduce the energy used in food transportation by saving the way food must travel from producer to consumer, (Peters et al., 2009) therefore, while saving energy, it reduces greenhouse gas emissions and carbon emissions.

As can be seen, urban agriculture provides many benefits in many areas. However, rather than benefits, raising awareness on urban agriculture and implementing it in the best way is a priority area that should be taken into consideration by both local governments and decision-makers.

3. LEGAL BACKGROUND OF URBAN AGRICULTURE

Sustainable planning and environmental legislation that encourages urban agriculture in cities should be developed (Bryld, 2003). Many cities in developed countries have recognized the benefits of urban agriculture and have developed planning and policy strategies to support food production (Lovell, 2010).

In the United States, for example, there are 39 UA laws in total among the 25 states that use the term in their legislation. Despite the fact that each of these laws is described differently by state law, they are classified into six policy categories. Grant programs for the creation of UA applications

- Tax Incentives
- Farm to Table Programs
- Urban Farms
- Community Gardens
- Urban Agriculture Incentive Zones (UAIZ)

Food Policy Councils (FPC) or Local Food Advocacy groups (Monaghan, 2020).

With the growing interest in healthy eating in Europe, the "Vitoria-Gasteiz Municipal Council" approved the "Agriculture-Food Strategy Municipal Action Plan" in 2017. Other European examples include the "Paris Sustainable Food Plan," which was developed between 2015 and 2020 for sustainable agriculture practices in municipal services in Paris, France's capital city (Menteş, 2019).

The food project, which is a food waste management plan that was accepted as part of the European Urban Laboratory's "urban revolutionary activities" in Heraklion, Greece, has been approved (Marouli, 2018). The Municipality of Rosario in Argentina, Spain, initiated the "Municipal Organic Agriculture Production Program" in 2002 (Soto, 2003).

The Christchurch City Council passed New Zealand's "Food Resistance Strategy" in 2014 (Toth et al., 2016). Almost all developing countries, urban agriculture lacks a legal foundation. Because its connection to the city has been overlooked as a result of rural life (Bryld, 2003; D. Maxwell et al., 1998; D. G. Maxwell, 1995). Therefore, urban agriculture needs to be enacted, policies revised and institutionalized so that it can be implemented and managed regularly (Bryld, 2003).

There is also no legal legislation relevant to urban agriculture in Turkey, as there are only a few examples of the incorporation of urban agriculture and urban applications, but peri-urban agriculture can be initiated through the enactment process.

Many villages in Turkey's metropolitan cities have been merged into the city limits as a result of Law No. 6360. Agriculture and agricultural production will inevitably continue under the name of peri-urban agricultural activity in these new neighborhoods (formerly defined as villages), which cannot be regarded as cities by only being included in the city boundary.

4. CONCLUSION AND DISCUSSION

The objective of urban agriculture implementation varies between developed and developing countries. Even though it is used in developed countries for landscaping, energy efficiency, and socialization, it is also used in developing countries to improve food security.

Through constructing cities that are more durable, productive, and safer in terms of food production, urban and peri-urban agricultural practices will play an important role in reacting to a variety of challenges facing developed countries (De Zeeuw, 2011).

Urban agriculture and peri-urban agriculture can be a sustainable and innovative solution as a productive land use model with many contributions such as reducing the urban heat effect, greening the city and supporting food production, and refreshing the city's air. As a summary, concepts of urban agriculture and future advantages of urban agriculture are addressed in this study.

Suggestions were made to decision-makers, metropolitan councils, and other local authorities, in order to increase the potential benefits of the peri-urban agriculture by allowing agriculture on the interfaces that serve as a transition between urban and rural areas.

To implement healthier urban and peri-urban agriculture in Turkey;

-In the process of urban agriculture land use, it should be included in the "Spatial Plans Construction Regulation."

-The General Directorate of Geographic Information Systems and the General Directorate of Spatial Planning should work together to promote urban agriculture in metropolitan areas as soon as possible.

- For a better implementation of urban agriculture, legal criteria should be reviewed, and decision-makers should develop urban agriculture regulations.

-The outputs of urban agriculture should be reviewed; more attention should be paid to its benefits and its disadvantages should be minimized.

- Once the existing regulatory obstacles to urban agriculture have been established, it is important to decide how to protect urban agriculture and to increase public knowledge of urban agriculture.

- Urban agriculture should be controlled and institutionalized by multidisciplinary teams as part of the city ecosystem.

- Urban agriculture; should be integrated into the food production system in all aspects (taking into account human life, past and possible natural disasters).

- Urban agriculture should be viewed as a component of the social food system, with voluntary partnerships and communities playing a role in bridging the gap between food production and consumption.

- Urban farmers should be provided with training and professional technical assistance, support should be provided in the production and processing stages, and the opportunity to sell their products in public places such as school canteens, markets and associations should be offered.

- Especially local governments should revise both infrastructure works and recreation activities in a way that supports urban agriculture.

- Providing land by the municipality to low-income groups in the city through renting and revitalizing production should be encouraged.

- Agriculture and agricultural-based activities should be established in areas that have acquired urban status but have not yet been urbanized as a result of Law No. 6360.

REFERENCES

Abdulkadir, A., Dossa, L., Lompo, D.-P., Abdu, N., & Van Keulen, H. (2012). Characterization of urban and peri-urban agroecosystems in three West African cities. *International journal of agricultural sustainability, 10*(4), 289-314.

Ackerman, K., Conard, M., Culligan, P., Plunz, R., Sutto, M.-P., & Whittinghill, L. (2014). Sustainable food systems for future cities: The potential of urban agriculture. *The economic and social review, 45*(2, Summer), 189–206-189–206.

Armar-Klemesu, M. (2000). Urban agriculture and food security, nutrition and health. *Growing cities, growing food. Urban agriculture on the policy agenda*, 99-118.

Balmer, K., Gill, J., Kaplinger, H., Miller, J., Peterson, M., Rhoads, A., . . . Wall, T. (2005). The diggable city: Making urban agriculture a planning priority.

Bell, S., Fox-Kämper, R., Keshavarz, N., Benson, M., Caputo, S., Noori, S., & Voigt, A. (2016). Urban allotment gardens in Europe. In (pp. 91-112). London: Routledge.

Bryld, E. (2003). Potentials, problems, and policy implications for urban agriculture in developing countries. *Agriculture and Human Values, 20*(1), 79-86.

Caplow, T. (2009). Building integrated agriculture: philosophy and practice. In: Urban futures 2030: Urban development and urban lifestyles of the future. *Heinrich Böll Foundation,* 48-51.

De Zeeuw, H. (2011). Cities, climate change and urban agriculture. *Urban Agriculture Magazine, 25*, 39-42.

Douglas, I. (2012). Urban ecology and urban ecosystems: understanding the links to human health and well-

being. *Current Opinion in Environmental Sustainability, 4*(4), 385-392.

FAO. (2012). Increasing Fruit and Vegetable Consumption Becomes a Global Priority *Food and Agriculture Organization News Room Focus*.

Galluzzi, G., Eyzaguirre, P., & Negri, V. (2010). Home gardens: neglected hotspots of agro-biodiversity and cultural diversity. *Biodiversity and conservation, 19*(13), 3635-3654.

Grewal, S. S., & Grewal, P. S. (2012). Can cities become self-reliant in food? *Cities, 29*(1), 1-11.

Haberman, D., Gillies, L., Canter, A., Rinner, V., Pancrazi, L., & Martellozzo, F. (2014). The potential of urban agriculture in Montréal: a quantitative assessment. *ISPRS International Journal of Geo-Information, 3*(3), 1101-1117.

Hodgson, K., Campbell, M. C., & Bailkey, M. (2011). Investing in healthy, sustainable places through urban agriculture. In (pp. 1-16): Funders' Network for Smart Growth and Livable Communities.

Kaufman, J. L., & Bailkey, M. (2000). *Farming inside cities: Entrepreneurial urban agriculture in the United States*. Massachusetts, ABD: Lincoln Institute of Land Policy Cambridge, MA.

Kortright, R., & Wakefield, S. (2011). Edible backyards: a qualitative study of household food growing and its contributions to food security. *Agriculture and Human Values, 28*(1), 39-53.

Lovell, S. T. (2010). Multifunctional urban agriculture for sustainable land use planning in the United States. *Sustainability, 2*(8), 2499-2522.

Marouli, C. (2018). *The A2U Food project*. Retrieved from Heraklion:

Maxwell, D., Levin, C., & Csete, J. (1998). Does urban agriculture help prevent malnutrition? Evidence from Kampala. *Food Policy, 23*(5), 411-424.

Maxwell, D. G. (1995). Alternative food security strategy: A household analysis of urban agriculture in Kampala. *World Development, 23*(10), 1669-1681.

Menteş, Y. (2019). Sürdürülebİlİr Kentsel Gelişimin Sağlanmasinda Kentsel Tarim Deneyİmlerİ, "Türkİye İçİn Önerİler". *Yüksek Lisans Tezi, Fen Bilimleri Enstitüsü, İnönü Üniversitesi Malatya*.

Monaghan, M. (2020). *Understanding the Goals of Urban Agriculture Policy in State Legislation*. Retrieved from

Mougeot, L. J. A. (2006). *Growing better cities: Urban agriculture for sustainable development*. Canada: IDRC.

Orsini, F., Kahane, R., Nono-Womdim, R., & Gianquinto, G. (2013). Urban agriculture in the developing world: a review. *Agronomy for sustainable development, 33*(4), 695-720.

Parece, T. E., & Campbell, J. B. (2017). Geospatial evaluation for urban agriculture land inventory: Roanoke, virginia USA. *International Journal of Applied Geospatial Research (IJAGR), 8*(1), 43-63.

Peters, C. J., Bills, N. L., Lembo, A. J., Wilkins, J. L., & Fick, G. W. (2009). Mapping potential foodsheds in New York State: A spatial model for evaluating the capacity to localize food production. *Renewable agriculture and food systems 24:72-84*.

Saha, M., & Eckelman, M. J. (2017). Growing fresh fruits and vegetables in an urban landscape: A geospatial assessment of ground level and rooftop urban agriculture potential in Boston, USA. *Landscape and urban planning, 165*, 130-141.

Saldivar-Tanaka, L., & Krasny, M. E. (2004). Culturing community development, neighborhood open space, and civic agriculture: The case of Latino community gardens in New York City. *Agriculture and Human Values, 21*(4), 399-412.

Smit, J., Nasr, J., & Ratta, A. (1996). Urban agriculture: food, jobs and sustainable cities. *New York, USA, 2*, 35-37.

Soto, G. (2003). Agricultura Orgánica: una herramienta para el desarrollo rural

sostenible y la reducción de la pobreza Memoria del Taller. In. Turrialba, Costa Rica.

Toth, A., Rendall, S., & Reitsma, F. (2016). Resilient food systems: a qualitative tool for measuring food resilience. *Urban ecosystems, 19*(1), 19-43.

Van Veenhuizen, R. (2006). Cities farming for the future. *Cities farming for future, Urban Agriculture for green and productive cities,(p 2-17). RUAF Foundation, IDRC and IIRP*.

Van Veenhuizen, R., & Danso, G. (2007). *Profitability and sustainability of urban and periurban agriculture* (Vol. 19): Food & Agriculture Org.

Intercontinental Geoinformation Days

igd.mersin.edu.tr

Anthropogenic intrusions leading to variability in Vegetated vs Non- vegetated land dynamics over the past two decades in India

Rahul Kashyap [1] Arvind Chandra Pandey[1*]

[1]*Department of Geoinformatics, School of Natural Resource Management, Central University of Jharkhand, Ranchi-835205, India*

Keywords
Forest
Cropland
Urban Area
Land cover dynamics
Decadal change

ABSTRACT

The increase in the human population, changing climate, natural hazards, extreme events, quest for resources has led to significant variability in the land cover dynamics. There has been a great deal of spatio temporal variability in the land use/ cover over the Indian landmass in past two decades. The study looks into the dynamics of land use/cover with focus on vegetated land vs non-vegetated land in light of human induced changes using MODIS land cover product. In order to detect the contribution of human induced changes, the dynamics of the human settlements in terms of urban area is analysed at three focal periods viz, 2001, 2010, and 2019. The difference in the decadal trend, show that the forest cover has increased by 1.1 % from 2001-10 to 2010-19. In contrast the cropland is decreased by 0.94 % from 2001-10 to 2010-19 whereas urban expansion is increased by 2.67%. Overall, the vegetated land has increased by 0.08 % and the non-vegetated land is decreased by 0.97 %. The population load requires resources to survive with concomitant decrease or reduced growth over vegetation areas.

1. INTRODUCTION

Rapid changes in ecosystems as a result of human activities, like tropical deforestation, are of great relevance to climate and global change (Arneth et al. 2010). Scenarios of future anthropogenic land cover and land use suggest continued changes as a result of the increasing demand for food and (bio) energy. Several previous studies have indicated the interactions between global land cover, the carbon cycle, and therefore the climate system.

Continuous monitoring of vegetation dynamics is crucial for understanding the biogeochemical processes and its possible effect on our climate system (Falkowski et al. 2000; IPCC, 2019). The changing energy balance is greatly affecting the terrestrial biosphere due to the climate variability and land use changes within the recent decades (FSI, 2019). Biodiversity, natural ecosystems, forestry and agricultural production are expected to be severely impacted thanks to climate variability and anthropogenic activity influenced land use changes within the future (Miura et al. 2008). Forest and agriculture account for nearly 80% of the geographic area of India, about 24.56% of which is forest and 55% of which is agricultural land (Reid et al. 2008). Agricultural production may be a key indicator for food security and a number of other studies have explored the connection between crop yields, NDVI and food security (Teal et. al. 2006).

There has been a great deal of spatio temporal variability in the land use/ cover over the Indian landmass in past two decades. The increase in the human population, changing climate, natural hazards, extreme events, quest for resources has led to significant variability in the land cover dynamics. The major concern of this study lies in examining the dynamics of the vegetated land vs non-vegetated land in light of human induced changes in the past two decades using MODIS based land use/cover product.

2. METHOD

The Terra and Aqua combined Moderate Resolution Imaging Spectroradiometer (MODIS) Land Cover Type (MCD12Q1) Version 6 data product

* **Corresponding Author**

(rahulkashyaprsm@gmail.com) ORCID ID 0000-0003-2655-8179
*(arvindchandrap@yahoo.com) ORCID ID 0000-0003-2796-0477

Cite this study

Kashyap R & Pandey A C (2021). Anthropogenic intrusions leading to variability in Vegetated vs Non- vegetated land dynamics over the past two decades in India. 2nd Intercontinental Geoinformation Days (IGD), 108-111, Mersin, Turkey

provides global land cover types at yearly intervals (2001-2019). The MCD12Q1 Version 6 data product springs using supervised classifications of MODIS Terra and Aqua reflectance data. The supervised classifications then undergo additional post-processing that incorporate prior knowledge and ancillary information to further refine specific classes. The "cropland" type within this study is that the IGBP classification scheme of the MCD12Q1 V006, and it had been used because cropland class reliability is >92% (Tucker et al. 2001).

MODIS classes are reclassified and classes pertaining to forests are merged together, likewise for the cropland. While, the rest of the classes are merged as others. The vegetated land comprises of the forest and cropland areas, while all other land use classes are termed non-vegetated land. In order to detect the contribution of human induced changes, the dynamics of the human settlements in terms of urban area is analysed at three focal points viz, 2001, 2010, and 2019. The focal period analyses, decadal change, fraction land cover change, overall change, and change in decadal trend in forest, cropland, urban and rest of the areas is analysed.

3. RESULTS

3.1. Focal Period Analyses

2001: In the year 2001, forest was estimated to cover 8.46 % of the land over in contrast to 58.09 % cropland area over the Indian landmass. The urban area occupied 1.04 % of land. Overall, it can be said that 66.55 % of vegetated area existed against 33.45 % non-vegetated area.

2010: In the year 2010, forest was estimated to cover 8.8 % of the land against 59.59 % cropland and 1.05 % urban area implying that 68.39 % of vegetated area in contrast to 31.06 % non-vegetated area.

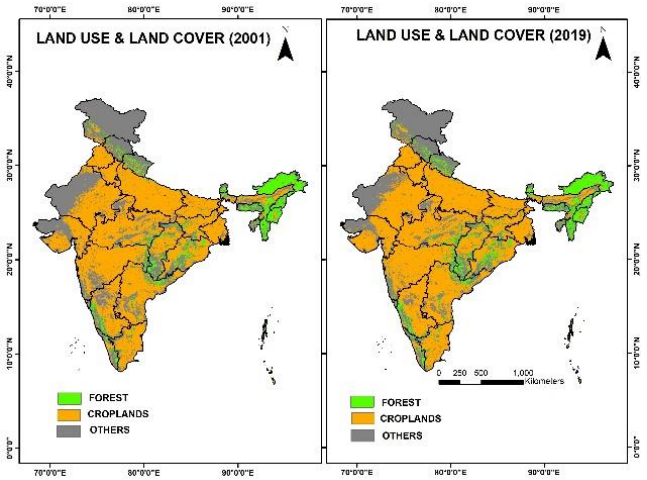

Figure 1. Land Use and Land Cover in 2001 and 2019

2019: In the year 2019, forest is estimated to cover 9.26 % of the land over the Indian landmass. The cropland made up 60.56 % of the Indian land area. The urban area occupied 1.1 % of land. Overall, it can be said that 69.82 % of vegetated area is seen and 30.16 % of the land is non-vegetated area.

3.2. Decadal Change

2001-2010: Forest cover has increased at 0.41% per year. The cropland records a lower increase at 0.257 % per year. The urban area also accounts for 0.18 % per year increase. Overall, the vegetated area cover has increased at 0.33 % per year, while the non-vegetated area termed as "others" has decreased at 0.55 % per year.

2010-2019: Forest cover has increased at 0.52 % per year. The cropland records a lower increase at 0.16 % per year. The urban area also accounts for 0.44 % per year increase. Overall, the vegetated area cover has increased at 0.34 % per year, while the non-vegetated area termed as "others" has decreased at 0.45 % per year.

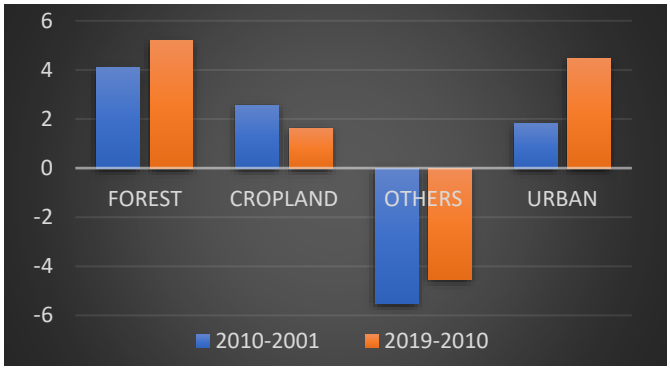

Figure 2. Decadal change in various land use & cover types in %

3.3. Change in terms of fraction of Indian land area

2001- 2010: Forest cover has increased by 0.34 % the rate of 0.03 % per year. The cropland also records a higher increase at 1.49 % at the rate of 0.149 % per year. The urban area also accounts for 0.016 % increase at the rate of 0.001 % per year. Overall, the vegetated area cover has increased by 0.915 %, at the rate of 0.09 % per year while the non-vegetated area termed as "others" has decreased by 1.84 % at the rate of 0.18 % per year.

2010-2019: Forest cover has increased by 0.45 % the rate of 0.04 % per year. The cropland also records a higher increase at 0.97 % at the rate of 0.09 % per year. The urban area also accounts for 0.04 % increase at the rate of 0.004 % per year. Overall, the vegetated area cover has increased by 0.71 %, at the rate of 0.071 % per year, while the non-vegetated area has decreased by 1.43 % at the rate of 0.14 % per year.

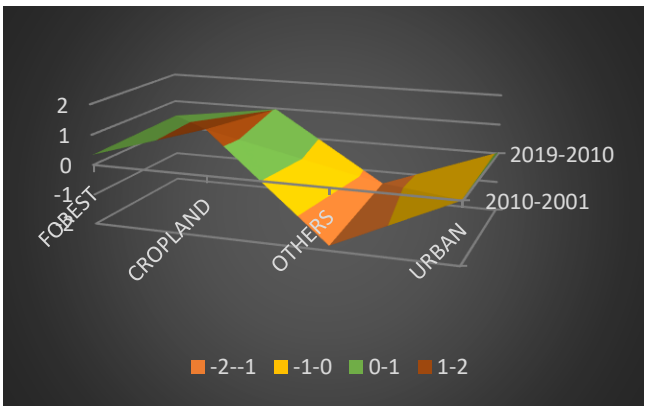

Figure 3. Decadal increase (+)/decrease (-) in fraction of Indian area in %

3.4. Gross Change

The forest cover has significantly increased by 9.52 % at the rate of 0.5 % per year over the years 2001-19. Cropland also records an increase of 4.24 % at the rate of 0.22 % per year over the last two decades. The urban area has grown by 6.35 % at the rate of 0.33 % per year. Overall, the vegetated area has increased by 6.88 % at the rate of 0.36 % per year. While, the non-vegetated land has decreased by 9.8 % at the rate of 0.51 % per year.

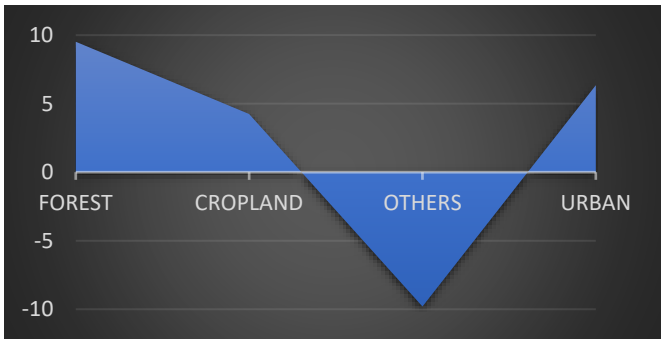

Figure 4. % Change in various land cover types (2019-2001)

The vegetated areas show an increase in the lower western Himalayas, along the eastern side in states of Jharkhand, Orissa, Chhattisgarh, MP in the central area. The parts along the western coast in Maharashtra, Karnataka, Kerala also shows increase in vegetated areas. Some patches in Andhra Pradesh and Tamil Nadu are also recorded.

The non-vegetated areas show an increase in North East in parts of Assam, Sikkim, in the western part in states such as Rajasthan, Gujrat, Maharashtra, Karnataka. Patches in eastern states such as Bihar, West Bengal, Jharkhand, Orissa, Chhattisgarh. It is also seen in areas of MP, Andhra Pradesh andTamilNadu.

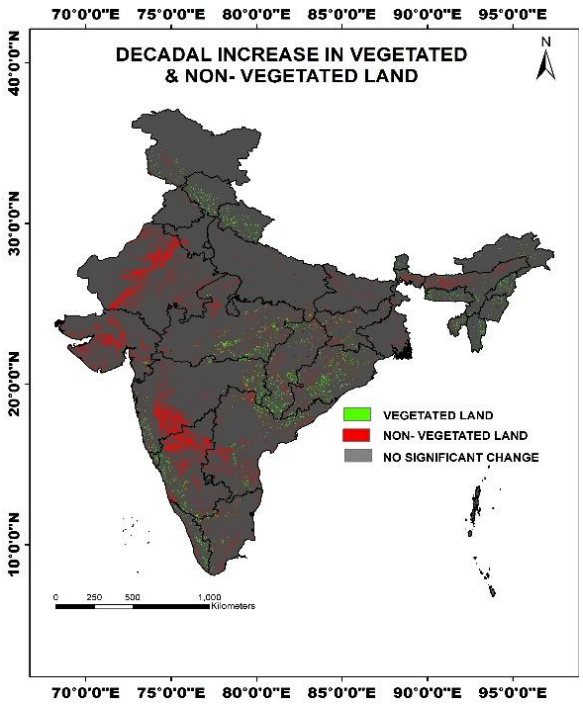

Figure 5. Decadal increase in vegetated and non-vegetated land

3.5. Trend in Decadal Change 3.5. Trend in Decadal Change

The difference in the decadal trend, show that the forest cover increase has increased by 1.1 % from 2001-10 to 2010-19. While, the cropland increase is decreased by 0.94 % from 2001-10 to 2010-19. The increase in urban expansion is increased by 2.67 %. Overall, the vegetated land increase has increased by 0.08 % and the non-vegetated land decrease is decreased by 0.97 %.

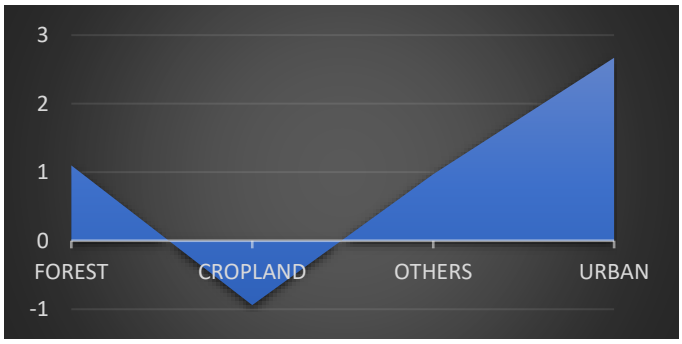

Figure 6. % Change in Decadal Change in various land cover types

4. DISCUSSION

A great deal of variability in the land cover dynamics is seen over the Indian landmass over the recent decades. Growing population and demand for resources along with the changing climate is basically the main cause trigging it. The forest cover has significantly increased by 9.52 % at the rate of 0.5 % per year over the years 2001-19. Cropland also records an increase of 4.24 % at the rate of 0.22 % per year over the last two decades. The urban area has grown by 6.35 % at the rate of 0.33 % per year. Overall, the vegetated area has increased by 6.88 % at the rate of 0.36 % per year. While, the non-vegetated land has decreased by 9.8 % at the rate of 0.51 % per year.

5. CONCLUSION

The difference in the decadal trend, show that the forest cover increase has increased by 1.1 % from 2001-10 to 2010-19. While, the cropland increase is decreased by 0.94 % from 2001-10 to 2010-19. The increase in urban expansion is increased by 2.67 %.Overall, the vegetated land increase has increased by 0.08 % and the non-vegetated land decrease is decreased by 0.97 %. Thus, a greater rate of growth in urban areas owing to greater population demand and at the same time a smaller growth rate in vegetated areas is seen over the Indian landmass over the past two decades. In order to meet the sustainable development goal, the vegetated areas should be growing at a faster rate than the urban growth. The population load requires resources to survive and these resources comes at the cost of slower growth in vegetation areas.

ACKNOWLEDGEMENT

The authors would like to acknowlege the data providing source for providing the data free of cost.

REFERENCES

Arneth A, Harrison S P, Zaehle S, Tsigaridis K, Menon S, Bartlein P J, Feichter J, Korhola A, Kulmala M, O'donnell D & Schurgers G (2010). Terrestrial biogeochemical feedbacks in the climate system. Nature Geoscience, 3(8), 525-532.

Carpenter S R, Mooney H A, Agard J, Capistrano D, DeFries R S, Díaz S & Whyte A (2009). Science for managing ecosystem services: Beyond the Millennium Ecosystem Assessment. Proceedings of the National Academy of Sciences, 106(5), 1305-1312.

Falkowski P, Scholes R J, Boyle E E A, Canadell J, Canfield D, Elser J, Gruber N, Hibbard K, Högberg P, Linder S & Mackenzie F T (2000). The global carbon cycle: a test of our knowledge of earth as a system. science, 290(5490), 291-296.

IPCC. Climate Change and Land: An IPCC Special Report on Climate Change, Desertification, Land Degradation, Sustainable Land Management, Food Security, and Greenhouse Gas Fluxes in Terrestrial Ecosystems; IPCC: Geneva, Switzerland, (2019).

ISFR. State of Forest Report 2019. Forest Survey of India (FSI); Ministry of Environment Forest & Climate Change, Government of India: New Delhi, India, (2019).

Miura T, Yoshioka H & Suzuki T (2008). Evaluation of spectral vegetation index translation equations for the development of long-term data records. In IGARSS 2008-2008 IEEE International Geoscience and Remote Sensing Symposium (Vol. 3, pp. III-712). IEEE.

Reid W V, Mooney H A, Cropper A, Capistrano D, Carpenter S R, Chopra K & Zurek M B (2005). Ecosystems and human well-being-Synthesis: A report of the Millennium Ecosystem Assessment. Island Press.

Teal R K, Tubana B, Girma K, Freeman K W, Arnall D B, Walsh O & Raun W R (2006). In-season prediction of corn grain yield potential using normalized difference vegetation index. Agronomy Journal, 98(6), 1488-1494.

Tucker C J, Slayback D A, Pinzon J E, Los S O, Myneni R B & Taylor M G (2001). Higher northern latitude normalized difference vegetation index and growing season trends from 1982 to 1999. International journal of biometeorology, 45(4), 184-190.

Intercontinental Geoinformation Days

igd.mersin.edu.tr

Usability of wearable mobile laser systems in cadastral studies

Seda Nur Gamze Hamal*[1], Binnaz Sarı [1], Ali Ulvi[1] Murat Yakar[2]

[1]*Mersin University, Institute of Science, Remote Sensing and Geographical Information Systems, Mersin, Turkey*
[2]*Mersin University Engineering Faculty Department of Geomatics Engineering, Mersin, Turkey*

Keywords
WMLS
Orthophoto
Point cloud
Photogrammetry
Cadastro

ABSTRACT

Lidar measurement systems have started to provide convenience in engineering and many multidisciplinary fields with their innovative approach. It allows to give positional information about difficult to access, narrow, small or closed areas. In addition, it enables map production in areas that cannot be measured with the GNSS device (where trees and housing are dense, etc.). The data obtained from the Wearable Mobile Laser System used in the study provides the ability to locally determine its own location and produce a map of the environment with the developed SLAM (Simultaneous Localization and Mapping) algorithm. At the same time, for the structures on the model, its usability in renovation works to improve existing cadastral work is discussed. In this study, the processing and accuracy criteria for cadastral studies were evaluated using the wearable lidar technology data in the Mersin University Çiftlikköy Campus region.

1. INTRODUCTION

The management of land and land has been of great importance since the first period when civilizations were established in the world. Accordingly, the work started to determine the borders, to establish and protect the property. By measuring the land plots and evaluating the measured data, it has been progressed on the axis of offering the right to use, use and disposition to its owner. Today; These studies are called cadastral activities or cadastre.

Social and environmental developments have gained a new dimension with the differentiation of human-soil relationship and land use. Cadastre 2014 study published by FIG; It is aimed to set standards in cadastre, to ensure public-private cooperation and to achieve digital transformation rather than classical measurements. Cadastre 2034 has started to be discussed with the vision of sustainable land management for the next 20 years. In this direction, sensitive, up-to-date, object-oriented, three-dimensional (3D) and four-dimensional (4D, 3D + time) cadastral concepts have been the primary goals. (Demir and Çoruhlu, 2009; Döner et al., 2007; Döner, 2015; Sultani and Şişman, 2014; Kaufmann et al., 2014; Yıldız et al., 2015)

99% of the cadastral works in Turkey are known to completion (Uzun and Çelik, 2011). However, the methods used and hardware that are expected from the cadastre (± 8 cm) accuracy insufficient to meet, incorrect or incomplete done some measurements, to find solutions to existing problems such as digitization of existing cadastral data and international standards adopted by Turkey (ISO 19 152, 19 112), Studies such as LADM, INSPIRE, Cadastre 2014 and beyond create the need for cadastral renewal. (Şahin et al., 2015; Çete and Yomralıoglu, 2013). These studies can be done with classical measurement methods, as well as with technological developments, providing the opportunity to be done with new methods and equipment (Döner et al., 2008; Karabin et al., 2017; Hao et al., 2011; Gura and Nedyakina, 2021).

In this study, the usability of laser scanning technology in renovation cadastre activities was examined. In this study, in addition to the points obtained by the total-station device with the data obtained by the wearable mobile (WMLS) laser scanning, the orthophoto obtained by the UAV photogrammetry was used in an integrated manner (Kaya et al., 2021; Ulvi et al., 2019;

* **Corresponding Author**

*(sedanurgamzehamal@gmail.com) ORCID ID 0000-0002-1050-3088
(binnaz452@gmail.com) ORCID ID 0000-0002-8240-9680
(aliulvi@mersin.edu.tr) ORCID ID 0000-0003-3005-8011
(myakar@mersin.edu.tr) ORCID ID 0000-0002-2664-6251

Cite this study

Hamal S N G, Sarı B, Ulvi A & Yakar M (2021). Usability of wearable mobile laser systems in cadastral studies. 2nd Intercontinental Geoinformation Days (IGD), 112-115, Mersin, Turkey

Yakar et al., 2016). Scans were carried out with WMLS and point cloud data belonging to the region were obtained. The vector drawings of the area were carried out in the light of the data obtained from two methods by using the orthophoto previously produced by the study team including the authors. Then, the accuracy of the study was examined by performing local measurements. The applicability of laser scanning method in cadastral studies has been tested by examining the results.

2. METHOD

In recent years, with the acceleration of the renewal cadastral under the sustainable land method, studies in this area have been started with new methods and equipment. Especially rapidly growing stock of construction and development of cities in Turkey are known to play an important role in making this work. With this urbanization pressure, the feasibility of cadastral studies with classical measurement methods is not possible due to the changing land conditions. Therefore, in this study, the feasibility of cadastral studies was tested with laser scanning technology (Otero et al., 2020; Williams et al., 2020), which offers a new and fast solution.

2.1. Study Area

Mersin University *Çiftlikköy* campus has been selected as the Faculty of Engineering test area. (Figure 1).

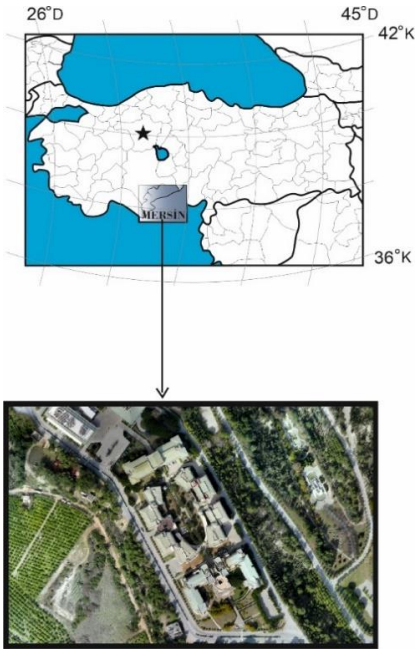

Figure 1. Study area

The WMLS device was used for reasons such as the presence of trees in an area of 18660 m2, the narrow distance between buildings, and the fact that conventional measurement methods can cause user-induced errors and take time. The fieldwork was completed in two sessions of 40 minutes in total.

2.2. Equipment

In this study, Gexcel Heron Lite Color wearable lidar scanner was used to test. Technical features of the device are given in Table 1. In addition, electronic length meter (total-station) and GNSS receiver were used.

Gexcel Heron Lite Color wearable lidar scanner is a measuring device with IMU integrated positioning system without the need for time of flight satellite navigation systems (Balenović et al., 2020; Döner and Bıyık, 2007). This device extracts the 3D point cloud of the area by detecting the different geometric properties of the objects around it. The map of the working area can be created in the local coordinate system. These products are produced with the SLAM algorithm, which is actively used to determine the map and location of the surrounding area. (Di Filippo et al., 2018; Zeybek, 2019; Güney and Sayın 2016).

Table 1. Technical features of Wearable Mobile Laser Systems

Features	Value
Panoramic camera	+
post processing software	Heron Desktop
lidar sensor	Velodyne VLP 16
IMU	+

2.3. Data Proccesing

In order to process the data obtained from field scans, the process was performed in the WMLS device's own software, Heron Desktop software.

In the process phase, the necessary odometer settings were made first. Odometer work flow is given in Figure 2.

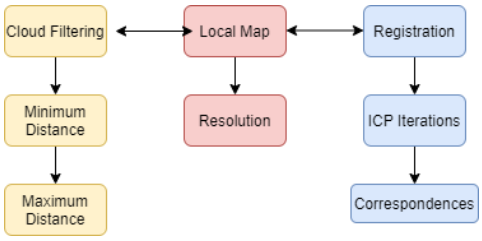

Figure 2. Odometer work flow

In the "cloud filtering" part of the first section, "minimum distance" and "maximum distance" settings; It is the section where it is adjusted to eliminate distortions that will occur according to the structure of the land, the location of the objects and environmental factors.

In the second part, the "local-map" settings determine the geometric criteria of the 3D point cloud map to be created.

The third part is the "Registration" part. In the laser scanning process, scans are carried out overlapped. In the data obtained, one of the measurements for the same object is taken as a reference (fixed) and all other scans are converted to the coordinate system of the reference point cloud. In the Registration section, the transformation parameters between two point clouds are calculated with points in the common scanning area. Therefore, "Correspondences" and "ICP iteration" are

important to reduce the minimum error and obtain a precise result.

The "create map" process is the process of creating an index map by splitting it into trajector map sets.

After the create map process, it was passed to the global optimization part. The ICP iteration number is chosen as default in the parameter adjustment with the alignment of the fragmented maps. The main purpose of this section is to increase the precision of accuracy. After parameter setting, links to fragmented maps are tied and connected to each other. All fragmented maps were connected in accordance with this condition and balancing was made by selecting the "optimize cluster".

Balanced point cloud data is transferred to the reconstructor software for the last step of geo-referencing. During the field survey, TAG points were purchased in areas where GCP was measured by GNSS and Total-station device. By using these target TAG points, the transformation from local coordinate to country coordinate system has been performed in Reconstructor software. The average error after conversion is ± 3cm.

3. RESULTS

In the study, a region within the Mersin University campus was scanned in a short time with the "Gexcel Heron Lite Color" scanner and 3D point cloud data was obtained (Figure 3).

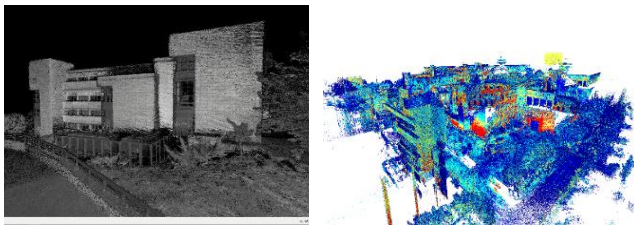

Figure 3. Point cloud data from WMLS

In the Recontructor program, 2D orthophoto image was obtained by using the point cloud data created (Figure 4). These orthophoto and orthophoto images produced with UAV were drawn in Netcad program and comparisons were made.

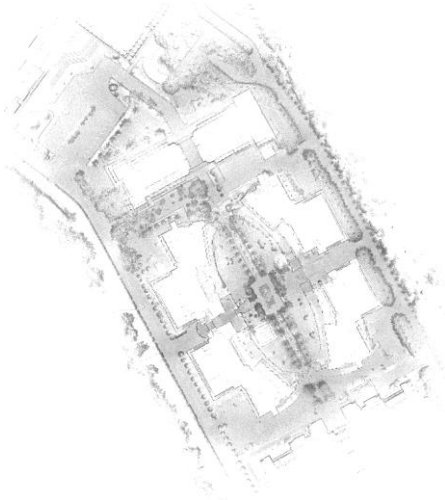

Figure 4. 2D orthophoto image obtained from WMLS

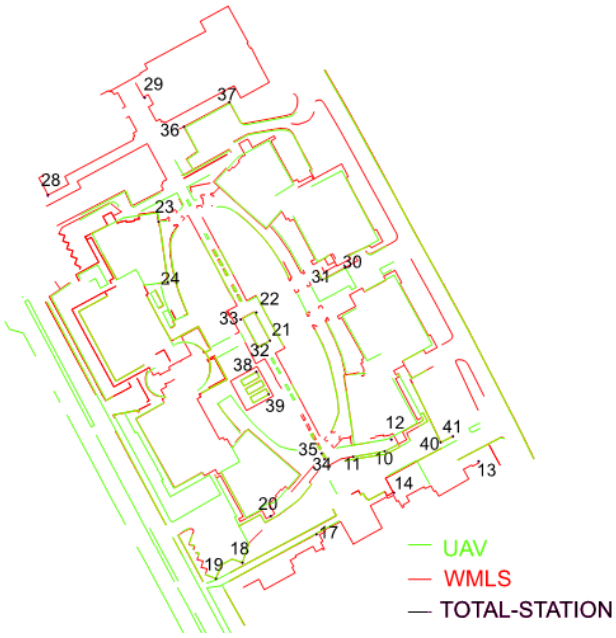

Figure 5. Vectorial drawing obtained from WMLS, UAV and Total-Station data

As a result of the vector drawings made on both orthophotos; These data were compared in terms of accuracy. First, drawings were made from the image produced from lidar, and then drawings were made on the image obtained from the UAV. For the accuracy of these drawings, measurements were carried out at the locations determined by ground measurement techniques during the field study phase. The same lengths were taken from both orthophotos and compared with the positional measurement data (Figure 5).

Table 2. Accuracy analysis of the lengths taken from the orthophoto

Point Numbers	Total Station V	WMLS [V_1]	UAV [V_2]	[V- V_1]	[V- V_2]
11-10	11.763	11.788	11.812	0.025	0.049
24-23	22.489	22.510	22.541	0.021	0.052
21-22	12.132	12.102	12.090	-0.030	-0.042
19-18	11.383	11.331	11.420	-0.052	0.037
30-31	9.556	9.552	9.561	-0.004	0.005
32-33	12.152	12.112	12.100	-0.040	-0.052
34-35	2.333	2.344	2.300	0.011	-0.033
36-37	19.044	19.05	19.088	0.006	0.044
38-39	9.378	9.444	9.434	0.066	0.056
40-41	5.022	5.07	4.990	0.048	-0.032

4. DISCUSSION and CONCLUSION

In this article, WMLS has been tested in the university campus area through mapping. It has been observed that moving objects (people, cars) in the environment have a negative effect on scans due to outdoor measurements. For this reason, it was determined that there should not be any moving objects close to the device during the measurement.

With the study, it has been observed that the mapping performance with WMLS is comparable with other

systems, and it is possible to reposition it by synchronizing with any point cloud.

As a result of the comparisons (Table 2), it is predicted that the orthophoto obtained from WMLS can be used for cadastral studies. In addition, in addition to the lidar method, it is seen that the orthophotos obtained from the UAV can be used in an integrated manner in order to obtain successful and more precise results.

It is more difficult to make correct drawings on orthophoto (UAV) in areas where construction is intense. Precise and complete information is not obtained about the features such as the floor area of the building, entrances, porches etc. In addition, it was not possible to draw the wooded and shaded areas on the orthophoto produced with the UAV.

WMLS; There are advantages and disadvantages of having all the details struck by the laser of the scanned area on the 2D orthophoto. The disadvantage of the data obtained by WMLS in the process is that the parameter values vary according to the field and scanning, and it depends on the experience of the operator.

While drawing with the WMLS orthophoto, going parallel with the point cloud provides a healthier drawing opportunity. In the 2D image, it is possible to see all the indentations and exits of the building such as balconies and porches. In addition, it was determined that the border lines (sidewalk, refuge, etc.) in the area where the trees are located are seen more clearly in 2D. Therefore, it is suggested that the WMLS device can be used in cadastral renewal works.

REFERENCES

Balenović I, Liang X, Jurjević L, Hyyppä J, Seletković A, & Kukko A (2020). Hand-Held Personal Laser Scanning–Current Status and Perspectives for Forest Inventory Application. Croat. J. Forest Eng.

BalenoviGüney C & Sayın S B (2016). Jeodezik Ölçme Ve Mekansal Karar Destek İçin Robotik Bir Yaklaşım. XVIII. Akademik Bilişim Konferansı.

Çete M & Yomralıoglu T (2013). Re-engineering of Turkish land administration. Survey Review, 45(330), 197-205.

Demir O & Çoruhlu Y E 2009. Determining the property ownership on cadastral works in Turkey. Land Use Policy, 26, 1, 112-120.

Di Filippo, A Sánchez-Aparicio, L J Barba, S Martín-Jiménez, J A Mora, R & González Aguilera D (2018). Use of a wearable mobile laser system in seamless indoor 3D mapping of a complex historical site. Remote Sensing, 10(12), 1897.

Döner F & Bıyık C (2007). Üç Boyutlu Kadastro. Jeodezi ve Jeoinformasyon Dergisi, (97), 53-56.

Döner F (2015). Evaluation of cadastre renovation studies in Turkey. Survey review, 47(341), 141-152.

Döner F, Thompson R, Stoter J, Lemmen C, Ploeger H & van Oosterom P (2008). 4D land administration solutions in the context of the spatial information infrastructure. In FIG Working Week, 14-19.

Gura D A & Nedyakina A P (2021). Geodesic provision for cadastral works: development prospects. In IOP Conference Series: Materials Science and Engineering (Vol. 1083, No. 1, p. 012057). IOP Publishing.

Hao M, Liu Z & Sun Y (2011). Assessment of mobile laser scanning data for building reconstruction in 3D cadastre. In 2011 International Symposium on Image and Data Fusion, 1-4.

Karabin M, Olszewski R, Gotlib D, Bakuła K & Fijałkowska A (2017). The new methods of visualisation of the cadastral data in Poland–. FIG Working Week 2017 "Surveying the world of tomorrow–From digitalisation to augmented reality.

Kaufmann J, Steudler D, Yomralıoğlu T, Uzun B & Demir O. Kadastro 2014.

Kaya Y, Yiğit A Y, Ulvi A & Yakar M. (2021). Arkeolojik Alanların Dokümantasyonununda Fotogrametrik Tekniklerinin Doğruluklarının Karşılaştırmalı Analizi: Konya Yunuslar Örneği. Harita Dergisi, 165, 57-72.

Otero R, Lagüela S, Garrido I, & Arias P (2020). Mobile indoor mapping technologies: A review. Automation in Construction, 120, 103399.

Şahin, H, Koçak B H, Osmanağaoğlu B İ, & Yildiz M T. (2015) Müfettiş Yardımcılığı Yetiştirme Programı Araştırma Çalışması Kadastronun Güncellenmesi, Yenilenmesi ve 22a Uygulamaları Uygulamadaki Sorunlar ve Çözüm Önerileri.

Sultani M Y & Şişman A. Kadastro 2014 İlkelerine Göre Afganistan Kadastrosunun İncelenmesi. Türkiye Arazi Yönetimi Dergisi, 2(2), 41-47.

Ulvi A, Yakar M, Yiğit A & Kaya Y. (2019). The Use of Photogrammetric Techniques in Documenting Cultural Heritage: The Example of Aksaray Selime Sultan Tomb. Universal Journal Of Engineering Science, 7(3), 64-73.

Uzun B & Celik N (2011). Kıyı Alanlarındaki Kamu Taşınmazlarının Yönetim Sorunları. 7. Kıyı Mühendisliği Sempozyumu (pp.447-458). Trabzon, Turkey.

Williams R D, Lamy M L, Maniatis G, & Stott E (2020). Three-dimensional reconstruction of fluvial surface sedimentology and topography using personal mobile laser scanning. Earth Surface Processes and Landforms, 45(1), 251-261.

Yakar M, Kabadayı A, Yiğit A Y, Çıkıkcı, K, Kaya Y & Catin S S (2016). Emir Saltuk Kümbeti Fotogrametrik Rölöve Çalişmasi Ve 3Boyutlu Modellenmesi. Geomatik, 1(1), 14-18.

Yıldız O, Çoruhlu Y, E & Demir O, 2015. A Visional Overview to Renovation Concept On Cadastral Works In Turkey, Sigma Journal Engineering and Natural Sciences, 33, 4, 503-519.

Zeybek M (2019). El-tipi LiDAR ölçme sistemleri ve 3B veri işleme. Türkiye Lidar Dergisi, 1(1), 10-15.

Intercontinental Geoinformation Days

igd.mersin.edu.tr

Checking Landsat 8 OLI's predictive power in the retrieval of chlorophyll-a and phycocyanin concentrations of a reservoir with high frequency field data

Güray Hatipoğlu[*1]

[1]*Middle East Technical University, Graduate School of Natural and Applied Sciences, Earth System Sciences, Ankara, Turkey*

Keywords
Remote sensing
water
chlorophyll-a
phycocyanin
landsat

ABSTRACT

Increased population, global warming, climate change, environmental pollution, agriculture, and many other issues make the monitoring of water bodies more and more critical with each day. Among the water quality variables to monitor, chlorophyll-a and phycocyanin are very crucial, as the former is strongly related to the phytoplankton dynamics, and the latter is an indicator of blue-green algae or cyanobacteria. As field trips are tiresome and difficult, satellite remote sensing methods have been developed continuously, yet most of the time their validation was insufficient since the aforementioned water quality variables may change dramatically with time. Hence, this study checked many commonly used algorithms reported to work well for chlorophyll-a retrieval with Landsat 8 OLI and an autosampler data which measures chlorophyll-a and phycocyanin in every 10 minutes. If not for the chlorophyll-a yet, a few band ratio algorithms and B1 and B6 of Landsat 8 OLI produced really promising prediction accuracies.

1. INTRODUCTION

The general issue in the remote sensing retrieval of chlorophyll-a (chla) is that global algorithms perform poorly on many different water bodies.

Tavares et al. (2021) constructed regionalized algorithms and reported superior performance over global ones, the best one was 2 band semi-analytical algorithm with red and near-infrared (NIR) bands of Sentinel-2 Multispectral Imager (MSI). Cui et al. (2020) too, considered regionally tuning the general algorithms after obtaining optical water type (OWT) and selecting an algorithm working best in that OWT for Bohai Sea. Still, OC4 algorithm of O'Reilly et al. (1998) was relatively successful even before regionalization. Matsushita et al. (2012) and Matsushita et al (2015) also made a similar approach, with having Case I and II differentiation in the former, and Maximum Chlorophyll Index (MCI) assigned category in the latter. Son and Kim (2018) also regionalized an algorithm after showing that OC4 was not good for their very low chla containing waters and generated a power function utilizing 4 bands in the blue-green region. Similar regionalization is applied by Al Shehhi et al. (2017) to account for the turbid atmosphere (i.e. dusty) of Arabia, and a power fit was obtained.

Moreover, there were uncountable study that developing/tuning new band algorithms, a few examples are Zhao et al. (2015), Huang et al. (2014), and Zhou et al. (2014). Among them, for instance, Rodríguez-López et al. (2020) checked many simple indices for Lake Laja chla retrieval, where chla concentrations were quite low, and found that combined use of normalized difference vegetation index (NDVI) and Green normalized difference vegetation index (GNDVI) yields very high correlation coefficient. For phycocyanin, Isenstein et al. (2020) used Landsat 7 ETM+ models for many groups of phytoplankton, and a model with R^2 of 0.83 was constructed against the square root of cyanobacteria volume in unit water volume.

One very common shortcoming of algorithm testing studies similar to above is the time difference between *in situ* sampling and satellite overpass. Chla, for instance, can vary in the order of minutes, but many studies worked with even a 2-day time difference. This study employs one dataset from Beaverdam Reservoir, Virginia, US with chla, phycocyanin, which are quite

* **Corresponding Author**

*(gurayhatipoglu@gmail.com) ORCID ID 0000 – 0002 – 7538 – 6265

Cite this study

Hatipoğlu G, (2021). Checking Landsat 8 OLI's predictive power for chlorophyll-a and phycocyanin concentrations of a reservoir with high frequency field data.. 2nd Intercontinental Geoinformation Days (IGD), 116-119, Mersin, Turkey

important for aquatic environments monitoring in 10-minute interval measurements. Owing to the relative smallness of the reservoir, it is impossible to retrieve anything with MODIS or Sentinel-3 satellites, but Landsat-8 OLI has sufficient spatial resolution. Landsat 8 OLI's bands and band ratio algorithms' predictive power for these variables are tested with almost simultaneous satellite match-ups to *in situ* data in this study.

2. METHOD

This section presents information about the study area, used *in situ* and satellite remote sensing data and the methods of the study.

2.1. Study Area

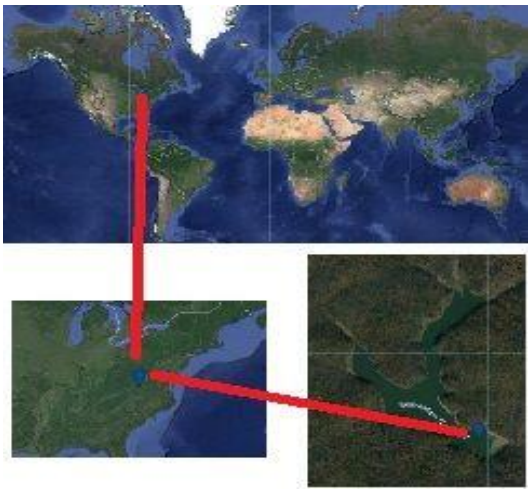

Figure 1. Location of the Beaverdam Reservoir (Google, n.d.)

Beaverdam Reservoir is situated roughly between 37.31 and 37.32 North latitudes, and -79.81 to -79.82 east longitudes. It is a secondary drinking water source for Roanoke, Virginia.

2.2. *in situ* Data

The part of the data matching up with the Landsat-8 OLI cloudless overpass was obtained from Carey et al. (2021). They collected *in situ* data via autosamplers that measure the water every 10 minutes. The chla, phycocyanin measurements were obtained via YSI EXO2 sonde. The mean, standard deviation, and range of these variables are in Table 1.

Table 1. Summary statistics of chlorophyll-a (chla) and phycocyanin (bga) data used in this study

Items	Mean	Standard Deviation	Range
chla(µg/L)	5.51	3.29	11.46
bga(µg/L)	0.27	0.16	0.49

2.3. Remote Sensing Data

Landsat 8 Operational Land Imager (OLI) top-of-atmosphere (TOA) reflectance (Chander et al. 2009) data were obtained via Google Earth Engine (Gorelick et al. 2017). (The atmospherically corrected data was not included in this study, as atmospheric correction itself heavily influences chla retrievals, and there might be algorithms that can still function well with TOA remote sensing data). 9 images of Landsat 8 OLI without clouds or other interferences were found within the period of *in situ* data presence. All images had Visible to NIR and short-wave infrared (SWIR) bands; B1,2,3,4 for coastal, blue, green, and red, respectively, then B5 as NIR, B6, and B7 as SWIR, B8 for the panchromatic band, B9 for cirrus detection, B10, and B11 for thermal bands (not used here). For the matched pixels, the correlogram between these bands is in Fig. 2.

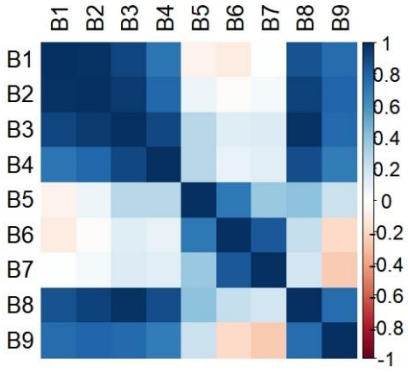

Figure 2. Correlogram of Landsat 8 OLI bands in this study's dataset

2.4. Methods

To check whether commonly applied band-ratio or other similar algorithms hold for high-frequency data match-ups as well, 10 widely used chla retrieval algorithms were chosen and presented in Table 2. (some of them mostly used for terrestrial purposes, but still retrieved chla).

Table 2. The indices used in retrieving chlorophyll-a (chla), and phycocyanin

Index	Structure	Reference
NDVI	(N-R)/(N+R)	(Rouse et al. 1973)
GNDVI	(N-G)/(N+G)	(Gitelson et al. 1996)
ARVI	(N-(R-(R-B)))/(N+(R-(R-B)))	(Kaufman & Tanre, 1992)
VARI	(G-R)/(G+R-B)	(Cheng et l. 2013)
VI Green	(G-R)/(G+R)	(Cheng et l. 2013)
GCI	(N/G)-1	(Gitelson et al. 2006)
NAVI	1-(Red/NIR)	(Carmona et al. 2015)
GDVI	NIR - Green	(Sripada et al. 2006)
EVI	2.5*((N-R)/(N+(6*R)-(7.5*B)+1)	(Huete et al. 2002)
NRVI	((R/N)-1)/((R/N)+1)	(Baret & Guyot, 1991)

Note: R stands for Red, G stands for Green, B stands for Blue, N stands for Near Infrared.
Note: ARVI index is used with coefficient of (R-B) as 1

The indices' performances were evaluated via R^2 adjusted values and Residual Standard Errors of the fitted linear models. As the dataset is very small yet, no training/test separation was done. All operations were done in R statistical environment (R Core Team, 2020).

3. RESULTS

Attempts to predict chla by indices failed. The following Table 3 shows relatively successful phycocyanin predictions.

Table 3. Performances of algorithms in retrieving phycocyanin concentration

Index	Adj R2 / RE for bga*
NDVI	(-)** 0.6081 / 0.1007
GNDVI	(-) 0.5564 / 0.1071
ARVI	(-) 0.5126 / 0.1123
VARI	(-) -0.09475 / 0.1683
VI Green	(-) -0.06856 / 0.1663
GCI	(-) 0.5 / 0.1137
NAVI	(-) 0.6301 / 0.09783
GDVI	(-) 0.4877 / 0.1151
EVI	(-) 0.5446 / 0.1085
NRVI	0.6081 / 0.1007

Note: *Adj R^2 stands for adjusted R^2, RE is residual standard error, bga is the phycocyanin concentration
Note: **(-) means that there is an inverse correlation

Table 4. Phycocyanin/chla ratio prediction performance

Index	Adj R^2 / RE for bgatochla*
NDVI	(-)** 0.3599 / 0.04354
GNDVI	(-) 0.3715 / 0.04314
ARVI	(-) 0.3122 / 0.04513
VARI	(-) -0.07602 / 0.05645
VI Green	-0.0718 / 0.05634
GCI	(-) 0.297 / 0.04563
NAVI	(-) 0.4405 / 0.0407
GDVI	(-) 0.606 / 0.03416
EVI	(-) 0.5324 / 0.03721
NRVI	0.3599 / 0.04354

Note: *Adj R^2 stands for adjusted R^2, RE is residual standard error, bgatochla is the ratio of phycocyanin to chla
Note: **(-) means that there is an inverse correlation

4. DISCUSSION

Even though chla was not successfully predicted in any algorithms, if one can modestly predict phycocyanin, and also the ratio of the phycocyanin to chla, it might be better than directly applying bands or indices to predict chla itself. Additionally, almost never used B1 coastal band predicts phycocyanin/chla with 0.5936 adjusted R^2 and 0.03469 residual standard error, and B6 shows similarly good performance of 0.5974 adjusted R^2 and 0.1021 residual standard error for phycocyanin retrieval itself (other bands' performances unreported, as they were very poor). Their linear model diagnostics, checking for any heteroscedasticity, very influential variables, were not bad, especially for the model with B6, albeit the good models for phycocyanin/chla ratio had influential one or two values. Additionally, as can be seen in Fig.2, B1 and B6 are only slightly and negatively correlated, so they are likely to carry different information. Hence, a new index to retrieve chla might be considered with either these B1 and B6 bands or NAVI and GDVI indices together with a much larger dataset.

5. CONCLUSION

Effective monitoring of the water bodies will be more and more widespread with more robust remote sensing retrieval of important water quality variables. This paper checked the predictive power of commonly used band-ratio algorithms, as well as the bands themselves, from Landsat 8 OLI to retrieve chla and phycocyanin concentrations from Beaverdam Reservoir in Virginia, US where there is a high-frequency sampler buoy that might be used to obtain satellite match-up with maximum 5 minutes of time lag.

Even though not for chla, there seem to be quite efficient ways to obtain phycocyanin, and also its ratio to chla via Landsat 8 OLI TOA reflectance. With an increased amount and availability of similar *in situ* data every day, algorithms including Band 1 and Band 6, or NAVI and GDVI indices should be developed for better retrieval of phycocyanin, which will make the monitor of cyanobacteria and its bloom much easier.

ACKNOWLEDGEMENT

The author is grateful to United States Geological Survey to distribute Landsat 8 OLI free for everyone, to Google Earth Engine team to allow everyone to access a wealth of remote sensing data very efficiently and with a cloud computing environment, to Cayelan C. Carey and her research team for making their data available in Environmental Data Initiative Repository with sufficient intellectual right access to use them after proper citation.

REFERENCES

Al Shehhi, M. R., Gherboudj, I., Zhao, J., & Ghedira, H. (2017). Improved atmospheric correction and chlorophyll-a remote sensing models for turbid waters in a dusty environment. *ISPRS Journal of Photogrammetry and Remote Sensing*, *133*, 46–60. https://doi.org/https://doi.org/10.1016/j.isprsjprs.2017.09.011

Carey, C.C., A. Breef-Pilz, and B.J. Bookout. (2021). Time series of high-frequency sensor data measuring water temperature, dissolved oxygen, pressure, conductivity, specific conductance, total dissolved solids, chlorophyll a, phycocyanin, and fluorescent dissolved organic matter at discrete depths in Beaverdam Reservoir, Virginia, USA in 2020 ver 1. Environmental Data Initiative. Retrieved in March 13, 2021 from: https://doi.org/10.6073/pasta/9a4877016583357cf04b8f68eb53b648.

Chander, G., Markham, B. L., & Helder, D. L. (2009). Summary of current radiometric calibration coefficients for Landsat MSS, TM, ETM+, and EO-1 ALI sensors. *Remote Sensing of Environment*, *113*(5), 893–903. https://doi.org/https://doi.org/10.1016/j.rse.2009.01.007

Cui, T. W., Zhang, J., Wang, K., Wei, J. W., Mu, B., Ma, Y., … Chen, X. Y. (2020). Remote sensing of chlorophyll a concentration in turbid coastal waters based on a global optical water classification system. *ISPRS Journal of Photogrammetry and Remote Sensing*, *163*, 187–201. https://doi.org/https://doi.org/10.1016/j.isprsjprs.2020.02.017

Gitelson, A. A., Kaufman, Y. J., & Merzlyak, M. N. (1996). Use of a green channel in remote sensing of global vegetation from EOS-MODIS. *Remote sensing of Environment*, *58*(3), 289-298.

Gitelson, A. A., Keydan, G. P., & Merzlyak, M. N. (2006). Three-band model for noninvasive estimation of chlorophyll, carotenoids, and anthocyanin contents in higher plant leaves. *Geophysical research letters*, *33*(11).

Google. (n.d.). Beaverdam Reservoir, Virginia. Retrieved March 14, 2021, from https://goo.gl/maps/tr5vKWwASiJeapAV9

Gorelick, N., Hancher, M., Dixon, M., Ilyushchenko, S., Thau, D., & Moore, R. (2017). Google Earth Engine: Planetary-scale geospatial analysis for everyone. *Remote Sensing of Environment*, *202*, 18–27. https://doi.org/https://doi.org/10.1016/j.rse.2017.06.031

Huang, C., Zou, J., Li, Y., Yang, H., Shi, K., Li, J., … Zheng, F. (2014). Assessment of NIR-red algorithms for observation of chlorophyll-a in highly turbid inland waters in China. *ISPRS Journal of Photogrammetry and Remote Sensing*, *93*, 29–39. https://doi.org/https://doi.org/10.1016/j.isprsjprs.2014.03.012

Huete, A., Didan, K., Miura, T., Rodriguez, E. P., Gao, X., & Ferreira, L. G. (2002). Overview of the radiometric and biophysical performance of the MODIS vegetation indices. *Remote sensing of environment*, *83*(1-2), 195-213.

Isenstein, E. M., Kim, D., & Park, M.-H. (2020). Modeling for multi-temporal cyanobacterial bloom dominance and distributions using landsat imagery. *Ecological Informatics*, *59*, 101119. https://doi.org/https://doi.org/10.1016/j.ecoinf.2020.101119

Kaufman, Y. J., & Tanre, D. (1992). Atmospherically resistant vegetation index (ARVI) for EOS-MODIS. *IEEE transactions on Geoscience and Remote Sensing*, *30*(2), 261-270.

Matsushita, B., Yang, W., Chang, P., Yang, F., & Fukushima, T. (2012). A simple method for distinguishing global Case-1 and Case-2 waters using SeaWiFS measurements. *ISPRS Journal of Photogrammetry and Remote Sensing*, *69*, 74–87. https://doi.org/https://doi.org/10.1016/j.isprsjprs.2012.02.008

Matsushita, B., Yang, W., Yu, G., Oyama, Y., Yoshimura, K., & Fukushima, T. (2015). A hybrid algorithm for estimating the chlorophyll-a concentration across different trophic states in Asian inland waters. *ISPRS Journal of Photogrammetry and Remote Sensing*, *102*, 28–37. https://doi.org/https://doi.org/10.1016/j.isprsjprs.2014.12.022

O'Reilly, J. E., Maritorena, S., Mitchell, B. G., Siegel, D. A., Carder, K. L., Garver, S. A., … McClain, C. (1998). Ocean color chlorophyll algorithms for SeaWiFS. *Journal of Geophysical Research: Oceans*, *103*(C11), 24937–24953.

R Core Team (2020). **R**: A language and environment for statistical computing. **R** Foundation for Statistical Computing, Vienna, Austria.

Rodríguez-López, L., Duran-Llacer, I., González-Rodríguez, L., Abarca-del-Rio, R., Cárdenas, R., Parra, O., … Urrutia, R. (2020). Spectral analysis using LANDSAT images to monitor the chlorophyll-a concentration in Lake Laja in Chile. *Ecological Informatics*, *60*, 101183. https://doi.org/https://doi.org/10.1016/j.ecoinf.2020.101183

Rouse, J., Haas, R.H., Schell, J.A., & Deering, D. (1973). Monitoring vegetation systems in the great plains with ERTS. Third Earth Resources Technology Satellite-1 Symposium- Volume I: Technical Presentations. NASA SP-351

Son, Y.-S., & Kim, H. (2018). Empirical ocean color algorithms and bio-optical properties of the western coastal waters of Svalbard, Arctic. *ISPRS Journal of Photogrammetry and Remote Sensing*, *139*, 272–283. https://doi.org/https://doi.org/10.1016/j.isprsjprs.2018.03.024

Sripada, R. P., Heiniger, R. W., White, J. G., & Meijer, A. D. (2006). Aerial color infrared photography for determining early in-season nitrogen requirements in corn. *Agronomy Journal*, *98*(4), 968-977.

Tavares, M. H., Lins, R. C., Harmel, T., Fragoso Jr., C. R., Martínez, J.-M., & Motta-Marques, D. (2021). Atmospheric and sunglint correction for retrieving chlorophyll-a in a productive tropical estuarine-lagoon system using Sentinel-2 MSI imagery. *ISPRS Journal of Photogrammetry and Remote Sensing*, *174*, 215–236. https://doi.org/https://doi.org/10.1016/j.isprsjprs.2021.01.021

Zhao, J., Temimi, M., & Ghedira, H. (2015). Characterization of harmful algal blooms (HABs) in the Arabian Gulf and the Sea of Oman using MERIS fluorescence data. *ISPRS Journal of Photogrammetry and Remote Sensing*, *101*, 125–136. https://doi.org/https://doi.org/10.1016/j.isprsjprs.2014.12.010

Zhou, L., Roberts, D. A., Ma, W., Zhang, H., & Tang, L. (2014). Estimation of higher chlorophylla concentrations using field spectral measurement and HJ-1A hyperspectral satellite data in Dianshan Lake, China. *ISPRS Journal of Photogrammetry and Remote Sensing*, *88*, 41–47. https://doi.org/https://doi.org/10.1016/j.isprsjprs.2013.11.016

Intercontinental Geoinformation Days

igd.mersin.edu.tr

Investigation and modeling of physical growth of urban areas using night-time light data

Samaneh Bagheri*[1], Sadra Karimzadeh[1], Bakhtiar Feizizadeh [1]

[1]*Department of Remote Sensing and GIS, University of Tabriz, Tabriz 5166616471, Iran*

Keywords
SUOMI NPP
NTL
NOAA

ABSTRACT

The expansion of urbanization and unbalanced urban growth has attracted the attention of many urban planners and decision makers to the issues and consequences of urban population growth. Due to the fact that human activities are accompanied by light during the day and night, so it is possible to study human activities using satellite images that show the light of the city. In this regard, the role of remote sensing techniques and data in identifying changes and urban growth and development in assessing population growth has been more brilliant than other methods. In this study, we will show that night light (NTL) is a way to evaluate the physical growth of cities using NPP images, travel distances and Landsat 7 and 8 images, and using remote sensing and GIS techniques. In this study, we examine population growth and travel distance and urban boundary changes over a 9-year period in two Iranian cities.

1. INTRODUCTION

The process of urbanization and urban growth in different parts of the world is the result of intertwined interactions between various social, economic, political, technological, geographical, and cultural factors. Recently, the development of Quantitative Urbanism and our increasing ability to collect and share data on many aspects of urban life have begun to supply us with better clues to the properties of cities. In this regard, the role of remote sensing techniques and data in identifying changes and population growth has been brighter than other methods. Nighttime light observations from remote sensing provide us with a timely and spatially explicit measure of human activities and therefore enable a host of applications such as tracking urbanization and socioeconomic dynamics, evaluating armed conflicts and disasters, investigating fisheries, assessing greenhouse gas emissions and energy use, and analyzing light pollution and health effects. In this study, we present a new multistage approach that demonstrates that we seek to evaluate the efficiency of night light measurement (NTL) in understanding the extent of urban boundary change and its development over a nine-year period. The purpose of this study is to present the application of satellite remote sensing (NTL) to determine the causes of changes and various factors affecting the development and increase of urban areas and comparisons between several locations.

2.MATERIAL, METHODS AND CASE STUDIES

In this study, the experimental framework for measuring urban growth consists of three stages: land cover production, night light classification, and travel time calculation. Each of these steps has its own processing. Each of these datasets has advantages and disadvantages. If logically combined, the three data sets can provide a more accurate estimate of the city's physical growth. The algorithm used in this study is called the BUNTUS algorithm (built-in, night light and travel time for urban size). In the following, we will show the study area and explain each step separately and we will examine their combination and the final result.

2.1.Case Studies

In this pilot study, we chose two cities (see Figure 1) that test different aspects of BUNTUS. The studies cities are the metropolises of IRAN: Tehran and Tabriz.

* **Corresponding Author**

*(samanehbagheri99@gmail.com) ORCID ID 0000-0003-3889-6685
(sadra.karimzadeh@gmail.com) ORCID ID 0000-0002-5645-0188
(Bakhtiar.Feizizadeh@gmail.com) ORCID ID 0000-0002-3367-2925

Cite this study

Bagheri S , Karimzadeh S & Feizizadeh B (2021). Investigation and modeling of physical growth of urban areas using night-time light data. 2nd Intercontinental Geoinformation Days (IGD), 120-122, Mersin, Turkey

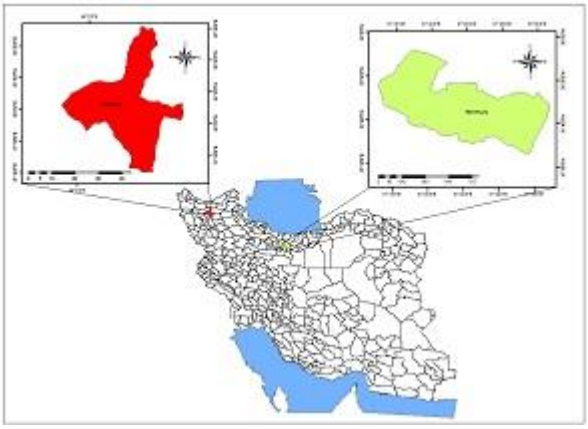

Figure 1. Study area

2.2. Land Cover Classification

For the land cover mapping, Landsat Enhancement Thematic Mapper (ETM), and Landsat Operational Line Imager (OLI)'s products have been used. ETM images were used to produce the ground cover map for 2012 and Landsat 8 images for the rest of the year. First, the necessary preprocessing such as radiometric and atmospheric correction were performed in ENVI image survey software, then the images were classified using the SVM method. At first, each image was classified into four classes, and then we divided those four classes into two classes to identify the built-in and non-created areas. In selecting the training data, Google Earth was used to help classify it correctly.

2.2.1. Accuracy Assessment

An error matrix was used to evaluate the accuracy of land cover produced through classification. The results showed that the accuracy of the four classified classes was between 85% and 90%.

2.2.2. Urban Area Generation

The land cover produced had 4 classes. A higher number of classes minimizes the effect of mixed pixels. We divided the 4 classes into two classes - built and unbuilt. The construct was assigned a value of 1 and everything else was assigned a non-constructed value of 0. Since our main focus was area construction, we re-evaluated the accuracy of the two classes. Our two-class classification was more than 90% successful in all datasets. Finally, Focal Statistics analysis was performed on the two-class image in ArcGIS software and it was ready to be collected with other data.

2.3. Nighttime Light Data Processing

Nighttime light (NTL) satellite images are a class of remote sensing products, globally available for multiple years. In this research, we use VIIRS images and various strategies. To find the DN threshold for urban areas. For multivariate analysis, we categorized NTL images into five classes to establish the relationship between DN and ground cover. We categorized the VIIRS datasets into five classes at their native resolutions of 742 meters. Using these thresholds, we classified VIIRS data into two classes.

2.4. Travel Distance Raster Creation

The road network provides a third view of urban extent since it measures the connectivity of space. Complete and accurate geospatial road network data is, therefore, a valuable dataset. Open Street Maps (OSM) provides the road network geospatial data at the global level at no cost (Muhammad Luqman & et al,2019). In the present study, OSM data were used which are easily accessible. To do this, a travel time layer was generated in QGIS software using the ORS tools. This tool calculates travel time without any restrictions such as traffic and based on the intended speed in each route. Eventually, it became a roster in ArcGIS software.

2.5. fusion of Datasets

Once three rasters were produced, we proceeded to merge those rasters. A simple sum of three rasters was generated according to the following formula:

$$DNout = DN_B + DN_{NTL} + DN_{TT}$$

Finally, we divided the generated layer into two classes according to the logical threshold. We selected the largest adjacent urban area, which included the urban core, and turned it into a vector polygon of data.

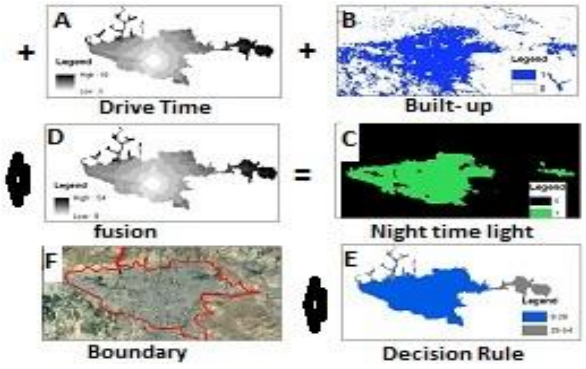

Figure 2. Fusion of three datasets (Tehran in 2020). Plate (A) represents the travel time raster (DNTT), plate (B) represents the built-up area (DNB), plate (C) represents the Nighttime Light classified raster (DNNTL), plate (D) represents the fusion of all three datasets (DNout), plate (E) represents the classified sum with a threshold value 1.5, and plate F represents the largest contiguous urban area boundary.

2. RESULTS

A little direct validation of BUNTUS is difficult. No other dataset has the resolution of time and place for complete comparison. More seriously, the definition of urban sprawl is arbitrary. Based on studies conducted on the two metropolises of Tehran and Tabriz in a period of nine years, the results showed that these two cities have not grown significantly in this period and have grown with a gentle slope.

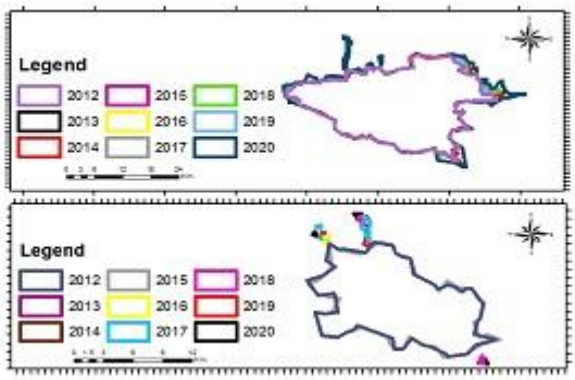

Figure 3. Urban area boundaries of two cities, 2012–2020

3. DISCUSSION

This program should be kept in mind when evaluating the usefulness of a data set such as BUNTUS. This is true for any urban data set because no single definition is sufficient for all applications, even if there is data to determine it. Our task here is to define an algorithm that is strong, consistent, and efficient enough to define global urban dispersion trends for many cities over decades. (Mohammad Loghman et al., 2019). The results of this study showed that the metropolises of Tehran and Tabriz did not experience significant physical growth in this period and had only a slight growth that occurred in different parts of the city. The area of the metropolis of Tehran in this 9-year period is about 66 square kilometers and the city of Tabriz It has increased by about 5 square kilometers.

4. CONCLUSION

The results of these studies show that, by combining Landsat information with night lights and travel time information, urban growth trends can be calculated. Due to the quality and availability of data variables and fully automated and public algorithms, this method makes it possible to achieve the growth of the urban border of all cities with it.

REFERENCES

Hao Wang & Hongrui Zhao & Shulong Jiang & Wenjia Wu (2016). The Research of China Urban Efficiency Based on Suomi-NPP Night-time Light Data. Procedia Environmental Sciences 36 (2016) 146 – 153

Bailang Yu & Christopher D. Elvidge & Chunyang He & Chenghu Zhou & Min Zhao & Wenting Cao & Weiming Cheng & Xuecao Li & Xi Li & Yuyu Zhou (2019). Applications of Satellite Remote Sensing of Nighttime Light Observations: Advances, Challenges, and Perspectives . Remote Sens. 2019, 11, 1971; doi:10.3390/rs11171971

Kevin R. Gurney & Muhammad Luqman & Peter J. Rayner (2019). Combining Measurements of Built-up Area, Nighttime Light, and Travel Time Distance for Detecting Changes in Urban Boundaries: Introducing the BUNTUS Algorithm. Remote Sens. 2019, 11, 2969; doi :10.3390/rs11242969

Intercontinental Geoinformation Days

igd.mersin.edu.tr

Rapid flood mapping with Sentinel-1 SAR images: A case study of Maritsa River

Ahmet Batuhan Polat*[1], Özgün Akçay [1]

[1]*Canakkale Onsekiz Mart University, Faculty of Engineering, Department of Geomatics Engineering, Canakkale, Turkey*

Keywords
Remote sensing
Flood mapping
Synthetic Aperture Radar
Sentinel-1
Polarization

ABSTRACT

Floods, one of the most devastating natural disasters, cause a large number of property and lives lost around the world every year. In general, the disaster caused by seasonal rains falling more than expected causes great damage to business lines such as farming. It is important to detect the flood areas as soon as possible due to occured flood disaster and provide aid to the damaged areas. In this study, it is aimed to quickly identify flood areas by using pre and during disaster event images obtained by remote sensing method. Then, these areas were visualized with the using of dB backscatter values. Radar images are used to detect flood areas due to low dB backscatter values on water surfaces. In this process using Synthetic Aperture Radar (SAR), the performances of different polarizations were also tested. Considering the results, the lowest backscatter value was obtained with VH polarization and it was demonstrated that the methods used in the study can be considered in rapid mapping of the flood areas.

1. INTRODUCTION

Maritsa River, is the partial of the border for Turkey and Greece. It starting from the Bulgaria and passes in Turkey, than it spills to Aegean Sea from the city of Edirne. When the rainfalls increased and causes to floods especially in the autumn and winter months, it is an important problem for the Greece and Turkey. Some severe floods occured in 2005, 2006 and 2007 in the area. Settlements and agricultural areas in the Turkey and Greece were heavily damaged from the floods (Derin 2020).

Flood is one of the most common destructive natural disasters on earth, causing loss of property and life (Li et al. 2018; Manavalan 2017). Remote sensing and satellite images are a common method for analyzing flood areas resulting from disasters, as they are cost-effective and provide real-time monitoring (Capolongo et al. 2019; Giustarini et al. 2016).

Remote sensing systems to be used for monitoring flood areas can be examined under two different headings: these are active and passive systems. Passive systems consist of optical satellites and contain rich information in image bands, so they have more preferable results in land cover mapping (Goffi et al. 2020). However, despite these results, optical satellite images frequently do not produce the desired results during flood disasters, because of the rain clouds restrict satellite view during the disaster period (Huang & Jin 2020). SAR images, which is an active system, are does not affect from the weather conditions. For this reason, it is the best remote sensing method to be used in cloudy weather conditions and to detect on the surface continuously (Shen et al. 2019; Marzano et al. 2011; Schumann et al. 2009). Also, smooth water surfaces can be easily detected in radar images. This is because the high scattering on a flat surface does not ensure that the returning microwave energy cannot be detected by the receiver (Martinis & Rieke 2015). Therefore, water surfaces perceived as flat by the sensor have more distinct dark pixels than different land surfaces.

SAR images have been used for years with different methods such as active contour models, threshold value approach and change detection to gather information and mapping in the flood events (Horritt et al. 2001; Hostache et al. 2012; Brivio et al. 2002). Among these methods, the use of threshold value filters all pixels to show backscatter values lower than a certain threshold value, giving fast and reliable results (Townsend 2002; Pulvirenti et al. 2012). In this way, flood mapping can be done quickly in floods that occur as a result of natural disasters and studies can be carried out in the relevant areas as soon as possible. Also Aciksarı and Akcay observed in their study in 2018 that the combined use of

* **Corresponding Author**

*(abpolat@comu.edu.tr) ORCID ID 0000-0002-7495-1998
(akcay@comu.edu.tr) ORCID ID 0000-0003-0474-7518

Cite this study

Polat A B & Akcay Ö (2021). Rapid Flood Mapping with Sentinel-1 SAR Images: A Case Study of Maritsa River. 2nd Intercontinental Geoinformation Days (IGD), 123-126, Mersin, Turkey

vertical and horizontal polarization increased the information perceived from the SAR image (Açıksarı & Akçay, 2018).

The aim of this study is to examine the back scattering values and present them visually with the threshold value in order to quickly flood mapping as a result of the floods in the Maritsa River. The images used were obtained on two different dates, before and during the flood. The histogram graph, minimum, maximum and average backscatter values of the scattering values were compared to determine the flood areas. In addition, VV and VH, which are different types of polarization in SAR images, were examined separately and the results were presented. Thereby, it has been tried to determine an optimal method to quickly identify flood areas with SAR images in sudden floods.

2. METHOD

Preprocessing steps were carried out by imaging the SAR images taken before and after the event with different polarizations as VV, VH and VV+VH/2. Afterwards, backscatter values were obtained from the SAR images and the flood areas were determined by applying the threshold value. Histogram graphics were examined separately for each image and polarization, and the mean and extreme values were compared.

2.1. Dataset and Study Area

The SAR images used for the study were obtained from the Sentinel-1A radar satellite provided free of charge by the European Space Agency(ESA). Sentinel-1 allows viewing SAR images in four different C-band imaging modes, with single or double polarization (Torres et al. 2012). Also, it has a spatial resolution up to 5 m, a coverage area of up to 400 km, and it passes through the same region in a short time. The acquisition dates of satellite images are given in Table 1.

Table 1. Image Acquisition Dates

Sentinel-1 SAR Image
30 October 2020 (Pre Event)
3 February 2021 (During Event)

As a study area, Maritsa River area has been selected which in the west of Turkey and has a border with Greece. The reason for being chosen as a study area is to affect by floods almost every year. The study area is shown in Figure 1.

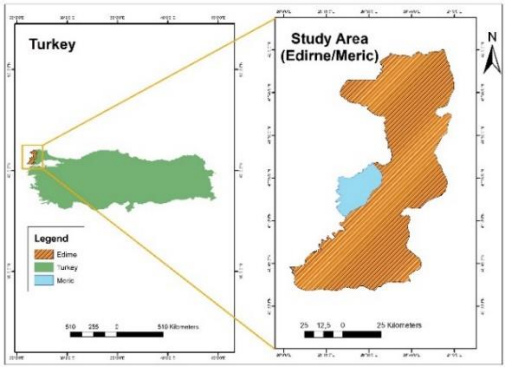

Figure 1. Study Area

2.2. Data Preprocess

Since raw SAR images are not suitable for direct use, they must go through a number of preprocessing steps. First, the orbit information of the SAR images were updated. Later, thermal noises in the images were removed. Than, the noises occurring in the image borders were removed. With the calibration performed after this process, the pixel values were directly associated with the radar backscatter. The Speckle Filter was applied to remove the speckles that negatively affect the image with the newly formed Sigmaσ values. While applying the Speckle Filter, a 7x7 size Lee Sigma filter was used. Finally, the terrain correction of the image was made and the corrected surface model was obtained. Preprocessing steps are shown in Figure 2.

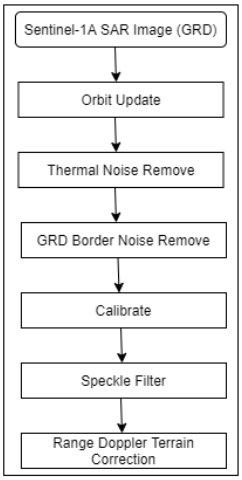

Figure 2. Preprocess Steps

After the preprocess steps, the backscatter values were filtered by using of the threshold values. Finally, the flood areas were obtained with filtered backscatter values for before and after the disaster. The images taken with different polarizations after the preprocessing steps are finished are shown in Figure 3.

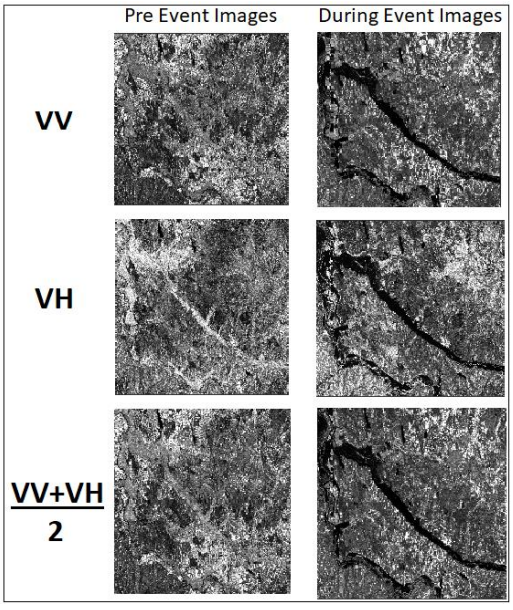

Figure 3. The acquisition of images obtained before and after the disaster in the study area with different polarizations

3. RESULTS

The extreme and average values of the backscatter values obtained from the images pre and during the event as a result of the operations performed are given in Table 2 and Table 3.

Table 2. Backscatter values of the image taken on October 30, 2020 (Pre event)

dB Values(Pre Event)	Minimum Value(dB)	Maximum Value(dB)	Mean Value(dB)
VV	-25,796	9,063	-8,9211
VH	-27,451	3,543	-16,8406
(VV+VH)/2	-25,906	6,265	-11,2236

Table 3. Backscatter values of the image taken on February 30, 2020 (During event)

dB Values (During Event)	Minimum Value(dB)	Maximum Value(dB)	Mean Value(dB)
VV	-26,547	6,22	-10,4023
VH	-27,647	-1,552	-18,0592
(VV+VH)/2	-26,729	3,881	-12,6127

Considering the backcatter values, it is seen that the lowest backscatter value is obtained from the image taken with VH polarization during the event with -27,647 dB value. Likewise, according to the average backscatter values, the lowest backscatter value was obtained from the VH polarization during the event. Histogram graphs of the backscatter values for all images are given in Figure 4.

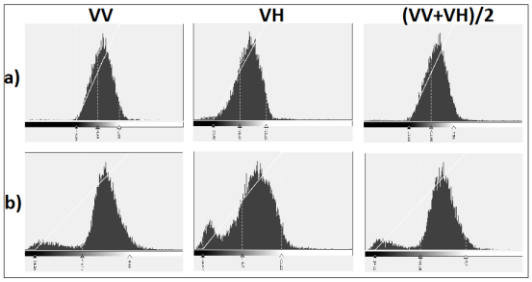

Figure 4. a) Histogram graphs of images taken pre event b) Histogram graphs of images taken during event

Finally, in the VH polarized image where the lowest backscatter values were obtained, the threshold value was applied to the dB backscatter values, and the flood areas were visualized for pre and during the event. The image of the flood areas is shown in Figure 5.

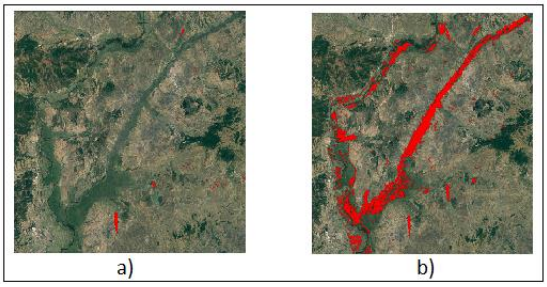

Figure 5. a) Pre event flood areas with the VH polarization b) During the event flood areas with the VH polarization

4. DISCUSSION

According to the dB backscatter obtained, the average values in all polarizations in the image taken during the event decreased. The reason for this is the increase in water areas and the low backscatter values obtained on water surfaces.

As a result of the comparisons made, the lowest backscatter value at minimum dB values was obtained from the image taken with VH polarization during the event with -27,647 dB. The highest minimum dB value was obtained with -25,796 dB as a result of the acquisition made with pre event VV polarization image. In average dB backscatter values, the value change in the image acquired with VV polarization was approximately 16.6%, in the image acquired with VH polarization approximately 7.2%, and a change of approximately 12.38% was observed in the acquisition using VV and VH polarizations together.

VH polarization more specifically determines the flood areas because it sends the signal vertically to the work area and receives the transmitted signal horizontally while it is received. By this way, different textural features are gathered from the image and different values are obtained from the reflected backscatter values.

5. CONCLUSION

In this study, one of the fastest methods for detecting the flood areas after sudden floods with SAR images was examined and the results obtained were analyzed. Optical satellite images are not always available during a flood disaster. The reason for this is the meteorological conditions that occurred during the event. Another advantage of using radar images for flood analysis is that due to the flat perception of water surfaces, smooth back reflection cannot be obtained and backscatter values are perceived as very low, and this advantage has been demonstrated in the study. As a result of the study, it was seen that the image acquisition polarization that most distinctly detected the flood areas was VH. The worst result was obtained from the image taken with VV polarization.

According to the results obtained in the study, SAR images provide the necessary facilities for the detection and analysis of the areas affected in a rapidly happening natural disaster such as a flood. In this way, threshold values can be determined from histogram graphs with the help of dB backscatter values in SAR images used for rapid flood mapping and areas can be displayed on the map. In future studies, it is aimed to establish the relationship of the work carried out with geographical information systems in the areas where flood disasters are experienced regularly. With this relationship, it is aimed to make risk analysis and discuss the precautions in the relevant region in order not to be affected by the destructive effects of flood waters.

REFERENCES

Açıksarı, E & Akçay, Ö (2018). İkili PolSAR Görüntülerinin Çok Zamanlı Ayrışma ve Kontrolsüz Sınıflandırma

Analizi. Çanakkale Onsekiz Mart Üniversitesi Fen Bilimleri Enstitüsü Dergisi, 4(2), 69-87(in Turkish).

Brivio P A, Colombo R, Maggi M & Tomasoni R (2002). Integration of remote sensing data and GIS for accurate mapping of flooded areas, Int. J. Remote Sens., 233 (3), pp. 143-1161, 10.1080/01431160010014729

Capolongo D, Refice A, Bocchiola D, D'Addabbo A, Vouvalidis K, Soncini A, Zingaro M, Bovenga F & Stamatopoulos L (2019). Coupling multitemporal remote sensing with geomorphology and hydrological modeling for post flood recovery in the Strymonas dammed river basin (Greece). Sci. Total Environ. 651, 1958–1968.

Derin M (2020). "Sınıraşan Sular Sorunu: "Meriç Örneği"". Meriç Uluslararası Sosyal ve Stratejik Araştırmalar Dergisi 4 :150-164(in Turkish).

Giustarini L, Hostache R, Kavetski D, Chini M, Corato G, Schlaffer S & Matgen P (2016). Probabilistic flood mapping using synthetic aperture radar data, IEEE Trans. Geosci. Remote Sens., 54 ,pp. 6958-6969.

Goffi A, Stroppiana D, Brivio P A, Bordogna G & Boschetti M (2020). Towards an automated approach to map flooded areas from Sentinel-2 MSI data and soft integration of water spectral features. Int. J. Appl. Earth Obs. Geoinf. 84, 101951.

Horritt M S, Mason D C & Luckman A J (2001). Flood boundary delineation from synthetic aperture radar imagery using a statistical active contour model, Int. J. Remote Sens., 22 (October 2014), pp. 2489-2507, 10.1080/01431160152497691

Hostache R, Matgen P & Wagner W (2012). Change detection approaches for flood extent mapping: how to select the most adequate reference image from online archives? Int. J. Appl. Earth Obs. Geoinf., 19 (1), pp. 205-213, 10.1016/j.jag.2012.05.003

Huang M & Jin S (2020). Rapid Flood Mapping and Evaluation with a Supervised Classifier and Change Detection in Shouguang Using Sentinel-1 SAR and Sentinel-2 Optical Data. Remote Sensing. 12(13):2073. https://doi.org/10.3390/rs12132073

Li Y, Martinis S, Plank S & Ludwig R. (2018). An automatic change detection approach for rapid flood mapping in Sentinel-1 SAR data. Int. J. Appl. Earth Obs. Geoinf. ,73, 123–135.

Manavalan R (2017). SAR image analysis techniques for flood area mapping-literature survey. Earth Sci. Inform. 10, 1–14.

Martinis S & Rieke C (2015). Backscatter Analysis Using Multi-Temporal and Multi-Frequency SAR Data in the Context of Flood Mapping at River Saale, Germany. Remote Sensing. 7(6):7732-7752. https://doi.org/10.3390/rs70607732

Marzano F S, Mori S, Weinman J A & Montopoli M (2011). Modeling polarimetric response of spaceborne synthetic aperture radar due to precipitating clouds from X- to Ka-band, IEEE Trans. Geosci. Remote Sens., 50 (3) pp. 687-703, 10.1109/TGRS.2011.2163942

Pulvirenti L, Chini M, Marzano F S, Pierdicca N, Mori S, Guerriero L, Boni G & Candela L (2012) Detection of floods and heavy rain using Cosmo-SkyMed data: the event in Northwestern Italy of November 2011 International Geoscience and Remote Sensing Symposium (IGARSS), (November 2011), pp. 3026-3029, 10.1109/IGARSS.2012.6350788

Schumann G, Bates P D, Horritt M S, Matgen P & Pappenberger P (2009). Progress in integration of remote sensing-derived flood extent and stage data and hydraulic models, Rev. Geophys., 47 (3), 10.1029/2008RG000274

Shen X, Anagnostou E N, Allen G H, Robert Brakenridge G & Kettner A J (2019). Near-real-time non-obstructed flood inundation mapping using synthetic aperture radar. Remote Sens. Environ. 221, 302–315.

Torres R, Snoeij P, Geudtner , Bibby D, Davidson M, Attema E,… Rostan F (2012). GMES Sentinel-1 mission. Remote Sensing of Environment, 120, 9–24. doi:10. 1016/j.rse.2011.05.028

Townsend P A (2002). Estimating forest structure in wetlands using multitemporal SAR, Remote Sens. Environ., 79 (2–3), pp. 288-304, 10.1016/S0034-4257(01)00280-2.

Intercontinental Geoinformation Days

igd.mersin.edu.tr

Assessment of spatiotemporal distribution of anchovy catches based on Vessel Monitoring System (VMS) and MODIS satellite data in the Gulf of Thailand

Nittaya Katekaew*[1,2], Jianzhong Lu[2], Anukul Buranapratheprat[3], Dudsadee Leenawarat [4]

[1]*Burapha University, Faculty of Geoinformatics, Chonburi, Thailand*
[2]*Wuhan University, State key Laboratory of Information Engineering in Surveying, Mapping and Remote Sensing, Wuhan, China*
[3]*Burapha University, Faculty of Science, Chonburi, Thailand*
[4]*Graduate School of Environmental Studies, Nagoya University, Aichi, Japan*

Keywords
Remote sensing
Spatial-Temporal distribution
Vessel Monitoring System (VMS)
Anchovy
Gulf of Thailand

ABSTRACT

This research was conducted to investigate spatiotemporal distribution of anchovy catches in the Gulf of Thailand in 2019 based on the data from Vessel Monitoring System (VMS) and fishing logbook. Generalized additive model (GAM) was used to analyze the relationship between environmental factors including sea surface chlorophyll-a (Chl-a) and sea surface temperatures (SST) from AQUA-MODIS satellite and fish catches from 3 fishing gears including falling net, surrounding net and lift nets during wet season and dry season 2019. The results showed that anchovy distribution and catches were intense in coastal areas, and the catch volume in dry season was larger than that in wet season. GAM analysis suggests that the highest fishing frequency be related to 0.1-0.8 mg/m^3 of Chl-a and 28.8-29.5 °C of SST in dry season. In wet season, high fishing frequency occurred in the area with Chl-a is 0.2-0.6 mg/m^3 and SST is 29.5-31.0 °C. This current study provides important information on the relationship of environmental factors to the distribution of anchovies, which can be used for sustainable management of anchovy resource fisheries.

1. INTRODUCTION

For commercial fisheries around the world, it is imperative to maintain a sustainable future, and to develop and implement an ecosystem management plan that allows it to take advantage of fish stocks while reducing the number of fishes caught (Hall, Alverson & Metuzals, 2000).

Anchovy, a small pelagic fish, plays an important role in marine ecosystems, not only as herbivorous fish consuming phytoplankton but also as a target fish for local commercial fisheries. Two genera of anchovy namely stelephorus and encrasicholina are found in the Gulf of Thailand (Department of Fisheries, 1993). Despite its small size, its catch volume and economic value are very high. In 2018, the total consumption of economic fish was 860,372 tons or 70.96 percent of the total fish volume, accounting for 24,866.91 million baht or 89.47 percent of the total fish cost, according to the statistics of the Department of Fisheries in Thailand. Anchovy had the highest catch volume of 162,555 tons (18.89%) worth 3,161.17 million baht (12.71%), followed by mackerel in the amount of 99,648 tons (11.58%) worth 3,059.10 million baht (12.30%) (Department of Fisheries, 2019).

The life cycle of anchovy, that is, spawning and foraging are associated with natural environments such as Chl-a and temperature near the coast (Department of Fisheries, 1993). The variations in environmental conditions could change the natural fluctuations of the anchovy stock especially in the coastal area where plankton is abundant and water temperature is varied. These relevant environmental information are essential for the study of the distribution of anchovy for fishery management (Safruddin et al., 2018). In this study, we use Vessel Monitoring System (VMS) data and fishing

* **Corresponding Author**

*(katekaew1559@gmail.com) ORCID ID 0000-0002-6039-8968
(lujzhong@whu.edu.cn) ORCID ID 0000-0002-6432-8481
(anukul_bu@hotmail.com) ORCID ID 0000-0001-7436-9175
(dudsadeelee@gmail.com) ORCID ID 0000-0002-8418-5262

Cite this study

Katekaew N, Lu J, Buranapratheprat A & Leenawarat D (2021). Assessment of spatiotemporal distribution of anchovy catches based on Vessel Monitoring System (VMS) and MODIS satellite data in the Gulf of Thailand. 2nd Intercontinental Geoinformation Days (IGD), 127-130, Mersin, Turkey

logbook to investigate the distribution of ancovy and the relationship of Chl-a, SST and fish catches. With high fishing statistics and enormous value, such studies are needed for the future sustainable use of this fishery resource.

2. METHOD

The study area is the Gulf of Thailand (Figure 1), a coastal sea located in the tropical zone influenced by monsoon seasons. The data in dry season (February-March) and wet season (July-August) 2019 are specified and used in the analysis.

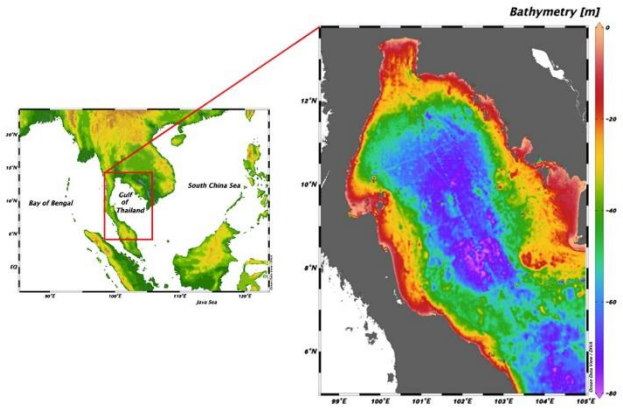

Figure 1 The Gulf of Thailand

2.1. Fishing Data

The tracking information of the fishing vessels was recorded with VMS, which reported the position of the vessels via navigation and communication satellites every 15 minutes to 1 hour. Catch data were obtained from the fishing logbook carried out by the Department of Fisheries. The information included types of fishing gears (falling net, surrounding net or lift nets), fish catch data consisted of fishing date, position, and catchweight (kg).

The vessel tracking information was checked with the fishing logbooks by comparing the locations from the GPS system noted by the fishermen and those from VMS. This was used to check the accuracy of the actual fishing points. The weight of anchovy obtained from the fishing logbook were used for calculations.

2.2. Satellite Data

Moderate Resolution Imaging Spectroradiometer (MODIS) satellite data including sea surface temperature (SST) and sea surface chlorophyll-a (Chl-a) of level 3 (4km) were used in the analysis. Only MODIS cloud-free images were taken into consideration.

2.3. Generalize Additive Model (GAM)

Information on the abundances and dynamics of the target fish population is effective for fishery management. It is also important to know how environmental factors affect the distributions of target population. International Council for the Exploration of the Sea (ICES) held a workshop in 1991 on the applications of spatial techniques for acoustic-survey data, where spatial statistical methods were discussed (ICES, 1993). One of the methods considered was generalized additive model (GAM). GAM is a non-parametric, regression technique not restricted by linear relationships, but flexible regardless of the statistical distribution of the data (Swartzman et al., 1995).

2.4. R Program

The environmental selections were predicted by the R program (R Development Core Team, 2017). The statistical model was constructed in the presence of anchovies based on the falling net, surrounding net, and lift net catches. The responding variable was anchovies in presence (fish number in kg) scenarios and the predictor factors were SST and Chl-a.

3. RESULTS

We make anchovy fishing points from VMS data during dry and wet season to determine where fishing vessels were operating in the Gulf of Thailand. Satellite data, Chl-a and SST were averaged for 3 months for each season to be used in the analysis and presented in the results.

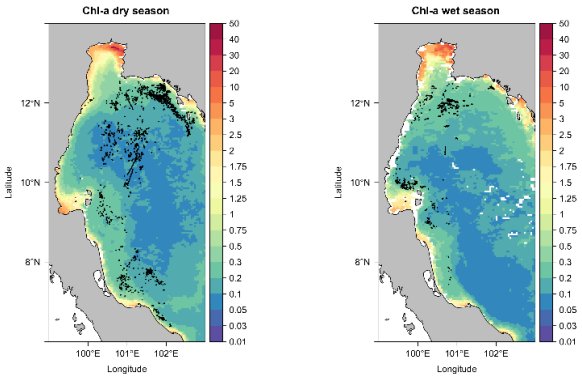

Figure 2 Anchovy fishing ground (Black points) overlaid on Chl-a in the Gulf of Thailand in dry and wet season

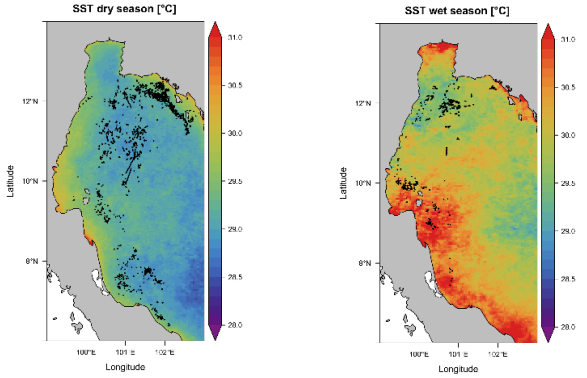

Figure 3 Anchovy fishing ground (Black points) overlaid on SST in the Gulf of Thailand in Dry and Wet Season

Chl-a was high in the upper Gulf of Thailand near the river mouths located in the northern coast and near the western coast of the central gulf in dry season (Figure 2). Chl-a in wet season was higher and spread wider across the upper Gulf of Thailand. However, the values in western coast of the central gulf in this season was low compared to those in dry season.

SST in dry season was lower than those in wet season (Figure 3). SST along the coastline around the gulf was found to be higher than that in other regions in both seasons.

The relationship between anchovy distribution and environmental factors including SST and Chl-a was analyzed using GAM. The results between dry and wet season were shown in Figure 4 and Figure 5.

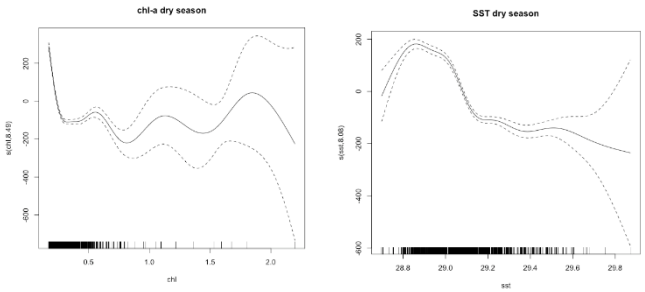

Figure 4 GAM-derived effect of model predictors (Chl-a and SST) in dry season indicates the 95% confidence intervals. The relative density of data points is shown by the rug plot on the x-axis.

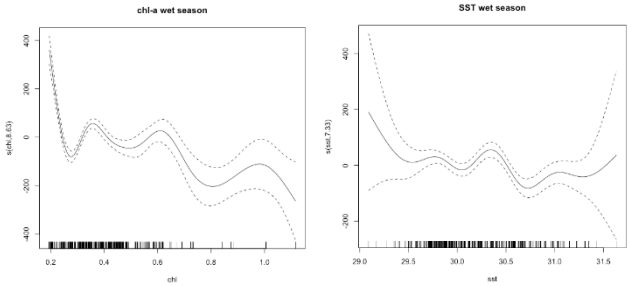

Figure 5 GAM-derived effect of model predictors (Chl-a and SST) in wet season indicates the 95% confidence intervals. The relative density of data points is shown by the rug plot on the x-axis.

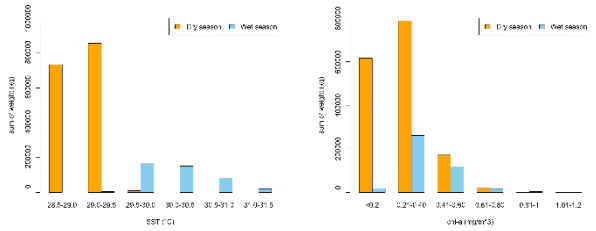

Figure 6 Sum of anchovy catches (kg) per Chl-a and SST in dry and wet season.

In dry season, the frequency of fishing operation of Chl-a was <0.2-0.6 mg/m^3 and high catch weight was 0.2-0.4 mg/m^3, and the frequency of fishing operation of SST was 28.5-29.5 °C and high catch weight was 29.0-29 °C. In the wet season, high fishing frequency had the Chl-a value in the range of 0.2-0.6 mg/m^3 and high catch weight during 0.2-0.4 mg/m^3 and SST is in the range of 29.5-31.0 °C and high catch weight in the range of 29.5-30.0 °C (Figure 4-6).

4. DISCUSSION

Spatial distribution of anchovies according to VMS data suggests that anchovies be found in the Gulf of Thailand in both dry and wet seasons. The fisheries area differed seasonally due to the different anchovy distribution. In wet season, the Gulf of Thailand is influenced by the southwest monsoon which prevails over Thailand from mid-May to mid-October. This monsoon brings moist air masses from the Indian Ocean to Thailand, causing cloudy and common rainfall, especially around the coast. As a result, this season has higher Chl-a than that in dry season, especially in coastal areas.

When the fishing sites from VMS data were overlaid with Chl-a map, it was found that the anchovy fishing spots were not in high Chl-a area. A study by Wang et al. (2010) found that high Chl-a concentrations are unsuitable for fish because they create a high-water density, which reduces the oxygen content in the water. However, Chl-a is an important indicator associated with the formation of areas where small marine fish concentrate for foraging (Lanz et al. 2009).

It was suggested that SST has the greatest influence on fish distribution. Previous studies have also indicated that SST is an indicator of fish aggregation and migration (Santos, 2000; Zainuddin, 2011). This present study also found that SST had a higher influence on fish distribution compared to Chl-a. However, Chl-a is essential as a food source for fish survival. Therefore, both parameters are critical for fish production.

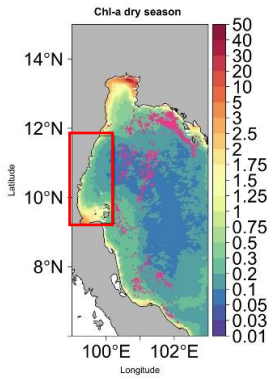

Figure 7 The red frame showing the area that prohibits the use of certain types of fishing gear.

The Department of Fisheries has imposed a ban on the use of certain fisheries that could affect the breeding of marine breeders in the Gulf of Thailand. This is a measure of aquaculture resource management during the spawning season from mid-February to mid-May.

The major goal is to maintain and restore aquatic animal resources in the central coast of the gulf. The measure covers an area of approximately 27,000 square kilometers, resulting in no fishing boats in this area during the rainy season.

GAM is an important tool in the study of relationships between oceanographic factors and the distribution of anchovies, as the expected relationships are often non-linear. GIS techniques were also used to analyze the distribution of small marine fish (Castillo et al 1996). We found that the environmental influence on the distribution of anchovies could be assessed according to statistical criteria. Therefore, the environmental factors involved in anchovy infestation become extremely important to understand the habitat needs.

The current study provides information and advice on the impact of environmental factors on anchovy proliferation for use in fisheries and sustainable management. Future work needed to be combined with other factors that may affect fertility and distribution of anchovies that were not considered in this study. Factors to consider include a large number of zooplanktons associated with the location of the anchovies, as they are linked to the density of zooplankton as well as wind direction that may influence the distribution of the anchovies.

5. CONCLUSION

The distribution of anchovies based on VMS data and the relationship between fish catches and environmental factors including Chl-a and SST in the Gulf of Thailand during dry and wet seasons of 2019 was concluded that:

1. Anchovy distribution and catches were intense in coastal areas, and the catch volume in dry season was larger than in that in wet season.

2. GAM analysis suggests that the highest fishing frequency be related to 0.1-0.8 mg/m3 of Chl-a and 28.8-29.5 °C of SST in dry season. In wet season, high fishing frequency occurred when Chl-a is 0.2-0.6 mg/m3 and SST is 29.5-31.0 °C.

ACKNOWLEDGEMENT

The authors would like to thank the Fisheries Department of Thailand for VMS and fisheries data, colleagues who contributed to the success of this research and article.

REFERENCES

Castillo J., Barbieri M. A., Gonzalez A., 1996 Relationships between sea surface temperature, salinity, and pelagic fish distribution off northern Chile. ICES Journal of Marine Science 53:139-146.

Department of Fisheries. 1993. Anchovy fisheries in Thailand. Department of Fisheries, Ministry of Agriculture and Cooperatives. 171 pages.

Department of Fisheries. 2019. Marine Capture Production Of Commercial Fishery 2018. Department of Fisheries, Ministry of Agriculture and Cooperatives. 5/2019

Hall MA, Alverson DL, Metuzals KI (2000) By-catch: Problems and solutions. Marine Pollution Bulletin 41: 204–219.

Lanz, E., Manuel, N.M., Juana, L.M. & Dworak, J.A. 2009. Small pelagic fish catches in the Gulf of California associated with sea surface temperature and chlorophyll. CalCOFI Report 50: 134-146.

Safruddin, Rachmat Hidayat, Mukti Zainuddin (2018). Effects of environmental factors on anchovies Stolephorus sp distribution in Bone Gulf, Indonesia. AACL Bioflux, 2018, Volume 11, Issue 2. 387-393

Santos, A.M.P. 2000. Fisheries oceanography using satellitecand airborne remote sensing methods: a review. FisheriescResearch 49: 1-20

Swartzman, G., Silverman, E., and Williamson, N. 1995. Relating trends in walleye pollock (Theragra chalcogramma) abundance in the Bering Sea to environmental factors. Canadian Journal of Fisheries and Aquatic Sciences, 52: 369–380.

Wang, W., Zhou, C., Shao, Q. & Mulla, D.J. 2010. Remote sensing of sea surface temperature and Chlorophyll-a:Implications for squid fisheries in the north-west Pacific Ocean. International Journal of Remote Sensing 31(17-18):4515-4530.

Zainuddin, M. 2011. Skipjack Tuna in relation to sea surface temperature and Chlorophyll-a concentration of Bone Bay using remotely sensed satellite data. Jurnal Ilmu dan Teknologi Kelautan Tropis 3(1) : 82-90.

*** R Development Core Team, 2017 R: A Language and Environmental for Statistical Computing. R Foundation for Statistical Computing. Vienna, Austria. http://www.R-project.org.

Intercontinental Geoinformation Days

igd.mersin.edu.tr

Use of photogrammetric techniques for virtual modeling of historical heritage. Application: Santa Bárbara Bridge (Almería, Spain).

Ahlem Nezreg*[1], Patricio Martínez-Carricondo [2], Fernando Carvajal-Ramírez [2], Francisco Agüera-Vega[2]

[1]*Department of Architecture, University of science and technology of Oran Mohamed Boudiaf, Bir El Djir 31000, Oran, Algeria;*
[2]*Department of Engineering, University of Almería (Agrifood Campus of International Excellence, ceiA3). La Cañada de San Urbano, s/n. 04120 Almería, Spain*

Keywords
Digital Photogrammetry
UAV
Virtual reconstruction
Cultural heritage
3D modeling
3D Technology

ABSTRACT

Photogrammetry using images from unmanned aerial vehicles (UAV) has revolutionized the conservation and dissemination of heritage, being increasingly used to document and preserve buildings of historical and cultural value, allowing a moment in time to be preserved for posterity. The aim of this study is the virtual reconstruction of the Santa Bárbara Bridge (Huércal Overa, Almería). For this purpose, two techniques was combined: on the one hand, photogrammetric techniques to carry out a survey of the current state, and on the other hand, architectural modeling software to reproduce the original state of the bridge. Complementarily, it has been essential to collect historical information that allows us to adjust to the reality built in its day.

1. INTRODUCTION

The use of photogrammetry for 3D reconstruction of cultural heritage elements has become an everyday tool in the world of archaeology and heritage conservation. The rapid and accurate acquisition of 3D models by photogrammetry with images from unmanned aerial vehicles (UAV) promotes heritage protection, constituting an effective tool for archaeological and architectural interest of data's collection.

In archaeology and architectural history, four different uses of 3D technologies have been identified: producing digital reconstructions, virtually analyzing reality-based data, calculating advanced spatial analyses, and disseminating research results (de Kleijn et al.2016). Through these technologies and the implemented methodology, any singular work of local history can be preserved for future generations, with reduced cost, in a timely manner and without causing additional damage to the current state of the work (Perez et al.2011). The main objective of the study is the virtual reconstruction of the Santa Barbara Bridge combining two techniques, on the one hand, the 3D modeling of the current state through UAV photogrammetry, and on the other hand, software for architectural modeling to reproduce the original state of the bridge. For this, it has been essential to collect historical information that allows us to adjust to the reality built in its day.

2. METHOD

2.1. Description of the building

The bridge of Santa Bárbara was built after the General Road Plan of 1864 in which it was presented the need to build 526 kms in the province of Almeria belonging to the General Road Network of the State.

The Santa Bárbara Bridge built on a flat spur on the Almanzora River, and cut by the route of the old road CN-340, controls the boxing of the Almanzora River to penetrate the first foothills of the Sierra de Almagro, (Quintero et al. 2018).

The iron bridge of Santa Barbara (Fig 1), was destroyed around October 1973 by a huge flood that Almeria suffered from it, But its iron construction and its almost indestructibility are evident in photos that attest of its imposing design.

* **Corresponding Author**

*(nezreg.ahlem@gmail.com) ORCID ID 0000-0002-6510-1625
(pmartinez@ual.es) ORCID ID 0000-0001-9556-7998
(carvajal@ual.es) ORCID ID 0000-0001-7791-0991
(faguera@ual.es) ORCID ID 0000-0003-0709-3388

Cite this study

Nezreg A, Martínez-Carricondo P, Carvajal-Ramírez F & Agüera-Vega F (2021). Use of photogrammetric techniques for virtual modeling of historical heritage. Application: Santa Bárbara Bridge (Almería, Spain). 2nd Intercontinental Geoinformation Days (IGD), 131-134, Mersin, Turkey

Figure 1. Santa Barbara Bridge before and after its destruction

2.2. Photogrammetric Survey

For the photogrammetric survey, a DJI Phantom 3 Professional drone was used with a camera model FC300X (3.61 mm), with a resolution of 4000 x 3000. The flight was carried out at a height of 33.1 m above ground level, taking a total of 841 photographs used to carry out the photogrammetric process between zenithal of the whole set and oblique photographs of detail in the areas of the abutments.

To obtain the support points for the topographic survey, a Trimble GPS with R6 receivers was used with the base located at the coordinates (591470.096, 4133789.004, 174.259) in the ETRS89 UTM30N system. A total of 25 support points were measured; however, only 15 points were used to adjust the photogrammetric project, keeping the rest for quality control. The photogrammetric process was carried out using Agisoft Metashape software version 1.6.1.10009, formerly called Agisoft Photoscan. This software performs photogrammetric processing of digital images and generates 3D spatial data for use in GIS applications, cultural heritage documentation and visual effects production, as well as for indirect measurement of objects of various scales. In the process of aligning images, the software is able to calibrate the camera, and this process allows to detect the points and obtain the orientation and position of the cameras (Fig 2). Thus a dense point cloud is obtained, a model or mesh is generated and then texture is applied (Marteau et al.2016). Finally, an orthophoto is generated where we can see the ground control points (GCPs) we have worked with. This orthophoto serves as a basis for measurements.

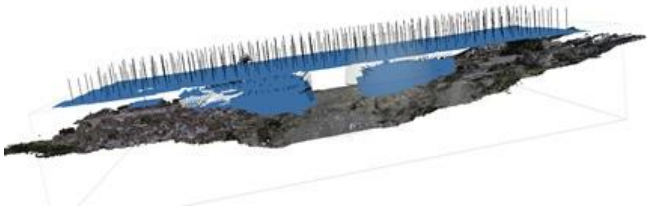

Figure 2. Image Processing in Agisoft Metashape

2.2.1. 3D modeling of the original state

The geometric complexity of the architectural features has been modeled manually from multiple sections of the dense point cloud through the 2D design and 3D modeling software "Autocad". CAD systems allow, through photogrammetric and topographic support, to establish the real position in space of the building, and to build the virtual model according to the inserted results (Cámara and Latorre 2003), Autocad allows to perform three-dimensional reconstructions of the buildings by generating polygons from a dense point cloud and rectify them to create the respective textures (Bacigalupo and Cessari 2003). The objective, in our case, is to extract the 2D geometry of the bridge from the 3D point cloud model data. The passage from Agisoft Metasahpe software to AutoCAD requires exporting the photogrammetric model in (*.rcs) format using the Recap software. From the upper section plane at different levels, the front and rear section planes, the geometry of the bridge is obtained (Fig. 3). The front section plane allows the height of the architectural elements to be obtained. Like the complete bridge, the extracted 2D drawings will be exported in (*.dwg) format to the Sketchup software, which is a face-based 3D modeling and graphic design program. The software allows importing the ground location through Google Earth, so the implementation of the model and terrain is according to the coordinates in reality (Meini et al. 2018).

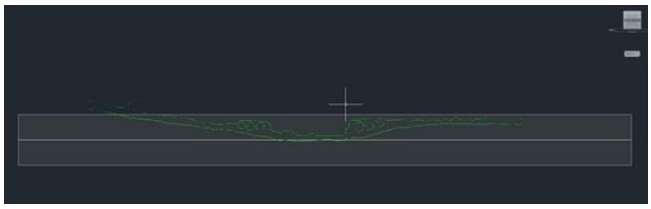

Figure 3. Back section with AutoCAD

In the absence of the original plans, photographs have been the main source for an objective modeling of the bridge. The modeling of the abutments is based on the import of the 2D plan, as well as the vertical section. As for the modeling of the bridge, bowstring type, it has a deck that is distributed in 13 equal spans, each span has a main support that has the same interior width as the arch, with two suspenders and a gusset connection point. It has been necessary to pre-dimension the arch due to lack of documentation. The ideal deflection (f) will be that which results in the smallest volume to the volume of the material according to Rebello (Fernandes et al. 2018).

F=Height, L=Arch span, H=Arch thickness, B=Arch width, 53.10/10= 5.310m ≤ F ≥ 53.10/5= 10.62m.

1.062/10= 0.1062m ≤ B ≥ 1.062/5= 0.212m

H = 0.02x53.10 = 1.062m

The 3D model was georeferenced and placed on the digital map imported from Google Earth, once the model was finished (Fig 4). The next phase was managed in the Lumion environment. Lumion is a powerful architectural visualization tool, allowing to build a 3D environment and add textures and materials, to get a real view of the model. Both software Sketchup and Lumion are compatible, therefore, the 3D model can be opened in Lumion in (*.skp) format (Meini et al. 2018).

Figure 4. Bridge modeling in Sketchup

3. RESULTS

The accuracy of the photogrammetric model is calculated from all the points not used for model fitting (CheckPoints) (Table 1). The holes appeared in the point cloud, have been solved with the help of MeshLab3, choosing the best closure algorithm for each of the holes, taking into account the dimensions and the position with respect to the model (Pierdicca 2018). The model obtained from Agisoft Metashape both in mesh level and texture has the level of accuracy sought, having a multitude of photographs in the most hidden areas, and the ability to move the UAV tool throughout the environment of the bridge.

Table 1. Accuracy obtained in each CheckPoint.

Label	XY error (m)	Z error (m)	Error (m)	Error (pix)
P10	0.0943959	-0.0056393	0.094564	0.252
P11	0.0477962	-0.130596	0.139068	0.464
P12	0.100177	-0.187536	0.212615	0.543
P13	0.0757485	-0.0689666	0.102441	0.667
P15	0.103087	0.217072	0.240306	0.486
P2	0.394938	-0.0392625	0.396885	0.528
P22	0.0505994	0.365492	0.368978	8.082
P23	0.0414179	0.0183191	0.045288	2.042
P24	0.026645	0.223695	0.225276	1.183
P3	0.18833	0.00776761	0.18849	2.777
P4	0.070044	-0.222663	0.23342	0.583
P5	0.122694	-0.100879	0.158841	0.031
P6	0.13204	-0.192194	0.23318	8.994
P7	0.0949744	-0.205719	0.226584	0.466
P8	0.210996	0.390464	0.443826	0.439

The position of the control points influences the accuracy of the model, so it is important to distribute the points throughout the study area (Caroti et al. 2015). The dense point cloud obtained by UAV photogrammetry using Agisoft Metashape, had a total of 44,966,257 points. The mesh obtained had a total of 5,165,417 faces and 2,589,219 vertices (Fig 5).

Figure 5. Dense point cloud Agisoft Metashape

The final model is georeferenced according to the real coordinates in sketchup, the same can be obtained directly from Autocad, in fact in this software, it is possible to draw complete 3D models of buildings, from photogrammetric models, detect several points where intervention is necessary, as well as the whole in a single coordinate system, located in its real position. Both software, Autocad and Sketchup, allow this in different ways but with the same objective (Cámara and Latorre 2003). The 3D model, and the sections obtained, can be considered as a basis for further detailing the project, because in the end, the most important thing is to have detailed technical information, not only based on the aesthetics of the model, but also on the geometry of its materials, its structure... (López et al. 2013).

The bridge has an arch span of about 53.10 m, and a maximum height of 9.55 m from the bottom of the arch to the deck. Both arches are braced together by 6 steel beams with an external section similar to the section of the arch in the last two, and increasing the section, in the center of the bridge. The deck has a width of 9.75m, it's composed of 6 longitudinal beams and 12 transverse beams of HEB type (800 x 300), the transverse beams are distributed at 4.085m each, where are also located the pendants (vertical suspenders), 24 in total, also carrying diagonal bracing. From these main supports, the diagonal suspenders, two for each, 44 in total, with St. Andrew's cross bracing. A rope-like profile connects the vertical and diagonal suspenders, this is the bowstring system. Figure 6 shows the final model of the Santa Barbara Bridge with Lumion, with the objective of achieving a photorealistic finish, which allows the construction of an information system of the engineering work, to which all documentation and georeferenced elaborations are incorporated.

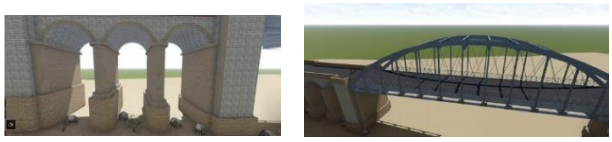

Figure 6. Renders obtained with Lumion software

4. DISCUSSION

The findings of the study show that UAV-assisted photogrammetric technique can be a complementary method to achieve a 3D model. The most important advantages of UAV-based photogrammetry are cost-effectiveness and flexibility, which allows obtaining 3D models with photorealistic textures with metric, topographic, texture, material properties and characteristics of the model, which invites to improve the capabilities of this technique for a better result, (Arias et al. 2005).

The objective of our study was to extract the maximum information with the help of the UAV technique to obtain a virtual reality of the bridge, and to obtain a rigorous documentation of the real estate, given that the structure of the bridge no longer exists, creating a model of the Santa Barbara bridge through photographs is probably the only way to return the building to its previous state, and therefore, this virtual model acquires a new perspective, to preserve the heritage, as well as the use of the UAV tool, the use of laser scanner, has proved to be a very useful tool that presents almost the same accuracy in areas that are located orthogonally to the shooting axis, on the contrary in areas with a vertical axis, the result is of lower quality with the UAV tool, but the latter presents superior results in areas of reduced accessibility (Martínez-Espejo et al. 2017).

In this study, several fields have been exploited in order to model the Santa Barbara Bridge in its original state, for this purpose photogrammetric data from the photogrammetric survey, topographic data from Google Earth, architectural data with the combination of the sections in Autocad and technical documentation projected in Sketchup were integrated. The old photographs have been the only source for the reproduction of the bridge, all this to obtain a three-dimensional reconstruction in order to obtain a model with optimal visualization quality.

5. CONCLUSION

Too many cultural heritage buildings around the world are in danger of being destroyed by natural processes or deliberate acts. UAVs and 3D technologies have provided ways to document history, preserving in the present time, what has been destroyed. With the destruction of the bridge, its original state has been permanently lost and preserving history is about remembering and learning from the past, bringing what is gone to birth again in the present. This project does just that, preserving the past, and giving life to the bridge, in addition with this methodology it is possible to detect pathologies in the constructive elements, as well as demonstrating that with this methodology, it is possible to obtain a restructured project that has been very convenient, that can be obtained in a reduced time and presents a photorealistic finish, as well as a technical documentation for conservation and archiving purposes.

ACKNOWLEDGEMENT

Thanks to the teachers and tutors for their patience and collaboration throughout the tests, providing the photogrammetric data with which the study could not have been done, and which have been of fundamental help in the realization of this research.

REFERENCES

Arias J, Herraez H, Lorenzo & C. Ordoñez (2005). Control of structural problems in cultural heritage monuments using close-range photogrammetry and computer methods. Computers and Structures, 83, 1754-1766.

A Bacigalupo C & Cessari L (2003). Survey techniques and virtual reality for the recovery plan. The International Archives of the Photogrammetry, Remote Sensing and Spatial Information Sciences, 40-42.

Cámara L, Latorre P, (2003). El Modelo Analítico Tridimensional obtenido por fotogrametría. Descomposición, manipulación y aplicaciones en el campo de la restauración arquitectónica. Arqueología de la arquitectura, 2, 87-96

Caroti G I, Martínez-Espejo Zaragoza I, & Piemonte A (2015). Accuracy assessment in structure from motion 3d reconstruction from uav-born images: the influence of the data processing methods. The International Archives of Photogrammetry, Remote Sensing and Spatial Information Sciences, 40(1), 103.

De Kleijn M, de Hond R & Martinez-Rubi (2016). A 3D spatial data infrastructure for Mapping the Via Appia. Digital Applications in Archaeology and Cultural Heritage. 3, 23-32.

Erenoglu, R. C., Akcay, O., & Erenoglu, O. (2017). An UAS-assisted multi-sensor approach for 3D modeling and reconstruction of cultural heritage site. Journal of Cultural Heritage, 26, 79-90.

Fernandes B P, Novello S M & Zacarias Pravia C M (2018). Um ábaco para pré-dimensionamento de seções de coberturas em arco treliçadas de perfis formados a frio. Revista de Estrutura do Aço 7(2).

Lancaster J (2018). Pre-and post-arson three-dimensional reconstructions of the Lichtenwalter schoolhouse, Green, Ohio. Digital applications in archaeology and cultural heritage, 8, 1-9.

López JAB, Barrera JA & Civanto JMM (2013) Documentación gráfica del patrimonio: Un paso adelante. XI Congreso internacional de expresión gráfica aplicada a la edificación, 590-594.

Marteau B, Vericat V, Gibbins C, & Batalla JR (2016). Application of Structure-from-Motion photogrammetry to river restoration: Application of SfM Photogrammetry to River Restoration. Earth Surface Processes and Landforms 42(3).

Martínez-Espejo Zaragoza I, Caroti G, Piemonte A, Riedel B, Tengen D & Wolfgang Niemeie W (2017). Structure from motion (SfM) processing of UAV images and combination with terrestrial laser scanning, applied for a 3D-documentation in a hazardous situation. Geomatics, Natural Hazards and Risk, 8(2), 1492-1504.

Meini M, Felice G Di & Petrella M (2018). Geotourism Perspectives for Transhumance Routes. Analysis, Requalification and Virtual Tools for the Geoconservation Management of the Drove Roads in Southern Italy, Goesciences, 8(19), 1–32.

Pérez JL, Mozas A, Cardenal Escarcena FJ, & López Arenas A (2011). Fotogrametría de bajo coste para la modelización de edificios históricos. Virtual Archaeology Review 2(3), 121.

Pierdicca R (2018). Mapping Chimu's settlements for conservation purposes using UAV and close range photogrammetry. The virtual reconstruction of Palacio Tschudi, Chan Chan, Peru, 8, 27-34.

Ramazan Cuneyt Erenoglua & Ozgun Akcay (2017). An UAS-assisted multi-sensor approach for 3D modeling and reconstruction of cultural heritage site. Journal of Cultural Heritage, 26, 79-90.

Quintero G, Mederos Martin A, Díaz C A & Bashore Acero C (2018). El poblado fortificado metalúrgico del Calcolítico Medio y final de Puente de Santa Bárbara (Huércal-Overa, Almería). Zephyrus, 81-71.

Intercontinental Geoinformation Days

igd.mersin.edu.tr

Investigation of the effects of vegetation indices derived from UAV-based RGB imagery on land cover classification accuracy

Muhammed Yusuf Öztürk*[1], İsmail Çölkesen[1]

[1]*Gebze Technical University, Engineering Faculty, Department of Geomatics Engineering, Kocaeli, Turkey*

Keywords
LULC
UAV
Phantom 4 pro
RGB indices
Random forest

ABSTRACT

The production of land use / land cover (LULC) maps using UAV images obtained by RGB cameras that offer high spatial resolution has recently increased. Vegetation indexes (VIs) are one of the important tools used to increase the limited spectral information of the UAV image in pixel-based classification. The aim of this study is to examine the effect of RGB-based VIs, called green leaf index (GLI), red-green-blue vegetation index (RGBVI) and triangular greenness index (TGI) which are frequently used in the literature, on the accuracy of thematic maps produced from UAV images. For this purpose, five different combinations comprising of RGB bands and VIs were formed. It was observed that the use of vegetation indices together with RGB bands increases the overall accuracy (OA) of the produced thematic maps in all cases. Additionally, the highest OA value was calculated from the thematic map produced using Dataset-5. The classification result of Dataset-4 consisting of RGB band and TGI, showed superior performance compared to Dataset-2 and Dataset-3, and a 0.1% difference was calculated between Dataset-5. Thus, this study has shown that the TGI index is more effective compared to GLI and RGBVI for thematic maps produced from a three-band UAV image.

1. INTRODUCTION

Gathering accurate and reliable land use and land cover (LULC) information about the Earth's surface is a prerequisite for the success of a wide range of applications carried out at local, regional and global scales (Colkesen and Ertekin 2020). Recent developments in the field of unmanned aerial vehicle (UAV) technologies and imaging sensor systems have led to a renewed interest in extracting required information about surface objects from high spatial resolution UAV images (Yao et al. 2019). Image classification is one of the effective ways for extracting meaningful information from the remotely sensed imagery and the main output of the process is thematic maps depicting LULC types of a given study area widely-used as main data source for land related studies.

Supervised pixel-based image classification that one of the popular classification techniques to produce LULC maps in the literature (Huth et al. 2012; Tehrany et al. 2014; Goldblatt et al. 2018). Pixel-based image classification is generally based on the assignment of the image pixels into pre-defined LULC classes using their digital numbers. The RGB-UAV-based platform is an alternative and low-cost aerial platform technology ensuring the capturing surface images at very high spatial and temporal resolutions. Although the RGB cameras are able to provide high spatial information about the surface, their spectral resolutions are limited for distinguishing spectrally similar pixels (Yang et al. 2020). In order to overcome this limitation, the auxiliary data such as vegetation index, texture features and principal components have been widely used in image classification process. Combinations of various vegetation indexes (VIs) and RGB bands are frequently used in the literature to improve the classification performance of RGB-UAV images (Sumesh et al. 2021). Many vegetation indexes based on different sensor specifications been developed since the launch of the first remote sensing satellite, Landsat. They are widely used for quantitative and qualitative evaluations of vegetation information (Xue and Su 2017).

The main purpose of this study is to analyse the effect of the use of RGB based vegetation indices on the classification accuracy. For this purpose, three popular vegetation indexes, namely green leaf index (GLI), red-green-blue vegetation index (RGBVI) and triangular

* **Corresponding Author**

*(m.ozturk2020@gtu.edu.tr) ORCID ID 0000 – 0001 – 6459 – 9356
(icolkesen@gtu.edu.tr) ORCID ID 0000 – 0001 – 9670 – 3023

Cite this study

Ozturk M Y & Colkesen I (2021). Investigation of the effects of vegetation indices derived from UAV-based RGB imagery on land cover classification accuracy. 2nd Intercontinental Geoinformation Days (IGD), 135-138, Mersin, Turkey

greenness index (TGI) were utilized. Classification results were evaluated using overall accuracy (OA), Kappa coefficient and F-score measurements.

2. STUDY AREA and DATASET

The study area covers the north-eastern part of Gebze technical University located in Gebze district of Kocaeli province. Within the boundaries of the study area, there are faculty buildings, other man-made structures, green vegetation and bare soil areas as shown in Figure 1. Study area consists of six main LULC classes: concrete including gray stone floor, road, gray and white roofs, forest class including deciduous trees, coniferous trees and grass, parkour including bicycle road, basketball and tennis court, shadow, soil and tile roof.

In this study, UAV-based high-resolution remote images were acquired by Phantom 4 Pro V2.0 drone equipped with a 20 MP RGB camera on 24 September 2020. "Pix4Dmapper" application was preferred for flight planning. The images collected from 80 m flight altitude with 80% forward overlap and %70 side overlap, resulting in ground sampling distance 2.3 cm. Agisoft PhotoScan software was used to process the obtained images and as a result, an 8-bit ortho-mosaic with a spatial resolution of 5 cm was produced.

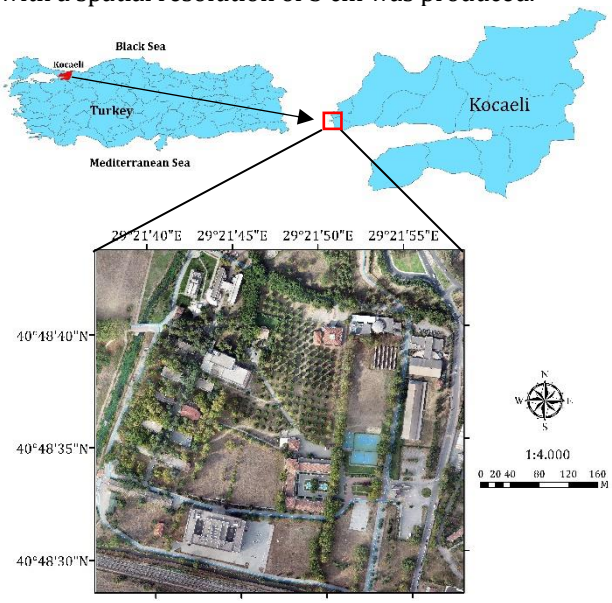

Figure 1. Study area

3. METHODOLOGY

In this study, the effect of the use of RGB based GLI, RGBVI and TGI vegetation indexes on the accuracy of thematic maps produced from UAV image were analyzed. For this purpose, training and validation pixels for each LULC classes were collected over UAV images. Random forest, one of the fast and robust ensemble learning algorithm, was utilized to construct classification model using training samples. Then, the data sets consisting of the combinations of UAV images and vegetation indexes were classified with the constructed classification model and thematic maps were produced. In order to conduct the accuracy assessment, OA, kappa coefficient and F-scores were calculated.

3.1. Random Forest (RF)

The RF algorithm, proposed by (Breiman 2001), is popular ensemble learning algorithm for produce thematic maps derived from pixel-based image classification procedure due to its robust and efficient performance (Nitze et al. 2015; Fu et al. 2017). RF utilizes multiple decision trees in that each tree trained using bootstrapped samples of input dataset for construct classification model and majority voting rule is applied to make the final prediction and simple majority rule is applied for final prediction (Colkesen and Kavzoglu 2017). Based on bootstrapping strategy, decision trees are trained using two thirds of input dataset and the remaining one-third of input dataset is utilized to evaluate the classification error (Tonbul et al. 2020). The results of each tree are aggregated, and final model output is composed.

3.2. Vegetation Indexes (VIs)

VIs are obtained from the mathematical equations applied to two or more spectral bands to emphasize the vegetation characteristics. Various VIs based on RGB bands have been developed. In this study, GLI, RGBVI and TGI indexes, frequently used in various studies in the literature, were evaluated.

GLI was developed for determinate wheat cover areas using 8-bit RGB camera. GLI values take values between -1 and +1. Negative values correspond to soil and lifeless features, whereas positive values correspond to green vegetation (Louhaichi et al. 2001).

$$GLI = \frac{2 \times Green - Red - Blue}{2 \times Green + Red + Blue} \quad (1)$$

RGBVI was developed for biomass estimation. It can be described as the normalized difference of the squared green spectral band and the product of blue×red bands (Bendig et al. 2015).

$$RGBVI = \frac{Green^2 - Blue \times Red}{Green^2 + Blue \times Red} \quad (2)$$

TGI, based on red, green and blue spectral bands, is sensitive to chlorophyll content at leaf and canopy (Hunt et al. 2011). Since this index uses the bands in the visible region, chlorophyll content can be estimated with TGI on images acquired from UAVs equipped with an RGB camera.

$$TGI = Green - 0.39 \times Red - 0.61 \times Blue \quad (3)$$

3.3. Accuracy Assessment

In this study, OA and kappa coefficient calculated from confusion matrix were utilized to evaluate the accuracy of the thematic maps produced. Additionally, F-score values were calculated using harmonic mean of

the user's accuracy and the producer's accuracy for analysis class-based measurements.

4. RESULTS

In this study, the effect of VIs on pixel based LULC classification of RGB image acquired by UAV was investigated. To achieve this purpose, three VIs (i.e., GLI, RGBVI and TGI) were calculated using equation given in section 3.2 and stretched to 0-255 pixel values. In order to construct classification model and evaluate accuracies of thematic maps, 5,000 pixels as training and 1,000 pixels as validation for each LULC class were selected on UAV image. Five datasets were created using RGB bands and different combination of VIs for evaluate classification results: Dataset-1 includes only RGB band, Dataset-2 consists of RGB bands and GLI, Dataset-3 consists of RGB bands and RGBVI, Dataset-4 consists of RGB bands and TGI and Dataset-5 corresponds to combination of RGB bands and all Vis considered. All datasets were classified with RF classifier and thematic maps were produced. Accuracy assessment results of each thematic map were given in Table 1. It should be noted that all classification process was done in R software.

Table 1. Accuracy assessment of thematic maps

LULC Class	F-scores				
	Dat-1	Dat-2	Dat-3	Dat-4	Dat-5
Concrete	91.3	91.8	92.4	92.4	94.6
Forest	97.5	97.0	96.9	97.2	96.7
Parkour	98.5	99.4	99.5	99.7	99.2
Shadow	89.2	90.4	90.0	90.5	89.9
Soil	79.5	81.2	79.5	80.0	80.0
Tile roof	84.5	85.8	85.9	87.2	87.3
OA	90.0	90.8	90.6	91.1	91.2
Kappa	0.88	0.89	0.89	0.89	0.89

As could be seen from table, the use of datasets consisting of VIs with UAV image increased the OA values in all case compared to use of only Dataset-1. In other words, the highest OA value was estimated as 91.2% (Kappa value of 0.89) from Dataset-5, whereas the lowest OA value was observed as 90.0% (Kappa value of 0.89) from Dataset-1. On the other hand, the OA value calculated from Dataset-4 was very close to the OA value of Dataset-5 (i.e., OA value of %91.1 and Kappa value of 0.89). Additionally, Dataset-2 and Dataset-3 were produced similar result with respect to the estimated OA values. These results showed that the TGI index performed more effectively in improving the classification results compared to other indexes. The results of class-based measurements (i.e., F-score) indicated that, when the highest F-score values were estimated for parkour class, the worst F-score values calculated for soil class. The reason why the class-level accuracy of the soil class is lowest may be that various substances that are mixed into the soil and have similar spectral properties with other LULC classes can be easily distinguished in the images obtained with the UAV. On the other hand, the addition of the aforementioned VIs to RGB bands increased the class-based accuracy of concrete and tile roof about 3%. Moreover, in thematic maps produced by classifying the data sets consisting of vegetation indexes and UAV images, the F-score values of forest class decreased.

Thematic maps produced by the RF classifier for each dataset were given in the Figure 2. According to visual analysis results, similar thematic maps were produced for each dataset. It is seen that the soil class is mixed with shadow and concrete classes. This visual result is consistent with the F-score values of the soil class. In addition, it is seen that the noise generated in the concrete class is reduced in the thematic map produced using Dataset-5 compared to other thematic maps.

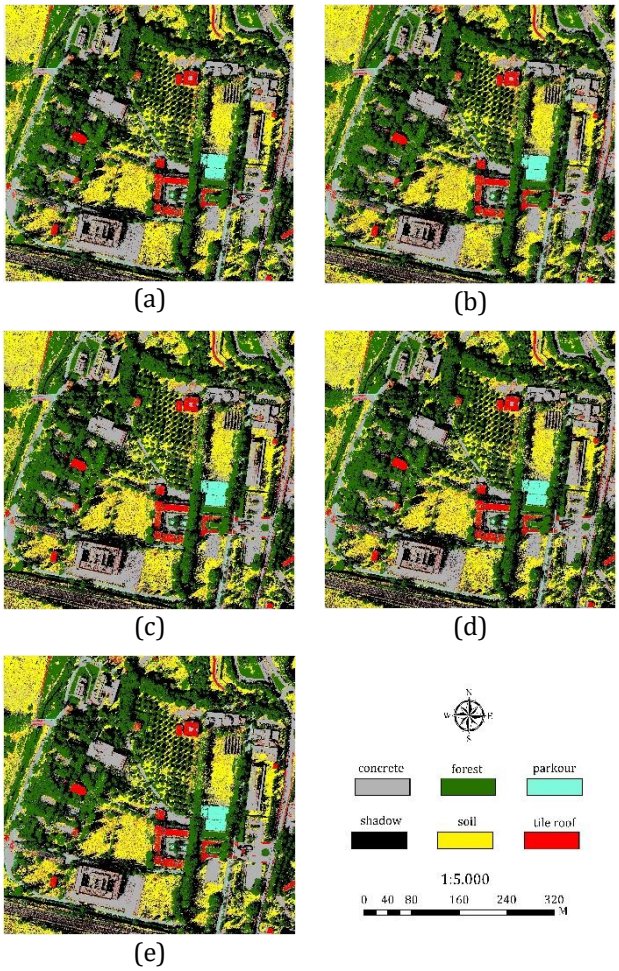

Figure 2. Thematic maps of (a) dataset-1, (b) dataset-2, (c) dataset-3, (d) dataset-4, (e) dataset-5

5. DISCUSSION AND CONCLUSION

In recent years, there has been an increasing interest in the production of thematic maps with UAV images using machine learning algorithms. Vegetation indices used to highlight the features of the Earth's provide a great advantage in increasing the spectral information in the pixel-based classification of RGB images. In this context, the effects of GLI, RGBVI and TGI indices used in various studies in the literature, on the thematic maps produced using UAV image with limited band number were evaluated. For this purpose, five datasets containing different combination of VI and UAV image was created and thematic maps of each dataset were produced by random forest classifier.

The following conclusions can be made by analyzing the classification results obtained. The accuracy of the thematic maps produced using VIs and RGB bands were increased about 1% compared to the thematic map accuracy derived from the classification of visible spectral bands only. This could be probably results of the increase in spectral information by means of vegetation indices usage. On the other hand, the estimated OA value in the dataset using the TGI index (i.e., Dataset-4) outperformed the results calculated from datasets using other indices (i.e., Dataset-2 and Dataset-3). Moreover, there is only 0.1% difference in OA between Dataset-4 and Dataset-5. According to these results, it can be said that TGI is the most effective index in classifying three-band UAV images for considered dataset used in this study.

REFERENCES

Bendig J, Yu K, Aasen H, Bolten A, Bennertz S, Broscheit, J, Gnyp M L & Bareth G (2015). Combining UAV-based plant height from crop surface models, visible, and near infrared vegetation indices for biomass monitoring in barley. International Journal of Applied Earth Observation and Geoinformation, 39, 79–87.

Breiman L (2001). Random Forests. In Machine Learning. 5–32, Chapman and Hall/CRC. https://doi.org/10.1023/A:1010933404324

Colkesen I & Ertekin O H (2020). Performance analysis of advanced decision forest algorithms in hyperspectral image classification. Photogrammetric Engineering & Remote Sensing, 86(9), 571–580.

Colkesen Ismail & Kavzoglu T (2017). The use of logistic model tree (LMT) for pixel- and object-based classifications using high-resolution WorldView-2 imagery. Geocarto International, 32(1), 71–86. https://doi.org/10.1080/10106049.2015.1128486

Fu B, Wang Y, Campbell A, Li Y, Zhang B, Yin S, Xing Z & Jin X (2017). Comparison of object-based and pixel-based Random Forest algorithm for wetland vegetation mapping using high spatial resolution GF-1 and SAR data. Ecological Indicators, 73, 105–117. https://doi.org/10.1016/j.ecolind.2016.09.029

Goldblatt R, Stuhlmacher M F, Tellman B, Clinton N, Hanson G, Georgescu M, Wang C, Serrano-Candela F, Khandelwal A K, Cheng W H & Balling R C (2018). Using Landsat and nighttime lights for supervised pixel-based image classification of urban land cover. Remote Sensing of Environment, 205(February 2017), 253–275.

Hunt E R, Daughtry C S T, Eitel J U H & Long D S (2011). Remote sensing leaf chlorophyll content using a visible band index. Agronomy Journal, 103(4), 1090–1099. https://doi.org/10.2134/agronj2010.0395

Huth J, Kuenzer C, Wehrmann T, Gebhardt S, Tuan V Q & Dech S (2012). Land cover and land use classification with TWOPAC: Towards automated processing for pixel- and object-based image classification. Remote Sensing, 4(9), 2530–2553. https://doi.org/10.3390/rs4092530

Louhaichi M, Borman M M & Johnson D E (2001). Spatially located platform and aerial photography for documentation of grazing impacts on wheat. Geocarto International, 16(1), 65–70.

Nitze I, Barrett B & Cawkwell F (2015). Temporal optimisation of image acquisition for land cover classification with Random Forest and MODIS time-series. International Journal of Applied Earth Observation and Geoinformation, 34(1), 136–146. https://doi.org/10.1016/j.jag.2014.08.001

Sumesh K C, Ninsawat S & Som-ard J (2021). Integration of RGB-based vegetation index, crop surface model and object-based image analysis approach for sugarcane yield estimation using unmanned aerial vehicle. Computers and Electronics in Agriculture, 180(July 2020), 105903.

Tehrany M S, Pradhan B & Jebuv M N (2014). A comparative assessment between object and pixel-based classification approaches for land use/land cover mapping using SPOT 5 imagery. Geocarto International, 29(4), 351–369.

Tonbul H, Colkesen I & Kavzoglu T (2020). Classification of poplar trees with object-based ensemble learning algorithms using Sentinel-2A imagery. Journal of Geodetic Science, 10(1), 14–22. https://doi.org/10.1515/jogs-2020-0003

Xue J & Su B (2017). Significant remote sensing vegetation indices: A review of developments and applications. Journal of Sensors, 2017, 1–17. https://doi.org/10.1155/2017/1353691

Yao H, Qin R & Chen X (2019). Unmanned aerial vehicle for remote sensing applications—A review. Remote Sensing, 11(12), 1443.

Jang G, Kim J, Yu J K, Kim H J, Kim Y, Kim D W & Chung Y S (2020). Cost-effective unmanned aerial vehicle (UAV) platform for field plant breeding application. Remote Sensing, 12(6), 998.

Intercontinental Geoinformation Days

igd.mersin.edu.tr

Prediction chlorophyll content of Zizania latifolia using hyperspectral data and machine learning

Adenan Yandra Nofrizal*[1], Rei Sonobe [1], Hiroto Yamashita [1], Akio Morita [1], Takashi Ikka [1]

[1]*Shizuoka University, Faculty of Agriculture, Shizuoka, Japan*

Keywords
Dimensionality Reduction
Zizania latifolia
Hyperspectral
Machine Learning

ABSTRACT

Chlorophyll content can be indicative of plant physiological activity and then changes in chlorophyll content have been used as a good indicator of disease as well as nutritional and environmental stresses on plants. Chlorophyll content estimation is one of the most applications of hyperspectral remote sensing data. Also, Random Forest (RF) has been applied to assess biochemical properties from remote sensing data; however, an approach integrating with dimensionality reduction techniques has not been fully evaluated. A total of 200 leaves were measured for reflectance and chlorophyll content and then the regression models were generated based on RF with three dimensionality reduction methods including principal component analysis, kernel principal component analysis and independent component analysis. This research clarified that PCA is the best method for dimensionality reduction for estimating chlorophyll content in *Zizania Latifolia* with a RMSE value of 5.65 ± 0.58 μg cm^{-2}.

1. INTRODUCTION

Chlorophyll pigments absorb sunlight and then their contents relate closely to primary production (Gitelson et al. 2006). Also, chlorophyll offers the information for assessing leaf nitrogen, an essential plant nutrient, due to the close relationship between them (Ramoelo et al. 2015; Kokali and Skidmore. 2015; Bungard et al. 2000) In addition, changes in the chlorophyll content of leaves are related to the effects of disease and nutritional and environmental stresses (Datt. 1999). Therefore, chlorophyll content is one of the most important indicators of photosynthetic activity among all biochemical variables.

To accurately measure chlorophyll content, spectrophotometric measurements using ultraviolet and visible spectroscopy or high-performance liquid chromatography measurements have been adopted widely, however, these techniques are expensive, labor-intensive and require bulky equipment. Although portable equipment such as the SPAD-502 Leaf Chlorophyll Meter (Konica Minolta Inc.) provides a simpler method of quantifying chlorophyll, leaf structure, water content and leaf pigment distribution make their output obscure (Peng et al. 1993). Thus, they are not suitable for quantifying chlorophyll content in Manchurian wild rice (*Zizania latifolia*), since this plant is one of silicicolous plants and leaf structure would be changed by the silica concentration of irrigated water.

On the other hand, remote sensing is one of the most attractive alternative options for this purpose and it has been revealed that hyperspectral data are useful for evaluating chlorophyll contents. Furthermore, it has been applied and evaluated for monitoring of biochemical properties based on hyperspectral indices and radiative transfer models (Lazaro. 2014; Wang. 2018). Accordingly, appraising hyperspectral reflectance to consider analyze chlorophyll contents with a variety a total slag fertilizer is required for restraint quality.

However, a dimension reduction is required to improve the usability of hyperspectral data, due to the high number of spectral bands (and some of them are highly correlated).

Besides dimension reduction, machine learning has been applied to evaluate vegetation properties (Chen. 2017; Doktor. 2014). Especially, Random Forest (RF), which is a regression technique that combines numerous decision trees to classify or predict the value of variable, has been used and reported its high performances for regression (Biau. 2016).

* **Corresponding Author**

*(adenan.y.nofrizal.20@shizuoka.ac.jp) ORCID ID 0000 – 0003 – 3176 – 0312
(sonobe.rei@shizuoka.ac.jp) ORCID ID 0000 – 0002 – 8330 – 3730
(yamashita.hiroto.16@shizuoka.ac.jp) ORCID ID 0000 – 0003 – 0571 – 8153
(morita.akio@shizuoka.ac.jp) ORCID ID 0000 – 0002 – 8418 – 2109
(ikka.takashi@shizuoka.ac.jp) ORCID ID 0000 – 0002 – 1845 – 5658

Cite this study

Nofrizal A Y, Sonobe R, Yamashita H, Morita A & Ikka T (2021). Prediction of chlorophyll content of Zizania latifolia using hyperspectral and machine learning. 2nd Intercontinental Geoinformation Days (IGD), 139-142, Mersin, Turkey

The objective main study is (1) to evaluate the potential hyperspectral data for estimation the chlorophyll of *Zizania Latifolia* and (2) to investigate the best dimensionality reduction method among Principal Component Analysis (PCA), Kernel Principal Component Analysis (KPC) and Independent Component Analysis (ICA).

2. METHOD

2.1. Study area and measurements

Manchurian wild rice (*Zizania latifolia*) plants were cultivated at within-row distances and inter-row spacing of 100 cm on a paddy field at Shizuoka University (Shizuoka, Japan, Figure 1) and grown in flooded conditions. As a basal fertilization, 18 kg of NH_4Cl, 12 kg of P_2O_5 and 12 kg of K_2O were supplied per 1000 m^2. Two further supplementary fertilizations were administered, consisting of 12 kg of NH_4Cl, 12 kg of P_2O_5 and 12 kg of K_2O, and 6 kg of NH_4Cl, respectively (per 1000 m^2). The soluble silicic acid content of the provided molten slag was 32% and the standard amount of slag fertilizer was 120 kg per 1000 m^2. The experiment included a control without slag and four slag fertilizer treatments: a standard amount of slag (1×Slag), and double (2×Slag), 4 times (4×Slag) and 8 times (8×Slag) the standard concentration. A total of 200 leaves (40 leaves from each treatment) were measured for reflectance and chlorophyll content on 2 and 5 October, 2020.

Hyperspectral reflectance was obtained using the FieldSpec4 (Malvern Panalytical, Almelo, Netherlands) and then a splice correction function was applied to minimize the inconsistency caused by the three detectors using ViewSpec Pro (Analytical Spectral Devices Inc., USA)..

Dimethyl-formamide was used the prepare extracts and their chlorophyll contents were quantified using a dual beam scanning ultraviolet-visible spectrometer (UV-1900, Shimadzu, Japan) and Porra's method (Porra. 1989)

Figure 1. *Zizania latifolia* and location of each treatment

2.2. Data Analysis

Performance evaluation was conducted for RF regression and all processes were implemented using R version 3.5.3 (R Team. 2020). RF regression creates multiple decisions tees called classification and regression trees (CART) based on randomly bootstrapped samples of training data (Breiman 2001) via generalization of the binomial variance (using a Gini index) and by nodes that are using by split variable from a group of randomly selected variable (Liaw. 2002). Since former research has described the effectiveness of RF (Hobbey. 2018; Johannson. 2014), it was also used in this research. RF differs from CART in growing non-deterministically to decorrelate the trees and lessen variance using two-stage randomization scheme related to a bootstrap sample and random variable selection. The number of trees (ntree) and the number of variables used to split the nodes (mtry) are normally established by the user. For tuning these hyperparameters, Bayesian optimization was applied using the Gaussian process.

2.3. Dimension Reduction Techniques

RF-based regression models were generated after dimension reduction techniques including Principal Component Analysis (PCA), Kernel Principal Component Analysis (KPCA) and Independent Component Analysis (ICA).

2.3.1. Principal Component Analysis (PCA)

PCA is the oldest and best-known technique of multivariate data analysis (Mishra. 2017). It was first coined by (Pearson. 1901), and produced independently by (Hotelling, 1933). PCA is the usual name for a technique which uses sophisticated underlying mathematical principles to transforms several probably correlated variables into smaller number of variables named principle components. The origin PCA lies in multivariate data analysis; however, it has a wide range of other applications. In general terms, PCA uses a vector space transform to reduce the dimensionality of large data sets. Using mathematical forecast, the original dataset, which may involve many variables (i.e the principal component). The central idea of PCA is to reduce the dimensionality of the data set in which there are many interrelated variables.

2.3.2. Kernel Principal Component Analysis (KPCA)

PCA only allows linear dimensionality reduction and then cannot be well represented in a linear subspace if the data has more complicated structures. Kernel PCA is the nonlinear form of PCA, which better exploits the complicated spatial structure of high-dimensional features (Benhart. 1997). The Radial Basis kernel function kernel, which is the typical general-purpose kernel, was applied and the kernel bandwidth was set to 0.1

2.3.3. Independent Component Analysis (ICA)

Independent component analysis (ICA) is closely related to PCA, whereas ICA finds a set of source variable that are mutually independent, PCA finds a set variable that are mutually uncorrelated (Dinesh. 2011). The independent component analysis technique is one of the most well-known algorithms which are used for solving this research. ICA is separating multivariate signal into additive subcomponent. This is done by assuming that the subcomponent is non-Gaussian signal and that they are statistically independent from each order

2.4. Statistical criteria

To evaluate the performance of the regression model, the root-mean-square error (RMSE, equation (1)) was applied.

$$\text{RMSE} = \sqrt{\frac{1}{n}\sum_{i=0}^{n}(\hat{y}_i - y_i)^2}, \quad (1)$$

Where n is number of samples, y_i is measured chlorophyll content and $\hat{y}_i$ is estimated chlorophyll content.

3. RESULTS AND DISCUSSION

3.1. Chlorophyll content

The measured chlorophyll content per leaf area (cm^2) ranged from 17.53 to 58.02 µg and the maximum value were obtained from the 2 × Slag treatment while the minimum values were from the control. Although there were significant differences in chlorophyll content between 2×Slag and other treatments ($p < 0.05$, Tukey-Kramer test), the other combinations did not differ significantly.

3.2. Spectral Reflectance and Correlation

Spectral reflectance in each fertilizer treatment shown in figure 2. It shown the control samples are highest reflectance values while the lowest values were from the 2 x Slag samples.

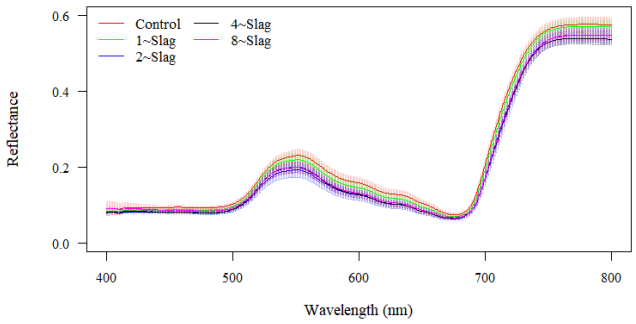

Figure 2. Spectral patterns for each slag fertilizer treatment

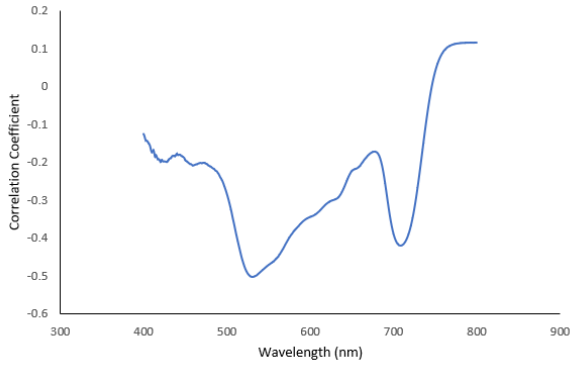

Figure 3. Correlation between spectral reflectance and chlorophyll content

Figure 3 illustrates correlations of each spectral reflectance wavelength with a chlorophyll content. For chlorophyll contents, negative correlations were confirmed near green peak and REIP, and the two bottoms were identified at 531 nm (r = -0.503) and at 709 nm (r = -0.420).

3.3. Accuracy Validation

Tables 1 shows statistics for the RMSE values calculated using regression models. Generally, PCA generally performed the best and PCA was selected as the best solution for estimating chlorophyll content 50 times, while KPCA was selected 12 times. Thus, it is not necessary to use kernel for expressing the relationships between chlorophyll content of *Zizania latifolia* and reflectance data from FielSpec4.

Table 1. Root-mean-square error (RMSE, µg cm^{-2}) for each regression model after 100 repetitions.

	PCA	KPCA	ICA
Minimum	4.49	4.90	4.36
Median	5.65	5.86	5.77
Mean	5.65	5.94	5.76
Maximum	7.33	7.54	7.37
Standard deviation	0.58	0.56	0.59

Figure 4 and 5 show the relationships between measured and estimated chlorophyll contents when the results of 100 repetitions were combined. The coefficient of determinations (R^2) were 0.47, 0.41 and 0.39 for ICA, KPCA, and PCA, respectively and then the advantage of ICA was confirmed. However, the differences were too small to claim that ICA should be applied.

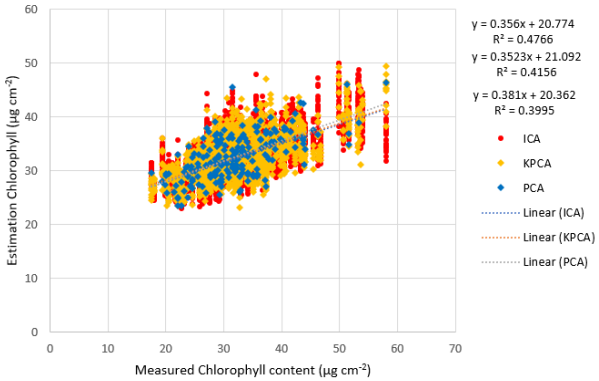

Figure 4. Relationship between estimation and measured chlorophyll contents.

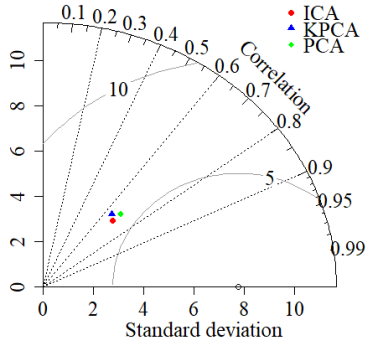

Figure 5. Taylor diagram showing the performance of each dimensionality reduction methods

4. CONCLUSION

This study has evaluated three dimension reduction techniques for estimating chlorophyll contents from reflectance. According of result, spectral reflectance had shown control sample are highest reflectance values more than another slag fertilizer treatment. However, PCA is the best method for dimensionality reduction for the estimation chlorophyll compared another advanced method such as ICA and KPCA.

REFERENCES

Benhart S, (1997). Kernel principal component analysis. Artifical Neural Networks-ICAN'97, 583-588

Biau G (2016). A Random Forest Guided Tour. Test, 25(5), https://doi.org/10.1007/s11749-016-0481-7x

Breiman L (2001). Random Forest. Mach.Math, 45, 4-45, https://doi.org/10.1023/A:1010933404324.

Bungard R A, Press M C & Scholes J D (2000). The influence of nitrogen on rain forest dipterocarp seedlings exposed to a large increase in irradiance. Plant Cell and Environment, 23(1), 1183-1194, https://doi.org/10.1046/j.1365-3040.2000.00642.x.

Chen X J, et all (2017). Spectral Characteristics and Species Identification of Rhododendros Using a Discrimnative Restricted Boltzmann Machine. Spectroscopy Letters, 50(2), 65-72, https://doi.org/10.1080/00387010.2017.1278709

Datt B (1999). Visible/near infrared reflectance and chlorophyll content in Eucalyptus leaves. International Journal of Remote Sensing, 20(14), 2741-2759, https://doi.org/10.1080/014311699211778

Dinesh K K & Naik N R (2011). An Overview of Independent Component Analysis and Its Applications. Informatica, 53, 63-81

Doktor D, et all (2014). Extraction of Plant Physiological Status from Hyperspectral Signatures Using Machine Learning Methods. Remote Sensing 6, 12(2), 12247-12274, https://doi.org/10.3390/rs61212247

Gitelson A, et all (2006). Relationship between gross primary production and chlorophyll content in crops: Implications for the synoptic monitoring of vegetation productivity. Journal of Geophysical Research-Atmospheres, 111(D8), https://doi.org/10.1029/2005jd006017

Hobbey E, et all (2018). Hotspot of soil organic carbon storage revealed by laboratory hyperspectral imaging. Science Report, 8(13), https://doi.org/10.1038/s41598-018-31776-w

Hotelling H (1933). Analysis of a complex of statistical variables into principal components. Journal of Educational Psychology, 24(6), 417-441, https://doi.org/10.1037/h0071325

Johansnon U, et all (2018). Regression conformal prediction with random forest. Machine Learning, 97(1-2), 1-22, https://doi.org/10.1007/s1099-014-5453-0

Kokali R F & Skidmore A K (2015). Plant phenolics and absorption features in vegetation reflectance spectra near 1.66 mu. International Journal of Applied Earth Observation and Geoinformation, 43, 55-83, https://doi.org/10.1016/j.jag.2015.01.010

Lazaro M, et all (2014). Retrieval of Biophysical Parameter with Heteroscedatic Gaussien Processes. IEEE Geosciences and Remote Sensing Letters, 11(4), 838-842, https://doi.org/10.1109/LGRS.2013.2279695.

Liaw A & Wiener M (2002). Classification and regression by random forest. R news, 2, 18-22

Mishra S P, et all (2017). Multivariate statistical data analysis-Principal Component Analysis (PCA). International Journal of Livestock Research, 7(5), 61-78, https://doi.org/10.5455/ijlr.20170415115235

Pearson K, (1901). On lines and planes of closet fit to systems of point in space. Philosophycal Magazine, 6(2), https://doi.org/10.80/14786440109462720

Peng S B, Garcia F V, Laza R C & Cassman K G (1993). Adjustment for Specific Leaf Weight Improves Chlorophyll Meter's Estimate of Rice Leaf Nitrogen Concentration. Agronomy Journal, 85(5), 987-990, https://doi.org/10.2134/agronj1993.00021962008500050005x

Porra R J, Thompson W A & Kriedeman P E. Determination of accurate extinction coefficients and simultaneous equations for assaying chlorophylls a and b extracted with four different solvents: verification of the concentration of chlorophyll standards by atomic absorption spectroscopy. Biochimica et Biophysica Acta (BBA)-Bioenergitics, 975(3), 384-385, https://doi.org/10.1016/S0005-2728(89)80347-0

Ramoelo A, et all (2015). Monitoring grass nutrients and biomass as indicators of rangeland quality and quantity using random forest modelling and World View-2 data. International Journal of Applied Earth Observation and Geoinformation, 43, 43-45, https://doi.org/10.1016/j.jag.2014.12.010

R Core Team (2020). R: A Language and environment for Statistic Computing. Vienna: R Foundation for Statistical Computing, Accesed 19 December 2020, http:/www.R-project.org./

Wang Z, et all (2018). Spatio Temporal Variations of Forest Phenology in the Qinling Mountains and Its Response to a Critical Temperature of 10 Degree C. Journal of Applied Remote Sensing, 12(4), https://doi.org/10.1117/1.JRS.12.022202

Intercontinental Geoinformation Days

igd.mersin.edu.tr

The effect of auxiliary data (slope, aspect and elevation) on classification accuracy of Sentinel – 2A image using random forest classifier

Furkan Bilucan *[1], **Taskin Kavzoglu** [1]

[1]*Gebze Technical University, Department of Geomatics Engineering, Kocaeli, Turkey*

Keywords
Remote sensing
Random Forest Classifier
Auxiliary data
DEM
Sentinel-2A

ABSTRACT

Land use/land cover (LULC) maps provide irreplaceable information about the earth's surface, and investigation of their accuracy has always been an attractive research topic. Furthermore, it is known that accuracy of LULC maps could be improved using auxiliary data. One of the prevalent auxiliary data is the digital elevation model (DEM) because the surface landscape is affected directly by topography. Slope, aspect and elevation which are the main characteristics of the land surface are extracted from DEM. In this study, the effects of slope, aspect and elevation on classification accuracy were analyzed. For this purpose, Sentinel-2A satellite image together with the DEM data from the ALOS PALSAR satellite was assessed as auxiliary data for the classification process. Seven LULC classes covering the bulk of the study area were specified as urban, road, forest, water, bare and soil lands, cultivated and non-cultivated land in the classification process. To avoid possible bias among the determined classes, 700 pixels for training and 300 pixels for testing were chosen for each class. Classification results revealed that the highest accuracy (96.19%) were obtained when spectral bands were used together with elevation, slope, aspect data.

1. INTRODUCTION

Remote sensing is one of the most powerful tools for monitoring the Earth's cover or natural resources. In addition, satellite images that are the main product of remote sensing technologies, are a significant source to obtain information about the Earth. Land use/land cover (LULC) maps can be produced in accordance with the purpose of working with the analysis of remotely sensed images. The most commonly used method for producing LULC maps is the classification of satellite images. Extraction of accurate information from remotely sensed imagery has been a significant exploration issue for researchers (Rwanga and Ndambuki, 2017). For a successful classification process, it is vital to select a dataset with high representativeness (Kavzoglu, 2009). Moreover, it is well known fact that LULC maps play fundamental role in many studies including estimating forest supplies, observing climate changes, crop production forecasting and assessing water quality. Therefore, auxiliary data are commonly applied to increase the classification accuracy of thematic maps (Sang et al. 2021; Hurskainen et al. 2019). It has been reported that auxiliary data such as digital elevation model (DEM) and its derivatives can improve the classification accuracy (Zhu et al. 2016; Nguyen and Pham, 2015). Land characteristics can have a considerable influence the accuracy of the classification result in areas with large topographic differences. Additionally, high topographic changes could cause pixels belonging to the same class to have different spectral values and pixels belonging to different classes to have similar spectral values (Fahsi et al. 2000). In this case, it brings about decrease in accuracy and errors to occur during the classification process. In light of this information, the main purpose of this study is to investigate DEM, which has a positive effect on thematic maps classification accuracy. Furthermore, five different datasets were created using Sentinel-2A image and DEM data. In accordance with the aim of study, 700 train and 300 test pixels were selected per class to produce thematic maps considering pixel-based image classification method. Random forest algorithm was applied to five datasets. Overall accuracy, F-score values and Kappa coefficient values were calculated to compare the performances on the constructed five datasets.

* **Corresponding Author**

*(f.bilucan2020@gtu.edu.tr) ORCID ID 0000 – 0001 – 7920 – 6914
(kavzoglu@gtu.edu.tr) ORCID ID 0000 – 0002 – 9779 – 3443

Cite this study

Bilucan F & Kavzoglu T (2021). The Effect of Auxiliary Data (Slope, Aspect and Elevation) on Land Use/Land Cover Classification Accuracy of Sentinel–2A Image Using Random Forest Classifier. 2nd Intercontinental Geoinformation Days (IGD), 143-146, Mersin, Turkey

2. METHOD

2.1. Study Area and Datasets

The study area covering an area approximately 537 km^2 land is located on Kocaeli province in Turkey (Figure 1). The study site basically covers seven essential LULC classes namely forest, bare and soil lands, road, water, urban, cultivated, and non-cultivated. Five datasets were created to evaluate the effect of elevation, slope and aspect on classification accuracy.

Description of five constructed dataset used in this study were given in Table 1. Dataset-I is the main dataset that includes Sentinel-2A image bands (i.e. band 2, 3, 4, 5, 6, 7, 8, 8A, 11, 12). Dataset-II was created by adding the slope feature to the Dataset-I (totally eleven bands). Dataset-III is the third dataset obtained by adding the aspect land features to the Dataset-I (totally eleven bands). Another dataset called Dataset-IV was produced using Dataset-I including spectral bands and elevation map. The last dataset named as Dataset-V was created using a combination of Sentinal-2A image bands together with topographical features of slope, elevation and aspect. DEM data at 12,5 m spatial resolution was obtained from the ALOS PALSAR satellite and employed in this study.

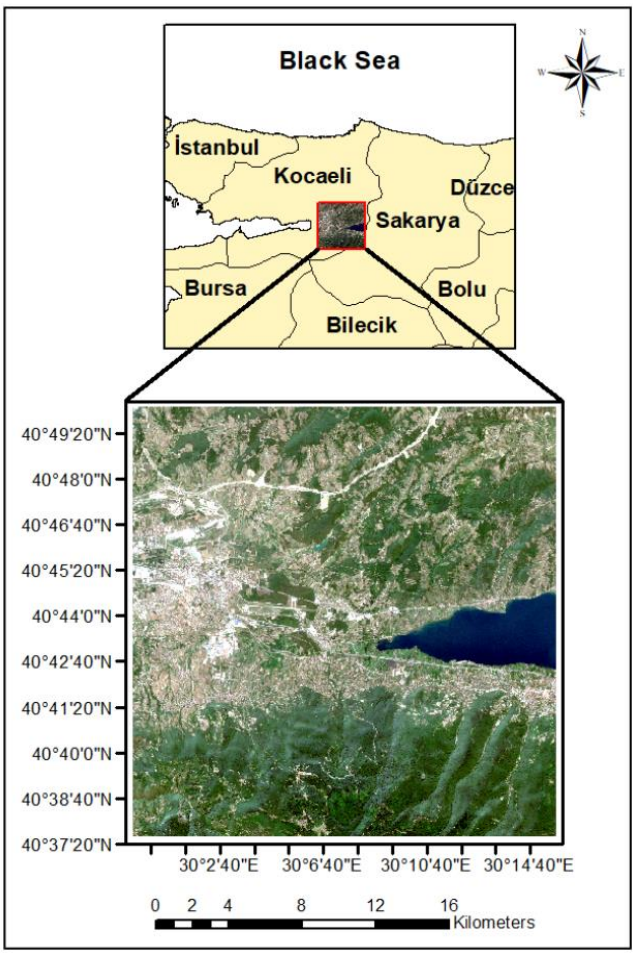

Figure 1. The study area, Kocaeli province of Turkey

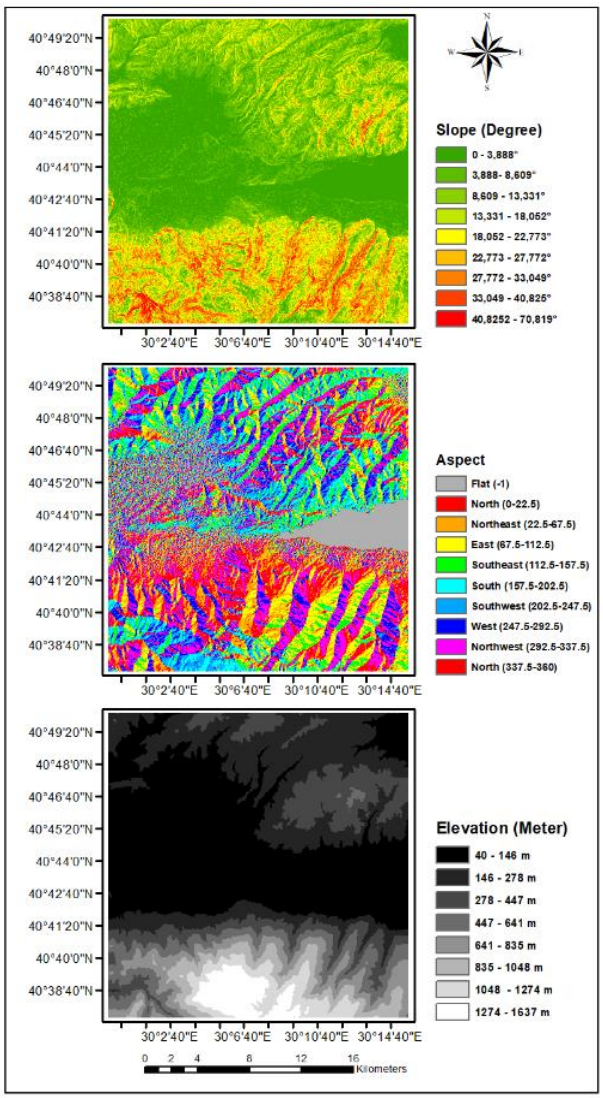

Figure 2. Slope, aspect and elevation feature maps

Table 1. Datasets used in this study

Datasets	Sentinel-2A bands	Slope	Aspect	Elevation
Dataset-I	√	-	-	-
Dataset-II	√	√	-	-
Dataset-III	√	-	√	-
Dataset-IV	√	-	-	√
Dataset-V	√	√	√	√

Slope, elevation and aspect features were derived from the DEM. The spatial resolution of the Sentinel-2A image bands was converted to 12.5 m spatial resolution by resampling method to combine with the topographical features. Slope is the angle of between any topographic surface with the horizontal plane and aspect is the position of the slopes against the sun. Additionally, vertical distance between sea level and any point on the land surface is defined as elevation. The slope in the study area varies from 0 and 70 degrees. Moreover, the study site has elevation values ranging from 40 to 1637 meters. In the aspect map produced for the study area, flat regions were represented by -1° and aspect map

delineates nine geographical directions as shown in Figure 2.

2.2. Random Forest Classifier

In random forest algorithm (RF), decision trees are used as the basic classifier; thus, a collective learning model is created by combining multiple decision trees (Breiman, 2001). The RF technique that is one of the collective learning algorithms has become popular in remote sensing due to the high accuracy it provides (Belgiu and Drâgut 2016; Kavzoglu 2017).

Random subsets are obtained from the original training dataset for training decision trees located in the forest. Almost two thirds of the generated subsets are used to form the decision tree structure, and the remaining part is used to test the validity of the model (Kavzoglu et al. 2020). Each decision tree receives one vote as a result of classification; hence, the structure of the tree is determined by number of votes received. If there are enough trees in the forest for a RF model, the probability of overfitting problem is reduced. It is also used not only in classification applications, but also in the regression applications.

3. RESULTS

In order to examine the effect of the auxiliary data on classification accuracy, RF classifier was applied to the constructed datasets. All classification processes were performed using sklearn library in Python programming language. The parameter n_estimators which is the number of trees in forest was selected as 100. The verbose and n_jobs parameters were selected as 1. Overall accuracies and Kappa coefficient values were calculated using standard confusion matrices (Table 2). The calculated F-score values for all LULC class were shown in Table 3 where the highest F-score values were estimated for the water class. It was observed that the highest classification accuracy was estimated with 96.19% overall accuracy using Sentinel-2A image bands, slope, elevation and aspect.

The thematic map was produced with the best performing Dataset-V (Figure 3). It was found that elevation is the most informative or the contributing one compared to other topographical features considering differences in classification accuracy. The second highest overall accuracy result was estimated the with 96.10% using Sentinel-2A image bands and elevation land feature (Dataset-IV).

Table 2. Accuracy assessment results (OA: Overall accuracy)

Datasets	OA (%)	Kappa(%)
Dataset-I	94.86	94.00
Dataset-II	95.67	94.94
Dataset-III	94.76	93.89
Dataset-IV	96.10	95.44
Dataset-V	96.19	95.56

Table 3. F-score values of the datasets (DS: Dataset)

Classes	DS-I (%)	DS-II (%)	DS-III (%)	DS-IV (%)	DS-V (%)
Urban	89.68	91.19	89.61	90.60	91.06
Road	94.58	95.07	94.60	95.38	95.05
Forest	97.68	99.34	97.68	99.17	99.34
Water	100	100	100	100	100
Bare soil	92.78	93.93	92.57	95.25	95.40
Cultivated	96.36	97.68	96.52	98.68	98.84
Non-cultivated	92.79	92.38	92.21	93.46	93.60

Results noticeably indicated that accuracy increased when elevation and slope features were used as auxiliary data. It should be highlighted that the aspect feature did not contribute to the solution by slightly decreasing the classification accuracy. To sum up, the worst classification result (94.76%) was obtained using Sentinel-2A image bands and aspect (Dataset-III).

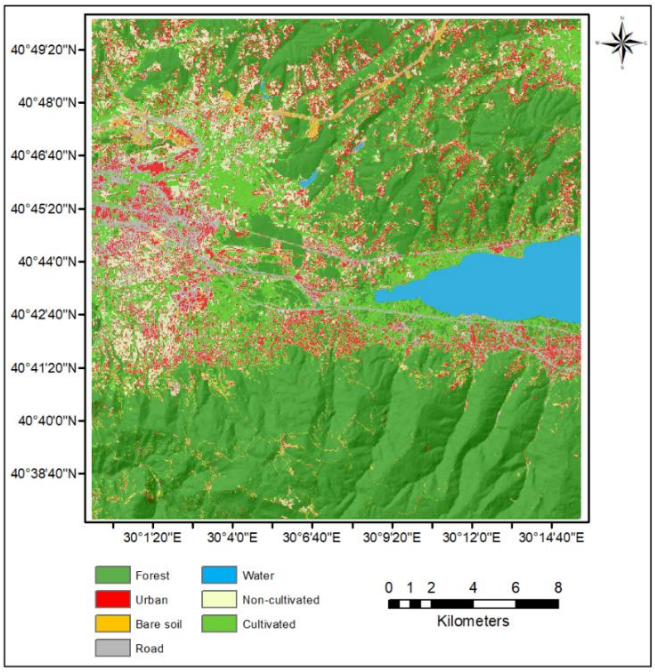

Figure 3. Thematic map produced with full dataset regression applications.

4. CONCLUSION

It is widely accepted that using auxiliary data is influential to enhance classification performance in remote sensing applications. In accordance with the aim of this study, the slope, aspect and elevation data were employed as auxiliary data to investigate their effect on classification result. Few researches focus on the impact of the slope, elevation and aspect on the classification result. In this study, pixel-based classification method was conducted using all datasets and some important results were reached. Firstly, Dataset-V was the most informative and contributing one compared to the other datasets since the highest accuracy was achieved with the use of this dataset. It should be emphasized that the second highest classification accuracy was achieved with the Dataset-VI that elevation used as auxiliary data. The

reason for this result is due to fact that the land elevation change is large in study area. It should be also noted that when slope, elevation and aspect were evaluated together in classification processes, overall accuracy increased significantly. To be more specific, improvement in overall accuracy was approximately 1.5%. This finding indicates that elevation was more informative in classification processes compared to the slope and aspect. Even though the elevation and slope features have positive influence on classification accuracy, aspect caused a slight as specified in Table 2.

As a result, the main purpose of this study is to evaluate the contribution and quantify the effectiveness of DEM derivatives in improving LULC classification using Sentinel-2A image. Results pointed out that slope, aspect and elevation extracted from DEM, could be used as auxiliary data to obtain more accurate thematic maps. It is clearly revealed that high topographic changes in land cover considerably influence the LULC map accuracy. To sum up, the use of slope and elevation information should be utilized for areas with high topographic changes to enhance classification performance.

REFERENCES

Belgiu M & Drâgut L (2016). Random Forest in remote sensing: A review of applications and future directions. ISPRS Journal of Photogrammetry and Remote Sensing, 114, 24-31.

Breiman L (2001). Random Forests. Machine Learning, 45(1), 5-32

Fahsi A, Tsegaye T, Tadesse W & Coleman T (2000). Incorporation of digital elevation models with Landsat-TM data to improve land cover classification accuracy. Forest Ecology and Management, 128(1-2), 57-69.

Hurskainen P, Adhikari H, Siljander M, Pellikka P K E & Hemp A (2019). Auxiliary datasets improve accuracy of object-based land use/land cover classification in heterogeneous savanna landscapes. Remote Sensing of Environment, 233.

Kavzoglu T (2009). Increasing the accuracy of neural network classification using refined training data. Environmental Modelling & Software, 24(7), 850-858.

Kavzoglu T (2017). Object-Oriented Random Forest for High Resolution Land Cover Mapping Using Quickbird-2 Imagery. In Handbook of Neural Computation, edited by Samui P, Roy S S & Balas V E, Amsterdam: Elsevier, Chapter 33, 607-619.

Kavzoglu T, Bilucan F & Teke A (2020). Comparison of Support Vector Machines, Random Forest and Decision Tree Methods for Classification of Sentinel-2A Image. 41st Asian Conference on Remote Sensing.

Nguyen T T H & Pham T T T (2016). Incorporating ancillary data into Landsat 8 image classification process: a case study in Hoa Binh, Vietnam. Environmental Earth Science, 75(5), 1-8.

Rwanga S S & Ndambuki M J (2017). Accuracy Assesment of Land Use/Land Cover Classification Using Remote Sensing and GIS. International Journal of Geosciences, 8(4), 611-622.

Sang X, Guo Q, Wu X, Xie T, He C, Zang J, Qiao Y, Wu H & Li Y (2021). The Effect of DEM on the Land Use/Cover Classification Accuracy of Landsat OLI Images. Journal of the Indian Society of Remote Sensing, 5.

Zhu Z, Gallant A L, Woodcock C E, Pengra B, Olofsson P, Loveland T R, Jin S, Dahal D, Yang L & Auch R F (2016). Optimizing selection of training and auxiliary data for operational land cover classification for the LCMAP initiative. ISPRS Journal of Photogrammetry and Remote Sensing, 122, 206-221.

Intercontinental Geoinformation Days

igd.mersin.edu.tr

Mangrove forests changes and responses to sea level rise based on remote sensing and GIS in PKWS, Cambodia

Nayelin Phorn*[1,2], Jianzhong Lu [2], Pakorn Petchprayoon [3]

[1] *Burapha University, Faculty of Geoinformatics, Chonburi Province, Thailand*
[2]*Wuhan University, State Key Laboratory of Information Engineering in Surveying, Mapping and Remote Sensing, Wuhan, China*
[3]*Burapha University, Faculty of Geoinformatics, Chonburi Province, Thailand*

Keywords
Mangrove forests
Sea Level Rise
Remote Sensing
GIS

ABSTRACT

Mangrove forests in Cambodia can be found along the coastline 435 km. Recently, mangroves have declined by anthropogenic activities and threatened to Sea level rise (SLR) caused by climate change. SLR was estimated to rise 40 to 60 cm in Koh Kong province by the end of the twenty-first century. Mangroves in Peam Krasop Wildlife Sanctuary (PKWS), Cambodia, will extract from 2015 to 2020 using sentinel-2 multi-temporal data with Random Forest classification. Moreover, the changes in mangroves also conducted using MOLUSCE. To predict the vulnerable mangroves area in 2020 due to future SLR based on Geospatial Model and SLR scenarios (40 cm, 60 cm, and 1 m). Mangroves in PKWS were estimated about 7157.90, 7495.21, 7337.47, 6436.26, 6761.66, and 7045.64 ha in 2015, 2016, 2017, 2018, 2019, and 2020. Furthermore, mangroves were increased by 337.31 ha during 2015-2016 but decreased about 157.74, 901.21 ha in 2017 and 2018. However, mangroves undertake to increased 325.40, 283.98 ha in 2019 and 2020. The total changes of mangroves were extremely decreased 112.26 ha from 2015 to 2020. When SLR by 40 and 60 cm, mangrove areas are projected to be inundated about 40.44 ha and reached 53.14 ha by 1 m, respectively.

1. INTRODUCTION

Mangrove forests can be found in the Southwestern part of Cambodia consists of four provinces such as Koh Kong province, Sihanoukville, Kampot, and Kep province (FAO, 2010). In recent years, mangrove forests were declined by anthropogenic activities, and threatened to future Sea level rise (SLR) caused by climate change (Ward et al., 2016). SLR in Cambodia, a 10 cm rise already observed in the last 40 years, and estimated to rise by 40 to 60 cm in Koh Kong by the end of the 21st century. Previous studies have indicated that SLR 1 m would lead to loss of 44 km^2 of coastline in Koh Kong and significantly raise the risk of severe flooding.

Remote Sensing (RS) has assisted as a supportable tool in mangrove forests studies can be found since 1956 (Kumar et al., 2013; Vaiphasa, 2006; Blasco et al., 2001). RS has evolved with the mangrove distribution mapping and monitors the extent of change in mangroves (Jia M, Tian J, Wang L, Yin D, et al. 2019). Until now, it provided the precise discussion of climate change factor impact on mangrove forests. Recently, research by Srivastava et al. (2015) showed that SLR was significantly affected to mangrove extent and mangrove species density by integrating remote sensing with meteorological data.

Thus, mapping the mangrove extent and analyzing the relationship between SLR and mangrove forests are essential for mangroves and as an indicator system for vulnerability assessment and conservation on coastal mangroves in Cambodia.

Due to these problems, the main purpose of this study is to apply the advanced technology of RS and GIS with proposed three objectives, 1) to extract mangrove forests in PKWS, Cambodia, from 2015 to 2020 derived from Sentinel-2 images with Random Forest Classification, 2) to analyze mangrove forests changes from 2015 to 2020 using MOLUSCE, and 3) to assess the vulnerable area of mangrove forests under different SLR scenarios using a Geospatial model based on IPCC's SLR projection.

* **Corresponding Author**

*(Nayelin.csw@gmail.com) ORCID ID 0000-0003-2632-329X
(lujzhong@whu.edu.cn) ORCID ID 0000 – 0002 – 6432 – 8481
(pakorn.pe@buu.ac.th) ORCID ID 0000-0001-8667-2868

Cite this study

Phorn N, Jianzhong L & Pakorn P (2021). Mangrove forests changes and responses to sea level rise based on remote sensing and GIS in PKWS, Cambodia. 2nd Intercontinental Geoinformation Days (IGD), 147-150, Mersin, Turkey

2. METHOD

2.1. Study Area

Peam Krasop Wildlife Sanctuary (PKWS) is a coastal wildlife sanctuary covering 25,897 ha and a unique supporting significant mangroves ecosystem located in Koh Kong Province in the Southwestern of Cambodia. PKWS is an area that concerns about the decline of mangrove forests and vulnerable to rising sea levels caused by climate change (Dara et al. 2009).

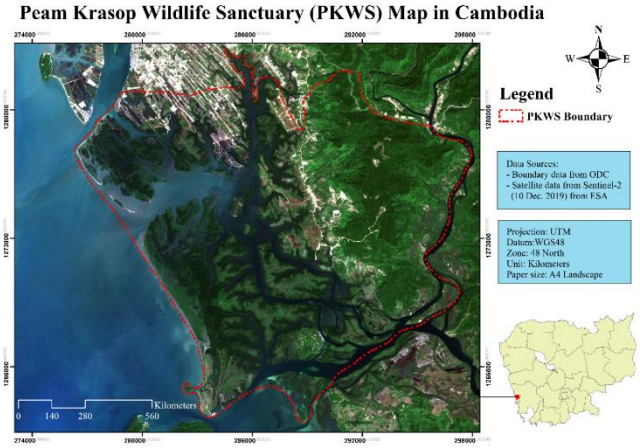

Figure 1. Map of study area

2.2. Data Acquisition

There are significant data include Sentinel-2A multi-temporal data from 2015 to 2020 derived from USGS and ESA. SRTM DEM was collected from USGS in 2014 with spatial resolution 1 Arc-Second Global covering with absolute vertical accuracy of less than 16m (RMSE of 9.73m). Sea level rise (SLR) under IPCC RCP 8.5 emission scenario based on AOGCMs model from CMIP5 are essential as the raster cells data for processing with SRTM DEM data to create a geospatial model of inundation level of SLR impact on mangrove forests areas.

Table 1. Summarized data acquisition

Data	Spatial resolution	Temporal coverage	References
Sentinel-2 L1C	10m	2015-2020	USGS & ESA
SRTM DEM	30 m	2014	USGS
SLR Rates	40cm, 60cm, 1m	The end of 21st century	IPCC's SLR scenarios

2.3. Data Processing

Mangrove forests extraction has been classified using Sentinel-2 images multi-temporal data with Random Forest by dzetsaka Plugin in QGIS. There are two steps for work procedures are training data and perform the type of classification. For training RF algorithm per every satellite image were 240 training data according to create a total of six classes.

There are three levels of land cover classification, land cover in level I, analysis of 6 classes include water body, mangrove forests, saltmarsh, forest lands, settlements, and other lands, and three land cover classes in level II, and one class in level III. The land cover classes level II are merge from land cover classes in level I which there are only three classes include water body, mangrove forests, and non-mangrove forests (merge of saltmarsh, forest lands, settlements, and other lands). For the land cover class in level III, there is only one class of mangrove forests class which other classes have been divided as the NoData.

After land cover classification has been completed, mangrove forests result in 2015 to 2020 were analyzed changed from mangrove forests class to other land cover classes every year between these time period (2015, 2016, 2017, 2018, 2019, 2020) using MOLUSCE in QGIS.

In the last part, mangrove forests extraction in 2020 was used to overlay with a geospatial model from SRTM DEM and SLR scenarios to determine the vulnerable area of mangrove forests in PKWS due to future SLR based on three different SLR scenarios were adopted such as SLR 40 cm, SLR 60 cm, and SLR 1 m.

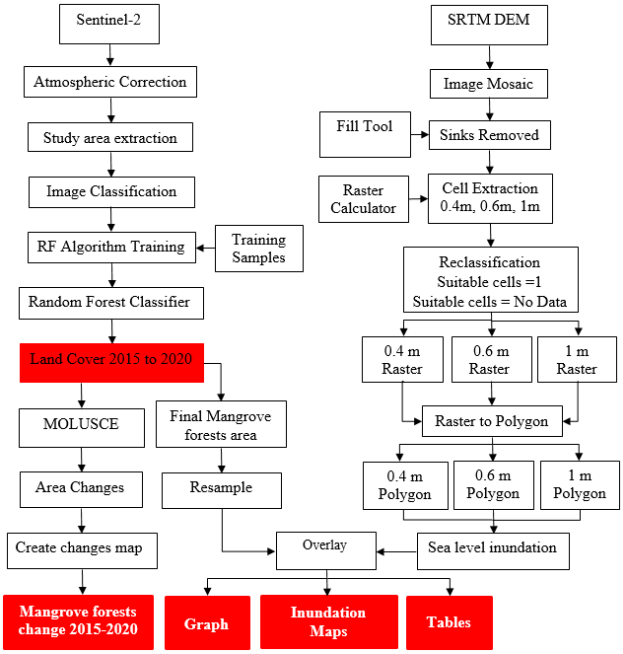

Figure 2. Methodology workflow.

2.4. Accuracy Assessments

For accuracy assessment of land cover classification was assessed using a confusion matrix from Random Forest algorithm training. Accuracy assessments calculated included overall accuracy (OA), kappa statistic, producer accuracy (PA), and user accuracy (UA) calculated using Confusion matrix online calculator based on Marco Vanetti (2007).

3. RESULTS

3.1. Mangrove Extraction

The result of mangrove forests maps in PKWS shown in green polygon (Tab.2, Fig.3). Mangrove forests area in PKWS were 7157.90, 7495.21, 7337.47, 6436.26, 6761.66 and 7045.64 ha in, 2015, 2016, 2017, 2018, 2019, and 2020.

The confusion matrix of the Random Forest algorithm indicated the mangrove forests class with Producer Accuracy around 99.962% and 99.996 in 2015 and 2016, and 100% from 2017 to 2020. The User Accuracy,

mangrove forests were estimated accuracy of 100% every year.

Table 2. Mangrove forests area (Hectare) from 2015 to 2020

Land cover	Area (Hectare)					
Year	2015	2016	2017	2018	2019	2020
Mangrove forests	7157.90	7495.21	7337.47	6436.26	6761.66	7045.64
PA (%)	99.96	99.96	100	100	100	100
UC (%)	100	100	100	100	100	100

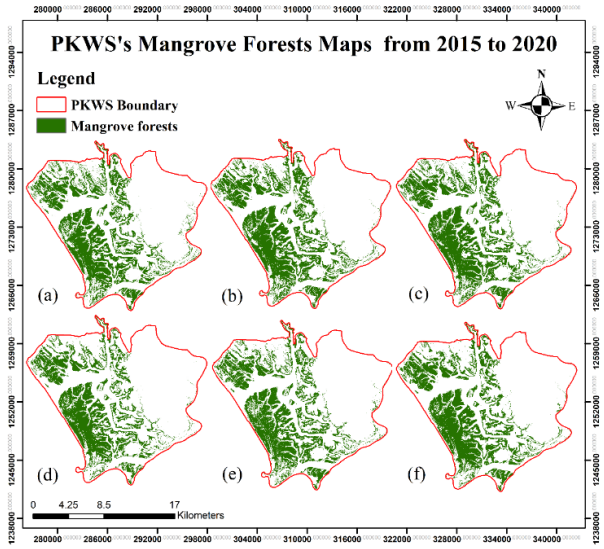

Figure 3. Land Cover Map of PWKS's mangrove forests from 2015 to 2020. (a) Classify 2015, (b) Classify 2016, (c) Classify 2017, (d) Classify 2018, (e) Classify 2019, (f) Classify 2020.

3.2. Mangrove Forests Change from 2015-2020

Mangrove forests estimated to decrease 112.26 ha occurred in PKWS from 2015 to 2020 due to mangrove forests converted to other land cover classes. Additionally, Mangrove forest areas converted to forest lands, other lands, settlements, and water, which were about -387.53, 115.78, 59.57, and -1.29 ha (Fig. 4, Tab. 3).

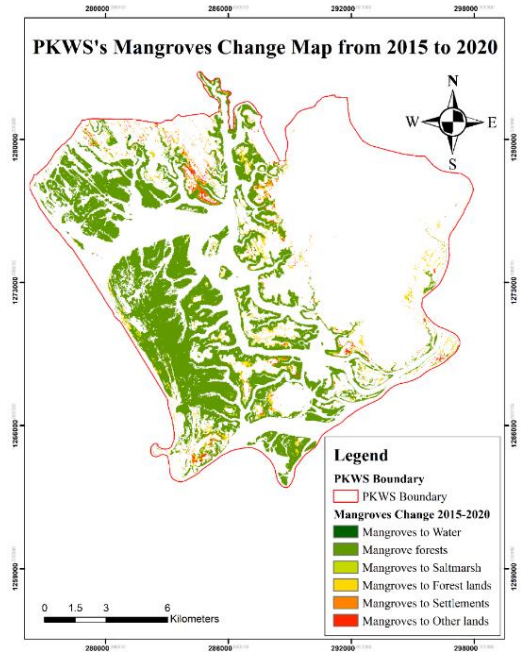

Figure 4. PKWS's Mangrove forests change 2015-2020

Table 3. Mangrove forests change (ha) from 2015 to 2020

Classes	2015	2020	Total
Mangrove to Water	15.62	14.33	-1.29
Mangrove forests	6281.89	6281.89	6281.89
Mangrove to Saltmarsh	167.05	618.96	451.91
Mangrove to Forest lands	505.22	117.69	-387.53
Mangrove to Settlements	60.27	0.7	-59.57
Mangrove to Other Lands	127.85	12.07	-115.78
Total (Hectare)	7157.9	7045.64	**-112.26**

3.3. Potential Inundation of SLR on Mangrove Forests Area

The results specify that potentially inundated mangrove areas will submerge by Sea level rise at the end of the twenty-first century for these different Sea level rise scenarios. Mangrove forests are projected to be inundated 40.44 ha by increasing SLR 40 cm and 60 cm by the end of the year 2100 and reached 53.14 ha by SLR 1 m, respectively.

Table 4. The potential inundation of different SLR scenarios vulnerable to mangrove forests areas in Peam Krasop Wildlife Sanctuary.

Mangrove forests areas	Sea Level Rise Scenarios		
	40 cm	60 cm	1m
Vulnerable area (hectare)	40.44	40.44	53.14

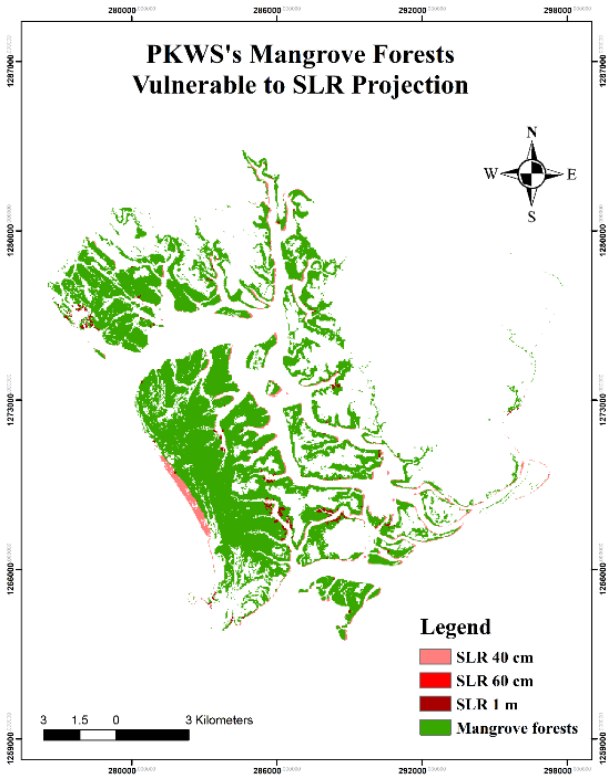

Figure 5. Analysis the inundation of mangrove areas in Peam Krasop Wildlife Sanctuary due three different SLR scenarios

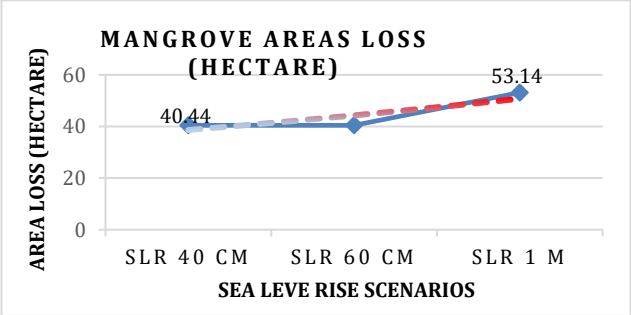

Figure 6. Total mangrove forests area loss under three different SLR scenarios in Peam Krasop Wildlife Sanctuary by the end of twenty-first century

4. DISCUSSION

In this study, mangrove forests maps of Peam Krasop Wildlife Sanctuary in Cambodia from 2015 to 2020 were produced. To the best of my knowledge, this is the first interesting topic conducted in Cambodia about the potential impact of Sea level rise to the mangrove forest areas in Cambodia based on Remote Sensing and GIS techniques. For conducted these mangroves maps from 2015 to 2020 defined from classification employed time-series data of multi-temporal Sentinel-2 L1C optical imageries with Random Forest classification in dzetsaka plugin that can be achieved an overall accuracy reach to 99%. This accuracy is based on the Random Forest algorithm training with 240 samples per satellite imageries.

For future work will focus on developing a geospatial model of combination DEM with high spatial resolution and Sea level rise data observing by tide gauge or altimeter satellite. This could be assessing the accuracy of this model in the future. This future work should be considering and research in more detail in Cambodia, while our research was the first knowledge about the vulnerable area of mangrove forests that will be affected by future Sea level rise using advanced technology of Remote Sensing (RS) and GIS model. Our research result might be accurate or not accurate depended on developing a geospatial model using the medium spatial resolution of DEM overlap with land cover's mangrove forests. The main reason to research as s study about the potential impacts of Sea level rise to mangrove forests, in the previous research studies, mostly used the lower accuracy DEM to create the GIS model to assess the impact of Sea level rise on land cover. Although this study is really important to enhance the mangrove forests changes and show resilience to future Sea level rise.

5. CONCLUSION

A quantitative of mangrove forests maps in Peam Krasop Wildlife Sanctuary between 2015 and 2020, result has shown mangrove forest areas estimated 7157.90, 7495.21, 7337.47, 6436.26, 6761.66, and 7045.64 ha in 2015, 2016, 2017, 2018, 2019, and 2020.

Either, mangrove forest areas in PKWS in this study were analyzed changed from 2015 until 2020 based on MOLUSCE. We contribute to mangrove forest area changes in this period. Mangrove forests increased by 337.31 ha between 2015 and 2016. In contrast, mangrove forests in PKWS were decreased 157.74 ha in 2017. Similarly, mangrove forests have continued to lose 901.21 ha from 7337.47 ha to 6436.26 ha in 2018. However, mangrove forests started increasing 325.40 ha in PKWS in 2019 increased from 6436.26 ha to 6761.66 ha. Mangrove forests continued to increase by approximately 283.98 ha in 2020 as well. The total long-term changes of mangrove forests in Peam Krasop Wildlife Sanctuary from 2015 to 2020, mangrove forests were lost about 112.26 ha from 7157.90 to 7045.64 ha.

Therefore, this study provides new knowledge about the vulnerable area of mangrove forests that will influence by future Sea level rise in Cambodia. Especially, lowly area of mangrove forests projected to inundate or impact areas about 4.44 ha by SLR 40 to 60 cm at the end of the twenty-first century and predicted to be inundated 53.14 ha by SLR 1 m.

ACKNOWLEDGEMENT

This work was supported by Geo-Informatics and Space Technology Development Agency (GISTDA), Burapha University, and Wuhan University.

REFERENCES

Blasco, F., Aizpuru, M., Gers, C., 2001. Depletion of the mangroves of continental Asia. Wetl. Ecol. Mang. 9, 255-266

Dara, A., Piseth, H., Mather, R., & Kim Sreng, K. (2009). Integrated assessment for identification of a preliminary zoning scheme for Peam Krasob Wildlife Sanctuary in southwest Cambodia.

IPCC, 2013: Summary for Policymakers. In: Climate Change 2013: The Physical Science Basis. Working Group I Contribution to the Fifth Assessment Report of the Intergovernmental Panel on Climate Change, eds. T. F. Stocker, D. Qin, G.-K. Plattner, M. Tignor, S. K. Allen, J. Boschung, A. Nauels, Y. Xia, V. Bex and P. M. Midgley, Cambridge University Press, Cambridge, UK and New York, NY, USA.

Jia, M., Wang, Z., Zhang, Y., Mao, D., Wang, C., 2018. Monitoring loss and recovery of mangrove forests during 42 years: the achievements of mangrove conservation in China. Int. J. Appl. Earth Obs. Geoinf. 73, 535–545.

Kumar, T., Panigraphy, S., Kumar, P., Parihar, J.S., 2013. Classification of flowrisstic composition of mangrove forests using hyperspectral data: case study of Bhitarkanika National Park, India. J Coast. Conserv. 17, 121-132.

Srivastava, P.K, Mehta, A., Gupta, M., Singh, S.K, Islam, T., 2015. Assessing impact of climate change on Mundra mangrove forest ecosystem, Gulf of Kutch, western coast of India: a synergistic evaluation using remote sensing. Theor. Appl. Climatol. 120, 685-700.

Vaiphasa, C., 2006. Consideration of smoothing techniques for hyperspectral remote sensing. ISPRS J. Photogramm. Remote Sens. 60, 91-99.\

Ward, R.D., Friess, D.A., Day, R.H., Mackenzie, R.A., 2016. Impacts of climate change on mangrove ecosystems: a region by region overview. Ecosyst. Health Sustain. 2 (4), e01211. https://doi.org/10.1002/ehs2.121

Intercontinental Geoinformation Days

igd.mersin.edu.tr

Effect of elevation on land surface temperature (LST) variation in Jos and Environs, Nigeria

Bello Abubakar Abubakar*[1], Sani Abubakar Abubakar [2]

[1] *Nigerian Defence Academy, Faculty of Arts and Social Sciences, Department of Geography, Kaduna, Nigeria*
[2] *Kaduna Polytechnic, School of Geodesy and Land Administration, Department of Photogrammetry and Remote Sensing, Kaduna, Nigeria*

Keywords
Land Surface Temperature
Elevation
Environmental Lapse Rate
Jos

ABSTRACT

Elevation is one of the factors causing temperature variation in different parts of the world. The increase in elevation usually resulted in the decrease in temperature, a phenomenon called Environmental Lapse rate (ELR). This research examines the effect of elevation on Land Surface Temperature (LST) in Jos and environs, Nigeria. Satellite data obtained from Shuttle Radar Topography Mission (SRTM) and Landsat 8 OLI/TIRS were used. The elevation of the study area was obtained from the SRTM data. The Landsat 8 data were used to derive the LST using single-channel algorithm. The relationship between elevation and LST was analysed using correlation analysis. The results showed that the study area is generally on a high elevation ranged from 550 metres to 1,800 meters above sea level. There was variation in the spatial distribution of the LST as a result of differences in elevation. The LST ranged from 19°C to 35°C was recorded in the highest and lowest elevation respectively. The LST decreased by 16°C for 1,250 meters increase in elevation indicating the effect of Environmental Lapse Rate (ELR). A moderate negative correlation was found between LST and elevation (r =0.46). Elevation was found to be a comfortable place of living as a result of the lower surface and air temperature.

1. INTRODUCTION

Currently, the rising of temperature as a result of climate change is affecting the world (Tofan et al. 2020; Me-Ead and McNeil 2016). Land Surface Temperature (LST) is one of the essential parameters considered in the study of climate change (Sumit et al. 2018). It is the skin temperature of the surface that involved the soil and vegetation surfaces (Sumit et al. 2018). The spatial and temporal variation of the LST is important in understanding the interaction between human activities and the environment (Thanh 2018; Stathopoulou and Cartalis 2009). The surface temperature has an impact on the air temperature (Koç et al. 2019; Song et al. 2017; Chrysoulakis et al. 2013). Air is heated when it contacts warm surfaces which make it rise up (Mitchell 2011; Lowry 1967). According to the United States Environmental Protection Agency (EPA), excess heat has effect on human heath causing discomfort and illness like heat exhaustion, heat stroke, heat cramps and heat related mortality. For instance, in the United States, from 1979-2003, over 8000 people died as a result of excess heat (EPA, 2017). In Europe, 20,000 lives were claimed by heat wave in 2003 mostly poor and elderly (Satterthwaite, 2008). Increase in temperature forces people to areas of comfort (Koç et al 2019).

Land cover type and elevation are some of the important factors responsible for the variability of the LST (Malb´eteau et al. 2017). Temperature tends to decrease with the increase in elevation (Xiaoxue et al. 2020; Bailey 1996). This decrease in temperature is referred to as the Environmental Lapse Rate (ELR) and for every 1,000 metres, there is a decrease of 5°C to 10°C (Sumit et al. 2018). Measurement of LST from the ground stations cannot represent the surface temperature of an area most especially developing countries that have few stations (Thanh et al. 2018). Satellite measurement provides a better result than the interpolated ground stations (Sumit et al. 2018; Cheval and Dumitrescu 2009). LST can be measured by the ground-based, air-born and satellite-based sensors (Denis et al. 2015). Some of the prominent satellite imageries used in retrieving the LST include Moderate Resolution Imaging Spectroradiometer (MODIS), Advanced Very High

* Corresponding author
*(abubakarbello1064@gmail.com) ORCID ID 0000 – 0003 – 3959 – 876X
(abu86sani@gmail.com) ORCID ID 0000 – 0002 – 7521 – 7365

Cite this study
Bello A. A & Sani A. A. (2021). Effect of elevation on land surface temperature (LST) variation in Jos and Environs, Nigeria. 2nd Intercontinental Geoinformation Days (IGD), 151-154, Mersin, Turkey

Resolution Radiometer (AVHRR), Advanced Spaceborne Thermal Emission and Reflection Radiometer (ASTER) and Landsat (Thanh et al. 2018). Many types of research on the LST were conducted on the flat surfaces focusing on the effect of land use/land cover on the LST variation. Relief is one of the factors that cause variation in the LST (Tofan et al. 2020; Gao et al. 2008). Twenty percent of the world continental surface is covered by the mountains (Malb´eteau et al. 2017; Meybeck et al. 2001). In Nigeria, the Jos plateau formed a major part of the north-central highlands. Elevation affects the climatic system of the area. Therefore, this research examines the effect of elevation on LST variation in Jos and environs.

2. METHOD

2.1 Study Area

The study area is located between Latitudes 9°17' and 10°23'N and Longitude 8°33' and 9°19'E covering an area of 5,324.62 km^2. It covers Jos North, Jos South, Bassa, Riyom, Barikin Ladi and Jos East Local Government Areas of Plateau State, North-central Nigeria. (Fig. 1). The climate is a tropical climate with a mean annual rainfall of 1,324mm with the highest rainfall recorded in July and August (Lekwot et al 2015). There is also a temperate climate as a result of the high altitude which is responsible for the low temperature with a monthly average temperature between 21°C and 25°C throughout the year (Isioye et al 2020). The coldest temperature is recorded during Harmattan from December to February while the warmest temperature is recorded between March and April (Lekwot et al 2015).

The vegetation is characterised by stunted trees with tall grasses and shrubs (Atipo et al 2020). The topography is characterised by highlands with different height ranges from 1,200 meters to 1,825 meters above sea level (Lakwot et al 2015). Jos plateau located in the city is the source of many rivers in Northern Nigeria like Kaduna, Gongola, Hadejia and Yobe rivers (Goyal and Pathirage 2018).

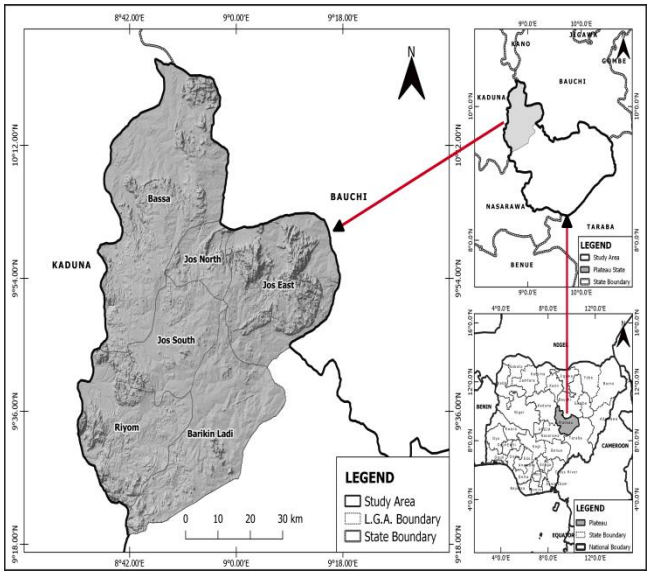

Figure 1. Map of the study area

2.2. Generation of Elevation

The elevation data were obtained from NASA's Shuttle Radar Topography Mission (SRTM). The 30 meters spatial resolution imagery was used to generate the Digital Elevation Model (DEM) using QGIS 3.14 'Pi'.

2.3. Calculation of LST

Landsat 8 (OLI/TIRS) acquired on the 13th November, 2020 was used retrieve the Land Surface Temperature (LST). The thermal band 10 was resampled to 30 meters resolution like other bands. Single-channel algorithm was used to derived the LST from the imagery (Palafox-Juárez et al. 2021).

Firstly, the spectral radiance of the top of the atmosphere was calculated followed by the brightness temperature from the absolute radiance values. The obtained results were converted to degree Celsius from degree Kelvin. Normalize Difference Vegetation Index (NDVI) was used to extract the surface emissivity to estimate the LST. Finally, the LST was calculated using the brightness temperature and surface emissivity. QGIS 3.14 'Pi' was used for the processing of the data.

3.4. Relationship Between LST and Elevation

The LST map was overlaid on the elevation map and the LST values and their corresponding elevation values were extracted. The values were used to assessed the relationship between the LST and elevation. Statistical Package for Social Science (SPSS) was used for the correlation analysis.

3. RESULTS

Figure 2 shows the elevation of the study area. The relief of the study area is unevenly distributed and ranged from 550 to 1,800 meters. The lowest elevation was found in Riyom in the south-west of the study area. A lower elevation of 800 meters was found in the north and eastern part of Jos East. Elevation ranged between 1,050 and 1,550meters was found mostly at the centre of the area in Jos North and South and extended to the southern part. The highest elevation was found in the east with a height of 1,800 meters.

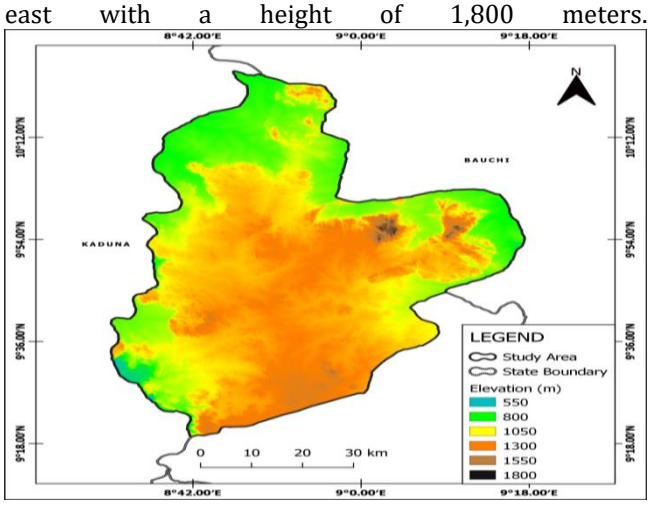

Figure 2. Elevation of the study area

2.3. Calculation of LST

Figure 3 shows the distribution of the surface temperature. The LST distribution varies and ranged from 19°C to 35°C. The highest surface temperature of 35°C was recorded in western Riyom, northern Bassa and Eastern Jos East with an elevation of 800 meters. A temperature ranged from 25.4°C to 28.6°C was found in most of the centre southern parts with a higher elevation ranged from 1,050 to 1,300 meters. Low surface temperature (22.2°C) was found in Barikin Ladi in the south with an elevation of 1,550 metres. The lowest surface temperature of 19°C was recorded in the highest points of the area with an elevation of 1,800 meters located in Jos East in the eastern part of the study area.

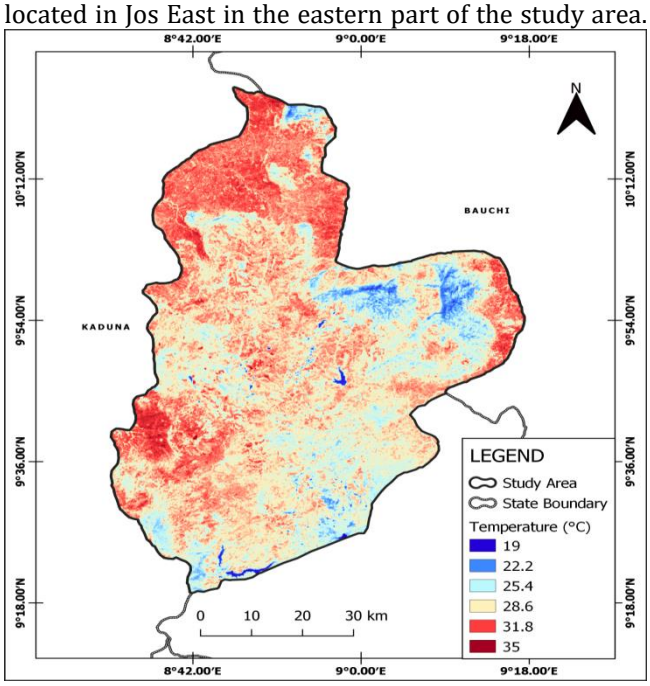

Figure 3. Land Surface Temperature of the Study Area

2.4. Relationship Between LST and Elevation

Figure 4 shows the relationship between LST and elevation. A weak linear relationship between the LST and elevation was observed. The correlation coefficient was r=0.46. The relationship shows that increase in elevation resulted to decrease in LST. The increase of 1,250 meters resulted to the decrease of 16°C.

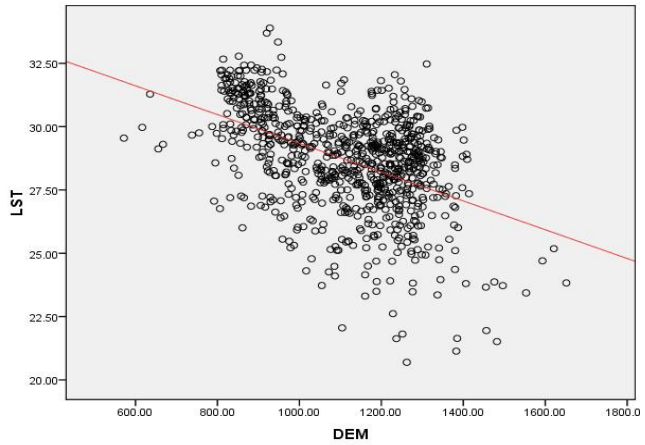

Figure 4. Scatter plot of LST and elevation

4. DISCUSSION

The elevation of the study area is generally high ranged from 550 meters to 1,800 meters. This is because of the highlands nature of the topography formed by the basement complex rocks. The study area also formed part of the north-central highland that is the sources of many rivers in Northern Nigeria (Goyal and Pathirage 2018). The elevation was reported to be ranged from 1,200 to 1,829 meters above sea level (Lakwot et al 2015).

The spatial distribution LST varies with elevation with 19°C and 35°C as the lowest and highest values respectively. The increase in elevation led to a decrease in LST. This is as a result of the Environmental Lapse Rate (ELR) effect where temperature decreases with an increase in altitude. For every 1000 meters of elevation, there is a decrease in temperature ranges from 5°C to 10°C (Sumit et al. 2018). The low air temperature on the high elevation lowered the surface temperature. The relationship between LST and elevation showed a moderate negative relationship with correlation coefficient r=0.46. This is because of the influence of elevation in decreasing the surface temperature. The high elevation is responsible for the temperate type of climate that makes the temperature of the study area lower throughout the year (Isioye et al 2020). The lower air temperature affects the surface temperature by lowering it. This result agreed with that of Sumit et al. (2018) that found a decrease of 3.5°C-4.6°C per 1,000 metres in Jaipur, India with a strong linear correlation (r=0.73-0.87) between LST and elevation. The moderate negative correlation found in the study area could be attributed to the interference of the terrain factors (aspect, slope and shaded relief), land use/land cover and weather condition.

5. CONCLUSION

This study examined the effect of elevation on LST variation in Jos and environs located in the North-central highland in Northern Nigeria. The study area is located on a high elevation raged from 550meters to 1,800 metres above the sea level. The LST ranged from 19°C to 35°C and varies spatially with elevation. The LST decreased with the increase in elevation indicating Environmental Lapse Rate (ELR). For the increase of 1,250 meters, there is a decrease of 16°C. Decrease in air temperature as a result of the increase elevation is responsible for the lower surface temperature. The relationship between LST and elevation showed a moderate negative linear relationship (r=0.46). Atmospheric condition, land use/ land cover and nature of topography influence the decrease of LST with the increase in elevation. High areas provide comfortable places for living because of the lower surface and air temperature.

REFERENCES

Atipo M, Olarinaye O, Awojoyogbe B & Kolo M (2020) High terrestrial radiation level in an active tin-mine at Jos South, Nigeria. J. Appl. Sci.

Environ. Manage., 24(3)435-442. https://dx.doi.org/10.4314/jasem.v24i3.6

Bailey R G (1996) *Ecosystem geography* (ed. Bailey, R. G.), 116-120, Springer

Cartalis C (2013). Sustainable urban metabolism as a link between bio- physical sciences and urban planning: The BRIDGE project. Landscape and Urban Planning, 112, 100-117.

Cheval S & Dumitrescu A (2009). The July urban heat island of Bucharest as derived from MODIS images. Theoret. Appl. Climatol., 96, 145-153.

Chrysoulakis N, Lopes M, San Jose R, Grimmond C S B, Jones M B, Magliulo V, Klostermann J E M, Synnefa A, Mitraka Z, Castro E A, Gonzalez A, Vogt R, Vesala T, Spano D, Pigeon G, Freer-Smith P, Staszewski T, Hodges N, Mills G & Denis M, Scotty S, & Thomas A (2015). Land surface temperature and surface air temperature in complex terrain. IEEE Journal of Selected Topics in Applied Earth Observations and Remote Sensing, 8(10), 4762-4774.

Environmental Protection Agency (2017). Heat Island Impact. Retrieved from http://www.epa.gov/heat-islands/heat-island-impacts.

Gao M, Qin Z, Qiu J, Liu S, Xu B, Li W & Yang X (2008). Retrieving spatial-temporal variation of land surface temperature in Tibetan Plateau for the years 2005-2006 from MODIS satellite data. 7110 (June 2014), 71101A-71101A – 10. https://doi.org/10.1117/12.800098.

Goyal S & Pathirage C (2018). Farmers perceptions of climate change related events in Shendam and Riyom, Nigeria. Economies, 6(70), 1-26. https://doi:10.3390/economies6040070.

Isioye O A, Akomolafe E A, Abubakar A Z & Dashe P (2020). Analysis of Urban Heat Island of Jos and environs using remotely sensed data. FUTY Journal of the Environment, 14(1), 121-138.

Koç A 1, Karahan A E & Bingül M B (2019). Determination of relationship between land surface temperature and different land use by CHAID analysis. Applied Ecology And Environmental Research, 17(3), 6051-6067.

Lekwot V E, Yakubu A A, Kwesaba D A & Sahabo A A (2015). An analysis of inner city decay: A study of some selected slums in Jos metropolis, Plateau State, Nigeria. International Journal of scientific and Technology Research, 4(2), 171-176.

Lowry W (1967). The climate of cities. Scientific American, 15-23.

Malb´eteau Y, Merlin O, Gascoin S, Gastellu J P, Mattar C, Olivera-Guerra L, Khabba S & Jarlan L (2017). Correcting land surface temperature data for elevation and illumination effects in mountainous areas: A case study using ASTER data over a steep-sided valley in Morocco. Remote Sensing of Environment, 189, 25-39.

Me-Ead C & McNeil N (2016). Graphical display and statistical modeling of temperature changes in tropical and subtropical zones. Songklanakarin. Journal of Science and Technology, 38(6), 715-721.

Meybeck M, Green P & Vo¨ro¨smarty C (2001). A new typology for mountains and other relief classes. Mountain Research and Development, 21(1), 34-45.

Mitchell B C (2011). Urbanization and land surface temperature in Pinellas County, Florida. M.A Dissertation, University of South Florida, United States of America.

Palafox-Juárez E B, López-Martínez J O, Hernández-Stefanoni J L & Hernández-Nuñez H (2021). Impact of urban land-cover changes on the spatial-temporal land surface temperature in a tropical city of Mexico. ISPRS International Journal of Geo-Information 10(76), 1-16. https://doi.org/10.3390/ijgi10020076

Satterthwaite D (2008). Climate change and urbanization: Effects and implications for urban governance. United Nations expert group meeting on population distribution, urbanization, internal migration and development. Population Division Department of Economic and Social Affairs United Nations Secretariat New York, 21-23 January 2008.

Stathopoulou M & Cartalis C (2009). Downscaling AVHRR land surface temperatures for improved surface urban heat island intensity estimation. Remote Sens. Environ., 113, 2592-2605.

Song J, Wang Z H, Myint S W & Wang C Y (2017). The hysteresis effect on surface-air temperature relationship and its implications to urban planning: An examination in Phoenix Arizona, USA. Landscape and Urban Planning, 167, 198-211.

Sumit K, Rohit G, Nivedita K & Aneesh M (2018). Assessment of land surface temperature variation due to change in elevation of area surrounding Jaipur, India. The Egyptian Journal of Remote Sensing and Space Sciences, 21, 87-94.

Thanh N P, Martin K & Trong P T (2018). Land surface temperature variation due to changes in elevation in Northwest Vietnam. Climate, 6 (28), 1-19. https//:doi:10.3390/cli6020028

Tofan A E P, Munawar M, Muhammad R T, Sarawuth C, Apiradee L & Don Mc N (2020). Land surface temperature assessment in Central Sumatra, Indonesia. Indonesian Journal of Geography, 52(2), 239-245. https://doi.org/10.22146/ijg.51327

Intercontinental Geoinformation Days

igd.mersin.edu.tr

Application of UAV-Based multispectral images for accessing oil palm trees health using online AI Platform

Hong Lay[*1,2,3], **Zhenfeng Shao** [2], **Sanara Hor** [3]

[1]*Burapha University, Faculty of Geoinformatics, Chonburi Province, Thailand*
[2]*Wuhan University, State Key Laboratory of Information Engineering in Surveying, Mapping and Remote Sensing, Wuhan, China*
[3]*Royal University of Agriculture, Faculty of Land Management and Land Administration, Phnom Penh, Cambodia*

Keywords
Oil palms
Multispectral
Object extraction
UAV
Vegetation indices

ABSTRACT

The oil palms are a major product in Cambodia to export local and worldwide which provides job opportunities and develops infrastructure over there. In this study, two plots of oil palms have collected by Unmanned Aerial Vehicle (UAV). The Artificial Intelligence (AI) online platform has been used to extracting oil palm trees from very-resolution imagery. In extracting oil palm tree is applied Picterra platform that it has to bring AI-powered for object detection and geospatial analysis. In this way, oil palm trees are counting automatically and manually, the result shows that high overall accuracy by automatically. The oil palm tree health is estimated by using vegetation indices that it has such as Green Normalized Different Red Edge (NDRE), Normalized Different Vegetation Index (GNDVI), and Normalized Different Vegetation Index (NDVI). Vegetation indices maps have been created from UAV-based multispectral images. It has estimated oil palm tree health using Green, Red, Red Edge, and Near-Infrared bands from the multispectral camera. The vegetation indices have been compared with maximum, minimum, mean, and standard deviation in vegetation and chlorophyll content. The NDVI indices are better than NDRE and GNDVI. The spectral profile has been created in both plots based on the pixel value of vegetation indices of reflectance and absorption.

1. INTRODUCTION

Oil palms are the product of the agriculture sector in Cambodia. Colchester et al. (2011) mention that the area coverage of oil palm plantations is 1188,00 ha of Economic Land Concessions in Cambodia. Mong Reththy Investment Cambodia Oil Palm Co., LTD (MRICOP) is the first company that the company has been invested in oil palm plantations coverage 11000 ha in Cambodia since 1995, according to (Saing et al. 2012). Four estates (Estate A, B, C & D) have been planted oil palm trees. As of 2016, oil palm trees have been planted on 15173 ha.

In estimating oil palm trees are popular which utilize Unmanned Ariel Vehicle (UAV) in this era. UAV has become an application in Photogrammetry and Remote Sensing (Yu et al. 2017). UAV has been demonstrated in agriculture that it provides multispectral bands of Parrot Sequoia Multispectral camera sensor. The sensor has been delivered Green band, Red band, Red Edge band, Near-Infrared band, and RGB camera. In the same way, (Raeva et al. 2019) assess those vegetation indices (NDRE, GNDVI & NDVI) with multispectral imagery from UAV. Therefore, multispectral imagery can be used in estimating oil palm tree health from UAV based on vegetation and chlorophyll content.

As shown above, UAV-based multispectral and very high-resolution imagery are essential for delivering into large oil palms area. The oil palm tree health is going to analyze a single tree and find where is allocated. Moreover, this research is going to apply UAV-based multispectral images to be detected and counted oil palm trees by using an online AI platform.

There are two objectives of the research as the following 1) to detect and count oil palm trees of very high-resolution images from UAV with an online AI platform and 2) to evaluate and compare oil palm trees health by Using NDRE, GNDVI, and NDVI indices in vegetation and chlorophyll content.

* **Corresponding Author**

*(layhong6363@gmail.com) ORCID ID 0000-0003-2091-0151
(shaozhenfeng@whu.edu.cn) ORCID ID 0000-0003-4587-6826
(hsanara@hotmail.com) ORCID ID 0000-0001-8801-6805

Cite this study

Lay H, Zhenfeng S & Hor S (2021). Application of UAV-Based multispectral images for accessing oil palm trees health using online AI Platform. 2nd Intercontinental Geoinformation Days (IGD), 155-158, Mersin, Turkey

2. METHOD

2.1. Area of Interest (AOI)

The oil palms are the largest area in Cambodia, the study cannot be detected the whole area of it. So, the study is going to collect 2 plots of the oil palms farm by using the UAV (DJI Matrice 100) at Mong Reththy Investment Cambodia Oil Palm Co., LTD, Sihanoukville, Cambodia. The location of the study area's latitude and longitude is 10.965651 North and 103.894319 East.

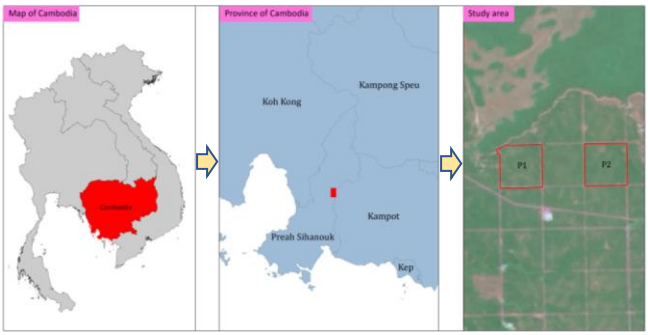

Figure 1. Map of the study area

2.2. Data Acquisition

Use DJI Matrice 100 to collect raw images of oil palm trees, that raw images get from RGB (Red, Green, and Blue bands) and multispectral camera (Green, Red, Red Edge, and Near-infrared bands (Table 1).

Table 1. DJI Matrice 100 flight planning

Plot	Front Overlap	Side Overlap	Height	Coverage
P1	75%	75%	150m	25 ha
P2	75%	75%	150m	25 ha

2.3. Research Framework

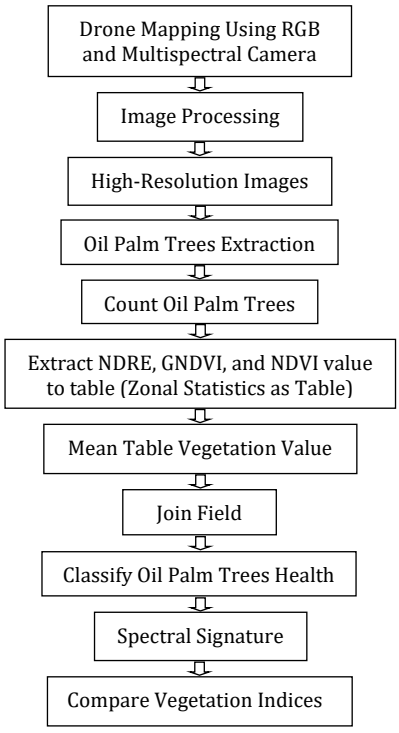

Figure 2. The workflow of the research

2.4. Vegetation Indices Calculation

The NDRE estimates tree leaf that it identifies chlorophyll absorption of Red wavelengths with the higher reflectance of NIR wavelengths, and the Red Edge wavelength to indicate chlorophyll content, according to (Carlson and Ripley 1997) (Equation 1).

$$NDRE = (NIR - REDGE) / (NIR - REDGE) \quad (1)$$

Where: NIR refers to Near-Infrared band and REDGE refers to Red Edge band.

According to (ESRI, 2020) Green Normalized Difference Vegetation Index (GNDVI) is a vegetation index that has been used in NIR and Green bands in estimating photosynthetic activity (Equation 2).

$$GNDVI = (NIR - Green) / (NIR + Green) \quad (2)$$

Where: NIR refers to the Near-Infrared band and Green refers to the Green band.

Karaburun (2010) explains that the well-known NDVI used for estimating green vegetation that refers to Normalized Different Vegetation Index (Equation 3).

$$NDVI = (NIR - Red) / (NIR + Red) \quad (3)$$

Where: NIR refers to the Near-Infrared band and RED refers to the Red band.

3. RESULTS &DISCUSSION

3.1. Oil Palm Trees Extraction

The result of oil palm tree extraction occurred in the polygon by using an online AI platform. The total of oil palm tree extraction of P1 is 4.70 ha and P2 is 4.10 ha. After oil palm trees are extracted, the next step counts the number of oil palm trees in both plots. Moreover, the number of oil palm trees counted automatically of P1 is 3456 trees and P2 is 3477 trees, and manually of P1 is 3447 trees and P2 is 3462 trees. See detailed at (Table 2) and on the map (Figure 3).

Table 2. Extracting and counting oil palm trees

Plot	Extraction	Automatically	Manually
P1	4.70 ha	3456 trees	3447 trees
P2	4.10 ha	3477 trees	3462 trees

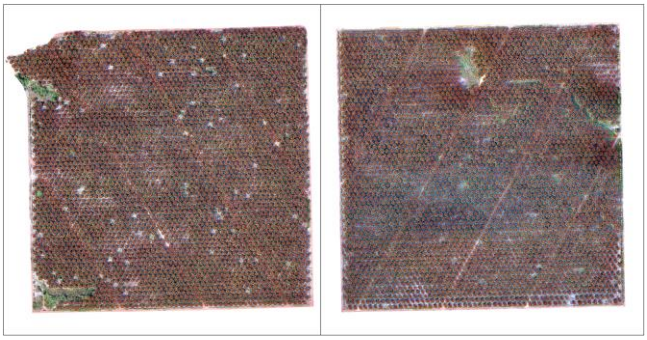

Figure 3. Map of oil palm trees extraction

3.2. Accuracy Assessment

The result of detecting oil palm trees is provided overall accuracy of P1 is 100% and P2 is 98.97%. Even though the oil palm tree detection appears high accuracy assessment but it shows missing detection and detects different objects. P1 is missing detection appears one oil palm tree and detects seven different objects on the unknown object. For P2 is missing detection appears one palm tree and fourteen different objects on the unknown trees. See detailed (Table 3).

Table 3. The overall accuracy of oil palm trees detection

Plot	Annotation	Testing	Training	Overall accuracy
P1	141	1	5	100%
P2	140	1	5	98.97%

3.3. Oil Palms Health Estimation

The result estimates oil palm tree health used and compared the vegetation indices that have Normalized Difference Red Edge (NDRE), Green Normalized Difference Vegetation Index (GNDVI), and Normalized Difference Vegetation Index (DNVI).

The NDRE used to identify leaf of oil palm tree that it called chlorophyll reflectance and absorbs at red edge and near-infrared. There are 3 classifies of oil palm trees chlorophyll estimation of P1 and P2 (Figure 4). P1 has such as low chlorophyll (0.14 – 0.29), medium chlorophyll (0.29 – 0.33) and high chlorophyll (0.33 – 0.44). P2 result shows that low chlorophyll (0.13 – 0.26), medium chlorophyll (0.26 – 0.31) and high chlorophyll (0.31 – 0.40).

GNDVI is determining water and nitrogen uptake into the plant canopy reflectance and absorbs at green and near-infrared. The classification for P1 is 3 classes and P2 is 3 classes of oil palm trees health estimation (Figure 5). P1 has such as unhealthy (0.41 – 0.65), moderately healthy (0.65 – 0.71), and very healthy (0.71 – 079). P2 shows on the map that moderately healthy (0.46 – 0.69) and Very healthy (0.69 – 0.78).

NDVI is estimated healthy by reflectance and absorbs at red and near-infrared. The classification for P1 is 3 classes and P2 is 2 classes of oil palm trees health estimation (Figure 6). P1 has such as unhealthy (0.33 – 0.71), moderately healthy (0.71 – 0.81), and very healthy (0.81 – 0.88). And P1 the result occurs that moderately healthy (0.54 – 0.81) and very healthy (0.81 – 0.88).

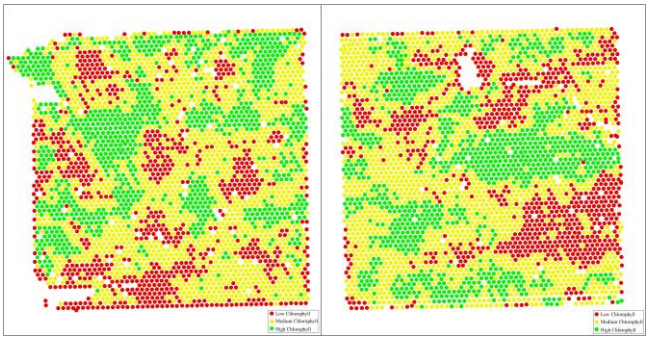

Figure 4. Map of NDRE

Figure 5. Map of GNDVI

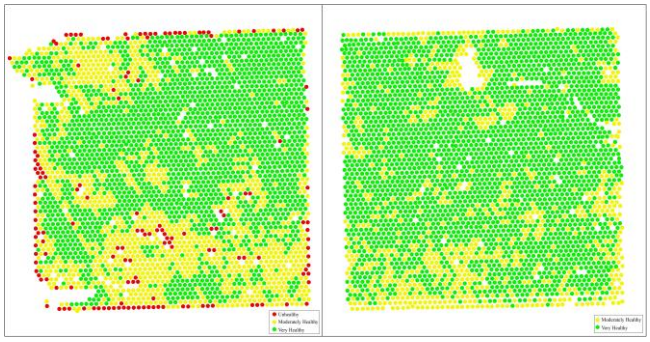

Figure 6. Map of NDVI

The compression of green band, red edge band, red band, and near-infrared band in the spectral signature of oil palm tree health based on GNDVI and NDVI indices. Use ten oil palm trees per one classify to compare the spectral profile of absorbs and emittance of each band. The result of P1 (Figure 7) shows that unhealthy absorbs low at Green and Red bands, and emittances low at Red Edge and Near-Infrared bans. Moderately healthy absorbs medium Green and Red bands, and emittances medium at Red Edge and Near-Infrared bands. Very healthy absorbs high at Green and Red bands, and emittances high at Red Edge and Near-Infrared bands.

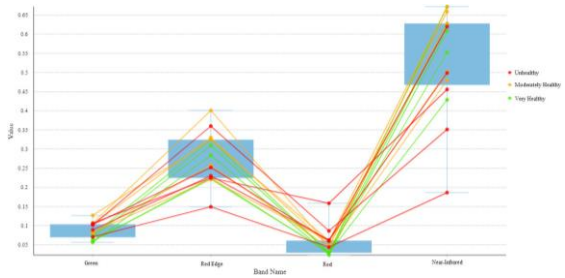

Figure 7. Comparison spectral profile of P1

Use ten oil palm trees per one classify to compare the spectral profile of absorbs and emittance. The result of P2 (Figure 8) shows that moderately healthy absorbs medium Green and Red bands, and emittances medium at Red Edge and Near-Infrared bands. Very healthy absorbs high at Green and Red bands, and emittances high at Red Edge and Near-Infrared bands.

After use vegetation index to estimate chlorophyll and health of oil palm trees. The result of P1 (Figure 9) shows that NDRE value Min is 0.14, Max is 0.14, Mean is 0.32, and Std Dev is 0.04. The value of GNDVI shows that Min is 0.41, Max is 0.79, Mean is 0.71, and Std Dev is 0.04. And the value of NDVI has such as Min is 0.33, Max is 0.88, Mean is 0.81, and Std Dev is 0.05.

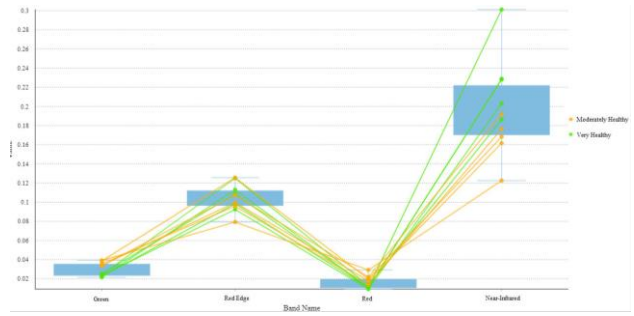

Figure 8. Comparison spectral profile of P2

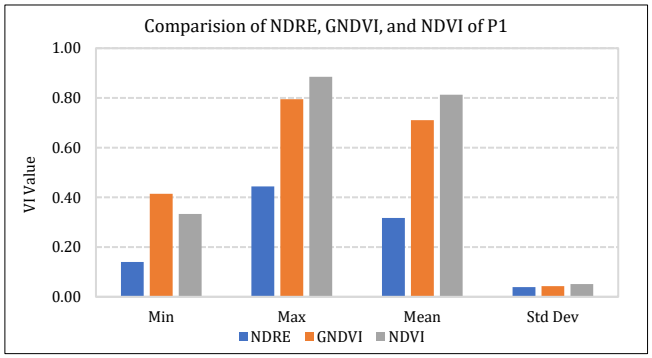

Figure 9. Comparison of vegetation indices of P1

The result of plot-2 (Figure 10) shows that the value of NDRE has such as Min is 0.14, Max is 0.41, Mean is 0.29, and Std Dev is 0.04. The value of GNDVI has such as Min is 0.46, Max is 0.78, Mean is 0.70, and Std Dev is 0.03. And the value of NDVI has such as Min is 0.54, Max is 0.88, Mean is 0.83, and Std Dev is 0.03.

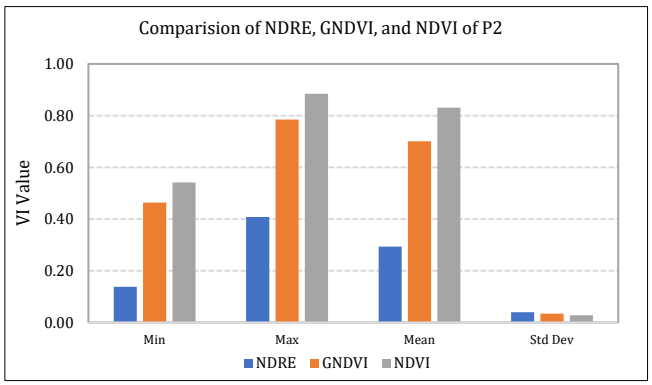

Figure 10. Comparison of vegetation indices of P2

4. CONCLUSION

In this research, a high-resolution image was applied to detect and count two plots of oil palm trees. A multispectral image was used to estimate and evaluate oil palm trees health at Mong Reththy Investment Cambodia Oil Palm Co., LTD, Sihanoukville Province, Cambodia. The high-resolutions was detected oil palm trees using an online AI platform found by Picterra. The comparison of NDRE, GNDVI, and NDVI indices in vegetation and chlorophyll content.

The result of oil palm tree extraction shows that the online AI platform is the performance for detecting area of interest in this study. It provided high accuracy in both plots but missing detection and detect different objects. Because a few objects are too small and blur, several trees are a similar texture as the oil palm trees. Therefore, the result of oil palm tree extraction occurs in a polygon that circles every single oil palm tree.

The result of oil palm trees health estimation shows that all vegetation indices can be evaluated healthy of the oil palm trees. The NDRE was used to analyze the chlorophyll of the oil palm tree. GNDVI analysis was used to determine oil palm trees that occur water and nitrogen uptake into the plant canopy. And NDVI was used to calculate oil palm tree health based on the value range of the index. Moreover, after vegetations index was used to compare that NDVI is the best performance than NDRE and GNDVI. Because it can help differentiate bare soil from grass or forest, detect plants under stress, and differentiate between crops and crop stages.

The high-resolution image from UAV is very important for counting oil palm trees. The online AI platform is useful for extracting, it is too simple. It occurs high accuracy assessment after used to detect oil palm trees tow plots. It can generate a large area on the online interface. The farm can apply the vegetation index to calculate the whole of oil palm areas by using multispectral images. Therefore, the farm can manage and estimate the yield of oil palm trees to produce it for the consumer.

ACKNOWLEDGEMENT

This work is supported by the National Key Research and Development Program of China with grant number 2018YFB2100501, the Key Research and Development Program of Yunnan province in China with grant number 2018IB023, the National Natural Science Foundation of China with grant number 42090012, 41771452, 417771454.

REFERENCES

Carlson, T. N., & Ripley, D. A. (1997). On the relation between NDVI, fractional vegetation cover, and leaf area index. Remote sensing of Environment, 62(3), 241-252.

Colchester, M., Chao, S., Dan, V. T., & Villanueva, J. (2011). Oil Palm Expansion in South East Asia. Bogor, Moreton-in-Marsh: Forest People Programme and Perkumpulan Sawit Watch.

Karaburun, A. (2010). Estimation of C factor for soil erosion modeling using NDVI in Buyukcekmece watershed. Ozean Journal of applied sciences, 3(1), 77-85.

Raeva, P. L., Šedina, J., & Dlesk, A. (2019). Monitoring of crop fields using multispectral and thermal imagery from UAV. European Journal of Remote Sensing, 52(sup1), 192-201.

Saing, C. H., Hem, S., Ouch, C., Phann, D., & Pon, D. (2012). Foreign investment in agriculture in Cambodia. Phnom Penh, Rome: Cambodia Development Resource Institute (CDRI), Food and Agriculture Organization of the United Nations (FAO).

Yu, X., Wu, X., Luo, C., & Ren, P. (2017). Deep learning in remote sensing scene classification: a data augmentation enhanced convolutional neural network framework. GIScience & Remote Sensing, 54(5), 741-758.

Intercontinental Geoinformation Days

igd.mersin.edu.tr

Sentinel-1 and -2 time-series data-fusion for olive tree identification in heterogeneous land surfaces using Google Earth Engine

Haydar Akcay*, Sinasi Kaya, Elif Sertel, Ugur Alganci, Samet Aksoy

Istanbul Technical University, Civil Engineering Faculty, Geomatics Engineering Department, Istanbul, Turkey

Keywords
Time-series data fusion
Sentinel-1 Sentinel-2
DVI red index (DVIR)
Random forest classification
Google earth engine

ABSTRACT

Olive, a crucial crop for the economies of Mediterranean countries, is expanded to Aegean, Mediterranean, Marmara, South-East and Black Sea regions of Turkey. Identification of olive trees in heterogeneous land surfaces, particularly in mountainous regions is essential for exploitation of un-grafted olive trees. In this study, several samples of olive tree, agriculture, bare-land, urban, forest and sparse vegetation fields located between Bayındır and Tire districts of Izmir province in Turkey, are randomly selected. Independent two sample sets are generated to train the classifier (70%) and for the validation (30%). Several data fusion combinations of time series of Sentinel-1 and Sentinel-2 satellite data with various spectral indices are performed with random forest classifier on Google Earth Engine environment. A new spectral index, named as "DVI Red index (DVIR)" is generated and experimented in the study, as well. Results demonstrated that "Sentinel-1, Sentinel-2 and 10 indices" data fusion performed best overall accuracy (95.5%) as "Sentinel-1 and new ratio index (DVIR)" data fusion performed highest user's accuracy (97.2%) for olive class. Of 10 spectral indices standalone classifications, DVIR ranked the first for overall accuracy (94.8%) and the third for olive class user's accuracy (84.4%).

1. INTRODUCTION

Olive, one of the most widely distributed crops around the world, is cultivated in each continent (Khan et al., 2018). It is crucial for the economies of Mediterranean countries and can be considered as a strategic crop (Akcay et al., 2019). Turkey is ranked fourth in 2017 with 2,100,000 tons of olive production in the world (FAO, 2019) and olive is the fourth most produced fruit following grape, apple and orange within the country (TUIK, 2019). Olive production is primarily a family business of which 320.000 families live off (Directorate General of Cooperatives of Turkey, 2018). Determination and continuous monitoring of olive trees particularly un-grafted ones are vital when evaluating olive as a strategic crop. It is time and labor-intensive work with traditional methods as olive is an indigenous crop of Mediterranean as well as exists in mountainous regions that are difficult to access. Hence, remote sensing is an efficient option and a very popular technique in order to overcome these challenges.

Sentinel-1 and -2 supply free data in the microwave and optical range of the electromagnetic spectrum in high spatial and temporal resolution. Recent studies exhibit the potential of Sentinel-2 satellite data for land cover determination with high accuracy. Besides, different studies experimented the performance of Sentinel-1 and Sentinel-2 data fusion of which were reported improvements in classification accuracy (Heckel et al., 2020).

Vegetation indices generally provide more sensitive results than individual spectral bands of satellite images (Avola et al., 2019). Numerous spectral indices are experimented to find the best index for separating different land covers or a specific one. For instance, Pena-Barragan et al. (2002) calculated various indices to identify cover crops, bare soil and olive trees and used (Blue+Green+Red)/3 ratio index to discriminate bare soil from vegetation cover and olive trees. Ettehadi et al. (2019) who focused on separating built-up areas from bare-lands exploited NDVI, SAVI and NDVIre for determination of vegetation cover. As such, several spectral indices are employed in different studies to find

* **Corresponding Author**

*(akcayhay@itu.edu.tr) ORCID ID 0000-0002-2404-2390
(kayasina@itu.edu.tr) ORCID ID 0000-0002-4962-0492
(sertele@itu.edu.tr) ORCID ID 0000-0003-4854-494X
(alganci@itu.edu.tr) ORCID ID 0000-0002-5693-3614
(aksoysa@itu.edu.tr) ORCID ID 0000-0001-6420-7316

Cite this study

Akcay H, Kaya S, Sertel E, Alganci U & Aksoy S (2021). Sentinel-1 and -2 time-series data-fusion for olive tree identification in heterogeneous land surfaces using Google Earth Engine. 2nd Intercontinental Geoinformation Days (IGD), 159-162, Mersin, Turkey

the best index to separate different land covers or a specific one.

In this study, multi-sensor time-series satellite data are utilized for identification of olive trees. In this regard, a total of 42 Sentinel-1 and Sentinel-2 satellite image pairs were accessed for 21 dates during two-year period between 2019 and 2021 in Google Earth Engine (GEE) platform. 10 different spectral indices, including a new experimental index, which we named as "DVI Red index (DVIR)" are calculated for each date and different combinations of bands and indices are stacked. Random forest classifier is performed to each stack. The results were assessed with accuracy assessment to compare the performance of different data fusions.

2. MATERIALS AND METHODS

2.1. Study Area

The study area is located between Bayındır and Tire districts of Izmir province in Turkey with a size of 225 km^2 (15 km x 15 km) (Fig. 1). North and south sides of the landscape are mountainous with heterogeneous plantations of which olive trees, sparse vegetation and bare-lands largely cover the area. Agricultural fields are mainly concentrated in the middle of the study site while olive trees also exist.

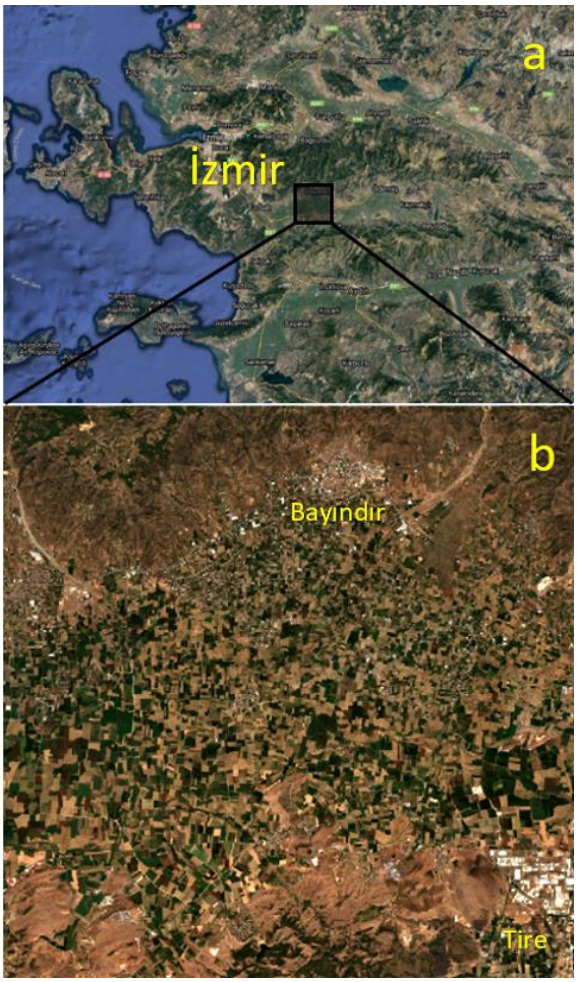

Figure 1. a) Study area from Google Earth© 2021 and b) Sentinel-2 (RGB: B4, B3, B2)

90 olive orchards, 70 agricultural parcels, 60 urban, 30 forest, 20 bare-land and 20 sparse vegetation fields are randomly selected from the study site such that samples for each class are scattered within the site. 70% and 30% of the sample sets are separated and used independently to train the random forest classifier and the validation of the classification, respectively.

2.2. Data Preparation

GEE (https://earthengine.google.com/), a cloud-based planetary scale geospatial analysis platform, is accessed and controlled through Internet-accessible application programming interface (API) (Gorelick et al., 2017). It enables exploiting several data collections of various remote sensing satellites (e.g. Landsat-5, -7, -8, Sentinel-1, -2, MODIS).

Sentinel-1 satellites are operating in C-band Synthetic Aperture Radar (SAR) and provide data at dual polarization (VH, VV) in Interferometric Wide Swath mode (IW) with 10 x 10 m pixel spacing (Torres et al., 2012). Sentinel-1 image collection on GEE platform includes calibrated and ortho-corrected Ground Range Detected (GRD) scenes of which images are processed using the Sentinel-1 Toolbox. Sentinel-2 satellites were launched in 2015 (S2A) and 2017 (S2B) and have 13 spectral bands with 10-, 20- and 60-m spatial resolutions (Laurin et al., 2018). Note that band 10 (SWIR-cirrus) is not available for level 2A products which are atmospherically corrected and provide bottom-of-atmosphere reflectance values.

In this study, a total of 42 Sentinel-1 and -2 satellite scenes (21 for each satellite sensor) between 01.01.2019 and 01.01.2021 were accessed in GEE environment. Closest image dates of each satellite were matched. VH/VV ratio band, radar vegetation index (RVI), normalized difference vegetation index (NDVI), Red-Edge NDVI (NDVIre), (Red+Green+Blue)/3 ratio index, difference vegetation index (DVI), normalized difference tillage index (NDTI), soil-adjusted vegetation index (SAVI), normalized difference built-up index (NDBI), bare soil index (BSI) and a new index named as "DVI red index (DVIR)" were calculated and included to Sentinel-1 and -2 data sets. Note that DVIR is generated using DVI and Red band which were noticed as distinctive when separating olive orchards. Table 1 shows the formulas of utilized spectral indices (B: Blue G: Green R: Red, NIR: Near-infared, SWIR: Shortwave-infrared).

Table 1. Spectral Indices

Index Name	Formula
NDVI	(NIR-R) / (NIR+R)
NDVIre	(RE1-R)/ (RE1+R)
(B+G+R)/3	(B+G+R)/3
DVI	NIR – R
NDTI	(SWIR1-SWIR2) / (SWIR1+SWIR2)
SAVI	(NIR-R) x (1+L) / (NIR+R+L) L=1.5
NDBI	(SWIR-NIR) / (SWIR+NIR)
BSI	((SWIR+R) - (NIR + B)) / ((SWIR+R) + (NIR + B))
RVI	4 x VH / (VV+VH)
DVIR	(R-DVI) / (R+DVI) = (2R-NIR) / NIR

2.3. Classification

Random forest (RF) classifier is a modern approach proved to perform fast and accurate for large and variegated data sets (Bargiel et al., 2017), and uses Classification and Regression Trees (CARTs) as working principle. A CART attempts to segment a predictor space into a number of homogenous regions which can be predicted by a generated rule set based on the input data. RF generates large number of CARTs based on various selections of the input data sets that are later summed up to one final result (Braun et al., 2015). Therefore, RF was selected as the classifier for the study.

Sentinel-2 images selected for the study are mostly cloud free. However, cloud mask was applied to the image collection as few parts of the scene covered by clouds. These regions, hence, were unclassified and displayed in white color in the classification image (Fig. 2). In the next step, Sentinel-1 and Sentinel-2 bands and calculated indices were combined. (21 dates, 4 Sentinel-1 bands/indices and 21 Sentinel-2 bands/indices). Therefore, an image with 21 x 25 = 525 layers were acquired. Different stack combinations were generated (e.g. S1, S2, S1+S2, S1+DVIR, S2+9 indices, S1+S2+10 indices) and random forest classification was implemented to each stack. 70% of samples were used for training the classifier and 30% of samples were used for the validation. It should be noted that the sample sets for training and the validation were divided and used independently. Table 2 demonstrates the accuracy metrics of each data fusion. Table 3 shows the confusion matrix of "S1 + S2 + 10 Indices" data fusion classification which performed the highest overall accuracy. Note that numbers refer to pixels of which an average olive orchard has approximately 50 pixels (with 10 m spatial resolution).

Table 2. Accuracy Metrics

Data Stack	User's Accuracy of Olive %	Overall Accuracy %	Kappa
S1+DVIR	97.2	94.2	0.92
S2+DVIR	93.2	94.9	0.93
S2	93.1	93.0	0.90
S2+9 indices	92.4	95.1	0.93
S1+S2+10 indices	91.4	95.5	0.94
S1+S2	91.2	94.7	0.93
(R+G+B)/3	86.1	91.8	0.89
BSI	85.3	88.2	0.84
DVIR	84.4	94.8	0.93
NDBI	83.5	87.1	0.82
NDVI	82.5	94.0	0.92
S1+NDVI	81.4	93.5	0.91
SAVI	79.2	92.0	0.89
DVI	76.1	90.7	0.87
NDVIre	65.2	85.2	0.79
NDTI	62.2	83.1	0.76
S1	55.5	66.4	0.52
S1+RVI	55.2	66.0	0.52
(VH/VV)	42.7	53.6	0.31
RVI	42.6	53.6	0.31

3. RESULTS

DVIR standalone classification succeeded 84.4% user's accuracy for olive class, following the (R+G+B)/3 ratio index (86.1%), and BSI (85.3%). Sentinel-1 standalone bands and RVI gave the lowest user's accuracies as expected (Table 2). S1+DVIR stack increased the accuracy remarkably and performed the highest user's accuracy (97.2%) as S1+NDVI, S1+(R+G+B)/3 and S1+BSI stacks remained at 81.4%, 82.3% and 82.7% respectively for olive class. S2+DVIR performed the second highest user's accuracy (93.2%) while S2 standalone classification performed 93.1% user's accuracy for olive class.

Regarding to overall classification accuracies, S1+S2+10 indices fusion succeeded the highest (95.5%) as S2+DVIR, S1+S2 and S1+DVIR stacks performed slightly lower accuracies of 94.9%, 94.7% and 94.2% respectively. DVIR standalone classification performed the highest (94.8%) compared to rest of the standalone index classifications.

Overall accuracy of DVIR standalone classification (94.8%) performed slightly higher than S1+DVIR (94.2%) but slightly lower than S2+DVIR stack (94.9%). This result can demonstrate the effectiveness of DVIR in land cover land use (LCLU) mapping. Fig. 2 describes the LCLU classification image of the study site.

Table 3. Confusion Matrix of "S1 + S2 + 10 Indices" Data Fusion Classification

Class	Bare-land	Agr.	Olive	Urban	Forest	Sparse Veg.	Total	User's Acc.
Bare-land	1208	0	1	21	0	0	1230	98.2
Agr.	0	2992	43	0	61	0	3096	96.6
Olive	0	3	1714	3	156	0	1876	91.4
Urban	1	5	1	220	0	0	227	96.9
Forest	0	0	0	0	477	0	477	100
Sparse Veg.	18	0	6	0	1	103	128	80.5
Total	1227	3000	1765	244	695	103		kappa
Producer's Acc.	98.5	99.7	97.1	90.2	68.6	100	kappa	0.94

4. DISCUSSION

As the purpose of the study was identifying olive orchards in heterogenous land surfaces with multi-sensor time-series data fusion, Sentinel-1 and -2 data were accessed and several spectral indices were calculated, combined and processed in Google Earth Engine environment. Results indicated that multi-sensor data fusion significantly increased the classification accuracy of SAR data. Furthermore, results show that just one optical index can improve the accuracy of SAR data more than %50 percent. For instance, S1+DVIR data fusion performed the highest user's accuracy for olive class (97.2%) whereas S1 and DVIR standalone classifications remained at 55.5% and 84.4% respectively. This explains the efficiency of SAR data when fused with optical indices. Hence, it is obvious that DVIR has significant role in identifying olive trees. It

should be noted that the positive impact of time-series data is also clear in this study. According to Table 3, olive mostly mismatched with forest class as expected. Because different tree groups including olive can be located in the same field (Fig. 2). Bare-land mismatched mostly with urban and sparse vegetation as expected. Large discrepancies between user's and producer's accuracies of forest and sparse vegetation classes are thought to be due to the lack of samples of these classes. Lastly, it was observed that joint use of (VH/VV) and RVI has negative effect on classification accuracy which may be explained with the negative effect of data redundancy.

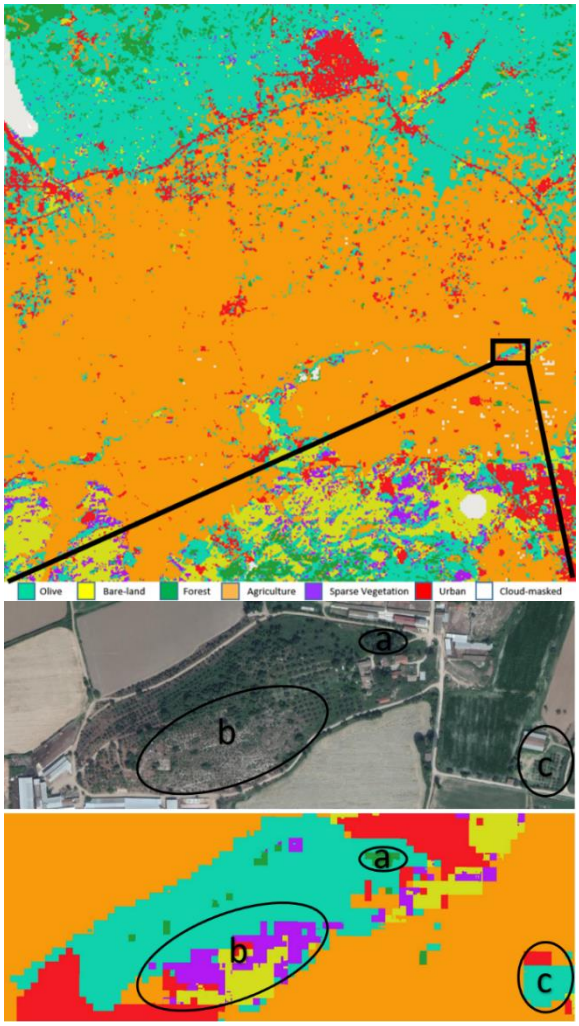

Figure 2. Classified image of "S1+S2+10 indices" data fusion. "Circle a" shows a group of trees, correctly classified as forest. In contrast, "circle b" demonstrates misclassification of olive class with sparse vegetation, agriculture, and bare-land. "Circle c" shows correct classification of urban and olive fields.

5. CONCLUSION

In this study, classification performances of data fusion of time series Sentinel-1, Sentinel-2 satellite data and several spectral indices experimented. It is observed that, DVIR has significant positive impact for not only in identifying olive trees but also land cover land use (LCLU) mapping. However, more comprehensive future works focused on DVIR are necessary to verify the efficiency of this index for both olive tree determination and LCLU mapping.

REFERENCES

Akcay, Haydar, et al. "Determination of Olive Trees with Multi-sensor Data Fusion." 2019 8th International Conference on Agro-Geoinformatics (Agro-Geoinformatics). IEEE, 2019.

Avola, G. et al., (2019). Remotely Sensed Vegetation Indices to Discriminate Field-Grown Olive Cultivars. Remote Sensing, 11(10), 1242.

Braun, A., and V. Hochschild. "Combined use of SAR and optical data for environmental assessments around refugee camps in semiarid landscapes." International Archives of the Photogrammetry, Remote Sensing & Spatial Information Sciences (2015).Breiman, L., Friedman, J.H., Olshen, R.A., Stone, C.J., 1984. Classification and Regression Trees. Belmont, Wadsworth.

Directorate General of Cooperatives of Turkey (2018). 2017 Yılı Zeytin ve Zeytin Yağı Raporu. http://koop.gtb.gov.tr/data/5ad06f17ddee7dd8b423eb2e/2017%20Zeytinya%C4%9F%C4%B1%20Raporu.pdf (Accessed 25 June 2019).

Earth Engine Data Catalog, https://developers.google.com/earth-engine/datasets/catalog (accessed on 28 March 2021).

Ettehadi P. et al., (2019). Separating Built-Up Areas from Bare Land in Mediterranean Cities Using Sentinel-2A Imagery. Remote Sensing, 11(3), 345.

FAO, 2019. Agricultural Statistics of the Food and Agriculture Organization of the United Nations, http://www.fao.org/faostat/en/#data/QC. (Accessed 27 June 2019).

Google Earth Engine, https://earthengine.google.com/ Accessed (30 March 2021).

Gorelick, Noel, et al. "Google Earth Engine: Planetary-scale geospatial analysis for everyone." Remote sensing of Environment 202 (2017): 18-27.

Heckel, Kai, et al. "Predicting forest cover in distinct ecosystems: The potential of multi-source Sentinel-1 and-2 data fusion." Remote Sensing 12.2 (2020): 302.

Khan, Aftab, et al. "Remote Sensing: An Automated Methodology for Olive Tree Detection and Counting in Satellite Images." IEEE Access 6 (2018): 77816-77828

Laurin, G. V. et al., (2018). Above-ground biomass prediction by Sentinel-1 multitemporal data in central Italy with integration of ALOS2 and Sentinel-2 data. Journal of Applied Remote Sensing, 12(1), 016008.

Peña-Barragán, J. M. et al., (2004). Assessing land-use in olive groves from aerial photographs. Agriculture, ecosystems & environment, 103(1), 117-122.

Torres, Ramon, et al. "GMES Sentinel-1 mission." Remote Sensing of Environment 120 (2012): 9-24.

TUIK, (2019). Turkish Statistical Institute, http://tuik.gov.tr/UstMenu.do?metod=temelist (Accessed 25 June 2019).

Intercontinental Geoinformation Days

igd.mersin.edu.tr

Temporal analysis and future prediction of CO_2 emissions of solid, liquid and gas fuels in Python with FBProphet model

Metin Kaynakli*[1], Mehmet Emin Tabar [2]

[1]*Bitlis Eren University, Vocational School of Technical Sciences, Department of Motor Vehicles and Transportation Technologies, Bitlis, Turkey*
[2]*Bitlis Eren University, Vocational School of Technical Sciences, Department of Architecture and Urban Planning, Bitlis, Turkey*

Keywords
FBProphet Model
Python
CO2 Emissions
Temporal Analysis
Fuels

ABSTRACT

Carbon emission simply means the release of carbon into the atmosphere. When it comes to carbon emission, many definitions come to mind, but talking about carbon emission is actually talking about greenhouse gas emission. Because greenhouse gas emissions are often calculated as carbon dioxide equivalents, they are often referred to as carbon emissions in any global warming or greenhouse gas impact debate. According to the predictions of the International Energy Agency, the demand for fossil fuels will increase until 2050 and a 130% increase in carbon emission values will be observed accordingly (O'Neill 2020). For this reason, very important problems such as global warming and climate change, which are beginning to be felt more and more, will become a bigger threat to the world in the coming years. In the study, the effects of solid, liquid and gaseous fuels on CO2 emissions were analyzed in time series using the FBProphet model and a future prediction was made.

1. INTRODUCTION

The concentration of greenhouse gases caused by humans in the atmosphere started to increase especially with the industrial revolution that started in the 1850s. As a natural consequence of this, an increase in energy demand has been observed and a significant increase has been observed in the use of fossil fuels to compensate this increase (Xie et al. 2013). When we look at the air temperatures, in the period from the 19th century until today, the air temperature has increased by 0.5 degrees on average.

As the years progress, greenhouse gas emissions increase and this has negative consequences for nature such as global warming. Energy production is the main cause of carbon emissions. Firms engaged in energy production resort to fossil fuels at a rate of 87% to provide the energy they need. It is known that solid, liquid and gaseous fuels also cause different levels of carbon dioxide emission. According to the "TUIK 2014 Greenhouse Gas Inventory", it was 132.5 million tons (equivalent to CO_2) in 1990, and this figure increased to 340 million tons (CO2 equivalent) in 2014 (Kılıç et al. 2018). In other words, the carbon emission of the energy sector increased by 156% between 1990 and 2014 (Mensah et al. 2018). To reduce this carbon dioxide emission, renewable energy sources should be used. Today, there are studies in many countries that have started to ban diesel and gasoline vehicles (Jochem et al. 2015). The use of fully electric vehicles instead of these vehicles is encouraged. It is thought that electric vehicles can significantly reduce CO_2 emissions, unlike diesel and gasoline cars.

When switching to electric vehicle technology, the question arises from where the needed energy will be met. It is thought that when the number of solar panels, wind power plants and hydroelectric power plants is increased, most of the energy needed can be met. For this reason, energy production from fossil fuels must be limited in order to prevent negative factors such as global warming and seasonal changes (Yilmaz and Yilmaz 2013).

In our study, by considering the role of solid, liquid and gaseous fuels in CO_2 emission amounts, the data were analyzed with time series and FBProphet model, and a future prediction was made as a result of this analysis.

* **Corresponding Author**

*(mkaynakli@beu.edu.tr) ORCID ID 0000 – 0001 – 8372 – 1345
(metabar@beu.edu.tr) ORCID ID 0000 – 0002 – 3234 – 5340

Cite this study

Kaynakli M & Tabar M.E (2021). Temporal analysis and future prediction of CO_2 emissions of solid, liquid and gas fuels in Python with FBProphet Model. 2nd Intercontinental Geoinformation Days (IGD), 163-166, Mersin, Turkey

2. METHOD

CO_2 emissions data for Turkey is taken from "https://data.worldbank.org/". The received data was transferred to Python software and a column matrix was created as date and emission data. The index data was added to this column matrix with the help of Python software. A fit model was created with the FBProphet model for this defined matrix. Period and freq value are defined in the model for the future forecast. The period was repeated as 34 years and a predictive value was found until 2050. In order to test the accuracy of the model, the entire model was defined as training data and the model predicted for the years whose CO2 emission value was known. CO2 emission data for the next 34 years were also predicted using time series. The FBProphet Model, made open source by Facebook, predicts the future with time series analysis (Chikkakrishna et al. 2019).

$$f(x) = g(x) + s(x) + h(x) + e(t)$$

FBProphet uses time as a regressor and tries to fit several linear and nonlinear functions of time as components (Chikkakrishna et al. 2019).

2.1. Total CO_2 Emissions

Total CO_2 emissions for Turkey are defined and a future forecast is made with the FBProphet model in Python. Total CO_2 Emissions are given in Table 1.

Table 1. Total CO_2 Emissions in Turkey

Index	Date	CO2 Emissions
0	01.01.1960	16820.529
1	01.01.1961	17363.245
2	01.01.1962	21631.633
...	...	...
54	01.01.2014	345908.110
55	01.01.2015	350337.846
56	01.01.2016	372724.881

Estimated future CO_2 emission values with the FBProphet model is given in Table 2.

Table 2. Total CO_2 Emissions FBProphet Outputs

Index	Ds	Trend	T_lower	T_upper	Yearly	Yhat
0	1960	13447.630	13447.630	13447.630	25200.766	11753.135
1	1961	9770.455	9770.455	9770.455	21823.579	12053.124
2	1962	6103.326	6103.326	6103.326	23249.486	17146.160
...	...	...	...	...	...	...
88	2048	67866.082	64788.927	71509.782	25474.416	70413.499
89	2049	68925.117	65688.232	72749.684	25723.441	71498.558
90	2050	69982.197	66573.648	74012.854	25943.213	72576.411

CO_2 emission estimation data are shown graphically in Fig. 1 and trend analysis is shown in Fig. 2.

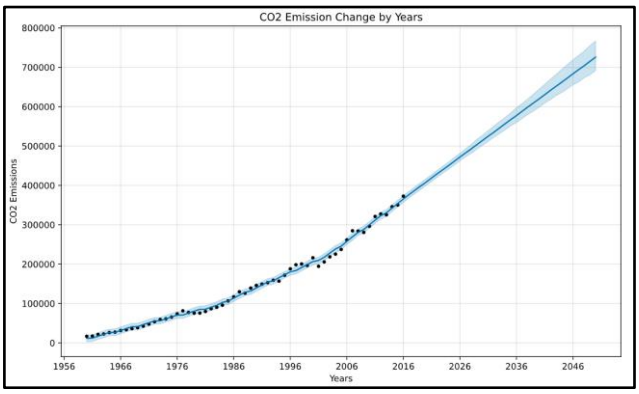

Figure 1. CO_2 Emissions Forecast

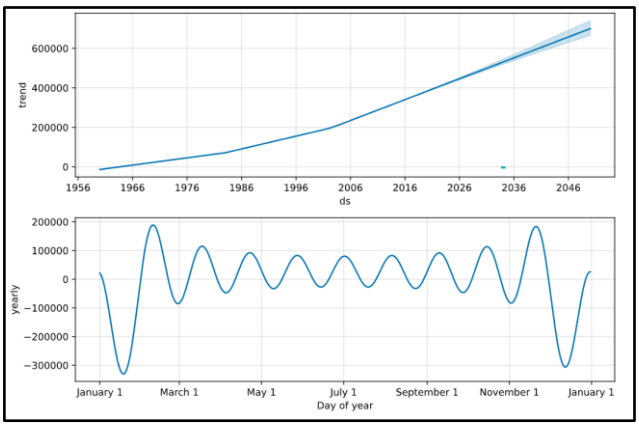

Figure 2. Trend Analysis

2.1.1. CO_2 Emissions from Solid Fuel Consumption

Emission values from solid fuels are shown in Table 3. CO_2 emissions from solid fuel consumption FBProphet outputs are shown in Table 4.

Table 3. CO_2 Emissions from Solid Fuel Consumption

Index	Date	CO_2 Emissions
0	01.01.1960	67.364290
1	01.01.1961	61.224921
2	01.01.1962	55.043228
...	...	...
54	01.01.2014	40.144175
55	01.01.2015	37.958718
56	01.01.2016	39.734168

Table 4. CO_2 Emissions from Solid Fuel Consumption FBProphet Outputs

Index	Ds	Trend	T_lower	T_upper	Yearly	Yhat
0	1960	8.453242	8.453242	8.453242	48.786464	57.239706
1	1961	7.023585	7.023585	7.023585	48.217769	55.241354
2	1962	5.597835	5.597835	5.597835	48.295549	53.893384
...	...	...	...	...	...	...
88	2048	4.729439	12.403263	2.785379	51.097074	46.367636
89	2049	4.637452	12.808790	3.163526	49.199019	44.561567
90	2050	4.545717	13.065674	3.539595	49.722226	45.176509

CO_2 emission from solid fuel estimation data are shown graphically in Fig. 3 and trend analysis is shown in Fig. 4.

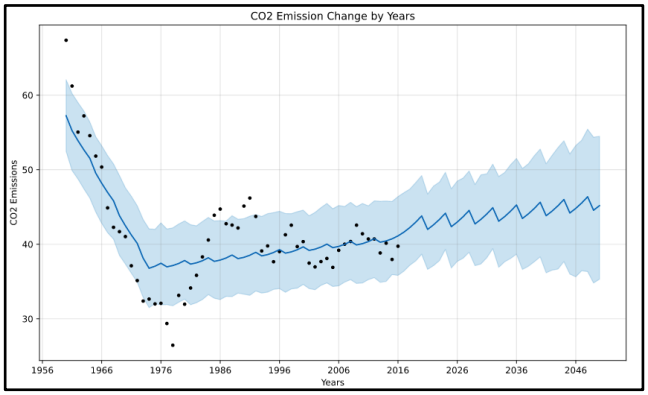

Figure 3. CO_2 Emissions from Solid Fuel Forecast

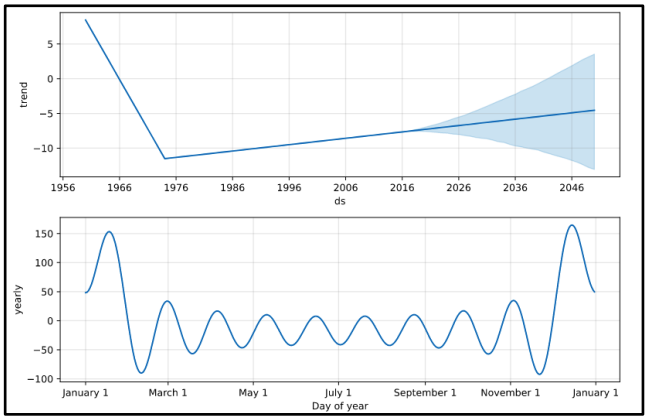

Figure 4. CO_2 Emissions from Solid Fuel Trend Analysis

2.1.2. CO_2 Emissions from Liquid Fuel Consumption

Emission values from liquid fuels are shown in Table 5. CO_2 emissions from liquid fuel consumption FBProphet outputs are shown in Table 6. CO_2 emission from liquid fuel estimation data are shown graphically in Fig. 5 and trend analysis is shown in Fig. 6.

Table 5. CO_2 Emissions from Liquid Fuel Consumption

Index	Date	CO2 Emissions
0	01.01.1960	26.596904
1	01.01.1961	32.946146
2	01.01.1962	39.599932
...	...	...
54	01.01.2014	22.964062
55	01.01.2015	26.127823
56	01.01.2016	26.663912

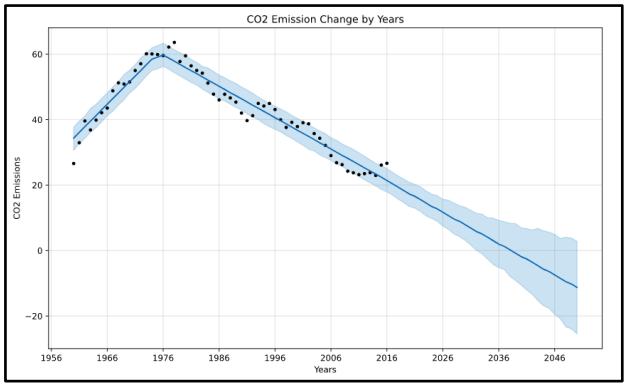

Figure 5. CO_2 Emissions from Liquid Fuel Forecast

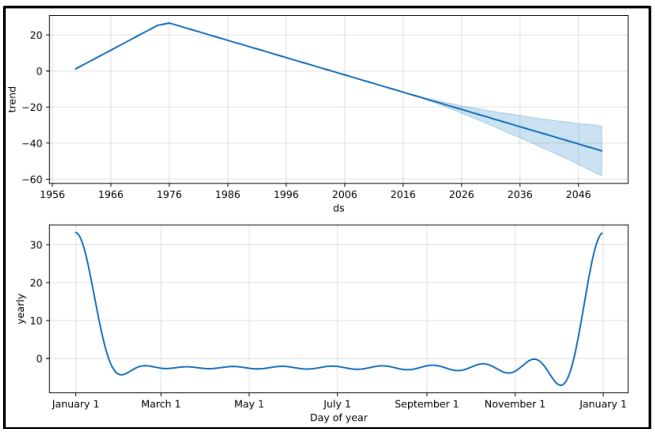

Figure 6. CO_2 Emissions from Liquid Fuel Trend Analysis

Table 6. CO_2 Emissions from Liquid Fuel Consumption FBProphet Outputs

Index	Ds	Trend	T_lower	T_upper	Yearly	Yhat
0	1960	1.207149	1.207149	1.207149	33.143364	34.350513
1	1961	2.931871	2.931871	2.931871	33.192160	36.124031
2	1962	4.651881	4.651881	4.651881	33.191892	37.843773
...	...	...	...	...	...	...
88	2048	42.368239	54.972443	29.763376	32.854304	9.513935
89	2049	43.327891	56.718477	30.035112	33.095079	10.232812
90	2050	44.284922	58.067588	30.565266	33.030788	11.254134

2.1.3. CO2 Emissions from Gaseous Fuel Consumption

Emission values from gaseous fuels are shown in Table 7. CO_2 emissions from gaseous fuel consumption FBProphet outputs are shown in Table 8.

CO_2 emission from gaseous fuel estimation data are shown graphically in Fig. 7 and trend analysis is shown in Fig. 8.

Table 7. CO_2 Emissions from Gaseous Fuel Consumption

Index	Date	CO2 Emissions
0	01.01.1960	0.000000
1	01.01.1961	0.000000
2	01.01.1962	0.000000
...	...	...
54	01.01.2014	26.620375
55	01.01.2015	25.746823
56	01.01.2016	23.510719

Table 8. CO_2 Emissions from Gaseous Fuel Consumption FBProphet Outputs

Index	Ds	Trend	T_lower	T_upper	Yearly	Yhat
0	1960	3.851375	3.851375	3.851375	2.886529	0.964847
1	1961	3.792307	3.792307	3.792307	3.299266	0.493041
2	1962	3.733399	3.733399	3.733399	3.243385	0.490014
...	...	...	...	...	...	...
88	2048	56.114847	51.847369	60.451480	1.201026	57.315873
89	2049	57.059376	52.592689	61.530913	2.585954	59.645330
90	2050	58.001325	53.297120	62.657709	2.204451	60.205775

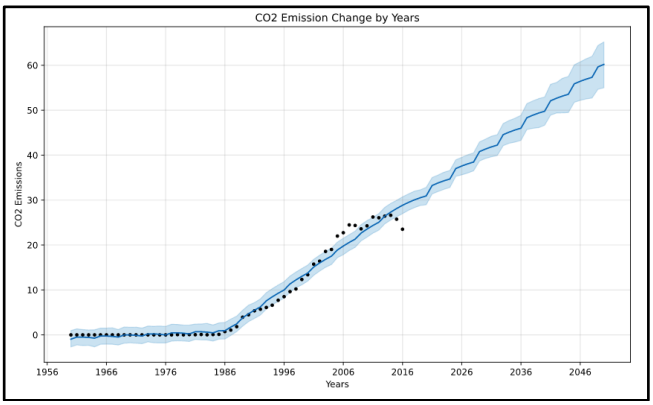

Figure 7. CO_2 Emissions from Gaseous Fuel Forecast

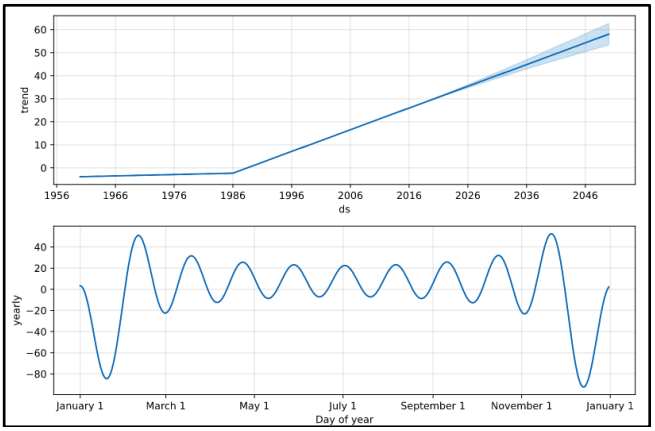

Figure 8. CO_2 Emissions from Gaseous Fuel Trend Analysis

3. RESULTS

The International Energy Agency has made a statement that the demand for fossil fuels will increase until 2050 and a 130% increase in carbon emission values will be observed accordingly. The carbon emission in 2016 is 372724.881. In our study, it was estimated that carbon emission in Turkey could increase by 94.720% until 2050. It is estimated that the CO2 emission of solid fuels will increase by 13,698%, that of liquid fuels will decrease by 57,793% and that of gaseous fuels will increase by 156,076%.

4. DISCUSSION

When the trend analyzes are examined, it is seen that the increase in CO_2 emission values are more in the autumn and winter transition months. This increase is likely due to residents' heating needs. The contribution of liquid fuels to CO_2 emissions will decrease with the transition to electric vehicles. The increase in the contribution of gaseous fuels to CO_2 emissions is due to the widespread use of natural gas. Therefore, alternative energy sources such as solar energy and hydroelectric power plants should be directed.

5. CONCLUSION

Continuing to use fossil fuels for needs such as warming and energy production will accelerate global warming and seasonal changes. Using renewable energy sources in energy production allows us to leave a more livable world to future generations. Therefore, renewable energy sources such as water, wind and solar energy should gradually replace fossil fuels.

REFERENCES

Chikkakrishna, N. K., Hardik, C., Deepika, K., & Sparsha, N. (2019). *Short-term traffic prediction using sarima and FbPROPHET.* Paper presented at the 2019 IEEE 16th India Council International Conference (INDICON).

Jochem, P., Babrowski, S., & Fichtner, W. (2015). Assessing CO2 emissions of electric vehicles in Germany in 2030. *Transportation Research Part A: Policy and Practice, 78*, 68-83.

Kılıç, E., Puig, R., Zengin, G., Zengin, C. A., & Fullana-i-Palmer, P. (2018). Corporate carbon footprint for country Climate Change mitigation: A case study of a tannery in Turkey. *Science of the total environment, 635*, 60-69.

Mensah, C. N., Long, X., Boamah, K. B., Bediako, I. A., Dauda, L., & Salman, M. (2018). The effect of innovation on CO 2 emissions of OCED countries from 1990 to 2014. *Environmental Science and Pollution Research, 25*(29), 29678-29698.

O'Neill, S. (2020). Global CO2 emissions level off in 2019, with a drop predicted in 2020. *Engineering (Beijing,China)*.

Xie, S.-P., Lu, B., & Xiang, B. (2013). Similar spatial patterns of climate responses to aerosol and greenhouse gas changes. *Nature Geoscience, 6*(10), 828-832.

Yilmaz, H., & Yilmaz, M. (2013). Forecasting CO2 emissions for Turkey by using the grey prediction method. *Sigma, 31*, 141-148.

Intercontinental Geoinformation Days

http://igd.mersin.edu.tr/2020/

Using analytical hierarchy process (AHP) for flood susceptibility mapping of Mersin, Turkey

Bilal Özay*[1], Osman Orhan [2]

[1]*Mersin University, Institute of Science and Technology, Department of Remote Sensing and GIS, Mersin, Turkey*

Keywords
Flood susceptibility
AHP
GIS Analysis
Multi Criteria Decision Making (MCDM)

ABSTRACT

Overflowing and flood disasters caused by excess water in the river beds cause a major problem. Increasing precipitation, along with the growth of cities, destruction of river beds, inadequate infrastructure and climate change, triggers overflowing and flood disasters. Overflowing and flooding on settlements can cause great damage and destruction. Flood maps, which are necessary to prevent these material and moral damages, determine the regions to be affected by the flood in advance and play an auxiliary role in the measures that can be taken there. Remote sensing and geographic information systems play a major role in obtaining and processing this information. Due to size and complexity of data obtained from field, GIS makes it easier for us to process data. And allows us to observe results much clear. In this study, Analytical Hierarchy Process used for flood susceptibility mapping of Mersin. 10 factors affecting flood have been used to prepare susceptibility map. Results showed us that coastal zone and close locations to river beds are under risk of flood. Since most of the built-up area located on or around these risk zones, it is required to take measures immediately.

1. INTRODUCTION

Disaster is natural or human-induced phenomenon that interrupts normal life and social activities, causes physical, social, cultural and economic losses in society, (Gündoğdu and Özçep, 2003). Thus, disasters defined by their impact on communities. Disaster is the result rather than the event itself(Ergünay, 2002).

Disasters cause damage and death, which can be reduced by disaster management. According to UNDP %90 of natural disasters occur in developing countries(Witschi-Cestari, 2002), which makes them more vulnerable when their economic situations considered.

Flood events are related to the climatic and physiographic structure of the region. In addition, roads and sidewalks that control the flow of water on the surface, and natural drainage areas blocked by buildings covering a large part of the ground increase the effect of flood by restricting the flow of water(Konrad and Booth, 2005; Fernandez and Lutz, 2010). Especially in dense residential areas, the effect of flooding is felt much more severely because the affected areas often include non-drainable surfaces and insufficient underground drainage channels(Selçuk et al, 2016).

Disaster management is important in order to predict, prevent and protect against flood disasters. It is not possible to stop disasters (Onuşluel and Harmancıoğlu, 2002) yet it is possible to reduce its impacts to minimum. For this purpose, it is required to prepare a susceptibility map. When adequate measures are taken in flood sensitive areas it is possible to greatly reduce effects of floods. For this reason, potential flood and overflow areas should be obtained with reliable methods and these data should be taken into consideration in making planning decisions at all scales, directing investment projects, and establishing settlement and land use policies (UNECE, 2000).

There are many studies to predict possible flood locations. It can be separated to two categories; modelling and multi-criteria decision analysis. Hecras (Manandhar, 2010) and Floodsim (Hadimlioglu et al, 2020) are popular programs among flood modelling applications. Analytical Hierarchy Process (Das, 2019; Vojtek and Vojteková, 2019; Swain et al, 2020) and Fuzzy weight(Hong *et al.*, 2018; Wang *et al.*, 2019) are popular among Multi-criteria decision analysis. Yet

* **Corresponding Author**

*(bilalozay7171@gmail.com) ORCID ID 0000-0001-8466-5664
(osmanorhan@mersin.edu.tr) ORCID ID 0000-0002-1362-8206

Cite this study

Özay B & Orhan O (2021). Using analytical hierarchy process (AHP) for flood susceptibility mapping of Mersin, Turkey. 2nd Intercontinental Geoinformation Days (IGD), 167-170, Mersin, Turkey

there is no such thing as best in between all these methods. Because every study area has different (unique) character. Quantity and quality of data is another decision maker between these methods.

Purpose of this research is to prepare a susceptibility map for Mersin, Turkey by using AHP. This study will be the first susceptibility map for Mersin by using AHP. There are different types of studies for flood in Mersin. These studies are about flood risk which is not same thing as susceptibility mapping. Flood risk analysis is an analysis to determine the possible damage 'if' flood occurs in that area. In susceptibility mapping our purpose is to find out sensitive locations for flood which means possible flood locations if requirements are meet.

2. MATERIALS and METHOD

2.1. Study Area

Mersin (Figure 1) is a city located in southern part of Turkey. The surface area of Mersin province is 15,620 km^2. Except for 50% of the Tarsus district, all of it is within the Eastern Mediterranean Basin boundaries. Mersin province, which is surrounded by the Mediterranean in the south, is separated from the inner parts of Anatolia by the high plateaus and peaks of the West and Central Taurus Mountains from the north. Mersin, Antalya Karaman and Konya are located within boundaries of Eastern Mediterranean basin.

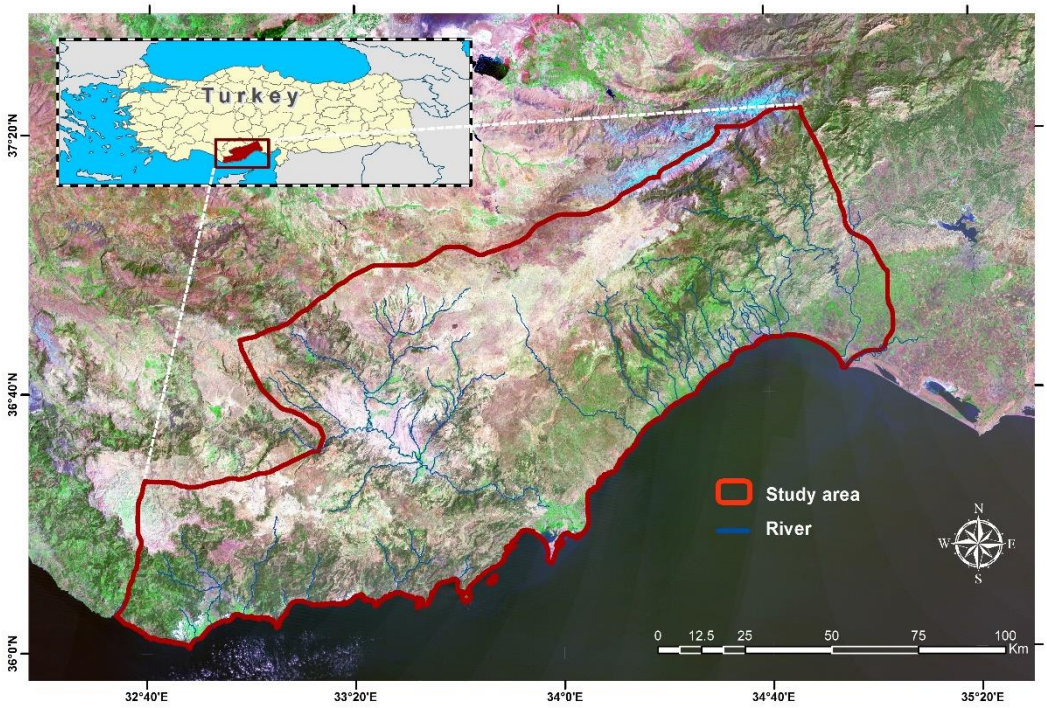

Figure 1. Study Area; Mersin, Turkey

According to 'Eastern Mediterranean Basin Flood Management Plan'; approximately 2.12% of Turkey's population is located within the basin, covering the provinces of Mersin has the largest population among the provinces. More than %90 of population of Mersin is located within the basin. The Eastern Mediterranean Basin generally has a Mediterranean climate with dry and hot summers and mild and rainy winters. It transitions to Central Anatolia Terrestrial Climate in the northern and upper parts. In these regions, summers are dry and hot, winters are cold and usually snowy. (DAHTYP, 2019).

2.2. Material

Elevation, slope, distance to river, distance to drainage, drainage density, landcover, TWI, SPI, aspect and curvature data have been used in this project to create a susceptibility map for Mersin. Elevation, slope, aspect and curvature produced from DEM (Yılmaz and Erdoğan, 2018) of Mersin. While landcover is a separate data, others produced with combination of DEM and river and/or stream lines.

Importance of each data can be explained as; Water accumulates in lowest elevation point of basin. Thus, as the elevation decreases chance of flood increases. Slope is effective on movement of water. Areas with lower slope accumulates water therefore it has higher risk for flood. River locations are natural path for water. Closest locations to river have higher risk of flood. Distance to drainage is similar with river. River is something that occurs on the ground level and drainage is a system operates underground. If water can access to underground level it will accumulate within drainage system. Drainage density defined as the total stream length per unit area. Higher density will increase the risk of flood. Land cover data has 5 groups. These groups were separated by their runoff, infiltration, evaporation and evapotranspiration. Highest risk

groups were artificial surfaces and water bodies. TWI represents the ratio of slope and specific basin area that describes the effect of topography on the distribution of soil moisture in an area. SPI is power of water flow. Regions with lower power will accumulate water so low SPI has higher chance of flood. Aspect is effective on soil moisture and hydrological conditions. Flat surfaces have highest risk, north, northeast and northwest 2nd in rank east and west are 3rd and south, southeast and southwest are the least flood risk areas. Curvature is our last data that has impact on flood. Curvature is shape of surface which can be convex or concave. For the values it has been separated in to 3 categories. Areas of between (-1)-1 values are highest risk areas, values below -1 comes 2nd and values above 1 comes in 3rd place in ranking of curvature.

2.3. Method

In this study Analytical Hierarchy Process has been used for flood susceptibility mapping. AHP is used in a multi-purpose decision-making situation with multiple criteria, in which a large number of decision makers are present, when choosing among many alternatives under certainty or uncertainty. Using a hierarchical model consisting of objectives, criteria, possible sub-criteria levels and options for each problem, AHP can be explained as a decision making and estimation method that is used if the decision hierarchy can be defined, and gives the percentage distributions of decision points in terms of factors affecting the decision.

Ranking of dataset for AHP is elevation(meter), slope(°), distance to river(meter), distance to drainage(meter), drainage density (km/km^2), land cover (level), TWI (level), SPI (level), aspect and (plan)curvature. Rank of dataset depends on expert opinion. While elevation has the highest rank, highest impact, and curvature is the lowest one. There are 2 weight calculation processes in AHP. One of them is between these 10 factors and other one is within every single factor. Also, every single factor has been grouped in to 5-10 classes depending on type of data. Range of classes determined based on expert opinions. In this step, every single group weighted according to their impact on flood. Weight of every single factor; Elevation (0,26), Slope (0,22), Distance to river (0,15), Distance to drainage (0,11), Drainage density (0,07), Landcover (0,06), TWI (0,03), SPI (0,02), Aspect (0,019), Curvature (0,014). For the last step in Arcgis program weight of factor and class have been multiplied to calculate the weight of every single pixel. Pixel size of every single parameter is 30x30 meters. Final calculation gave us the susceptibility map of Mersin.

3. RESULTS

Figure 3 shows the susceptibility map of Mersin. It has been produced by multiplying parameter's weight and group's weight. Coastal locations and surroundings of rivers are most sensitive areas according to this research. Figure 2 shows us conditioning factors of this research. It can be clearly observed even through those maps because highest risk groups in every single conditioning factor were located within those areas.

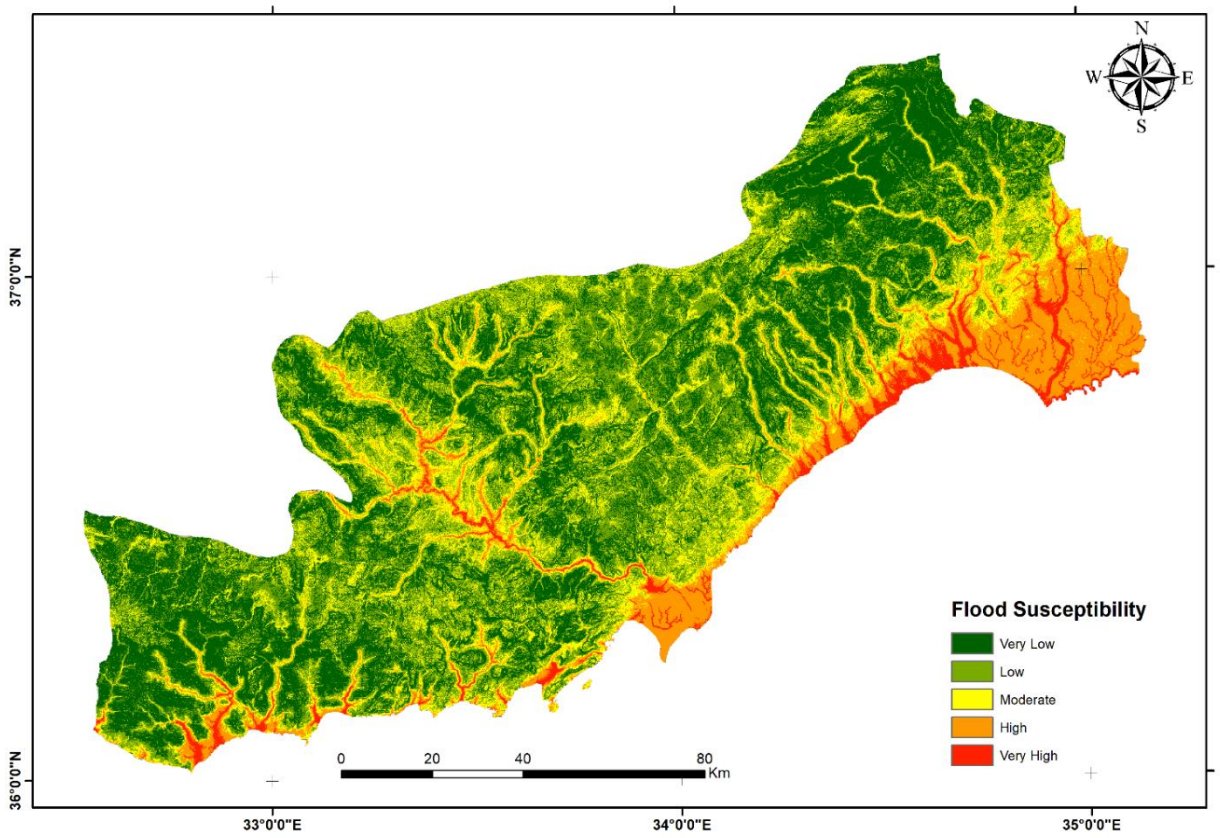

Figure 3. Flood susceptibility map of Mersin

Susceptibility map shows that Mersin is under risk by % 3,07 Very high, %11,42 High, %18,67 Moderate, %31,48 Low and %35,34 Very low. These percentages were calculated by pixel ratios.

But more than %50 population of Mersin and especially high populated districts are under risk of flood.

4. DISCUSSION

AHP is a simple and executable weighting technique that depends on expert's opinion. Assigning weights for parameters may introduce some uncertainty. Analytical Hierarchy Process can be used for regional and local susceptibility analysis(Liu *et al.*, 2018).

Study area (Mersin) is a coastal zone with low elevation. Most of the built-up areas of districts were constructed over river zones by drying them. Especially high populated districts such as akdeniz, mezitli, toroslar, yenişehir. Elevation, distance to river and drainage density are important factors for flood susceptibility mapping. Thus, high risk within these parameters creates greater risk for flood.

High and very high risk zones validated by checking flood events of Mersin. Validation showed us that floods occur on sensitive (high and very high) areas of susceptibility map.

5. CONCLUSION

Flood is one of the most destructive natural disasters worldwide. Thus, prediction of flood areas is important to foreseen future risks. Method and materials can be different while preparing a susceptibility map. There is no such thing as best in method. Every study area requires a pre research to find out which method is better for that zone. Another factor for choosing method is materials that will be used. Finding all datasets is not possible for every study area. Quantity and quality of datasets a big factor while choosing suitable method.

Flood susceptibility map can be used for land selection of investments, agricultural activities, industrial zones, residential zones. Being able to see sensitive locations will allow us to prepare for risks in existing developed areas.

REFERENCES

(DAHTYP), T.C. Tarım Ve Orman Bakanlığı Su Yönetimi Genel Müdürlüğü, (2019) Doğu Akdeniz Havzası Taşkın Yönetim Planı,

Das, S., (2019), Geospatial mapping of flood susceptibility and hydro-geomorphic response to the floods in Ulhas basin, India, Remote Sensing Applications: Society and Environment 14 60–74 Contents

Ergünay O. (2002), Afete Hazırlık ve Afet Yönetimi. Türkiye Kızılay Derneği Genel Müdürlüğü Afet Operasyon Genel Merkezi (AFOM) 3-17 Ankara (in Turkish)

Fernandez, D.S., and Lutz, M.A., (2010). Urban flood hazard zoning in Tucuman Province, Argentina, using GIS and multicriteriadecision analysis. Engineering Geology, 111, 90-98

Gündoğdu O, Özçep F. (2003), Yaşanan Önemli Depremlerin Işığında Afet Yönetimi Problemi ve Değerlendirilmesi, Türkiye 15. Jeofizik Kurultayı ve Sergisi; Bildiri Özetleri Kitabı, 111, 20-24 Ekim, İzmir (in Turkish)

Hadimlioglu, I.A.; King, S.A.; Starek, M.J., (2020), FloodSim: Flood Simulation and Visualization Framework Using Position-Based Fluids. *ISPRS Int. J. Geo-Inf. 9*, 163

Hong, H., Tsangaratos, P., Ilia, I., Liu, J., Zhu, A-X., Chen, W., (2018), Application of fuzzy weight of evidence and data mining techniques in construction of flood susceptibility map of Poyang County, China, Science of the Total Environment 625, 575–588 Contents

Konrad, C.P., and Booth, D.B., (2005). Hydrologic changes in urban streams and theirecological significance. American Fisheries Society Symposium, 47, 157-177

Kowalzig, J., (2008). Climate, poverty, and justice: What the Poznań UN climate conference needs to deliver for a fair and effective global deal. Oxfam Policy Pract. Clim. Change Resil. 4 (3), 117–148.

Manandhar, B., (2010), Flood plain analysis and risk assessment of Lothar Khola, MS Thesis, Tribhuvan University Institute of Forestry Pokhara, Nepal

Selçuk, L., Selçuk, A. S., Kasapoğlu, D. (2016), Coğrafi bilgi sistemleri (CBS) tabanlı çok kriterli karar analizi (Çkka) kullanılarak, Van ili merkez ilçelerinin kentsel taşkın duyarlılık değerlendirmesi, Van/Türkiye, Yerbilimleri, 37 (1), 1-18 (in Turkish)

Swain, K.C., Singha, C., Nayak, L. (2020), Flood Susceptibility Mapping through the GIS-AHP Technique Using the Cloud. ISPRS Int. J. Geo-Inf., 9, 720.

(UNECE), Statistical and Economic Commission for Europe, (2000), "Relief, Planning and Reconstruction in The Wake of Hurricane Mitch", Conference of European Statisticians, UN/ECE Work Session on Methodological Issues Involving the Integration of Statistics and Geography, Neuchatel, Switzerland.

Vojtek, M.; Vojteková, J. (2019), Flood Susceptibility Mapping on a National Scale in Slovakia Using the Analytical Hierarchy Process. Water, 11, 364.

Wang, Y.; Hong, H.; Chen, W.; Li, S.; Pamučar, D.; Gigović, L.; Drobnjak, S.; Tien Bui, D.; Duan, H., (2019), A Hybrid GIS Multi-Criteria Decision-Making Method for Flood Susceptibility Mapping at Shangyou, China. Remote Sens., 11, 62.

Witsschi-Cestari, A, (2002). "Acil Durum Yönetimine UNDP Açısından Bakış," Uluslararası Acil Durum Yönetimi Sempozyumu, Ankara, T.C. Başbakanlık Türkiye Acil Durum Yönetimi Genel Müdürlüğü Yay. , 33. (in Turkish)

Yılmaz, A, Erdoğan, M. (2018). DESIGNING HIGH RESOLUTION COUNTRYWIDE DEM FOR TURKEY. International Journal of Engineering and Geosciences, 3 (3), 98-107

Intercontinental Geoinformation Days

igd.mersin.edu.tr

Analysing influence of abandoned mining sites on land use land cover and the terrain in Jos, Nigeria

Adamu Bala *[1], **Samuel Sule Garba** [2], **Taiye Oluwafemi Adewuyi** [3], **AbdulAzeez Alıyu Onotu** [1]

[1]*Ahmadu Bello University, Faculty of Environmental Design, Department of Geomatics, Zaria, Nigeria*
[2]*University of Maiduguri, Faculty of Engineering, Department of Geomatics, Maiduguri, Nigeria*
[3]*Nigerian Defence Academy, Faculty of Art and Social Science, Department of Geography, Kaduna-Nigeria*

Keywords
Geospatial techniques
Abandoned Mining Sites
Land Use Land Cover
Terrain
Degraded Land
Jos

ABSTRACT

This research used Geospatial techniques in analysing the influence of abandoned mining sites on Land Use Land Cover (LULC) and the Terrain in Jos South, Nigeria. Thus, the objectives were to determine how the abandoned mining sites relate to the neighbouring land use and analyse the topography of the terrain in the neighbourhood of the degraded sites. The study analysed abandoned mining (land degraded) sites using multi-sensor satellite imageries of Landsat 8 (2016), SPOT 5 (2012), and SRTM DEM data of the study area. Maximum Likelihood Supervised classifications of land cover and land degradation features using Landsat 8 and SPOT 5 imageries were carried out to determine the area of land that had been affected by mining-induced activities. Finally, detailed terrain analyses such as slope and aspect were carried out. The results of the LULC classification revealed a total land cover of 512.10km^2 with mine ponds occupying about 10.01km^2. Terrain analyses revealed that the spatial location of the degraded sites is irrespective of the terrain because most of the degraded sites occurred because of mining activities; which can be done whether at high or low land. It was however suggested that certain land uses such as block industries, water treatment plants, and fish farms should be sited around the seasonally inundated mine pond.

1. INTRODUCTION

Henssen (2014) defined land as an area of the surface of the earth together with the water, soil, rocks, minerals, and hydrocarbons beneath or upon it and the air above it. It embraces all things which are linked to a fixed area or point on the surface of the earth. Components of land include the soil, vegetation, groundwater, air, wildlife. Each of these components plays a substantial role in bestowing a quality on the land through their interaction with one another (Christopher, 2015).

Proper mining started on the Jos Plateau as far-off as 1902 through Tin and Columbite as the foremost targets (Gyang and Ashano, 2009). The Tin Mining industry on the Jos Plateau has triggered widespread manmade environmental damage, with gigantic tracks of pastoral land systematically ruined in the pursuit of minerals. These activities have negative consequences on the land and hence have instigated environmental degradation in quite a lot of parts of the study area. Some of these dangers affected the environment resulting in land degradation, devegetation, water, and air pollution.

Related researches have been carried out in the past (Jonathan and Joshua, 2013; Edun and Davou, 2013; Adedeji *et al*., 2014; Igbokwe *et al*., 2008; Haruna and Solomon, 2011; and Owolabi, 2020). These research attempts mostly centred on the evaluation of the effects of post-mining activities and gully erosion on the environment.

Bearing in mind the importance of sustainability of any land and the environment in general, and also the rate at which the abandoned mining sites in the study area are affecting the LULC and terrain, this research analysed the influence of Abandoned Mining Sites on Land Use Land Cover and Terrain in the study area, to proffer solutions on how suitable restoration, reclamation, or rehabilitation can be carried out.

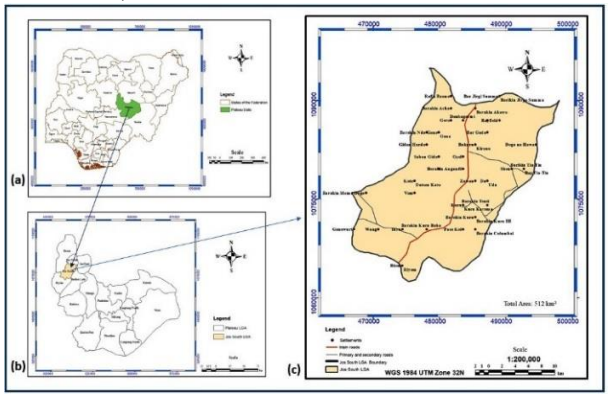

Figure 1: (a)Nigeria (b)Plateau State (c) Jos South LGA (the study area)

* **Corresponding Author**

*(abala@abu.edu.ng) ORCID ID 0000-0002-9666-5722
(ssgarba@unimaid.edu.ng) ORCID ID 0000-0003-3424-2975
(toadewuyi@nda.edu.ng) ORCID ID 0000-0001-7234-9090
(aoaliyu@abu.edu.ng) ORCID ID 0000-0003-1653-1634

Cite this study

Bala A, Garba S.S., Adewuyi, T.O. & Aliyu, A.O. (2021). Analysing Influence of abandoned mining sites on land use land cover and the terrain in Jos, Nigeria. 2nd Intercontinental Geoinformation Days (IGD), 171-174, Mersin, Turkey

The study area (shown in Figure 1) is the Jos South Local Government area which bounded by Latitude (9°34'22"N to 9°54'40"N) and Longitude (8°39'55"E to 8°59'13"E). It covers a total area of 512 km^2. It has a cool climatic condition known as mountain climate. 18°C is the average mean daily temperature, reaching up to 36^{0}C.

2. METHOD

2.1 Reconnaissance field survey and Ground truthing

Ground truthing and signature extraction were carried out before the supervised maximum likelihood classification of the merged imagery.

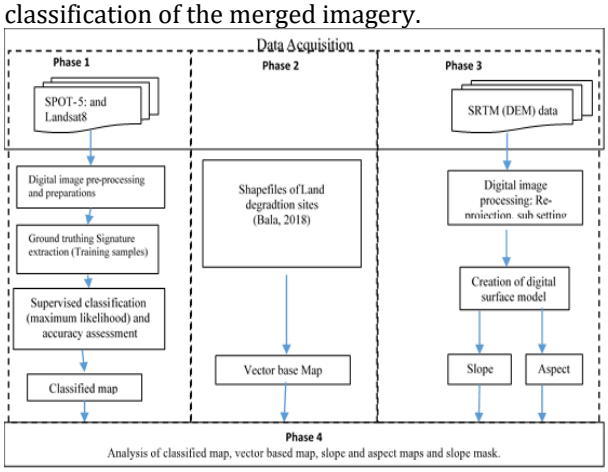

Figure 2: A flow diagram of the steps used in the research (after; Bala, 2018)

2.2 Materials Used

A description of different types of data sets dataset utilised for this research is given in Table 1.

Table 1: Datasets and their sources:

DATA NAME	RESOLUTION	DATA DATE	DATA SOURCE	PURPOSE	DESCRIPTION
SPOT 5	2.5 m	7/12/2012	Office of the Surveyor-General of the Federation	LULC mapping and analysis	3 bands multispectral image: NIR, red and green
Landsat 8: OLI and TIRS	15, 30& 100m	11/2/2016	http://www.glovis.usgs.gov/	Collateral data for LULC mapping	11 bands multispectral image
Digital Elevation Model (DEM)	20 m in both H and V directions	-	Office of the Surveyor-General of the Federation	Terrain visualization and analysis	A raster DEM covering the study area.
Vector files of land degraded sites	-		Bala, 2018	Extracting the land degraded sites	shapefiles
Study area vector file	-	-	National Centre for Remote Sensing, Jos	To demarcate the study area	Jos South local government boundary shapefile

2.3 Image Classification

The merged SPOT 5 and Landsat 8 multispectral images were classified instead of classifying SPOT5 alone because the Landsat 8 is dated 2016 whereas SPOT5 is dated 2012, hence it will be more current to employ both for the classification (Olumide, 2007).

The six (6) identified classes are shown in Table 2.

Table 2: A description of the six adopted land classes

Training sample	Code	Color assign	Description
Mine pond	1	Blue	Land surface occupied by stagnant water body without tributaries which are caused as a result of excavation/mining of earth material e.g. lake
Settlement	2	Red	Commercial, industrial, residential places, etc.
Bare exposed Rocks	3	Gray	Land consisting of rocky and stony materials.
Farmland	4	Lemon	Land occupied or related to agriculture or farming activities.
Bare degraded land	5	Yellowish	A bare surface that consists of exposed excavated earth surface material with no vegetation.
Vegetation	6	Light green	Shrubs and other vegetation that is not used for farming activities.

2.4 Analyses of Terrain in the Neighbourhood of the Abandoned Mining Sites

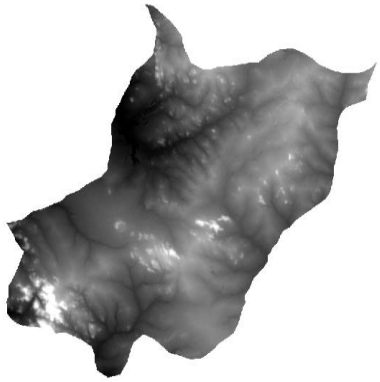

Figure 3: A subset of DEM of the study area

The DEM data scene was clipped to match the study area (see Figure 3). The slope was calculated for each cell in raster images (ESRI, 2017a). Thereafter, the slope and aspect maps were generated based on Eqn. 1 and 2 (ESRI, 2017b).

$$Percent\ of\ slope = (Rise \div Run) \times 100 \quad \text{(Eqn. 1)}$$

$$Degree\ of\ slope, \theta = \tan^{-1}(Rise \div Run) \quad \text{(Eqn. 2)}$$

3. RESULTS

3.1 Analyses of Land Use Classification in the Neighbourhood of Degraded Area

The overall map accuracy and the Kappa coefficient accuracy were 77.82% and 73.16% respectively.

The degradation that affected different land cover types was determined by overlaying the land cover data with the vector files of the abandoned mining sites. Special attention was paid to land cover classes that coincided with degraded areas such as inundation and bare degraded land because such areas represent land cover types that were likely to have been affected by degradation.

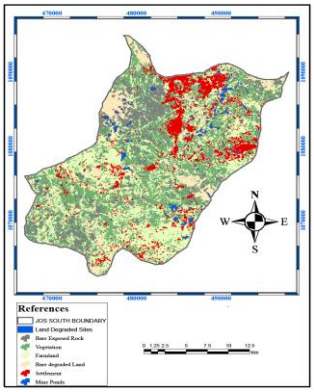
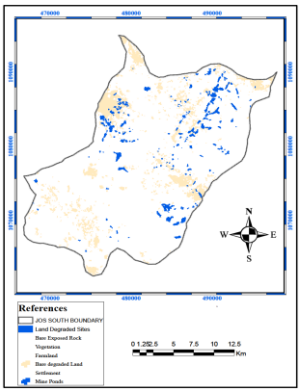

Figure 4: Land cover map; Figure 5: Relationship between Bare Degraded land and Abandoned mining sites

In Figure 4, the settlement areas were concentrated in the central upper part of the area and are shown in red colour. Similarly, the mine ponds (degraded) were dispersed all over the area characterizing where mining activities are taking place. Again, the presence of rocky covers indicated that the study is characterized by steep terrain. Farmlands and vegetation covers are found all over the area and are displayed in light green and green.

In Figure 5, the relationship between bare land cover and degradation is that this land cover is not much influenced by degradation because rock outcrops do not get easily eroded or excavated, except where quarry activities (blasting and crushing) are carried out turning this land cover to big gullies and inundated due to rainfall.

Table 3: LULC distribution of the fused imagery

LULC CLASS	AREA (Km²)	AREA (%)
Mine pond	10.0052	1.95
Settlement	35.7792	6.99
Exposed Rock Outcrop	212.809	41.56
Farmland	92.9401	18.15
Bare degraded land	38.4006	7.50
Vegetation	122.163	23.85
TOTAL	**512.0971**	**100**

Source: (Geomatic Department, ABU Zaria, 18/6/2018)

Mine ponds and bare degraded lands account for a total of 9.45%, these are the most obvious land degraded covers with less economic activities going on (Table 3).

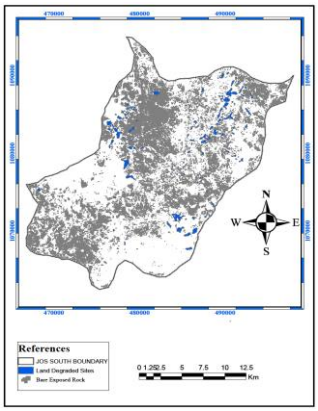
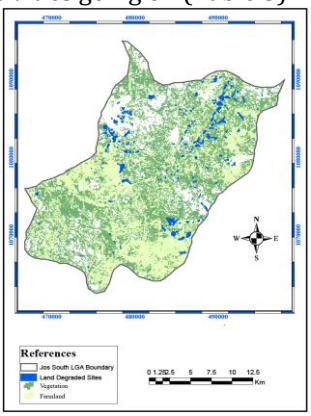

Figure 6: rock outcrop & Abandoned mining sites; Figure 7: Vegetation, Farmland &Abandoned mining sites

The rock cover in Figure 6 is largely spread across the area and covered a total of 41.56%. This land cover could be referred to as degraded areas because it is barren and agricultural activities are seldom carried out. Some areas are turned into quarry areas where rocks are blasted and crushed for economic purposes.

In Figure 7, farming activities make the topsoil susceptible to erosion. This results in gulling as witnessed in many parts of the areas. Also, some farmlands have been disturbed due to tin mining activity. Also, large portions of the vegetation cover are cleared annually for farming purposes and searching for minerals, resulting in vegetation degradation, deforestation, and severe damage.

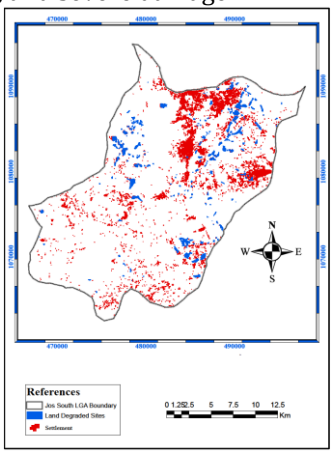

Figure 8: Relationship between Settlements and Land degraded sites

In Figure 8, settlements are not properly planned; some houses are built indiscriminately near the abandoned mine pits without due consideration to dangers such may posit. Most of the area is rocky hence houses cannot be constructed easily.

3.2 Analyses of the Terrain in the Neighbourhood of the Degraded Sites

The high elevation of the area contributes to land degradation because when heavy rainfalls, water moves from the upstream carrying sediments down the lowland. The resultant high overflow on the steep slopes aggravates soil erosion and ultimately causes the land cover to depreciate resulting in degradation of the area.

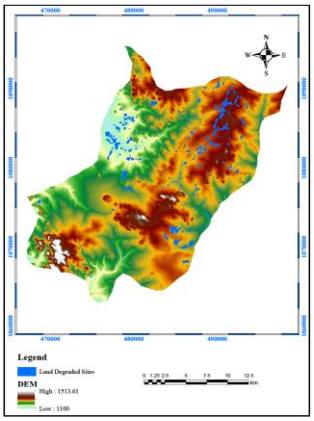
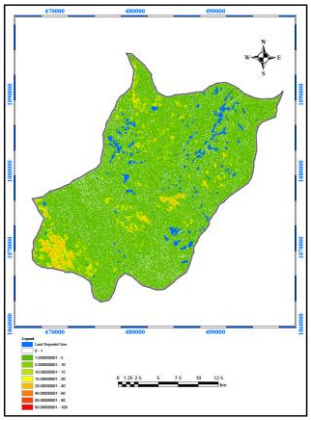

Figure 9: Overlay Maps (Degraded Sites & DEM); Figure 10: Slopes derived from DEM

Figure 9 is the overlay of the digitized degraded sites on the elevation model. This revealed the abandoned mining ponds spread randomly in the study area. It can

be observed that the spatial location of the sites is irrespective of the elevation.

The slope map in Figure 10 shows the configuration of the terrain in terms of depth and height. It implied that land covers with depths (e.g. derelict ponds) have slope values of 0 to 0.99, which further describes that the study area is characterized by excavated surfaces, gully, and abandoned mines that have become derelict ponds (filled with water and stagnant).

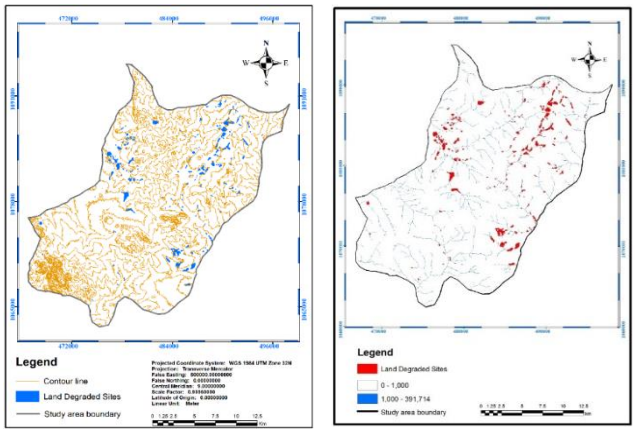

Figure 11: Degraded sites overlaid on contours; Figure 12: Degraded sites overlaid on the flow accumulation

From Figure 11, the spatial location of the sites is irrespective of the contour values as some sites are located on a steep slope while others are on a gentle slope.

Figure 12 shows the stream networks derived from flow accumulations. It is observed that most of the stream networks were connected with the degraded sites which proves the fact that most of the degraded sites are seasonally inundated.

4. DISCUSSION

The high elevation of the area contributes to land degradation which affects the LULC. In addition to elevation, slopes that were affected by degradation were identified because mountain surfaces inherently have steep slopes. The steepness of the slope is significant in the study of land degradation mainly because of the impacts of soil erosion caused by water on the slopes. Most of the degraded sites occurred as a result of mining activities; the major condition or criteria for mining minerals is its availability hence mining activities can be done whether at high or low land.

5. CONCLUSION

The study has effectively analysed the influence of Abandoned Mining Sites on Land Use Land Cover and Terrain in the study area using existing abandoned mining sites vector files, maximum likelihood supervised classification and digital elevation model data. The study revealed that the spatial location of the degraded sites is irrespective of the terrain because most of the degraded sites occurred as a result of mining activities; which can be done whether at high or low land. There are certain appropriate LULC in the neighbourhood that could be utilized productively, for example, block industries, water treatment plants, fish farming, and other economic activities should be sited around the seasonally inundated mine pond, so that they can be more useful.

ACKNOWLEDGEMENT

The authors wish to acknowledge the Office of the Surveyor-General of the Federation (OSGOF), Abuja; and the USGS for providing them with Satellite Imageries.

REFERENCES

Adedeji, O. H., Adebayo, H. O. and Sotayo, E. I. (2014). Assessment of Environmental Impacts of Inland Sand Mining in Parts of Ogun State, Nigeria. *Ethiopian Journal of Environmental Studies* and *Management, 5*(7).doi:http://www.dx.doi.org/10.4314/ejesm.v7i5 .2Bala, A. (2018) "Geospatial Analyses of Land Degradation Sites in Jos South LGA of Plateau State". M.Sc. thesis submitted to the Ahmadu Bello University, Zaria. Available on http://kubanni.abu.edu.ng/jspui/handle/12345678 9/11107

Christopher O. A. (2015). Land-Use management. Available on http://www.unaab.edu. ng. Accessed on 17th June, 2015.

Edun, E. O., and Davou, D. D. (2013). Inventory of Abandoned Mine Ponds/Dams on the Jos-Bukuru North-Central Nigeria Using G.I.S and Remote Sensing Technique. *The International Journal of Engineering and Science*, *2*(5): 62-71.

Environmental System and Research Institute (ESRI) (2017a). *How Slope Works.* ESRI ArcGIS Desktop help.

Environmental System and Research Institute (ESRI) (2017b). *How Aspect Works.* ESRI ArcGIS Desktop.

Gyang, J.D, and Ashano, E.C (2009). Effects of Mining on Water Quality and the Environment; a case study of parts of the Jos Plateau, North Central Nigeria. Continental *Journal Environmental Sciences, 3:* 33-42.

Haruna, M.D. and Solomon J.N. (2011). An Assessment of Mining Activities Impact on Vegetation in Bukuru Jos Plateau State Nigeria Using Normalized Differential Vegetation Index (NDVI). *Journal of Sustainable Development, 4*(6). doi:10.5539/jsd. v4n6p150

Henssen, J. (2014). *Basic Principles of the Main Cadastral Systems in the World*. Retrieved from https://www.fig.net/commission7/reports/events/ delft_ seminar_ 95/paper2.html. Accessed on 23rd. September, 2020.

Jonathan O. and Joshua B. (2013). Geospatial application in mapping gully erosion sites in Jos, Plateau State, Nigeria. *Journal of Scientific Research and Essay (SJSRE)*, *2* (6): 85-95.

Olumide, M.A. (2007). *Land use and land cover change detection with remote sensing and GIS at metropolitan Lagos, Nigeria (1984-2002).* Leicester, England: ProQuest LLC.

Owolabi, A. (2020). Assessment of Terrain and Land Use/Land Cover Changes of Mine Sites using Geospatial Techniques in Plateau State, Nigeria. *Journal of Mining and Environment (JME), 11(4): 935-948. DOI: 10.22044/jme.2020.9668.18*

Intercontinental Geoinformation Days

igd.mersin.edu.tr

2D Flood modeling with the help of GIS: Mersin / Lamas River

Vahdettin DEMİR*[1], Aydın ALPTEKİN [2], Mehmet Özgür ÇELİK [3], Murat YAKAR [3]

[1]*KTO Karatay University, Faculty of Engineering, Civil Engineering Department, Konya, Turkey*
[2]*Mersin University, Faculty of Engineering, Geological Engineering Department, Mersin, Turkey*
[3]*Mersin University, Faculty of Engineering, Geomatics Engineering Department, Mersin, Turkey*

Keywords
Flood modeling
Mersin
Lamas River
HEC-RAS 2D
CBS

ABSTRACT

A flood is a natural disaster that causes damage to the surrounding lands, settlements and living creatures by not fitting the amount of water in the riverbed for various reasons. Flood disasters all over the world and second in terms of loss of life and property in Turkey, located between meteorological disasters in the first place. To reduce the material and moral damages of floods affecting our lives, it is necessary to know the mechanism that turns the flood into a disaster and to take precautions before the flood occurs. In this study, Lamas River Basin, where floods were experienced many times in the past, was chosen as the study area. 2D flood modeling was performed with Geographical Information Systems and HEC-RAS-2D program. As a result of the modeling, flood depth and propagation maps were obtained for different flood return periods (Q_{50}, Q_{100} and Q_{500}).

1. INTRODUCTION

Flood is a natural disaster that interrupts economic and social activities in the region by damaging surrounding lands, settlements, infrastructure facilities, and living creatures, due to reasons such as excessive rainfall, rapid melting of the existing snow, landslide, uncontrolled water release from the dam, and by changing the cross-section of the riverbed. It ranks second among all disasters and first among meteorological disasters in terms of loss of life and property in the world and our country. When the current data are examined, the economic loss caused by the floods is approximately 300 million TL every year. When examining the flood events and effects that occurred in our country between 1975 and 2015; it was observed that 1209 floods occurred, 720 people lost their lives, and 893.993 hectares of land were submerged. The year when the most flood occurred was 2015 (122 times) and the most casualties were in 1995 with 164 people. The total number of floods experienced between 1975 and 2002 is 487, and the total loss of life is 493. The total number of floods evaluated in the 2003-2015 period was 722, and the total loss of life was 227 (DSI 2017).

The precipitation regime is changing with global warming and climate change. This situation causes precipitation to turn into natural disasters. Floods from natural disasters are not a problem that can be eliminated completely. Therefore, preventive measures should be taken against floods, especially in urban areas, upstream and downstream of rivers. Globally, there has been a growing interest in recent years to predict floods, manage impacts and mitigate associated damage. Reducing the damage caused by floods requires different strategies in different areas. Therefore, targets and measures used in flood risk management should be diversified and regionalized (Hooijer et al. 2004). The purpose of flood modeling and risk analysis is to minimize the loss of life and property caused by floods (Petrow et al. 2006). It is also the protection of river ecology (Rubinato et al. 2019). The nature of the flood hazard is often defined by causation, in other words the probability and magnitude of the flood event. Flood risk is a function of flood vulnerability (Merz et al. 2007). Rapid and unplanned urbanization, insufficient infrastructure systems and changes in precipitation characteristics due to climate change create more areas that will be affected by floods in our country and around the world (Willems et al. 2012). Losses of lives, injuries, psychological traumas and deterioration in social life occur in these areas due to floods. In addition, floods can cause damage to public and private properties, infrastructure systems such as sewerage and superstructure systems such as roads and bridges

* **Corresponding Author**

*(vahdettin.demir@karatay.edu.tr) ORCID ID 0000-0002-6590-5658
(aydinalptekin@mersin.edu.tr) ORCID ID 0000-0002-5605-0758
(mozgurcelikmersin.edu.tr) ORCID ID 0000–0003– 4569– 888X
(myakar@mersin.edu.tr) ORCID ID 0000-0002-2664-6251

Cite this study

Demir V, Alptekin A, Çelik M. Ö, & Yakar M (2021). 2D flood modeling with the help of GIS: Mersin / Lamas River. 2nd Intercontinental Geoinformation Days (IGD), 175-178, Mersin, Turkey

(Demir and Ülke Keskin 2020) For these reasons, city planners should primarily assess the flood risk for new settlements.

The Hydrologic Engineering Centers River Analysis System (HEC-RAS) software is frequently used in flood modeling worldwide. Yazıcılar and Onder (1998), Tate et al. (2002), Sheffer et al. (2008) have used HEC-RAS software to map flood areas. In this study, the Lamas river flowing into the Mediterranean and situated in the Eastern Mediterranean Region of Turkey was designated as the work area. There have been many major floods in this area in the past. The last recorded floods occurred in January 1959, December 2001, and October 2006, and there were great financial and emotional damage in the floods. Therefore, this study aims to perform two-dimensional modeling of 50-, 100- and 500-years flood return periods of Lamas River with the help of the HEC-RAS program, which can work integrated with GIS systems and GIS systems and hydraulic calculations can be made.

2. MATERIAL and METHOD

2.1. Study Area

Mersin is located to the west of Adana, the southeast of Karaman the southwest of Niğde, the south of Konya and the east of Antalya. The surface area of Mersin province is 15.853 km^2. Except for 50% of the Tarsus district, all of it is within the boundaries of the Eastern Mediterranean Basin. Mersin province, which is surrounded by the Mediterranean in the south, is separated from the inner parts of Anatolia by the high plateaus and peaks of the West and Central Taurus Mountains from the north (URL 2021). Lamas River (Limonlu) is located in Erdemli district. This river takes its source from the Yüğlük Mountain in the region of Karaaydın. The Lamas River, which joins the Aksıfat River, flows into the Mediterranean from the Limonlu district (CVSB 2016; SYGM 2019). For this reason, the river gave its name to the Limonlu district. Its length is 99 km. The annual average flow rate is 6.25 m^3/s (SYGM 2019). The study area is included in Figure 1.

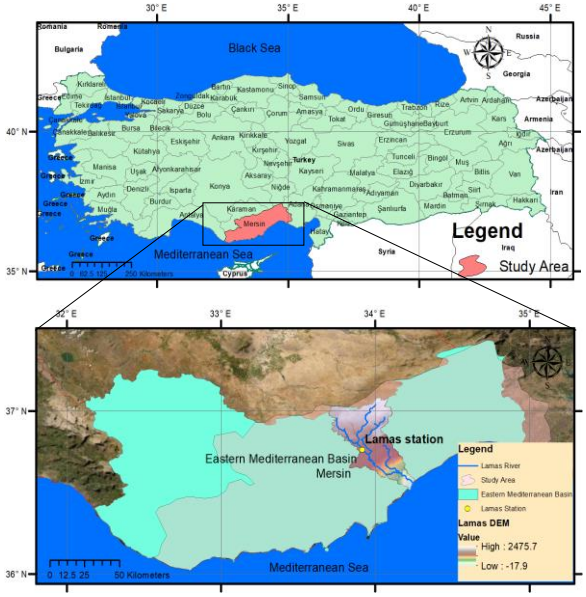

Figure 1. Study Area

2.2. HEC-RAS 2D

HEC-RAS is a program that can model 2D flow developed by the United States Army Corps of Engineers. HEC-RAS models the flood flow using full 2D Saint Venant equations and 2D diffusion wave equations (Quiroga et al. 2016).

$$\frac{\partial \zeta}{\partial t}+\frac{\partial p}{\partial x}+\frac{\partial q}{\partial y}=0 \tag{1}$$

$$\frac{\partial p}{\partial t}+\frac{\partial}{\partial x}\left(\frac{p^2}{h}\right)+\frac{\partial}{\partial y}\left(\frac{pq}{h}\right)=\frac{n^2 pg\sqrt{p^2+q^2}}{h^2}-gh\frac{\partial \zeta}{\partial x}+pf+\frac{\partial}{\rho\partial x}(h\tau_{xx})+\frac{\partial}{\rho\partial y}(h\tau_{xy}) \tag{2}$$

$$\frac{\partial q}{\partial t}+\frac{\partial}{\partial y}\left(\frac{q^2}{h}\right)+\frac{\partial}{\partial x}\left(\frac{pq}{h}\right)= \frac{n^2 qg\sqrt{p^2+q^2}}{h^2}-gh\frac{\partial \zeta}{\partial y}+qf+\frac{\partial}{\rho\partial y}(h\tau_{yy})+\frac{\partial}{\rho\partial x}(h\tau_{xy}) \tag{3}$$

Where h is the water depth in meters, p and q represents the specific flow in the x and y directions (m^2/s), ζ is the water surface elevation (m), g is the acceleration due to gravity (m/s^2), n is the Manning friction coefficient, ρ is the density of water (kg/m^3), τ_{xx}, τ_{yy} and τ_{xy} are components of effective shear stress and f is the Coriolis effect (Kamboh et al. 2016).

3. RESULTS

Flood modeling includes several processes. Modeling requires a digital elevation model, flow rates calculated for different return times of the Lamas river, baseline map of the region and Manning friction coefficients. In the study, the digital elevation model was obtained from the General Directorate of State Hydraulic Works (Figure 2).

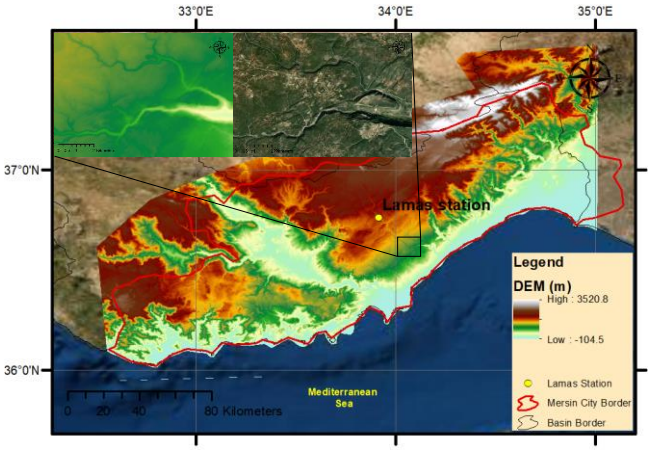

Figure 2. Digital Elevation Model (DEM)

The resolution of the DEM is 10 meters (Fig. 1). Flow networks and basin boundaries have been obtained using ArcGIS-Hydrology tools. For detailed information, the proposed study can be examined (Çay et al. 2018). Flood return periods are determined according to statistical and deterministic methods. In this study, flood return periods were obtained from the Eastern Mediterranean Flood Management Plan. According to this report, the study area is in flood risk areas (SYGM 2019). Flood return periods are given in Table 1.

Table 1. Flood values of different return periods of Lamas River.

Return period	Q_{50}	Q_{100}	Q_{500}
Flood (m^3/s)	29.1	36.3	51.5

Manning friction coefficients were taken as 0.04 as an average value in the study. The distribution area (km^2) in the study area of Q_{50}, Q_{100} and Q_{500} return periods is given in Table 2. Flood modeling was carried out in the HEC-RAS 2D program using 25 meters of calculation areas (mesh).

Table 2. Flood areas

Return period	Q_{50}	Q_{100}	Q_{500}
Area (km^2)	3.46	3.57	3.82

According to Table 2, an important area (with 3.46 km^2) is affected in modeling the Q_{50} flow rate. As a percentage, the Q_{50} flow rate constitutes 96% of the Q_{100} flow rate and 90.5% of the Q_{500} flow rate. The maps of floods in the study area are shown in Figures 3-5.

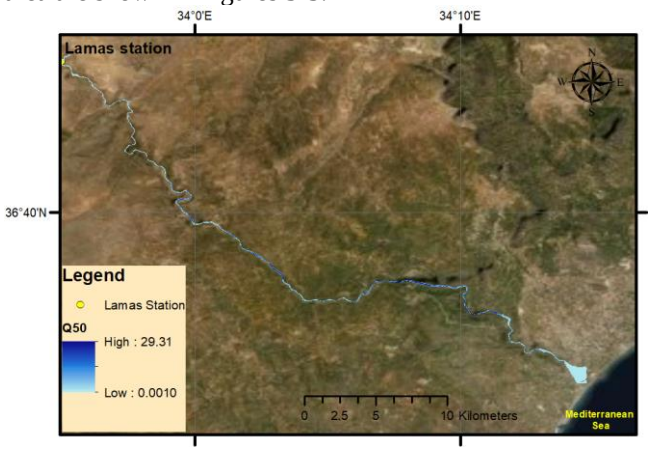

Figure 3. Flood propagation map for Q_{50}

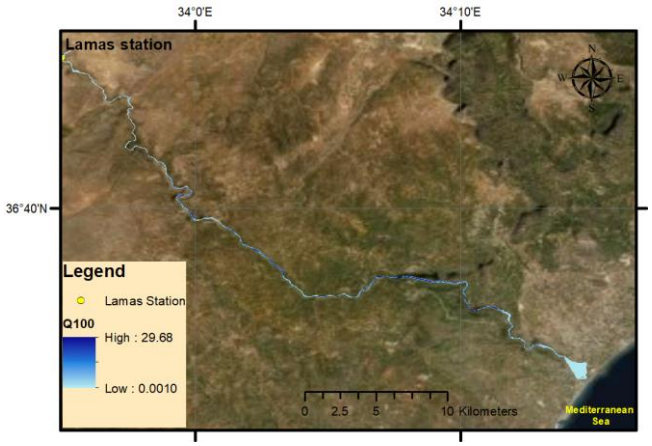

Figure 4. Flood propagation map for Q_{100}

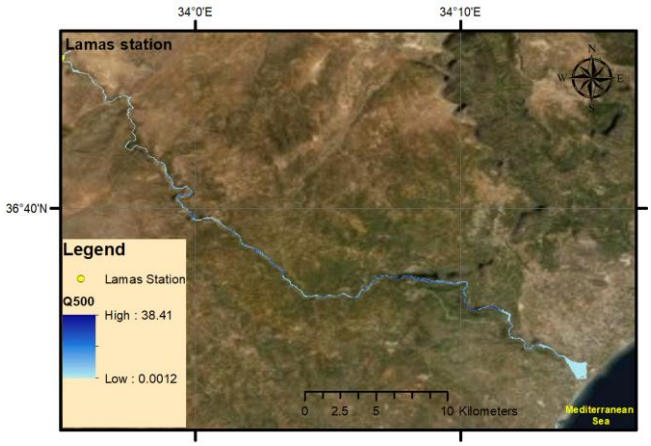

Figure 5. Flood propagation map for Q_{500}

When Figure 3-4 is examined, it is seen that the flood flow rate with 50 years and larger flood flow rates are overflowing from the river bed. Especially towards the downstream part, the right and left sides of the study area are inundated. Although the river sections are sufficient in the upstream sections, the river sections are insufficient in the downstream section. In the HEC-RAS 2D modeling, it is seen that the flow cannot follow the curves of the river downstream. As a result, water heights of up to 1-1.5 meters can be seen on the right and left sides of the river. These overflows are more common in the region to the east of the river. The reason for this situation is that the eastern region is located at a lower elevation. Besides, the flood spread could not pass to the Mediterranean from the highway between Mersin and Antalya and caused pooling in the downstream region.

4. DISCUSSION

Lamas river, which is the study area, is an important region that can be affected by floods according to the basin management plan. In the related plan, the Lamas river was studied together with the Sulukluk river and only in the downstream region. In this study, only the effect of the Lamas river was investigated in upstream and downstream regions. Thus, the model used was studied for the first time in the region. The results obtained are compatible and supportive of the plan. In the report, it was stated that all greenhouse areas could be submerged and the highway passing through the region could act as a set, causing high water depths in the greenhouse area behind it (Figure 6).

Figure 6. The greenhouse area affected by the flood

5. CONCLUSION

In this study, 3 different (Q_{50}, Q_{100} and Q_{500}) flood return period Mersin/Lamas river were modeled with the HEC-RAS 2D package program that can perform 2-dimensional flood modeling. The height model in the analysis was obtained from the General Directorate of State Hydraulic Works. Food return periods were taken from the basin management plan. In the modeling, the constant 0.04 Manning friction coefficient was defined on 25-meter meshes. After hydraulic calculations were made in HEC-RAS, all results data were brought together in ArcGIS and flood propagation maps were created.

As a result of the modeling, it was determined that the area located in the downstream part of the Lamas river after the Q_{50} flow rate was significantly affected by the flood. In the Mediterranean Region, regulations that can carry at least Q_{100} flood flow rates should be made in urban areas. Water heights of up to 1.5 meters were determined in the downstream parts of the study area. Cross-section arrangements should be made that can carry the waters of this height. Besides, it is suggested that the pooling that occurs in the Mersin-Antalya highway region can be reduced with new channels that can be opened on this road.

ACKNOWLEDGEMENT

The authors thank KTO Karatay University, Mersin University, General Directorate of State Hydraulic Works, and their staff for all their support.

REFERENCES

Çay, F., Demir, V., & Sevimli, M. F. (2018). Determination of the river basin boundaries with the help of GIS in Turkey. 13th International Congress on Advances in Civil Engineering, 1-8, Izmir, Turkey

CVSB (2016). Evaluation report of pollution prevention studies in the Eastern Mediterranean Basin, Ministry of Environment and Urbanization, Ankara. (in Turkish)

Demir V & Keskin A Ü (2020). Obtaining the manning roughness with terrestrial-remote sensing technique and flood modeling using FLO-2D, a case study Samsun from Turkey. Geofizika. 37(2),131-156. https://doi.org/doi.org/10.15233/gfz.2020.37.9

DSI (2017). Flood management. Republic of Turkey Ministry of Forestry and Water Affairs. (in Turkish)

Hooijer A, Klijn F, Pedroli G B M, & Van Os A G (2004). Towards sustainable flood risk management in the Rhine and Meuse river basins: synopsis of the findings of IRMA-SPONGE. River Research and Applications, *20*(3), 343–357. https://doi.org/10.1002/rra.781

Kamboh S A, Sarbini I N, Labadin J, & Eze M O (2016). Simulation of 2D Saint-Venant equations in open channel by using MATLAB. Journal of IT in Asia, 5(1), 15–22. https://doi.org/10.33736/jita.47.2015

Merz B, Thieken A H, & Gocht M (2007). Flood risk mapping at the local scale: concepts and challenges flood risk management in Europe, 25, 231–251. https://doi.org/10.1007/978-1-4020-4200-3_13

Petrow T, Thieken A H, Kreibich H, Merz B & Bahlburg C H (2006). Improvements on flood alleviation in Germany: lessons learned from the Elbe Flood in August 2002. Environmental Management, 38(5), 717–732. https://doi.org/10.1007/s00267-005-6291-4

Quiroga V M, Kure S, Udo K, & Mano A (2016). Application of 2D numerical simulation for the analysis of the February 2014 Bolivian Amazonia flood: Application of the new HEC-RAS version 5. RIBAGUA - Revista Iberoamericana Del Agu, 3(1), 25–33. https://doi.org/10.1016/j.riba.2015.12.001

Rubinato M, Nichols A, Peng Y, Zhang J, Lashford C, Cai Y Peng, Lin P Zhi & Tait S (2019). Urban and river flooding: Comparison of flood risk management approaches in the UK and China and an assessment of future knowledge needs. Water Science and Engineering, 12(4), 274–283. https://doi.org/10.1016/j.wse.2019.12.004

Sheffer Y, Rico N A & Eıızel M (2008). The palaeoflood record of the Gardon River. France: A comparison with the extıeme 2002 flood event. Geomorvhology, 98(1–2), 71-83.

SYGM (2019). Eastern Mediterranean Basin flood management plan. General Directorate of Water Management, Ankara. (in Turkish)

Tate E C, Maidment D R, Olivera F & Anderson D J (2002). Creating a terrain model for floodplain mapping. Journal of Hydrologic Engineering, *7*(2), 100–108. https://doi.org/10.1061/(ASCE)1084-0699(2002)7:2(100)

URL (2021). *Mersin.ktb.gov*. https://mersin.ktb.gov.tr/TR-73136/mersin.html (Date of Access: 06.04.2021) (in Turkish)

Willems P, Arnbjerg-Nielsen K, Olsson J, & Nguyen V T V (2012). Climate change impact assessment on urban rainfall extremes and urban drainage: Methods and shortcomings. Atmospheric Research, 103, 106–118.https://doi.org/10.1016/j.atmosres.2011.04.003

Yazıcılar, F., & Önder, H. (1998). Taşkın yatakları planlamasında HEC-RAS Bilgisayar programı ile su yüzü profili hesaplanması-Bartın Nehrinde bir uygulama. 1–21. Su Mühendisliği Problemleri Semineri (in Turkish)

Intercontinental Geoinformation Days

igd.mersin.edu.tr

Using modern methods to determine the suitable area for rain harvesting

İldeniz Leyla ÖZTÜRK*[1], Lütfiye KUŞAK[2]

[1]Mersin University, Geomatics Engineer, Mersin, Turkey
[2]Mersin University, Engineering Faculty, Department of Geomatics Engineering, Mersin, Turkey

Keywords
Rain Harvest
Depletion of Underground Water Resources
Modern Techniques
Agricultural Land
Geostatistical Analysis

ABSTRACT

In addition to the efficient use of our water resources, it is important to ensure the recycling of the water we use in order not to deplete our fresh water resources, which are decreasing today, and to leave healthy and sufficient water to future generations. The purpose of using the rainwater harvesting system is to create a reliable, low-cost, practical water obtaining system in areas where there is no water and cannot meet the desired needs. Rain harvest; It enables groundwater to be fed, increases our living standards, increases agricultural production, benefits the creatures living in nature, prevents climatic changes, floods, water pollution, and enables us to obtain drinking water. The aim of this study is to determine the area suitable for rain harvesting for the agricultural lands of Karahacılı Village in Yenişehir district of Mersin province. Specific criteria will be selected in the study to evaluate potential RWH sites. In addition, suitable and unsuitable areas will be identified and criteria will be determined for this. Both biophysical and socio-economic criteria must be considered to ensure the success of RWH techniques and to facilitate the adoption of new RWH technology by local farmers. Choosing appropriate socio-economic parameters is critical to achieve desired results.

1. INTRODUCTION

Water is the most important and basic life source of all living organisms living in the ecological system on earth. Throughout history, the birth and development regions of many civilizations have been on the waterfront. Proximity to water resources has maintained its importance from past to present and has had a direct impact on the development of societies (Aghaloo and Chiu 2020; Teston et al. 2018; Agarwal et al. 2001). Especially the ancient Egyptian civilization established around the Nile River actively used this water resource and this river has been the basis for many scientific studies. In addition, it has also contributed to the formation of activities that directly affect human life and social order (determination of the flood time, development and protection of private property, etc.). The rough and unconscious use of water harms the country's natural resources (Alwan et al. 2020; Teston et al. 2018; Akaydın Sel 2017; Al-shabeeb 2016). Due to the unconscious use of water in thousands of decares of land in the world, agriculture has become impossible and yield losses have occurred (Bashar et al. 2018; Teston et al. 2018 Campisano et al. 2017). The advantages of the rain harvesting method are that it is simple and economical, and the water transmission losses are low. In the water harvesting method, water collection areas are roofs, courtyards, streets and squares, small soil surfaces, sloping areas and large basins that feed seasonal flows (Salameh 2018). The water storage medium is divided into underground storage and storage on the soil surface (Guillaume et al. 2017; Guyassa et al. 2017; Ekinci 2015). While soil, sediment and cisterns are used for underground storage, tanks, reservoirs and pools are used as storage media on the soil surface. The rain harvesting system is limited and prone to little rainfall. Therefore, limited precipitation is among the main limiting factors of the method (Can and Yilmaz 2019; Datta 2015; Gould et al. 2014).

The aim of this study is to determine the area suitable for rain harvesting for the agricultural lands of Karahacılı Village in Yenişehir district of Mersin province. In the study, certain criteria will be selected to evaluate potential RWH sites (these are precipitation, temperature, land use, slope, aspect, soil type, soil depth and drainage density). In addition, suitable and unsuitable areas will be identified for this (agricultural

* **Corresponding Author**

*(idenizleylaa@gmail.com) ORCID ID 0000-0003-0598-9316
(Lutfiyekusak@mersin.edu.tr) ORCID ID 0000-0002-7265-245X

Cite this study

Ozturk I L & Kusak L (2021). Using modern methods to determine the suitable area for rain harvesting. 2nd Intercontinental Geoinformation Days (IGD), 179-182, Mersin, Turkey

areas, Distances to roads, urban areas, faults and drainage networks) criteria will be set. Both biophysical and socio-economic criteria need to be considered to ensure the success of RWH techniques and to facilitate the adoption of new RWH technology by local farmers. Choosing appropriate socio-economic parameters is critical to achieve desired results (Toosi et al. 2020; Velasco-Muñoz et al. 2019; Lani et al. 2018; Vema et al. 2018; Tamaddun 2018). RWH structures cannot be applied in drainage networks for environmental, technical and financial reasons. The acceptable distance from the roads should be considered to avoid any possibility of future conflict between the road development and the constructed structures. It is very important to exclude urban areas from being selected as RWH sites for safety reasons (eg conflicting with floods and land uses). In addition, agricultural land (cultivated areas) are both economically and environmentally valuable resources and should be excluded simply because they cannot be disturbed by water collection systems, but proximity to rainwater harvesting systems can be an advantage if appropriate safety measures are maintained.

2. METHOD

In this study, biophysical factors of rainfall, land use, slope, aspect, soil type, soil depth and drainage intensity were selected to assess potential RWH sites (Hajjar et al. 2020; Hafizi et al. 2018; Hassani et al. 2016). In addition, six socio-economic factors were used to identify unsuitable areas, including distances to farmland, roads, urban areas, wells, faults and drainage networks (Yeniçeri 2018; Yosef and Asmamaw 2015). The most common RWH systems that are widely used and shown to be successful will be considered. Selected socio-economic factors and common RWH systems will be conducted on the basis of similar studies. Next, optimum locations will be proposed for each type of RWH system based on the specific requirements of each system.

2.1. Data Collection and Pre-Processing

The sources of the main factors that will be used to determine suitable sites for RWH are shown in Table 1.

Table 1. Data and sources to be used in this study

Data name	Scale	Sources
Precipitation	Data (Excel File)	Meteorology
Drainage	5m	Spatial Data Infrastructure
Road map		Spatial Data Infrastructure (open street map)
Geology	1:250000	Ministry of Agriculture National Soil and research institute
Land Use		CORINE (2018)
Slope	5 m	DEM Data
Aspect	5 m	DEM Data (Soil map)

Raw data will come from various government agencies, a field study. Monthly precipitation data will be collected from the Meteorology unit. Annual average precipitation will be calculated for each station. Maps will be created in ArcGIS environment using 5m DEM data and 3D Analyst tool. Soil map and drainage density map of the study area will be created according to slope, aspect, rainfall, soil infiltration feature and arrow. In addition, thematic layers such as existing water areas will be prepared using ArcGIS software.

2.2. Analytical Hierarchy Process (AHP)

An Analytical Hierarchy Process (AHP) method will be used to generate the potential RWH map. AHP is a method used to analyze and organize complex decisions based on professional knowledge and practice. The relative importance of each criterion will be determined by consulting experts on the importance of selected criteria for Rain harvesting using a scale from 1 to 9.

2.2.1. Layer selection:

In this study, slope, aspect, land use / cover, soil type, precipitation criteria, soil depth and drainage density criteria will be used.

Precipitation

The most influential factor for the high RWH potential is precipitation. Average annual precipitation data is one of the prerequisites for large-scale RWH structures. More rainfall in an area results in higher RWH potential. Higher precipitation values indicate higher water volume and higher potential flow and consequently higher potential for local flow capture using RWH structures (Toosi et al. 2020; Hofman-Caris et al. 2019; Nguyen and Han 2017).

Slope

Surface runoff and seepage will be greatly affected by the topography of the basin. Slope has a direct impact on runoff formation and conversion from precipitation to runoff. As the slope increases, the RWH opportunity time decreases due to increasing flow rates. Ideally, the slope of a basin should be as gentle as possible for a high RWH potential. Often areas with slopes greater than 5% are subject to more erosion; Therefore, it is necessary to consider erosion control measures in areas where the basin has a steeper slope (Toosi et al. 2020; Krois and Schulte 2014).

Soil Type

One of the main criteria for RWH planning is soil. Naturally poorly drained clay soils produce higher amounts of runoff, while sandy soils generate less runoff (Toosi et al. 2020).

Soil Depth

Soil depth is considered to be representative of water storage capacity (i.e. deeper soils have more water storage capacity). Areas with shallow soils are potentially more suitable for RWH technologies than deep ones, as they have lower infiltration (higher flow coefficient) and produce more water (Toosi et al. 2020).

Land Use

The effect of different land use and vegetation on the amount and velocity of different runoff flowing downhill. Dense vegetation, forests and closed areas increase the amount of water infiltration and water withdrawal, while urban and pasture-covered areas increase the amount of runoff. Since the infiltration effect is already explained by soil type, a lower weight has been assigned to land use (Toosi et al. 2020).

Drainage Density

Dense drainage networks can play a crucial role in collecting rainwater. The concentration time is significantly related to the drainage density, such that areas with higher drainage density are more suitable for RWH as it provides a system through which the flow can flow and harvest immediately. Drainage density is considered the least important factor (Toosi et al. 2020).

2.2.2. Socio-Economic Criteria

Both biophysical and socio-economic criteria need to be considered to ensure the success of RWH techniques and to facilitate the adoption of new RWH technology by local farmers. Choosing appropriate socio-economic parameters is critical to achieve desired results. RWH structures cannot be applied in drainage networks for environmental, technical and financial reasons. The acceptable distance from the roads should be considered to avoid any possibility of future conflict between the road development and the constructed structures. It is very important to exclude urban areas from being selected as RWH sites for safety reasons (eg conflicting with floods and land uses). In addition, agricultural land (cultivated areas) are both economically and environmentally valuable resources and should be excluded simply because they cannot be disturbed by water collection systems, but proximity to rainwater harvesting systems can be an advantage if appropriate safety measures are maintained (Toosi et al. 2020).

3. CONCLUSION

Rainwater Harvesting (RWH) is becoming one of the most promising alternative freshwater resources that can potentially be captured and used, especially in arid and semi-arid regions. This study is the preliminary information of the system to be established and its analyzes are ongoing. Using the biophysical and socio-economic factors, the appropriate RWH areas will be determined with the GIS-based AHP method and additional methods and it will be determined whether the existing areas are suitable or not.

REFERENCES

Afet ve Risk Dergisi 1(2), 2018, (126-136).

Agarwal, A., Narain, S., & Khurana, I. (Eds.). (2001). Making water everybody's business: practice and policy of water harvesting. Centre for Science and Environment.

Aghaloo, K., & Chiu, Y. R. (2020). Identifying Optimal Sites for a Rainwater-Harvesting Agricultural Scheme in Iran Using the Best-Worst Method and Fuzzy Logic in a GIS-Based Decision Support System. *Water*, *12*(7), 1913.

Akaydın Sel, K. (2017). *Yağış sularının konut ölçeğinde sürdürülebilir tasarım kapsamında incelenmesi* (Doctoral dissertation). Yüksek Lisans Tezi, Haliç Üniversitesi, İstanbul.

Al-shabeeb, A. R. (2016). The use of AHP within GIS in selecting potential sites for water harvesting sites in the Azraq Basin—Jordan. *Journal of Geographic Information System*, *8*(1), 73-88.

Alwan, I. A., Aziz, N. A., & Hamoodi, M. N. (2020). Potential water harvesting sites identification using spatial multi-criteria evaluation in Maysan Province, Iraq. *ISPRS International Journal of Geo-Information*, *9*(4), 235.

Bashar, M. Z. I., Karim, M. R., & Imteaz, M. A. (2018). Reliability and economic analysis of urban rainwater harvesting: A comparative study within six major cities of Bangladesh. *Resources, Conservation and Recycling*, *133*, 146-154.

Campisano, A., Butler, D., Ward, S., Burns, M. J., Friedler, E., DeBusk, K., Han, M. (2017). Urban rainwater harvesting systems: Research, implementation and future perspectives. *Water research*, *115*, 195-209.

Can, A., Yilmaz, Ü. (2019). Yağmur Suyu Potansiyeli Ve Kullanim Suyu Olarak Değerlendirilmesi. 14. Ulusal Tesisat Mühendisliği Kongresi.

Datta, N. (2015). Evaluating impacts of watershed development program on agricultural productivity, income, and livelihood in bhalki watershed of Bardhaman District, West Bengal. *World Development*, *66*, 443-456.

Ekinci, B. (2015). Su Kaynaklarinin Verimli Kullanilmasina Yönelik Örnek Ülke Uygulamalari Ve Ülkemizde Bu Çalişmalarin Uygulanabilirliği. Orman ve su işleri bakalığı, Ankara.

Gould, J., Qiang, Z., Yuanhong, L. (2014). Using every last drop: rainwater harvesting and utilization in Gansu Province, China. *Waterlines*, 107-119.

Guillaume, J. H., Helgeson, C., Elsawah, S., Jakeman, A. J., Kummu, M. (2017). Toward best practice framing of uncertainty in scientific publications: A review of W ater R esources R esearch abstracts. *Water Resources Research*, *53*(8), 6744-6762.

Guyassa, E., Frankl, A., Zenebe, A., Poesen, J., Nyssen, J. (2017). Effects of check dams on runoff characteristics along gully reaches, the case of Northern Ethiopia. *Journal of hydrology*, *545*, 299-309.

Hafizi Md Lani, N., Yusop, Z., & Syafiuddin, A. (2018). A review of rainwater harvesting in Malaysia: prospects and challenges. *Water*, *10*(4), 506.

Hajjar, H., Kilinç, İ. K., Ülker, E. (2020). Rainwater

Harvesting Potential in Public Buildings: A Case Study in Katip Celebi University. *Türk Doğa ve Fen Dergisi*, *9*(Özel Sayı), 167-172.

Hassani, A. N., Katibeh, H., Farhadian, H. (2016). Numerical analysis of steady-state groundwater inflow into Tabriz line 2 metro tunnel, northwestern Iran, with special consideration of model dimensions. *Bulletin of Engineering Geology and the Environment*, *75*(4), 1617-1627.

Hofman-Caris, R., Bertelkamp, C., de Waal, L., van den Brand, T., Hofman, J., van der Aa, R., & van der Hoek, J. P. (2019). Rainwater harvesting for drinking water production: a sustainable and cost-effective solution in The Netherlands?. *Water*, *11*(3), 511.

Krois, J., Schulte, A. (2014). GIS-based multi-criteria evaluation to identify potential sites for soil and water conservation techniques in the Ronquillo watershed, northern Peru. *Applied Geography*, *51*, 131-142.

Lani, N. H. M., Syafiuddin, A., Yusop, Z., Bin Mat Amin, M. Z. (2018). Performance of small and large scales rainwater harvesting systems in commercial buildings under different reliability and future water tariff scenarios. *Science of The Total Environment*, *636*, 1171-1179.

Nguyen, D. C., & Han, M. Y. (2017). Proposal of simple and reasonable method for design of rainwater harvesting system from limited rainfall data. *Resources, Conservation and Recycling*, *126*, 219-227.

Salameh, E. (2008). Over-exploitation of groundwater resources and their environmental and socio-economic implications: the case of Jordan. *Water International*, *33*(1), 55-68.

Tamaddun, K., Kalra, A., & Ahmad, S. (2018). Potential of rooftop rainwater harvesting to meet outdoor water demand in arid regions. *Journal of Arid Land*, *10*(1), 68-83.

Teston, A., Geraldi, MS, Colasio, BM ve Ghisi, E. (2018). Brezilya'daki binalarda yağmur suyu hasadı: bir literatür taraması. *Su*, *10* (4), 471.

Toosi, A. S., Tousi, E. G., Ghassemi, S. A., Cheshomi, A., & Alaghmand, S. (2020). A multi-criteria decision analysis approach towards efficient rainwater harvesting. *Journal of Hydrology*, *582*, 124501.

Velasco-Muñoz, J. F., Aznar-Sánchez, J. A., Batlles-delaFuente, A., & Fidelibus, M. D. (2019). Rainwater harvesting for agricultural irrigation: An analysis of global research. *Water*, *11*(7), 1320.

Vema, V., Sudheer, K. P., Chaubey, I. (2018). Hydrologic design of water harvesting structures through simulation-optimization framework. *Journal of hydrology*, *563*, 460-469.

Yeniçeri, M. (2018). Yağmur sularının hasadı ve aktif olarak tarımsal sulamada kullanılması.

Yosef, B. A., & Asmamaw, D. K. (2015). Rainwater harvesting: An option for dry land agriculture in arid and semi-arid Ethiopia. *International Journal of Water Resources and Environmental Engineering*, *7*(2), 17-28.

Intercontinental Geoinformation Days

igd.mersin.edu.tr

Analysis of carbon absorption amount of urban forests by spatial interpolation methods

Elif Akyel[*1], **Fatih Kenar** [2]

[1] *Izmir Katip Celebi University, Faculty of Engineering and Architecture, Geomatics Engineering, İzmir, Turkey*
[2] *Izmir Katip Celebi University, Faculty of Social and Human Sciences, Geography, İzmir, Turkey*

Keywords
Urban Forests
Geographic Information Systems (GIS)
Oxygen Production
Carbon Absorption

ABSTRACT

As a result of increasing urbanization as of the 20th century, people's need for green space is increasing. It can be said that the concept of Urban Forest has emerged as a natural result of increasing urbanization both in the world and in our country. In a study conducted by the World Health Organization, it is emphasized that at least 9m² green area per person is necessary for a healthy society. In this context, the concept of urban forests, which provides the opportunity to offer the social functions of forests to people, gains importance day by day. The Urban Forests project started to be implemented in our country in 2003. With this project, a total of 64 urban forests have been established in 55 provinces and 9 districts until the end of 2008. The oxygen produced, the carbon dioxide consumed and the carbon absorption of 64 urban forests that constitute the analysis area of this study were calculated. As a result of interpolation studies carried out in Geographical Information Systems (GIS), maps showing the contribution of urban forests to the environment were created and all these factors were analyzed on a spatial basis.

1. INTRODUCTION

The urbanization of the world population to increase the need of people for green areas in areas close to the city (Konijnendijk, 2003). The concept of urban forestry, which emerged in line with this need, aims to ensure the development of cities in harmony with the natural environment through urban planning (Johnston, 1996). Urban forests are areas created naturally or artificially in and around the city, ensure functional contributions and aesthetics to the city structure, and providing recreational opportunities for people living in the city (Ayaşlıgil, 2007). The purpose of creating urban forests is to improve the urban landscape and provide recreational opportunities for health and sports (Kowarik & Körner, 2005).

In addition to the contributions of urban forests to the social life of people, they also have many effects on nature. Forests help the harmonious functioning of nature with the carbon dioxide they consume and the corresponding carbon absorption amount. Climate change, which causes this function to deteriorate, is proportional to the amount of carbon released into the atmosphere. Today, many measures are taken to reduce carbon emissions. These forests, which increase the air quality, provide absorption by the leaves or the soil surface, the excretion of aerosols and particles on the leaf surface, and the movement of particles in the direction of the vegetation coast as a result of slowing air movements. Transported particles keep carbon dioxide emissions at a significant rate (Öner, N., Ayan, S., Sivacioglu, A., & Imal, B. (2007). This helps prevent air pollution.

Data obtained from the Forest Regional Directorate were used in the study. Assessment of the contribution of 64 urban forests to the environment established by the ministry constitutes the purpose of the study. In this context, the oxygen produced by the forests, the carbon dioxide consumed and the carbon absorption amount maps were created. The average carbon absorption amount of urban forests was calculated as 642.93 tons. Considering the resulting data, Antalya Urban Forest was determined as a forest area with a higher absorption amount of 15000 tons of carbon.

2. METHOD

The changing habits of people cause urbanization problems, food crises, decrease in natural resources such as soil, water and climate change. One of the reasons of climate change is the gases that accumulate in the atmosphere and cause greenhouse effect. Carbon

*Corresponding Author

*(elif.akyel@ikc.edu.tr) ORCID ID 0000 – 0002 – 9355 – 7478
(fatih.kenar@ikc.edu.tr) ORCID ID 0000 – 0001 – 9648 – 1475

Cite this study

Akyel E. & Kenar F. (2021). Analysis of carbon absorption amount of urban forests by spatial interpolation methods. 2nd Intercontinental Geoinformation Days (IGD), 183-185, Mersin, Turkey

emissions as the main cause of climate change mainly arises as a result of diffusion into the atmosphere of these gases, especially carbon dioxide. Increasing green areas helps reduce carbon emissions. As of 2019, there are 22.3 million hectares of forest in our country. In addition to these areas, there are 64 urban forests that form the scope of this study with the Urban Forests project developed by the Forest Regional Directorate.

In the study, the carbon dioxide consumed by urban forests, the corresponding carbon emission and the amount of oxygen produced were visualized in the GIS. Inverse Distance Weighted (IDW) technique, which allows analysis on spatial basis, was used in the creation of maps. Maps produced with this technique reveal the contribution of urban forests across the country to the environment. In addition, as a result of the analysis made using the data of the existing forests, the amount of oxygen produced by the areas near the forests, the rate of carbon dioxide consumption and the amount of carbon emission can be estimated.

Carbon dioxide consumption and oxygen production shown with different colors in GIS are effective factors in determining carbon absorption. When the map created as a result of the analysis is evaluated, the parameter that has more effect on the amount of emission on the basis of the region and the province was determined.

2.1. Inverse Distance Weigthed (IDW) Interpolation Method

IDW, which is a non-geostatistical method, is frequently preferred in studies. It is used to determine the value of unknown points based on known points. Estimates are made taking into account the distance function. The estimated values are a function of the distance and size of the nearby points, and the importance and effect on the cell to be estimated decreases with increasing distance (Taylan, E & Damçayırı, D. 2016).

IDW has been the common form in GIS systems, although a variety of weighted functions are used. IDW is a complete intermediate value generator (interpolator) such that it consolidates the values of the data. The IDW estimator is as follows (Loyd C.D., 2007; Demircan, Alan, & Şensoy, 2011).

$$Z(X_0) = \frac{\sum_{1=1}^{n} z(X_i).d_{i0}^{-r}}{\sum_{i=1}^{n} d_{i0}^{-r}} \qquad (1)$$

The location X_0, where the predictions are made is a function of n neighboring measurements giving the number of neighboring measurements. ($z(X_i)$ and i=1,2,…,n,); r is the exponential value that determines the assigned weight of each of the observations, and d_{i0} is the distance that separates the observation location X_i and the prediction location X_0. As the exponent grows, the assigned weight of observations far from the prediction location shrinks; increasing the denominator indicates that the forecasts are very similar to the nearest observations (Demircan, Alan, & Şensoy, 2011). The formula was calculated in ArcGIS, and as a result, relevant maps were created.

3. RESULTS & DISCUSSION

In the study, 64 urban forests created within the scope of the Urban Forests project carried out by the Forest Regional Directorate were handled. IDW interpolation method was used to determine the spatial models of the variance that emerged in the contribution of these forests to the environment. Maps were obtained that reveal the created models effectively.

On the maps, oxygen production and carbon dioxide consumption, which are factors affecting carbon emissions, are visualized by interpolating with GIS.

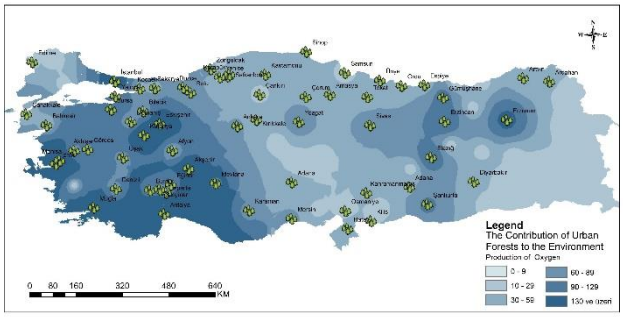

Figure 1. Oxygen Production Map of Urban Forests

Fig. 1 contains the oxygen production map of urban forests. When the map is examined, it can be said that the amount of oxygen production is high, especially in the southwestern part of the country. In the inner and eastern parts of the country, the amount of oxygen produced by urban forests is lower than other regions. On the other hand, Erzurum Urban Forest, which is established on an area of 717 hectares, stands out in that region with 600 tons of oxygen production. Antalya Urban Forest is the forest with the highest contribution to the ecosystem with 8367 tons of oxygen production. On the other hand, Yenice Urban Forest located in Karabük with 0.8 tons was the forest with the lowest oxygen production.

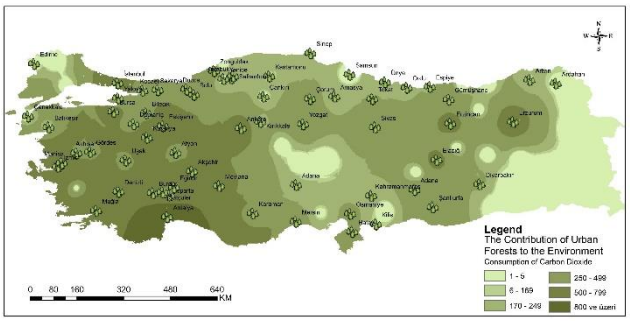

Figure 2. Carbon Dioxide Consumption Map of Urban Forests

In Fig. 2 there is a map showing the carbon dioxide consumption of urban forests. When the map is interpreted, it can be said that the marine urban forests in the southwestern part provide a higher rate of carbon dioxide consumption. The urban forest with the highest carbon dioxide consumption is the Antalya Urban Forest with 55000 tons of consumption. The least consumption amount was Karabük Yenice Urban Forest with 6 tons. This situation is similar to the oxygen production map in Fig. 1. The insufficiency of urban forests in the eastern

parts of the country can also be observed in the carbon dioxide consumption rate map.

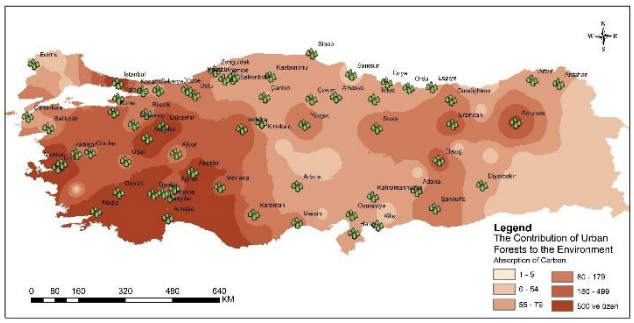

Figure 3. Carbon Absorbation Map of Urban Forests

The carbon absorption amounts of the Urban Forests are given in the map in Fig. 3. Carbon dioxide consumption rate is one of the important parameters affecting carbon absorption. This situation causes the maps in Fig. 2 and Fig. 3 to be similar.

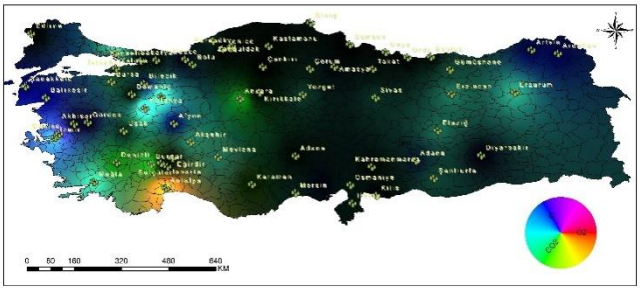

Figure 4. Carbon Absorption Map by Oxygen Production and Carbon Dioxide Consumption of Urban Forests

Urban forests control the carbon dioxide and oxygen balance, which are important for the world ecosystem, resulting from carbon absorption and fossil fuels (Nowak 1993). The global carbon cycle is defined as one of the biogeochemical cycles that enable the concentration of carbon dioxide, one of the greenhouse gases, to balance in the atmosphere. Forests play a role in this global cycle. Urban forests, which store carbon in soil and vegetation, exchange carbon with the atmosphere through photosynthesis and respiration (Brown 1997).

The map in Fig. 4 was created in order to determine the parameter affecting carbon absorption more on the basis of urban forests by evaluating the oxygen production and carbon dioxide consumption amounts together.

4. CONCLUSION

Problems such as the acceleration of population growth, urbanization, and traffic increase the need for natural habitats of people. Urban forests, which are areas where people who want to get away from their stressful lifestyle can interact with nature, gain importance day by day. In our country, the Urban Forests project has been put into effect by the Forest Regional Directorate. 64 urban forests have been established so far within the scope of the project, and this number is planned to be increased in the coming years. Urban forests have many contributions to the environment. Forests that increase oxygen production help to maintain carbon balance by reducing carbon dioxide consumption.

The total oxygen production of urban forests, which have an average oxygen production of 330.59 tons, evaluated within the scope of the study, is 21158 tons. Forests whose total carbon dioxide consumption was 55000 tons, the average consumption amount was determined as 148.79 tons. In forests where a total of 41148 tons of carbon is stored, an average of 642.93 tons is absorbed. The forest with the highest amount of carbon storage was the Antalya Urban Forest. 15000 tons of carbon is stored in this forest. The lowest absorption amount among urban forests was determined as Yenice Urban Forest in Karabük with 2 tons.

Reasons such as industrialization, population growth and the use of fossil fuels cause an increase in greenhouse gases consisting of carbon dioxide, methane and ozone. The main reason for global warming is these gases released into the atmosphere. By regulating the carbon balance of forests in the city atmosphere, it makes it possible to slow down global warming. 64 urban forests contribute to the global cycle. In addition, the number of urban forests in the Eastern and Southeastern Anatolia Region is quite low. Establishing urban forests in these regions is important in terms of their contribution to the natural environment.

REFERENCES

Ayaşlıgil T (2007). Kent Ormanlarının Rekreasyonel Amaçlı Kullanımı ve İstanbul İli Örneğinde İrdelenmesi. YTÜ Mim. Fak. E-Dergisi, 2(4), 213-236.

Brown S (1997). Ormanlar ve İklim Değişikliği: Karbon Rezervi Olarak Ormanlık Alanların Rolü, XI. Dünya Ormancılık Kongresi Bildirileri, Antalya.

Demircan M, Alan İ & Şensoy S (2011). Coğrafi Bilgi Sistemleri Kullanılarak Sıcaklık Haritalarının Çözünürlüğünün Artırılması, TMMOB Harita ve Kadastro Mühendisleri Odası 13. Türkiye Harita Bilimsel ve Teknik Kurultayı, Ankara.

Johnston M (1996). A Brief History of Urban Forestry in the United States. Arboricultural Journal: The International Journal of Urban Forestry, 257-278.

Konijnendijk C C (2003). A Decade of Urban Forestry in Europe. Forest Policy and Economics, 5(2), 173-186.

Kowarik I & Körner S (2005). Wild Urban Woodlands: New Perspectives for Urban Forestry. Berlin: Springer.

Loyd C D (2007). Local Modelsfor Spatial Analysis, CRC Press, 21-22p.

Nowak D J (1993). Atmospheric Carbon Reduction by Urban Trees, Journal of Environmental Management, 37(3), 207-217.

Öner N, Ayan S, Sivacioglu A & Imal B (2007). Kent Ormancılığı ve Kent Ormanının Çevresel Etkileri. (203, Dü.) Kastamonu Üni., Orman Fakültesi Dergisi, 7(2), 190.

Taylan E & Damçayırı D (2016). Isparta Bölgesi Yağış Değerlerinin IDW ve Kriging Enterpolasyon Yöntemleri ile Tahmini. Teknik Dergi, 27(3), 7551-7559.

Intercontinental Geoinformation Days

igd.mersin.edu.tr

Analysis urban green space classification using landscape pattern analysis based on GIS and remote sensing in Pattaya, Thailand

Sopaphan Chinnabut*[1], Nengcheng Chen [2], Haoran Zhang [3]

[1]*Burapha University, Geoinformatics, Chonburi, Thailand*
[2]*Wuhan University, State Key Laboratory of Information Engineering in Surveying, Mapping and Remote Sensing, Wuhan, China*
[3]*Geo-Informatics and Space Technology Development Agency, Bangkok, Thailand*

Keywords
Urban green space
Landscape pattern analysis
Digitization
GIS
Pattaya, Thailand

ABSTRACT

This research explores the urban green space (UGS) classification and analyze the quantity and distribution of UGS using landscape pattern analysis based on GIS and remote sensing in Pattaya city, Thailand. The useful of the classification for UGS planning and management was interpreted through landscape pattern analysis. In this study, use satellite image interpretation, land use map of Pattaya City was used as a based. Digitization for six criteria have natural green space, amenity green space, function green space, linear green space, economy green space and abandoned green space were identified to explore the classification. field survey provided information to validate the interpretations. Landscape pattern was based on landscape metrics analyzed using FRAGSTAT 4.2. The result show that the land scape structure of the Pattaya city is unreasonable, the amenity green space is seriously lacking and the distribution is not balanced. The proportion of abandoned green space is high but useless and the landscape diversity index is low. Landscape pattern analysis has allowed to interpret what category needs attention to improve their quality and quantity as well as to protect them from any land use development, guideline to manage the sustainable green space in Pattaya.

1. INTRODUCTION

Urban green space (UGS) is one of the important elements in cities for environmental conservation and it has a good impact on the environment and its accurate estimation is of significance to guide the future urban planning management and environmental protection. UGS provides benefits to the city that helps mitigate these negative effects (Ridder, 2004),

During the process of urbanization flocked into the ever-expanding cities and created artificial and impervious surfaces to substitute natural areas. The proportion of urban green space did not keep up with the speed of urban growth (Pauleit et al., 2005), which brought large pressure to the urban environment and led to a gradual reduction in the quality of life (Grimm et al., 2008; Johnson, 2001).

The Thai government established a mega project called the Eastern Economic Corridor (EEC) with 3 model provinces, including Chachoengsao, Chonburi and Rayong provinces. Pattaya is a part of ECC in Chonburi, Thailand. EEC is a pilot project for the economic development of Thailand's Eastern Seaboard. The result will enhance Pattaya's accessibility, will make Pattaya the heart of the eastern region, with the number of tourists visiting the EEC region to rise to 46.7 million over the next few years. Moreover, most of the land use of Pattaya is urban and built-up land, on the other hand, forest and water are the low proportion. As the population growth increases over time, the green space should be developed along with the ECC project for the good quality of life of the people in Pattaya.

Due to the long-term effects of many factors such as human activities and urban development. Due to its strong real-time performance, high precision and visualization, Geographic Information System, Global Positioning System and Remote Sensing Technology (3S) technology are widely used in the research on urban green space landscape pattern. Many scholars have made outstanding achievements in the research on green space landscape patterns in megapolises and provincial capitals (Liao, 2019). But the exploration of green-land landscape patterns in small and medium-sized cities is still rare.

* **Corresponding Author**

*(62910175@go.buu.ac.th) ORCID ID 0000 – 0001 – 7047 – 7056
(cnc@whu.edu.cn) ORCID ID 0000 – 0002 – 3521 – 9972
(haoran@gistda.or.th) ORCID ID 0000 – 0001 – 8829 – 7109

Cite this study

Chinnabut S, Chen N & Zhang H (2021). Analysis urban green space classification using Landscape pattern analysis based on GIS and remote sensing in Pattaya, Thailand. 2nd Intercontinental Geoinformation Days (IGD), 186-189, Mersin, Turkey

The objective are to explore the UGS classification that represent the structure and function and to analyze the quantity and distribution of UGS using landscape pattern analysis in Pattaya, Thailand.

2. METHOD

2.1. Study area

The study area is Pattaya, a city in Thailand "Fig. 1". It is on the east coast of the Gulf of Thailand, within, but not part of, Bang Lamung District in the province of Chonburi, which is located in the coordinates of 12° 55' 39.3888'' N and 100° 52' 37.4988'' E. Pattaya city is a self-governing municipal area. A total area of 50.19 square kilometers. As of 2019 it had a population of 119,532. Therefore, the population density is around 2,238 per square kilometers. There are 4 - 5 times latent population more than the number of reality (about 400,000 - 500,000 people) without reporting to Civil Registration. The annual average temperature is 27.7 °C and the average humidity is 77% during the year. The annual rainfall is 1117.6 mm. km2. Pattaya is at a low altitude of only 1.5 meters above sea level, and the temperatures are warm throughout the year. The topography is flat with a lack of hills and mountains, and most of the agriculture lands were marshlands earlier.

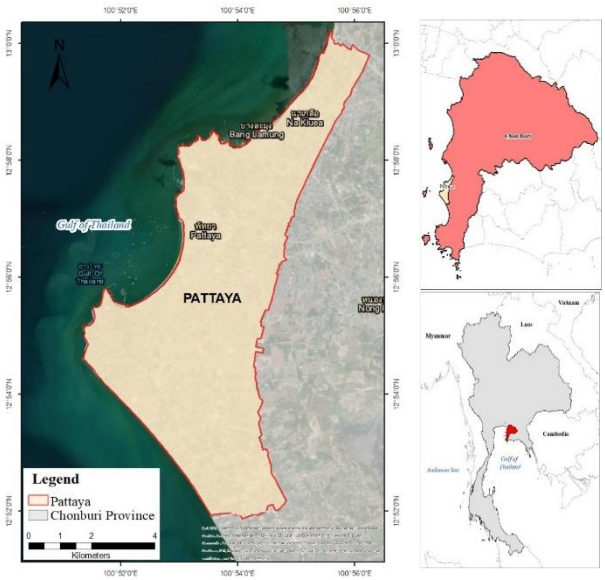

Figure 1. Location of study area in Pattaya, Thailand.

2.2. Methodology

Research designed to study urban green space classification using landscape pattern analysis. The main procedure of the proposed methodology is diagrammatized in "Fig. 2" and a detailed depiction is given in the following four sub-sections. This thesis has 4 conceptual frameworks which are data acquisition, data pre-processing, data analysis and data result.

2.2.1. Data acquisition

A Pléiades satellite data to study the urban green space map was downloaded from EOS are available at https://eos.com/pleiades-1/, on December 12th, 2019. This dataset has a spatial resolution (pixel size) of 2m., for the multispectral waveband images. Additionally, the Pleiades datasets includes a very high-resolution 0.5m panchromatic image. Also, a 30m resolution Digital Elevation Model was produced from the Pleiades stereo images in "Table 1".

This study was collected Land use data (Shape files), on October, 2018. That source from Land Development Department (LDD) in Thailand was shown in "Table 2". most of the land use of Pattaya is urban and built-up land with an area 44.86 km2 or 90.13% of the total area in Pattaya, on the other hand, forest and water are the low proportion. This data support the next steps to make it accurate.

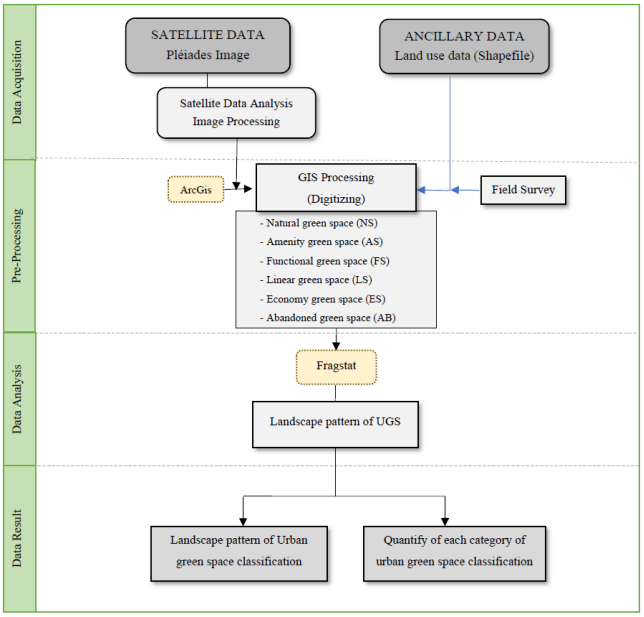

Figure 2. Diagram framework in this research.

Table 1. Characteristics of the utilized satellite data.

Dataset	Spectral channels	Spatial resolution (m)
Pleiades	Panchromatic (470-830nm)	0.5
	Blue (430-550nm)	2
	Green (500-620nm)	2
	Red (590-710nm)	2
	Near-infrared (740-940nm)	2

Table 2. Proportion of Land use types in Pattaya.

Type of LS	Area (km²)	Area (&)
A: Agriculture	0.69	1.38
F: Forest	0.28	0.56
U: Urban	44.86	90.13
W: Water	0.10	0.21
M: Miscellaneous	3.84	7.72
Total	49.77	100

2.2.2. Data pre-processing

Digitizing is the process of interpreting and converting paper map or image data to vector digital data. In manual digitizing you trace the lines or points from the source media. The UGS classifications were digitized by using digital instrument with the ArcMap10.2.2.

Digitization can visual interpretation on the color difference, roughness of texture, size, shape, pattern of

dispersion, relationship with surrounding objects and digitize the data, modify data and make a database in the geographic information system. Manual Digitizing is still a useful technique because of its ability to accurately copy maps in poor condition. Computers have a higher risk of error when interpreting information contained on a faded, stained or poor quality map or image. Manual Digitization is limited by the visual acuity and accuracy of the digitizer. In this research, urban green space classification was digitized into 6 type. Detail, definition and second class were shown in "Table 3".

Table 3. Classification of UGS system in Thailand

First Class	Second class
NS	rivers, streams, canals, lakes, mountains, forests.
AS	park, garden, sports field, outdoor activity, botanical garden, zoo, golf course
FS	domestic garden, housing estate, institutional ground (school yards, college yards), burial ground, landfill space
LS	green buffer, green belt, green traffic island, other linear features.
ES	Perennial garden, Economic forest gardens, shopping mall, housing estate.
AB	Abandoned green space, waiting for development.

Note: NS: Natural green space, AS: Amenity green space, FS: Function green space, LS: Linear green space, ES: Economy green space, AB: Abandoned green space

2.2.3. Data analysis

Analysis of landscape pattern of each category of UGS. In the FRAGSTATS (McGarigal et al., 2012), was conducted to quantify of each criteria of urban green spaces and to interpret the useful of the classification for UGS planning and management. In this analysis, landscape pattern analysis was conducted for the whole city in Pattaya. This paper selects relevant landscape pattern index, outputs indexes which can reflect the landscape space accurately and comprehensively. Six landscape metrics were chosen that we are describing. The numeric characters in "Table 4".

Table 4. Landscape metrics used in the analysis.

Class-level	
metrics	Description
CA	Total Class Area
AREA_MN	Mean Patch Area
NP	Number of patches
PD	Patch density

Landscape-level	
metrics	Description
SHDI	Shannon's Diversity Index
SHEI	Shannon's Evenness Index

3. RESULTS

The study area in Pattaya have total area of 50.19 km^2. According to tha data in "Table 5". The total area covered by urban green space is 8.3174 km^2 or 16.57% of the total area in Pattaya. The proportion of abandoned green space (AB) is the highest (63.69%), followed by functional green space (FS) (19.84%), natural green space (NS) (8.44%), Linear green space (LS) (4.96), Amenity green space (AS) (2.43) and economy green space (ES) is the lowest (0.64%).

Table 5. Analysis of the proportion of each category of urban green space in Pattaya, Thailand

Type of UGS	Area (km^2)	Area%
NS	0.7018	8.44
AS	0.2020	2.43
FS	1.6499	19.84
LS	0.4128	4.96
ES	0.0533	0.64
AB	5.2976	63.69
Total	8.3174	100

Table 6. Analysis of the composition and patches type level of urban green space landscape

Type of UGS	CA (ha)	NP	PD	Area_MN	SHDI	SHEI
NS	68.40	167	3.37	0.41		
AS	20.23	68	1.37	0.30		
FS	164.60	479	9.67	0.34		
LS	36.80	207	4.18	0.18		
ES	5.29	14	0.28	0.38		
AB	504.27	509	10.28	0.99		
Total	799.60	1444	29.15	2.60	0.30	0.20

According to the data in "Table 6", Landscape pattern analysis revealed that abandoned green space has the highest number of patches and patch density, followed by functional green space, linear green space, natural green space, and amenity green space while economy green space is the lowest. Also abandoned green space has the highest mean patch area, followed by natural green space, economy green space, functional green space and amenity green space while the lowest is linear green space.

As previously mentioned, most of the abandoned green space, area is much larger than other green space but this type of green area does not benefit the environment, that unuse land for waiting develope and useless in city. For functional green space and linear green space are not bad. There is a lack of public land or amenity green space and economy green space.

4. DISCUSSION AND CONCLUSION

This study intended to explore and distribution the UGS classification that represent the structure and function using landscape pattern analysis in Pattaya, Thailand. It was digitized from high resolution image satellite into 6 type of UGS and use FRAGSTAT to compute landscape pattern with the indices found that the analysis showed the proportion of amenity green space and economy green space are 2.43%, 0.64%, respectively, also the landscape pattern value it indicates that these type of Pattaya is extremely scarce. also

The function of amenity green space overlaps with many others, in particular parks and gardens and natural

areas can also provide informal opportunities for children's play where there are no other facilities. It is important therefore to consider the provision of amenity green spaces in the context of urban planning and management.

ACKNOWLEDGEMENT

This research was supported by Burapha University, Wuhan University, and Geo-Informatics and Space Technology Development Agency (GISTDA) who provided insight and expertise that greatly assisted the research.

REFERENCES

Byrne J & Sipe N (2010). Green and open space planning for urban consolidation—A review of the literature and best practice. Urban Research Program. Issues papers11. Griffith University, Brisbane (in Australia).

Clémence V & Jérémie L & Pierre-Yves L (2016). Patterns of landscape change in a rapidly urbanizing mountain region. https://doi.org/10.4000/cybergeo.27800

Emil P T & Lausted V K (2013). Classification and valuation of urban green spaces—A hedonic house price valuation. Journal of Landscape and Urban Planning, 120, 119– 128

Gaffin S R, Khanbilvardi R & Rosenzweig C (2009). Communication development of a green roof environmental monitoring and meteorological network in New York City. Journal of Forestry Research, 20, 79-82.

Jiaqi L (2019). Landscape pattern analysis of urban green space based on the new green space classification standard Take Danzhou City, Hainan Province as an example. Journal of Earth and Environmental Science. https://doi:10.1088/1755-1315/300/2/022169

Kristen P & Yvette L D (2015). Monitoring forest cover spatial patterns with aerial imagery. Colorado State University, Fort Collins (in USA).

Lee A C K, Jordon H C & Horsley J (2015). Value of urban green spaces in promoting healthy living and wellbeing. prospects for planning. Risk Management and Healthcare Policy, 8, 131-137.

McGarigal K, Cushman S A, Neel M C & Ene E (2002). FRAGSTATS: Spatial Pattern Analysis Program for Categorical Maps; University of Massachusetts, Amherst (in USA).

Najihah A & Arif A S (2018). Developing urban green space classification system using multi-criteria: The case of Kuala Lumpur city, Malaysia. Journal of Landscape Ecology, 20,16-36. https://doi: 10.1136/bmj.39093.464190.55

Office of Natural Resources and Environmental Policy and Planning (2014). Standard of Urban Green Space and Species Plants suitable for green space.

Pham U D & Nakagoshi N (2008). Application of land suitability analysis and landscape ecology to urban greenspace planning in Hanoi, Vietnam. Urban Forestry and Urban Greening, 7, 25-40.

Pongpattananurak N (2014). Prioritizing Forest Complexes of Thailand Using Landscape Metrics. Journal of Thai Journal Forest, 33 (2), 61-76.

Toke E P (2013). Classification and valuation of urban green spaces—A hedonic house price Valuation. Landscape and Urban Planning. https://doi.10.1016/j.landurbplan.2013.08.009

Wang H & Peng C (2012). Study on the landscape pattern of green land in Zhuzhou City, Hunan Province. Journal of Central South University of Forestry and Technology, 32 (07), 64 - 68.

Intercontinental Geoinformation Days

igd.mersin.edu.tr

Trend analysis of temperature and precipitation data of 9 stations located in Mediterranean region

Cavit Berkay Yılmaz [*1], **Vahdettin Demir** [1], **Mehmet Faik Sevimli** [1], **Fikret Demir** [2] **Murat Yakar** [3]

[1]*KTO Karatay University, Engineering Faculty, Civil Engineering Department, Konya, Turkey*
[2]*Turkish State Meteorological Service, Ankara, Turkey*
[3]*Mersin University Engineering, Faculty, Geomatics Engineering Department, Mersin, Turkey*

Keywords
Trend
Temperature
Precipitation
Mediterranean region

ABSTRACT

Trend is defined as a statistically significant decrease or increase in the measured values of a parameter over the time series. Since hydrological values are of randomly changing character over time, special methods should be used to investigate the tendency to decrease or increase. In this study, Linear Trend and Modified Mann-Kendall trend analyzes were examined using the annual average temperature data (℃) and the annual total precipitation data (mm) between the years 1960-2020 of 9 stations in the Mediterranean Region. Study was performed in 95% confidence interval. According to the results of the study carried out there are increasing trends in temperature data in 8 of the 9 stations and no trend in precipitation data.

1. INTRODUCTION

Climate changes affect the entire ecosystem over time, causing significant changes in hydrometeorological parameters. For this reason, performing analysis of these parameters is of vital importance in detecting extreme situations that may occur over time. İçel (2009), in her study examined the temperature and precipitation values and extreme cases in the eastern Mediterranean coast and determined an increasing trend in 11 stations and stated that this increase is more apparent after the year 1992. Bahadır (2011), studied the temperature and precipitation trend changes in the Mediterranean Region with the Growth Curve and ARIMA model and determined all stations revealed an increase in temperature and a decrease in precipitation. Gönençgil and İçel (2014), in their study, they carried out investigations using ANOVA method for precipitation data of 11 stations located on the Eastern Mediterranean coast between 1975-2006 and as a result of these investigations, they found a decrease in the annual total precipitation and the annual total number of rainy days. Çelik (2019), in his study, conducted drought analyzes (SPI) for 15 stations located on the Mediterranean coast between 1967 and 2016 and found extreme climate conditions were frequently experienced. Yücel et al. (2019), in their study, they determined statistically significant increasing trends in temperature data and statistically decreasing trends in precipitation data. In this study, Linear Trend and Modified Mann-Kendall trend analysis methods were used to determine statically significant trends and analysis was performed in 95% confidence interval.

2. METHOD

Mediterranean Region covers the 3 major basins, namely he Eastern Mediterranean basin, the Antalya basin and the Western Mediterranean basin. The region is of great importance in agriculture and tourism. The region, which has a Mediterranean climate, receives hot and dry summer and warm and abundant rainfall in winter seasons.

Detailed information of stations was given in Table 1. and station location were shown on map in Fig. 1.

Figure 1. Station locations

* **Corresponding Author**

(cavitberkayyilmaz@gmail.com) ORCID ID 0000-0002-2734-2073
*(vahdettin.demir@karatay.edu.tr) ORCID ID 0000-0002-6590-5658
(mehmet.faik.sevimli@karatay.edu.tr) ORCID ID 0000-0002-4676-8782
(fidemir@mgm.gov.tr) ORCID ID 0000-0001-7675-9492
(myakar@mersin.edu.tr) ORCID ID 0000-0002-2664-6251

Cite this study

Yılmaz C B, Demir V, Sevimli M F, Demir F & Yakar M (2021). Trend analysis of temperature and precipitation data of 9 stations located in Mediterranean region. 2nd Intercontinental Geoinformation Days (IGD), 190-193, Mersin, Turkey

Table 1. Statistical information about temperature and precipitation data

No	Data	Period	Std. Dev.	Skew.	Kurt.
17238 Burdur	Temp.	1960-2020	0.73	0.25	-0.32
	Pre.	1960-2020	85.30	0.02	-0.59
17240 Isparta	Temp.	1960-2020	0.81	0.14	0.04
	Pre.	1960-2020	142.06	0.42	0.26
17255 Kahramanmaraş	Temp.	1960-2020	0.91	-0.17	-0.21
	Pre.	1960-2016	171.22	0.69	0.25
17292 Muğla	Temp.	1960-2020	0.58	0.02	-0.47
	Pre.	1960-2020	280.05	0.18	0.00
17302 Antalya	Temp.	2001-2020	0.55	0.72	0.39
	Pre.	2006-2020	451.59	-0.30	-1.49
17340 Mersin	Temp.	1960-2020	1.03	0.20	-0.93
	Pre.	1960-2020	182.46	0.53	0.03
17351 Adana	Temp.	1960-2020	0.57	0.28	0.54
	Pre.	1960-2020	202.51	0.72	0.38
17355 Osmaniye	Temp.	1986-2020	0.64	-0.23	0.01
	Pre.	1986-2020	168.43	0.35	0.18
17372 Antakya	Temp.	1960-2020	0.64	-0.20	0.03
	Pre.	1960-2020	185.29	0.28	-0.22

When Table 1. containing statistical information on temperature and precipitation data is examined, it is seen that the temperature data of the stations are distributed symmetrically except for 1 (17302 /Antalya) station. When the same examination is applied to the kurtosis coefficients, it is seen that all 9 stations are flatter (Platykurtic) than the normal distribution curve. For precipitation data, it is seen that the stations are distributed symmetrically except for 3 (17255/Kahramanmaraş, 17340/Mersin, 17351/Adana) stations. When the same examination is applied to the kurtosis coefficients, it is seen that all 9 stations are flatter (Platykurtic) than the normal distribution curve.

2.1. Linear Trend Test

Linear Trend test is a parametric test that assumes the data is normally distributed and used to determine the presence or absence of a trend in a time series (Karabulut and Cosun 2009). This method's application is mainly based on graph and the line (Eq. 1) fitted to this graph to determine the trend curve (Yağbasan et al. 2020).

$$y_i = ax_i + b \quad (1)$$

In Eq. 1. "a" represents slope and "b" represents the intersection point with the y axis (Demir 2018). "a" and "b" values are calculated using Eq. 2. and 3.

$$a = \frac{\sum_{i=1}^{N} x_i y_i - N\bar{x}\bar{y}}{\sum_{i=1}^{N} x_i^2 - N\bar{x}^{-2}} \quad (2)$$

$$b = \bar{y} - a\bar{x} \quad (3)$$

In Eq. 2. and 3. variables "N" represents the number of data in the series, "$\bar{x}$" represents the average of "x" variables, "$\bar{y}$" represents the average of "y" variables, "x_i" represents the "x" value in the "i-th" row, "y_i" represents the "y" value in the "i-th" row.

Trend existence is decided by applying "t" distribution and "t" test (Eq. 4.).

$$f(t) = \frac{\Gamma(\frac{v+1}{2})}{\sqrt{v\pi}\Gamma(\frac{v}{2})}(1+\frac{t^2}{v})^{-\frac{v+1}{2}} \quad (4)$$

The calculated "t" value is compared with the "$t_{critical}$" value corresponding to the 95% significance level (Demir 2018).

2.2. Modified Mann-Kendall Test

In the original Mann-Kendall test, although the procedure is assumed to be independent, a correlation is observed in most of the hydrological events and the presence of positive autocorrelation increases the possibility of detecting a significant trend (Yağbasan et al. 2020). In order to eliminate this situation variance value is calculated with the help of Eq. 5 and 6. (Hamed and Rao 1998).

$$\frac{n}{n_s^*} = 1 + \frac{2}{n(n-1)(n-2)}\sum_{i=1}^{n-1}(n-i)(n-i-2)\rho_s(i) \quad (5)$$

$$V(S) = Var(S)\frac{n}{n_s^*} = \frac{n(n-1)(2n+5)}{18}\frac{n}{n_s^*} \quad (6)$$

And the rest of the test is carried out similiarly to the original Mann-Kendall test. After application calculated "Z" value compared with the "$Z_{critical}$" value to check statistically significant trend presence (Yılmaz et al. 2020).

3. RESULTS

In this study, Linear Trend and Modified Mann-Kendall trend analyzes were examined using the annual average temperature data (°C) and the annual total precipitation data (mm) between the years 1960-2020 of 9 stations in the Mediterranean Region. The obtained results were mapped with the help of ArcGIS software and visualized. The main purpose of this application is to concretize the trend results obtained and to determine their distribution over the region. Results from trend tests for temperature data are shown in Table 2.

Table 2. Trend test results for temperature data

No	Test	Critical Value	Result	Trend
17238 Burdur	LT	±1.67	3.77	Increasing
	MMK	±1.96	3.21	Increasing
17240 Isparta	LT	±1.67	3.23	Increasing
	MMK	±1.96	2.41	Increasing
17255 Kahramanmaraş	LT	±1.67	7.87	Increasing
	MMK	±1.96	6.11	Increasing
17292 Muğla	LT	±1.67	4.20	Increasing
	MMK	±1.96	3.06	Increasing
17302 Antalya	LT	-	-	-
	MMK	-	-	-
17340 Mersin	LT	±1.67	14.60	Increasing
	MMK	±1.96	8.00	Increasing
17351 Adana	LT	±1.67	3.92	Increasing
	MMK	±1.96	3.70	Increasing
17355 Osmaniye	LT	±1.69	2.97	Increasing
	MMK	±1.96	2.71	Increasing
17372 Antakya	LT	±1.67	3.55	Increasing
	MMK	±1.96	3.43	Increasing

-: Not enough data for trend analysis.
LT: Linear Trend Test
MMK: Modified Mann-Kendall Test

When the Linear Trend test results (Table 2.) for temperature data were examined, it was determined that increasing trends were found in 8 stations and the results obtained were found to be significant at 95% of the confidence interval. And the results of the Modified Mann-Kendall trend test (Table 2.) were examined, it was determined that increasing trends were found in 8 stations and the results obtained were found to be significant at 95% of the confidence interval. The results of the examination of both test shows increasing trends in 8 stations and there are extreme cases of increasing trends in 2 stations (17255/Kahramanmaraş, 17340/Mersin). Maps of Linear Trend and Modified Mann-Kendall Tests are shown in figures 2 and 3.

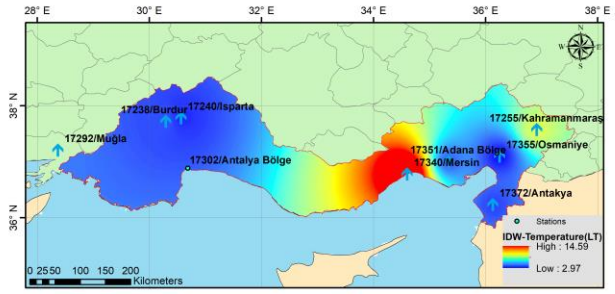

Figure 2. Map of the Linear Trend test results for temperature data

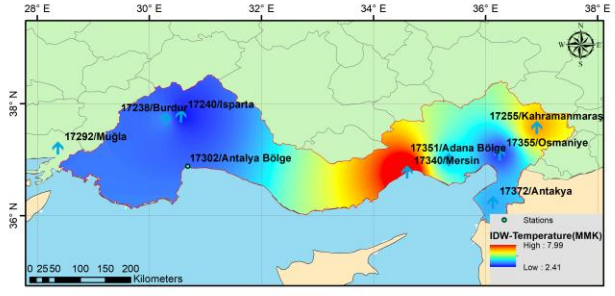

Figure 3. Map of the Modified Mann-Kendall trend test results for temperature data

Results from trend tests for precipitation data are shown in Table 3.

Table 3. Trend test results for precipitation data

No	Test	Critical Value	Result	Trend
17238 Burdur	LT	±1.67	-0.04	No trend
	MMK	±1.96	0.13	No trend
17240 Isparta	LT	±1.67	-1.50	No trend
	MMK	±1.96	-0.78	No trend
17255 Kahramanmaraş	LT	±1.67	0.52	No trend
	MMK	±1.96	0.46	No trend
17292 Muğla	LT	±1.67	-1.13	No trend
	MMK	±1.96	-0.87	No trend
17302 Antalya	LT	-	-	-
	MMK	-	-	-
17340 Mersin	LT	±1.67	0.71	No trend
	MMK	±1.96	0.67	No trend
17351 Adana	LT	±1.67	-0.31	No trend
	MMK	±1.96	-0.21	No trend
17355 Osmaniye	LT	±1.69	-0.68	No trend
	MMK	±1.96	0.03	No trend
17372 Antakya	LT	±1.67	-0.76	No trend
	MMK	±1.96	-0.68	No trend

-: Not enough data for trend analysis.
LT: Linear Trend Test
MMK: Modified Mann-Kendall Test

When the Trend test results (Table 3.) for precipitation data were examined, it was found that there was no significant trend in 95% of the confidence interval at any of the stations. Since there is no statistically significant trend in any of the trend test results for the precipitation data no map has created.

As for the test results for individual stations, only 17340/Mersin station will be examined as an example.

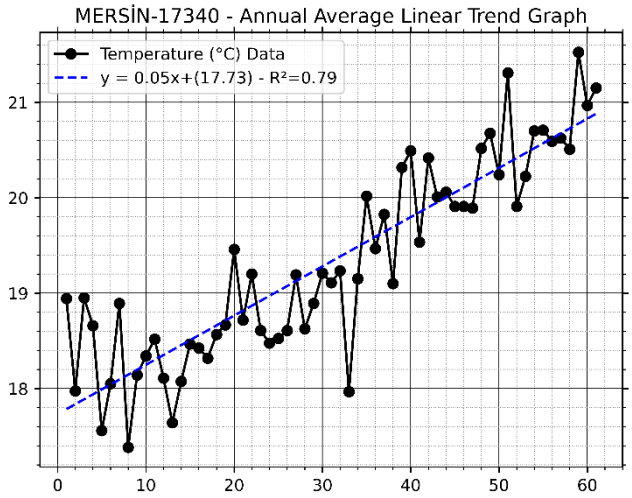

Figure 4. Linear Trend test graph for temperature data

As it is shown in Fig. 4 when the annual average temperature graph is examined a clear increase in temperature data over the years and statistically significant extreme case of increasing trend is observed for both tests (Table 2).

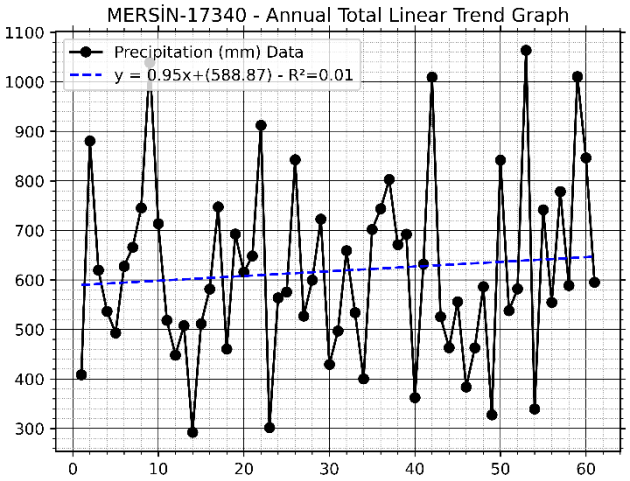

Figure 5. Linear Trend test graph for precipitation data

And an increasing trend can be observed for precipitation data. But this observation is not statistically significant for both tests (Table 3).

4. DISCUSSION

While temperature data generally gives high R^2 results, the R^2 values obtained from precipitation data is much lower. This means the linear projection of linear trend test does not fit well to the high fluctuations of precipitation data. But trend results obtained from tests are quite compatible for both tests. Increasing trends in temperature data expected to increase more in the near future (Bahadır 2011). These increasing trends in temperature data indicates an increase of demand in limited water resources (Yücel et al. 2019) and the relationship between temperature and humidity might affect the number of storms that will occur in the future (İçel 2009). For temperature data the stations that shows trend presence are in accordance with other studies (Yücel et al. 2019).

5. CONCLUSION

When results from both tests examined for temperature data, both tests show an increasing trend in 8 stations and 2 (17255/Kahramanmaraş, 17340/Mersin) of these stations has an extreme case of increasing trends. When the same examination was applied to the precipitation results no significant trend was detected in any of the stations for both tests.

ACKNOWLEDGEMENT

We would like to express our gratitude to Turkish State Meteorological Service for providing the data for Mediterranean Region.

REFERENCES

Bahadır M (2011). Türkiye'de iklim değişikliğinin iklim bölgelerine yansımasında kuzey-güney yönlü sıcaklık ve yağış değişim öngörüleri. Journal of Akademik Bakış, 26.

Çelik A M (2019). Akdeniz kıyılarında ekstrem nemli ve kurak mevsimlerin dağılımı (1967-2016). Academic Platform Journal of Engineering and Science, 7-1, 56-66.

Demir V (2018). Karadeniz Bölgesi yağışlarının trend analizi. MS Thesis, Ondokuz Mayıs University, Samsun (in Turkish).

Gönençgil B & İçel G (2014). Türkiye'nin Doğu Akdeniz kıyılarında yıllık toplam yağışlarda görülen değişimler (1975-2006). Turkish Geographical Review, 55, 1-12.

Hamed K H & Rao A R (1998). A Modified Mann-Kendall trend test for autocorrelated data. Journal of hydrology, 204(1-4), 182-196. DOI: 10.1016/S0022-1694(97)00125-X

İçel G (2009). Türkiye'nin Doğu Akdeniz kıyılarında sıcaklık ve yağış trend analizleri ve ekstrem hadiseler. PhD Thesis, İstanbul University, İstanbul (in Turkish).

Karabulut M & Cosun F (2009). Kahramanmaraş ilinde yağışların trend analizi. Turkish Journal of Geographical Sciences, 7(1), 65-83.

Yağbasan Ö, Demir V & Yazıcigil H (2020) Trend analyses of meteorological variables and lake levels for two shallow lakes in central Turkey. Water, 12(2), 1–16.

Yılmaz C B, Demir V & Sevimli M F (2020) Karadeniz yağışlarının Kuzey Atlantik Salınımı ile ilişkisi. Gazi Journal of Engineering Sciences, 6(3), 248-254.

Yücel A, Atılgan A & Öz H (2019) Trend analysis in temperature, precipitation and humidity: The case of Mediterranean Region. Scientific Papers. Series E. Land Reclamation, Earth Observation & Surveying, Environmental Engineering, 8, 91-98.

Intercontinental Geoinformation Days

igd.mersin.edu.tr

Creating and evaluating pollution distribution map in Aegean Region by using geographical information system (GIS) and air quality data

Ömer BİLGİNER*[1], Elif AKYEL [1], Güzide Miray PERİHANOĞLU [2], Sena TEKAVCU [3]

[1]*Izmir Katip Celebi University, Faculty of Engineering and Architecture, Department of Geomatics Engineering, Izmir, Turkey*
[2]*Van Yüzüncü Yıl University, Security Vocational School, Emergency and Disaster Management Program, Van*
[3]*Istanbul Technical University, Faculty of Civil Engineering, Department of Geomatics, Istanbul, Turkey*

Keywords
Air Pollution
Air Quality
GIS
Sulfur Dioxide
Particulate Matter

ABSTRACT

Air pollution is defined as an environmental problem that occurs as a result of foreign substances such as dust, smoke and gas exceeding normal amounts in the atmosphere and affecting the health of living things adversely. Air pollution, which is one of the leading environmental problems today, threatens future generations seriously. Air pollution is shown as the most important cause of global warming and has negative effects on other living things, especially human health. The causes of air pollution in our country can be shown as rapid and unplanned urbanization, wrong location in the industrial zone and pollutants from the chimneys. In this study, the data obtained from the air monitoring stations in the provinces of the Aegean region were evaluated in the Geographical Information System and the location analysis of particulate matter (PM) and sulfur dioxide (SO_2) causing air pollution was performed. The data used in this study has been mapped through being obtained from Republic of Turkey Ministry of Environment and Urbanisation National Air Quality Monitoring Network. Spatial distribution maps of air pollution were created by making spatial analysis of pollutants in the region with the help of the Geographical Information System and it was determined whether the pollutant parameters tend to increase or decrease.

1. INTRODUCTION

Global warming is the biggest threat to the world. Global warming is the increase in the temperature of the Earth's surface and atmosphere as a result of the increase in the amount of greenhouse gases (carbon dioxide, methane, ozone) released into the atmosphere (Başıbüyük et al. 2017). The biggest reason for the increase in global warming in recent years is industrialization. Especially since the 20th century, industrialization has increased rapidly in order to improve living standards and as a result of this increase, irreversible damages to nature have occurred.

Air pollution, which is one of the leading global warming and environmental problems today, seriously threatens future generations. Air pollution is defined as an environmental problem that occurs as a result of the increase of foreign substances such as dust, smoke and gas in the atmosphere to more than normal amounts and negatively affects the health of living things (Akyürek et al. 2013).

Air pollution can be divided into two groups as natural and artificial causes (Zencirci and Işıklı 2017). Among the artificial causes, human activities such as industrial factories, mining, transportation can be cited. Natural causes are natural processes such as volcanic eruptions and forest fires. Natural causes have a local impact on air pollution. Artificial causes affect the world on a global scale. Therefore, artificial causes are the most important factor in air pollution.

In the past, air pollution only affected industrial areas. Air pollution is seen as the most important problem in settlements with the effect of the increasing population. The first death case from air pollution was recorded in London in 1873 and it was stated that these deaths increased every year (Altıkat et al. 2011). In 2020, there was a decrease in industrial production due to the Covid-19 pandemic. As a result of this decrease, a significant decrease in air pollution was detected (Baysan and Yavaş 2020). The causes of air pollution in our country can be shown as unplanned and rapid urbanization,incorrect

* **Corresponding Author**

*(omer.bilginer@ikcu.edu.tr) ORCID ID 0000 – 0001 – 5789 – 7929
(elif.akyel@ikcu.edu.tr) ORCID ID 0000-0002-9355-7478
(gm.perihanoglu@yyu.edu.tr) ORCID ID 0000-0002-2730-590X
(tekavcu19@itu.edu.tr) ORCID ID 0000-0001-9622-0144

Cite this study

Bilginer O, Akyel E, Perihanoglu G M & Tekavcu S (2021). Creating and evaluating pollution distribution map in Aegean Region by using geographical information system (GIS) and air quality data. 2nd Intercontinental Geoinformation Days (IGD), 194-197, Mersin, Turkey

choice of location in an industrial zone and pollutants coming out of chimneys (Garipağaoğlu 2003).

Air pollutants are seen as an international problem as they are spread by wind. Air pollutants are shown as carbon monoxide (CO), sulfur dioxide (SO_2), hydrocarbons (HK), nitrogen oxides (NOx) and particulate matter (PM) (Finlayson and Pitts 1986). Sulfur dioxide (SO_2) is a gas that enters the atmosphere as a result of the combustion of fossil fuels and volcanic eruptions. It has the property of being a poisonous gas for all living things (Akan and Morcalı 2017). Sulfur dioxide occurs as a result of the use of coal for heating purposes, and where urbanization occurs, sulfur dioxide is known to have a higher value. Particulate matter (PM) is solid or liquid particles that can be emitted in the atmosphere and suspended in the air. PM is divided into aerodynamic diameters in terms of mass and composition (Akyürek et al. 2013). PM10 notation is used to describe particles that are 10 micrometers or smaller, which have been selected for this study.

In this study, spatial distribution maps of Particulate Matter and Sulfur dioxide causing air pollution were created by evaluating the data from January, February and March in 2018 and 2019 from the Air Monitoring Station in the provinces in the Aegean Region in the Geographical Information System and it has been determined whether it has a decreasing trend.

2. METHOD

2.1. Study Area

In this study, the distribution of SO_2 and PM10 substances, which are among the air pollutants, in the Aegean Region according to the data in January, February and March of 2018 and 2019 were examined.The study area covers İzmir, Manisa, Aydın, Denizli, Muğla, Afyonkarahisar, Kütahya and Uşak provinces within the borders of the Aegean Region. The Aegean region is the second largest industrial region in Turkey after Marmara region. It is seen that these sectors have a significant share in air pollution due to the intensification of the automotive, oil and mining industry in the Aegean region.

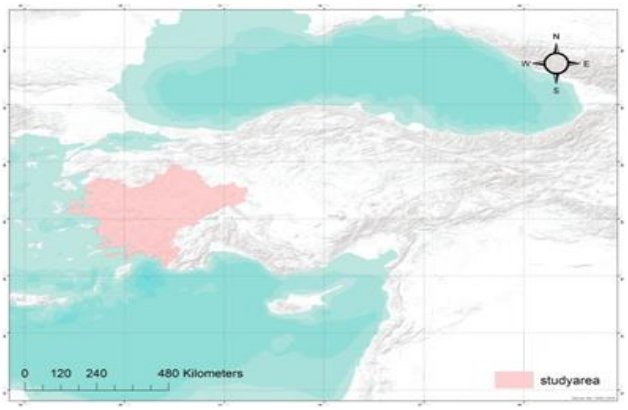

Figure 1. Study Area

2.2. Materials

The data to be used in the study were obtained from observation stations in provinces in the Aegean Region. The data were downloaded from the database of the Republic of Turkey Ministry of Environment and Urbanization National Air Quality Monitoring Network website and saved in excel table format.

2.3. Method

In this study, spatial analysis of air pollutants SO_2 and PM10 were mapped using Inverse Distance Weighting (IDW) interpolation method in ArcGIS program.The values of the points that need to be estimated with IDW are calculated by averaging the values of the sample points around each point (Göğsu and Hastaoğlu 2019). The effect of the points closer to the points to be predicted is greater, and more distant points have less effect. The IDW estimator can be given by equation (1).

$$Z(X_0) = \frac{\sum_{i=1}^{n} z(X_i).d_{i0}^{-r}}{\sum_{i=1}^{n} d_{i0}^{-r}} \quad (1)$$

The location X_0 where the predictions are made is a function of the neighboring measurements n. d is the distance separating observation location X_i and prediction location x_0, and r is the parent that determines the assigned weight of observations. As the exponent grows, the weights of observations at a distance to the point where it should be estimated become smaller. The increase in the exponent suggests that the estimates are very similar to the closest observations (Demircan et al. 2011).

3. RESULTS

Data of SO_2 and PM10 items found in the study area by IDW interpolation method. PM10 and SO_2 distributions are shown in Fig. 2, 3, 4 and 5.

When Fig. 2 and 3 are examined, it is seen that the amount of PM10 increases in Kütahya and decreases in Afyon and Uşak. The most important reason for the high air pollution in Kütahya is the coal-fired thermal power plants in the city. Air pollution limit value of PM10 is 40 µg / m3 (microgram / cubic meter) in our country (Vural 2021). When Fig. 2 and 3 are examined, it is seen that the PM10 limit amount has been exceeded in the Aegean Region.

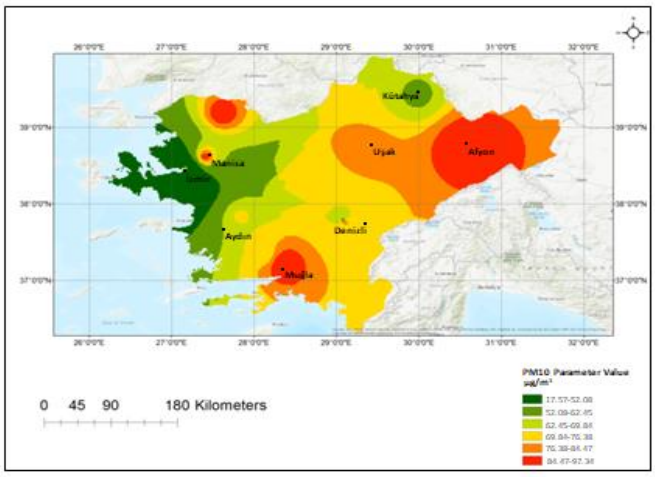

Figure 2. PM10 Distribution in January, February and March 2018

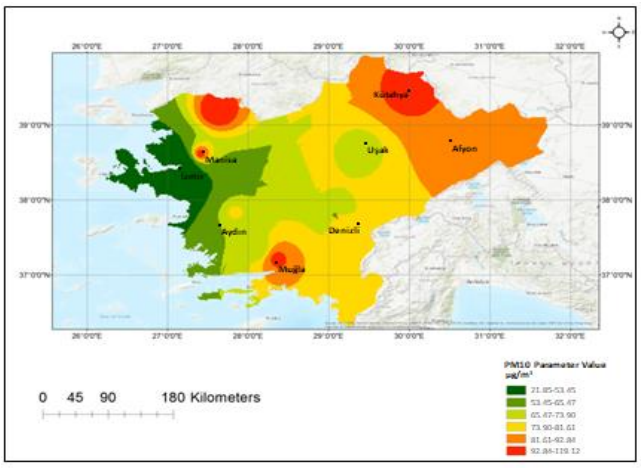

Figure 3. PM10 Distribution in January, February and March 2019

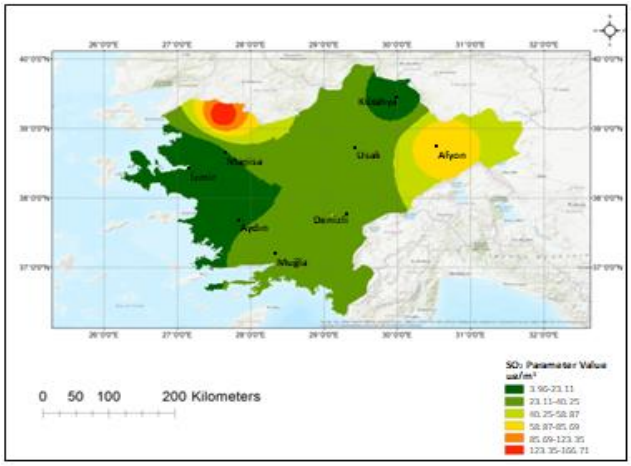

Figure 4. SO_2 Distribution in January, February and March 2018

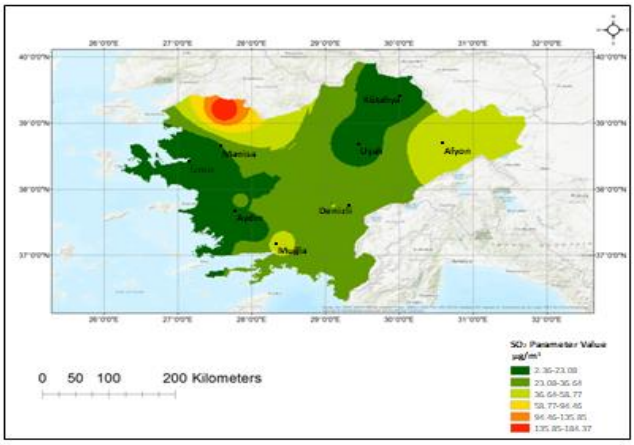

Figure 5. SO_2 Distribution in January, February and March 2019

When Fig. 4 and 5 are examined, it is seen that the distribution of SO_2 in the provinces in the Aegean Region has decreased in 2019 compared to the previous year. The air pollution limit value of SO_2 is 20 µg / m3 (microgram / cubic meter) in our country (Vural 2021). It is seen that many provinces in the Aegean Region exceed this limit value. Considering the years 2018 and 2019, İzmir is the cleanest province in the region in terms of SO_2 amount.

4. CONCLUSION

Today, air pollution, which has negative effects on human health, is a global threat that affects future generations. Industrialization, increase in the number of vehicles, rapid population growth and urbanization cause a rapid increase in air pollution. Fuels used in industrial production and coal used for heating can be shown among the reasons for the high level of air pollution in the region during the winter months. In order to improve the air quality, especially the increase of natural gas should be encouraged. If natural gas cannot be made widespread, the use of high-calorie coal for heating should be encouraged and attention should be paid to thermal insulation in buildings.

Air pollution causes respiratory diseases in humans. Effective strategies for preventing air pollution should be determined and implemented in order to protect human health in the region. Industrial facilities should be located outside of the settlements and the prevailing wind direction should taken into consideration.

REFERENCES

Akan D S & Morcalı M H (2017). Kahramanmaraş Hava Kirliliği Kaynaklarının İzlenmesi ve Belirlenmesi. KSU Mühendislik Bilimleri Dergisi, 20(2).

Akyürek Ö, Arslan O & Karademir A (2013). SO_2 ve PM10 Hava Kirliliği Parametrelerinin CBS ile Konumsal Analizi: Kocaeli Örneği. TMMOB Coğrafi Bilgi Sistemler Kongresi, Ankara.

Altıkat A, Torun F E & Bayram T T (2011). Küresel Kirlilik: Dünya, Avrupa Birliği ve Türkiye'de Hava Kirliliği Örneği. Erciyes Üniversitesi Fen Bilimleri Enstitüsü Dergisi, 27(2): 134-149.

Başıbüyük G Ö, Ay F & Acar S (2017). Küresel Isınma ve Küresel Isınmanin Yaşlılar Üstündeki Etkisi. Türkiye Sosyal Araştırmalar Dergisi (1): 203-218.

Baysan C & Yavaş S P (2020). COVID-19 ve Hava Kirliliği; Karantina Boyunca Ne Oldu? ESTÜDAM Halk Sağlığı Dergisi. 2020;5(COVID-19 Özel Sayısı):35-46.
Bilgi Sistemleri Kongresi, Ankara.

Demircan M, Alan I & Sensoy S (2011). Increasing Resolution Of Temperature Maps By Using Geographic Information Systems (GIS) And Topography Information. 5th Atmospheric Science Symposium, Istanbul.

Finlayson-Pitts J B & Pitts, N J (1986). Atmospheric Chemistry: Fundamentals and Experimental Techniques. Wiley Publishing Co.

Garipağaoğlu N (2003).Türkiye'de Hava Kirliliği Sorununun Coğrafi Bölgelere Göre Dağılımı, Doğu Coğrafya Dergisi, 8(9).

Göğsu S & Hastaoğlu K Ö (2019)Ters Mesafe Ağırlıklı Enterpolasyon Yönteminde Güç Fonksiyonu. TMMOB Harita ve Kadastro Mühendisleri Odası 17. Türkiye Harita Bilimsel ve Teknik Kurultayı, Ankara.

Vural E (2021). Güneydoğu Anadolu Bölgesi İllerinin CBS Kullanarak Hava Kalitesinin Mekânsal Değişiminin İncelenmesi (2007-2019). Doğal Afetler ve Çevre Dergisi, 7(1): 124-135.

Zencirci S A & Işıklı B (2017). Hava Kirliliği. Türk Dünyası Uygulama Ve Araştırma Merkezi Halk Sağlığı Dergisi 2(2),24-36.

Intercontinental Geoinformation Days

igd.mersin.edu.tr

Determination of effective predisposing factors using random forest-based gini index in landslide susceptibility mapping

Alihan Teke*[1], Taskin Kavzoglu [1]

[1]*Gebze Technical University, Department of Geomatics Engineering, Kocaeli, Turkey*

Keywords
Landslide susceptibility
Machine learning
Random forest
Feature importance
Factor selection

ABSTRACT

Landslide susceptibility mapping is a multi-phase procedure that includes several key steps, one of which is the correct determination of landslide predisposing factors. In the current literature, however, there is no global consensus or framework about the selection of these factors. In this study, the effectiveness of predisposing factors was investigated using the Random Forest-based Gini index to generate landslide susceptibility models. For this purpose, 16 predisposing factors, representing the morphological, lithological, and environmental characteristics of the study area, were initially utilized and measured their importance scores calculated by utilizing the Gini index. Then, three models (RF-1, RF-2, and RF-3) including 50%, 75%, and the whole of the factors, were produced based on the importance scores. To select the optimum one among these models, their performances were assessed employing two accuracy assessment metrics, namely overall accuracy (OA) and area under curve (AUC). The validation results revealed that AUC obtained using RF-1, RF-2, and RF-3 models were calculated as 85.85%, 96.70%, and 90.66% respectively. Also, the statistical significances of the models were evaluated using McNemar's test, which revealed that all models were statistically different from each other.

1. INTRODUCTION

At a global scale but particularly in mountainous zones, landslides have drastically shaped and modified the local terrain due to the deformations they create (Geertsema et al. 2009). As a result of these surface displacements, both human life and man-made structures including settlements, infrastructure, superstructure, and also ecological integrity are under threat. In addition to these adverse influences, landslides also lead to tremendous economic damages and the devastation of natural resources (Schuster & Fleming, 1986). Therefore, implementing the necessary preparedness strategies and generating emergency action plans are of utmost significance in the pre-disaster phase given all the above-mentioned issues (Gómez & Kavzoglu, 2005). In this context, landslide susceptibility maps are highly functional tools that can display the distribution of landslide-susceptible and non-landslide zones and enable the reactivation of idle fields. Thus, landslide susceptibility maps provide valuable supports to public enterprises in terms of both preventing financial losses and safeguarding human beings (Kavzoglu et al. 2014).

Given the complex dynamics of landslides, the performances of landslide susceptibility maps depend primarily on the determination of convenient and robust landslide predisposing factors. In the literature, generally, the selection of these factors is executed with the aid of expert judgment or utilizing available geo-environmental data sets (e.g. lithology map, road networks). However, some factors in the data set may reduce the accuracy of models, which lead to adversely affect the reliability of the produced landslide susceptibility maps. Furthermore, unnecessary features not only increase the computational complexity of the model, but also extend the processing time.

To alleviate the aforementioned challenges, the feature selection paradigm has been recently gained popularity as an effective solution. Broadly speaking, FS approaches discard superfluous variables from the data set, and thus, more comprehensible models are generated. Consequently, both the predictive performance and reliability of the landslide susceptibility maps can be enhanced. Due to these wide-ranging benefits, feature selection algorithms have been

* **Corresponding Author**

* (a.teke2020@gtu.edu.tr) ORCID ID 0000 – 0003 – 4048 – 329X
(kavzoglu@gtu.edu.tr) ORCID ID 0000 – 0002 – 9779 – 3443

Cite this study

Teke A & Kavzoglu T (2021). Determination of Effective Predisposing Factors Using Random Forest-Based Gini Index in Landslide Susceptibility Mapping. 2nd Intercontinental Geoinformation Days (IGD), 198-201, Mersin, Turkey

intensively employed in landslide susceptibility zonation studies (Hu et al. 2021; Kavzoglu et al. 2015; Sahin 2020).

The main motivation of this current work is to determine the optimal landslide predisposing factor subset using feature importance scores obtained by the Gini index of Random Forest (RF). To achieve this object, three models consisting of 50%, 75%, and the whole of the factors were established based on the importance order of 16 landslide causative factors. To determine the optimal subset of factors, two accuracy assessment metrics, namely overall accuracy (OA) and area under curve (AUC) were calculated. Finally, McNemar's test was employed to statistically analyze the performance differences of the three models.

2. METHOD

2.1. Study Area and Datasets

The Arakli district of Trabzon province situated in the northeast part of Turkey, between latitudes 40° 57′ N and 40° 31′ N; longitudes 39° 49′ E and 40° 04′ E, was selected as the region of interest (Fig. 1). It covers an area of about 479 km^2, the large part of the study area is mountainous with elevations varying 0 to 2876m and slopes up to about 70°. In addition to the morphological characteristics, heavy rainfall is one of the most significant agents that predispose to the occurrence of landslides in the study area (Sahin et al. 2017). Furthermore, anthropogenic influences such as the construction of superstructure, infrastructure and deforestation make a substantial contribution to the occurrence of mass movement.

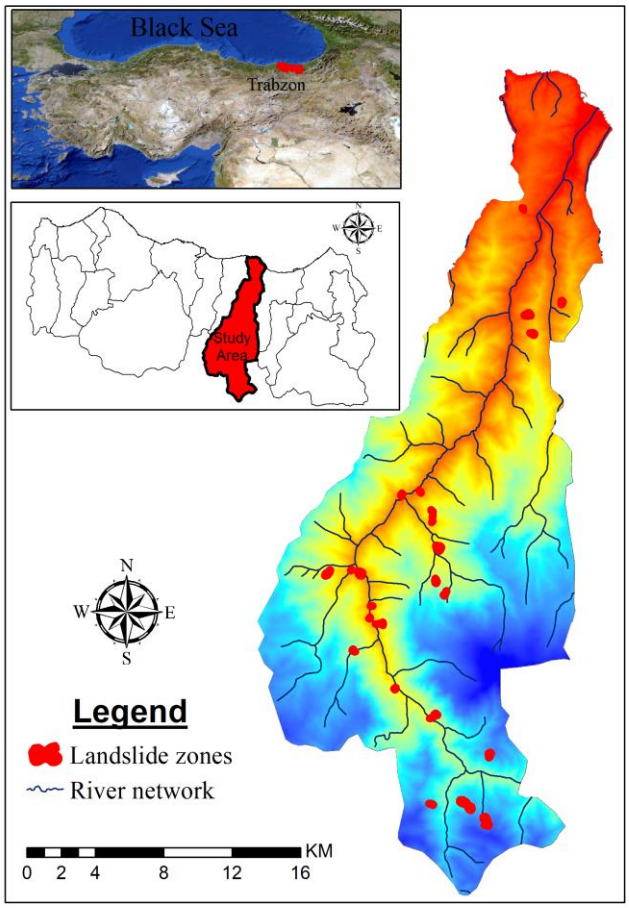

Figure 1. Location map of the study area and landslides

In the process of reliable and accurate generation of landslide susceptibility maps, one of the key steps is the preparation of the landslide predisposing factors (Kavzoglu et al. 2020). In this study, slope, topographic roughness index (TRI), elevation, distance to roads, distance to rivers, profile curvature, aspect, valley depth, normalized difference vegetation index (NDVI), lithology, topographic wetness index (TWI), stream power index (SPI), road density, topographic position index (TPI), drainage density, and plan curvature were determined as primary landslide predisposing factors to generate landslide susceptibility map.

2.2. Random Forest

Random forest (RF), proposed by Breiman (2001), is a solid ensemble learning approach whose working principle is essentially based on combining many decision trees. In addition to its capability to perform versatile tasks such as classification, regression, and unsupervised learning, RF has been extensively employed for feature selection applications. It reduces the variance and enhances the generalization, resulting from the bagging methodology. To assess the predictive performance of the model, about two of thirds of the instances or simply in-bag instances are employed for the model training phase while remaining (i.e. out-of-bag) instances are employed for the internal cross-validation procedure (Kavzoglu et al. 2018).

In the current literature, several metrics, which are relatively cost-effective, have been proposed to calculate factor importance scores using RF (Fabris et al. 2018). Among them, the Gini index (or mean decrease impurity) is widely preferred by researchers to measure the importance of features. Gini index is essentially a splitting function used by the RF algorithm in order to specify which feature to split on throughout the learning stage (Qi 2012).

In the domain of the earth sciences and geomorphological researches, the RF technique has become quite popular and attracted wide interest owing to its unique abilities in coping with complicated and inconsistent real-world problems. From the perspective of landslide susceptibility mapping studies, recent works have demonstrated a broad application of the RF (Merghadi et al. 2020). Although RF algorithms have been utilized for regression and classification purposes, studies in which RF is employed as a feature selection algorithm are rare to find in the field of landslide susceptibility mapping.

3. RESULTS

In this study, a RF-based feature selection algorithm was adopted to detect the most efficient landslide contributing factors. In parallel with this purpose, 16 factors were initially included in the modeling process. Then, the importance value of each factor was calculated using the Gini index, as shown in Table 1. Results revealed that the slope had the greatest importance score of 0.358. Other significant factors were determined as TRI (0.222) and elevation (0.100). On the other hand,

plan curvature (0.009), drainage density (0.015), and TPI (0.018) were found to be the least effective ones.

Considering the importance scores, three models (RF-1, RF-2, and RF-3) including 75%, 50%, and the whole of the factors were produced (Table 1). Whereas the RF-1 model had all factors in the data set, RF-2 and RF-3 factors had %75 and %50 of the data set, respectively. Among these models, to seek the best ones, each model was independently trained using the RF classifier.

Table 1. Three models formed with different factors based on factors importance scores

Factors	RF-1	RF-2	RF-3	Importance Score
Slope	√	√	√	0.358
TRI	√	√	√	0.222
Elevation	√	√	√	0.100
Distance to Roads	√	√	√	0.038
Distance to Rivers	√	√	√	0.035
Profile Curvature	√	√	√	0.032
Aspect	√	√	√	0.030
Valley Depth	√	√	√	0.028
NDVI	√	√	X	0.027
Lithology	√	√	X	0.027
TWI	√	√	X	0.027
SPI	√	√	X	0.027
Road Density	√	X	X	0.025
TPI	√	X	X	0.018
Drainage Density	√	X	X	0.015
Plan Curvature	√	X	X	0.009

Evaluation of performances has been considered as an essential tool in obtaining information about the reliability of landslide susceptibility maps. Therefore, two accuracy assessment measures including OA and AUC were calculated in order to compare the predictive performances of three models. According to the results of the accuracy assessment, the RF-2 model had the greatest OA with 93.28% and followed by the RF-3 and RF-1 models with 83.48% and 75.02, respectively (Table 2). Similarly, when it comes to the AUC value, the RF-2 model had the highest AUC value 96.70% followed by the RF-3 (90.66%) and RF-1 (85.85) models, as shown in Fig. 2.

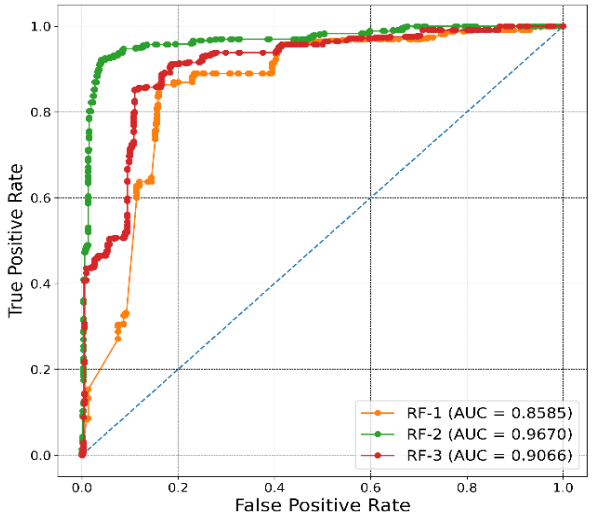

Figure 2. ROC curve analysis of the models

Table 2. Performance evaluation of the models

Models	OA (%)	AUC (%)
RF-1	75.02	85.85
RF-2	93.28	96.70
RF-3	83.48	90.66

Table 3. McNemar's test results for the models

	RF-1	RF-2	RF-3
RF-1	-	154.58	72.75
RF-2		-	78.22
RF-3			-

Apart from these accuracy assessment measures, the statistical significance of the difference between the performances of the models was also analyzed using McNemar's test. If the estimated statistical value is higher than the chi-square table value (3.84 for a 95% confidence interval), it can be inferred that the difference between the results of the two independent models is statistically significant. In other words, the model outperforms the other model. According to the estimated statistical significance test results, it was observed that three models yielded statistically different results. More specifically, when analyzed the statistical significance of the RF-1 and RF-2 models, the statistical value is estimated as 154.58, which clearly indicates statistical significance in performances.

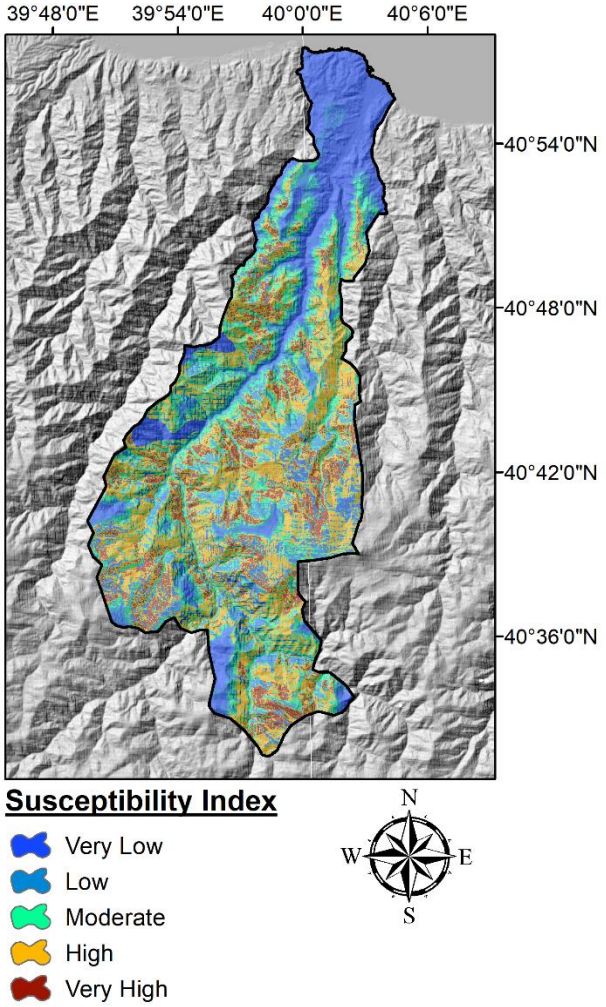

Figure 3. Landslide susceptibility map produced using optimal landslide predisposing subset including 12 factors

4. CONCLUSION

In this current study, the effectiveness of predisposing factors was analyzed using the RF-based Gini importance scores to create a more robust and accurate landslide susceptibility map for the Arakli district of Trabzon Province, Turkey. For this purpose, three models consisting of 50%, 75%, and the whole factors in the data set were produced based on the importance order of features obtained by utilizing the Gini index algorithm. Two accuracy assessment (OA and AUC) and a statistical significance test was used to make a sound comparison of the model performances.

According to the indication of the study, some considerable inferences can be drawn. Firstly, it was observed that the RF-2 model consisting of 12 landslide causative factors (slope, TRI, elevation, distance to roads, distance to rivers, profile curvature, aspect, valley depth, NDVI, lithology, TWI, and SPI) were found to be more efficient than other models. Thus, 25% of the whole data set was curtailed, which also alleviated the training time and model complexity. Besides, it can be clearly concluded that using whole conditioning factors caused the curse of dimensionality, also called the Hughes phenomenon. When utilized RF-3 model containing 50% of the whole data set, a significant decrease in the model performance by about 10% was observed. As a result, the RF-2 model with 93.28% OA, which is determined as the optimal model, was employed in the generation of the landslide susceptibility map of the study area. Secondly, the slope was found to be the most important causative factor, which is compatible with many previous types of research. Thirdly, it can be observed that RF algorithms employed with the correct features were yielded highly accurate results. This indication proves the robustness of the RF algorithm. In summary, the correct identification of predisposing factors, which is one of the critical issues in the determination of landslide susceptibility, was carried out utilizing the RF-based Gini index algorithm and the landslide susceptibility map with high accuracy and reliability was attained.

REFERENCES

Breiman L (2001). Random forests. Machine Learning, 45(1), 5-32.

Fabris F, Doherty A, Palmer D, De Magalhães JP & Freitas AA (2018). A new approach for interpreting Random Forest models and its application to the biology of ageing. Bioinformatics, 34(14), 2449-2456.

Geertsema M, Highland L & Vaugeois L (2009). Environmental impact of landslides. Landslides-Disaster Risk Reduction, 1, 589-607.

Gómez H & Kavzoglu T (2005). Assessment of shallow landslide susceptibility using artificial neural networks in Jabonosa River Basin, Venezuela. Engineering Geology, 78(1-2), 11-27.

Hu X, Mei H, Zhang H, Li Y & Li M (2021). Performance evaluation of ensemble learning techniques for landslide susceptibility mapping at the Jinping county, Southwest China. Natural Hazards, 105(2), 1663-1689.

Kavzoglu T, Colkesen I & Sahin EK (2018). Machine Learning Techniques in Landslide Susceptibility Mapping: A Survey and a Case Study. Landslides: Theory, Practice and Modelling. Advances in Natural and Technological Hazards Research, 50,283-301.

Kavzoglu T, Sahin EK & Colkesen I (2015). Selecting optimal conditioning factors in shallow translational landslide susceptibility mapping using genetic algorithm. Engineering Geology, 192, 101-112.

Kavzoglu T, Sahin EK & Colkesen I (2014). Landslide susceptibility mapping using GIS-based multi-criteria decision analysis, support vector machines, and logistic regression. Landslides, 11, 425-439

Kavzoglu T, Teke A & Bilucan F (2020). Effectiveness of machine learning algorithms in landslide susceptibility mapping: A case study of Trabzon Province, Turkey. 41st Asian Conference on Remote Sensing.

Merghadi A, Yunus AP, Dou J, Whiteley J, ThaiPham B, Bui DT, Avtar R & Abderrahmane B (2020). Machine learning methods for landslide susceptibility studies: A comparative overview of algorithm performance. Earth-Science Reviews, 207, 103225.

Qi Y (2012). Random forest for bioinformatics. Ensemble Machine Learning: Methods and Applications, Springer (2012), 307-323.

Sahin EK (2020). Assessing the predictive capability of ensemble tree methods for landslide susceptibility mapping using XGBoost, gradient boosting machine, and random forest. SN Applied Sciences, 2, 1-17.

Sahin EK, Ipbuker C & Kavzoglu T (2017). Investigation of automatic feature weighting methods (Fisher, Chi-square and Relief-F) for landslide susceptibility mapping. Geocarto International, 32(9), 956-977.

Schuster RL & Fleming RW (1986). Economic losses and fatalities due to landslides. Bulletin of the Association Engineering Geologists, 23(1), 11-28.

Intercontinental Geoinformation Days

igd.mersin.edu.tr

Trend analysis of precipitation data using Mann Kendall and Sen's slope tests

Osman Enes Gunes*[1], Aslan Cihat Basara [1], Yasemin Sisman [2]

[1]Ondokuz Mayis University, Institute of Graduate Studies, Department of Geomatics Engineering, Samsun, Turkey
[2]Ondokuz Mayis University, Faculty of Engineering, Department of Geomatics Engineering, Samsun, Turkey

Keywords
Trend Analysis
Homogeneity Test
Standart Precipitation Index
Mann Kendall Test
Sen's Slope Test
Precipitation Data

ABSTRACT

Changes in precipitation occur due to global or local climate changes. Studying this change is very important for human life. Rainfall is very important in meeting essential needs such as agricultural activities and clean water resources. Therefore, trend analysis in precipitation data is important. In this study, in order to examine whether there is a trend in the precipitation data of Erbaa Plain (Turkey), first homogeneity test was performed and then the standard precipitation index was calculated. The calculated data were analyzed using the Mann-Kendall test and Sen's Slope test. Monthly precipitation data for 40 years covering the years 1981-2020 were used in the study. Precipitation data were analyzed according to 90% confidence interval. Trends were detected in January and September in monthly precipitation series

1. INTRODUCTION

Change in meteorological data is a complex natural hazard that causes drought and affects ecosystems and society in many ways. In order to minimization the effects of drought as a result of meteorological variability, water resources management strategies should be developed and drought risk should be assessed (Beden et al.2020). Meteorological events on earth have unfixed feature. Therefore the size and consequences of meteorological changes cannot be easily predicted (Coskun 2019).

Various analysis methods such as time series, regression analysis and machine learning are used in the analysis of meteorological data. In this study, one of the analysis methods, time series methods were used. The precipition, known as most important meteoeological data, was selected as study topic.

Changes in precipitation in a residential area can lead to important problems affecting human life. Change has significant effects on clean water resources and agricultural activities. Efficient use and control of water is provided by the correct evaluation and analysis of the meteorological data. In order to meet the needs, the management of water resources that change depending on time and quantity parameters is very important. Thus, the meteorological data should be examined on the presence of any trend (Yüce et al. 2017). While, the continuous decrease in precipitation values, disasters can be observed such as drought and desertification, the continuous increase precipitation values, disasters such as landslides and floods are seen. Therefore, trend analysis and disaster risk maps in rainfall data have great importance (Beden et al.2020; Basara et al.2020).

In this study, precipitation analysis of the Erbaa Plain, which has a high importance in terms of agricultural activities in Tokat province, located in the Middle Black Sea Region, was performed using time series.

2. MATERIAL AND METHOD

In this study, precipitation data of Erbaa plain of Erbaa, given fig.1, district of Tokat province were used as application data. The precipitation data were taken from the NASA Langley Research Center (LaRC) POWER project. Monthly precipitation data for the 40-year period covering the years 1981-2020 were obtained from the website of the project. Standard Homogenity Test SNHT, Standard Precipitation Index (SPI), Mann-Kendall Trend Test, Sen's Slope Test were used as methods in the study.

* **Corresponding Author**

*(osmanenesgunes@gmail.com) ORCID ID 0000-0001-8656-4701
(aslancihatbasara@gmail.com) ORCID ID 0000 – 0001 – 6644 – 6097
(ysisman@omu.edu.tr) ORCID ID 0000 – 0002 – 6600 – 0623

Cite this study

Gunes O.E, Basara A.C & Sisman Y (2021). Trend analysis of precipitation data using Mann Kendall and Sen's slope test. 2nd Intercontinental Geoinformation Days (IGD), 202-205, Mersin, Turkey

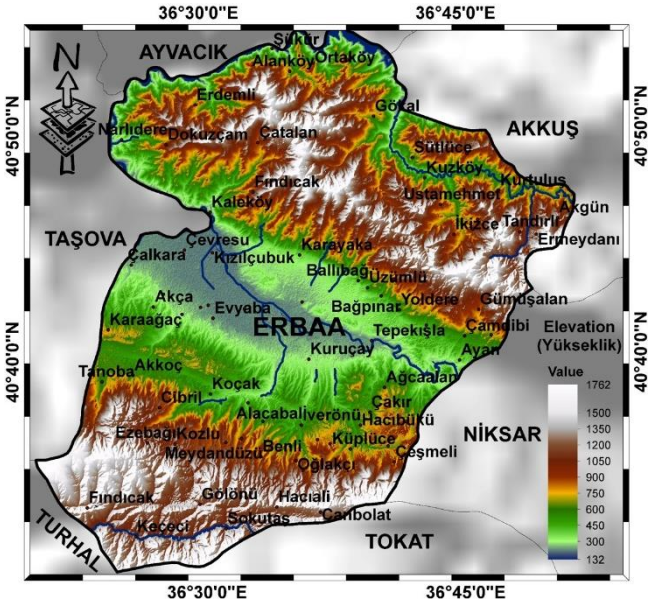

Figure 1. Location Map

2.1. Standart Normal Homogenity Test (SNHT)

The Standard Normal Homogeneity test (SNHT) method is used in the tests of many climatic and hydrological sizes (Alexandersson 1986). A point "c" from the analyzed series is divided into two by reference and Equation 1 is calculated with the help of Equation 2 If the change occurs at a 'h' point, T (c) reaches its maximum value at the point c = h. The test statistic is as in Equation 3. If the test value exceeds the table value, it is rejected. In this case, it is decided that the data are not homogeneous.

$$T(c) = c.\bar{z_1}^2 + (n-c).c.\bar{z_2}^2 \quad c = 1, \dots, n \quad (1)$$

$$\bar{z_1} = (\sum_{i=1}^{c} \frac{y_i - \bar{y}}{\sigma})/c \text{ ve } \bar{z_2} = (\sum_{i=1+c}^{n} \frac{y_i - \bar{y}}{\sigma})/(n-c) \quad (2)$$

$$T_0 = max_{1 \le c \le n} T(c) \quad (3)$$

2.2. Standart Precipitation Index (SPI)

The Standard Precipitation Index (SPI) was proposed in 1993 and is used to identify and monitor drought in regions with varying climate (Mckee et al. 1993). If the data is in a normal distribution, the difference of precipitation from the mean can be divided by the standard deviation to determine the abnormalities in the regions. SPI account are calculated using Equation 4. The SPI values are classified according to Table 1.

$$SPI = \frac{(x_i - x_i^{ort})}{\sigma} \quad (4)$$

Table 1. SPI Classification

SPI Value	Drought Category
≥ 2	Extremely Humid
1.5 to 1.99	Very Humid
1.0 to 1.49	Moderately Humid
0.50 to 0.99	Lightly Humid
-0.49 to 0.49	Normal
-0.99 to -0.50	Lightly Drought
-1.0 to -1.49	Moderate Drought
-1.5 to -1.99	Very Drought
≤ −2	Extreme Drought

2.3. Mann Kendall Test

The Mann-Kendall method is a non-parametric method that is processed according to the presence or absence of change in parameters in a time series (Mann 1945; Kendall 1975). It is determined whether there is a trend in the daha using Mann Kendall test (Beşel and Tanır Kayıkçı 2019). In this method, the order of the data is compared (Gilbert 1987). One of the advantages of the test is that the data does not need to any distribution.

Mann-Kendall test is calculated using Equation 5 and Equation 6. The variance calculation of the test statistic with a normal distribution is calculated using Equation 7. In order to determine the significance of the test and probability function are calculated using Equation 8-9.

$$S = \sum_{k=1}^{n-1} \sum_{j=k+1}^{n} sgn(x_j - x_k) \quad (5)$$

$$sgn(x_j - x_k) = \begin{cases} 1 & (x_j - x_k) > 0 \\ 0 & (x_j - x_k) = 0 \\ -1 & (x_j - x_k) < 0 \end{cases} \quad (6)$$

$$Var(S) = \frac{n(n-1)(2n+5)}{18} \quad (7)$$

$$Z = \begin{cases} \frac{S-1}{\sqrt{Var(S)}} & S > 0 \\ 0 & S = 0 \\ \frac{S+1}{\sqrt{Var(S)}} & S < 0 \end{cases} \quad (8)$$

$$F(Z) = \frac{1}{2\pi} e^{\frac{-z^2}{2}} \quad (9)$$

2.4. Sen's Slope Test

The direction and size of the trend in the data are determined using the Sen's Slope test (Sen 1968). If there is a linear trend in the time series, the actual slope (change in unit time) can be determined using a nonparametric method. This method can be applied to records that are not affected by data errors or extreme values and where there are missing values (Yu et al. 1993).

The median is calculated using Equation 10 in Sen's Slope test. If the number of data (N), is an odd or even, Equation 11 and 12 are applied, respectively.

$$Q_i = \frac{(x_j - x_k)}{(j-k)} \quad (10)$$

$$Q = Q_{(N+1)/2} \quad (11)$$

$$Q = \frac{1}{2}\left[Q_{N/2} + Q_{(N+2)/2}\right] \quad (12)$$

3. RESULTS

In the first stage of the study, the Standard Homogeneity Test (SNHT) was applied to determine the suitability of the values in the data set for analysis. Then SPI values were calculated for drought classification. The Mann-Kendall test was applied to determine the direction of trends and statistical significance levels in the data series. In the last stage, Sen's Slope test was applied to determine the trend directions. This process

was made for monthly and annual total precipitation series. The work flow chart of the study is given in Figure 2.

Figure 2. Flow Chart

Homogeneity testing was done using the R-Studio program. Results are given in Table 2. It was found that the data were homogeneous and suitable for analysis.

Table 2. Homogeneity Analysis Result

P-value	alpha	SNHT
0.466	0.05	Homogeneous

According to Table 2, it was decided that the data were homogeneous since P-value selected significance value (0.05). The calculation and classification of SPI values of application data are calculated using Equation 4 and Table 1. The results are given in Table 3.

Table 3. Annual SPI Classes

Year	SPI Class	Year	SPI Class
1981	Lightly Drought	2001	Normal
1982	Lightly Humid	2002	Normal
1983	Normal	2003	Normal
1984	Moderate Drought	2004	Moderately Humid
1985	Moderate Drought	2005	Lightly Humid
1986	Very Drought	2006	Moderate Drought
1987	Normal	2007	Normal
1988	Lightly Humid	2008	Normal
1989	Moderate Drought	2009	Extremely Humid
1990	Moderate Drought	2010	Lightly Humid
1991	Lightly Humid	2011	Moderately Humid
1992	Normal	2012	Very Humid
1993	Moderate Drought	2013	Very Drought
1994	Normal	2014	Normal
1995	Normal	2015	Lightly Drought
1996	Lightly Humid	2016	Moderately Humid
1997	Normal	2017	Lightly Drought
1998	Lightly Humid	2018	Normal
1999	Moderately Humid	2019	Lightly Drought
2000	Lightly Humid	2020	Very Drought

From the Table 3, Extremely Humid in 1 year, Very Humid in 1 year, Moderately Humid in 4 years, Lightly Humid in 8 years, Normal in 13 years, Lightly Drought in 4 years, Moderate Drought in 6 years, Very Humid in 3 years rainfall was observed. There was no rainfall in the Extreme Drought class.

Mann-Kendall Test results of the monthly total precipitation data set are given in Table 4.

Table 4. Monthly Mann Kendall Trend Analysis Results

Months	MK-z Tau	MK-P Value	MK Hypo-thesis
January	0.297	0.007	Refuse
February	-0.108	0.328	Accept
March	0.162	0.142	Accept
Aprıl	-0.136	0.217	Accept
May	0.151	0.169	Accept
June	0.181	0.100	Accept
July	0.001	0.991	Accept
August	0.003	0.981	Accept
September	0.196	0.075	Refuse
October	-0.090	0.415	Accept
November	-0.110	0.316	Accept
December	0.074	0.499	Accept

Sen's Slope Test results for the monthly total precipition data set are given in Table 5.

Table 5. Monthly Sen's Slope Trend Analysis Results

Months	Sen's Slope	Sen's Type of Trend
January	0.033	Increase
February	-0.007	No Trend
March	0.018	Increase
Aprıl	-0.016	Decrease
May	0.013	Increase
June	0.017	Increase
July	0.000	No Trend
August	0.000	No Trend
September	0.018	Increase
October	-0.010	Decrease
November	-0.018	Decrease
December	0.007	No Trend

Trend charts obtained as a result of the analysis are given in Figure 3-5.

4. DISCUSSION AND CONCLUSION

In this study, monthly precipitation data of Erbaa Plain in mm were used. SNHT was applied to monthly precipitation data and H_0 hypothesis was accepted since P = 0.466 value was higher than significance level 0.05 value. It was seen that the data were suitable for analysis.

The SPI values were analyzed with Mann-Kendall trend test, which is one of the non-parametric tests, as monthly. The analysis was made according to 10% significance level. According to the trend analysis, an increasing trend was determined in January and September. Although not statistically significant, an increasing trend was observed in March, May and June. A downward trend was observed in February, April, October and November.

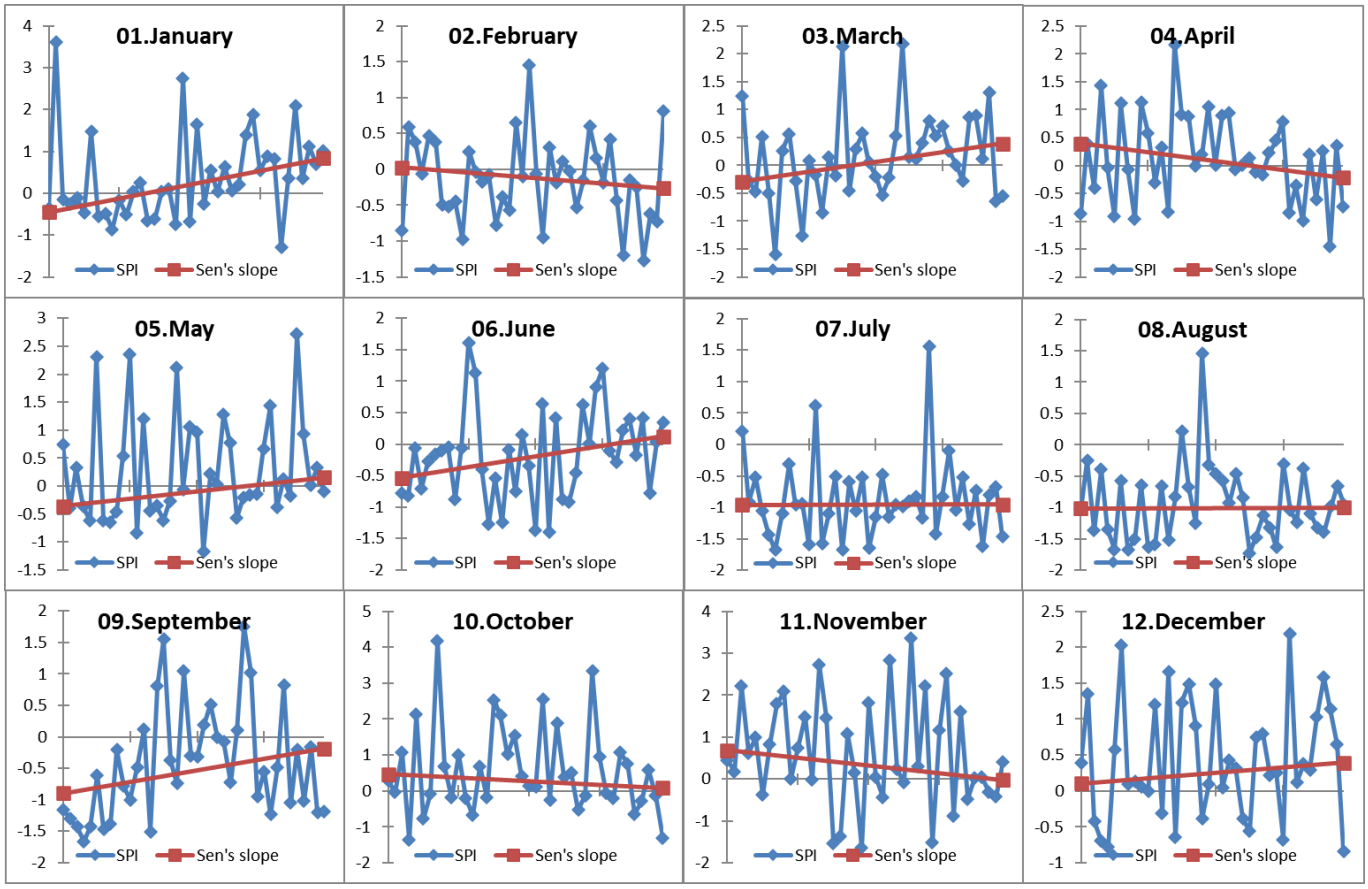

Figure 3. Monthly Trend Graphs

The SPI values were analyzed with the Sen's Slope trend test, which is one of the non-parametric tests, for monthly with 10% signifidance level. According to the analysis results, Mann Kendall z values and Sen's Slope values show parallelism.

While there is generally increasing precipitation in the Erbaa Plain, droughts have been observed in recent years (2016-2020). It has been observed that the decreasing tends was in the autumn months, when the region receives the most precipitation. Also, an increasing trend was observed in the summer months, when the lowest rainfall was observed throughout the year. The plans should be made in order to reduce the damages that may occur due to the negative effects of climate change. Similar studies done for other regions of Turkey and hydrological and climatological elements. In this way, the formation and effects of climate changes can be observed on a wider scale and contribute to the planning to be made.

REFERENCES

Alexandersson, H. (1986). A homogeneity test applied to precipitation data. Journal of climatology, 6(6), 661-675.

Basara A.C., Tabar M.E. & Sisman Y. (2020). GIS-Based Landslide Susceptibility Mapping Using Frequency Ratio and AHP Methods. Intercontinental Geoinformation Days (IGD), 223-226, Mersin, Turkey.

Beden, N., Demir, V., Keskin, A.Ü. (2020). Samsun İlinde SPI ve PNI Kuraklık İndekslerinin Eğilim Analizi. DEUFMD 22(64), 107-116.

Beşel, C, Tanır Kayıkçı, E. (2019). Serisel Korelasyonun Toplam Zenit Gecikmesi Zaman Serilerinde Parametrik Olmayan Trend Belirleme Üzerindeki Etkisi. Gümüşhane Üniversitesi Fen Bilimleri Enstitüsü Dergisi, 9 (1), 180-188.

Coşkun, M. (2019). İklim Değişmeleri ve Küresel Isınma, 12. Bölüm, Yer Bilimi Kitabı, Ed. Mete Alim-Serkan Doğanay, Pegem Akademi, Ankara.

Gilbert, R. O. (1987), Statistical methods for environmental pollution monitoring, Van Nostrand Reinhold, New York.

Kendall, M. G. (1975), Rank Correlation Methods, Charles Griffin, London.

Mann, H. B. (1945), Non-parametric Test Against Trend, Econometrika, 13, 245-259.

Mckee, T. B., Doesken, N. J., Kleist, J., (1993). The relationship of drought frequency and duration to time scales, AMS 8th Conf. Appl. Climatol., 17-22.Ocak.1993, California, 179–184.

Sen, P. K. (1968). Estimates of The Regression Coefficient Based on Kendall's Tau. J. Am. Stat. Assoc., 63, 1379–1389.

Yu, Y.S., Zou, S., Whittemore, D., (1993), Non-Parametric Trend Analysis of Water Quality Data of Rivers in Kansas, Journal of Hydrology 150: 61-80.

Yüce, Ş., M. Ünsal, ve M. I. Yüce (2017), Seyhan havzası yıllık akım verilerinin eğilim analizi, IX. Ulusal Hidroloji Kongresi, 4-6 Ekim 2017, Diyarbakır.

Intercontinental Geoinformation Days

igd.mersin.edu.tr

Investigation of the shadow effect of urbanization on green areas with shadow impact analysis

Halil İbrahim Şenol[*1]

[1]*Harran University, Faculty of Engineering, Department of Geomatics Engineering, Şanlıurfa, Turkey*

Keywords
3D GIS
Shadow Impact Analysis
Smart Cities
Urban Development

ABSTRACT

Today, the use of information technologies has made life easier and helps people to take precautions against problems that may arise in the future. 3D GIS (Geographic Information Systems) is also used for various purposes to facilitate human life today. One of these goals is to improve the foresight ability in plans. In the studies carried out until today, the power of 3D GIS to produce solutions to various problems in the world is revealed. In this study, the effects of urban shadowing because of wrong urbanization have been investigated by using the power of 3D GIS. The data was provided via OSM (Open Street Map), which is an open-source map provider. The obtained data were analyzed and a park which is the surrounding area is not yet developed was determined. In the aim of the study, new buildings were added around the park by evaluating the direction of urban growth and possibilities, and the effect of the shadow it created on the sunbathing time of the park was investigated. The details of the work carried out are given in detail in the following stages.

1. INTRODUCTION

Unplanned and rapid urbanization is one of the major problems in developed and developing countries. Migration from rural areas to cities has caused the cities to grow in an unplanned manner. Unplanned urbanization resulting from migration causes difficulties in processing urban data and making plans. Therefore, the concept of "Smart City" has been introduced to make future city plans smooth and effective and to make them sustainable. The smart city is one of the most current concepts of the last twenty years. The smart city can also serve as a decision support tool for better planning and management of infrastructure requirements.

3D city models, which are generally used for visualization purposes, can also be used effectively for planning and development purposes (Şenol et al., 2018; Şenol ve Kaya, 2019). Today we live in a fast-developing world. For this reason, it is vital to take preventions in the planning stages. Problems that can be predicted during the planning phase can be easily observed with 3D GIS and its solutions.

However, it is still difficult to get the correct data. Although open-source data sharing is advanced, they still do not have enough skills to give accurate results. Elevation information, which is especially important for a subject such as 3D GIS, is not yet available in most of these data. For this reason, researchers have generally paid for the data access. However, although there are free data provided by local governments, it cannot be said that these data are very healthy. There is still a regular 3D GIS data shortage in the majority of our country.

While forming the basis of this research, we will first talk about 3D GIS and some of its uses. 3D GIS has been used for shadow and solar analysis for several years. 3D city models are used to estimate how much a building is exposed to the sun (Redweik et al., 2013; Eicker et al., 2014; Santos et al., 2014). 3D city models provide geometric information such as the slope, direction, and area of the roof used as input for the study of sun exposure time (Biljecki et al., 2015).

However, some researchers may use dense point clouds instead of 3D city models for solar energy studies (Gooding et al., 2015). Both forms of research (point cloud and 3D model) allow us to design an urban settlement to maximize sunbathing of a neighborhood (Vermeulen et al., 2015) and estimate the capacities of decentralized energy resources in crisis management practices (Aarsen et al., 2015). . Besides, 3D city models

* **Corresponding Author**

*(hsenol@harran.edu.tr) ORCID ID 0000-0003-0235-5764

Cite this study

Şenol H, İ. (2021). Investigation of the shadow effect of urbanization on green areas with shadow impact analysis. 2nd Intercontinental Geoinformation Days (IGD), 206-209, Mersin, Turkey

with window details can be used to estimate indoor lighting (Saran et al., 2015).

Visualization is one of the main purposes of 3D GIS and 3D city models. Thanks to model production, we can easily present features that are impossible to present in a 2D environment in 3D models (Köninger & Bartel, 1998, Ellul & Altenbuchner, 2014). In this way, the perspective of decision-makers and users on city plans has changed and the model experience has been a factor in decision making. Also, the use of 3D models based on visualization is available in various fields. Such as rainwater harvesting in development areas (Yiğit et al., 2020), solar impact analysis (Büyüksalih et al., 2017) etc.

3D city models are also indispensable for many visibility analyzes, such as determining the line of sight between two points in an urban area and predicting the volume of view (Lonergan & Hedley, 2016; Peters et al., 2015). 3D city models can also be used to predict sky visibility. An example of this can be the degree to which the surrounding buildings cover the sky from the perspective of the person.

Estimating building shadows is also frequently used in urban planning applications (Zhou et al., 2019). The analysis of building shadows is also important in positioning the buildings to be designed solar energy panels and estimating the energy potential (Strzalka et al., 2012; Eicker et al., 2015). This use case is closely related to the prediction of the sun exposure of buildings described earlier, and they are often used together.

In this study, a park which is located in Diyarbakır, Turkey and the construction around it has not been completed yet was selected. Two scenarios are presented according to the existing structures around the park and the predicted structures expected to be built in the future, and the shadow effects of these scenarios on the park have been analyzed.

2. METHOD

Although shadow impact analysis is a method that can be used for predicting future scenarios, it is still a new method and is not common. In line with this study, firstly the field of study was determined and Open Street Map, which provides open-source GIS data, was examined to obtain the data of the determined study area. Open Street Map is an open-source and external user-supported map platform. For this reason, the data provided by the system may not always provide accurate data since it is user-sourced.

For this reason, after selecting an area belonging to Diyarbakır, which is the study area, the accuracy of the data was compared via Google Street View, and also the missing building floor height data were obtained through this platform. Building heights and sun angle are of great importance in the shadow effect analysis. For this reason, the study area was chosen as a park in the east-west direction and with a small number of buildings around it (Figure 1).

In this direction, using the tools provided by ArcGIS Solutions, first the basic structures and then the proposed structures were introduced to the system. While the buildings were entered into the system, the height of the buildings was given by using the CityEngine software and simple models were produced. Thanks to these 3D models, shadow effect analysis, which is a 3D analysis, can be done easily. The models produced are colored and divided as follows;

- The green zone is the park area,
- Blue structures are existing buildings and
- Red structures are the proposed buildings (Figure 2).

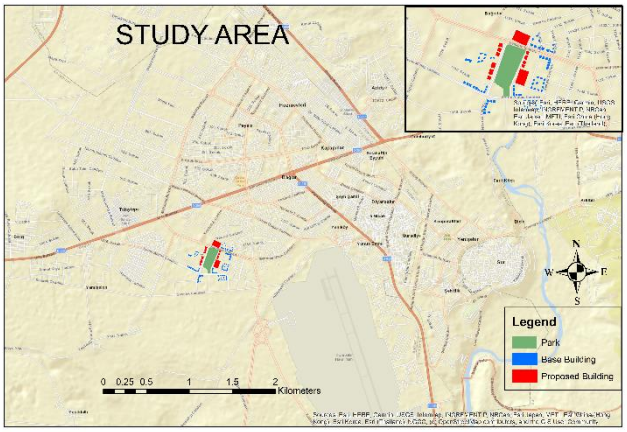

Figure 1. Study Area

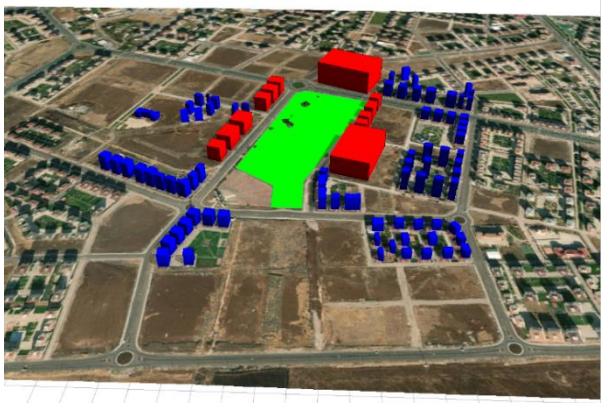

Figure 2. 3D model of the study area

2.1. Shadow Impact Analysis

ArcGIS Pro software was used for shadow impact analysis and previously created 3D models were transferred to the software. To ensure the accuracy of the analysis, attention was paid to the height of the building and the geographical accuracy of the structures.

The shadow movements of the 3D models that were included in the shadow impact analysis were observed according to two separate situations. To compare the shadows obtained in two different situations, first, the basic structures were analyzed and the shadow conditions were revealed, and then the effect of the proposed structures on the park was investigated if they were built in the area. All the sun conditions of the buildings were examined and their effect on the park was analyzed (Figure 3).

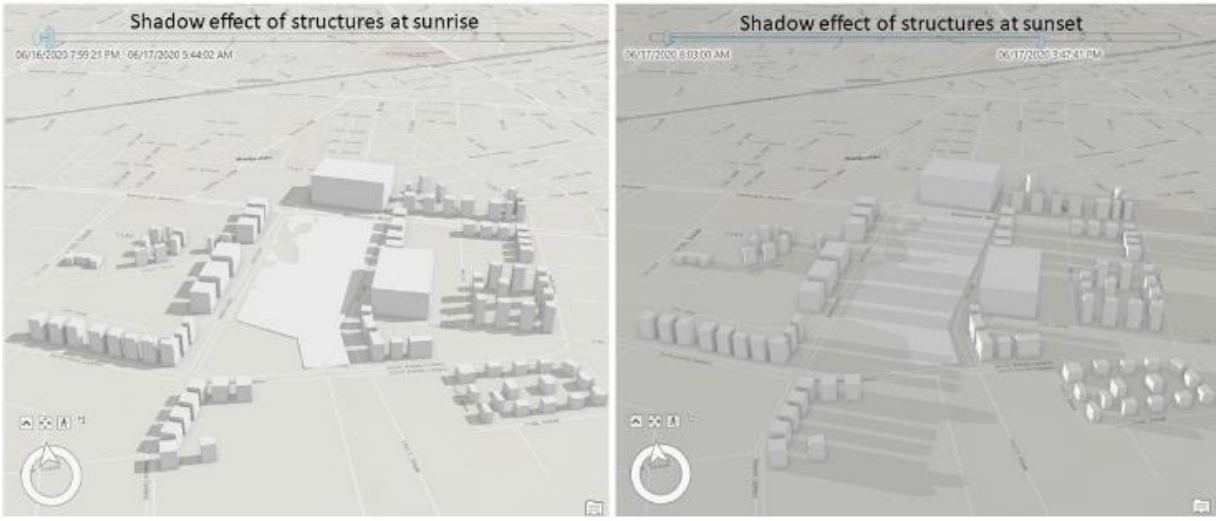

Figure 3. Shadow effect at different times of the day

As seen in Figure 3, the effect of the proposed buildings on the park is serious. This can limit the possibility of providing sunlight to people, which is one of the biggest features of green space. In the analysis results, the sunshine duration was analyzed and the shadow boundaries formed on the park were revealed. First, the shadow areas created by the existing buildings were analyzed (Figure 4), then the shadows created by the proposed buildings were analyzed too (Figure 5).

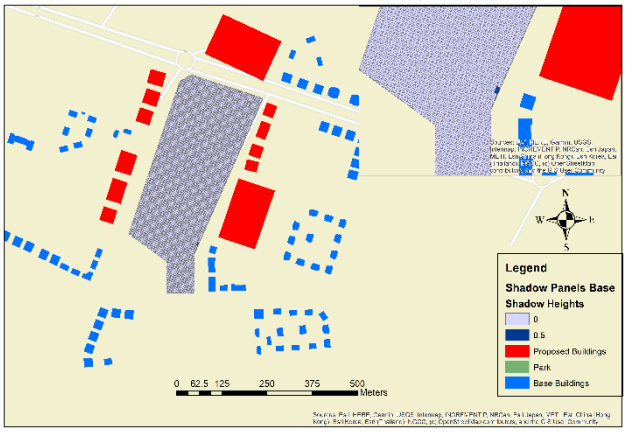

Figure 4. Shadow effect of base buildings on the park

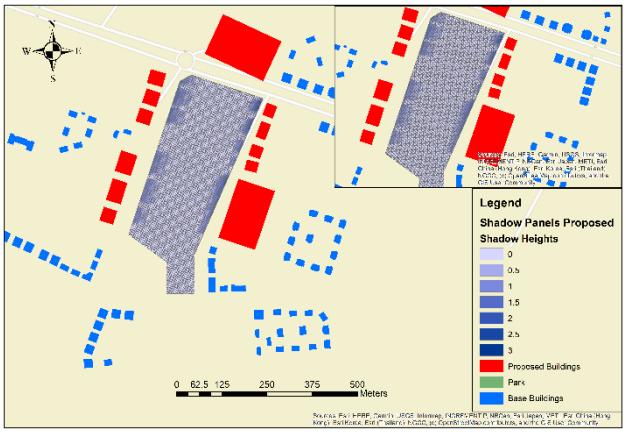

Figure 5. Shadow effect of proposed buildings on the park

When the shadow situations affected by two different building types are analyzed, it is obvious that the new buildings that can be built around the park will cause serious shadowing effects. Also, considering the shadow durations, it can be considered that building heights can be a factor in this shading. For this reason, the two shadow conditions were compared with a separate analysis, and the amount of shading was revealed (Figure 6).

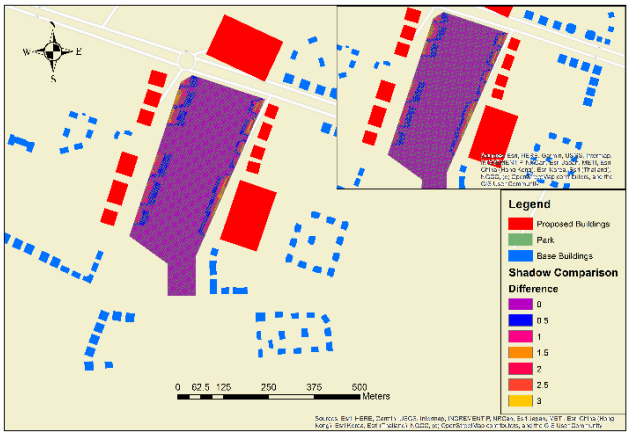

Figure 6. Comparison of shadow effects of different scenarios

3. RESULTS and DISCUSSION

When the shadowing times and amounts on the park are examined, although it is seen that there is a serious accumulation of shadows, the amount of shading remained at a certain level since the building heights in the region have a certain limit. However, the shadowing effect is serious in areas that are constantly under the shadow. When the shadow areas are examined in the generated raster file, the shadow areas are revealed and the number of shadows produced are compared in Figure 7. Shade areas are divided into areas that are mostly shaded, have equal shade and sun duration, and are not shaded.

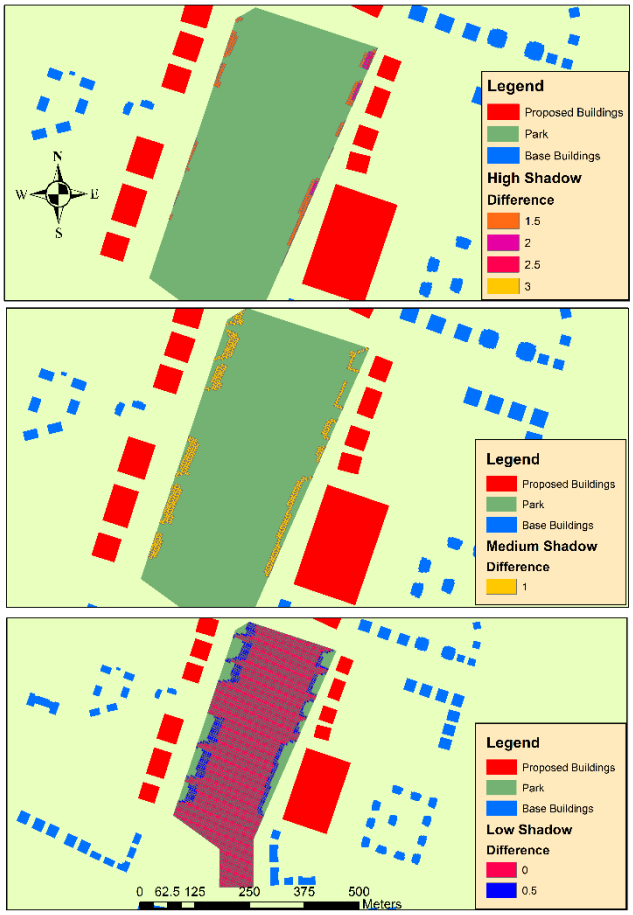

Figure 7. Amounts of shadows were obtained as a result of the analysis.

4. CONCLUSION

Nowadays, the increasing amount of degradation in green areas and the green area needs of people have led people to take various measures in the protection of these areas. Shade is an important factor in the benefit of green spaces and decreases the sunbathing effect. It is not correct to limit sunbathing periods due to construction, especially in this period, during which many studies have been conducted on the beneficial use of solar energy. For this reason, the shading periods of places open to human use such as parks should also be taken into consideration while making city plans. In future studies, sunbathing effect and solar energy utilization times can be investigated by comparing shadow and sun effects.

REFERENCES

Aarsen, R., Janssen, M., Ramkisoen, M., Biljecki, F., Quak, W., & Verbree, E. (2015). Installed base registration of decentralised solar panels with applications in crisis management. The International Archives of Photogrammetry, Remote Sensing and Spatial Information Sciences, 40(3), 219.

Biljecki, F., Stoter, J., Ledoux, H., Zlatanova, S., & Çöltekin, A. (2015). Applications of 3D city models: State of the art review. ISPRS International Journal of Geo-Information, 4(4), 2842–2889.

Buyuksalih, G., Bayburt, S., Baskaraca, A. P., Karim, H., & Rahman, A. A. (2017). Calculating solar energy potential of buildings and visualization within unity 3d game engine. International Archives of the Photogrammetry, Remote Sensing and Spatial Information Sciences, 42(4/W5).

Eicker, U., Monien, D., Duminil, É., & Nouvel, R. (2015). Energy performance assessment in urban planning competitions. Applied Energy, 155, 323–333.Eicker, U., Nouvel, R., Duminil, E., & Coors, V. (2014). Assessing passive and active solar energy resources in cities using 3D city models. Energy Procedia, 57(896), e905.

Ellul, C., & Altenbuchner, J. (2014). Investigating approaches to improving rendering performance of 3D city models on mobile devices. Geo-Spatial Information Science, 17(2), 73–84.

Gooding, J., Crook, R., & Tomlin, A. S. (2015). Modelling of roof geometries from low-resolution LiDAR data for city-scale solar energy applications using a neighbouring buildings method. Applied Energy, 148, 93–104.

Köninger, A., & Bartel, S. (1998). 3D-GIS for urban purposes. Geoinformatica, 2(1), 79–103.

Lonergan, C., & Hedley, N. (2016). Unpacking isovists: a framework for 3D spatial visibility analysis. Cartography and Geographic Information Science, 43(2), 87–102.

Peters, R., Ledoux, H., & Biljecki, F. (2015). Visibility Analysis in a Point Cloud Based on the Medial Axis Transform. UDMV, 7–12.

Redweik, P., Catita, C., & Brito, M. (2013). Solar energy potential on roofs and facades in an urban landscape. Solar Energy, 97, 332–341.

Santos, T., Gomes, N., Freire, S., Brito, M. C., Santos, L., & Tenedório, J. A. (2014). Applications of solar mapping in the urban environment. Applied Geography, 51, 48–57.

Saran, S., Wate, P., Srivastav, S. K., & Krishna Murthy, Y. V. N. (2015). CityGML at semantic level for urban energy conservation strategies. Annals of GIS, 21(1), 27–41.

Şenol, H. İ., & Kaya, Y. (2019). İnternet Tabanlı Veri Kullanımıyla Yerleşim Alanlarının Modellenmesi: Çiftlikköy Kampüsü Örneği. Türkiye Fotogrametri Dergisi, 1(1), 11-16.

Şenol, H. İ., Ernst, F. B., & Akdağ, S. (2018). Kentsel Dönüşüm Alanlarının Geotasarım Yöntemi ile Planlanması: Eyyübiye Örneği. Harran Üniversitesi Mühendislik Dergisi, 3(3), 63-69.

Strzalka, A., Alam, N., Duminil, E., Coors, V., & Eicker, U. (2012). Large scale integration of photovoltaics in cities. Applied Energy, 93, 413–421.

Vermeulen, T., Knopf-Lenoir, C., Villon, P., & Beckers, B. (2015). Urban layout optimization framework to maximize direct solar irradiation. Computers, Environment and Urban Systems, 51, 1–12.

Yiğit, A. Y., Orhan, O., & Ulvi, A. (2020). Investigation of The Rainwater Harvesting Potential at the Mersin University, Turkey. Mersin Photogrammetry Journal, 2(2), 64-75.

Zhou, K., Lindenbergh, R., & Gorte, B. (2019). Automatic shadow detection in urban very-high-resolution images using existing 3D models for free training. Remote Sensing, 11(1), 72.

Intercontinental Geoinformation Days

igd.mersin.edu.tr

Spatial flood analysis to determine possible economic damage: Case study of the European side of Istanbul

Buğrahan ÖZCİHAN [1], Enes Doğukan ÖZGENER [1], İlker KARAKAP [1], Levent Doğukan ÖZLÜ [1], Yusuf Göktuğ BAĞCI[1], Ömer AKIN *[1], Hande DEMİREL [1]

[1]*Istanbul Technical University, Faculty of Civil Engineering, Department of Geomatics Engineering, Istanbul, Turkey*

Keywords
Flood Analysis
Geographic Information System (GIS)
Economic Impact
Spatial Risk Assessment

ABSTRACT

Floods are one of the natural disasters that affect people's lives and cause enormous environmental and economic damage. Istanbul has been frequently exposed to the devastating effects of floods from past to present, especially in terms of human losses and damage to infrastructure. Although various precautions have been taken by the authorities to prevent losses, such as improving stream and infrastructure, none of them have been able to mitigate the effects of floods to a great extent. One of the solutions is to collect spatial and economic data obtained from different sources into a single spatial database and present this synthesized information to decision-makers in an understandable form using Geographic Information Systems (GIS). In this study, a possible flood disaster that may occur on the European side of Istanbul is simulated using spatial flood analysis methods and the results of the disaster are presented. After the inundated areas are identified, the economic dimension is calculated and compared with past events for the validation of risk assessment. According to the results, total damage of more than $500 million is estimated for a possible full-scale flood event on the European side of Istanbul.

1. INTRODUCTION

Istanbul, one of the most densely populated metropolises in the world, has experienced many flood disasters between 1989-2009 (Turoglu 2011). In the study of flood disasters, climate change, increasing concretion, unplanned urbanization, insufficient infrastructures, flood proclivity of topography, and settlements in riverbeds can be mentioned as the main causes. According to Sahin and Sag (2015), soil structure, economic activities, land use and population characteristics are also effective on occurrence of flood. Flooding is often caused by heavy rainfall and, depending on the infrastructure, can cause severe damage to roads, buildings, and the residents of the affected neighborhoods. The main reason why these impacts of disasters could not be prevented is not the determination of possible flood zones or the failure to perform necessary analyzes, but the fact that different sources of information are not presented and analyzed in a spatial environment.

The proposed solution to prevent or manage the impact of a possible flood event is to collect spatial and economic data from different sources in a single spatial database, analyze this information using Geographic Information Systems (GIS) and present it to decision makers in an understandable form. In this study, flood analyzes are carried out in the GIS environment and a spatial risk assessment is made by using economic input data for the areas identified as the result of the analyzes. The costs of several affected components of the infrastructure are estimated for the European side of Istanbul and compared with past events to validate the methodology. A temporal comparative pricing strategy is followed by using the economic dimension of past floods, such as the Ayamama flood that occurred in 2009 (Ozcan 2017). All types of data used in the study are obtained from open-source database. Since detailed information on infrastructure (type, construction material, etc.) could

* **Corresponding Author**

*(ozcihan17@itu.edu.tr) ORCID ID 0000-0002-4540-3140
(ozgener16@itu.edu.tr) ORCID ID 0000-0002-2293-5662
(karakap16@itu.edu.tr) ORCID ID 0000-0002-7128-2100
(ozlul17@itu.edu.tr) ORCID ID 0000-0001-7121-8101
(bagciy16@itu.edu.tr) ORCID ID 0000-0002-5145-9925
(akinom@itu.edu.tr) ORCID ID 0000-0002-8109-0313
(hande.demirel@itu.edu.tr) ORCID ID 0000-0003-0338-791X

Cite this study

Ozcihan B, Ozgener E, Karakap I, Ozlu L, Bagci Y, Akin O & Demiral H (2021). Spatial analyses of inundated areas in European side of Istanbul due to a possible flood and its possible economic damage. 2nd Intercontinental Geoinformation Days (IGD), 210-213, Mersin, Turkey

not be obtained from any open-source database, this dimension of risk assessment could not be merged with the results of this study.

Further sections are organized as follows: In the next section, the study area, data, flood analysis methods, and the economic dimension of the analysis are described. In section 3, spatial and quantitative estimations are presented and findings are interpreted. Finally, the subject is concluded in the last section.

2. METHOD

2.1. Study Area and Data

Istanbul is the most populous city in Turkey and due to its high population, it holds many problems related to flooding. One of these problems is the impact of flooding on residential areas resulted from the unplanned urbanization. Flood disasters in recent years have caused many casualties and millions of dollars of damage. When the past events of Istanbul were examined, it was found that the floods caused more damage on the European side than on the Asian side according to the Istanbul Development Agency (2010). Also, there is more quantitative economic data about past events. Therefore, the European side of Istanbul was selected as the study area to implement and validate the methodology.

The data used in the study were obtained entirely from open-source database. OpenStreetMap data were used to identify water bodies, buildings, roads, and Point of Interests (POI). For such studies, Digital Elevation Model (DEM) is an important input to determine the characteristics of topography and flood impacts. One of the most important factors affecting the accuracy of flood analyzes is the resolution of DEM. Paid data such as LIDAR DEM have higher resolution than Shuttle Radar Topography Mission (SRTM) or other freely available DEM data. The use of high-resolution DEM could significantly increase the accuracy of the analysis. However, in this study, to follow the open-source approach, the SRTM DEM with a spatial resolution of 30m x 30m was chosen as the most suitable data and obtained from USGS Earth Explorer. The unit prices needed for the economic analysis were obtained from Cost Table of the Department of Revenue Management. This analysis can be applied to any region where the required data are available. Study area and data are shown in Fig. 1.

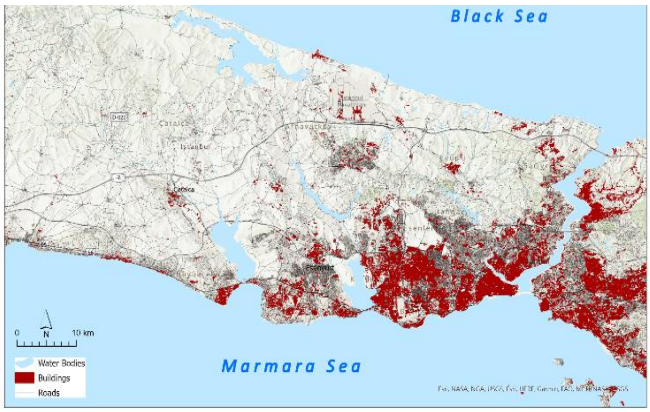

Figure 1. Study area and Data

2.2. Methodology

2.2.1. Flood analysis

The analysis process starts with the determination of inundated areas using the DEM and continues with the estimation of the economic dimension for roads and buildings using unit costs of these components. Workflow is shown schematically in Fig. 2.

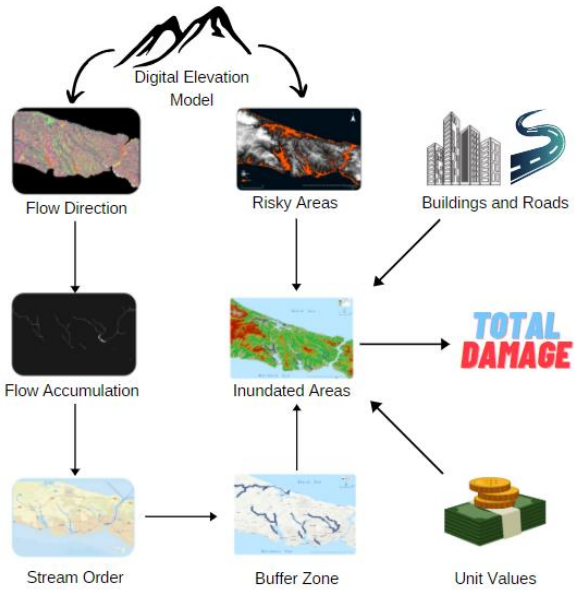

Figure 2. Schema of followed workflow

To perform the analyses shown in Fig. 2, ArcGIS Pro Hydrology Toolbox was used. By using fill operation, small imperfections of the DEM data have been removed. Then, the flow direction from one cell to the others and the amount of water collected in each cell were calculated with flow accumulation and direction analysis. Finally, stream orders representing a kind of evacuation line of Istanbul during the flood disaster were determined. In the further steps, the flood impact distance was determined to be 500 meters with the help of legal regulations (Legal Gazette, 1984). This distance was used to perform the buffer analysis for the stream orders. According to Ozcan (2017), the water had risen 6-7 meters during the last flood in Ayamama Stream in 2009. Based on this information, the heights of the streams in Istanbul were obtained from the DEM and the rise height of the water was added to the elevation of the streams. As a result of this process, areas below 25 meters were determined as risk zones in the DEM data. Then, the inundated areas were obtained at the intersection of the buffer zone and the at-risk areas. Finally, the flooded roads and buildings were determined by intersecting the inundated areas with the buildings and roads.

2.2.2. Economic analysis

Within the scope of this study, an economic analysis was conducted using the unit damage costs for buildings and roads identified in Legal Gazette of Turkey No: 31231 (Legal Gazette, 2021). Although there are many types of buildings affected by flooding, they were classified into

four main classes as house, workplace, shopping center, and educational buildings.

By using unit prices for different types of buildings, the total cost per unit square meter of each affected building was determined. Roads were also examined under 3 main classes, referred to as primary, secondary, and tertiary. Primary roads consist of high-cost highways, secondary roads are two-way roads that connect to primary roads, and tertiary roads are smaller and simpler roads outside of urban areas. Damage costs for the three main types of roads were calculated based on the cost of roads built in the past years. In this way, the structural economic damage costs of buildings and roads were calculated.

3. RESULTS

The inundated areas determined by the flood analysis are shown in Fig. 3.

Figure 3. Map of inundated areas

As shown in Fig. 3, there are mainly five different regions to be affected by the flood. According to map of inundated areas in Fig. 3, affected districts are Arnavutköy, Avcılar, Büyükçekmece, Çatalca, Eyüpsultan, Kağıthane and Küçükçekmece. To see the effects of the flood, a 3-dimensional model was also created for the illustration of the flood as shown in Fig. 4.

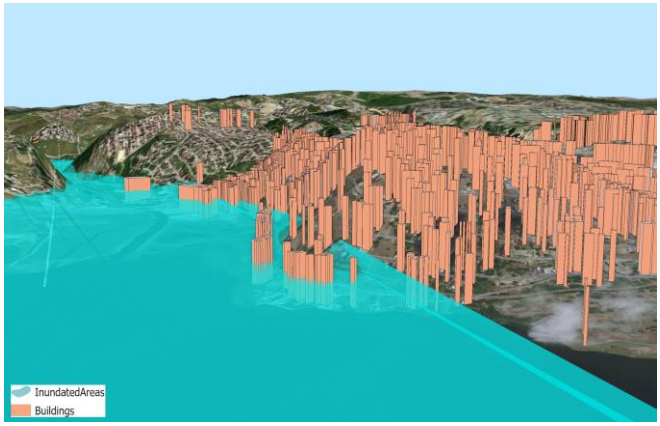

Figure 4. 3D model example of flood

With the help of the 3D model, it is possible to have a better view of the flood by observing the land shape and the flood together. In the context of this study, the analysis performed with the 3D model is not detailed. However, when sufficient data is available, it enriches the study by adding a different perspective to the analysis.

When the simulated flood area is examined in detail, it was found that 1326 buildings, 139.31 km^2 of the residential area, and 586 km of roads are affected. A part of the affected roads and buildings are shown in Fig. 5.

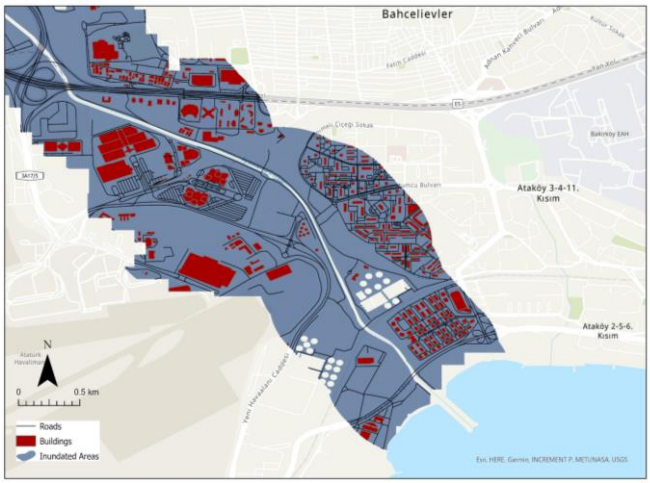

Figure 5. Inundated roads and buildings in the Ayamama region

While calculating the economic damages caused by the flood, the road and building data were calculated separately by using the unit prices for roads and the prices for building repairs obtained from the Cost table of the Department of Revenue Management. Damage to primary, secondary, and tertiary roads was calculated as $ 420 million and damage of different building types was calculated as $ 100 million in total. The costs of the different types of roads and buildings are shown in Fig. 6 and the comparison of these components is shown in Fig. 7. The total damage caused by the flood was determined to be $ 520 million, as shown in Fig. 7.

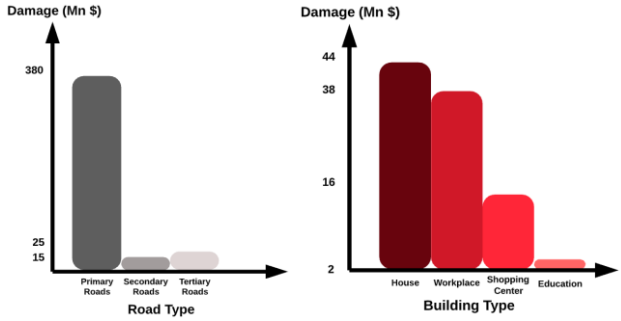

Figure 6. Calculated damage for roads and buildings

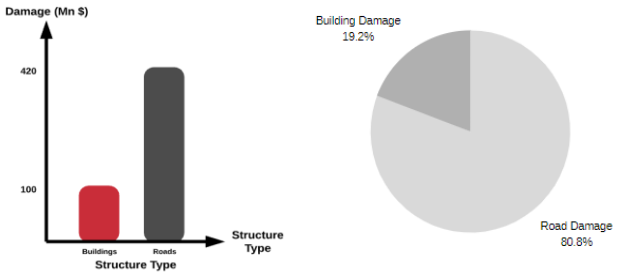

Figure 7. Graphical representations of the total damage of roads and buildings

Finally, to make the accuracy assessment, the calculated economic damage was compared with the real economic damage of the flood that occurred in the Ayamama River region in 2009 (Ozcan 2017), and the accuracy rate of 87% was obtained.

4. CONCLUSION

Determination of the inundated areas that occurred due to flooding and their economic damage is very important in terms of taking measures to minimize the impacts. In this paper, the areas that will be inundated by possible flooding on the European side of Istanbul are spatially determined and the economic impacts are calculated to be presented to decision-makers by using completely open-source data. The applied methodology can be implemented for any city in the world where data is available and the results can be shared with decision-makers. By using such spatial decision-making systems, precautions should be taken to reduce the destructive power of floods that seriously harm people.

REFERENCES

Istanbul Development Agency (2010). Appendices of Istanbul Regional Plan

Legal Gazette of Turkey (1984). The Law 2981: Some Procedures to be Applied to the Buildings that Differ to the Zoning and Slum Legislation and the Amendment of an Article of the Zoning Law No. 6785 (Republic of Turkey Legal Gazette, 8 March 1984, No: 18335)

Legal Gazette of Turkey (2021). Approximate Unit Costs of Structures Used in Archıtecture and Engineering Services in 2021 (Republic of Turkey Legal Gazette, 24 March 2021, No: 31433)

Ozcan O (2017). Taşkın Tespitinin Farklı Yöntemlerle değerlendirilmesi: AYAMAMA Deresi Örneği. Doğal Afetler Ve Çevre Dergisi, 3(1), 9-27.

Sahin I & Sag, F (2015). The economic impact of flood disaster between 1980-2015 years: The sample of Turkey. Eurasian Academy of Sciences Eurasian Business & Economics Journal 3, 71-82

Turoglu H (2011). Flashfloods and Floods in Istanbul. Ankara University Journal of Environmental Sciences, 3(1), 39-46

Intercontinental Geoinformation Days

igd.mersin.edu.tr

Analysis and investigation on spatio-temporal dynamic pattern of drought in Thailand

Arpakorn Wongsit[*1], **Nengcheng Chen** [2], **Tanita Suepa** [3]

[1]*Burapha University, Geoinformatics, Chonburi, Thailand*
[2]*Wuhan University, State Key Laboratory of Information Engineering in Surveying, Mapping and Remote Sensing, Wuhan, China*
[3]*Geo-Informatics and Space Technology Development Agency, Bangkok, Thailand*

Keywords
Drought
SPI
NDVI
VCI
Thailand

ABSTRACT

The spatio-temporal analysis to evaluate drought conditions in Thailand from 2000 to 2020 using indices, are SPI, NDVI, and VCI derived from MODIS based on GEE platform. This study found that NDVI could be used to assess and monitor the drought conditions in these regions. The correlation analysis between the SPI and VCI indicates the potential of VCI in measuring the direct impact of rainfall on vegetation dynamics. Analysis showed that VCI was found to be stronger in providing a detailed description of the vegetation dynamics with the corresponding level of precipitation received. The average NDVI was 0.59, the highest in 2017 at 0.74, and the lowest value at 0.39 in 2001. The average VCI was 54%, the highest in 2017 at 86%, and the lowest value at 21% in 2001. SPI is obtained from the rainfall data. The SPI value of -2.11 was the lowest with the drought severity level in 2004 and in 2000 was the highest SPI of 1.12 where were moderate to extreme wet with no drought severity level.

1. INTRODUCTION

The dynamic nature of drought causes difficulties in planning, monitoring, predicting, and providing support to the drought-stricken areas (Thiruvengadachari and Gopalkrishna 1993). The drought affects people and agriculture at the local scale as well as impacts on the economy, society, and environment. The impact of drought on precipitation, soil, agricultural fields, and water reservoirs is analyzed by hydrologic, agricultural, meteorological, and socio-economic terms (Hayes et al. 2012). Drought's problem in Thailand is not a new issue but a crucial repetitious problem. The country has been experiencing drought for decades, this is a natural disaster that appears in many areas and a vital damaging problem that obstructed national development. The areas experiencing drought greatly tend to have a shortage of water for consumption and agriculture where Thai farms primarily rely on natural rainwater. The declining crop yield causes a shortage of agricultural products and processed products for both domestic consumption and export. In other words, the drought not only directly impact to the economy but also indirectly impact to the society and culture (Meteorological Department 2011). Remote sensing provides invaluable geo-information for drought conditions with the capability of obtaining satellite images from the past to recent date, it is a relatively cost-effective method. Also, it is a source of timely continuous geo-referenced information to monitor the condition of large-scale areas especially for such remote areas (Jiao et al. 2016) with limited data to possibly create periodic and accurate drought condition maps of related areas. While MODIS data from Terra satellite is widely used for drought monitoring applications and to explore spatiotemporal drought patterns with satellite derived indices that offer effective opportunities of collecting huge volume of data and fulfill lacking area data to cover Thailand completely.

Hence, the spatiotemporal analysis of drought for this study is applied by MODIS derived indices from Google Earth Engine (GEE) to provide the Normalized Difference Vegetation Index (NDVI) (Gu et al. 2007). Vegetation Condition Index (VCI) can be obtained from NDVI and establishment of the relationship between the rainfall derived data. The amount of rainfalls, known as Standardized Precipitation Index (SPI), is conducted to obtain the sensitive indices responding to the drought condition and to assess spatiotemporal of drought. This is to correlate between MODIS satellite data derivatives and meteorological index. This study applies the GEE

* **Corresponding Author**

*(62910177@my.buu.ac.th) ORCID ID 0000-0002-5558-1557
(cnc@whu.edu.cn) ORCID ID 0000-0002-3521-9972
(tanita@gistda.or.th) ORCID ID 0000-0002-5560-0965

Cite this study

Wongsit A, Chen N & Suepa T (2021). Analysis and investigation on spatio-temporal dynamic pattern of drought in Thailand. 2nd Intercontinental Geoinformation Days (IGD), 214-217, Mersin, Turkey

platform to automatically retrieve and analyze drought which requires long term data and good coverage of the region exposed to drought conditions. GEE is a cloud-based platform for planetary-scale geospatial analysis to store and proceed geographic data sets. It is accessible to create multi-temporal maps or conduct time series analysis by using the available satellite images in the platform by its processing capability and coding approach (Gorelick et al. 2017). Thus, GEE platform provides feasible tools and extensive geospatial data which are proficiently fit drought monitoring purposes. The GEE application automatically retrieves data that is useful to access the data scripts. This will be utilized for developing the methods and kind of data used in the countries with inadequate observation data.

Therefore, the main aim of this study to evaluate drought conditions in Thailand for a twenty-one-year period from 2000 to 2020 using main indices, which are widely used for droughts to analyze the spatio-temporal drought with the indices from satellite data in order to represent the drought rapidly is NDVI and VCI which derived indices from MODIS satellite data derived indices based on GEE platform and SPI from meteorological index which is obtained from the rainfall data, are also selected for this study as well. The representative vegetation indices are selected for the study including NDVI, VCI, and SPI. Based on the selected indices, spatiotemporal drought over Thailand is characterized using online-based remotely sensed datasets ranging from 2000 to 2020 period. Indicators such as the SPI and NDVI can be generated the best correlation-anticipation relationship for early signs of drought impacts and drought monitoring purposes (Measho et al. 2019).

2. METHOD

2.1. Study area

The study area focuses on Thailand country, located in the center of mainland of Southeast Asia (Fig. 1). This located wholly within the tropics. Thailand encompasses with diverse ecosystems including the hilly forested areas of the northern frontier, the fertile rice fields in the central plains, the broad plateau of the northeastern part and the rugged coasts along the narrow southern peninsula. There are 77 provinces and over 69 million people. Thailand has a land area of 513,115 sq.km, bounded within 5°37′N - 20°27′N Latitudes and 97°22′E - 105°37′E Longitudes. Thailand bordered by Myanmar and the Andaman Sea to the west, Laos to the northeast, Cambodia to the southeast, the Gulf of Thailand and Malaysia to the South.

2.2. Data Acquisition

Datasets analyzed the Spatial-temporal distribution of drought conditions in Thailand is shown in Table 1. The integration of remotely sensed data with meteorological datasets, MODIS-derived NDVI in the GEE platform and SPI derived from rainfall data for the period of 30-years from 1990 to 2020 for 126 rain-gauge stations to generate the correlation to determine the spatiotemporal drought patterns in Thailand for 21-years period from 2000 to 2020.

Table 1. Dataset characteristics and source used

Dataset	Variables	Spatial resolution	Temporal resolution	Source
Precipitation (rain gauge stations)	SPI	95 stations	Monthly	TMD
Terra-MODIS (MOD13Q1)	NDVI/ VCI	250-m	16-Day	GEE

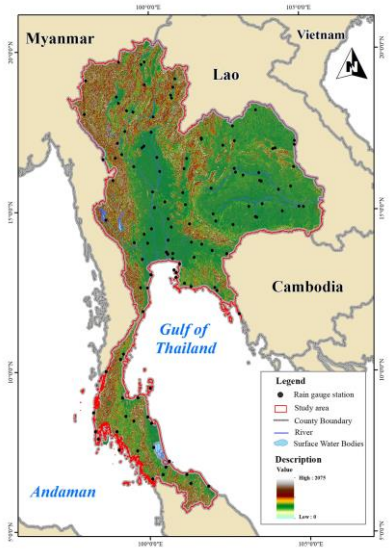

Figure 1. This is topography map of Thailand.

2.3. Data Pre-processing

2.3.1. Computation of NDVI

From 16-day MOD13Q1 V6 images, monthly NDVI were calculated using surface reflectance (ρ) from MODIS red and near infrared by dividing the difference between them and their sum.

$$NDVI = \frac{\rho\text{NIR} - \rho\text{RED}}{\rho\text{NIR} + \rho\text{RED}}$$

where ρRED and ρNIR are spectral reflectance measurements that were acquired in the red and near-infrared regions, respectively. NDVI ranges from −1 to +1, with +1 indicating healthy vegetation cover, lower values representing stressed vegetation, negative values representing open water or high moisture content, and 0.1 value, indicating bare soil. The valid data was used in the analysis is thus from 0.1 to 1.0

2.3.2. Computation of VCI

The VCI derived from NDVI (Reddy et al. 2020) was widely used for detecting the onset of drought, its intensity, duration, and impact (Kogan 1995) In the study, atmospherically corrected NDVI products derived from MODIS 250 m. time series data of growing season were used to generate monthly VCI and subsequently mean VCI for the growing season during the period from 2000 to 2020. VCI provides the information on the current status of vegetation compared with the historical maximum and minimum, the following equation was used to derive VCI

$$VCI = \frac{NDVIi - NDVImin}{NDVImax - NDVImin} \times 100$$

where NDVIi represents the mean Vegetation Index values in a certain year, NDVImin and NDVImax are the multiple-year minimum and maximum NDVI values calculated for each pixel from 2000 to 2020. VCI provides the deviation of each pixel from the historical NDVI values. VCI value is being measured in percentage ranging from 1 to 100. VCI value below 35% indicates severe drought condition, 35 to 50%shows the drought condition, and 50 to 100% indicates above normal condition of vegetation (Kogan 1995).

2.3.3. Computation of SPI

The calculation of this index is based on long-term precipitation data. The SPI can be calculated in the monthly, 3-month, 6-month, 9-month and 12-month interval. For this study, monthly rainfall data for the period of 31 years from 1990 to 2020, for 126 rain-gauge stations were used to compute 3-month SPI using the software developed by the National Drought Mitigation Center (UNL. 2018). The 3-month SPI was computed by using the following mathematical equation to assess the wet and dry conditions based on precipitation variables.

$$SPI = \frac{Xij - Ximean}{\sigma}$$

where, Xi is the precipitation for the ith station and jth observation, Ximean is long-term average rainfall of ith station, and σ is standard deviation.

The 3-month SPI raster was used to reflect the impacts of drought on different water-related sector makers (WMO, 2012) mean 3-month SPI raster for the period, and the same was used for further analysis with the vegetation indices derived from time-series MODIS datasets. Meteorological and soil moisture conditions (agriculture) respond to precipitation anomalies on relatively short timescales. Classification of SPI proposed by McKee et al. (1993), i.e., extremely wet (≥ 2.00), very wet (1.50 to −1.99), moderately wet (1.00 to −1.49), near normal (−0.99 to 0.99), moderately dry (−1.00 to −1.49), severely dry (−1.50 to −1.99), and extremely dry (≤− 2.00) was adopted to define the wet and dryness intensities of the study area.

2.4. Data analysis for spatio-temporal drought

In order to specifically understand the drought conditions and vegetation development, more emphasis was given to the main season (Measho et al. 2019), which was mapped in detail view and in comparison, to the average drought conditions of the last 20 years based on MODIS NDVI datasets. Moreover, time-series VCI maps of all the years were generated and interpreted to identify areas of drought vulnerability at a pixel level of analysis. SPI is used to determine meteorological drought, but it can be helpful for finding parallel drought patterns with VCI. It is one of the most commonly used indices for characterizing drought dynamics applied similar drought categories with an aggregated dataset of SPI is a recommended index for drought purposes for identifying spatio-temporal drought patterns in Thailand from 2000 to 2020.

3. RESULTS

3.1. Meteorological datasets

Precipitation data collected rainfall data from TMD. Selected 95 stations that have the amount of rainfall data for the full 30 years from 126 rainfall gauge stations. The average monthly rainfall was 20-250 mm and the highest monthly average rainfall between May to September (180-250 mm). The average of 21-year annual precipitation is more than 1,600 mm/year. and the average precipitation is in the range of 1,300-1,900 mm per year, with the highest average in 2019 at 1,995 mm. and the lowest mean value in 2017 at 1,329 mm. below the average over the last 21-years (Fig. 2). SPI from 95 rainfall data each station that has the amount of rainfall data for the full 30 years from 126 rainfall gauge stations, the average SPI 3-month. The average monthly SPI 3-month value was between -2.211 to 1.263. The average SPI-3 value with the drought severity level where was the lowest in December 2004 was -2.211 follow by April 2016 was -1.565 and December 2002 was -1.194 and the highest SPI in June 2000 was 1.126 follow by June 2017 was 1.127 and April 2000 was 1.057 where were moderate to extreme wet with the no drought severity level. (Fig. 3).

3.2. Remotely sensed datasets

The average NDVI in 2000–2020 was 0.59 from the range of 0.30 – 0.75, the highest average in October 2017 at 0.74 and the lowest average value in June 2001 at 0.39 (Fig. 4). The average VCI in 2000–2020 was 54.31% from the range of 81-86%, the highest average in October 2017 at 86.26% and the lowest average value in June 2001 at 21.75% (Fig. 5).

3.3. Correlation of meteorological datasets and Remotely sensed datasets

The correlation analysis between mean 3-month SPI and mean NDVI during 2000-2020 shows a positive correlation with a correlation coefficient (r) of 0.37 (Fig. 6). It indicates that a low rainfall pattern clearly affects the vegetation conditions. The correlation analysis between mean 3-month SPI and mean VCI during 2000-2020 showed a positive correlation with a correlation coefficient (r) of 0.31 (Fig. 7). It is evident from the analysis that SPI trends are in agreement with the VCI patterns.

4. CONCLUSION

This study intended to evaluate drought conditions in Thailand for a twenty-one-year period from 2000 to 2020 using main droughts indices to analyze the spatio-temporal drought with the indices found that the analysis showed that NDVI could be used as an indicator to assess and monitor the drought conditions in semi-arid and arid regions. The correlation analysis between the mean 3-month SPI and VCI indicates the potential of VCI in measuring the direct impact of rainfall on vegetation dynamics. Analysis showed that VCI was found to be stronger in providing a detailed description of the vegetation dynamics with the corresponding level of precipitation received.

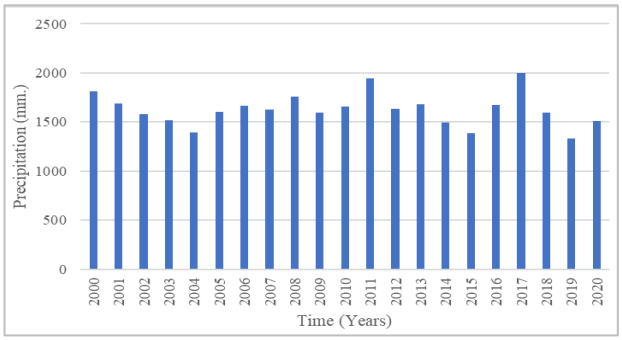

Figure 2. Annual precipitation data

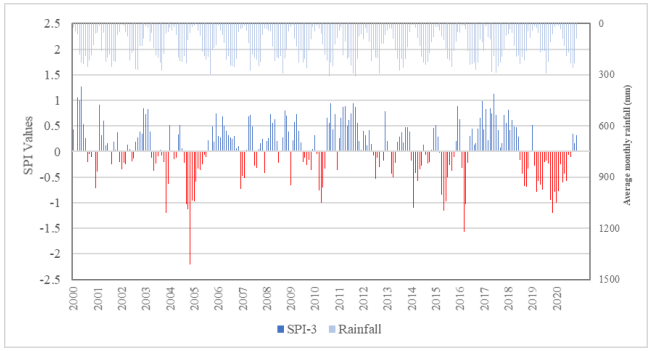

Figure 3. Average 3-month SPI

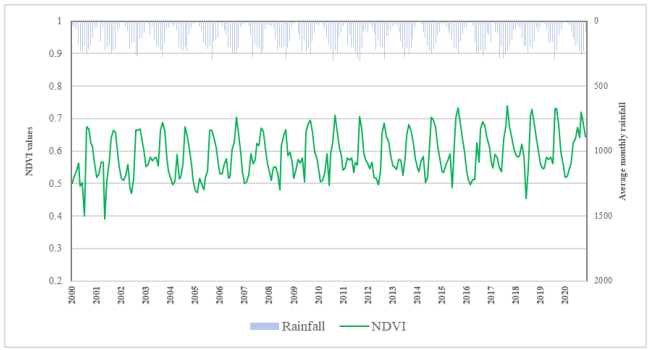

Figure 4. Average NDVI (2000 - 2020)

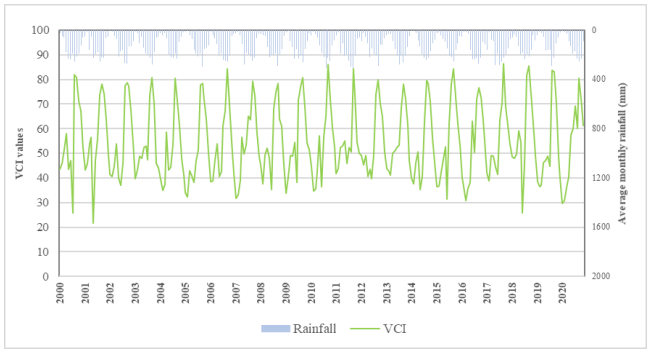

Figure 5. Average VCI (2000 - 2020)

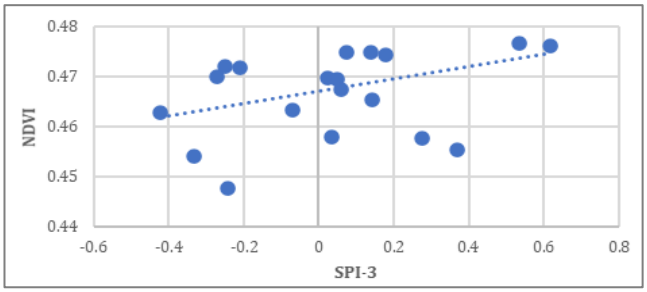

Figure 6. The correlation analysis between mean SPI-3 and mean NDVI in 2000-2020

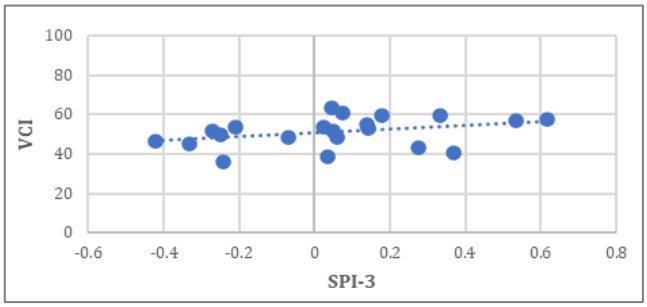

Figure 7. The correlation analysis between mean SPI-3 and mean VCI in 2000-2020

ACKNOWLEDGEMENT

This research was supported by Burapha University, Wuhan University, and Geo-Informatics and Space Technology Development Agency (GISTDA). The author is thankful to the Thai Meteorological Department (TMD) for providing rainfall data in Thailand.

REFERENCES

Gorelick N et al (2017). Google Earth Engine: Planetary-scale geospatial analysis for everyone. Remote Sensing of Environment, 202, 18–27.

Gu Y et al (2007). A five-year analysis of MODIS NDVI and NDWI for grassland drought assessment over the central Great Plains of the United States. Geophysical Research Letters, 34(6), 1–6.

Hayes M J et al (2012). Drought monitoring: Historical and current perspectives. Remote Sensing of Drought: Innovative Monitoring Approaches, 1–19.

Jiao W et al (2016). Evaluating an enhanced vegetation condition index (VCI) based on VIUPD for drought monitoring in the continental United States. Remote Sensing, 8(3).

Kogan F N (1995). Application of vegetation index and brightness temperature for drought detection. Advances in Space Research, 15(11), 91–100.

Measho S et al (2019). Spatiotemporal analysis of vegetation dynamics as a response to climate variability and drought patterns in the Semiarid Region, Eritrea. Remote Sensing, 11(6).

METEOROLOGICAL DEPARTMENT (2011). Study on Drought Index in Thailand Agro - meteorological Academic Group. 551.

Reddy et al (2020). Assessment of spatiotemporal vegetation dynamics in tropical arid ecosystem of India using MODIS time-series vegetation indices. Arabian Journal of Geosciences, 13(15).

Thiruvengadachari S. & Gopalkrishna H R (1993). An integrated pc environment for assessment of drought. International Journal of Remote Sensing, 14(17), 3201–3208.

UNL (2018). The SPI Generator application.

WMO (2012). Standardized Precipitation Index User Guide. Svoboda, M., Hayes, M. and Wood (Eds.), World Meteorological Organization Report WMO-No. 1090, Geneva, Switzerland.

Intercontinental Geoinformation Days

http://igd.mersin.edu.tr/2020/

Using terrestrial liDAR data in 3D CAD modeling applications

Lütfiye Karasaka*[1], Neslişah Ulutaş[2]

[1]*Konya Technical University, Faculty of Engineering and Natural Science ,Department of Geomatics Engineering, Konya, Turkey*
[2]*Konya Technical University, Institute of Graduate Studies, Konya, Turkey*

Keywords
LIDAR
Terrestrial Laser Scanning
Point Cloud
ArchitecturalDocumentation
3D-Modeling

ABSTRACT

Preserving historical and cultural artifacts through generations is essential for maintaining the roots and ensuring the development of any civilization.Conservation and restoration works are crucial in order to save numerous historical and cultural heritages in our country and the world and also pass on them from generation to generation. Nowadays, the increasing development in measurement technologies and the integration of photogrammetry into architectural applications have provided different perspective in architectural documentation applications. In this context, Terrestrial laser scanning method is a current method used in documentation studies today. The most important advantages of terrestrial laser scanning in this study are as follows: -the point cloud data obtained by terrestrial laser scanners provides the opportunity to reach the correct data at the desired frequency in a short time, -obtaining appropriate and practical results for the targeted study,- the possibility of using scanners in different working areas. In this context, laser scanners have become one of the popular methods in which effective and successful results are obtained in architectural documentation projects such as survey, restitution and restoration. Within the scope of this study, ''Ali Efendi Muallimhanesi'', which is one of the historical and cultural heritage of Konya province, was scanned with a terrestrial laser scanner and a architectural survey was carried out with the help of the obtained scanning data.

1. INTRODUCTION

Our country has an extremely rich and important cultural potential that contains numerous historical and cultural artifacts (Ministry of Culture and Tourism, 2021). Although today's modern buildings are designed to withstand various events, historical structures have suffered many natural or human-induced damages until today. Architectural documentation studies for the transfer of these precious historical artifacts from the past to the present have proven to be an effective and useful method for the reconstruction and preservation of the building (Kuswaha et al.2020). Nowadays, different perspectives have been obtained in architectural documentation applications thanks to the increasing developments in measurement technologies and the integration of photogrammetry into architectural applications. Terrestrial laser scanning method has become a more effective and current method compared to traditional measurement methods for architectural documentation studies. Terrestrial laser scanning technique is basically evaluated within the LIDAR (Light Detection and Ranging) system(Yakar et al. 2020). LIDAR technology is the name given to a remote sensing technology, commonly known as laser scanning technology, referred to as beam capture and distance determination (Sevgen 2018). TLS is a method based on obtaining the XYZ coordinates of many points as a result of sending laser pulses to the target object and measuring the distance between the device and the target (Costabile et al. 2021; Gumilar et al. 2020; Uzun and Spor 2019). Using 3D point cloud data obtained by laser scanning method, the following studies can be performed through CAD applications: basic measurement data, orthophoto image extraction, 2D or 3D drawings, solid surface models, 3D animations, texture covered 3D model extraction.It is seen that high resolution 3D point cloud data is used in architectural survey studies, in the production of orthopho to ready for CAD drawing (Hassan 2019; Lin et al. 2019; Bonfanti et al. 2013).

In this study, 3D CAD drawings of Ali Efendi Muallimhane, one of the historical and cultural works of Konya province, were created from high resolution 3D point cloud data and their orthophotos.

***Corresponding Author**

*(lkarasaka@ktun.edu.tr) ORCID ID 0000-0002-2804-3219
(nesliulutas@hotmail.com) ORCID ID 0000-0002-8941-3690

Cite this study

Karasaka L & Ulutaş N (2021). Using terrestrial liDAR data in 3D CAD modeling applications . 2nd Intercontinental Geoinformation Days (IGD), 218-221, Mersin, Turkey

2. METHOD

2.1. Terrestrial Laser Scanner Method

Terrestrial laser scanning technology is a method that samples or scans objects directly, precisely and automatically obtaining 3D coordinates (x, y, z) with the help of LiDAR technology. (Costabile et al. 2021;Beg 2018;Bonfanti et al. 2013). It is based on a system that scans the target object in series of points within limited angles in horizontal and vertical directions and enables it to be displayed as point clouds (Lichti and Gordon 2004). The location of a point is determined by the time it takes for the LiDAR signal to hit the target and the beam reflected from the target back to the scanner (Equation1). Scanner centered polar coordinates are obtained as a result of these operations. These polar coordinates are converted into cartesian coordinates (Figure1).

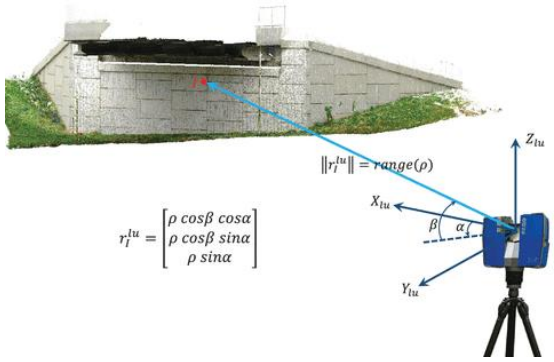

Figure 1. A typical pulsed laser telemeter, the operating principle.(Lin et al. 2019).

$$\Delta R = c\frac{\Delta t}{2} \quad (1)$$

R: the distance between point A and point B
c: the velocity of electromagnetic radiation
r: measured time interval

As a result, the point cloud formed by millions of points is obtained .These point clouds contain different resolutions, sampling densities and attributes as well as different scenes and objects(Kuswaha et al. 2020; Beg 2018).

2.2. Usability of Terrestrial Laser Scanners in Architectural Documentation Studies

High resolution 3D point cloud data is frequently used in documentation studies of historical and cultural heritage such as survey, restitution and restoration (Wojtkowska et al. 2021). In the documentation process of a building, terrestrial laser scanners are frequently preferred in architectural facade scans because they provide an accuracy of mm level. Thanks to this point cloud data representing the structure, 3D coordinate data of objects or structures that are difficult to survey can be obtained (Okuyucu and Çoban 2019; Kersten et al. 2009; Hassan 2019). Architectural documentation studies are carried out within certain standards. The survey work to be carried out with 3D point cloud data of any object or area to be recorded shows the feature of base data for restitution and restoration works to be carried out in the future. Using this data, the 3D model of the object or structure to be scanned can be recorded and stored. When compared with traditional measurement methods, it is seen that models created with point cloud data make accurate measurements at a rate of 99.9%. Thanks to this method, in which the most complex geometries of the structures are revealed exactly, the process-result relationship in architectural documentation processes works extremely quickly. (Uzun and Spor 2019).

With the transfer of the obtained point cloud data of the object or structures to the CAD program, the preparation of floor plans and section drawings and technical drawing operations can be performed. Thanks to the high quality orthophotos obtained from the point cloud data, 2D technical drawings can be made in architectural survey studies. In this way, the details of the object or the building can be shown on the 3D point cloud data, and the current state of the building can be completed in the form of architectural survey work. Restitution studies can be prepared for problematic sections by integrating with previously obtained photographs and data obtained during the survey on the works that have been destroyed or structurally damaged(Uzun and Spor 2019).

Today, there are many software (AutoCAD, Sketchup, etc.) that offer the opportunity to work on point cloud. For example, AutoCAD software provides certain improvements and enhancements when working over the point cloud.With the point cloud plugin, using clipping tools, an existing area on the cloud can be focused and drawings can be made on the cropped area with the help of points. The cropped area includes any objects left within this area, along with the crop border. In addition, since these clipped areas now show a cross-section feature, they allow object creation with using point clouds depending on the density of the cloud.Another drawing method is to correctly identify the dynamic user-defined coordinate system on the target surface to be drawn(Prota Altar 2021).

2.3. Study Area

The determined working site called ‘‘Ali Efendi Muallimhanesi’’ is located opposite to the northern entrance of Şerafettin Mosque in Karatay District of Konya Province. The ‘Muallimhane’, which was built by Hacı Ali in the early 15th century, was initially named ‘Daru'l Kurra’, and depending on the need, the school and ‘Daru'l Huffaz’sections were opened and turned into an educational institution that includes levels that complement each other. It was allocated to Konya Provincial Mufti in February 2015 by Konya Governorship for use in Quran and Islamic Related Services(Konya Metropolitan Municipality 2021).

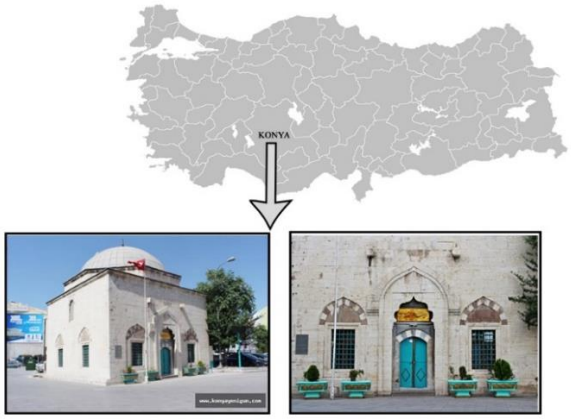

Figure 2. Study area , "Ali Efendi Muallimhanesi", Konya

3. APPLICATION

In this study, Faro Laser Scanner X-330 Hdr was used. The scanner is a suitable device for 3D documentation and land surveys (Faro 2021).

Scanning operations of the target object were carried out from the station points determined in such a way that one or more facade of the target can be seen and from the appropriate distance. The process of combining the scan data and creating the point cloud cluster for the target object has been completed in the faro scene software. From this stage on, the survey drawings of the façades of the building were made by taking 2D orthophotos obtained from the point cloud data (Figure 5). In addition,a drawing has been made illustrating the details of the building that has been made through points with the help of point cloud.

4.RESULTS

Preserving cultural heritage is a requisite duty for all civilizations around the World (Moussa et al. 2013). In order to keep the traces of civilizations alive, it is extremely necessary to pass on historical and cultural artifacts from generation to generation.

The terrestrial laser scanning method has become the reason of preference for many disciplines with its potential to obtain cost effective, high-accuracy data in a short time (Okuyucu and Çoban 2019). Laser scanners, which ensure that the architectural documentation studies are carried out in a healthy way and in the specified standards, have become preferred by users in our country and in the world.

In the last few years, 2D representation of historical and cultural heritage and 3D modeling studies have accelerated the design processes thanks to the developing CAD software. Technical drawings, analyzes and simulations can be obtained with CAD software, which includes many modules that allow 2D and 3D work. Thanks to the point cloud function that comes with the AutoCAD software used within the scope of the study, points in the point cloud can be captured and 3D visualization can be done. It is extremely important that the software enables 3D drawing through the point cloud.

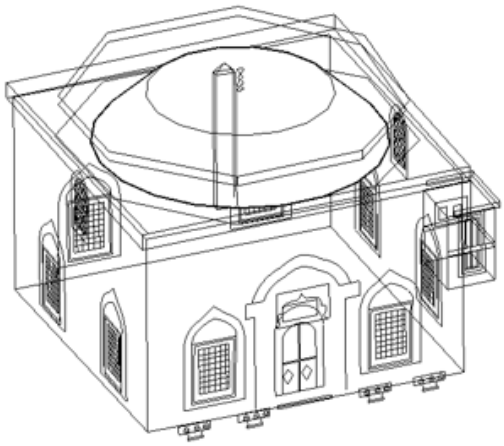

Figure 3. Drawing made by using Point Cloud

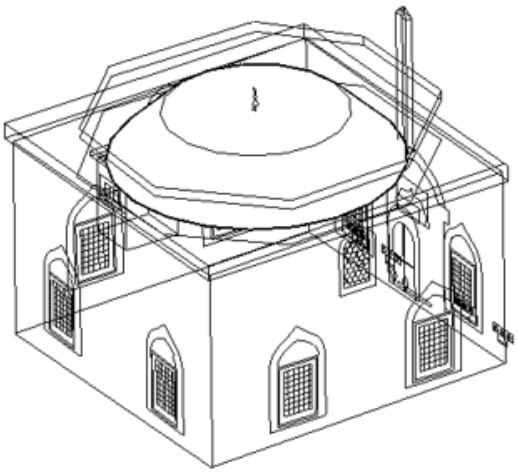

Figure 4. Drawing made by using Point Cloud

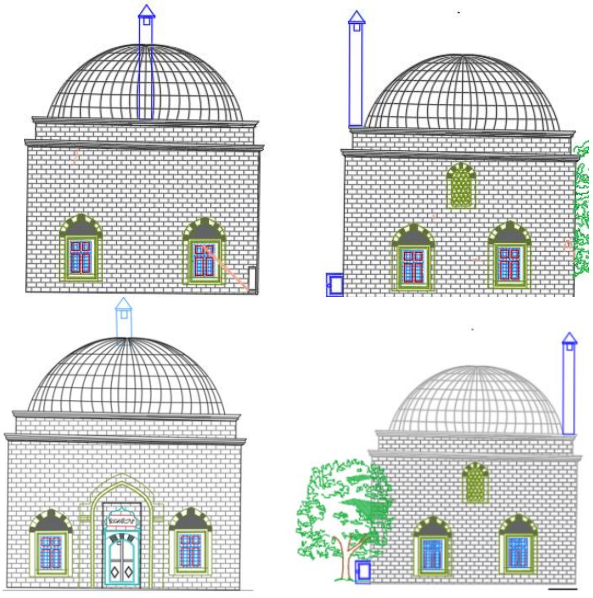

Figure 5. Architectural drawings of building facades made by using orthophoto

However, in accordance with the standards accepted in the survey studies, it is not possible to show the details of the building exactly in the drawings to be obtained by this method. This is due to the fact that points in a

frequent and complex arrangement do not allow the drawing of the details of the building. In order to make 2D drawings for use in survey studies, orthophotos are produced over the desired sections from the point cloud data. In this way, 3D data is reduced to 2D data in the most accurate way. By means of orthophotos obtained, 2D or 3D technical drawings, 3D models in the form of solid surfaces and animations can be obtained (Guidi et al.2019).

In addition, floor plans and section drawings of the whole building can be obtained easily. In this study, meaningful drawings have been created in which the details of the object can be reflected more easily as a result of the drawing made using orthophotos.

In our country, 3D modelling studies are preferred in documenting our historical and cultural heritage values. With the constantly developing CAD software facilities, the opportunity to work on 3D point cloud data will become easier and the details of complex objects will be drawn more easily. In this way, studies conducted over point clouds can provide different dimensions and new gains to heritage documentation studies.

ACKNOWLEDGEMENT

We would like to thank to Azim Metin, Geomatics Engineer for providing the scanned data of the study area.

REFERENCES

Beg A (2018). 3 Boyutlu Modellemede Yersel Lazer Tarama ve İnsansız Hava Araçları Verilerinin Entegrasyonu ve Kilistra Antik Kenti Örneği. MS Thesis, Selçuk University, Konya (in Turkish).

Bonfanti C, Chiabrando F & Rinaudo F (2013). TLS Data For 2D Representatıon and 3D Modelıng. Dıfferent Approaches Tested In The Case Of San Gıovannı In Saluzzo (Cn) Italy. ISPRS Annals of Photogrammetry, Remote Sensing and Spatial Information Sciences. II-5/W1. 37-42.10.5194/isprsannals-II-5-W1-37-2013.

Gumilar I, Hawaari T, Sidiq T P & Lukmanulhakim A (2020). As-built drawing generation of LFM building ITB using terrestrial laser scanner. IOP Conference Series: Earth and Environmental Science. 500. 012053. 10.1088/1755-1315/500/1/012053.

Hassan T A & Fritsch D (2019). Integration of Laser Scanning and Photogrammetry in 3D/4D Cultural Heritage Preservation -A Review. 10.30845/ijast.v9n4p9.

Kersten T P, Hinrichsen N, Lindstaedt M, Weber C, Schreyer K & Tschirschwitz F (2014). Architectural Historical 4D Documentation of the Old-Segeberg Town House by Photogrammetry, Terrestrial Laser Scanning and Historical Analysis Digital Heritage. Progress in Cultural Heritage: Documentation, Preservation, and Protection, Springer, Heidelberg, pp. 35-47.

Kushwaha S K P, Dayal K R, Raghavendra S, Pande H, Tiwari, S, Agrawal S & Srivastava S K (2020). 3D Digital Documentation of a Cultural Heritage Site Using Terrestrial Laser Scanner—A Case Study. In Applications of Geomatics in Civil Engineering (pp. 49-58). Springer, Singapore.

Lichti D D &Gordon S J (2004). Error Propagation in Directly Georeferenced Terrestrial Laser Scanner Point Clouds for Cultural Heritage Recording, Proceedings of FIG Working Week, s.on CD, Athens, Greece, 22-27.

Lin Y J, Ayman H, Bullock D & Prezzi M (2019). Application of High-Resolution Terrestrial Laser Scanning to Monitor the Performance of Mechanically Stabilized Earth Walls with Precast Concrete Panels. Journal of Performance of Constructed Facilities. 33. 04019054. 10.1061.

Okuyucu Ş & Çoban G (2019). Afyonkarahisar Dinar Bademli Köyü Cami Röleve Projesinin Lazer Tarama Yöntemiyle Hazırlanması. The Turkish Online Journal of Design Art and Communication, 9(2),249-262.

Sevgen S (2018). Lidar Verilerinden Bina Çatı Düzlemi Otomatik Çıkarım Modeli Geliştirme.PhD Thesis, Karadeniz Technical University, Trabzon (in Turkish).

Uzun T & Spor Y (2020). Yersel Lazer (Nokta Bulut) Tarama Yöntemi ile Rölöve– Restitüsyon-Restorasyon Projesi Hazırlama Süreci ve Bir Örnek Elazığ Harput. 15.

Wojtkowska M, Kedzierski M & Delis P (2021). Validation of terrestrial laser scanning and artificial intelligence for measuring deformations of cultural heritage structures. Measurement, 167, 108291.

Yakar M, Kuşak L & Ünel F B (2020). Ölçme Bilgisi II. Atlas Akademi.

Konya Metropolitan Municipality, 2021.
https://www.konya.bel.tr/, Accesed Date: 01.03.2021

Culture and Tourism Ministry Official Website , 2021.
https://www.ktb.gov.tr/: Accesed Date:03.02.202

Prota Altar 2020.http://www.protabilgisayar.com.tr/, Accesed Date: 13.12.2020

Intercontinental Geoinformation Days

http://igd.mersin.edu.tr/2020/

Road extraction through satellite imagery processing and visual interpretation

Aikaterini Karagianni[*1]

[1]*Aristotle University of Thessaloniki, Faculty of Engineering, School of Civil Engineering, Lab. of Photogrammetry–Remote Sensing, Thessaloniki, Greece*

Keywords
Remote sensing
Road extraction
Urban planning
Digital processing
Visual interpretation

ABSTRACT

Road extraction plays an important role in urban planning and city extension issues, as well as in road monitoring, traffic management and map updating. Technological advances may offer a wealth of data and techniques that could be implemented in road delineation and extraction projects. Among the various methods that have been developed for this purpose, remote sensing techniques and especially digital processing of satellite data could contribute significantly in this direction. This paper presents the study of a road network which concerns the city of Kastoria and its surroundings located in northwestern Greece. The study is of particular interest due to the city's physiognomy depicted in its structure and the special character of the road network in the city center. Landsat 8 imagery was used in order to detect and delineate the linear features through spatial enhancement, while semi-automatic techniques were applied to SPOTmaps products to extract the road network. The resulted data present the efficiency of using satellite imagery for road network delineation and combined with other data could be used in further studies concerning road maintenance and extension, change detection issues, as well as for cultural and touristic purposes.

1. INTRODUCTION

Among the various elements that play an important role in urban and peri-urban development is the extraction of information related to the corresponding road network. Technological advances may offer a variety of data and techniques that could be used for road delineation and extraction. Remote sensing could contribute significantly in this direction (Cleynenbreugel 1990; Wang et al. 2016).

Digital processing of optical satellite images and visual interpretation could offer valuable information regarding the road network of an area, its structure, possible changes over time, as well as the road connections it offers (Karagianni 2019).

Several approaches have been implemented in order to delineate road structures on satellite imagery which are closely correlated with the regional characteristics of the study area as well as the relevant technological development (Alshehhi et al. 2017; Hong et al. 2019). While some methods require extended time to be performed, others require extensive knowledge in terms of computational or programming literacy. Therefore, fast and effective techniques are valuable, especially in preliminary studies.

This paper presents the study of a road network which concerns the city of Kastoria and its surroundings located in northwestern Greece. The long history of the city and its wider area, as well as the special structure of the road network in the historic districts of the city center make this study of particular interest (Lazaridou and Karagianni 2014).

Landsat 8 imagery and SPOTmaps products were used in order to detect and delineate the linear features, while semi-automatic techniques were applied to extract the road network. The efficiency of using satellite imagery for road network delineation is presented in the results, which could be combined with other data in order to be used in further studies concerning road maintenance and extensions, change detection issues, as well as for cultural and touristic purposes.

2. STUDY AREA AND SATELLITE DATA

2.1. Study Area

Study area is located in medium-high altitude (630m) in the north western part of Greece, region of Western Macedonia and it concerns Kastoria city and its

* **Corresponding Author**

*(aikateck@civil.auth.gr) ORCID ID 0000-0003-3423-5265

Cite this study

Karagianni A (2021). Road extraction through satellite imagery processing and visual interpretation. 2nd Intercontinental Geoinformation Days (IGD), 222-225, Mersin, Turkey

surroundings (Fig. 1). The city is located on a peninsula at the western shore of Lake Orestiada and it has a long cultural history, which is depicted in its structure (old city, newer city and urban extension). The lake which surrounds the city is included in the Natura 2000 network offering unique habitats for many endangered fauna and avifauna species (Ponce de León 2015).

The city has a high architectural and urban value. Rich elements of Byzantine culture (Byzantine Justinian walls and medieval churches) as well as traditional mansions of the 17th and 18th centuries, unique for their architectural design are located in the city center (Doltso & Apozari traditional districts) (Moutsopoulos 1989).

Figure 1. The location of the Regional Unit of Kastoria in Greece (left image) and the city of Kastoria in the red circle (right image) (Karagianni 2019)

2.2. Satellite Data

The data employed for this study concern Landsat 8 satellite imagery and SPOTmaps products covering the study area.

Landsat 8 satellite was launched on February 11, 2013 and carries two instruments: The Operational Land Imager (OLI) sensor and the Thermal Infrared Sensor (TIRS). These sensors both provide improved signal-to-noise (SNR) radiometric performance, quantized over a 12-bit dynamic range (4096 potential grey levels in an image compared with only 256 grey levels in previous 8-bit instruments). Improved signal to noise performance enables better characterization of land cover state and condition (USGS 2012). Satellite data acquired from Landsat 8 consist of eleven spectral bands with a spatial resolution of 30 meters for Bands 1 to 7 and 9. The resolution for Band 8 (panchromatic) is 15 m and for Bands 10, 11(thermal bands) is 100 m. Among the eleven spectral bands, Landsat 8 includes one band that measures the near infrared (Band 5-NIR) and two bands that cover different slices of the shortwave infrared (Bands 6 and 7-SWIR).

The image data that have been used in this study were downloaded free of charge from U.S. Geological Survey (USGS-Earth Explorer). They were acquired on 14-03-2014 (path: 185, row: 32) with level processing 1T-Standard Terrain Correction (systematic radiometric and geometric accuracy) and projection information: UTM, zone 34, spheroid & datum WGS 84. The image has excellent quality (image quality: 9).

The SPOT satellite observation system was designed in 1977 by CNES (Center National D'Etudes Spatiales) in France with the participation of Sweden and Belgium. It was the first European Earth-observation satellite programme. The system consists of a series of satellites and terrestrial installations for the control and programming of satellites, as well as the production and distribution of images. SPOT satellites are equipped with two independent imaging instruments (series of detectors operating with pushbroom scanning technique). They collect multispectral and panchromatic imagery, offering high geometric accuracy. Each image covers a square of 60 km or 120 km on a side with a ground resolution of 10 m for SPOT 1 to SPOT 4 and 2.5 m for SPOT 5.

The SPOTmaps data that have been used in this study were provided by the Technical Services Division of Kastoria Prefecture and they were acquired on 20-12-2012. SPOTmaps products derive from SPOT 5 color satellite images and include orthorectified coverage at a resolution of 2.5 m (Airbus Defence and Space 2013). They consist of three spectral bands and projection information: WGS84/UTM zone 34N. These color products are obtained after merging two separate images, a panchromatic image with 2.5 m resolution and a multispectral image (three spectral bands) with 10 m resolution.

3. DIGITAL PROCESSING METHODS

Delineation and extraction of the road network were done by implementing digital processing through non-automatic and semi-automatic techniques. Visual interpretation performed before and after the processing also contributed to the study.

Enhancement techniques are often used in feature extraction, locating areas or objects on the ground and gaining useful details. Image enhancement refers to the creation of new images from the original data, in order to increase the information that can be visually interpreted from the data (Lillesand and Liefer 1987). Spatial enhancement modifies the pixel values based on neighboring pixel values. It is largely related to spatial frequency within an image, which is the difference between the higher and lower value of a continuous group of pixels. Among the various techniques available, edge and line detection is a significant enhancement technique in digital image processing, especially in the study of urban features or in linear features mapping, such as road networks (Karagianni 2019).

In the first stage of the study, spatial enhancement techniques were applied to Landsat 8 imagery (after subsetting the data according to the area of interest) in order to improve the appearance of the image and facilitate the extraction of useful information regarding the linear features which are highlighted. Spatial enhancement operations improve the interpretability of features within the data by modifying neighborhood pixel values based on the value of a targeted pixel. Convolution filtering uses a matrix to average small sets of pixels across the image in order to change the spatial frequency characteristics (ERDAS Field Guide 2013).

The original Landsat 8 image subset, as well as the resulted image subset after the implementation of a 3x3 convolution filter, are presented in Fig. 2 and Fig.3 respectively. Edge detection processing highlighted linear features (including the road network) and urban features.

Subsequently, road extraction could be performed manually using the enhanced image as a base in order to create a vector layer which would contain the road network.

Figure 2. The original multispectral image covering the study area (color composite RGB: 4-3-2) (Karagianni 2019)

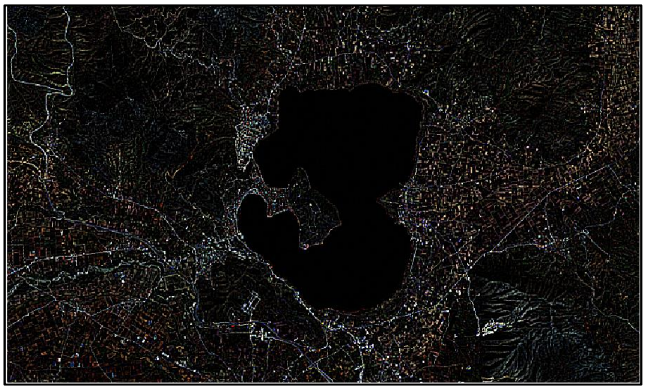

Figure 3. The final image after convolution filtering for edge detection (Karagianni 2019)

For the digitization of various features as well as related changes (changes in road networks, changes in infrastructure networks, urban development issues, etc.) classic, manual digitization techniques are frequently used, which can often be time-consuming and tedious.

Extraction of information from satellite images in vector format (digitization of linear elements and boundaries, such as road network, lake outline, etc.), could be accomplished through semi-automatic digitization techniques, in addition to the manual detection/design process through visual interpretation only. In this way, the process is simplified while the required time is reduced.

Most image processing software offer add-on modules that could facilitate the extraction of linear features through assisted digitization reducing the required amount of non-automated workload when collecting different types of features.

In this study, a module offered by Erdas Imagine software was used in order to digitize the road network of the study area. This interactive tool is guided by the operator who recognizes features from the screen image (IMAGINE Easytrace™ User's Guide 2010). The process was performed in SPOTmaps image as it offers higher spatial resolution and consequently higher accuracy in the results.

The definite and nearly constant width, as well as the similar texture (pattern) along the extension of the road network were exploited in order to draw ribbon features by centerlines, setting the appropriate parameters.

Boundary features such as road edges were detected through the discontinuity of intensity or color which indicated different areas, as well as due to the consistent texture (whiter or blacker than the background). Vertices were automatically inserted between the neighboring manually measured vertices based on the underlying raster imagery, in comparison to the classical digitizing method in which manually measured vertices are only used. The results were saved in a vector file. In Fig. 4 the digitized road network is presented in yellow color, while in Fig. 5 the area of the city extension is shown (subset of the newer part of the city) which presents a more organized structuring.

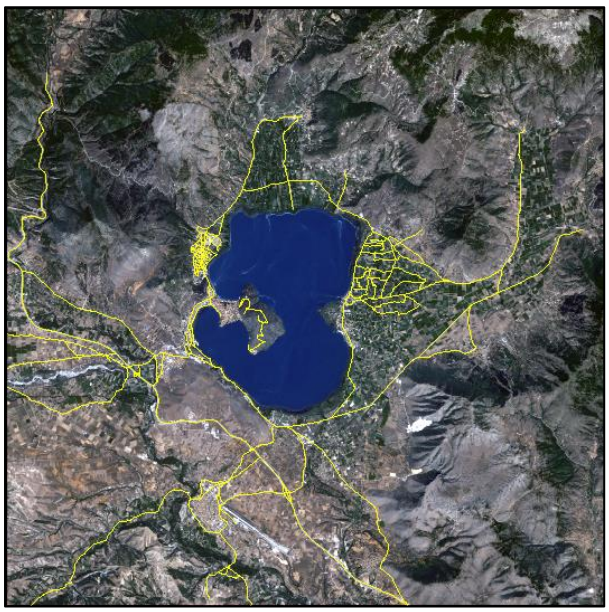

Figure 4. Road network of the city of Kastoria and the wider area (yellow line) on the SPOTmaps satellite product (Karagianni 2019)

Figure 5. Road network of the city extension (yellow line) on the SPOTmaps satellite product subset (Karagianni 2019)

4. DISCUSSION-CONCLUSION

Several methods could be applied to satellite images in order to delineate and extract road networks for urban planning and road monitoring. In the selection of the most appropriate method several parameters should be taken into account, such as the type of the project, the study area, the available time and the required workload, as well as the final cost and the specialization of the personnel. Therefore, the need to search for easy, fast and efficient tools is imperative.

Spatial filters could be used to sharpen or emphasize the edges in the image, offering effective results especially in preliminary studies which do not require special details but must be carried out in a short time. In this study, convolution filtering for edge detection was applied in order to delineate the linear features. The resulting image after spatial enhancement presents an improved appearance and is suitable for the delineation of linear features. The road network is effectively highlighted facilitating the subsequent manual extraction process.

Semi-automatic digitization offers satisfactory results in the urban areas of the imagery, where the urban fabric presents organized structuring (as shown in Fig. 5). Satisfactory results are also obtained in areas where there is a strong differentiation between the road network and the environment (road network in cultivated areas, in the mountainous area of the peninsula or in bare ground areas).

In intricately structured areas presenting a more anarchic structuring (road network of narrow width and shading interference), the semi-automatic method appears to have weaknesses in digitization as there are difficulties in finding the edges (center of urban fabric on the peninsula). Similar problems also arise when attempting to digitize sections of the road network with variable width or large differences in texture.

Especially in multispectral images, features that are normally sharp enough to be clearly visible on the screen may not be properly detected, as the module processes image intensity information only (large color differences may not correspond to large intensity differences). This issue could be solved if one of the color bands is used for digitization or if the image is digitally enhanced before digitization. Additional corrections to digitization can also be made manually, combining the semi-automatic with the manual process.

Through semi-automatic digitization, the process is facilitated and the amount of non-automated workload required when collecting different types of features could be reduced, providing products which could be efficiently combined with other types of data for road maintenance and extension, change detection issues, as well as for cultural and touristic purposes.

ACKNOWLEDGEMENT

The author wishes to thank the former Technical Services Division of Kastoria Prefecture (now Directorate of Technical Works, Regional Unit of Kastoria) for providing the SPOTmaps products.

REFERENCES

Airbus Defence and Space (2013). SPOTMaps products.

Alshehhi R, Marpu P R, Woon W L & Mura M D (2017). Simultaneous extraction of roads and buildings in remote sensing imagery with convolutional neural networks. ISPRS Journal of Photogrammetry and Remote Sensing, 130, 139-149. https://doi.org/10.1016/j.isprsjprs.2017.05.002

Cleynenbreugel J van, Fierens F, Suetens P, Oosterlinck A (1990) Delineating road structures on satellite imagery by a GIS-guided technique. Photogrammetric Engineering and Remote Sensing, 56, 893-898.

ERDAS Field Guide™ (2013) U.S.A: Intergraph Corporation, Erdas Inc.

IMAGINE Easytrace™ User's Guide (2010) ERDAS Inc.

Hong M, Guo J, Dai Y, & Yin Z (2019). A novel FMH model for road extraction from high-resolution remote sensing images in urban areas. Procedia Computer Science, 147, 49-55, ISSN 1877-0509. https://doi.org/10.1016/j.procs.2019.01.183

Karagianni A (2019). Research on the potentials of remote sensing techniques and interpretation of optical satellite data in civil engineering issues. Doctoral Thesis, Aristotle University of Thessaloniki (in Greek) 83-85, 94-97.

Lazaridou M & Karagianni A (2014). Visual satellite imagery interpretation for the city of Kastoria. 1st International Geomatics Applications Conference (GEOMAPPLICA), 279-285, Skiathos, Greece.

Lillesand T M and Kiefer R W (1987) Remote Sensing and Image Interpretation. 2nd ed. New York: John Wiley and Sons, Inc.

Moutsopoulos N (1989). Kastoria: Greek Traditional Architecture, Melissa Publishing House, Athens.

Ponce de León P (2015). Institutional framework and protection of traditional settlements-the case of Kastoria. Protection of Traditional Settlements and Contemporary Architectural Design. Conference on Society for the Environment and Cultural Heritage, 1-13, Kastoria, Greece.

USGS (2012). A Global Land-Imaging Mission. U.S. Geological Survey Fact Sheet, 1-4.

Wang W, Yang N, Zhang Y, Wang F, Cao T & Eklund P (2016). A review of road extraction from remote sensing images. Journal of Traffic and Transportation Engineering (English Edition), 3(3), 271–282. https://doi.org/10.1016/j.jtte.2016.05.005

Intercontinental Geoinformation Days

igd.mersin.edu.tr

Construction of 3D modeling based on vertical and oblique unmanned aerial vehicle imagery for efficient national park management

Changhui Lee[1], Taeheon Kim [2], Jueon Park [3], Youkyung Han[4]

[1]*Kyungpook National University, School of Convergence and Fusion System Engineering, Sangju 37224, Korea*
[2]*Kyungpook National University, Department of Convergence and Fusion System Engineering, Sangju 37224, Korea*
[3]*Kyungpook National University, Department of Geospatial Information, Daegu 41566, Korea*
[4]*Seoul National University of Science and Technology, Department of Civil Engineering, Seoul 01811, Korea*

Keywords
Remote sensing
UAV
3D modeling
National park management

ABSTRACT

In order to efficiently manage large forest areas, a large number of people and budgets are required. Additionally, areas where access is difficult cannot be managed. The management of forest areas using a unmanned aerial vehicle (UAV) has the effect of solving existing limitations. In this study, 3D modeling was carried out on October 22, 2020, using images acquired by UAV for Yongha Campsite located in Wolaksan National park, Chungcheongbukdo province, South Korea. Considering the lack of matching points in image matching due to the nature of forest areas, the ratio of image overlap was set high during UAV flight plan establishment, and vertical and oblique images were acquired by UAV. Afterwards, we validated the usability of the data based on a 3D model.

1. INTRODUCTION

As rapid urbanization progresses from the end of the 20th century, the proportion of green land, which used to be a large part of the country, has reduced to a great extent (Park and Choi 2016). Since the introduction of the Nation Park System in 1967 in Korea, 22 national parks have been designated and managed to preserve the environment, culture, history and heritage. The total area of the national park is 6,726 km, which covers 6.6% of the total area of the South Korea (Kim, 2008). Although the Korean government manages national parks by assigning managers, however, it is difficult to efficiently manage the larger through on-site surveying. This causes serious problems every year, such as economic losses caused by theft of expensive forestry products and damages to the natural environment caused by illegal campers dumping garbage. In addition, the importance of managing and preserving national parks has been emphasized due to the recent increase in the number of campers who enjoy camping.

Currently, various techniques for management of national parks replace the field. Among them, unmanned aerial vehicles(UAV), one of the critical technologies of the fourth industrial revolution are being presented as an advanced method for managing national parks. UAV can quickly acquire high quality data about area of interest. In addition, it is possible to produce orthophoto and digital surface models using images acquired by UAV. Especially, a three-dimensional (3D) model can be built based on images acquired by UAV to be able to manage the national parks by expressing them in realistic.

In this study, we aim to verify usability by constructing a 3D map to efficiently manage the national parks using UAV. To this end, images were acquired by setting the altitude and the ratio of overlap high in consideration of difficulty in extracting matching points of the forest area that have similar features. In addition, vertical and oblique images were obtained by adjusting the camera angle, and the utilization of the 3D models in the forest area was verified after constructing 3D models based on the acquired images.

2. SELECTION OF RESEARCH AREA AND ESTABLISHMENT OF FLIGHT PLAN

The Yongha Campsite in Wolaksan national park located in Chungcheongbukdo province, South Korea was selected as a research area for the construction of 3D models and verification of utilization of forest areas using UAV (Fig. 1).

* **Corresponding Author**

*(lch970914@gmail.com) ORCID ID 0000 – 0001 – 5665 - 4001
(rlaxogjs77@gmail.com) ORCID ID 0000 – 0003 – 1743 – 5134
(wndjs0614@gmail.com) ORCID ID 0000 – 0002 – 8797 – 1437
(han602@seoultech.ac.kr) ORCID ID 0000 – 0001 – 6586 – 8503

Cite this study

Lee C H, Kim T H, Park J E & Han Y K (2021). Construction of 3D modeling based on unmanned aerial vehicle imagery for efficient national park management. 2nd Intercontinental Geoinformation Days (IGD), 226-229, Mersin, Turkey

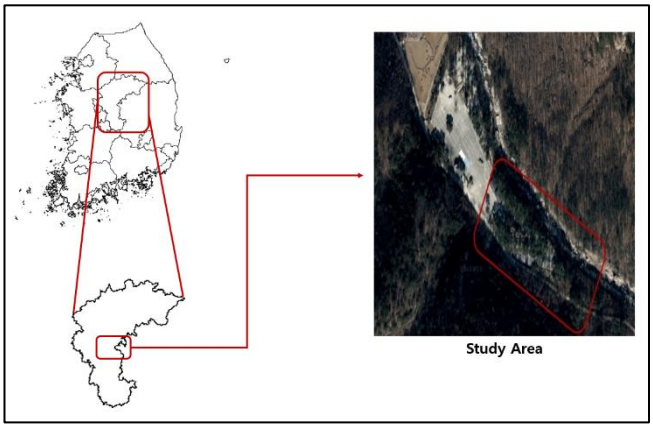

Figure 1. Study Area

The UAV used in this study is Inspire 2 model manufactured by DJI, and the Zenmuse X4S. The-optical sensor was mounted on the UAV platform and the data was acquired around 1 p.m. on October 22, 2020. The detailed specifications are given in Table 1.

Table 1. Specification of UAV and camera used in study

Inspire 2		Zenmuse X4S	
			
Weight	3,440g	Weight	253g
Flight altitude	≤ 2,500m	Resolution	5472 × 3648
Flight time	27min	Sensor	Optical
Speed	≤ 94km/h	Focal Length	8.8mm

For image acquisition, UAV as automatically flown using the Pix4d Capture application, and longitudinal (plan 1) and lateral (plan 2) flight routes were set for each angle to obtain images of the same area. Fig. 2 illustrates the flight route at the time of image acquisition.

Figure 2. Flight route of UAV

3. METHOD

3.1. Data Acquisition

The UAV image were acquired around 1 p.m. at the time of flight, with an altitude of 70 meters and a forward and side overlap of 80%. Both vertical and oblique images were acquired under the same flight conditions. Generally, the side overlap is set around 70~90%, the forward overlap is set as 60%. However, the study area was located in the forest area within the national park, therefore, many feature points of images cannot be matched during the image matching process, which can lead to a problem of reduced accuracy for 3D model. For this reason, to extract more matching points from the images, the flight was carried out by increasing the ratio of image overlap and altitude of UAV. Moreover, oblique images were acquired based on a flight plan 1, and 2 with an angle of 45°. Vertical images were acquired only with a flight plan 1. Fig. 3 shows parts of oblique and vertical images acquired by UAV.

Vertical image **Oblique image**

Figure 3. Vertical images and oblique images acquired by UAV

3.2. Construction of 3D Model

In this study, for constructing 3D models, photoscan software from Agisoft was used. Image processing is performed in the UAV image matching software using Scale-Invariant Feature Transform (SIFT) algorithm. The SIFT method finds features such as building corners or road intersections in the image, and utilizes this information to estimate the position of the image relative to the sturcture from motion (SfM) algorithm to determine the 3D position. The SfM algorithm is a technique that enables the sequential adjustment of the matched images through the SIFT algorithm to restore the target and the photographed location relationship at the same time (Aicardi et al., 2016). After conducting the image matching, a 3D model was constructed using the build tiled model function in photoscan software. This function can visualize 3D models at high resolutions, and build 3D models based on dense clouds or mesh data.

4. RESULTS

To find models applicable for the efficient national park management, we compared the number of point clouds and dense clouds. In addition, we carried out an analysis comparing visual differences between models. The extracted numbers of point and dense clouds per model are provided in Table 2.

Table 2. Number of point and dense clouds per model

Case	3D model components	Number of point clouds	Number of dense clouds.
A	Longitudinal 90 ° & Lateral 45° & Longitudinal 45°	218,652	159,973,964
B	Longitudinal 90° & Lateral 45°	209,943	139,631,410
C	Longitudinal & Lateral 45°	188,924	154,428,719
D	Lateral 45°	139,236	106,211,703
E	Longitudinal 90°	74,269	28,240,041
F	Longitudinal 45°	40,568	82,155,116

Table 2. shows that the more images acquired by 45°, and 90° angles with flight plan 1, and 2 are used together, the more point clouds and dense clouds can be extracted.

Table 3. Image of 3D model per m odel components.

	Point cloud of 3D model	Dense cloud of 3D model
A		
B		
F		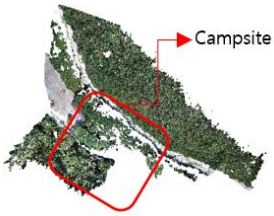

Among the results of generated 3D model, Case F failed to construct a 3D model in the densely wooded campsite area, because of the least point clouds and dense clouds (Table 3). Conversely, Case A has the numerous point and dense clouds, resulting in the effective construction of a 3D model.

In a 3D model using only vertical images (Fig. 4), the information of side texture was mostly distorted or missed. On the other hand, in the case of using vertical and oblique images, the side texture of the campsite was successfully generated, as shown in Fig. 5.

Through previous results, we can confirm that the 3D model based on vertical and oblique images is successfully generated. However, there was a problem of data loss at the edge of the 3D model, as shown in Fig. 6. It is judged to be a problem caused by not maintaining the degree of overlap on the edge when acquiring UAV images. Neverthless, the 3D model based on vertical and oblique images can express the detailed terrain as well as trees, which are clearly identified as shown in Fig. 7.

Figure 4. Missing data when using vertical images only

Figure 5. 3D model when constructed using both vertical and oblique images

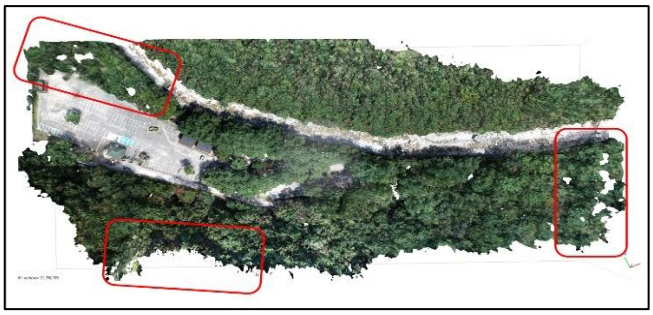

Figure 6. Modeling failure due to lack of image overlap

Figure 7. Forest area magnification image of Case A

5. CONCLUSION

In this study, we constructed a 3D model by mixing vertical and oblique images of campgrounds located within national parks taken using UAV. To evaluate the constructed 3D model, we compared with 3D models constructed with only vertical or oblique images. As a result, we could confirm that using both the vertical and oblique images together to generate the 3D model

showed better in representing the detailed terrain including each tree object.

From the constructed forest 3D model, we were able to provide visual data for the safety, efficient conservation, and management of the natural environment of the national park users. It can have the following advantages for applications point of view.

First, a 3D map can be used for efficient conservation and management of forest areas. It can save a lot of budget by reducing manpower in the national park management.

Second, it is meaningful that 3D maps of forest areas can be produced quickly without additional equipment other than UAV. If a quick 3D map is produced for the area in the event of a disaster, it will be a great help in disaster monitoring work.

Further research will be conducted to improve the performance of 3D map side textures by adjusting flight conditions and setting camera angles with diverse. Moreover, we have a plan to build a higher density forest 3D model using GCP data together to be used simultaneously with other geographic information system data.

ACKNOWLEDGEMENT

This study was carried out with the support of ´R&D Program for Forest Science Technology (Project No. 2021328B10-2122-AA03) provided by Korea Forest Service (Korea Forestry Promotion Institute).

REFERENCES

Aicardi I, Chiabrando F, Grasso N, Lingua A M, Noardo F & Spano A (2016). UAV photogrammetry with oblique images: First analysis on data acqusition and processing. International Archives of the Photogrammetry, Remote Sensing & Spatial Information Sciences, 41.

Kim T I (2008). Comparison of economic value between Mountain and Marine National Park - Focused on Mt. Juwang and Dadohae Marine National Park. Journal of the Korean Institute of Forest Recreation, 12(4), 9–18.

Park S, Chol G Y (2016). Urban sprawl in the Seoul Metropolitan Region, Korea since the 1980s observed in satellite imagery. Association of Korean Geographers, 5(3), 331-343.

Intercontinental Geoinformation Days

igd.mersin.edu.tr

Photogrammetric analysis of multispectral and thermal close-range images

Özgün Akçay[*1]

[1]*Canakkale Onsekiz Mart University, Faculty of Engineering, Department of Geomatics Engineering, Canakkale, Turkey*

Keywords
Photogrammetry
Remote sensing
Multispectral images
Thermal images
Close-range

ABSTRACT

Sensors capable of multispectral and thermal imaging beyond visible bands offer many analysis possibilities for environmental monitoring. Different sensor images constitute an important source of information especially in the fields of agriculture, forestry, geology and energy. Photogrammetric studies have been affected by this development in recent years and have been used in the production of multispectral and thermal models besides the RGB model. However, due to geometric and radiometric resolution differences, it is difficult to combine or evaluate models produced from different types of sensors. In this study, the three-dimensional test field images obtained with RGB, multispectral and thermal sensors were oriented and modeled photogrammetrically. The accuracies of the control points on the produced models were compared and discussed. When the results are examined, control point accuracy was obtained as almost similar as in the RGB model after the orientation based on automatic feature matching. Automatic feature detection and matching in thermal images were not robustly produced due to low geometric resolution. For this reason, manual measurements were performed in thermal images, and the photogrammetric orientation and adjustment process was done accordingly.

1. INTRODUCTION

Recently, multi-sensor modeling and analyzes have been carried out with terrestrial and UAV-based close-range photogrammetry. Although multispectral and thermal lightweight cameras are relatively low resolution compared to RGB cameras, photogrammetric products three-dimensional models and orthophotos have been considered for monitoring and inspection in many areas such as forestry, agriculture and archaeology.

The multispectral data were processed with a photogrammetric pipeline to create triband orthoimages to extract some Vegetation Indices (VI) such as the Normalized Difference Vegetation Index (NDVI), the Green Normalized Difference Vegetation Index (GNDVI), and the Soil Adjusted Vegetation Index (SAVI), examining the vegetation vigor for each crop (Candiago et al., 2015). Saura et al. (2019) also analysed a vineyard with UAV based multispectral imagery and produced the Digital Elevation Model and NDVI to collect information about the agricultural production such as moisture and biomass density. Minařík & Langhammer (2016) proposed a methodology for assessment of spatial and qualitative aspects of forest disturbance based on the multispectral sensor Tetracam camera with the UAV photogrammetry.

On the other hand, photogrammetric studies which consider both RGB and thermal images are seen. Ribeiro-Gomes et al. (2017) evaluated the use of the Wallis filter for improving the quality of the thermal photogrammetry process using structure from motion software. Despite the low resolution of the thermal imagery compared to RGB imagery, forest structural elements were extracted using both point clouds (Webster et al. 2018). Van der Sluijs et al. (2018) revealed the morphology and daily to annual dynamics of thaw-driven mass wasting phenomenon using photogrammetric terrain models and orthomosaic time series.Zefri et al. (2018) studied about the use of thermal and visual imagery taken by UAV in the inspection of photovoltaic installations. Biass et al. (2019) provided detail in characterizing the emplacement of a compound pāhoehoe lava flow using SfM photogrammetry techniques to visible and thermal data sets .

Studies in which multispectral and thermal three-dimensional photogrammetric models and their analysis

* **Corresponding Author**

*(akcay@comu.edu.tr) ORCID ID 0000-0003-0474-7518

Cite this study

Akcay Ö (2021). Photogrammetric analysis of multispectral and thermal close-range images. 2nd Intercontinental Geoinformation Days (IGD), 230-233, Mersin, Turkey

are performed together can also be found in the literature. Erenoglu et al. (2017) developed a novel methodology extracting and distinguishing material features from UAS-based multi-sensor data photogrammetry for the cultural heritages. Edelman (2018) explored the feasibility to obtain visible, infrared, hyperspectral and thermal 3D registrations of simulated crime scenes using photogrammetry for use in forensic practice. Raeva et al. (2019) carried out unmanned flights with a fixed-wing platform with two different sensors – multispectral and thermal in order to examine two main crops cultivated area. Turner et al. (2020) investigated geological discontinuities in hard rock masses using UAV-mounted thermal and multispectral cameras.

In this study, the three-dimensional test field images obtained with RGB, multispectral and thermal sensors were oriented photogrammetrically and the accuracies of the control points on the obtained models were compared. In particular, the effects of sensors on photogrammetry as a result of modeling with multispectral and thermal images were discussed.

2. METHOD

All photogrammetric experiments were carried out on the three-dimensional test field as shown in Fig. 1. There are coded targets of Photomodeler and Agisoft Metashape software on the test area in dimensions of 85 cm x 85 cm x 20 cm. As indicated in the workflow in Fig. 2, firstly, the coordinates of the control points were calculated on the test field. Then, photogrammetric models were created by taking test field images with Sony visible range, Mapir multispectral and Optris thermal cameras. The features of the cameras used in the study are shown in Table 1. Although the resolutions of RGB cameras and multispectral cameras are close to each other, it is seen that the resolution of the thermal camera is quite low compared to the others. In the results section, the accuracies produced from photogrammetric models are presented.

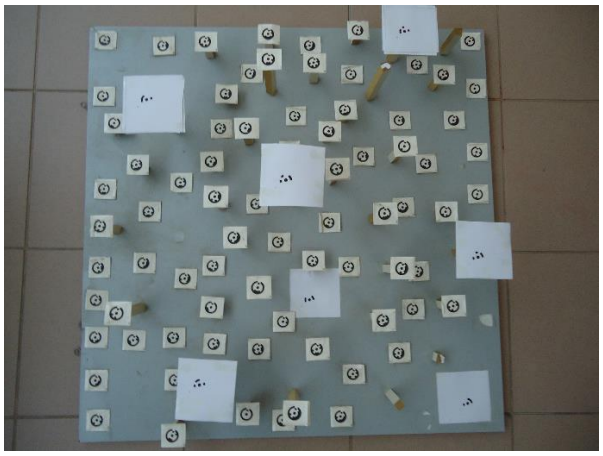

Figure 1. Three dimensional test field

Table 1. Sensor specifications

Name	Band type	Resolution (pixel)
Sony	Red Green Blue	4320 x 3240
Mapir	Orange Cyan NIR	4000x3000
Optris	Thermal	382 x 288

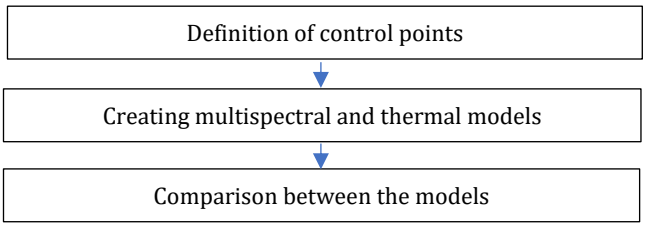

Figure 2. Workflow for photogrammetric analysis

2.1. Photogrammetric Control Points

The coordinates of the control points were also produced by the photogrammetric method. By using 10 images taken with the RGB camera, 75 coded targets were automatically measured with Photomodeler, then the orientation and bundle adjustment processes were completed. Measurements of 7 coded targets (CP1, CP2, CP4, CP6, CP8, CP10 and CP12) belonging to Agisoft software were performed by manual photogrammetric method and model coordinates were generated. After the distance between the targets P1 and P8 was determined with a precision ruler, the model coordinate system was transformed into the local coordinate system defined in the metric system. In Agisoft software, 10 image orientations were re-processed with coded targets, and X, Y, Z coordinates of control points and their errors were defined (Table 2). It is seen that the point location accuracies are about 1 mm.

Table 2. Control points in the local coordinate system

No	X (m)	Y (m)	Z (m)	Error (m)
CP1	0.3750	-0.2895	-0.8057	0.0009
CP2	0.3557	0.0122	-0.6887	0.0013
CP4	0.0197	0.1448	-0.6212	0.0013
CP6	-0.1406	-0.2054	-0.6868	0.0011
CP8	0.0570	-0.0760	-0.8068	0.0012
CP10	0.2448	0.4398	-0.7356	0.0012
CP12	-0.2293	0.3003	-0.6830	0.0013

2.2. Multispectral and Thermal Models

First, radiometric calibration of the multispectral camera images was performed. The 12 images obtained as a result of the calibration were automatically oriented and optimized by the coded targets in Agisoft software. In addition, dense point clouds were produced (Fig. 3).

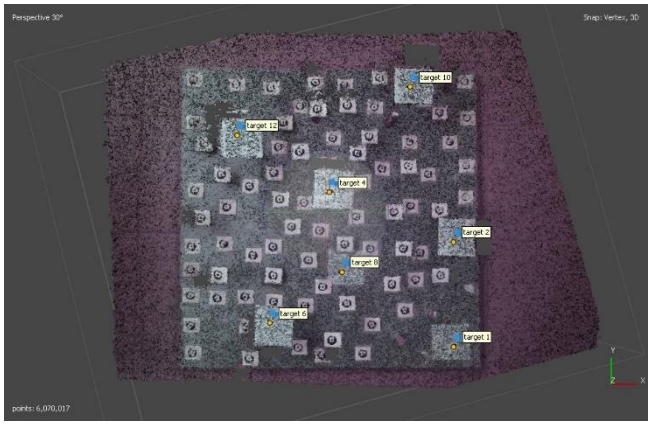

Figure 3. Multispectral dense cloud point

Since the spectral range of thermal camera images is different than RGB and multispectral sensor images, it was not possible to automatically measure the coded targets in the Agisoft software. Due to noise and radiometric distortions on the thermal images, automatic feature detection and matching was not sufficient for orientation. Fig. 4 shows the views of the same features on different thermal images. 7 coded targets and 11 other targets were manually measured on 13 thermal images. The selectivity of some targets for manual measurements has been increased by coins.

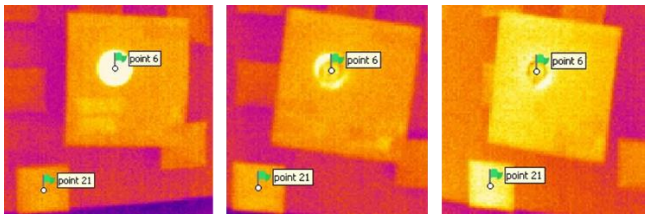

Figure 4. Same features on different thermal images

Fig. 5 explicitly depicts distortions and photogrammetric measurements points in a thermal image. By measuring a total of 18 common points on the images, orientation and optimization were implemented. Dense point clouds could not be produced due to insufficient automatic matching based on the thermal image.

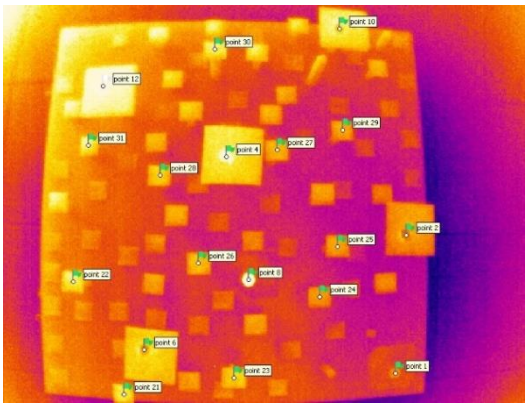

Figure 5. A thermal image and measurement points

3. RESULTS AND DISCUSSIONS

When pixel errors were examined in Table 3 and Fig. 6, it is seen that photogrammetric measurement accuracies are similar in all image types. In other words, the accuracy of manual measurements made in thermal and automatic measurements on RGB and multispectral images produced similar results. In some control points, it is also observed that manual thermal measurements are better than automatic multispectral measurements.

Table 3. Errors of control points in pixel unit

No	RGB	Multispectral	Thermal
CP1	0.231	0.343	0.523
CP2	0.276	0.476	0.29
CP4	0.215	0.293	0.278
CP6	0.252	0.558	0.29
CP8	0.192	0.144	0.334
CP10	0.174	0.299	0.337
CP12	0.289	0.598	0.386

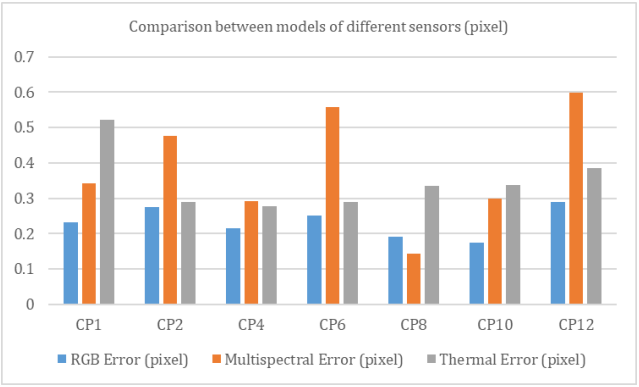

Figure 6. Comparison between in pixel unit

However, when metric accuracies are analyzed in Table 4 and Fig. 7, it is seen that RGB and multispectral results differ significantly from thermal results. Although RGB stands out in terms of accuracy, the results obtained from multispectral images are also very consistent. This is due to the fact that one pixel size of the thermal camera sensor is larger than other sensors.

Table 4. Errors of control points in millimeter unit

No	RGB	Multispectral	Thermal
CP1	0.9	1.7	2.9
CP2	1.3	1.6	3.5
CP4	1.3	1.1	3.1
CP6	1.1	0.7	4.8
CP8	1.2	1.2	1.5
CP10	1.2	1.3	1.8
CP12	1.3	1.5	1.7

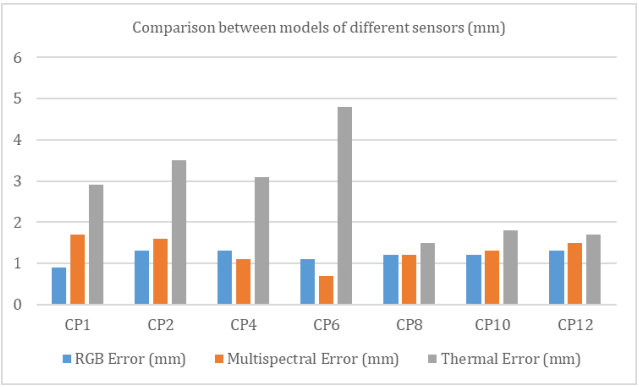

Figure 7. Comparison between errors in millimeter unit

4. CONCLUSIONS

In photogrammetry, besides three-dimensional RGB models, multispectral and thermal models are also successfully produced. In particular, radiometric corrections on multispectral and thermal images are important in terms of geometric positioning accuracy. Due to the difficulties in automatic processing of thermal images, manual point measurement is mandatory, so there is a loss of time and accuracy in model production. The low resolution of thermal images makes it difficult to combine and analyze them with RGB and multispectral models. In the future, studies should be carried out to increase the resolution of thermal models with RGB and multispectral camera images.

REFERENCES

Ribeiro-Gomes, K., Hernández-López, D., Ortega, J. F., Ballesteros, R., Poblete, T., & Moreno, M. A. (2017). Uncooled thermal camera calibration and optimization of the photogrammetry process for UAV applications in agriculture. Sensors, 17(10), 2173.

Webster, C., Westoby, M., Rutter, N., & Jonas, T. (2018). Three-dimensional thermal characterization of forest canopies using UAV photogrammetry. Remote Sensing of Environment, 209, 835-847.

Van der Sluijs, J., Kokelj, S. V., Fraser, R. H., Tunnicliffe, J., & Lacelle, D. (2018). Permafrost terrain dynamics and infrastructure impacts revealed by UAV photogrammetry and thermal imaging. Remote Sensing, 10(11), 1734.

Zefri, Y., ElKettani, A., Sebari, I., & Ait Lamallam, S. (2018). Thermal infrared and visual inspection of photovoltaic installations by UAV photogrammetry—application case: morocco. Drones, 2(4), 41.

Edelman, G. J., & Aalders, M. C. (2018). Photogrammetry using visible, infrared, hyperspectral and thermal imaging of crime scenes. Forensic science international, 292, 181-189.

Biass, S., Orr, T. R., Houghton, B. F., Patrick, M. R., James, M. R., & Turner, N. (2019). Insights into pāhoehoe lava emplacement using visible and thermal structure-from-motion photogrammetry. Journal of Geophysical Research: Solid Earth, 124(6), 5678-5695.

Candiago, S., Remondino, F., De Giglio, M., Dubbini, M., & Gattelli, M. (2015). Evaluating multispectral images and vegetation indices for precision farming applications from UAV images. Remote sensing, 7(4), 4026-4047.

Minařík, R., & Langhammer, J. (2016). USE OF A MULTISPECTRAL UAV PHOTOGRAMMETRY FOR DETECTION AND TRACKING OF FOREST DISTURBANCE DYNAMICS. International Archives of the Photogrammetry, Remote Sensing & Spatial Information Sciences, 41.

Saura, J. R., Reyes-Menendez, A., & Palos-Sanchez, P. (2019). Mapping multispectral Digital Images using a Cloud Computing software: applications from UAV images. Heliyon, 5(2), e01277.

Erenoglu, R. C., Akcay, O., & Erenoglu, O. (2017). An UAS-assisted multi-sensor approach for 3D modeling and reconstruction of cultural heritage site. Journal of cultural heritage, 26, 79-90.

Raeva, P. L., Šedina, J., & Dlesk, A. (2019). Monitoring of crop fields using multispectral and thermal imagery from UAV. European Journal of Remote Sensing, 52(sup1), 192-201.

Turner, R. M., MacLaughlin, M. M., & Iverson, S. R. (2020). Identifying and mapping potentially adverse discontinuities in underground excavations using thermal and multispectral UAV imagery. Engineering Geology, 266, 105470.

Intercontinental Geoinformation Days

igd.mersin.edu.tr

Tree detection from high-resolution unmanned aerial vehicle (UAV) images

Halil İbrahim Şenol*[1], Abdurahman Yasin Yiğit [2], Yunus Kaya [1]

[1]*Harran University, Faculty of Engineering, Department of Geomatics Engineering, Şanlıurfa, Turkey*
[2]*Mersin University, Faculty of Engineering, Department of Geomatics Engineering, Mersin, Turkey*

Keywords
Remote sensing
UAV
Photogrammetry
Extraction
Tree detection

ABSTRACT

In parallel with the advancement of technology, important developments are taking place in the field of data collection and data processing about the earth, as in many other fields. The data collection stage, which takes a long time with traditional methods, can be completed in a very short time with modern techniques. Satellite images, terrestrial data collection tools, and unmanned aerial vehicles (UAVs) are actively used in studies to determine the characteristics of the earth. UAVs are popular due to their high resolution and fast data collection capacity. Products obtained from UAVs can also be processed based on modern image processing techniques. In this way, it is possible to get meaningful and usable information from the images obtained. The development of fast and easy data collection methods brings along the big data problem. Although long times are spent processing data, success in processing images is low. For this reason, automatic processing of data obtained with modern techniques increases the quality of the result and saves time. In this study, trees were detected over the image of a wooded area obtained with a UAV. The data obtained by the UAV are separated from other objects in the field by object-based classification in eCognition software. In object-oriented classification, the data are grouped at the segmentation stage. Later, segments with similar characteristics were classified according to certain index values. As a result of the study, control data was generated in the eCognition software. Using this data, accuracy analysis was made with the help of an error matrix and the kappa statistic was found to be 78%.

1. INTRODUCTION

Nowadays, with the use of aerial photographs, satellite images, and LiDAR data, it has become quite easy to produce data on the land structure, vegetation, and other details. According to terrestrial data collection techniques, although these methods facilitate data collection and access, the process of this data and integrating it into geographic information systems has not progressed at the same time (Şasi ve Yakar, 2018).

To speed up the data processing phase, many studies have been carried out on the classification of the earth's surface (Yilmaz et al., 2014; Yilmaz et al., 2014). The studies have continued for many years on a pixel-based basis. In the pixel-based classification, the neighborhood relationships and color values of the pixels were examined, and the classes were created by grouping the pixels with similar values. However, today, due to the high resolution of both aerial photographs and satellite data, pixel-based classification methods have not been able to give sufficiently detailed results. Since the pixel-based approach examines only the spectral values of the pixels in the classification phase of these images, which contain intense information, it could not produce clear data on vegetation and details. Instead of the pixel-based approach, a new and highly accurate object-oriented approach has begun to be used. Using additional data on object structures, this approach creates meaningful objects by grouping pixels into segments.

When the studies on the determination of wooded areas were examined, it was seen that many different approaches were used. Woodland areas were classified first in the studies carried out. It was observed that the feature that separates wooded areas from green areas on the earth is the height data, and the feature that

* **Corresponding Author**

*(hsenol@harran.edu.tr) ORCID ID 0000-0003-0235-5764
(ayasinyigit@mersin.edu.tr) ORCID ID 0000-0002-9407-8022
(yunuskaya@harran.edu.tr) ORCID ID 0000-0003-2319-4998

Cite this study

Şenol H. İ., Yiğit A. Y. & Kaya Y. (2021). Tree Detection from High Resolution Unmanned Aerial Vehicle (UAV) Images. 2nd Intercontinental Geoinformation Days (IGD), 234-237, Mersin, Turkey

distinguishes wooded areas from other high objects is color data. During the detection of wooded areas, an object-based classification approach was used, and the wooded areas were detected automatically.

Gupta and Bhadauria (2014) aimed to classify agriculture, buildings, and wetlands, especially wooded areas. Multi-resolution segmentation and closest neighborhood approaches were used in the study. They mentioned that the parameters used in multiresolution segmentation play an important role in affecting the accuracy. As a result of this study, the accuracy rate regarding the classification of wooded areas is about 97%.

Jamil and Bayram (2017) mentioned in their study that tree segmentation is an active and ongoing research area in the field of photogrammetry and remote sensing. They stated that it is more difficult due to the similarities between various tree species, both within and between classes.

When the literature is examined, it has been observed that Near Infrared (NIR) band is used in addition to Red-Green-Blue (RGB) bands in image-based tree detection. In the studies, non-vegetation areas were initially removed using the traditional Normalized Difference Vegetation Index (NDVI), then average shift segmentation was applied to transform the pixels into meaningful homogeneous objects. Then the segments were assigned to the appropriate classes.

In this study, tree detection was investigated by applying object-based classification and segmentation methods using images containing high-resolution RGB bands and height data obtained from the UAV.

2. METHOD

There are many methods in the literature for detail extraction and object classification studies (Blaschke et al.2014; Ma et al.2017; Luo et al.2020). The pixel-based classification method has been used in most of the studies until recently (Moosavi et al.2014; Tehrany et al.2014; Gupta and Bhadauria 2014). Pixel-based approaches work on each pixel and extract information from remotely sensed data based on spectral information only (Gupta and Bhadauria 2014; Tehrany et al.2014; Khatami et al.2016; Louargant et al.2018). The main purpose of this method is to automatically combine each pixel in the image according to the land attributes (Guan et al.2014; Senthilkumaran and Vaithegi (2016). The problems faced by pixel-based approaches are overcome by object-based image classification. In Object-Based information, an image is interpreted not only according to a single-pixel but also according to the harmony between neighboring pixels. Object-oriented information extraction depends not only on spectrum character but also on geometry and structure knowledge (Wei et. Al. 2005; Gupta and Bhadauria 2014). Unlike pixel-based classification, the object-based classification method does not work directly on individual pixels. This method works through clusters of many pixels, meaningfully grouped by the segmentation process. It then uses these clusters instead of pixels as classification elements (Carleer and Wolff 2006). These clusters are created homogeneously; classify them by considering their characteristics such as spectral reflection, shape, size, and texture. Objects can be distinguished in a more meaningful way by considering the properties between neighboring pixels. More accurate results can be obtained by using the classification tree with rule-based processing capability (Blaschke et al. 2011). In object-based classification, besides the spectral and textural information used in pixel-based classification methods, shape characteristics and neighborhood relations are also used.

The most important and first stage in object-based classification is segmentation. Segmentation is the process of grouping pixels with similar spectral properties and creating image objects. The purpose of segmentation is to divide the image into different subsections and to create meaningful objects from the image (Baatz et al. 1999; Definiens 2012).

In this study, the multi-resolution segmentation algorithm is used as the segmentation method. In multi-resolution segmentation, image objects are divided into small pieces based on average heterogeneity for a given resolution. Later, these segments are assigned to classes by classifying with certain rule sets. The process of assigning a tag to each pixel and object in an image is called classification. In this case, by focusing on an object-based photo or image categorization, by applying the Mean-Shift segmentation method to the input image, segments are provided. The properties (spectral, textural, and spatial) of each object are created by making use of the classification results. Finally, categorization operations are created using the feature set.

The classification and detail extraction process was done in eCognition Developer software. While classifying the segments formed, the normalized surface model (nDSM) obtained from digital products and various indexes which were found to be valid as a result of literature research were used.

With the help of these indexes used, each segment is labeled as classified or unclassified. After generating the result class, the data density is reduced by combining neighboring segments assigned to the same class with the merge command.

After the end of the classification process, the tree class was exported as vectorial and generalized in geographic information systems (GIS) software. With this process, vectorial data with pixel-by-pixel fracture became more homogeneous.

To calculate the accuracy of the classification process, control data was generated in eCognition Developer software and accuracy analysis was performed with the help of an error matrix. The agreement between the accuracy analysis and the classification was calculated.

3. RESULTS and DISCUSSION

The object-oriented image analysis method provides a system that captures objects according to distinctive features such as shape, color, texture in the image. This method provides the ability to distinguish various objects in the image such as buildings, trees, roads, and vehicles. The object-oriented classification method

includes segmentation and classification stages (Bergsjö 2014). While the segmentation process allows the target classes on the image to be collected in the same segment, the second stage requires the classification of objects.

The most important step in object-based classification is segmentation. Segmentation is the process of grouping pixels with similar spectral properties and creating image objects. The purpose of segmentation is to subdivide the image and create meaningful objects from the image (Baatz et al. 2000). There are various segmentation methods in the literature. In this study, a multi-resolution segmentation algorithm is used. After the images were separated into significant segments, the properties of each segment were tested and the responses of each feature in each image band and image segment were analyzed. The analysis enabled the determination of the boundary values that best represent the class based on the feature that captures the distinction of the related class. Thus, the classification continued with the limits set in the relevant membership function, and this step was made cyclically until the best classification representing real-world conditions was obtained. The indexes used in the classification process are given in Table 1. Also, nDSM was used in the study, except for indexes. The classes created are shown in Figures 1 and 2.

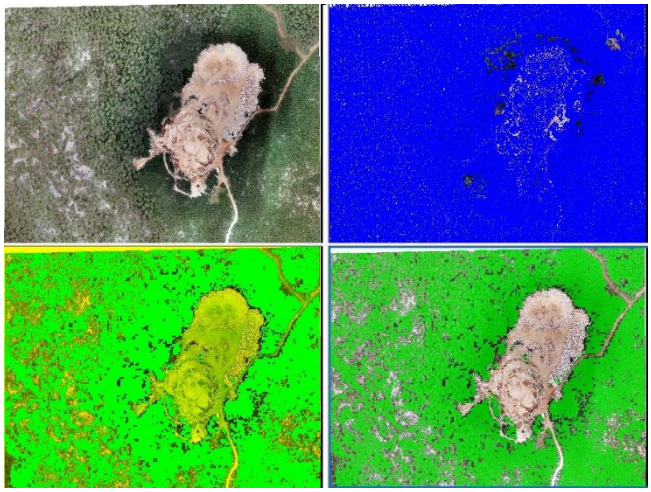

Figure 1. This is an example of figure formatting

Finally, an accuracy analysis was conducted to determine the compatibility of the classes with the real space. Accuracy analysis is the last step in measuring the accuracy and reliability of the classification.

To check the classification quality and accuracy, the Kappa coefficient, which is the most common accuracy estimation parameter, was calculated with the error matrix approach based on the TTA mask, and the pixels assigned to the tree classes at a rate of 78% were found to be compatible.

Table 1. RGB band index (R:red-G:Grenn-B:Blue)

Name	Short Name	Formula	Reference
Common Band Ratio	CBR	$(R+G+B)/3$	Çömert et al. 2017
Excess green index	EGI	$(2xG)-B-R$	Woebbecke et al. 1995
Green Leaf area index	GLI	$((2xG)-B-R)/((2xG)+B+R)$	Hunt et al. 2013
Green Ratio Index	GRI	$G/(B+G+R)$	Sonnentag et al. 2012
(The Synthetic NDVI) (Green Red Vegetation Index)	sNDVI GRVI	$(G-R)/(G+R)$	Motohka et al. 2010
Vegetation Adjusted Reflectance Index	VARI	$(G-R)/(B+G+R)$	Gitelson et al. 1996
Excess red vegetation İndex	ERVI	$(1.4\ x\ R)-G$	Mao et al. 2003

4. CONCLUSION

With the development of photogrammetric methods and computer software, it has become possible to produce high-resolution structural and spectral data on forest areas using images obtained by UAV. Products derived from this process could evaluate and measure forest structure at the tree level at a significantly lower cost than sources such as LiDAR, satellite, or aerial imagery. Detecting trees and determining their locations are among the common uses of remote sensing and photogrammetry applications. Thanks to the high resolution of the products obtained by UAV, the research field is still up to date. However, most of the studies use UAV data with not only RGB bands but also NIR bands. In this study, the performance of only visible bands (RGB), canopy height models (nDSM), multiple resolution segmentation, and rule sets in tree extraction was investigated.

When the results were examined, it was observed that segmentation using only spectral information was less accurate than the approach involving the use of an elevation model. In other words, the use of models such as nDSM has a significant effect on the accuracy of tree detection. Besides, the size of the segmented trees also influenced the optimum resolution. It was also observed that the density of deciduous or coniferous trees and forest species did not affect the accuracy of segmentation.

Finally, large trees tend to be divided into more segments, while smaller trees tend to split in small numbers. The importance of spatial resolution has been found to compartmentalize trees of different sizes. Also, this research; proved that the size of trees and bands such as NIR tape should be used in addition to RGB tapes and showed that it deserves further investigation in the future. One of the results of the study is that different band indexes influence the accuracy of tree detection.

REFERENCES

Baatz M & Schape A (2000). Multi resolution segmentation: an optimization approach for high quality multi scale image segmentation. Proceedings of Twelfth Angewandte Geographische Informations verarbeitung'in İçinde, (J. Strobl, T. Blaschke, G. Griesebner Ed.), Wichmann-Verlag, Heidelberg, ss.12−23.

Bergsjö J (2014). Object based change detection in urban area using KTH-SEG. Bachelor Thesis, Kth Royal Instıtute Of Technology, Stockholm.

Blaschke T & Geoffrey J H (2011). Qihao Weng ve Bernd Resch, Collective Sensing: Integrating Geospatial Technologies to Understand Urban Systems-An Overview, Remote Sensing, 2011, 3, 1743-1776.

Blaschke T, Hay G J, Kelly M, Lang S, Hofmann P, Addink E & Tiede D (2014). Geographic object-based image analysis–towards a new paradigm. ISPRS journal of photogrammetry and remote sensing, 87, 180-191.

Carleer A P & Wolff E (2006). Urban land cover multi-level region-based classification of VHR data by selecting relevant features. International Journal of Remote Sensing, 27(6), 1035-1051.

Çömert R, Avdan U & Şenkal E (2012). İnsansız hava araçlarının kullanım alanları ve gelecekteki beklentiler. Uzaktan Algılama ve Coğrafi Bilgi Sistemleri Sempozyumu, Zonguldak, (In Turkish).

Definiens (2012). Definiens Developer XD 2.0.4. Reference Book, Definiens AG, München, Germany, https://www.imperial.ac.uk/media/imperialcollege / medicine/facilities/film/Definiens-Developer-Reference-Book-XD-2.0.4.pdf , (03.04.2020).

Gitelson A Y, Kaufman Y J & Merzylak M (1996). Use of a green channel in remote sensing of global vegetation from eos-modis. Remote Sensing of Environment, 58, 289-298.

Guan H, Li J, Yu Y, Chapman M & Wang C (2014). Automated road information extraction from mobile laser scanning data. IEEE Transactions on Intelligent Transportation Systems, 16(1), 194-205.

Gupta N & Bhadauria H S (2014). Object Based İnformation Extraction From High Resolution Satellite İmagery Using eCognition, International Journal of Computer Science Issues (IJCSI), 11, 139.

Hunt E, Raymond Jr, Doraiswamy P C, McMurtrey J E, Daughtry C ST & Perry E (2013). A visible band index for remote sensing leaf chlorophyll content at the canopy scale. Publications from USDA-ARS / UNL Faculty, 1156.

Jamil A & Bayram B (2017). Tree Species Extraction and Land Use/Cover Classification From High-Resolution Digital Orthophoto Maps, IEEE Journal of Selected Topics in Applied Earth Observations and Remote Sensing, 11, 89-94.

Khatami R, Mountrakis G & Stehman S V (2016). A meta-analysis of remote sensing research on supervised pixel-based land-cover image classification processes: General guidelines for practitioners and future research. Remote Sensing of Environment, 177, 89-100.

Louargant M, Jones G, Faroux R, Paoli J N, Maillot T, Gée C & Villette S (2018). Unsupervised classification algorithm for early weed detection in row-crops by combining spatial and spectral information. Remote Sensing, 10(5), 761.

Luo W, Xing J, Milan A, Zhang X, Liu W & Kim T K (2020). Multiple object tracking: A literature review. Artificial Intelligence, 103448.

Ma L, Li M, Ma X, Cheng L, Du P & Liu Y (2017). A review of supervised object-based land-cover image classification. ISPRS Journal of Photogrammetry and Remote Sensing, 130, 277-293.

Mao W, Wang Y & Wang Y (2003). Real-time detection of between-row weeds using machine vision, In 2003 ASAE Annual Meeting (p. 1). American Society of Agricultural and Biological Engineers.

Moosavi V, Talebi A & Shirmohammadi B (2014). Producing a landslide inventory map using pixel-based and object-oriented approaches optimized by Taguchi method. Geomorphology, 204, 646-656.

Motohka T, Nasahara K N, Oguma H & Tsuchida S (2010). Applicability of green-red vegetation index for remote sensing of vegetation phenology. Remote Sensing, 2, 2369-2387.

Şasi A & Yakar M (2018). Photogrammetric modelling of hasbey dar'ülhuffaz (masjid) using an unmanned aerial vehicle. International Journal of Engineering and Geosciences, 3(1), 6-11.

Senthilkumaran N & Vaithegi S (2016). Image segmentation by using thresholding techniques for medical images. Computer Science & Engineering: An International Journal, 6(1), 1-13.

Sonnentag O, Hufkens K, Teshera-Sterne C, Young A M, Friedl M & Braswell B H (2012). Digital repeat photography for phenological research in forest ecosystems. Agricultural and Forest Meteorology, 152, 159–177.

Tehrany M S, Pradhan B & Jebuv M N (2014). A comparative assessment between object and pixel-based classification approaches for land use/land cover mapping using SPOT 5 imagery. Geocarto International, 29(4), 351-369.

Wei W, Chen X, & Ma A (2005, July). Object-oriented information extraction and application in high-resolution remote sensing image. In Proceedings. 2005 IEEE International Geoscience and Remote Sensing Symposium, 2005. IGARSS'05. (Vol. 6, pp. 3803-3806).

Woebbecke D M, Meyer G E, Von B K & Mortensen D A (1995). Color indices for weed identification under various soil, residue, and lighting conditions. Trans. ASAE 38, 259–269.

Yilmaz, H. M., Yakar, M., Mutluoglu, O., & Yildiz, F. (2004). Selection of the most suitable sizes of ground control points in the satellite images. In ISPRS Congress Istanbul (pp. 12-13).

Yilmaz, I., Bildirici, I. O., Yakar, M., & Yildiz, F. (2004). Color calibration of scanners using polynomial transformation. In XXth ISPRS Congress Commission V, Istanbul, Turkey (pp. 890-896).

Intercontinental Geoinformation Days

igd.mersin.edu.tr

Supervised machine learning classification in Google Earth Engine: Time series analysis in Akkuyu, Turkey

Muzaffer Can İban*[1], Şafak Bozduman [2], Ezgi Şahin [2]

[1]*Mersin University, Faculty of Engineering, Department of Geomatics Engineering, Mersin, Turkey*
[2]*Mersin University, Institute of Science, Department of Remote Sensing and Geographic Information Systems, Mersin, Turkey*

Keywords
Supervised Classification
Machine Learning
Remote Sensing
Land Use and Land Cover
Google Earth Engine
Nuclear Power Plants

ABSTRACT

This paper tests the potential of the Google Earth Engine platform and Sentinel-2 data to classify and monitor land use and land cover nearby a nuclear power plant construction which is being eroded in Akkuyu district of Mersin Province in Turkey. After classification study, the performance of different supervised machine learning classification algorithms are compared. According to the accuracy assessment results, the random forest classifier has performed slightly better classification than other classifiers. According to the numerical results, Akkuyu NPP project has doubled the footprint of built-up areas. The project has brought a significant deforestation and filling areas on the seashore.

1. INTRODUCTION

The classification of land use and land cover (LULC) presents crucial information to comprehend the relationships between humankind and environment. Remote sensing (RS) and geographic information systems (GIS) have been regularly used for mapping and monitoring LULC, thanks to a wide range of free data and software. Nowadays, many researchers are able to implement more precise and accurate LULC change analysis with the help of high-resolution RS products. Lambin et al. 2001; Mas, 1999)

RS and geospatial big data approach can help to understand the continuous change on earth's surface. Such big data requires time-series composite images, which brings higher variability in the spectra of different LULC classes. Conventional approach to implement multi-temporal big data processing has required to satellite-data searching, downloading and storing. Besides, computational processing capacities need to be powerful enough to manage all data and to run different complex classifiers (Tamiminia et al. 2020).

European Space Agency's Copernicus Program has launched several satellite missions including Sentinel-1,2,3 and 5 satellite constellations. The scientific community, governments and private sectors have used Sentinel-2 data for land use and land cover monitoring. Sentinel-2 offers improved data compared to other low to medium spatial resolution satellite images, especially in temporal and spatial resolution (Gascon et al 2017).

To handle satellite imagery there are two different system architecture: on one hand cluster-based high performance computing where a single image is processed and stored by the co-operation of several computers. On the other hand, there are cloud-based platforms where the capabilities of supercomputers can be achieved without owning a good storage and processing system.

The Google Earth Engine (GEE) platform is a free cloud-based tool of Google where the users can access and process petabyte scales of remotely sensed data by using Javascript and Python coding on its own user interface. GEE takes advantage of Google's computational infrastructure to reduce operational time and provide a repository for script storing and sharing. The GEE data catalogue allows access to multiple satellite data and satellite-derived products (Gorelick et al. 2017).

This paper was conceived with two main objectives: (1) to test the potential of the GEE platform and Sentinel-2 data to classify and monitor land use and land cover nearby a nuclear power plant (NPP) construction which is being eroded in Akkuyu district of Mersin Province in Turkey; (2) to compare and assess the performance of different supervised machine learning (ML)

* **Corresponding Author**

*(caniban@mersin.edu.tr) ORCID ID 0000 – 0002 – 3341 - 1338
(safak.bozduman@gmail.com) ORCID ID 0000 – 0003 – 0359 – 9090
(ezgisahin.9600@gmail.com) ORCID ID 0000 – 0002 – 7455 – 8141

Cite this study

İban M C, Bozduman Ş & Şahin E (2021). Supervised machine learning classification in Google Earth Engine: Time series analysis in Akkuyu, Turkey. 2nd Intercontinental Geoinformation Days (IGD), 238-240, Mersin, Turkey

classification algorithms in terms of the obtained classification accuracy.

2. MATERIALS AND METHODS

2.1. Study Area

Akkuyu NPP is under construction on Mediterranean Sea coast in Mersin Province, Turkey. It will be Turkey's first nuclear power plant. Therefore, it is crucial to monitor the impact of such a mega-project on LULC of the surrounding area. As seen in "Fig. 1", the image classification frame is selected as a 25 x 15 km rectangle around the NPP construction site. However, LULC change analysis is implemented in 1-km and 5-km buffers centered on the site.

Figure 1. Image Classification Frame

2.2. Image Classification

Via GEE platform, the least cloudy Sentinel-2 MSI Level 2-A images were obtained from scihub for 2017, 2019 and 2021 in order to visualize the LULC change in biannual time series. Each LULC class (water bodies, built-in areas, agricultural areas, forests and barren land) are trained in pixel-wise approach. For each class, a set of 100 points are selected and marked on images. 75 of them are used for training and 25 points are used for testing.

GEE platform has built-in supervised machine learning image classification functions. These are classification and regression trees (CART)(Lawrance and Wright 2001), random forest (RF) (Pal 2005) and support vector machines (SVM) (Mountrakis et al. 2011). All these classification algorithms were executed on three different images with the same training and testing set of points. The hyper-parameters of ML algorithms are kept as default and they are not tuned on GEE platform.

After obtaining the classified images, the images are clipped to aforementioned buffer frames.

3. RESULTS

Table 1 shows the overall accuracy and kappa coefficients for the classifications of three different images with SVM, CART and RF classifiers.

Table 1. Accuracy Assessment

Years	ML Algorithm	Overall Accuracy	Kappa Coefficient
2017	SVM	0.74	0.67
	CART	0.81	0.75
	RF	0.86	0.83
2019	SVM	0.69	0.61
	CART	0.85	0.81
	RF	0.89	0.87
2021	SVM	0.81	0.77
	CART	0.84	0.79
	RF	0.89	0.87

"Fig. 2" and "Fig.3" shows the LULC classification maps of the region in 2017, 2019 and 2021 images with three classifying ML algorithms.

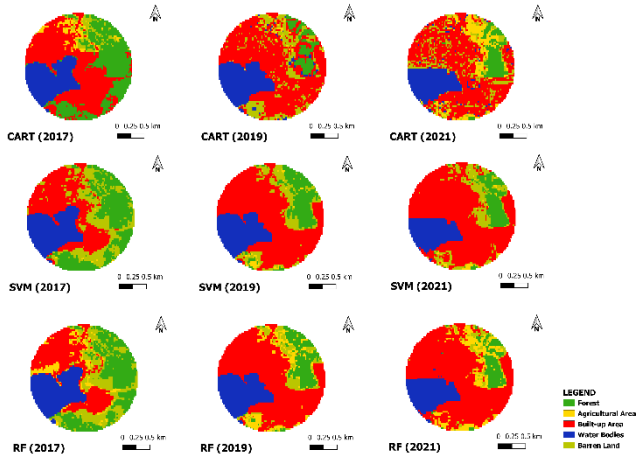

Figure 2. LULC Classification Maps in 1-km Buffer Zone

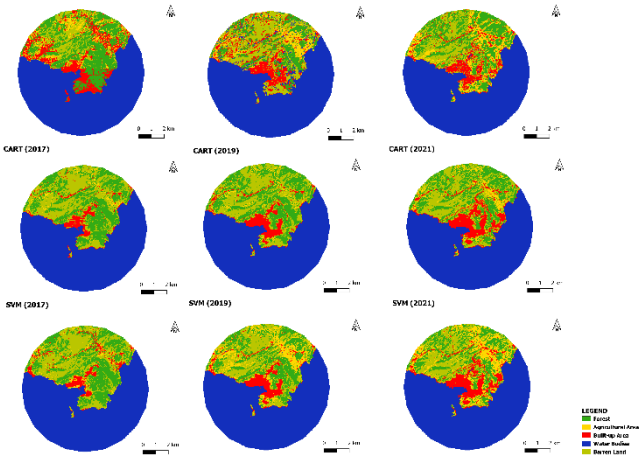

Figure 3. LULC Classification Maps in 5-km Buffer Zone

Table 2 shows the percentage of each LULC classes in the classification maps. By this table, it is possible to investigate the LULC change between 2017 and 2021 during the construction phase

Table 2. LULC Analysis

Buffer Zones	Year	ML	Forest (%)	Agriculture (%)	Built-up (%)	Water Bodies (%)	Barren Land (%)
1 km	2017	SVM	26.66	0.23	31.81	19.73	21.56
		CART	29.25	4.39	43.08	18.65	4.62
		RF	25.93	7.52	26.50	19.85	20.20
	2019	SVM	13.88	1.43	54.40	17.57	12.71
		CART	6.81	1.62	55.67	19.62	16.28
		RF	11.49	8.72	54.19	17.76	7.85
	2021	SVM	10.05	1.53	60.96	14.35	13.11
		CART	8.50	10.45	49.45	16.77	14.82
		RF	7.99	10.88	61.57	14.99	4.58
5 km	2017	SVM	18.71	1.52	4.07	54.70	21.01
		CART	20.02	5.02	10.30	54.43	10.23
		RF	18.09	2.44	4.35	54.73	20.38
	2019	SVM	18.05	2.07	5.79	54.48	19.61
		CART	10.50	5.55	8.82	57.51	17.61
		RF	15.38	9.16	5.79	54.64	15.02
	2021	SVM	16.00	3.60	8.43	54.06	17.90
		CART	16.62	7.57	7.23	54.57	14.00
		RF	13.40	11.35	8.46	54.30	12.48

4. DISCUSSION AND CONCLUSIONS

According to the accuracy assessment results, the RF classifier has performed slightly better classification than SVM and CART classifiers. Even though CART classifier gives a better result than SVM, LULC classification maps derived from CART classifier seems to be over-trained. In contrast, RF and SVM classifiers enable to obtain a descent distribution of LULC classes.

According to the numerical results of LULC change analysis between 2017 and 2021, Akkuyu NPP project has doubled the footprint of built-up areas. The project has brought a significant deforestation and filling areas on the seashore. The operating NPP is expected to absorb more population, which may lead to new development areas, and more loss in forest and agricultural lands.

REFERENCES

Gascon, F., Bouzinac, C., Thépaut, O., Jung, M., Francesconi, B., Louis, J., ... & Fernandez, V. (2017). Copernicus Sentinel-2A calibration and products validation status. Remote Sensing, 9(6), 584.

Gorelick, N., Hancher, M., Dixon, M., Ilyushchenko, S., Thau, D., & Moore, R. (2017). Google Earth Engine: Planetary-scale geospatial analysis for everyone. Remote sensing of Environment, 202, 18-27.

Lambin, E. F., Turner, B. L., Geist, H. J., Agbola, S. B., Angelsen, A., Bruce, J. W., ... & Xu, J. (2001). The causes of land-use and land-cover change: moving beyond the myths. Global environmental change, 11(4), 261-269.

Lawrence, R. L., & Wright, A. (2001). Rule-based classification systems using classification and regression tree (CART) analysis. Photogrammetric engineering and remote sensing, 67(10), 1137-1142.

Mas, J. F. (1999). Monitoring land-cover changes: a comparison of change detection techniques. International journal of remote sensing, 20(1), 139-152.

Mountrakis, G., Im, J., & Ogole, C. (2011). Support vector machines in remote sensing: A review. ISPRS Journal of Photogrammetry and Remote Sensing, 66(3), 247-259.

Pal, M. (2005). Random forest classifier for remote sensing classification. International journal of remote sensing, 26(1), 217-222.

Tamiminia, H., Salehi, B., Mahdianpari, M., Quackenbush, L., Adeli, S., & Brisco, B. (2020). Google Earth Engine for geo-big data applications: A meta-analysis and systematic review. ISPRS Journal of Photogrammetry and Remote Sensing, 164, 152-170.

Intercontinental Geoinformation Days

igd.mersin.edu.tr

Analysis of the effect of training sample size on the performance of 2D CNN models

Elif Ozlem Yilmaz[1], Taskin Kavzoglu*[1]

[1]*Gebze Technical University, Faculty of Engineering, Department of Geomatics Engineering, Kocaeli, Turkey*

Keywords
Remote sensing
CNN
Deep Learning
Image Classification
Sample Size

ABSTRACT

Hyperspectral remote sensing plays a significant role in the research of Earth observation owing to rich spectral information. Convolutional Neural Networks have been commonly used in hyperspectral image classification with the rapid development of deep learning algorithms. In this study, the effect of sample size on the performance of 2D CNN models was analyzed using freely available Pavia hyperspectral data for a 9-class classification problem. Thematic maps were produced with different number of samples and the accuracies of the thematic maps were compared. The results were verified for the effectiveness of different number of samples considering accuracy metrics (overall accuracy, F-score and Kappa coefficient). As a result, overall accuracies of 86.42, 91.84, 94.20 and 95.36% were produced for Deep Learning models using 50, 100, 200 and 400 samples, respectively.

1. INTRODUCTION

Deep learning, which is defined as a sub-branch of machine learning, has become a popular application in remote sensing in recent years, as these algorithms handle complex problems with higher accuracy, especially for image classification. Compared to traditional classification methods, deep learning models have achieved higher accuracies in classifying hyperspectral datasets (Paoletti et al. 2019). Since the architecture of deep learning models is flexible, this has a positive impact on the learning ability of these architectures. Another reason for the widespread use of the deep learning approach is the development of Graphics Processing Unit (GPU) hardware of computers (Paoletti et al. 2020). The concept of deep learning was originated from the artificial neural networks (ANNs). ANNs have been long employed for many problems with varying levels of success. Their black-box nature, optimal parameter selection, initial network size and pruning strategies have limited their use, particularly in remote sensing studies (Kavzoglu and Mather 1999). ANNs are data-dependent models focusing on training data characteristics, not the abstract values estimated from the samples as in the case of statistical methods (Cetin 2004). Therefore, training data must be representative or should be processed via refining to be representative (Kavzoglu 2009).The ANNs are formed by combining input, hidden, and output layers (Wang and Raj 2017). The connections between neurons is usually provided by the backpropagation method (Kavzoglu and Mather 2003). The term "deep" is used in Deep Learning because the increase in the number of hidden layers indicates that the model is getting deeper.

In image classification applications, spectral and spatial properties obtained from satellite images are jointly evaluated by deep learning methods. Thus, considering such properties of the data increases the accuracy of the thematic maps (Zhao and Du 2016). Image classification using deep learning methods may be divided into three parts: (i) dataset preparation, (ii) neural network model training, and (iii) classification using the trained model (Zhang et al. 2016). Moreover, deep learning algorithms learn the relationship between input data and labeled data using feature maps. In the literature, the neural network architecture, namely Deep Belief Network, Recurrent Neural Network, Autoencoder, and Convolutional Neural Network, have been commonly used for image processing such as segmentation, detection and classification (Du and Li 2018; Khan et al 2017; Merchant 2020; Sildir et al. 2020; Wang et al. 2020; Wu and Prasad 2017).

The purpose of this study is to analyze the performance of 2D CNN model using hyperspectral dataset by considering the different number of samples (i.e. 50, 100, 200 and 400). To meet this objective, the result of thematic maps generated by 2D CNN model was

* **Corresponding Author**

(eoyilmaz@gtu.edu.tr) ORCID ID 0000-0002-6853-2148
(kavzoglu@gtu.edu.tr) ORCID ID 0000-0002-9779-3443

Cite this study

Yilmaz E O & Kavzoglu T (2021). Analysis of the effect of training sample size on the performance of 2D CNN models. 2nd Intercontinental Geoinformation Days (IGD), 241-244, Mersin, Turkey

assessed based on overall accuracy, Kappa coefficient and F-score value.

2. CONVOLUTIONAL NEURAL NETWORKS

The Convolutional Neural Network (CNN) model has been widely used as the architecture of Deep Learning model (Vali et al. 2020). The main difference of the architecture of CNN models from other neural networks is that CNN includes convolution filters (Khan et al. 2018). The model of CNN has a great capacity to extract the features of the big data, such as hyperspectral imagery.

The architecture of the CNN model, a feed-forward neural network, consists of several combinations of dense, pooling, flattening, convolutional, and dropout layer (Yılmaz 2020). The convolutional layer is used for feature map extraction from a large dataset. The dense layer connects neurons in the previous and next layer. The pooling layer reduces the large data but keeps only the substantial information. The flattening layer converts multidimensional properties into a one-dimensional vector. Moreover, the dropout layer is used to prevent overfitting in the deep learning models (Srivastava et al. 2014). In addition to this architecture, other training parameters namely optimization, activation and learning rate also used in CNN models during the training stage (Yılmaz 2020).

3. STUDY AREA AND DATASET

In this study, a well-known Pavia University hyperspectral dataset was used to test the influence of using different numbers of training samples in the training stage. The dataset was obtained by a Reflective Optics Spectrographic Image System (ROSIS) sensor, which has 610x340 pixels with 1.3 meters spatial resolution (Fig. 1). The original dataset includes 115 spectral bands, but 12 bands were removed because they comprised noisy data.

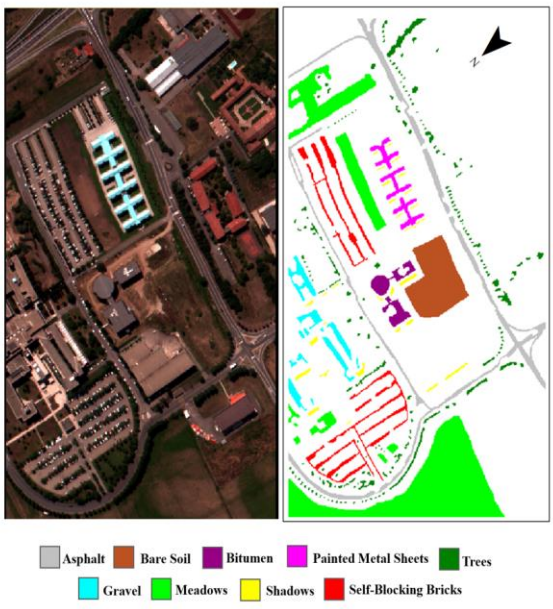

Figure 1. The study area and ground reference data for Pavia University hyperspectral imagery.

The reference dataset of Pavia image was generated for nine major land use/cover (LULC) classes and 42,776 labeled samples were available. The classes of LULC, namely asphalt, meadows, gravel, trees, painted metal sheets, bare soil, bitumen, self-blocking bricks, and, shadows, are given Table 1.

Table 1. The number of samples from reference data.

LULC Classes	Number of Samples
Asphalt	6,631
Meadows	18,649
Gravel	2,099
Trees	3,064
Painted metal sheets	1,345
Bare soil	5,029
Bitumen	1,330
Self-blocking bricks	3,682
Shadows	947
Total	42,776

Before classifying the Pavia University hyperspectral dataset using 2D CNN model, the first step was to randomly divide the dataset into three subsets: the first (training dataset) with 75% of the samples, the second (validation dataset) with 15% of the samples to evaluate the overall accuracy of the thematic maps and the third (test dataset) with %10. Thus, 50, 100, 200, and 400 samples for each reference class were randomly selected from the training dataset. It should be noted that the application of classification was performed using Jupyter Notebook with Python Language.

4. RESULTS

In this study, LULC classification was performed using the 2D CNN model. In order to build the user-defined model, input, batch, convolutional, flattening, dropout and dense layers were generated (Fig. 2.). It should be noted that a patch size of 5x5 was chosen for all the applications of 2D CNN models. Moreover, the training dataset was set according to the determined patch size. In order to train the deep learning model quickly, the training dataset was normalized before the model training phase. The unit parameters of the dense layer were chosen as 64 and 128 considering a trial-and-error approach. Moreover, the activation functions of ReLU and Softmax were employed in the processing stage.

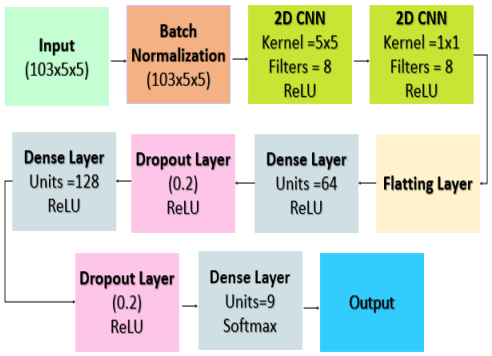

Figure 2. 2D CNN model adopted in this study.

The produced thematic maps representing 9 LULC classes were generated with 2D CNN model using 50, 100, 200 and 400 samples (Fig. 3.).

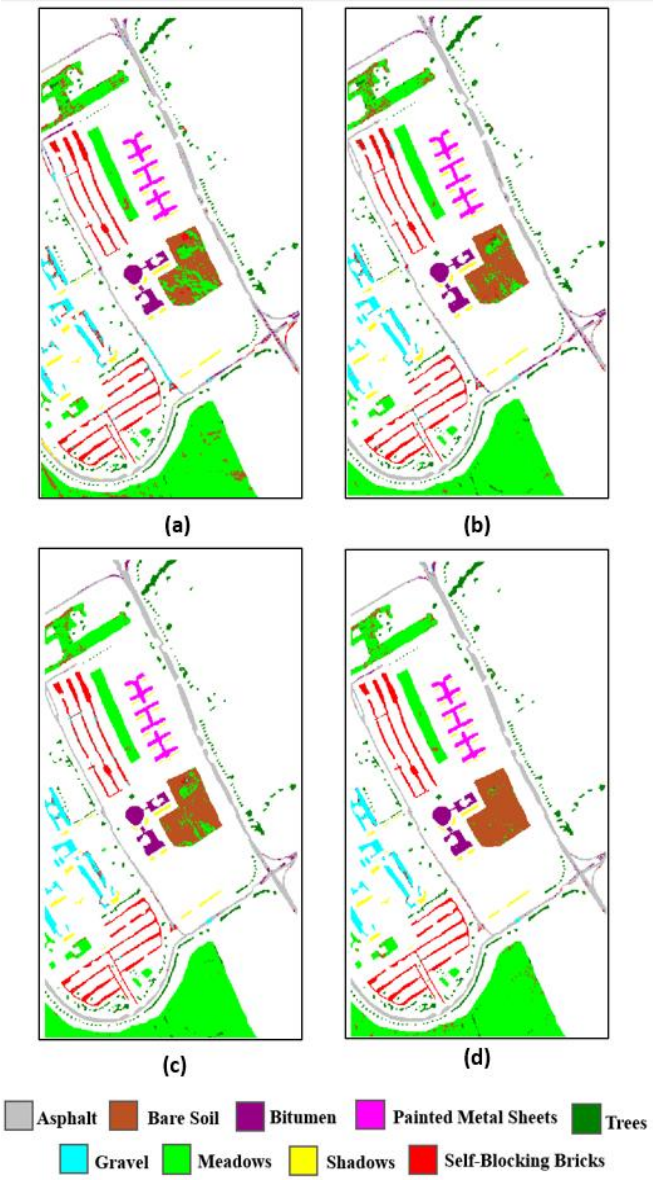

Figure 3. Thematic maps produced with 2D CNN model by using (a) 50 samples, (b) 100 samples, (c) 200 samples, (d) 400 samples.

To analyze the accuracy assessment of the thematic maps, the overall accuracies and Kappa coefficients were calculated by using the reference dataset. The overall accuracies of the thematic maps generated using 50, 100, 200 and 400 samples were estimated to be 86.42, 91.84, 94.20 and 95.36 respectively. Also, Kappa coefficients were calculated as 0.82, 0.89, 0.92 and 0.94, respectively (Table 2). Furthermore, F-score values were produced to evaluate the estimated accuracy of each LULC class. As can be seen in the table, the LULC classes with the highest F-score value (1.00) was calculated for the painted metal sheets for all number of samples combination and shadow classes, except for the case of 50 samples. The LULC classes with the lowest F-Score values belong to the bare soil (0.68), gravel (0.77) and bitumen (0.79) classes for 50 samples. From the visual analysis of the thematic maps produced, it was observed that the gravel class was mixed with the self-blocking brick class for 50 samples. It was also observed that the meadow and bare soil classes were mixed together due to similar spectral characteristics. The thematic map created with 100 samples had the lowest F-score values (0.82) with the bitumen and bare soil classes. Moreover, it was observed that the bare soil class was mixed with meadows class in the thematic map produced with both 200 and 400 samples.

Training times for different sizes of training samples were recorded and shown in Table 2. In the models using 50, 100 and 200 samples, the training processes lasted 500.5, 500.4 and 500.3 seconds, respectively. However, the slowest training period of the model took about 930 seconds for 400 samples. The reason could be related to the large sample size of the dataset employed during the training.

Table 2. Accuracy assessment for the thematic maps produced with 2D CNN model.

LULC Classes	Number of Samples			
	50	100	200	400
Asphalt	0.87	0.93	0.97	0.96
Meadows	0.91	0.94	0.95	0.96
Gravel	0.77	0.87	0.91	0.95
Trees	0.93	0.95	0.95	0.97
Painted metal sheets	1.00	1.00	1.00	1.00
Bare soil	0.68	0.82	0.85	0.89
Bitumen	0.79	0.82	0.91	0.91
Self-blocking bricks	0.87	0.91	0.94	0.97
Shadows	0.93	1.00	1.00	1.00
Overall Acc. (%)	86.42	91.84	94.20	95.36
Kappa Coef.	0.82	0.89	0.92	0.94
Training Time (sec)	500.5	500.4	500.3	937.2

5. CONCLUSION

The deep learning methods have been widely used in remote sensing applications, including object detection, image segmentation and image classification. Superior performances have been reported in the literature for the classification of hyperspectral images with deep learning algorithms. In this study, Pavia University hyperspectral image dataset was classified using 2D CNN models with 50, 100, 200 and 400 samples. In addition, thematic maps were generated by the deep learning model using a 5x5 patch size, then accuracy measurements were conducted. The 2D CNN model with 400 samples resulted in a significant increase in overall accuracies (~9%), particularly compared to 50 samples per class. The findings in this study revealed that samples per class employed in the training stage of 2D CNNs can have significant impact on the achieved accuracy. Poor performances were observed for the cases where limited training data were available for training.

REFERENCE

Du J & Li Z (2018). A hyperspectral target detection framework with subtraction pixel pair features. IEEE Access, 6, 45562–45577.

https://doi.org/10.1109/ACCESS.2018.2865963

Kavzoglu T & Mather P M (1999). Pruning artificial neural networks: An example using land cover classification of multi-sensor images. International Journal of Remote Sensing, 20(14), 2761–2785. https://doi.org/10.1080/014311699211796

Kavzoglu T & Mather P M (2003). The use of backpropagating Artificial Neural Networks in land cover classification. International Journal of Remote Sensing, 24(23), 4907–4938. https://doi.org/10.1080/0143116031000114851

Cetin M, Kavzoglu T & Musaoglu N (2004) Classification of multi-spectral, multi-temporal and multi-sensor images using Principal Components Analysis and Artificial Neural Networks: Beykoz case. Proceedings of 20th Congress of the International Society of Photogrammetry and Remote Sensing, Istanbul, 12-23 July 2004.

Kavzoglu T (2009). Increasing the accuracy of Neural Network classification using refined training data. Environmental Modelling and Software, 24(7), 850–858. https://doi.org/10.1016/j.envsoft.2008.11.012

Khan M J, Yousaf A, Javed N, Nadeem S & Khurshid K (2017). Automatic target detection in satellite images using Deep Learning. Journal of Space Technology, 7(1), 44–49.

Khan S, Rahmani H, Shah S A A & Bennamoun M (2018). A guide to Convolutional Neural Networks for computer vision. Synthesis Lectures on Computer Vision, 8(1), 1–207. https://doi.org/10.2200/s00822ed1v01y201712cov015

Merchant M A (2020). Classifying open water features using optical satellite imagery and an object-oriented convolutional neural network. Remote Sensing Letters, 11(12), 1127–1136. https://doi.org/10.1080/2150704X.2020.1825869

Mosavi A, Ardabili S, & Várkonyi-Kóczy A R (2020). List of Deep Learning Models. In Lecture Notes in Networks and Systems, 101, 202–214. https://doi.org/10.1007/978-3-030-36841-8_20

Paoletti M E, Haut J M, Plaza J, & Plaza A. (2019). Deep learning classifiers for hyperspectral imaging: A review. ISPRS Journal of Photogrammetry and Remote Sensing, 158, 279–317. https://doi.org/10.1016/j.isprsjprs.2019.09.006

Paoletti M E, Haut J M, Tao X, Miguel J P & Plaza A. (2020). A new GPU implementation of support vector machines for fast hyperspectral image classification. Remote Sensing, 12(8), 1257. https://doi.org/10.3390/RS12081257

Sildir H, Aydin E, & Kavzoglu T (2020). Design of Feedforward Neural Networks in the classification of hyperspectral imagery using superstructural optimization. Remote Sensing, 12(6), 956. https://doi.org/10.3390/rs12060956

Srivastava N, Hinton G E, Krizhevsky A, Sutskever I & Salakhutdinov R (2014). Dropout: a simple way to prevent neural networks from overfitting. Journal of Machine Learning Research, 15, 399–421. https://doi.org/10.1016/B978-1-4832-1446-7.50035-2

Vali A, Comai S & Matteucci M (2020). Deep Learning for Land use and land cover classification based on hyperspectral and multispectral Earth observation data: A review. Remote Sensing, 12(15), 2495. https://doi.org/10.3390/rs12152495

Wang H & Raj B (2017). On the Origin of Deep Learning. Computer Science - Machine learning, 1–72. Retrieved from http://arxiv.org/abs/1702.07800

Wang J, Zheng Y, Wang M, Shen Q & Huang J (2020). Object-scale adaptive Convolutional Neural Networks for high-spatial resolution remote sensing image classification. IEEE Journal of Selected Topics in Applied Earth Observations and Remote Sensing, 14, 283–299. https://doi.org/10.1109/JSTARS.2020.3041859

Wu H & Prasad S (2017). Convolutional Recurrent Neural Networks for hyperspectral data classification. Remote Sensing, 9(3), 298. https://doi.org/10.3390/rs9030298

Yılmaz E Ö (2020). Uzaktan algılanmış verilerin derin öğrenme yöntemiyle sınıflandırılması. MS Thesis, Gebze Technical University, Kocaeli (in Turkish).

Zhang L, Zhang L & Du B (2016). Deep Learning for remote sensing data: A technical tutorial on the state of the art. IEEE Geoscience and Remote Sensing Magazine, 4(2), 22–40. https://doi.org/10.1109/MGRS.2016.2540798

Zhao W & Du S (2016). Learning multiscale and deep representations for classifying remotely sensed imagery. ISPRS Journal of Photogrammetry and Remote Sensing, 113 (March 2016), 155–165. https://doi.org/10.1016/j.isprsjprs.2016.01.004

Intercontinental Geoinformation Days

igd.mersin.edu.tr

Documentation of cultural heritage with backpack lidar usage on photogrammetric purpose

Kasım Erdal[1], Hasan Bilgehan Makineci*[1]

[1]*Konya Technical University, Engineering Faculty, Geomatics Engineering Department, Konya, Turkey*

Keywords
Backpack Lidar
Cultural Heritage
Documentation
GNSS/IMU Integration
3D Model

ABSTRACT

Modelling historical artefacts' external and internal structures together is a task that can be done with many sessions with classical terrestrial laser scanners. Backpack Lidar Systems are a proper newly applied alternative method in large areas of use and historical buildings where many sessions should be held with terrestrial laser scanner systems. These systems quickly acquire coordinate data and omega, kappa and phi angles differences with internal GNSS / IMU components and save time and cost following photogrammetric mentality. In this research, using Backpack Lidar System; The exterior and interior structure of the village mosque, which is an Ottoman artefact built in 1899 at the Dumanoluğu Village in the Şiran District of Gümüşhane City, was modelled in 3D. With its integrated camera, the point data has been coloured and made suitable for architectural survey studies. The village mosque's exterior scan was completed within seven minutes, and the interior scan within five minutes. 2.041.971 points were obtained in the external scanning, and 821.306 points in the internal scanning. Four GCPs were used for the mosque's exterior screening. The point clouds obtained were combined and modelled.

1. INTRODUCTION

For centuries, human beings have built important structures for protection, shelter and meeting their basic needs. These structures have suffered partial or total deterioration due to wars, natural conditions and people throughout history. Every society has an absolute duty to transfer the cultural heritage of humanity to future generations and protect it in the best way. Living in a geography that has hosted the most important civilisations of human histories, such as Anatolian lands, imposes a much more important responsibility.

It is a great necessity to use sufficient technological infrastructure and human resources to protect and transfer all cultural artefacts in the borders of our country to future generations. For this purpose, developing and increasing the use of photogrammetric methods can be seen as a duty. All methods such as photogrammetric techniques, Unmanned Aerial Vehicles (UAV), terrestrial, mobile and air-assisted lidar systems, and satellite data can be used to preserve and document cultural heritage (Kaya et al., 2021; Ulvi et al., 2019; Makineci 2016; Yaman and Kurt 2019).

All photogrammetric methods have advantages and weaknesses according to the area of use and purpose. According to the literature, it is possible to talk about the success of terrestrial laser scanning systems, which have been widely used in recent years in cultural heritage documentation. However, the problems that develop to the loss of time and the increase in the number of sessions lead to new alternatives (Zeybek 2019). Backpack Lidar systems carried by human assistance are also an essential alternative issue of recent times. In this study, the success of these systems was demonstrated by documenting a mosque's internal and external architectural features in a short time using Backpack Lidar.

2. MATERIALS AND METHOD

2.1. Study Area

The historical village mosque belonging to the Dumanoluğu Quarter of Gümüşhane Province, Şiran District, located in the east of the Black Sea Region, Turkiye, was chosen as the study area.

* **Corresponding Author**

(kerdal.245@gmail.com) ORCID ID 0000-0001-6024-7361
*(hbmakineci@ktun.edu.tr) ORCID ID 0000-0003-3627-5826

Cite this study
Erdal K & Makineci H B (2021). Documentation of cultural heritage with backpack lidar usage on photogrammetric purpose. 2nd Intercontinental Geoinformation Days (IGD), 245-248, Mersin, Turkey

2.2. Backpack Lidar System

In this study, the Greenvalley Libackpack DGC50 backpack LIDAR system was used. When the backpack LIDAR models are analysed, it is seen that they generally have a single laser sensor and a panoramic camera. Unlike the general, the Libackpack DGC50 model has two laser sensors (one horizontal and one vertical), with a panoramic camera and GNSS/IMU receiver. With the GNSS receiver in the LIDAR system, point data is obtained in coordinates during the sessions held in outdoor dimensions (Fig 1).

The GNSS receiver in the laser scanner works with the PPK method. While providing access to the satellite data required for the PPK, the ground station operating with the static method is used simultaneously. In this way, the horizontal position of the obtained point data can be obtained up to ±7 cm. In addition, the properties of the Lidar used in the study are shown in Table 1 (greenvalleyintl.com 2021).

Table 1. Greenvalley Libackpack DGC50 specs

Dimension (mm)	1010 X 344 X 252
Battery	5700 mAh
Weight	10.3 kg
Working hours	~2 h
Laser Sensor	VLP16 × 2
Accuracy	±3 cm
Vertical FOV	-90°~90°
Horizontal FOV	0°~360°
Measuring range	100 m

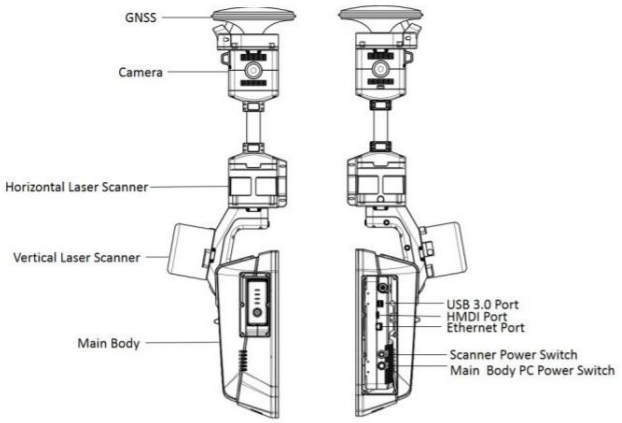

Figure 1. Greenvalley Libackpack DGC50 Profile

2.3. Workflow of Study

The general workflow of the study is divided into fieldwork and office work. There are Ground Control Points (GCPs) used in fieldwork and operations for generating lidar data. Office work includes adjustment of GCPs and analysis of point cloud (fig 2).

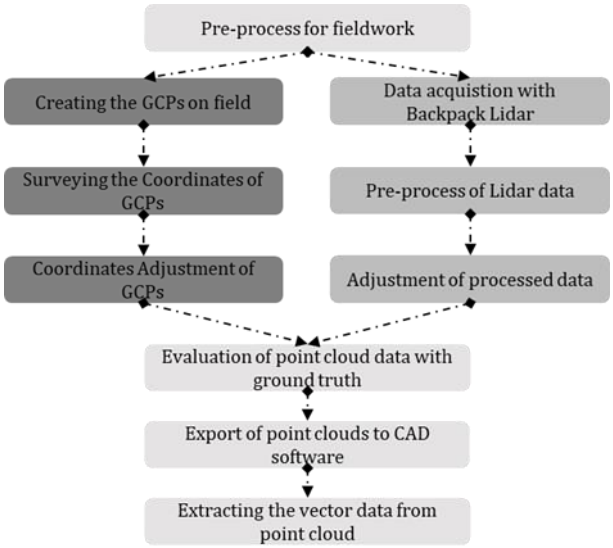

Figure 2. Workflow of fieldwork and office work

Lidar system is started around the historical monument to be scanned outdoors. Since the Greenvalley Libackpack DGC50 consists of a laser scanner + panoramic camera + GNSS components, some issues need to be considered before starting data collection. Check that the camera is ready and make sure that the recording process has begun. It is checked that the GNSS receiver is connected to a sufficient number of satellites and that it is ready. It is necessary to wait at least 3 minutes before starting data collection; It is expected to obtain the satellite data required for an accurate coordinating process of the point cloud. After waiting, data is created to be collected after the "8" mark is made slowly on the ground to perform GNSS calibration.

3. RESULTS AND DISCUSSIONS

In the research, external and internal scanning was carried out to obtain and document the point cloud of the mosque. The external scan of the mosque was completed within 6 minutes (fig 3), and the internal scan within 4 minutes (fig 4). 2.041.971 points were obtained in the external scanning, and 821.306 points were obtained in the internal scanning.

Today, terrestrial laser scanners are used for historical artefacts, archaeological excavations, etc. It is frequently used in many modelling studies. Terrestrial laser scanners are installed at many points in the area to be scanned, so fieldwork takes a long time. The increase in the number of processes in office work takes a long time due to the efforts to combine the point clouds obtained from different points (Ulvi et al., 2019). When we examine other models of handheld laser scanners, it can be obtained from the laser scanner we use in our work for a long time due to hand-held and single laser scanner fatigue. Less point cloud is obtained from the obtained point cloud (Yaman and Kurt 2019).

Figure 3. The external scan of the mosque

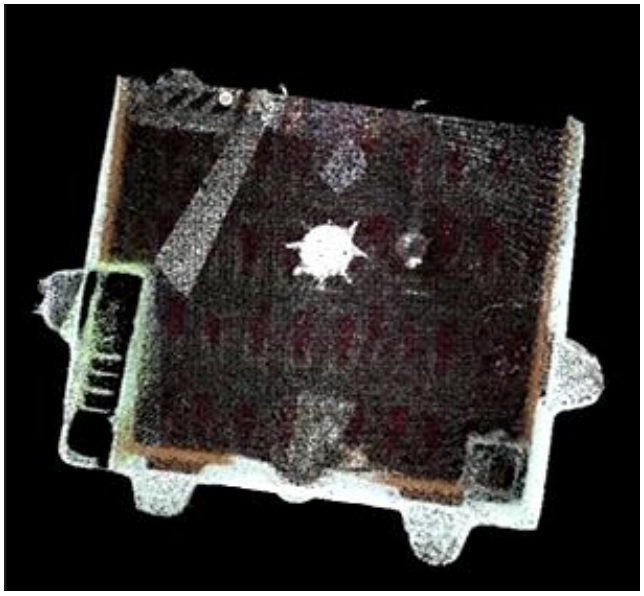

Figure 4. The internal scan of the mosque

Using photogrammetric studies according to the National Large Scale Map Production Regulation (BÖHHBÜY 2018); It is necessary to use a minimum of 4 checkpoints, up to 30% of the GCP number. Since the point cloud data collected with the GVI Libackpack DGC50 is coordinated, adjustment is not performed in this study. Considering the minimum number of GCPs, 4 GCPs were measured in the exterior scanning of the historic mosque. Error-values of the determined GCPs is given in Table 2.

Table 2. Minimum, Maximum, Mean Errors of GCPs

	Horizontal (X, Y) (cm)	Vertical (Z) (cm)
Min Error	0.020	0.004
Max Error	0.082	0.077
Mean Error	0.047	0.041

The coordinated point cloud is transferred to CAD software. The drawing process (vectorisation of structure) is performed in CAD. In this way, vector data is obtained. The walls of the historical mosque can be obtained in vector form, as in Figure 5.

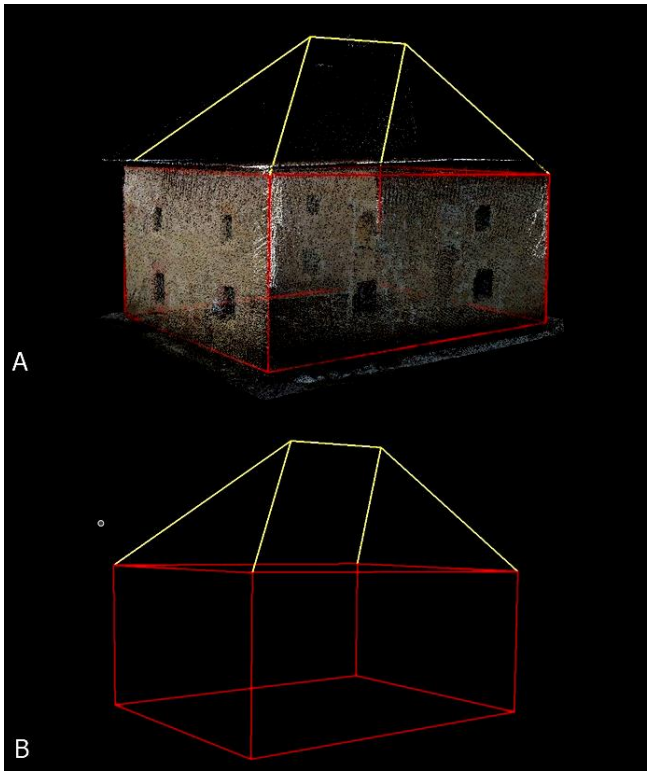

Figure 5. Vectorisation of Structure A: Vectors with point cloud and B: Only vectors

4. CONCLUSION

This study aimed to determine that the documentation and modelling of historical buildings can be carried out quickly and effectively with Backpack Lidar. Well-to-do results have been demonstrated with the fieldwork and office work carried out for this purpose.

ACKNOWLEDGEMENT

The authors declare their appreciation to Küre Engineering, which made an essential contribution to obtaining the data.

REFERENCES

Kaya, Y., Yiğit, A. Y., Ulvi, A., & Yakar, M. (2021). Arkeolojik Alanların Dokümantasyonununda Fotogrametrik Tekniklerinin Doğruluklarının Karşılaştırmalı Analizi: Konya Yunuslar Örneği. Harita Dergisi, 165, 57-72.

Makineci, H. B. (2016). İnsansız Hava Araçları Lidar Etkileşimi. Geomatik, 1(1), 19-23.

Ulvi A, Varol F & Yiğit A Y (2019). 3D modeling of cultural heritage: the example of Muyi Mubarek Mosque in

Uzbekistan (Hz. Osman's Mushafi). International Congress on Cultural Heritage and Tourism (ICCHT), 115-123, Bishkek, Kyrgzstan.

Yakar M, Yılmaz H M & Mutluoglu O (2014). Performance of photogrammetric and terrestrial laser scanning methods in volume computing of excavation and filling areas. Arabian Journal for Science and Engineering, 39, 387-394. https://doi.org/10.1007/s13369-013-0853-1

Yaman, A., & Kurt, M. (2019). Tarihi ve kültürel mirasların belgelenmesi ve üç boyutlu modellenmesi için Geoslam yersel lazer tarayıcının kullanım olanaklarının araştırılması: Aksaray İli Ulucami Örneği. Türkiye Lidar Dergisi, 1(1), 5-9.

Zeybek, M. (2019). El-tipi LiDAR ölçme sistemleri ve 3B veri işleme. Türkiye Lidar Dergisi, 1(1), 10-15.

https://greenvalleyintl.com/wp-content/uploads/2020/10/LiBackpackDGC50.pdf

https://www.mevzuat.gov.tr/MevzuatMetin/3.5.20181962.pdf

Intercontinental Geoinformation Days

igd.mersin.edu.tr

Extraction of high-precision built-up areas from SENTINEL-2B imagery via multi-index approach and fuzzy C-means algorithm

Bachri Imane*[1], Zonkouan Badjo Ruth Virginia [2], Benbouziane Abdelmajid [3], Raji Mohammed [4], Hakdaoui Mustapha [1], Beh Ibrahim Diomande [2]

[1]*Hassan II University of Casablanca, Faculty of Science Ben M'sik, Laboratory of Applied Geology, Geomatics and Environment, Casablanca, Morocco*
[2] *Alassane Ouattara University, Laboratory of Demography and Spatial Dynamics, Bouaké, Ivory Coast*
[3]*Hassan II University of Casablanca, Faculty of Science Ben M'sik, Laboratory of Sedimentary Basin Dynamics and Geological Correlations, Casablanca, Morocco*
[4]*Hassan II University of Casablanca, Faculty of Science Ben M'sik, Laboratory of Laboratory of Geodynamics of Ancient Chains, Casablanca, Morocco*

Keywords
Built up area
High spatial resolution
Sentinel-2B
Multi-index
FCM

ABSTRACT

Accurate Urban built-up area information is required for a wide range of applications, in particular risk prevention and city planning. However, the extraction of built-up urban areas using high spatial resolution multispectral image, such as Sentinel-2, remains a significant challenge due to spectral confusion and intra-urban variability with other types of land cover, especially between built-up areas and bare land. As a result, in this work, we aim to increase built up accuracy mapping for Tan-Tan city (Southern of Morocco) by using six spectral indices, including Normalized Difference Building Index (NDBI), New Built Up (NBI), and Normalized Difference Tillage Index (NDTI) for urban area, and Normalized Difference Vegetation Index: NDVI, linked to vegetation, as well as the Bare Soil Index (BSI) and Dry Bare-Soil Index (DBSI) for bare land by means of Fuzzy C Means (FCM) algorithm. The six spectral indices were extracted from Sentinel-2 during the dry season and were combined to generate six multi-index datasets. Herein empirical results show that DBSI index works with NDBI, while BSI works better with NDTI. Therefore, the two multi-index datasets DBSI/ NDVI / NDBI and BSI/ NDVI / NDTI were suitable for built-up extraction in dry season in preferring order. Their overall accuracies were 85.28%, and 83.99%, respectively.

1. INTRODUCTION

Although urban areas make up only a small percentage of the world's total land area, their population density and resource use rates are much higher than in surrounding areas, necessitating better resource management practices. Understanding the spatial distribution and development of urban areas is critical for urban planning and resource planning, and mapping the built-up areas is among the most basic tasks needed for this (Ettehadi Osgouei et al., 2019) . When carrying out using traditional methods like field surveying and aerial photography, such mapping practice necessitates a significant amount of resources.

Satellite imagery is essential for the study of urban development, and the evolution of sensors towards very high spatial resolution provides an extremely rich set of metrics and sub-metric data, creating new challenges in remote sensing. With the advent of such images, the content of the data to be exploited has become much denser over the last ten years. The transition from medium to high resolution has been accompanied by a redefinition of the stakes in civil and military applications. Within a metric resolution image, the

* **Corresponding Author**
*(bachri.imane@gmail.com) ORCID ID 0000-0001-6146-5213
ORCID ID 0000-0002-4901-9920
ORCID ID 0000-0002-2759-2080
ORCID ID 0000-0002-2866-0188
ORCID ID 0000-0002-3598-7672

Cite this study
Bachri I, Zonkouan Badjo R.V, Benbouziane A, Raji M, Hakdaoui M & Beh Ibrahim D (2021). Extraction of high-precision built-up areas from SENTINEL-2B imagery via multi-index approach and fuzzy C-means algorithm. 2nd Intercontinental Geoinformation Days (IGD), 249-252, Mersin, Turkey

notion of object has become accessible. However, the extraction of built-up urban areas using high spatial resolution multispectral image remains a significant challenge due to spectral confusion and intra-urban variability with other types of land cover, especially between built-up areas and bare land. These detection accuracy problems require additional data other than the satellite image itself, digital elevation models (DEMs), reference images, LIDAR data, or other (Zhang et al., 2013). The aim of this study is to extract and detect urban areas using a multispectral image of high spatial resolution (HR) Sentinel-2 for the city of Tan-Tan based on a multi-index approach including the Normalized Difference Building Index, the New Building Index, the Normalized Difference Tillage Index, and the Normalized Difference Vegetation Index and the index of bare soils and the index of dry bare soils.

2. MATERIALS AND METHODS

2.1. Study Area

Tan-Tan is a Moroccan city, located in the region of Guelmim Essmara, southwest Morocco, 330 km south of the city of Agadir, this city has a mild and temperate climate is located between two wadis that flow into the ocean: Oued Drâa and Oued Chebika bordered by sand dunes. The city of Tan-Tan had 60,698 inhabitants according to the 2004 census.

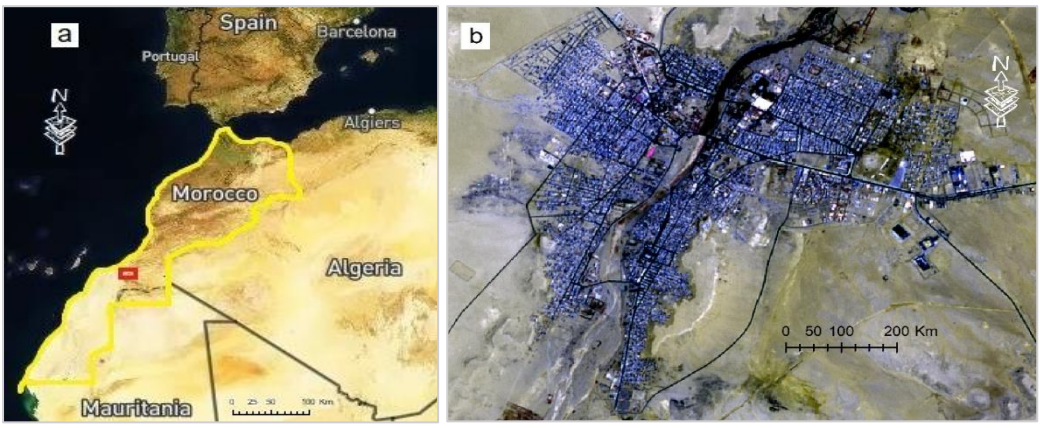

Figure 1. a. Location of study area Tan-Tan; **b**. Natural color composite (RGB 4-3-2) Sentinel-2B image.

2.2. Data Used

Sentinel-2 is a high-resolution multispectral imaging mission. It is based on a constellation of Sentinel-2A and Sentinel-2B, flying in the same orbit but 180° out of phase, and is designed to give a high revisit frequency of 5 days at the equator to observe the Earth's surface. The onboard sentinel-2 optical instrument has 13 spectral bands: four at 10 m, six at 20 m, and three at 60 m spatial resolution (Table 1). In the present work, the cloud-free Sentinel-2B images were downloaded for free from the Copernicus Open Access Hub website. The multispectral image acquired on June 30, 2020 level 1c was atmospherically corrected, resampled to 20 m using the nearest neighbor technique, clipped according to the study area, and exported in GeoTIFF format.

Sentinel-2 images were chosen based on the fact that Sentinel-2 is a free cost satellite imagery provides high accuracy for built-up areas due to its high spatial resolution compared to others multispectral images. Furthermore, several studies have shown that Sentinel-2 image outperforms Landsat OLI image for urban mapping utilizing a variety of indices.

Table 1. Sentinel-2 spectral bands showing the central wavelength, with the resolution

Spectral Bands	Central Wavelength	Resolution
B1- Coastal Aerosol	443 nm	60 m
B2- Blue	490 nm	10 m
B3- Green	560 nm	10 m
B4- Red	665 nm	10 m
B5- Vegetation Red Edge	705 nm	20 m
B6- Vegetation Red Edge	740 nm	20 m
B7- Vegetation Red Edge	783 nm	20 m
B8- NIR	842 nm	10 m
B8A- Vegetation Red Edge	865 nm	20 m
B9- Water Vapor	945 nm	60 m
B10- SWIR-Cirrus	1375 nm	60 m
B11- SWIR	1610 nm	20 m
B12- SWIR	2190 nm	20 m

3. METHOD

The proposed method for extraction of built-up areas using sentinel-2B imagery consisted of three main steps: pre-processing of satellite imagery, processing including extraction of spectral indices and their combination as well as classification, and the last one is analysis of results.

3.1. Pre-processing of Sentinel-2B imagery

The Sentinel-2B level 1c image bands were converted from Top-of-Atmosphere (TOA) reflectance values to Bottom-of-Atmosphere (BOA) reflectance via Sen2Cor plugin. The corresponding spectral bands were considered in this process: blue, green, red, near infrared (NIR), shortwave infrared 1 (SWIR-1) and shortwave infrared 2 (SWIR-2). The SWIR-2 band has a resolution of 20 m; hence, it was resampled to 10 m resolution

utilizing the nearest neighbor method. Then, the image was clipped according to the study area These steps were performed using the SNAP 8.0.0 software provided by European spatial agency (ESA).

3.2. Sentinel-2B processing

3.2.1. Spectral indices used

The spectral indices part of multispectral transformations that consist in transforming the luminance measured at the satellite sensor into meaningful quantities in the environmental domain. Due to the type of multispectral satellite data, it can describe the state of a phenomenon. An index is a numerical variable describing the intensity or extent of a phenomenon that is too complex to be broken down into a manageable number of parameters. Table 2 contains the six spectral indices used in this research. The SAGA GIS software was employed to calculate the six spectral indices used. The results of the spectral indices presented in Figure 2.

Table 2. Different spectral indices used in this research on Sentinel-2B image.

Index Name	Formula on sentinel-2 image	References
Bare Soil Index (BSI)	$\frac{(B11+B4)-(B8+B2)}{B11+B4+B8+B2}$	(Roy et al., 2002)
Dry Bare Soil Index (DBSI)	$\frac{(B11-B3)}{(B11+B3)}-NDVI$	(Rasul et al., 2018)
New Built Up (NB)	$\frac{\boldsymbol{B11*B4}}{\boldsymbol{B8}}$	(Chen et al., 2010)
Normalized Difference Built-up Index (NDBI)	$\frac{(B11-B8)}{(B11+B8)}$	(Zha et al., 2003)
Normalized Difference Vegetation Index (NDVI)	$\frac{(B8-B4)}{(B8+B4)}$	(Rouse et al., 1974)
Normalized Difference Tillage Index (NDTI)	$\frac{(B11-B12)}{(B11+B12)}$	(Van Deventer et al., 1997)

3.2.2. Multi-index combinations

An informal analysis of different combinations of spectral indices as components of the multi-index dataset was used to determine the most appropriate index combination. Table 3 illustrated the correlation between different indices. They discovered a strong association between the bare soil indices BSI and DBSI. That is, the two bare soil indexes generate nearly identical information over Tan-Tan region. The NDTI , NBI, NDBI indices, on the other hand, has poor associations with both the BSI and DBSI indices. The NDVI and NDTI, NDBI indices have a mean correlation. Based on the correlation between the six spectral indices, the spectral difference between the three main land cover classes (bare land, vegetation, urban area) could be expected to increase by overlaying two distinct combinations DBSI/NDVI/NDBI and BSI/NDVI/NDTI. The Quantum GIS 3.18 software was utilized to generate the required spectral layer stacking proposed.

Table 3. Values of correlation between spectral indices used in the research.

	BSI	DBSI	NBI	NDBI	NDTI	NDVI
BSI	1.00000	0.98416	0.23987	0.13283	0.44765	-0.26974
DBSI	0.98416	1.00000	0.32804	0.30715	0.43765	-0.26421
NBI	0.23987	0.32804	1.00000	0.21163	-0.48695	-0.47264
NDBI	0.13283	0.30715	0.21163	1.00000	-0.42525	0.56775
NDTI	0.44765	0.43765	-0.48695	-0.42525	1.00000	0.57795
NDVI	-0.26974	-0.26421	-0.47264	0.56775	0.57795	1.00000

Figure 2. Spectral indices result used (a) BSI (b) DBSI (c) NBI (d) NDBI (e) NDVI (f) NDTI (g) DBSI/NDVI/NDBI (h) BSI/NDVI/NDTI

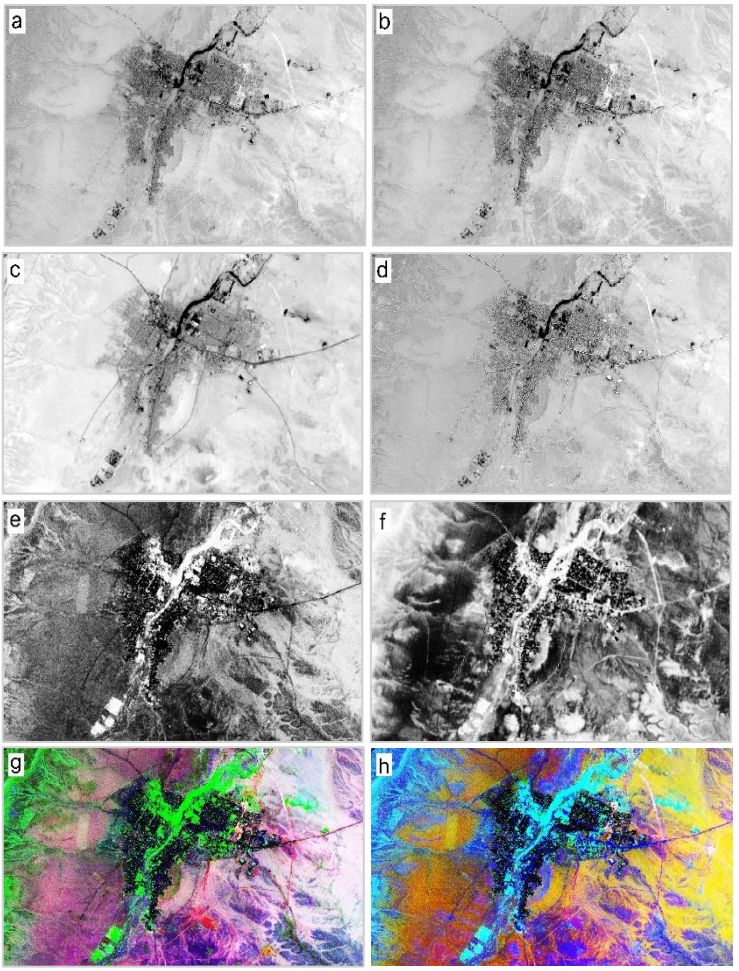

4. RESULTS AND DISCUSSIONS

The results of the built-up area extracted utilized Sentinel-2B image and multi-index datasets created via Fuzzy C-Means Algorithm can be seen from the treated images in Figure 3.

The statistics that is, produced accuracy (PA), user's accuracy (UA), overall accuracy, and kappa coefficient produced from the result of the classified images are shown in Table 4 et 5. Based on the Accuracy of mapping of each types of data in Table 5, the multi-index datasets DBSI/NDVI/NDBI generated an overall accuracy of 85.28% and a coefficient kappa of 0.89, the multi index datasets BSI/NDVI/NDTI generated an overall accuracy of 83.99% and a coefficient kappa of 0.8 and the sentinel-2B image generated overall accuracy of 53.71% and a coefficient kappa of 0.67.

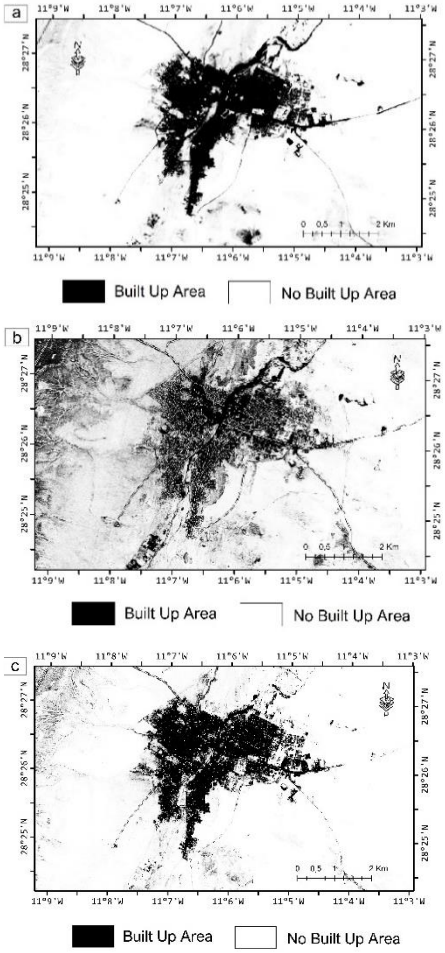

Figure 3. Results of the built-up area extracted of Sentinel-2B image and multi-index datasets created via Fuzzy C-Means Algorithm (a) Sentinel-2B image (b) data-set DBSI/NDVI/NDBI (c) dataset BSI/NDVI/NDTI

Table 4. Classification accuracies of the different approaches for the Tan-Tan region

Data	Sentinel-2B		DBSI/NDVI/NDBI		BSI/NDVI/NDTI	
Accuracy types	PA (%)	UA (%)	PA (%)	UA (%)	PA (%)	UA (%)
Built-Up	67.91	9.75	90.12	96.21	83.73	82.98
Bare land	47.49	71.20	97.52	75.69	87.52	97.65

Table 5. Tan-Tan region's total accuracy and Kappa statistics

Data Type	Overall Accuracy	Kappa
Sentinel-2B	53.71%	0.67
DBSI/NDVI/NDBI	85.28%	0.89
BSI/NDVI/NDTI	83.99%	0.80

According to the visual analysis of the results shown in Figure 3, it was apparent that the Sentinel-2B image and the multi-index created, distinguished built-up land from other land cover types differently. Both multi-index datasets created DBSI/NDVI/NDBI and BSI/NDVI/NDTI, which were derived from Sentinel-2B images and checked for built-up using mapping fuzzy c means classifier in Tan-Tan (arid region), showed high precision, rapid, and automatic classification of built-up class. Nevertheless, based on the statistical results (the overall accuracy and the Kappa coefficient) the best result was obtained by using the DBSI/NDVI/NDBI multi-index.

5. CONCLUSION

Extraction of built up areas using high resolution image has been the biggest issue in mapping urbanized areas due to spectral confusion and intra-urban variability with other types of land cover. In this study a multi-index approach for extracting of built up areas from Sentinel-2B satellite images in dry region was suggested. The Fuzzy C Means algorithm was used to classify the multi-index images generated with various index combinations. The DBSI/NDVI/NDBI combination greatly improved the misclassification of bare lands as built-up areas, according to the findings of this study (Overall accuracy 85.29% and kappa coefficient 0.89). but we must not neglect the fact that the combination BSI/NDVI/NDTI also generated good results(Overall accuracy 83.99% and kappa coefficient 0.8). These results indicate the effectiveness of the suggested multi-index. More research is expected to incorporate multi-polarization SAR Sentinel 1 data in order to use SAR data to distinguish between bare fields and built-up areas.

REFERENCES

Chen, J., Li, M., Liu, Y., Shen, C. & Hu, W. (2010). Extract residential areas automatically by new built-up index. *2010 18th International Conference on Geoinformatics, Geoinformatics 2010*. https://doi.org/10.1109/GEOINFORMATICS.2010.5567823

Ettehadi Osgouei, P., Kaya, S., Sertel, E. & Alganci, U. (2019). Separating Built-Up Areas from Bare Land in Mediterranean Cities Using Sentinel-2A Imagery. *Remote Sensing*, *11*(3). https://doi.org/10.3390/rs11030345

Rasul, A., Balzter, H., Ibrahim, G. R. F., Hameed, H. M., Wheeler, J., Adamu, B., Ibrahim, S. & Najmaddin, P. M. (2018). Applying Built-Up and Bare-Soil Indices from Landsat 8 to Cities in Dry Climates. *Land*, *7*(3). https://doi.org/10.3390/land7030081

Rouse, J. W. . J., Haas, R. H., Schell, J. A. & Deering, D. W. (1974). Monitoring Vegetation Systems in the Great Plains with Erts. *NASSP*, *351*, 309. https://ui.adsabs.harvard.edu/abs/1974NASSP.351..309R/abstract

Roy, P., Rikimaru, A. & Miyatake, S. (2002). Tropical forest cover density mapping. *Tropical Ecology*, *Vol 43*, 39–47.

Van Deventer, A. P., Ward, A. D., Gowda, P. H. & Lyon, J. G. (1997). *Using Thematic Mapper Data to Identify Contrasting Soil Plains and Tillage Practices*.

Zha, Y., Gao, J. & Ni, S. (2003). Use of normalized difference built-up index in automatically mapping urban areas from TM imagery. *International Journal of Remote Sensing*, *24*(3), 583–594. https://doi.org/10.1080/01431160304987

Zhang, J., Li, P. & Xu, H. (2013). Urban built-up area extraction using combined spectral information and multivariate texture. *International Geoscience and Remote Sensing Symposium (IGARSS)*.

Intercontinental Geoinformation Days

igd.mersin.edu.tr

The availability of local laser technique in forest management planning

Mücahit Emre ORUÇ*[1], İldeniz Leyla ÖZTÜRK [1], Ali ULVİ[1]

[1]*Mersin University, Geomatics Engineer, Mersin, Turkey*

Keywords
Forest management plan
TLS
Point cloud
3D model

ABSTRACT

Studies in forestry in Turkey have great importance between humanity and life. In this direction, many forestry studies are carried out. The purpose of these studies is to protect forest areas and to ensure their continuity. The forestry organization continues to work urgently in line with this purpose. As a result of the researches, it is seen that old methods are lacking in time and cost in the forest management plan and many forestry studies. Nowadays, researches have been made on the use of the old methods, the use of terrestrial laser technology, which is seen as costly but actually offers positive opportunities at a low cost in line with the purpose to be used. In this study, how the methods used in forest management plans can contribute to the forestry sector with terrestrial laser scanning, which is one of today's technologies, and the sensitivity of devices and software that can be used in this direction are scrutinized. The data obtained as a result of the study were compared with the old methods and the usability of the terrestrial laser scanning method was examined.

1. INTRODUCTION

Turkey has rich forest areas where the various types of wood. The importance given to forest areas in Turkey are progressing in the past with today's sustainable and innovation studies. As a result of research conducted in the presence of Turkey Forests, Global Forest Resources Assessment prepared a 5 year (Global Forest Resources Assessment-FRA) in 2020 according to the report; While it rises to 27th place in the world ranking in the forest existence ranking, it is ranked 1st in Europe and 6th in the world among the countries that increase forest existence (URL-2; URL-3). Forest assets in Turkey in the past 18 years, 2.1 million hectares have been increased. Turkey's 2023 target is visionary in forested areas are planned to correspond to 30% of my area of the country. The areal value of this ratio corresponds to approximately 23.4 million hectares (URL1).

Forestry adversely affected to Turkey's contribution to the protection of forest ecosystems is needed in many areas.Forest management; It is a science that investigates how, when and in what criteria forests can be used and how to obtain more efficiency from forests in order to ensure continuity of forests (Kaplan and Şeylan 2007).

Referring to the historical development of forest management in Turkey when there is no regular continuity until 1857. With the reform edict issued in 1856, many studies were carried out in many areas. When these studies were found, it was desired to benefit from forestry movements to contribute to the conditions. In order to ensure the continuity of developments in the field of forestry, schools for educational purposes were opened and the personnel to work in this field were technically trained. Important steps have been taken in the field of forestry by bringing foreign experts from other countries in order to enact the necessary legislation for the implementation of innovations (Eler 2008).

Despite all these steps taken; It is known that there are problems in determining forest boundaries, preserving, managing and transferring current forest assets to future generations and in preparing forest management plans. In this context, studies to be carried out in forest areas are of utmost importance. Today, in parallel with the advancing technological developments in these studies, different and new methods have been used in addition to the classical methods from the past. Among these methods are remote sensing and Geographic Information Systems (GIS), photogrammetry and LIDAR (light detection and ranging / Laser Imaging Detection and Ranging).

* **Corresponding Author**

*(mucahitemre27@gmail.com) ORCID ID 0000-0003-2454-9279
(idenizleylaa@gmail.com) ORCID ID 0000-0003-0598-9316
(aliulvi@mersin.edu.tr) ORCID ID 0000-0003-3005-8011

Cite this study

Oruc M E, Ozturk I L & Ulvi A (2021). The availability of local laser technique in forest management planning. 2nd Intercontinental Geoinformation Days (IGD), 253-256, Mersin, Turkey

The LIDAR method offers high resolution data regardless of the sparse and frequent forest areas. In this context, the study was completed with the terrestrial laser scanner using the LIDAR technology in the study area determined in the study, and the data belonging to the area were obtained precisely and quickly. By processing these data, the usability of the terrestrial laser scanner in forest areas was examined and the results were examined.

1.1. Study Area

As a study area, measurements were carried out in a forested area within the campus of Mersin University.

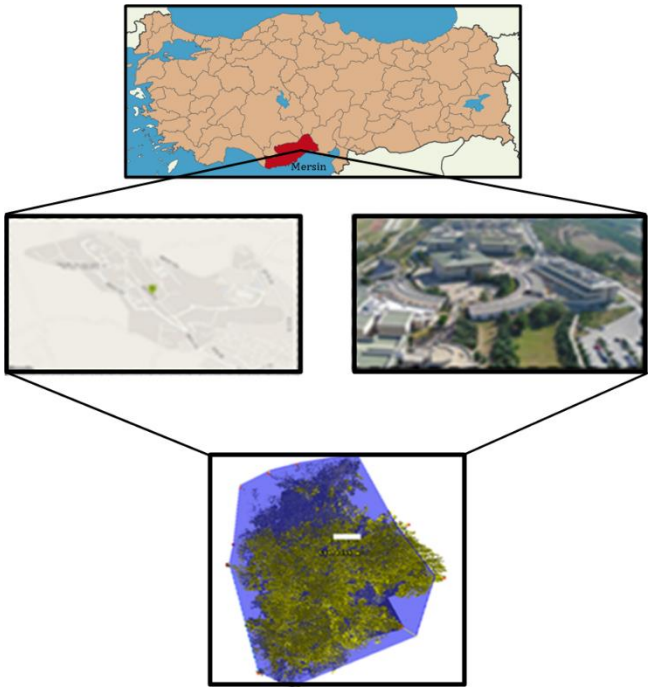

Figure1. Study Area

2. METHOD

The terrestrial laser scanning (YLT) method was used in the study. The distance between the object and the device is measured with the laser beam emitted from the laser scanner device. Thus, the point cloud of the scanning area can be obtained and three (3D) models of the desired object can be produced (Kaya et al. 2021; Çelik et al. 2020;; Kaya and Yiğit et al. 2020; Yiğit and Ulvi 2020; Yakar et al. 2015). The distance between the laser scanning device and the object can be determined by means of the optical source, which is called the laser beam. It has properties (monochromaticity, compatibility, divergence, reflection, density) that distinguish the laser beam from normal light. Thanks to these features, data about the shape and size of real objects can be easily collected and analyzed.
By means of mirrors, also known as laser optical scanning mechanism, the scanning of the object or the surface is performed by directing the laser beam in horizontal and vertical directions. The capacity of a laser scanner to deflect the laser beam in horizontal and vertical directions is given as the viewing angle in the technical information. In order to create a three-dimensional model of an object, it may be necessary to use more than one scanning station with different viewing angles. The result obtained as a result of scanning is a point cloud consisting of millions of points that vary in proportion to the product measuring distance. Information such as point cloud data, location information, density information, RGB value, scan angle, number of reflections, reflection size.

Figure 2. TLS method

In the TLS method, measurement can be performed from one point or several points with the terrestrial laser scanner. Although the measurements made from a single point are very practical, they are not preferred much in practice. Since scanning is performed from only one direction, it is highly possible that complete and healthy data regarding the scanned object cannot be obtained. Therefore, this application is not used except in compulsory cases. Instead, it is scanned from more than one point (Ulvi et al. 2020; Ulvi et al. 2019; Watt and Donoghue 2005;). In this study, scanning was not carried out from a single point, the scans were carried out at more than one station point. Scan data has been processed in point cloud and a variety of commercial and open source software that enables 3D modeling.

2.1. Data Collection and Pre-Processing

The determined working area was realized with the terrestrial laser scanner faro focusS 350 model. A forest area has been chosen as the study area. Testing the applicability of the ylt method played an important role in selecting such a field. As a result of the literature research, it was concluded that there are mainly pine trees in the forests in the Mediterranean region and the trunk length of these trees is long and therefore the tree branches will not prevent scanning. Therefore, the application was carried out in the pine area located in the Mersin University Çiftlikköy campus. The laser scanner was positioned to take the trunk parts of the trees from every angle with frequent sessions, and the measurement process was completed by performing a total of 11 sessions (Figure 3).

The perimeter of the tree trunk was measured from the reference points determined with the help of a rope by marking the reference points at 50, 100, 150 cm heights of the tree trunks and the values were measured with the help of a steel tape measure (Figure 4).

Figure 3. Study area scanning examples

Figure 4. Field Work / reference height applications taken from trees

The necessary data for the processing of the data were obtained by field measurements. FARO SCENE software which is a commercial software and various programs were used in the process of data processing. The scans made by processing the data in the software were combined. The point cloud of the study area was obtained as a result of the merging. A solid model was created through the obtained point cloud. Body circumferences and diameter values of the tree were measured on the 3D model.

Faro Scene software used for data processing has been developed to process scans obtained from all laser scanning devices.

The software offers opportunities such as automatic object recognition of objects found in scans, technical features such as recording and positioning in scans. It was transferred to the software after the scans made.

First, the process operation was applied. At this stage, the process of merging data with cloud to cloud point merging method has been completed. Considering the combined data, a simpler data was obtained by deleting the noise pollution data found in scans other than what was desired. This process is the noise removal process and as a result of the process, it provides the user with the opportunity to obtain a simpler and more usable data. After this stage, solid model (mesh) was created from the generated point cloud.

3. CONCLUSION

In this study, since a forested area was preferred, the point cloud obtained was combined with high resolution and low error, and a point cloud and solid model were obtained. However, it has been determined that a single software is not sufficient for software. On the other hand, since the surface shapes in the study area have various geometric shapes and the leaf regions in the upper parts of the tree are scattered and thin coniferous, a healthy data could not be obtained in the point cloud.

The sensitivity of the laser scanner used in this study was examined by comparing the measurements of the reference points marked on the body parts of the tree with a steel tape measure and the measurements made from the 3D solid model produced from the scans.

With the results obtained, error values were calculated and values very close to the results obtained by local methods were obtained. Since more area can be scanned in a short time in the Ylt method and the volume calculations of the trees will be calculated more easily with the software used, the use of the Ylt method is envisaged.

REFERENCES

Çelik, M. Ö., Hamal, S. N. G., & Yakar, İ. (2020). Yersel Lazer Tarama (Ylt) Yönteminin Kültürel Mirasın Dokümantasyonunda Kullanımı: Alman Çeşmesi Örneği. Türkiye Lidar Dergisi, 2(1), 15-22.

Kaplan, S. Y., & Şaylan,(2007). G. T. D. Yerleşim Alanları Civarındaki Ormanların Yerinden Yönetimi Sorunu (Doctoral dissertation, Ankara Üniversitesi Sosyal Bilimler Enstitüsü Sosyal Çevre Bilimleri Anabilimdalı) Doktora Tezi.

Kaya, Y., Yiğit, A. Y., Ulvi, A., & Yakar, M. (2021). Arkeolojik Alanların Dokümantasyonununda Fotogrametrik Tekniklerinin Doğruluklarının Karşılaştırmalı Analizi: Konya Yunuslar Örneği. Harita Dergisi, 165, 57-72.

Kaya Y & Yiğit, A. Y. (2020). Dijital El Kameraları Kullanılarak Kültürel Mirasın Belgelenmesi. Türkiye Fotogrametri Dergisi, 2(2), 33-38.

Türkiye'de orman amenajman yönetmeliğinin tarihsel gelişimi. Türkiye Ormancılık Dergisi, 9(2), 89-98.

Ulvi, A., Yakar, M., Yiğit, A., & Kaya, Y. (2019). The Use of Photogrammetric Techniques in Documenting Cultural Heritage: The Example of Aksaray Selime Sultan Tomb. Universal Journal Of Engineering Science, 7(3), 64-73.

Ulvi, A., Yakar, M., Yiğit, A. Y., & Kaya, Y. (2020). İHA ve Yersel Fotogrametrik Teknikler Kullanarak Aksaray Kızıl Kilise'nin 3 Boyutlu Nokta Bulutu ve Modelinin Üretilmesi. Geomatik Dergisi, 5(1), 22-30

URL1:https://www.ogm.gov.tr/tr/haberler/turkiye-orman-varligini-artiran-ulkeler-siralamasinda-avrupa-da-1-inci-dunyada-ise-6-sirada

URL2:http://www.fao.org/documents/card/en/c/ca9825en/

URL-3:http://www.gonder.org.tr/?p=9782

Ünal, E. L. E. R. (2008). Türkiye'de orman amenajman yönetmeliğinin tarihsel gelişimi. Türkiye Ormancılık Dergisi, 9(2), 89-98.

Yakar, M., Orhan, O., Ulvi, A., Yiğit, A. Y., & Yüzer, M. M. (2015). Sahip Ata Külliyesi Rölöve Örneği. TMMOB Harita ve Kadastro Mühendisleri Odası, 10.

Yiğit, M. (2016). Orman amenajman planları kullanılarak ormanların zamansal değişiminin incelenmesi: olur şefliği örneği (Master's thesis, Artvin Çoruh Üniversitesi, Fen Bilimleri Enstitüsü).

Yiğit, A. Y., & Ulvi, A. (2020). İHA Fotogrametrisi Tekniği Kullanarak 3B Model Oluşturma: Yakutiye Medresesi Örneği. Türkiye Fotogrametri Dergisi, 2(2), 46-54.

Intercontinental Geoinformation Days

http://igd.mersin.edu.tr/2020/

Monitoring the stability of highway cut slopes utilizing drone photogrammetry

Ufuk KADER[1], Arif Oguz ALTUNEL[*2]

[1]Geomatics Engineer, Municipal Infrastructure Affairs, Kastamonu, Turkey
[2]Kastamonu University, Department of Forest Engineering, Kastamonu, Turkey

Keywords
Drone photogrammetry
Digital surface models
Slope stability

ABSTRACT

Roads have long been an integral asset for civilization. A lot of things have been said, drawn and shown regarding what and what not to do while drafting the routes. No matter how conscientious they are planned and laid out, mishaps occur while placing them on terrain. The demand to tie two points with the shortest possible route, create cut slopes and embankments. They both are bolstered with engineering reinforcements, however the cut slopes, which are always in sight while driving through, gave way in majority of time if those engineering principles are not sufficiently applied. Slope failure occurs when the downward movements of material due to gravity and shear stresses exceeds the shear strength. Therefore, factors exploiting these critical dynamics, increase the chances of slope failures. Six crumbling cut slopes en route to Karabuk from Kastamonu province were investigated in terms of the stability dynamics. Through stereo photogrammetric evaluation, digital surface models, which were sensitive to 0.08 to 0.22 m ground resolutions were constructed. Additionally, soil samples to understand the physical and chemical compositions of the cut slopes were taken from two depths; 0-15 cm and 15-30 cm. Analyses of the models showed that the considerable parts of all of the cut slope areas were graded over 87%, which was the collapse threshold for unprotected or untreated soil surfaces. Lab analyses showed that the binding agents e.g. organic matters, lime, etc. were rather weak because no vegetation to stabilize the already steep cut slopes was present on any of them.

1. INTRODUCTION

Roads are the foremost infrastructural need for the societies to establish secure transportation and commerce. The principle road building approach is to connect two points with the shortest possible route ((Umrao et al. 2015), however, geologic and topographic conditions are not always favorable for this principle to be laid down, flawlessly. In order to draft and materialize a road route, the mentioned difficulties must be eliminated so that a reasonably through right of way is constructed (Gorcelioglu, 2004). Due in fact to the geologic and topographic terrain conditions faced in majority of our country, the routes are planned and constructed over not so ideal ground, thus many cut-slopes and the corresponding embankments have to be devised to finalize the roadbed, effectively. In order to control the slope stability problems resulting from the steep slopes during construction, engineering solutions must be entegrated into the projects (Senturk, 1989). Six such cut slopes, which have long been eroding especially during wet seasons, were investigated to determine the underlying reasons trigerring the mass movements year after year. Drone photogrammetry was used to efficiently model the slopes along with the soil analses for composition and physical characteristics.

2. STUDY AREA

Six cut slopes varying in size on Kastamonu-Karabük intercity road were investigated for slope failure in this study.

* **Corresponding Author**

(ufukkader@outlook.com) ORCID ID 0000-0002-8020-0031
*(aoaltunel@kastamonu.edu.tr) ORCID ID 0000-0003-2597-5587

Cite this study

Kader U & Altunel A O (2021). Monitoring the stability of highway cut slopes utilizing drone photogrammetry. 2nd Intercontinental Geoinformation Days (IGD), 257-259, Mersin, Turkey

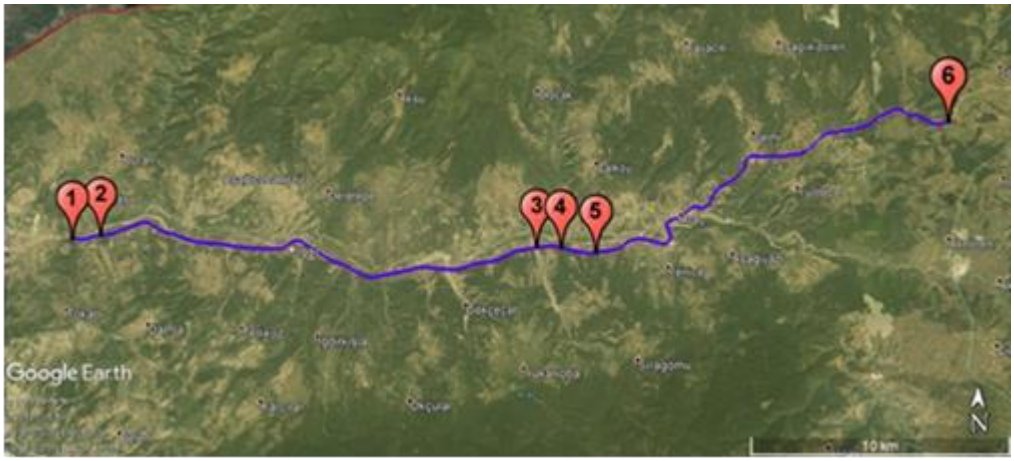

Figure 1. Studied cut slope locations on the intercity road en route to Kastamonu from Karabuk

3. METHODOLOGY

Each cut slope was individually flied over utilizing a preprogrammed drone, DJI Phantom 3 Professional, to model the surface(s), meticulously. Simultaneously, soil samples were collected from the upper undisturbed edges of the slope areas. The samples were taken from two depths, 0-15 cm and 15-30 cm to analyze the physical and chemical compositions of the slope surfaces. In majority of the studies conducted to assess the slope stability, the term, factor of safety, (FS), is rather important in better understanding and definition (Duncan et al. 2014). When FS is explained in terms of the slope gradient intervals; "stable", "critical range" and "fail certain", can be grouped as followed: < 87%, 87% < x < 148% and 148% < , respectively (Zakaria et al. 2018) (Figure 2).

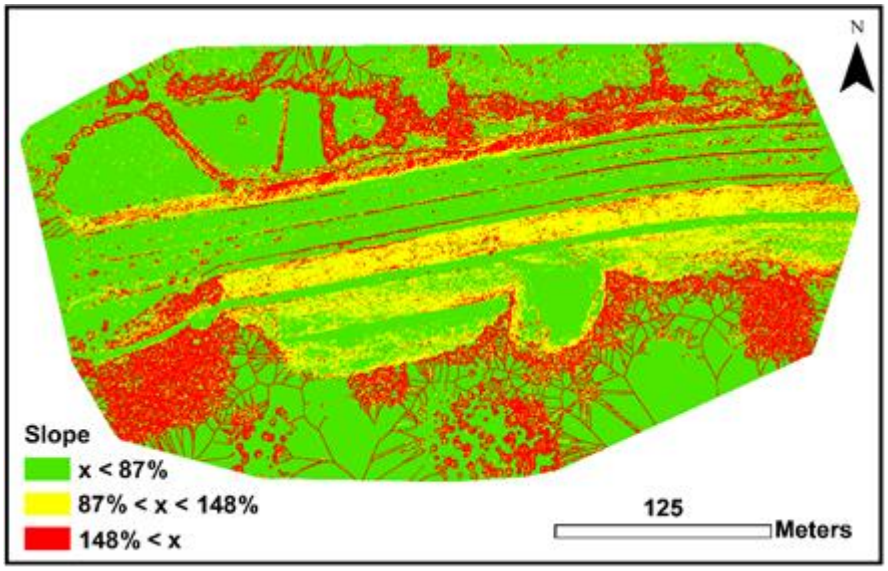

Figure 2. Site 2 slope classification resulting from 0.09 m DSM

4. RESULTS

Six digital surface models (DSM) with relatively high spatial resolutions; 0.22 m for site 1, 0.09 m for site 2, 0.08 m for site 3, 0.1 m for site 4, 0.14 m for site 5 and 0.15 m for site 6, were constructed for slope classification analyses. Slope classes were generated as a function of the vertical elevation gain/loss within a given horizontal distance, thus each slope area was dissected according to the slope classes specified above, and the acreages were calculated, accordingly (Table 1).

As clearly visible and suspected from the visual observations, the cut slopes were unfortunately not constructed to stay stable in the long run. The acreage amounts regarding the "critical" and "fail certain" slope classes were obviously less than the ones aggregated in "stable" slope class in all cut slope surfaces, however, we all know how erosion which might innocently start in a rather small part of a catchment, could trigger large mass movements when the favorable conditions materialize. When the acreages were compared percentagewise, stable parts vs. unstable parts, the results were nowhere near innocent. The worst was in site 6 in which exactly one third of the entire slope area was on the unstable slope classes. The least affected one still amounting almost one fifth of the entire slope area on the unstable slope classes was site 5. It was not clear from the results of this study that the very existence of these dangerous slope classes was initially there or were gradually developed due in fact from the relentless

atmospheric effects hammering on the bare slope surfaces. However, if this conclusion was the result of the imperviousness during the construction or unavoidable circumstances due to some other constrains e. g. the need to remove more vegetation beyond the upper reaches of the slopes to lengthen the slope surfaces, and the excessive amount of surface stripping needed to compensate the steepness, the current situation in the studied cut slopes or in many others alike has not been good in terms of the functions assigned to them in the first place.

Soil analyses conducted on all of the cut slope surface areas showed that clay heavy two investigated depths lacked rather less binding agents, organic matter and lime. The vegetation removed during the grading left the slope surfaces vulnerable to precipitation. The already weak organic matter formed under the coniferous stands was quickly washed away when the slope surfaces were prepared, terraced or graded. Generally, sponge like this top coat on soil surfaces limited the surface runoff better dissipating the water. The same organic matter on unstable slopes, on the other hand, was quickly ravaged by the same water.

Table 1. Cut slope surface area classifications based on the "stable", "critical" and "fail certain" slope percentages

	Site 1 classification	Site 2 classification	Site 3 classification
Slope (%)	Acreage (m^2)	Acreage (m^2)	Acreage (m^2)
x < 87	214144.72	86265.87	53830.06
87 < x <148	21279.15	8250.08	4822.65
148 < x	37574.47	9693.67	7132.64
Total area (m^2)	272998	104210	65785
	Site 4 classification	Site 5 classification	Site 6 classification
Slope %	Acreage (m^2)	Acreage (m^2)	Acreage (m^2)
x < 87	61416.33	119506.33	70197.90
87 < x <148	6707.54	8687.10	7343.13
148 < x	11507.16	13875.62	15692.90
Total area (m^2)	79631	142069	93234

5. DISCUSSION and CONCLUSION

When the cut slopes were left to stand on their own, they were mostly furnished with engineering reinforcements to keep them from crumbling if the gradients were steeper than the proven safe. However, these have been rather expensive protective measures, which have been overlooked frequently. When either the cut slopes or the embankments were left untreated, they would eventually erode jeopardizing the lifespan of the main infrastructure that they had actually been erected to protect. Whenever vegetation was removed on flat or inclined surfaces, erosion has become a problem varying in severity depending on the steepness. Six cut slopes investigated in this study were just manifesting the types of such adversities. The soil eroding from the slope surfaces was overflowing the retaining walls installed at the slopes' bottom heels. Although furnished with some terracing, they were all on bare soil without any protective measure. Such slopes must first be seeded immediately after construction to form a perennial shrub cover with long root systems. A balanced mix of deciduous and coniferous tree species must also be planted to bolster the protection in the long run. Drones have been very powerful and practical in purpose build such case studies. The precision they provided, was only surpassed by light detection and ranging (LIDAR). For periodic status monitoring, there is no better priced alternative to drone remote sensing today. All considered, the cut slopes and embankments must be built with the utmost attention they deserve because there are means to capture the misdeed, flawlessly.

REFERENCES

Duncan, J. M., Wright, S.G., & Brandon, T.L. (2014). Soil Strength and Slope Stability. 2nd edition. John Wilet and Sons, Inc. 333 s.

Gorcelioglu, E., (2004). Orman Yolları-Erozyon İlişkileri, İ.Ü. Orman Fakültesi yayınları, İ.Ü. Y. No: 4460, O.F. Y. No: 476, İstanbul.

Senturk, N. (1989). Yol inşaatında Zemin Etüdlerinin Önemi, Or. Müh. Dergisi, Yıl 26, Sayı II, s. 26-29, Ankara.

Umrao, R. V., Singh, R., & Singh, T. N. (2015). Stability evaluation of hill cut slopes along national highway-13 near Hospet, Karnataka, India. Georisk: Assessment and Management of Risk for Engineered Systems and Geohazards, 9(3), 158-170.

Zakaria, Z., Sophian, I., Sabila, Z. S. & Jihadi, L. H., (2018). Slope Safety Factor and Its Relationship with Angle of Slope Gradient to Support Landslide Mitigation at Jatinangor Education Area, Sumedang, West Java, Indonesia. IOP Conf. Series: Earth and Environmetal Sciences 145: 012052.

Intercontinental Geoinformation Days

igd.mersin.edu.tr

Using drone mapping to analyze risky areas and predict LULC at Sichang Island, Chonburi province, Thailand

Suwatcharapong Surasanpreedee[*1,2,3] **Kitsanai Charoenjit**[*1] **Zhenfeng Shao**[*2]

[1]*Burapha University, Geoinformatics, Chonburi, Thailand*
[2]*Wuhan University, State Key Laboratory of Information Engineering in Surveying, Mapping and Remote Sensing, Wuhan, China*
[3]*Geo-Informatics and Space Technology Development Agency, SCGI: Sirindhorn Center for Geo-Informatic, Chonburi, Thailand*

Keywords
UAV
Remote sensing
LULC
Risky area
CA-MAKOV model

ABSTRACT

Thailand is a country located in Southeast Asia, the Thai government wants to become the economic leader of ASEAN, so there is an economic development plan named EEC (Eastern Economic Corridor), a megaproject with a huge investment but the Thai government is focusing only on the mainland. The researchers determined that there is still an area that is more outstanding than other islands (Gulf of Thailand), Sichang Island, located in Chonburi Province, has sufficient potential for development. This research study the knowledge of Geoinformatics, remote sensing, and aerial imagery from the drone are used to conduct research, to determine the potential of the development of the Sichang Island area. These include finding risky areas on the island and predicting future LULC in the next 10 years by using aerial imagery from drones as a base. The results were obtained, there is a village in the community in highly risky area (flood and land-slides combined) 2.865 % of Sichang area, and the prediction of the future LULC is the continuous expansion of urban-build up area 9.348%.

1. INTRODUCTION

The Thai government established a mega project called the Eastern Economic Corridor (EEC) with 3 model provinces, Chachoengsao. Chon Buri and Rayong provinces, with only focus on the mainland but still has an important island called “Sichang” in the area of Chonburi Province and is also a district in Chonburi Province as well. These island that is unique in culture, tradition and tourism. Therefore, in response to the government's policy of driving the economy in this region, it is appropriate to prepare the information of digital geographic information system of Sichang Island but the spatial area study is small-scale (only around 6.5 square kilometers). If using satellite images (free data) such as Landsat or Sentinel, the resolution is not enough. If we use very high-resolution satellite imagery, then there will be many budgets of buying satellite imagery data. For this reason, with this solution. It is advisable to use an unmanned aerial vehicle (UAV) or drone to capture aerial imagery because the drone has the advantage such as it helps to save budget and time. Drone is currently able to capture images. We can choose the time period to flying. Current drone price not expensive and getting cheaper according to the advancement of technology. Nowadays drone is becoming more popular equipment in geo-informatics system.

Research objectives:

1. Assessing the location of natural disaster risk areas (complex, landslides, floods) in Sichang Island, Chon Buri province, Thailand
2. Predict LULC for next 10 years in Sichang Island, Chon Buri province, Thailand

In this study, Map of Sichang Island, which is located in the coordinates 13 ° 38 ′ 59″ N - 100 ° 48 ′30 E, was produced. Given in Fig 1.

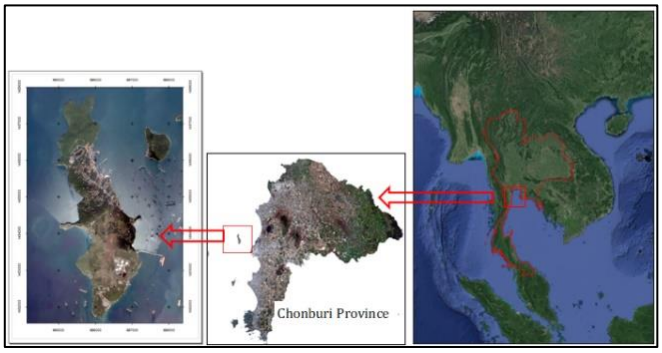

Figure 1. Location Map

2. METHOD

This thesis has 5 conceptual frameworks which are (1) area study (2) data collection (3) data processing (4)

* **Corresponding Author**

*(62910174@go.buu.ac.th) ORCID ID 0000 – 0003 – 0689 – 2284
(kitsanai@go.buu.ac.th) ORCID ID 0000 – 0003 – 4290 – 6778
(shaozhenfeng@whu.edu.cn) ORCID ID 0000 – 0003 – 4587 – 6826

Cite this study

Surasanpreedee S, Charoenjit K & Shao Z (2021). Using drone mapping to analyze risky areas and predict LULC at Sichang Island, Chonburi province, Thailand. 2nd Intercontinental Geoinformation Days (IGD), 260-263, Mersin, Turkey

data analysis and (5) conclusion. The most difficult step is step (2). After we choose the area study, Sichang Island. The data collection on Sichang is done by UAV or drones. Flying for capture many images, taking full 1 day for total area of the island, different from other thesis, that use satellite imagery which is much easier, just download the information from some website in a short time. But this method takes the advantage in steps 3 and 4, are easier than other methods because the images from drone have very height resolution, allowing for easier processing and analysis and are more accurate result. There are two processes in step 4, the process of finding risky areas on Sichang Island and the process of predicting LULC in the next 10 years on Sichang Island.

Table 1. Data sources.

Sensor	Date	Resolution	Source
Drone	2019/09/01	7 cm.	Drone DJI Phantom4.
Ortho RGB aerial photo	1999, 2009	50 cm.	Royal Thai Survey Department
Landsat 8 OLI	2019/09/28	30 m.	https://earthexplorer.usgs.gov/

2.1. Data collection step

Drone data: The researcher used Drone DJI-Phantom 4 to capture aerial images of whole Sichang Island area, flying at altitude 200 meters from the ground. The image, with a resolution of about 7cm., flew drone on October 1, 2019, taking 1 day to collect all areas in the Island. the steps are as follows: (1) Select a drone "DJI Phantom 4" (2) Select Application DJI Go 4, made a connection between I-Pad (or smart phone) and Drone for basic control (3) For flying Drone to mapping, we use the automatic PIX-4D Mapper application to make it, set the height to 200 meters. (4) When planning to fly, must not fly against the direction of the wind, because the area is an Island in the middle of the sea, when flying high, there is a chance that strong wind, is the reason for lose battery power and reduced working time of the drone.

Ortho RGB aerial photography at Sichang Island: Data Raster (spatial resolution 50 cm, 3 Bands) Year 2009 from Royal Thai Survey Department.

Other information: are used to make decisions in the Sichang Island risk areas table (AHP)(Jin-Yu, Zhong-bin, & Qing-yun, 2008), such as include Rainfall data, slope, soil type (capacity of water flowing through the soil), distance from the reservoir, and geological data.

2.2. Data processing

Drone data: take aerial photos from the drone to mosaic via application "PIX 4D Mapper" which will get the base map for this research. This step is most important, after the drone has finished taking aerial photos, many data is stored on the SD card of the drone, moving the data to computer, and then using PIX 4D Mapper to manage (mosaic) all photos, there are 3 steps: (1) rayclouds (2) volumes (3) mosaic editor. In this step, we will get a mosaic image of Sichang Island. After that, resample the image resolution (7 centimeters) to 1 meter in order to facilitate the calculation of the computer. and clip the area by only real Sichang boundary. (obtained the shapefile boundary from the digitizing drone image)

Ortho RGB aerial photography at Sichang Island, Resample the image resolution from 50 centimeters to 1 meter (Must have the same size and number of pixels as the Drone image) because it is a requirement to calculate the area of future changes via CA-MAKOV model. Create a new shape file by digitizing, based on drone image. Identify by visually because resolution 1 meters can already be seen clearly.

Data for make decisions AHP, DEM calculations, slope calculations, distance of water sources can be found on drone data. NDVI values used data from Landsat satellite image. Other information can be found on the Thailand government agencies website such as Land Development Department, Meteorological Department. and then resample resolution to 1 meter again.

2.3. Data analysis

2.3.1. Assessing the location of natural disaster risk areas (landslides, floods)

Manipulate in Arc-GIS program**.** Calculate two types of risk value, which are flood and landslide. After getting results from both types of risk areas map, then combine them together to find complex risk areas again.

Risky areas (flood), the data used include elevation, slope, soil type (capacity of water flowing through the soil), distance from the reservoir, and geological data.

Risky areas (land slide), the data used include Rainfall data, slope, soil type (capacity of water flowing through the soil), distance from the reservoir, and geological data. Prove C.R. value < 0.1 Therefore, the consistency of comparison is within acceptable values. (Flood = 0.084, Land slide = 0.030). Take the boundary of Sichang Island (obtained from the digitize image from the drone) to clip with all data layers, so every layer is same size. Make all 7 layers of data into raster data and assign values 1,3,5 (Risk level height = 5, medium = 3, low = 1), in this step, we will see the color difference shown in each data layer. After that just reclassify to only 3 types. Layers of information are combined with Arc GIS to create risk maps area. Use the previously calculated Eigenvector as the weight for each criterion (multiply). Use the map algebra function in Arc GIS to manage risk mapping, selected spatial analysis tools >map algebra >raster calculator. After getting the risk map (land slide and flood), bring both of them to the combined risk area map. By using 1:1 weighting. Use the map algebra function in Arc GIS again. In the final step, you will get a combined risk map. The equation used to calculate the risk area:

Flood risk area = 0.131x (Elevation) + 0.205x (slope angle) +0.320 x (drainage) + 0.131x (land use) + 0.047x (Lithology) + 0.120x (distance from the reservoir) + 0.045x(NDVI)

Landslide risk area = 0.256x (Precipitation) + 0.194x (slope angle) +0.255 x (drainage) + 0.136x (land use) + 0.042x (Lithology) + 0.060x (distance from the reservoir) + 0.057x(NDVI)

Complex risk areas = 0.5x (landslide prone areas) + 0.5x (flood-prone areas)

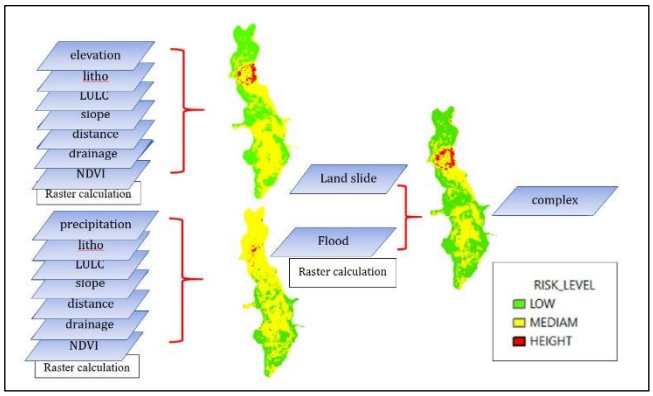

Figure 2. The process of creating risk area map, land slide, flood, complex

2.3.2. Predict land use land cover for next 10 years

High-resolution image from the drone (resemble to 1 meter) as a base to classify (by digitize) Sichang LULC area into 4 types (no agriculture area on Sichang Island) which are (1) forest area (2) miscellaneous area (3) urban and buildup (4) water body. Classify by visual identification. For my proposal the file type is img. We can exactly identify LULC types by visually because the Sichang Island map (resolution 1 meters) can already be seen very clearly. Another benefit of using very high-resolution images from the drone is the ability to know the details until the object type is well identified. Such as the width of the road or drain gutters on the side of the road etc.

Use Ortho RGB aerial photography at Sichang Island (resemble 1 meter) as a base to classify (by digitizing) the Sichang area into 4 types. Sorting types must be the same as for drone classification. The file is img. type. Identify LULC types by visually. Next Step of digitizing Sichang LULC from Drone image or Ortho RGB image. Add data (1) Sichang map layers from drone and Ortho RGB(Royal Thai Survey Department) (2) shapefile boundary from the digitizing drone image. Begin with the digitizing urban-build up area, which consists of urban areas, buildings, roads, alleys, docks etc. Digitizing water body area, which consisting of reservoir, pond etc. Digitizing forest area, which consisting of forest, brake, group of trees, shrubs etc. Union urban and buildup, water, forest area together, check every area not overlap by intersect method. Perform by geoprocessing. Do not allow any overlapping areas because this will negatively affect the conversion of polygon to raster files. Shapefile boundary from the digitizing drone image, use this shapefile erase the union area from union Forest, Urban-build up, Water body area, the output is miscellaneous area. Union forest, miscellaneous, urban and buildup, water area together. Do not allow any overlapping areas. Before converting the file to raster. Must be ordered in the attribute table strictly. The adjustment is edit feature> start editing> open attribute table> set value 1 2 3 4 for Forest miscellaneous urban water respectively. Converse polygon to raster. Last step is check that the sequence of LULC types is as needed. (1=forest, 2 = miscellaneous, 3 = urban buildup, 4 = water body)

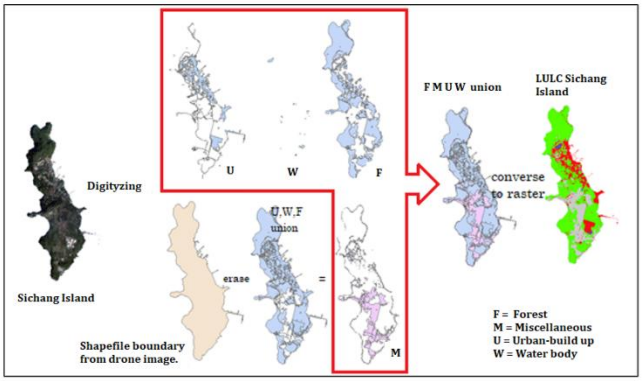

Figure 3. Sequencing process for digitizing LULC.

Make both images (Year 2009, 2019) have the same area and number of pixels, same columns and lows value, image resolution (at 1 meter) and in the same type of classification (1) Forest (2) Miscellaneous area (3) urban areas (4) Water body and must be arranged in sequence. (every file must be img.file). Export 2 file .img about LULC Sichang Island map (year 2009 2019) to new folder and set the name's folder. For the next step, we will work entirely on this folder only, set value extent raster dataset and spatial reference = size (original), cell size = 1,1 no data = 5, format = IMAGIN image (.img file)

IDRISI: MAKOV Chain step. Example predict Year 2029 (used base map on year 2009 compere year 2019) Use the IDRISI program to calculate future LULC area changes. The first step is to create a new folder, separated into working folders. Converse .img file to .rst file Import image by Geotiff/tiff (depend on ArcGIS version) or .img file. This proposal is .img file. Open new .rst file that got from the value of the previously obtained map in ArcGIS for check value, for 2 images (2009, 2019) must be in equal every class and same area and same resolution. Reclassify both map at 4 type again. (in ArcGIS). Set the Label value to an integer only. (in ArcGIS)

Return to IDRISI again. Run MAKOV Chain. Selected a base image as 2009(Ortho RGB aerial photography) compared to 2019 (image from the drone). Defines the gap of both years, 10 years and set the predicted year as the future for the next 10 years. Do not select maps from browsing button. The maps that we use must only come from the same folder we created, otherwise the IDRISI program will not calculate, all operations will be in the same folder. When we finished this MAKOV step. We get conditional probability map, transition area matrix, transition probability matrix. Class number 1 2 3 4 means Forest(F), Miscellaneous(M), Urban and Built-up(U), Water body(W) chronologically number.

IDRISI: Run program CA-Markov Model at Modeling> Environmental/Simulation Models >Time Series > CA_MARKOV.(Eastman, 2003) Selected a base map 2009 (image from the drone) compared 2 part. Use The transition area, conditional probability map that is a result from Markov chain step. Select cellular automata filter type standard 5x5 contiguity filter. The time used in calculations depends on the number of cellular automata interaction, we will get the LULC map of Sichang Island in the future for the next 10 years (dividing land use into 4 types). Export any file, file format, .img or .tiff

Check the accuracy of the prediction map by the map year 1999 compared with 2009, to predict the 2019

map. It's mean we have to generate LULC year 1999 again. The results are compared with the actual map data obtained from drone. The Drone and Ortho RGB aerial photo, result accuracy is 93.61% The satellite images Landsat 5, result accuracy is 62.68% (before use raster calculation, must resample resolution to 1 meter).

3. RESULTS

3.1. Complex risky area maps.

Complex risk maps (Integrated landslide and flood risk) have a low-risk area with a total area of 3.436 square kilometers. medium-risk with a total area of 2.648 square kilometers, high risk with a total area of 0.1795 square kilometers (2.865 %), shown in the figure 4.

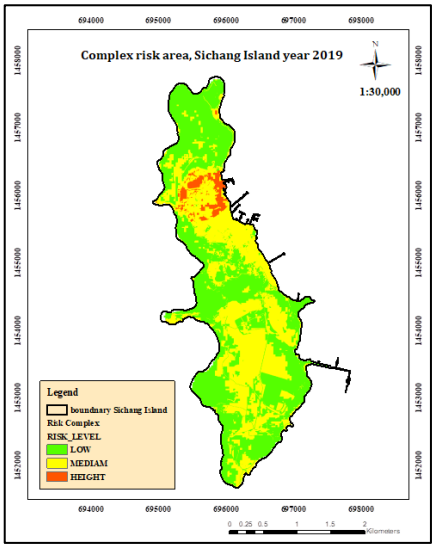

Figure 4. Complex risk area map.

3.2. Predict of changes in LULC next 10 years

Predict year 2029 of changes in LULC of Sichang Island during year 2009 and year 2019, This table describes changes LULC area. The unit is square meters, from what has changed to what, what is still the same, example is Urban-build up area from year 2019(Note the horizontal space in the letter U, number is 1,075,934 m^2) to year 2029(Notice the vertical position in the letter U, number is 1,176,780) increase 100,846 m^2. Forest and Miscellaneous area become Urban-build up area 67,7256 and 33,262 m^2, not change and still urban area 1,075,793 m^2 and change to water body area 141 m^2, results as follows:

Table 2. Transition area matrix.

Year	2029				
2019	F	M	U	W	Total(m^2)
F	3,770,646	64507	67,7256	2,056	3,904,934
M	107,654	1,264,744	33,262	1,013	1,406,673
U	0	0	1,075,793	141	1,075,934
W	0	0	0	36,685	36,685
Total	3,878,300	1,329,252	1,176,780	39,894	6,424,226

4. DISCUSSION

This research used aerial imagery from a drone is basically, divided into 2 parts, the first part is calculated for the risky area, the second part predicts the LULC for the next 10 years, which is relative with the 10-year economic development plan of Thailand as well. Using the CA-MAKOV model theory calculations(White, Engelen, & Uljee, 1997), past photographs map must be compared, an aerial photograph of 50 centimeters, Ortho RGB resolution. (researchers requesting support from the Royal Thai Survey Department). For the first time, the researcher used data from Landsat 5 satellite, which has a resolution of 30 meters, when calculating the error value was too large, so when we had the drone images, if we wanted to predict the LULC with CA-MAKOV model, the entire map image must same resolutions map. This is because the Si Chang Island area is approximately 6.5 km^2, with very little space compared to other studies, so flying drones to build a database is the right answer.

5. CONCLUSION

Complex risk maps (Integrated landslide and flood risk) have high risky area 2.9%. Which has a community area in this risky area with a total of 1 village. The Thai government agency at Sichang Island should prepare plans to accommodate future disaster situations.

LULC predictions for the next 10 years can be concluded that there is a slight decline in forest areas, less miscellaneous areas, more urban and construction areas, constant water supply areas, indicating that there is an enlargement of the city. The government should use the budget to support the construction of roads and public utilities to support the increasing number of tourists, transport and goods, environmental protection, planning to eliminate waste caused by tourists, etc.

ACKNOWLEDGEMENT

I would like to thanks Dr. Zhenfeng Shao, supervised this research. This work is supported by the National Key Research and Development Program of China with grant number 2018YFB2100501, the Key Research and Development Program of Yunnan province in China with grant number 2018IB023, the National Natural Science Foundation of China with grant numbers 42090012, 41771452, 41771454, and would like to thanks Dr. Kitsanai Charoenjit, co-advisor that provides technical support our Drone (DJI Phantom4).

REFERENCES

Eastman, J. R. (2003). IDRISI Kilimanjaro tutorial. *Manual Version, 14*, 61-123.

Jin-Yu, G., Zhong-bin, E. Z., & Qing-yun, S. N. (2008). Study and applications of analytic hierarchy process [J]. *China Safety Science Journal (CSSJ), 5*, 026.

White, R., Engelen, G., & Uljee, I. (1997). The use of constrained cellular automata for high-resolution modelling of urban land-use dynamics. *Environment and Planning B: Planning and Design, 24*(3), 323-343.

MERSİN UNIVERSITY

IGD
Intercontinental Geoinformation Days

ISBN: 978-625-44303-2-9 | http://igd.mersin.edu.tr/2020/